J. Astrophys. Astr. (2001) 22, 1–8

GMRT Detection of HI 21 cm-line Absorption from the Peculiar Galaxy in Abell 2125

K. S. Dwarakanath[1] * & F. N. Owen[2] †
[1]*Raman Research Institute, Bangalore 560 080, India*
[2]*National Radio Astronomy Observatory, Socorro, NM 87801, USA*

Received 2000 October 27; accepted 2001 February 05.

Abstract. Using the recently completed Giant Meterwave Radio Telescope, we have detected the HI 21 cm-line absorption from the peculiar galaxy C153 in the galaxy cluster Abell 2125. The HI absorption is at a redshift of 0.2533, with a peak optical depth of 0.36. The full width at half minimum of the absorption line is 100 km s^{-1}. The estimated column density of atomic Hydrogen is $0.7\times10^{22}(T_s/100)$ cm^{-2}. The HI absorption is redshifted by $\sim$ 400 km s^{-1} compared to the [OIII] emission line from this system. We attribute this to an infalling cold gas, or to an out-flowing ionised gas, or to a combination of both as a consequence of tidal interactions of C153 with either a cluster galaxy or the cluster potential.

Key words: Galaxies: active — galaxies: clusters: individual (A2125) — galaxies: star-burst — radio lines: galaxies.

1. Introduction

Abell 2125 is a rich cluster of galaxies (Abell Class 4) at a redshift of 0.246. Recently detailed optical and radio studies of this cluster were published (Dwarakanath & Owen 1999, Owen *et al* 1999). These studies have detected 27 radio galaxies in this cluster above a 20 cm luminosity limit of 1.4×10^{22} W Hz^{-1} (H_o = 75 km s^{-1} Mpc^{-1}, q_o = 0.1). In projection, these radio galaxies extend over $\sim$ 5 Mpc along a band running from the northeast to the southwest of the cluster center. About half of these galaxies show signs of star formation, with the largest concentration of them in the southwest clump $\sim$ 2 Mpc in projection from the cluster center. There is a bimodal distribution of the 27 cluster members in radio luminosity, with the majority below a spectral luminosity at 20 cm of 10^{23} W Hz^{-1}. Star formation is primarily responsible for the radio emission of these galaxies. Rest of the members

*e-mail: dwaraka@rri.res.in
†e-mail: fowen@nrao.edu

with a spectral luminosity above this value owe most of their radio emission to an AGN activity in them.

In Fig. 1 a radio image of the central region of the cluster is reproduced from Dwarakanath & Owen (1999). All the sources in this figure are cluster members. The brightest source in this figure (C153) has a peak flux density of 23.2 mJy/beam and is within 30″ ($\sim$ 100 kpc) in projection from the cluster core. This is the second brightest radio source in the cluster with a 20 cm spectral luminosity of 3.3×10^{24} W Hz^{-1}. Most of this radio emission arises in the core of this galaxy. The core is essentially unresolved at a resolution of $\sim 1.8''$. However, faint extended radio emission can be seen towards northwest and southeast directions. This galaxy has a ratio of [NII] to H_α consistent with an AGN (Owen *et al.* 1999). But, the value of the continuum break around 4000 Å(D(4000)), and the value of B–R (color) are very small and consistent with star formation as well as AGN activity. The star formation rates implied by the H_α and O[II] lines are consistent with each other but are a factor of 50 too small to account for the observed radio emission (Owen *et al.* 1999). This discrepancy can arise either because the star formation rates are under-estimated due to dust in C153, or most of the radio emission from C153 is due to an AGN activity. In comparison with the blue luminosities and colors of other cluster members where the star formation rates estimated by the optical lines and the radio continuum agree, it is apparent that dust obscuration is unlikely to be significant in C153. Most of the radio emission from C153 must therefore be due to an AGN activity at its center.

Since there is star formation and AGN activity in C153, we might expect to detect some of the cold gas feeding the AGN. Such a cold gas could be in a torus close to the nucleus. Alternatively, we might expect to detect the HI in the interstellar medium of the host galaxy. Such a system with multiple HI absorption components was indeed detected in Hydra A (Dwarakanath, Owen & van Gorkom 1995). Infall velocities of HI absorption components up to 400 km s^{-1} have been detected in radio elliptical galaxies (van Gorkom *et al.* 1989, van der Hulst *et al.* 1983, Shostak *et al.* 1983). This in-falling HI gas has been attributed to cold gas loosing its angular momentum due to frictional drag on it by the pressure supported hot gas in the ellipticals. Interactions and mergers are quite common in cluster galaxies (Lavery & Henry 1994, Dressler *et al.*1994, Couch *et al.* 1994, Wirth, Koo & Kron 1994). Such interactions can lead to disturbed morphologies and chaotic velocity fields of the interacting galaxies. In-flow and/or out-flow of ionised and/or atomic gas is expected from such galaxies. It is interesting to explore if C153 displays any such phenomena.

2. GMRT Observations

The Giant Meterwave Radio Telescope (GMRT) located at Khodad near Pune in India, is an aperture synthesis instrument consisting of 30 fully steerable parabolic dishes of 45 m diameter. Six antennas are distributed along each of the three arms

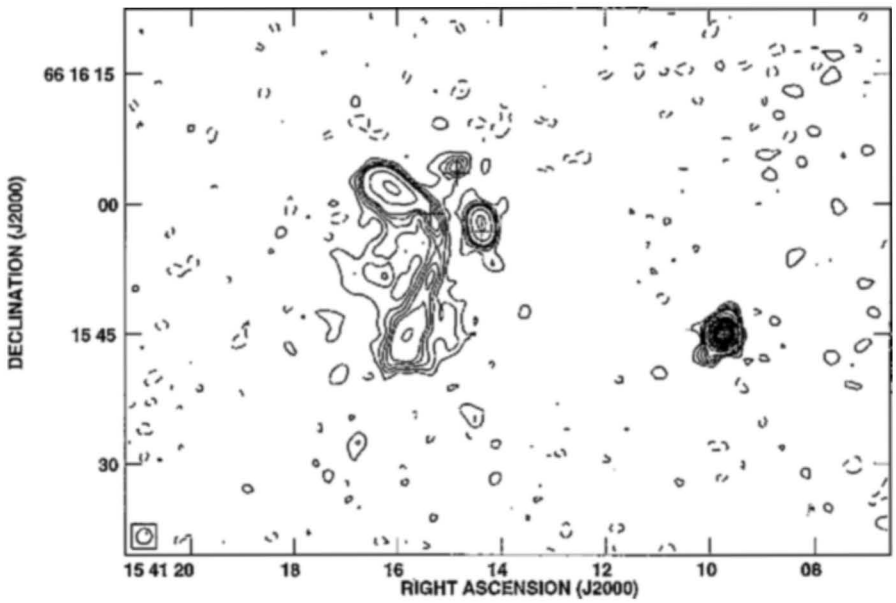

Figure 1. Radio image of the center of Abell 2125. This is a 20 cm image made with the VLA in its A configuration with a resolution $\sim 1.8''$. The crosses mark the positions of optical identifications. The brightest source in this figure (C153) has a peak continuum surface brightness of 23.2 mJy/beam and is within $\sim$ 100 kpc (in projection) from the cluster core. This source shows signs of star formation although it is an AGN. The rms in this image is $\sim$ 30 μJy/beam. The contours are in steps of 60 μJy/beam from –120 to 300 μJy/beam (excluding 0), in steps of 0.6 mJy/beam from 0.6 to 3 mJy/beam, in steps of 1.5 mJy/beam from 4.5 to 15 mJy/beam, and in steps of 3 mJy/beam from 18 to 30 mJy/beam. The synthesised beam is at the bottom left corner.

of a rough Y and the remaining 12 antennas are more or less randomly placed in a compact cluster near the center of the Y. The center of the Y, called the "Central Square" has a minimum baseline of $\sim$ 100 m and a maximum baseline of $\sim$ 1 km. The maximum baseline of the GMRT array is $\sim$ 25 km (Swarup *et al.* 1991). Currently the antennas have dual polarised feeds at 5 frequencies viz., 150, 230, 327, 610, and 1420 MHz. The 1420 MHz feed is a broad-band corrugated horn covering the frequency range of 900–1450 MHz continuously. The full width at half maximum of the primary beams of the GMRT dishes at 20 cm is $\sim 25'$.

For the current observations the antennas were pointed at α(J2000) = $15^h41^m09^s$ and δ(J2000) = $66^o15'44''$. The backend used was a 30 station FX correlator which produces 128 spectral channels across the chosen baseband bandwidth. Any band-

width which is $2^n \times$ 62.5 KHz with n taking integer values between 0 and 8 can be chosen. In the present observations, a bandwidth of 8 MHz centered at 1134 MHz was used. This 8 MHz band covered a velocity range of $\sim$ 2000 km s^{-1} at the redshift of 0.2526 of C153. The corresponding velocity resolution is $\sim$ 15.7 km s^{-1}. Although most of the 30 antennas were included in the observations, the total number of antennas that were used in the final analysis was 14 with a maximum baseline of $\sim$ 2.5 km. The integration time on the source was $\sim$ 4 Hr. Gain and bandpass calibrations were carried out by observing the VLA calibrator 1634+627 once an hour. The absolute flux densities were estimated by observing 1331+305 (3C 286).

The raw data from the telescope was converted to FITS format and analysed using the Astronomical Image Processing System (AIPS – developed by the National Radio Astronomy Observatory). The channels from the flat portion of the spectrum and which were free from line absorption were used to estimate the continuum visibilities. Spectral-line visibilities in each of the spectral channels were obtained by subtracting the estimated continuum contribution from the observed visibilities. A continuum image and a spectral cube were made using AIPS. The synthesised beam was $36'' \times 22''$ at a position angle of -22^o. The r.m.s. value in the spectral cube was 1.5 mJy/beam/channel, close to the expected value. The spectral cube was featureless except for the absorption line in the galaxy C153. The spectral cube was Hanning smoothed with a resulting r.m.s. of 0.9 mJy/beam/channel. The spectrum towards C153 from this cube is displayed in Fig. 2. The velocity resolution in this spectrum is $\sim$ 32 km s^{-1}.

The HI absorption line is at a redshift of 0.2533, or, at a systemic velocity of 66550 km s^{-1}. The best-fit Gaussian gives a full width at half minimum of 100 km s^{-1}. The peak optical depth is 0.36 and the corresponding HI column density is 0.7 $\times$ $10^{22}(T_s/100)$ cm^{-2}. The corresponding HI mass in a sphere of radius 1 kpc is $\sim 10^8 M_\odot$.

3. Discussion

The most interesting aspect of the HI absorption in C153 is that it is redshifted by $\sim$ 400 km s^{-1} w.r.t. the velocity of the [OIII] emission line, but is within $\sim$60 km s^{-1} of the H_α and [OII] emission lines (Owen, under preparation). The errors in the redshift estimates based on the optical lines are expected to be $\sim$60 km s^{-1} making the velocity difference between the HI absorption line and the [OIII] emission line significant. The [OII] and the [OIII] line emission appear to come from a more extended, disturbed region than the HI absorption and the Hα emission lines. There can be different scenarios accounting for the observed differences in the velocities and in the spatial extents of different lines. There can be an outflow of [OIII] emitting gas while the HI absorption, the Hα, and the [OII] lines are at rest w.r.t. the galaxy, or there can be an in-fall of the gas seen in HI absorption, Hα, and [OII] lines while the [OIII] emitting gas is at rest, or there can be a combination of

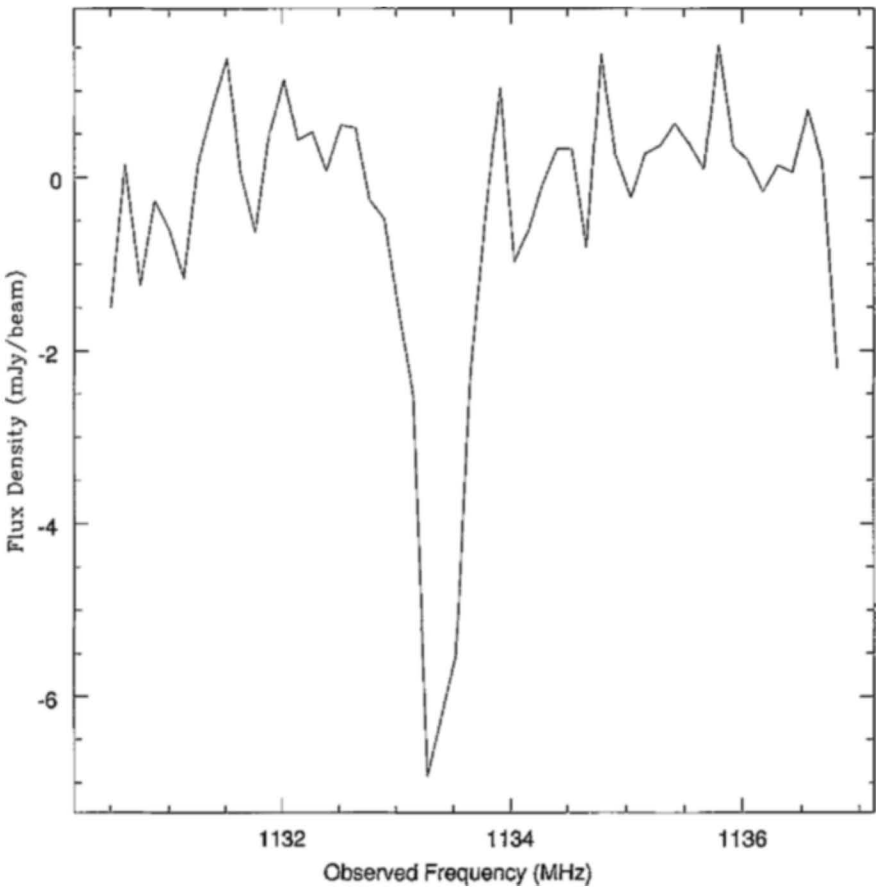

Figure 2. The HI 21 cm-line absorption in C153 obtained using the GMRT. The zero on the y-axis corresponds to the peak continuum surface brightness of C153 of 24.1±1.5 mJy/beam and is in excellent agreement with 23.2±0.075 mJy/beam estimated from earlier VLA observations (Dwarakanath & Owen 1999). The spectrum was obtained at α(J2000) = $15^h41^m09.83^s$, and δ(J2000) = $66^o15'44.1''$. The original spectrum was Hanning smoothed and alternate channels plotted to obtain the spectrum shown here with a velocity resolution of $\sim$ 32 km s^{-1}. The peak absorption has an optical depth of 0.36 and corresponds to a redshift of 0.2533. The [OIII] emission line from this system is blue shifted w.r.t. the HI absorption line by $\sim$ 400 km s^{-1}.

these two situations. Any model that attempts to explain the current observations should also account for the width, and the HI column density of the absorption line. We consider the following physical models and discuss their plausibilities in the context of the current observations : (a) a gas torus close to the AGN, (b) the interstellar medium of the host galaxy, (c) an interacting, intervening cluster galaxy, and (d) tidal interactions with the cluster potential.

If the HI absorption is due to a gas torus surrounding the AGN, both the width, and the column density of the HI line can be explained. A rotating gas torus of dimensions comparable to the linear size of the central radio continuum source can easily account for the observed width of the HI absorption line. While the linear size of the radio continuum source is unknown, it is expected to be less than 1 kpc based on the earlier observations with the VLA (Dwarakanath & Owen 1999). For e.g., a gas torus of HI density $\sim$ 20 cm^{-3}, and of extent $\sim$ 100 pc with a circular velocity $\sim$ 250 km s^{-1} surrounding a radio continuum source of comparable extent can account for the observed width and column density of the HI absorption line. The HI absorption will be essentially at rest w.r.t. the AGN since there is no systematic motion involved other than the circular motion of the torus. The Hα emission could come from ionised part of the torus. However, the spatially extended [OII] and [OIII] emission must have a different origin. Thus, a gas torus has a limited scope in explaining the current observations.

If the HI absorption is due to the interstellar medium of the host galaxy, then, for an assumed spin temperature of 100 K, the total column density of HI in the line is comparable to the integrated HI column density along the line of sight at low galactic latitudes ($|b| < 5°$) in the Galaxy (Dickey & Lockman 1990). This similarity in the column densities indicates that the HI absorption in C153 could also be due to the line of sight gas in its galaxy. However, the observed HI column density requires a near edge-on alignment of the disk of the galaxy to our line of sight which has a rather small probability. In addition, since the circular motion of the disk-gas is not expected to have any significant component of velocity along the line of sight, the HI absorption is expected at a velocity not too far from the systemic velocity. It is possible to account for some inward velocities by gravitational in-fall of the cold HI gas due to loss of angular momentum. This loss of angular momentum is due to the frictional drag on the cold gas by the surrounding hot gas (Gunn 1979). This model has been adapted by van Gorkom *et al.*(1989) to account for the HI in-fall velocities observed in radio ellipticals. In their adaptation of this model, they assume spherical cold clouds moving in circular orbits through pressure supported hot gas. These clouds experience a frictional drag and acquire radial in-fall velocities. Geometrical consistency demands that the radial velocity be not more than $1/(2\pi)$ times the circular velocity. While small HI in-fall velocities $\sim$ 50 km s^{-1} observed in some radio ellipticals can be explained by this model, larger HI in-fall velocities observed by them in these ellipticals must have a different origin. Note that there is one example (viz., NGC 315) of an HI absorption redshifted by $\sim$ 400 km s^{-1} w.r.t. the systemic velocity (Shostak *et al* 1983). In this case, the column density is 4.6×10^{20} cm^{-2} and the line width is < 5 km s^{-1}. These values are typical of interstellar clouds in the Galaxy. In the case of NGC315 one is witnessing a single cloud along the line of sight which is presumably in a state of free-fall to its center. However, in the present case, the HI column density is 15 times larger, and the line is 20 times wider. This cold gas presumably has a different origin. Even if we assume that the HI absorption is at rest w.r.t. the galaxy (C153), thus alleviating the difficulties in accounting for its

large in-fall velocities, the requirement of near edge-on alignment of the galaxy to our line of sight to account for the observed HI column density makes this model less probable.

Absorption due to an intervening cluster galaxy alleviates the difficulties encountered in the two scenarios mentioned earlier. Galaxies in clusters are known to undergo interactions, and mergers. If a dwarf galaxy of HI mass $\sim 10^8$ $M_\odot$, and of size a few kpc is interacting, and falling into C153, it can explain the current observations. The in-fall velocity of the dwarf will be at least as much as the escape velocity from C153. The escape velocities from galaxies can be greater, or, of $\sim$400 km s^{-1}. Such an in-falling dwarf can easily explain the observed redshift of the HI absorption line, if we attribute the observed velocity difference between the HI absorption and [OIII] emission to an in-falling cold HI gas. The width of the HI absorption line simply results from the rotation of the dwarf. Given a sufficient size for this dwarf of a few kpc, its alignment with the AGN need not be as critical as in the earlier scenario (case (b)) to give rise to the HI absorption. A consequence of such an interaction is a disturbed morphology of the galaxies. Indeed, C153 shows a disturbed morphology as seen in the HST images. In addition, such an interaction can pull off gas from the outer regions of galaxies due to tidal interactions, and cause an outflow of gas. This can also account for the observed difference in the velocities of HI absorption and [OIII] emission lines. However, there is one drawback in this picture. The galaxy C153 is within $\sim$ 100 kpc in projection from the cluster core. If C153 is indeed close to the cluster core, i.e., no projection effects, then a dwarf galaxy in-fall into C153 is less likely in the core of a high velocity dispersion ($\sim$900 km s^{-1}) cluster like Abell 2125. This drawback is less serious if C153 were to be in the outer regions of the cluster.

If C153 is not in the outskirts of the cluster but is indeed close to the core then we can advance the following alternative scenario. The observed galaxy density distribution in Abell 2125 and its X-ray intensity distribution obtained from ROSAT PSPC observations are very similar (Owen *et al.* 1999). The galaxy C153 is within $\sim$ 100 kpc from the peaks of these two distributions. Since C153 has a velocity $\sim$ 1500 km s^{-1} w.r.t. the cluster mean and is in the dense core of the cluster, both tidal stripping and ram-pressure stripping are expected to be very effective. Recent simulations show that stripped gas quite often falls back onto the galaxy (Barnes & Hernquist 1998, and references therein). In such a situation, redshifted HI absorption from the in-falling cold gas is expected. Alternatively, the stripping can lead to an outflow of gas which is seen in the lines of [OIII] emission. Thus, this model can account for both in-falling cold gas and out-flowing ionised gas. A consequence of tidal stripping and ram-pressure stripping is a disturbed morphology of C153 which is seen in its HST images. Future VLBA images in radio continuum and in the 21 cm-line of HI as well as imaging in the optical emission lines could throw more light on the nature of this source.

Acknowledgements

The Giant Meterwave Radio Telescope is the result of dedicated efforts of a large number of people at the National Center for Radio Astrophysics, Pune and at the GMRT site, Khodad. N.V.G. Sarma and his team at the Raman Research Institute, Bangalore were responsible for designing and building the broad-band 21 cm feeds and receivers for the GMRT. We thank Rajaram Nityananda and K. R. Anantharamaiah for stimulating discussions and useful comments on the paper.

References

Barnes, J. E., Hernquist, L., 1998, *Astrophys. J.*, **495**, 187.
Couch, W. J., Ellis, R. S., Sharples, R. M., Smail, I., 1994, *Astrophys. J.*, **430**, 121.
Dickey, J. M., Lockman, F. J., 1990, *Ann. Rev. Astron. Astrophys.*, **28**, 215.
Dressler, A., Oemler, A. Jr., Butcher, H. R., Gunn, J. E., 1994, *Astrophys. J.*, **430**, 107.
Dwarakanath, K. S., Owen, F. N., van Gorkom, J. H., 1995, *Astrophys. J. Lett.*, **442**, L1.
Dwarakanath, K. S., Owen, F. N., 1999, *Astron. J.*, **118**, 625.
van Gorkom, J. H., Knapp, G. R., Ekers, R. D., Ekers, D. D., Laing, R. A., Polk, K. S., 1989, *Astron. J.*, **97**, 708.
Gunn, J. E. 1979, In *Active Galactic Nuclei*, edited by C. Hazard and S. Mitton (Cambridge University, Cambridge), p 213.
van der Hulst, J. M., Golisch, W. F., Haschick, A. D., 1983, *Astrophys. J. Lett.*, **264**, L37.
Lavery, R. J., Henry, J. P., 1994, *Astrophys. J.*, **426**, 524.
Owen, F. N., Ledlow, M. J., Keel, W. C., Morrison, G. E., 1999, *Astron. J.*, **118**, 633.
Shostak, G. S., van Gorkom, J. H., Ekers, R. D., Sanders, R. H., Goss, W. M., Cornwell, T. J., 1983, *Astron. Astrophys.*, **119**, L3.
Swarup, G., Ananthakrishnan, S., Kapahi, V. K., Rao, A. P., Subrahmanya, C. R., Kulkarni, V. K., 1991, *Curr. Sci.*, **60**, 95.
Wirth, G. D., Koo, D. C., Kron, R. G., 1994, *Astrophys. J. Lett.*, **435**, L105.

J. Astrophys. Astr. (2001) 22, 9–20

Observation of Ultra Low Hard X-ray Flux from Cyg X-1 – A Possible Partial Occultation of the X-ray Source

R. K. Manchanda *

Tata Institute of Fundamental Research, Colaba, Mumbai - 400 005, India

Received 2000 June 1; accepted 2000 September 5.

Abstract. The black hole candidate Cyg X-1 was observed in ultra low state on March 30, 1997 using Large Area Scintillation counter Experiment (LASE) in the hard X-ray energy region of 20–180 keV. During the 30 minute exposure a combined signal of 68 sigma was obtained, however, the measured flux at 50 keV was lower by a factor of 2 than the minimum flux reported so far. Using the recent orbital ephemeris of the source, our snap-shot observations were made at $\phi_{5.6} = 0.915$, which corresponds to the binary minimum revealed by the ASM light curves. The daily average data from the BATSE detectors give the source intensity level to be higher by a factor of 5. Very low flux values measured in the present experiment suggest that the hard X-ray source may have been partially occulted by the primary companion during its transit near the X-ray minimum.

Key words: Accretion, accretion disks – X-rays: stars – black hole candidate: individual– Cyg X-1.

1. Introduction

Cyg X-1 is the brightest X-ray binary source in the hard X-ray and soft gamma ray energy region to date, and is the best candidate for stellar mass black holes. In spite of extensive studies during the last 35 years, the X-ray source still remains enigmatic. Apart from the 5.6^d binary orbital period (Dolan *et al.* 1979), the source also exhibits a 294^d periodicity (Manchanda 1983, Priedhorsky *et al.* 1983, Kemp *et al.* 1983, Kemp *et al.* 1987). Intensity variability down to millisec time scales, and chaotic rapid variations have been observed from the source. Spectral variability in hard X-rays on time scales of minutes has been reported in the literature (Tanaka & Lewin 1995 and references therein).

The source shows two distinct spectral states, 'X-ray low' and 'X-ray high',

*e-mail:ravi@tifr.res.in

depending on the low energy flux below 10 keV and the power law index changes from 1.5 to $\sim 3-4$ between the two states. During its low state, the X-ray spectrum is dominated by photons up to several hundred keV. However, the HEAO-C observations during September 1979 to July 1980 revealed the presence of a 'super-low' state in which both the soft X-ray and hard X-ray flux dropped simultaneously (Ling *et al.* 1983). Three distinct intensity levels namely 'X-ray low' (γ_1), 'X-ray high' (γ_2) and 'X-ray very high' (γ_3), have been suggested on the basis of the power density spectrum analysis (PDS) of the source intensity and the strength of the quasi-periodic oscillations (Tanaka 1989; van der Klis 1995). Cyg X-1 went through an extended low luminosity level (γ_0) in 1994 during which the 45–140 keV flux decreased to almost 25% of the normal X-ray high state value (Ling *et al.* 1997). Discrete intensity states for source is a simplified description for deriving the model parameters, the BATSE light curve of the daily averaged intensity suggests a continuous luminosity variation of the source.

The binary period of 5.6^d for the source has been established from the optical observations and the X-ray sinusoidal binary light curve has been recently observed from the RXTE data (Pooley *et al.* 1999). No clear dip due to the eclipsing by the primary companion has been seen either in the optical data or the soft X-ray light curve. Cygnus X-1 is also one of the most variable high energy source, and no systematic spectral studies at high energies with its binary phase have been made so far. The model fitting for the broad band X-ray spectrum of the source itself has been a matter of great debate. While the low energy components are modeled with galactic absorption for a black body input spectrum with a K_α fluorescence emission line due to Iron at 6.7 keV, high energy continuum has been fitted both with Comptonized power law, addition of a reflection component and two component Comptonized spectra (Chitnis *et al.* 1998).

The snap-shot X-ray spectrum obtained during the present experiment is much steeper than the canonical power index $\alpha \sim 2$, suggestive of the 'mid' or 'low' state. The total luminosity of the source was also found to be lower by a factor of about 2 compared to the measurements even during the super low state. Since the present observations correspond to the minimum in binary light curve as seen in the ASM phase data, and the daily averaged intensity of the source in the 45–150 keV energy band on the day of our observation was by a factor of 5 higher (BATSE archival data), the present observations suggest a partial eclipsing of the hard X-ray emission region of the source near the minimum phase. The source spectrum has a peculiar knee-shaped profile and we discuss the physical conditions, which can lead to this behaviour.

2. Experimental details

The observations were made with a Large Area Scintillation counter Experiment (LASE) which is designed to study fast variations in the flux of X-ray sources in the hard X-ray energy region up to 200 keV. The payload consists of three large area

X-ray detector modules mounted on a servo-controlled platform. The detectors are a specially designed combination of thin and thick large area NaI(Tl) scintillation counters configured in back-to-back geometry. Each of the detector modules has a geometrical area of 400 cm^2 and the thickness of the prime detector is 3mm. The active anti-coincidence shield is provided by a 30 mm thick crystal. The field of view of each module is $4.5^o \times 4.5^o$ and is defined by demountable mechanical slat collimator specially designed with a sandwiched material of lead, tin and copper. Each module along with the collimator is further encased with a passive shield. Each detector is designed as a stand-alone unit with independent on-board subsystems for HV power and data processing. LASE payload is fully automatic with an on-board star tracker and requires no ground control during the flight. The detector modules have 100% detection efficiency in the operative energy region and the back-to-back configuration gives 80% reduction in the detector background. The details of the detector design, associated electronics, control sub-systems and the in-flight behaviour of the instrument are presented elsewhere (D'Silva *et al.* 1998). The response matrix of each detector was constructed from the pre flight calibration of the detectors at different X-ray line energies using a variety of radioactive sources Am^{241} (24.7 keV and 59.6 keV), Ba^{133} (32.4 keV and 81 keV), Cd^{109} (22.1 keV and 97.5 keV). To calibrate the high energy end of chosen energy range, we used highly accurate 'divide by two' attenuators in the detector outputs and observed the 300 keV and 357 keV lines from Ba^{133}. In addition, an Am^{241} source is mounted on the payload for periodic calibration of the payload by command during the flight. Accepted events from various detectors are pulse height analyzed and time tagged with 25 μsec resolution and are transmitted to the ground on a 40 kbit PCM/FM link. The 3σ sensitivity of the LASE telescope in the entire energy range up to 180 keV is $\sim 1.5 \times 10^{-6} cm^{-2} s^{-1} keV^{-1}$ for a source observation of 10^4 sec.

The balloon flight was launched on 30 March 1997 from Hyderabad, India (cut-off rigidity 16.8 GV) and reached a ceiling altitude of 3.3 mbs. A number of X-ray sources Her X-1, GR 1744-28, GS 1843+00, GRS 1905+105, Cyg X-1 and Cyg X-3 were observed during the experiment. Cyg X-1 was in the field of view of the two detectors for a total period of 30 minutes during 0530 to 0600 UT. The background was derived from two observations of a blank field before and after the source pointing. The present observation of the source corresponds to MJD 50536.07.

3. Results and Discussion

The counting rate profile from the two detectors during the source observation is shown in Fig. 1. The data are plotted as the total counts in the entire energy band versus bin number ($\sim$ 30sec) for each detector. The top panel gives the azimuthal information about the source acquisition and the tracking during the observation. The source observation interval is marked by the arrows. It is clearly seen from

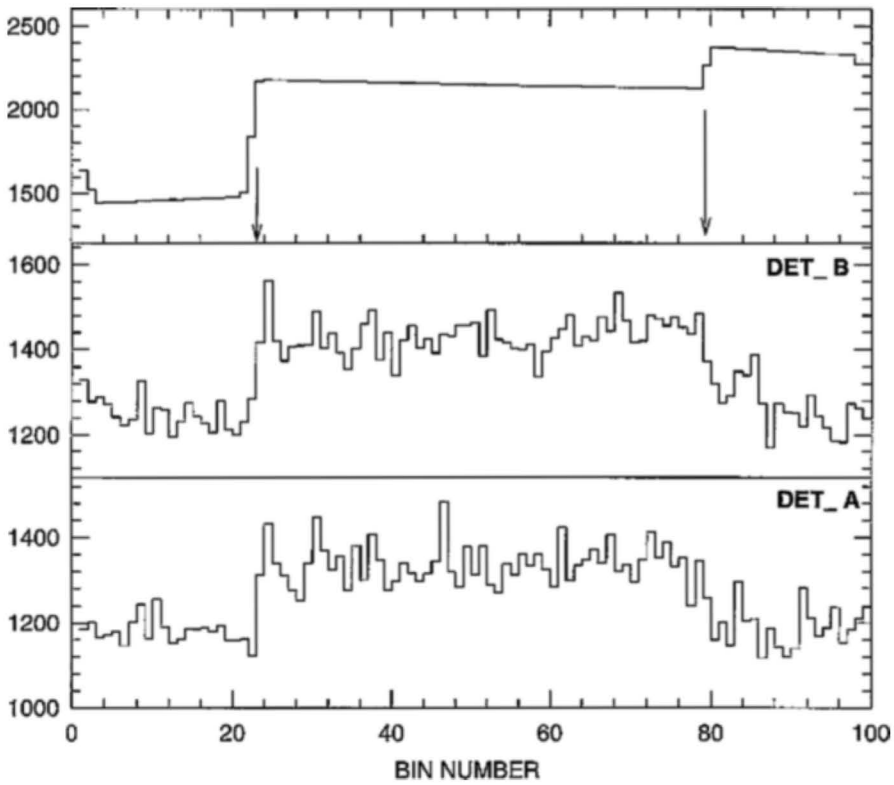

Figure 1. The counting rate profile of the two detectors during the observation of Cyg X-1. The top panel gives the target tracking and is marked by arrows. The bin size is $\sim$ 30 sec. Y-axis gives the integral counts for the detectors and azimuth shaft-encoder value for the upper panel.

the figure that the observed counting rate registered a significant increase as soon as the detectors acquired the target and an excess of $\sim$ 6 ct. s^{-1} was recorded due to the source. A total excess of 11070 and 12750 counts was obtained in each of the two detectors and corresponds to a combined statistical significance of 68σ in the 20–180keV energy band. The source contribution was divided in 16 energy bins and corrected for the atmospheric absorption of 3.3 mbs corresponding to the float altitude, window transmission, detection efficiency and the energy resolution of each detector. An additional correction of 10% due to the systematic effects was applied to data below 26 keV.

The combined deconvolved hard X-ray spectrum of the source is shown in Fig. 2. The observed spectra of the source obtained during 'X-ray low/hard' (γ_1), 'X-ray high/soft' (γ_2) and super low state (γ_0) are also plotted in the figure for comparison. The high state spectrum is taken from the HEXTE data on board RXTE satellite

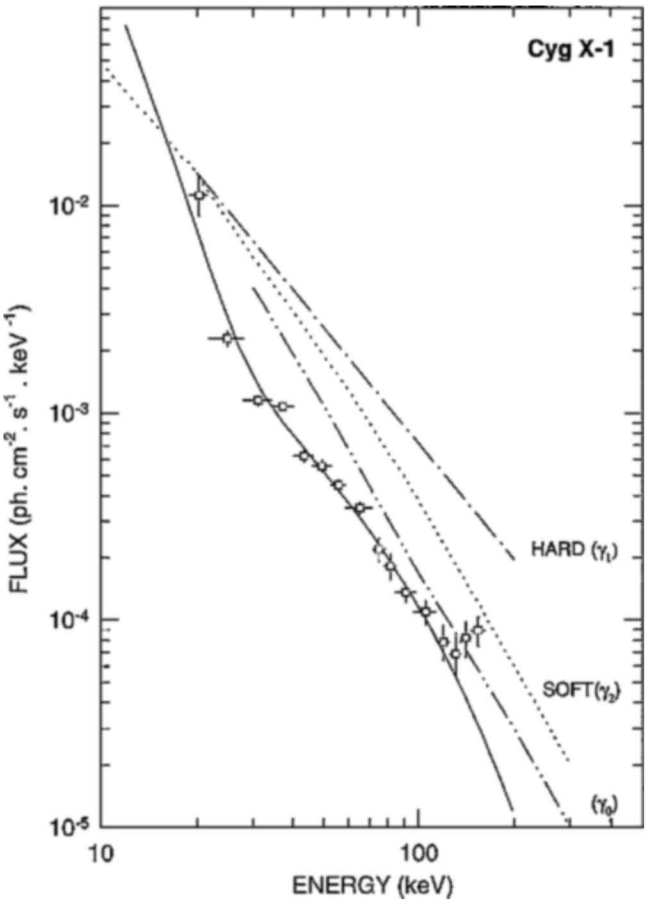

Figure 2. Hard X-ray spectrum of Cyg X-1. 'X-ray high/soft', 'X-ray low/hard' and super low state spectra are shown for comparison. Solid line represents a two temperature thermal fit.

(Cui *et al.* 1998). The low state spectrum (Ubertini *et al.* 1991, Ling *et al.* 1997) and super low state data corresponds to Ling *et al.*(1997) and Phlips *et al.* (1996). It is seen from the figure that the present data show a peculiar knee-shaped spectral profile and is quite different from the observations made so far. It is interesting to note that the low energy point compares well with the other data while the data above 30 keV are a factor of ~5-7 lower than the high state spectrum and a factor of 2 lower than the super low state. In order to further establish that the observed features in the spectrum of Cyg X-1 are genuine and that there was no other unknown systematic effect, we have plotted the observed spectrum of Cyg X-3 in Fig. 3, which was tracked after Cyg X-1. The data of Rao *et al.* (1991) obtained using a xenon filled proportional counter telescope are also shown for comparison. It is

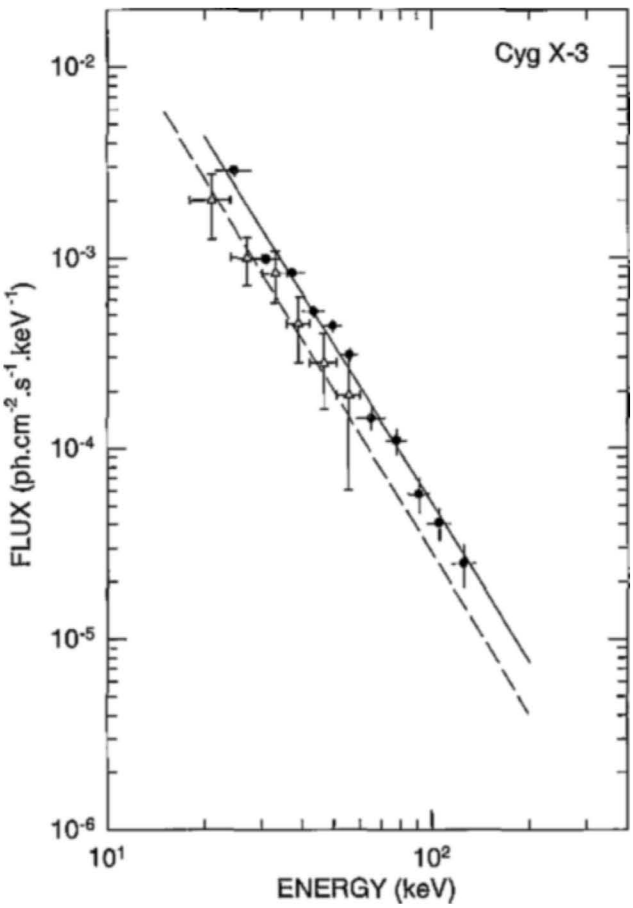

Figure 3. Hard X-ray spectra of Cyg X-3. The data of Rao *et al.* (1991) are shown for comparison (△). The dotted line gives the best fit spectrum (11.3 $E^{-2.8}$) by the authors.

clear from Fig. 3 that both data agree completely both in magnitude and in the spectral shape. This comparison clearly supports the reliability of data presented in Fig. 2.

It is seen from Fig. 2, that the entire data can not be fitted to a simple mathematical function either with a single power law of the form $\frac{dN}{dE} = K\ E^{-\alpha}$ ph. cm^{-2} s^{-1} keV^{-1} or a thermal spectrum of the type $\frac{A}{E}.e^{-E/kT}$. However above 40 keV the data can be reasonably represented by either of the two forms. The best fit model parameters for a 'forced fit' with single power law are $K = 1.8 \pm 0.2 \times 10^{-1}$ and $\alpha = 1.95 \pm 0.2$ for $\chi^2 \sim 2.3$ per degree of freedom thereby suggesting a composite fit. The spectral index of 1.95 ± 0.2 compares well with that of 'X-ray low' state value of ~ 2.1 (Ubertini *et. al.* 1991, Ling *et al.* (1997) and is not surprising as the source was observed to be in the X-ray low/hard state since October 1996

(RXTE archival data). Similarly, a simple exponential function with a kT≈35 keV can be fitted to the data above 40 keV with a poor χ^2 value and the temperature compares well with the value of kT=36±6 keV reported by Ubertini *et al.* (1991). No acceptable fit to the entire data was found even for a composite two component spectrum. A combined mathematical function with two temperatures fitted to the data is shown in Fig. 2 for illustration. The composite fit parameter values are $A_1 \sim 12$ kT~3.54 keV, $A_2 \sim 7.3 \times 10^{-2}$ and kT value of 52 keV for a χ^2 value of 4.7. Similarly the best attempt with two component power law fit to the data corresponded to spectral indices of $\alpha_1 = 1.76 \pm 0.06$ and $\alpha_2 = 2.76 \pm 0.1$ and with the roll over energy $E_r \sim 26 \pm 2$ keV. The estimated luminosity of the source in the 20–200 band at the time of present observations is 2×10^{36} ergs/sec, assuming a source distance of 10 kpc.

In order to pinpoint the cause of disparity between the present measurements and the earlier data and its possible relation to its binary nature, we have plotted the binary light curve of Cyg X-1 in Fig. 3. The data shown in the lower panel are taken from Pooley *et al.* (1999) who have made a comparative study of orbital modulation in the X-ray and radio bands. The top panel corresponds to the phasogram computed from the BATSE daily average intensity of the source along with the present observation. For computing the 5.6^d phase, we have used the spectroscopic ephemeris of P=$5^d.599847 \pm 0^d.000018$ and T=JD 2441874.703 ±0.009 (Brocksopp *et al.* 1999). It is seen from Fig. 4, that the epoch of our observation $\phi_{5^d.6} = 0.91$ does correlate to the minimum in the ASM light curve. Since the daily average intensity of the source obtained from the BATSE data does not show any large variation during the binary cycle of present observation and the average flux is higher by a factor of 5, we conclude that there may be a partial eclipsing of the hard X-ray emission region around the source. As discussed later, the knee-shaped spectral profile in the hard X-ray region is consistent with this conclusion. This feature might have been missed in the past experiments due to long integration intervals used to derive hard X-ray spectra because of the low sensitivity of the detector systems. High sensitivity of the present instrument allows snap-shot spectra of the bright X-ray sources with high statistical significance.

The wide band X-ray spectrum of Cygnus X-1 in the energy range 2–500 keV is very complex and requires multiple functions to fit the different sub-sets of the data and gives an acceptable value of χ^2. Cui *et al.* (1997) have fitted the high state spectrum with a black body, broken power law and a high energy cut-off, while Chitnis *et al.* (1998) obtained the best χ^2 value with the addition of reflection component and an ad hoc edge at 7.76keV. In these models the black-body component with kT~ 0.3 keV accounts for 35% of the observed flux in the 2–10keV band. A variety of physical models for black hole candidate X-ray sources describing the dynamical and thermodynamical properties of mass accretion like advection dominated accretion flow, Comptonization due to bulk motion, super Keplarian boundary layers and sub Keplarian mass flow, on to the compact objects have been discussed in literature (Narayan & Yi 1994; Titarchuk 1994; Chakrabarti & Titarchuk 1995). In the case of Cyg X-1, the X-ray photons are believed to orig-

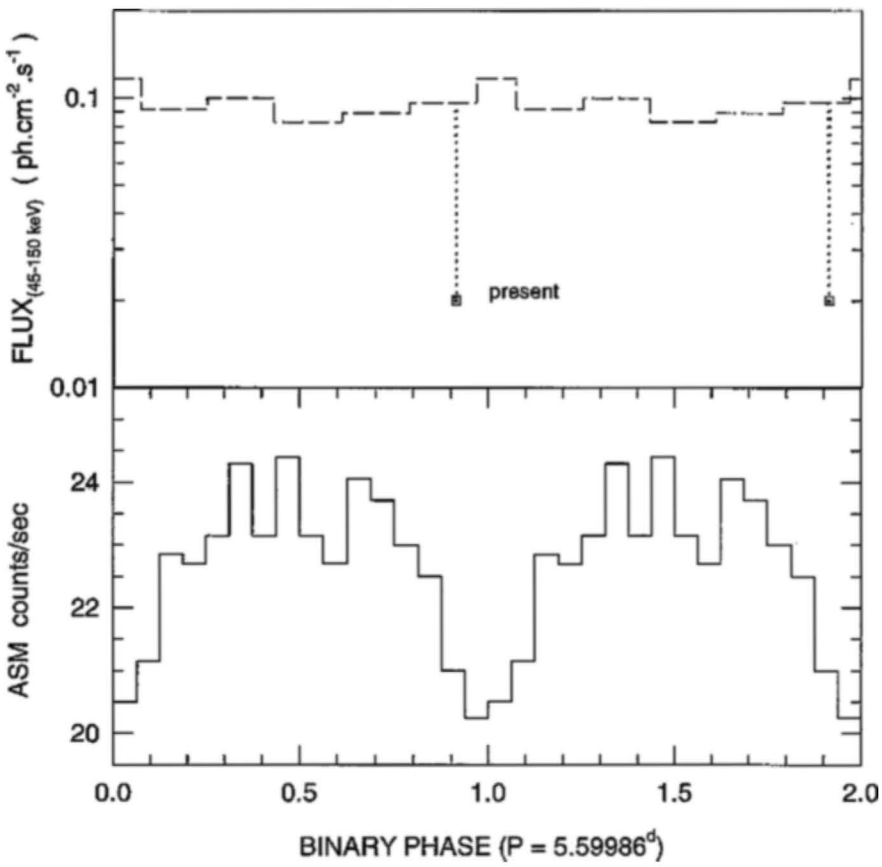

Figure 4. Binary phase histogram for Cyg X-1. See text for details

inate in two different sites. The low energy photons below 10 keV are emitted in optically thick accretion disk, while the hard X-ray photons originate in the Inverse Compton scattering process of the low energy photons in the hot corona around the X-ray object (Sunyaev & Titarchuk 1980, Liang & Nolan 1984). In order to fit the X-ray high/soft (γ_2) state, a two temperature concentric spherical geometry is adopted for the corona models, in which the photons between 25 and 300keV originate in the outer corona and the inner core contributes photons between 25 keV and 2 MeV (Skibo & Dermer 1995; Ling *et al.* 1997).

In a hot plasma, multiple scattering will control the energy exchange between electron and photon only if the plasma is very tenuous, since the bremstrahlung and recombination losses are $\propto \rho^2$ and Thompson scattering goes as $\propto \rho$; where ρ is the number density. If $4kT_e > h\nu$, the seed photons will be upgraded in energy. Even for a Maxwellian distribution of electrons with $kT_e \ll m_e c^2$, the energy shift during each collision is given by $\frac{\nu'}{\nu} \sim 1 + \frac{4}{3}[\gamma^2 - 1]$. Therefore, multiple

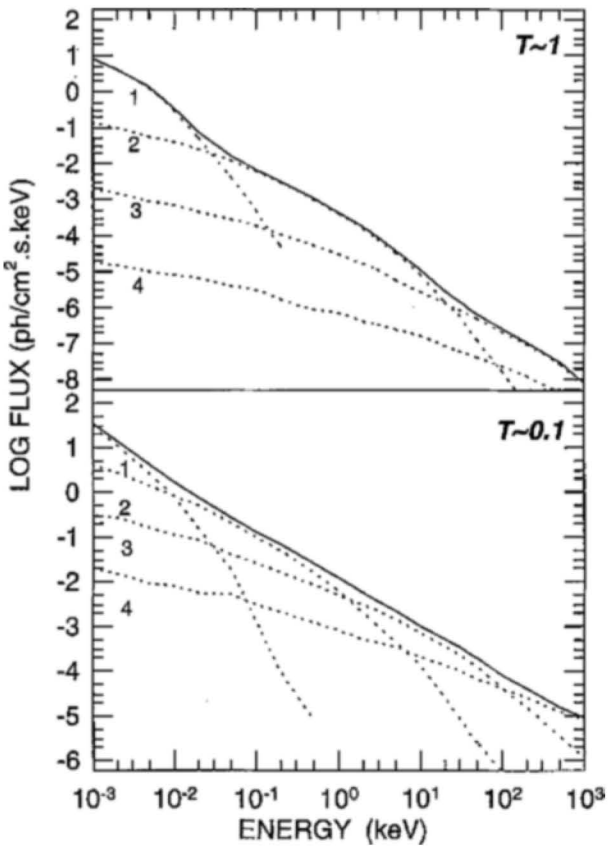

Figure 5. Sample curves for Comptonization of low energy photons in a cloud of weekly relativistic plasma for two values of optical depths and differing number of scattering.

scattering even by a Maxwellian gas can lead to very high photon energies. In a non-relativistic plasma where $kT_e \ll m_e c^2$ and $\tau \gg 1$, the average number of scattering for the seed photon $n_s \sim \tau^2$ and the probability density for multiple scattering is given as; $P(n_s) \propto \exp[\frac{n_s \pi^2}{3(\tau+\frac{2}{3})^2}]$. The emergent spectrum therefore, develops into a unified power law from the ensemble of spectra produced by the photons scattered by differing number of times. Both analytical and Monte-Carlo solutions for the spherical cloud and disk-shape geometry have been discussed in literature in relation to Cyg X-1 (Shapiro 1973; Sunyaev & Titarchuk 1980, Pozdnyakov *et al.* 1983, Hua & Titarchuk 1995) In the disk shape medium the output spectrum is a power law for $h\nu \sim kT_e$ and above $h\nu \gg kT_e$ it can be represented by Wein's distribution function given as $(\frac{h\nu}{kT_e})^3.e^{-h\nu/kT_e}$. A sample computation of Comptonization of the low energy photons in a weekly relativistic plasma for two values of optical depth is shown in Fig. 5. The dotted curves give the individ-

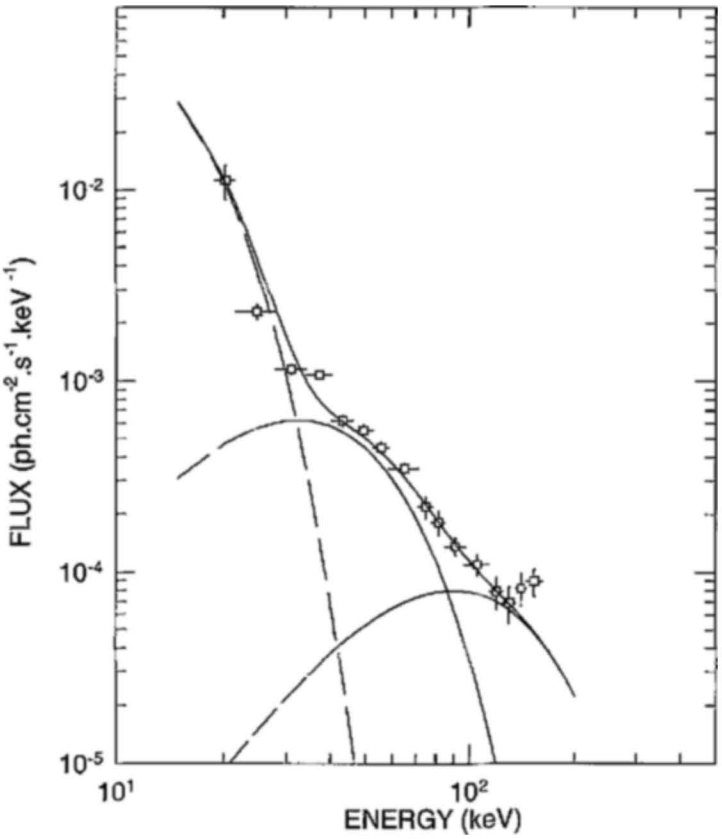

Figure 6. The spectral fit to the present data with multi-component Wien distribution function. Individual curves correspond to kT value of 2.8, 11.8 and 30 keV respectively.

ual contribution due to events with differing scattering number (Pozdnyakov *et al.* 1983).

It is clear from Fig. 5, that in the absence of any one of the individual components, the resultant spectrum will exhibit a sudden dip in the corresponding energy band. Therefore, in the physical model of hard X-ray generation due to Comptonization of the seed photons, it is possible to synthesize knee-shaped spectral profile by preferred selection of photon species, which have undergone differing number of scattering collisions. In a hot plasma with kT_e= 27 keV, an input seed photon with 1 keV energy requires about 20 scatterings to reach the maximum value of $3kT_e$ =81 keV.

It is therefore suggestive that the spectral shape seen in the present measurement is an ensemble with missing spectral components in which the input photons have gone through less number of scatterings. This can arise in an eclipsed geometry of the emitting region, where a part of the photons in the forward cone are

blocked and only albedo photons with a large average scattering angle are seen in the visibility cone. A large average scattering angle should in turn only arise in large number of scatterings. Fig. 5 shows the observed data fitted with a three component Wien spectrum. The best-fit parameters correspond to the kT value of 2.8, 11.8 and 30 keV. It is seen from the figure that multi-component Wien's function gives a very close fit to the data. The highest plasma temperature inferred from the present fit agrees well with the best fit kT_e value of 26.5 keV inferred by Sunyaev & Titarchuk (1980) in their original paper and derived temperatures during the X-ray low/hard state.

4. Summary

In this paper we have presented hard X-ray observations of Cyg X-1 which are radically different than the earlier measurements. Orbital analysis shows that the present data were taken in the minimum phase and the observed low flux indicates a possible partial eclipse of the hard X-ray emission region. The observed spectrum has a knee-shaped profile and can arise by selective summation of the multiple components in a physical model in which the hard X-ray emission arises due to Inverse Compton scattering of the seed photons.

Acknowledgements

I thank J. A. R. D'Silva, P. P. Madhwani, N. V. Bhagat, B. G. Bagade and Ms. N. Kamble for their support in fabrication of the payload and flight support. I also thank the staff at the TIFR balloon facility, Hyderabad for fabricating the balloon and conducting a successful balloon flight. BATSE and the RXTE instrument teams are thanked for making the data available on public archives.

References

Brocksopp, C., Tarasov, A. E., Lyuty, V. M., Roche P., 1999, *Astron. Astrophys*, **455**, 623.

Chitnis, V. R., Rao, A. R. & Agrawal P. C., 1998, *Astron. Astrophys.*,**331**, 251.

Cui, W., Heindl, W. A., Rothschild, R. E., Zhang, S. N. Jahoda K. & Focke W., 1997, *Ap. J.*, **474**, L57.

Dolan, J. F., Crannel, C. J., Dennis, B., Frost, K, & Orwig L. E., 1979, *Ap. J.*, **230**, 551.

D'Silva, J. A. R., Madhwani, P., Tembhurne N. & Manchanda, R. K., 1998, *Nucl. Instr. Meth.*, **A 412**, 342.

Giles, D. R. & Bolton, C. T., 1982, *Ap. J.*, **260**, 240.

Hua, X. M. & Titarchuk, L., 1995, *Ap. J.*, **449**, 188.

Kemp, J., Barbour, M. S., Hanson, G. D., Terrell, D. & Walker E. N. , 1983, *Ap. J.*, **100**, L75.

Kemp, J. C., Kartskaya, E. A., Kumisiashvili, M. I., Lyutyi, V. M., Kharuzina T. S. & Cherepsshchuk A. M., 1987, *Soviet Astronomy*, **31**, 170.

Liang, E. P. & Nolan, P. L., 1984, *Space Sci. Rev.*, **38**, 353.
Ling, J. C., Mahoney, W. A., Wheaton, Wm. A., Jacobson, A. S., Kaluziensky, L., 1983, *Ap. J.*, **275**, 307.
Ling, J. C., Wheaton, W. A., Wallyn, P., *et al.*, 1997, *Ap. J.*, **484**, 375.
Manchanda, R. K., 1983, *Astrophys. Space Sci.*, **91**, 435.
Narayan, R. & Yi, I., 1994, *Ap. J.*, **428**, L 13.
Phlips, B. F., Jung, G. V. & Leising M. D. *et al.*, 1996, *Ap. J.*, **465**, 907.
Pooley, G. G., Fender, R. P. & Brocksopp, C., 1999, *Mon. Not. R. Astr. Soc.*, **302**, L1.
Pozdnyakov, L A., Sobol I. M. & Sunyaev R. A., 1983, *Space Sci. Rev.*, **2**, 189.
Priedhorsky, W. C. & Terrel, J. & Holt, S. S., 1983, *Ap. J.*, **270**, 233.
Rao, A. R., Agrawal, P. C. & Manchanda, R. K., 1991, *Aston. Astrophys.*, **241**, 127.
Shapiro, S. L., 1973, *Ap. J.*, **180**, 531.
Skibo, J. G., Dermer, C. D., 1995, *Ap. J.*, **455**, L25.
Sunyaev, R. A. & Titarchuk L. G., 1980, *Astron. Astrophys.*, **86**, 121.
Tanaka, Y. 1989, in Proc. 23rd ESLAB Symposium on Two Topics in X-ray Astronomy, ed. J. Hunt & B. Battrick (Paris: ESA), 3
Tanaka, Y. & Lewin, W. H. G., 1995, in X-ray Binaries, ed. W. H. G. Lewin, J. van Paradijs & E. P. J. van den Heuvel, Cambridge Uni. Press, 126.
Titarchuk, L. G., 1994, *Ap. J.*, **434**, 570.
van der Klis, M. , 1995, in X-ray Binaries, ed. W. H. G. Lewin, J. van Paradijs, & E. P. J. van den Heuvel, Cambridge Uni. Press, 126.
Ubertini, P., Bazzano, A., La Padula, C., Manchanda, R. K. & Polcaro, V. F., 1991, *Ap. J.*, **383**, 263.

J. Astrophys. Astr. (2001) **22**, 21–34

Using HI to Probe Large Scale Structures at z $\sim$ 3

Somnath Bharadwaj [1*], Biman B. Nath [2†] & Shiv K. Sethi [3‡]
[1] *Department of Physics and Meteorology & Center for Theoretical Studies, I.I.T. Kharagpur, 721 302, India*
[2] *Raman Research Institute, Bangalore 560 080, India*
[3] *Harish-Chandra Research Institute, Chhatnag Road, Jhusi, Allahabad 211 019, India*

Received 2000 March 14; accepted 2000 October 21.

Abstract. The redshifted 1420 MHz emission from the HI in unresolved damped Lyman-α clouds at high z will appear as a background radiation in low frequency radio observations. This holds the possibility of a new tool for studying the universe at high-z, using the mean brightness temperature to probe the HI content and its fluctuations to probe the power spectrum. Existing estimates of the HI density at $z \sim 3$ imply a mean brightness temperature of 1 mK at 320 MHz. The cross-correlation between the temperature fluctuations across different frequencies and sight lines is predicted to vary from $10^{-7}\,\mathrm{K}^2$ to $10^{-8}\,\mathrm{K}^2$ over intervals corresponding to spatial scales from 10 Mpc to 40 Mpc for some of the currently favoured cosmological models. Comparing this with the expected sensitivity of the GMRT, we find that this can be detected with $\sim$ 10 hrs of integration, provided we can distinguish it from the galactic and extragalactic foregrounds which will swamp this signal. We discuss a strategy based on the very distinct spectral properties of the foregrounds as against the HI emission, possibly allowing the removal of the foregrounds from the observed maps.

Key words: Cosmology: theory, observations, large scale structures—diffuse radiation.

1. Introduction

The problem of determining the distribution of matter on large scales in the universe and understanding the large scale structure (LSS) formation is of prime importance

*e-mail: somnath@phy.iitkgp.ernet.in
†e-mail: biman@rri.ernet.in
‡e-mail:sethi@mri.ernet.in

in modern cosmology. Observing the angular positions and redshifts of galaxies has been the most straightforward method of mapping the LSS in the present day universe (Peebles 1993; Peebles 1980), but the interpretation of these observations is complicated by the fact that the relation between the distribution of galaxies and the distribution of underlying matter is not fully understood (Bardeen *et al.*1986). Other direct methods use galaxy clusters or super-clusters as tracers to map the large scale structures. A large variety of techniques have been developed and applied to quantify the distribution of galaxies, and amongst these the correlation functions (two-, three-point correlation functions, etc) and their Fourier counterparts (power spectrum, bi-spectrum, etc.) have been most popular (Peebles 1980). Much of the work comparing the observations with different theories has been based on these.

An alternative approach is to use observations of fluctuations in the diffuse extragalactic background radiation at different wavelengths to probe the large scale structure. Here, the observations of anisotropies in the cosmic microwave background radiation (CMBR) have been most important. These observations probe the clustering of matter at the last scattering surface (e.g. Bond 1996), and combined with the information from the galaxy surveys, they have been successful in narrowing down the allowed class of theoretical models of LSS formation (e.g., Peacock 1999 and reference therein). The study of diffuse background at other wavelengths has been used to infer the clustering properties of matter at more recent epochs. Shectman (1974) observed fluctuations in the optical background; the results of this observation are consistent with predictions from galaxy counts (Peebles 1980). This method has also been applied to far-infrared background (Kashlinsky *et al.* 1997) and recently the first detection of fluctuations in this background has been reported (Kashlinsky *et al.* 1999). Gorjian, Wright & Chary (1999) have recently reported a tentative detection of a near-infrared background. There are similar predictions for fluctuations in the X-ray background (Barcons *et al.*1998, 2000).

In this paper we investigate the possibility of using the extragalactic background radiation at low radio frequencies (meter wave) to probe the LSS. This is largely motivated by the fact that the Giant Meter-wave Radio Telescope (GMRT; Swarup *et al.*1991) which is designed to observe in several frequency bands in the interval 150 MHz to 1420 MHz has recently started functioning. This frequency range corresponds to the 1420MHz emission from HI in the redshift range $0 \leq z \leq 8.5$. Absorption studies along sight lines to quasars indicate that most of the HI in the redshift range $0 \leq z \leq 3$ is in damped Lyman-α (DLA) clouds and the density of HI in DLAs has been determined reasonably well from absorption studies (Lanzetta, Wolfe & Turnshek 1995). Although the HI emission from individual DLAs at high z is too faint to detect using presently available telescopes, the redshifted HI emission from unresolved DLAs will contribute to the background radiation at low frequencies. In this paper we investigate how the brightness temperature of this radiation is related to the density and peculiar velocity of the HI. We consider the possibility of detecting correlations in the fluctuations in this component of the background radiation and using this to probe LSS at high z.

The possibility of observing the redshifted 21 cm emission from HI at high z has been discussed earlier by many authors in a large variety of contexts. One of the first papers (Sunyaev & Zel'dovich 1975) considers the possibility of meter-wave observations to detect protogalaxies and protoclusters at $z \leq 10$. There have been several attempts to detect the HI in proto-clusters and proto-super clusters (see Subrahmanyan & Anantharamaiah 1990 and reference therein).

More recently Subramanian & Padmanabhan (1993) have calculated the abundance of protoclusters as a function of the redshifted HI flux density for various redshifts for both the CDM and HDM models. In a later paper Kumar, Padmanabhan & Subramanian (1995) have calculated the line profile of the HI emission from a spherically symmetric protocluster. Bagla, Nath & Padmanabhan (1997) and Bagla (1999) have used a combination of N-body simulations and a model for the behaviour of the baryons to calculate the abundance and the expected flux from the HI in structures like protoclusters at high redshifts. A major uncertainty in all of these works is in the assumptions about the HI content of the universe at high redshifts. The main focus of all of these works has been on individual peaks of the density fluctuations (protoclusters) which will manifest themselves as detectable features in low-frequency radio maps. Subramanian & Padmanabhan (1993) have also studied the possibility of detecting the excess variance in radio images due to the density fluctuations in the HI at high z.

Katz, Weinberg & Hernquist (1999) have used smoothed particle hydrodynamic simulations to study the distribution of HI gas at high z and they consider the possibility of detecting HI emission from galaxies at $z > 2$.

Tozzi *et al.*(2000) and Shaver *et al.*(1999) have studied the possibility of detecting the HI in the IGM at $z > 5$. The state of the HI at these redshifts is unknown and these works are based on different scenarios for the reionization of the universe.

The work presented here differs significantly from the previous papers in that:

(1) It is restricted to $z < 3.5$ where the HI content of the universe is well determined from DLA absorption studies. We use the results of these observations as inputs to our calculations.

(2) Instead of looking at the possibility of detecting individual features (as has been the focus of a large number of previous papers) we have studied the statistical properties of the fluctuations in the brightness temperature in low frequency radio maps. The statistical quantity we have studied is the cross-correlation between the temperature fluctuations along different lines of sight in the radio map made at different frequencies. Individual features corresponding to protoclusters are rare events and protoclusters with flux in the range $1.5 - 3\,\mathrm{m\,Jy}$ are predicted to occur with abundances in the range $10^{-8} - 10^{-7}\,\mathrm{Mpc}^{-3}$ in the CDM model (Subramanian & Padmanabhan 1993). Even small density fluctuations will contribute to the cross-correlation signal and our proposal has the advantage of simultaneously using the signal in all the pixels in all the frequency channels across the bandwidth of observation.

The structure of the paper is as follows: in §2 we discuss the basic formalism of calculating the brightness temperature and fluctuations in the redshifted 21 cm radiation, in §3 we discuss the numerical results for two currently favoured cosmological models. In §4, the observational difficulties in the presence of galactic and extragalactic foregrounds are presented, and we discuss a possible strategy for overcoming these. §5 gives a summary of our main results.

2. Formalism

We treat the HI in damped Lyman-α (DLA) systems as a continuous distribution with $n_{\rm HI}(\mathbf{x},\mathbf{t})$ denoting the comoving number density of HI atoms in the excited state of the hyperfine transition. Such a treatment is justified in a situation where the resolution of the observations is not sufficient to detect individual DLAs. In addition, the fact that the HI actually does not have a continuous distribution but is distributed in discrete objects can, if required, be taken into account when calculating statistical measures of the fluctuation in the HI distribution.

The HI emission which is at a frequency $\nu_e = 1420$MHz in the rest frame of the gas it is emitted from is redshifted to a frequency ν for an observer located at the origin of the coordinate system. Taking into account the effects of both the expansion of the universe as well as the peculiar velocity $\mathbf{v}(\mathbf{x},t)$ of the HI at the time of emission and $\mathbf{v}(0,t_0)$ of the observer at the present time, the comoving coordinate $\mathbf{x}$ of the HI and ν are related by

$$\mathbf{x} = \mathbf{n}\, c \int_{\frac{\nu}{\nu_e(1-W)}}^{1} \frac{da}{a^2 H(a)} \tag{1}$$

in a spatially flat universe. Here $\mathbf{n} = \mathbf{x}/x$ is a unit vector along the line of sight to the HI, $W(\mathbf{x}) = \mathbf{n}\cdot[\mathbf{v}(\mathbf{x},t) - \mathbf{v}(0,t_0)]/c$ accounts for the effects of the peculiar velocities and

$$H(a) = \frac{\dot{a}(t)}{a(t)} = H_0\sqrt{\Omega_{m0}a^{-3} + \lambda_0} \tag{2}$$

is the Hubble parameter at the epoch when the scale factor has value a.

When discussing observations of the redshifted HI emission, it is convenient to use $\boldsymbol{\nu} = \mathbf{n}\nu$ to simultaneously denote the frequency and the direction of the observation. The vector $\boldsymbol{\nu}$ fixes both the comoving position $\mathbf{x}$ of the HI from where the radiation originates and the time t at which the radiation originates, and we shall use ν and $(\mathbf{x},t)$ interchangeably. Here we calculate how $T(\nu)$ the brightness temperature of the radiation is related to the density $n_{\rm HI}(\mathbf{x},t)$ and the the peculiar velocity $\mathbf{v}(\mathbf{x},t)$ of the HI.

The energy flux in the frequency interval $d^3\nu$ can be calculated if we know the number of excited HI atoms in the comoving volume d^3x from where the radiation originates and it is given by

$$\text{Flux} = \frac{h_P\, \nu_e\, A_{21}\, n_{\rm HI}(\mathbf{x},t)\, d^3x}{4\,\pi\, r_L^2(\mathbf{x})}. \tag{3}$$

Here r_L is the luminosity distance which is given by

$$r_L(\mathbf{x}) = x\,[1 - W]\,\frac{\nu_e}{\nu}. \tag{4}$$

The flux is also related to the specific intensity as follows

$$\text{Flux} = \frac{I(\boldsymbol{\nu})}{\nu^2} d^3\nu \tag{5}$$

which allows us to calculate the specific intensity to be

$$\frac{I(\boldsymbol{\nu}_1)}{\nu^2} = \frac{h_P\,\nu_e\,A_{21}\,n_{\rm HI}(\boldsymbol{\nu})}{4\,\pi\nu_e^2} \left\{\frac{1}{[1 - W(\nu)]}\frac{\nu}{x}\right\}^2 \left|\frac{\partial \mathbf{x}}{\partial \boldsymbol{\nu}}\right| \tag{6}$$

where $|\frac{\partial \mathbf{x}}{\partial \boldsymbol{\nu}}|$ is the Jacobian of the transformation from $\boldsymbol{\nu}$ to $\mathbf{x}$ given in equation (1).

It should be noted here that the effect of the peculiar velocity $(i.e. W)$ can be neglected if we restrict the analysis to scales which are much smaller than the horizon. This is not true for the spatial derivatives of the peculiar velocities which appear in the Jacobian and we retain such terms in our analysis. Calculating the Jacobian gives us

$$\left|\frac{\partial \mathbf{x}}{\partial \boldsymbol{\nu}}\right| = \left(\frac{x}{\nu}\right)^2 \frac{c}{H(\frac{\nu}{\nu_e})}\frac{\nu_e}{\nu^2}\left[1 - \frac{\nu_e}{\nu}\frac{(\mathbf{n}\cdot\nabla)(\mathbf{n}\cdot\mathbf{v})}{H(\frac{\nu}{\nu_e})}\right]. \tag{7}$$

Equations (6) and (7) allow us to calculate the brightness temperature of the radiation

$$T(\boldsymbol{\nu}) = \left(\frac{c^2}{2k_B}\right)\frac{I(\boldsymbol{\nu})}{\nu^2} \tag{8}$$

which gives us

$$T(\boldsymbol{\nu}) = \frac{T_{21}N_{21}(\boldsymbol{\nu})}{8\pi}\frac{A_{21}}{H(\frac{\nu}{\nu_e})}\left(\frac{\nu_e}{\nu}\right)^2\left[1 - \frac{\nu_e}{\nu}\frac{(\mathbf{n}\cdot\nabla)(\mathbf{n}\cdot\mathbf{v})}{H(\frac{\nu}{\nu_e})}\right] \tag{9}$$

where $T_{21} = h_p\nu_e/k_B$ and $N_{21}(\boldsymbol{\nu}) = (c/\nu_e)^3\,n_{HI}(\boldsymbol{\nu})$ is the number of HI atoms in the excited state in a comoving volume $(21\text{cm})^3$.

The number density $n_{\rm HI}(\boldsymbol{\nu})$ can be written as a sum of two parts, namely the mean $\bar{n}_{HI}(\nu)$ and the fluctuation $\Delta n_{HI}(\boldsymbol{\nu})$. We assume that the fluctuation in the number density of HI can be related to the perturbations in the underlying dark matter distribution $\delta(\boldsymbol{\nu})$ through a time dependent linear bias parameter $b(\nu)$ which gives us

$$N_{21}(\boldsymbol{\nu}) = \bar{N}_{21}(\nu)[1 + b(\nu)\delta(\boldsymbol{\nu})]\,. \tag{10}$$

We use this to calculate the isotropic part of the temperature

$$\bar{T}(\nu) = \frac{2.38\,\text{K}h^{-1}\,\bar{N}_{21}(\nu)}{\sqrt{\Omega_{m0}(\frac{\nu_e}{\nu})^3 + \lambda_0}}\left(\frac{\nu_e}{\nu}\right)^2 \tag{11}$$

and the fluctuation

$$\Delta T(\boldsymbol{\nu}) = \bar{T}(\nu)\left[b(\nu)\delta(\boldsymbol{\nu}) - \frac{\nu_e}{\nu}\frac{(\mathbf{n}\cdot\nabla)(\mathbf{n}\cdot\mathbf{v})}{H(\frac{\nu}{\nu_e})}\right]. \tag{12}$$

Now, in the linear theory of density perturbations, both the perturbation and the peculiar velocity can be expressed in terms of a potential i.e.

$$\delta(\mathbf{x},t) = D(t)\nabla^2\psi(\mathbf{x}) \tag{13}$$

and

$$\mathbf{v}(\mathbf{x},t) = -f(\Omega_m)H(t)a(t)D(t)\nabla\psi(\mathbf{x}) \tag{14}$$

where $D(t)$ is the growing mode of linear density perturbations (Peebles 1980). In a spatially flat universe the function f can be well approximated by the form (Lahav *et al.* 1991)

$$f(\Omega_m) = \Omega_m^{0.6} + \frac{1}{70}[1 - \frac{1}{2}\Omega_m(1+\Omega_m)] \tag{15}$$

where the time dependence of Ω_m can be expressed as

$$\Omega_m(\nu) = \left(\frac{H_0}{H(\frac{\nu}{\nu_e})}\right)^2\left(\frac{\nu_e}{\nu}\right)^3\Omega_{m0}\,. \tag{16}$$

Using this and defining a time dependent linear redshift space distortion parameter $\beta(\nu) = f(\Omega_m)/b(\nu)$ we can express the fluctuation in the temperature as

$$\Delta T(\boldsymbol{\nu}) = \bar{T}_A(\nu)b(\nu)D(\nu)\left[\nabla^2 + \beta(\nu)(\mathbf{n}\cdot\nabla)^2\right]\psi(\mathbf{x}). \tag{17}$$

We next calculate the cross-correlation between the temperature fluctuations along two different lines of sight $\mathbf{n_1}$ and $\mathbf{n_2}$ at two different frequencies ν_1 and ν_2. The quantity we consider is the correlation

$$w(\boldsymbol{\nu_1},\boldsymbol{\nu_1}) = \langle\Delta T(\boldsymbol{\nu_1})\Delta T(\boldsymbol{\nu_1})\rangle \tag{18}$$

which is a function of the two frequencies ν_1, ν_2 and θ the angle between the two lines of sight. Using equation (17) and defining $\phi(x_{12}) = \langle\psi(\mathbf{x_1})\psi(\mathbf{x_2})\rangle$ to be the two point correlation of the potential $\psi(\mathbf{x})$, we obtain

$$w(\boldsymbol{\nu_1},\boldsymbol{\nu_2}) = \bar{T}_1\bar{T}_2D_1D_2b_1b_2\left[\nabla^2 + \beta_1(\mathbf{n_1}\cdot\nabla)^2\right]\left[\nabla^2 + \beta_2(\mathbf{n_2}\cdot\nabla)^2\right]\phi(x_{12}) \tag{19}$$

where $x_{12} = \mid \mathbf{x_1} - \mathbf{x_2} \mid$ and we have used the notation $\bar{T}_1 = \bar{T}(\boldsymbol{\nu_1})$, etc.

The function $\phi(x)$ is related to the correlation of the perturbations in the underlying dark matter distribution, and $\xi(\mathbf{x}_1,t_1,\mathbf{x}_2,t_2) = \langle\delta(\mathbf{x}_1,t_1)\delta(\mathbf{x}_2,t_2)\rangle$ the two point correlation of the perturbation in the dark matter density at the point $\mathbf{x_1}$ at the epoch t_1 and $\mathbf{x_2}$ at the epoch t_2 can be written in terms of the potential ϕ as

$$\xi(\mathbf{x}_1,t_1,\mathbf{x}_2,t_2) = D(t_1)D(t_2)\tilde{\xi}(x_{12}) = D(t_1)D(t_2)\nabla^4\phi(x_{12})\,. \tag{20}$$

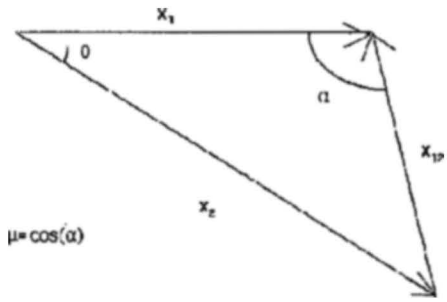

Figure 1. This shows the various distances and angles involved in calculating $w(\nu_1, \nu_2, \theta)$, where ν_1 can be converted to $\mathbf{x}_1$ using equation (1).

We have introduced the function $\tilde{\xi}(x_{12})$ so that we can write $\xi(\mathbf{x_1}, t_1, \mathbf{x_2}, t_2)$ as a product of two parts, one which has the temporal variation and another the spatial variation. Equation (20) can be inverted to express the different derivatives of $\phi(x_{12})$ which appear in equation (19) in terms of moments of $\tilde{\xi}(x_{12})$ which are defined as

$$\tilde{\xi}_n(x_{12}) = \frac{n+1}{x_{12}^{n+1}} \int_0^{x_{12}} \tilde{\xi}(y) y^n dy \,. \tag{21}$$

The form of the angular correlation is further simplified if we restrict θ to be very small. Under this assumption $\mathbf{n_1} \simeq \mathbf{n_2}$, and we use $\mathbf{n}$ to denote the common line of sight. We also use $\mu = \mathbf{n}\cdot(\mathbf{x_1} - \mathbf{x_2})/\mathbf{x_{12}}$ for the cosine of the angle between the line of sight $\mathbf{n}$ and the vector $\mathbf{x_1} - \mathbf{x_2}$ joining the two points between which we are measuring the correlation. The relation between the different distances and angles is shown in figure 1, and we have $x_{12} = \sqrt{x_1^2 + x_2^2 - 2x_1x_2\cos(\theta)}$ and $\mu = (x_1 - x_2\cos(\theta))/x_{12}$. Using these we finally obtain the following expression for the two point correlation of the temperature

$$\begin{aligned} w(\nu_1, \nu_2, \theta) &= \bar{T}_1\bar{T}_2 D_1 D_2 b_2 b_2 \left\{ \left[(1+\beta_1\mu^2)(1+\beta_2\mu^2) \right] \tilde{\xi}(x_{12}) \right. \\ &+ \left[(\frac{1}{3} - \mu^2)(\beta_1 + \beta_2) + (\frac{1}{2} - 3\mu^2 + \frac{5}{2}\mu^4)\beta_1\beta_2 \right] \tilde{\xi}_2(x_{12}) \\ &- \left. \left[\frac{3}{10} + 3\mu^2 - \frac{7}{2}\mu^4 \right] \tilde{\xi}_4(x_{12}) \right\} . \end{aligned} \tag{22}$$

3. Predictions for different models

The density of HI ($\Omega_{\rm HI}$) in DLAs has been determined reasonably well for $0 \leq z \leq 3$ from absorption studies (Lanzetta, Wolfe & Turnshek 1995) and they find that the observed evolution of $\Omega_{\rm HI}$ is well approximated by $\Omega_{\rm HI}(z) = \Omega_{\rm HI0}\exp(\alpha z)$ with $\Omega_{\rm HI0} = 0.18 \pm 0.04 \times 10^{-3}h^{-1}$ and $\alpha = 0.60 \pm 0.15$ for $q_0 = 0$, and

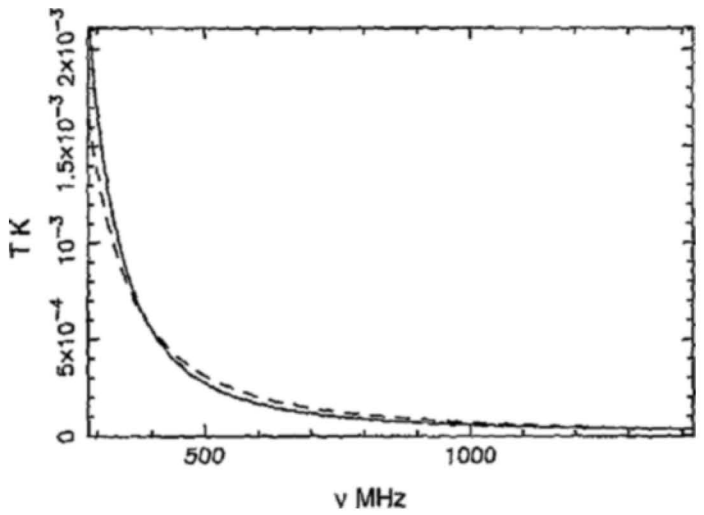

Figure 2. This shows the isotropic part of the brightness temperature at different frequencies. The solid line shows model (I) and the dashed line model (II) of section 3.

$\Omega_{\rm HI0} = 0.19 \pm 0.04 \times 10^{-3} h^{-1}$ and $\alpha = 0.83 \pm 0.15$ for $q_0 = 0.5$, We have used this to calculate the isotropic part of the background brightness temperature due to the redshifted HI emission (equation 17). We have considered two spatially flat FRW cosmological models with parameters (I) $\Omega_{m0} = 1.0$ and $\lambda_0 = 0$, and (II) $\Omega_{m0} = 0.3$ and $\lambda_0 = 0.7$, with $h = 0.5$ in both cases. It should be pointed out that the fits given in Lanzetta *et al.* (1995) are not valid for the model with a cosmological constant, and we use the $q_0 = 0$ fit in this case. Figure 2 shows the brightness temperature as a function of frequency for both the cases.

We find that the temperature increases rapidly as we go to lower frequencies (higher z) and it is around 1 mK at $\nu \sim 330$MHz which corresponds to $z \sim 3$. The increase in the temperature is a direct consequence of the increase of HI density with increasing redshift. The HI density is not very well determined at $z > 3$ and there is evidence that $\Omega_{\rm HI}$ falls off at higher redshifts (Storrie-Lombardi *et al.* 1996).

We next consider $w(\nu_1, \nu_2, \theta)$ the cross-correlation in the temperature fluctuation at different frequencies which we have calculated for the two cases discussed above. We have calculated the dark-matter two point correlation function (equation 20) using the analytic fitting form for the CDM power spectrum given by Efstathiou, Bond & White (1992). For case (I) we use a value of the shape parameter $\Gamma = 0.25$ and for (II) we use $\Gamma = 0.14$. The power spectra are normalized using the results of Bunn & White (1996) based on the 4-year COBE data. It should be noted that the redshift evolution of the matter correlation function and $f(\Omega_m)$ are quite different in the two cases that we have considered. The predictions for $w(\nu_1, \nu_2, \theta)$

are shown in figures 3 and 4. We have assumed that the HI faithfully traces the matter distribution and set $b(\nu) = 1$ throughout.

In our analysis we have kept ν_1 fixed at 320MHz and let ν_2 vary over a band of 16MHz centered around ν_1, while θ takes values upto 2°. In order to measure $w(\nu_1, \nu_2, \theta)$ over this range we would need radio images of the background temperature fluctuation in a 2° × 2° field at different frequencies in a 16MHz band centered around 320MHz and $w(\nu_1, \nu_2, \theta)$ could be estimated using

$$w(\nu_1, \nu_2, \theta) = \langle \Delta T_{\nu_1}(\mathbf{n_1}) \Delta T_{\nu_2}(\mathbf{n_2}) \rangle \tag{23}$$

where $\Delta T_{\nu_1}(\mathbf{n_1})$ refers to the temperature fluctuation along the direction $\mathbf{n_1}$ in the image made at frequency ν_1, and the angular brackets denote average over all pairs of directions $\mathbf{n_1}$ and $\mathbf{n_2}$ which are separated by an angle θ. The central frequency, bandwidth and angular range have been chosen keeping in mind the Giant Meter wave Radio Telescope (GMRT, Swarup *et al.*1991) which has recently become operational. The frequency intervals and angular separation can be converted to a corresponding comoving length-scale and in case (I) 1MHz = 8.9Mpc and $1^{'}$ = 1.8Mpc, while in case (II) 1MHz = 16.0Mpc and $1^{'}$ = 2.7Mpc. The linear theory of density perturbations which we have used here can be applied at scales $\geq$ 10Mpc, which covers most of the region shown in the figures.

We find that $w(\nu_1, \nu_2, \theta)$ is between $10^{-7}\mathrm{K}^2$ and $10^{-8}\mathrm{K}^2$ when the comoving-distance corresponding to the separation in frequencies and direction is less between 10Mpc and 40Mpc beyond which it falls off. The cross-correlation between the temperature fluctuations is expected to be larger at small scales where the linear theory of density perturbations will not be valid and we have not considered these scales here. The temperature fluctuations are anti-correlated when the separation in frequencies exceeds the angular separation. This occurs because of the effect of

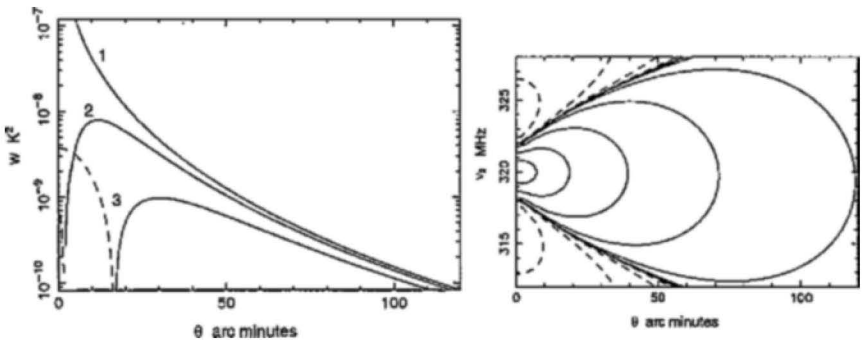

Figure 3. For $\Omega_{m0} = 1, h = 0.5$, (a) shows $w(\nu_1, \nu_2, \theta)$ in K^2 vs. θ with $\nu_1 = 320$MHz and curves (1),(2) and (3) corresponding to $\nu_2 = 320$MHz, 322MHz and 324MHz respectively; (b) shows contours of equal $w(\nu_1, \nu_2, \theta)$ at logarithmic intervals of w with $\nu_1 = 320$MHz. Here 1MHz = 8.9Mpc and $1^{'}$ = 1.8Mpc. The dashed lines show negative values of w.

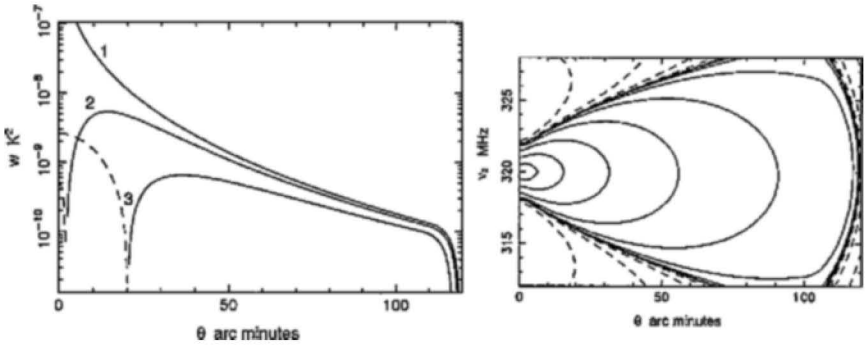

Figure 4. For $\Omega_{m0} = 0.3, \lambda_0 = 0.7, h = 0.5$, (a) shows $w(\nu_1, \nu_2, \theta)$ in K^2 vs. θ with $\nu_1 = 320$MHz and curves (1),(2) and (3) corresponding to $\nu_2 = 320$MHz, 322MHz and 324MHz respectively; (b) shows contours of equal $w(\nu_1, \nu_2, \theta)$ at logarithmic intervals of w with $\nu_1 = 320$MHz. Here 1MHz = 16.0Mpc and $1^{'} = 2.7$Mpc. The dashed lines show negative values of w.

the peculiar velocity which produces a "distortion" very similar to the effect it has on the two-point correlation function in redshift surveys.

4. Observational prospects

In this section we discuss the prospects of actually observing the background radiation from the HI in damped Lyman-α clouds. Our discussion is restricted to observations at around 320 MHz largely because we have reliable estimates of the HI content at $z \leq 3$ and there are indications that $z \simeq 3$ might be the redshift where the HI content of the universe is maximum (Storrie-Lombardi *et al.* 1996). Another reason for our choice of this frequency range is that the GMRT (Swarup *et al.* 1991) which is already functioning at these frequencies is expected to have an angular resolution of $10^{''}$ and reach noise levels of 100μK in around 10 hrs of integration. The angular resolution and sensitivity of the GMRT will be sufficient for detecting both the isotropic component as well as the correlations in the component of the background radiation arising from the HI at $z \simeq 3$ (Figs. 2, 3 and 4) provided we can distinguish this component from the contribution due to other sources.

4.1 *Galactic and extra-galactic foregrounds*

Any observations at low frequencies will have a very large contribution from the synchrotron radiation from our own galaxy. Observations at 408 MHz (Haslam *et al.* 1982) with resolution 1°x1° indicate a minimum temperature of $\simeq$ 10 K at 408 MHz. Using $T \propto \nu^{-2.7}$ as indicated by the spectral index of galactic synchrotron radiation, the temperature at $\nu \simeq 320$ MHz is $\simeq$ 20 K. Comparing this number with the expected background from redshifted HI radiation (Fig. 2) the galactic foreground is seen to be several orders above the expected signal. Another

quantity of interest to us is the fluctuations in the galactic radiation at angles $\lesssim 1°$. However as the resolution of Haslam maps is $\simeq 1°$ it cannot be used to make any predictions about the fluctuations at the angular scales of interest.

Another source of contamination is the continuum radiation from unresolved extragalactic sources (the resolved ones will be removed from the image before analysis) and we use results from the recent FIRST survey (for details see White *et al.* 1997 and references therein) to estimate this. Tegmark & Estathiou (1996) provide an analytic fit for the number of sources per unit flux ϕ[mJy] per steradian in this survey, and at flux levels $\phi \ll 100$mJy this can be approximated by

$$\frac{dn}{d\phi} = \frac{5.24 \times 10^5}{\text{mJy sr}} \left(\frac{\phi}{0.75\text{mJy}}\right)^{-1.65} . \tag{24}$$

We use this to estimate the total contribution from sources fainter than 100 μJy, and converting this to brightness temperature we find that the continuum emission from unresolved radio sources is expected to produce a background radiation with brightness temperature $\sim .1$K at 1.5 Ghz. For the purposes of estimating an order-of-magnitude we assume this value to be representative of what we expect at $\sim$ 320 MHz.

The two-point correlation function of the sources detected by FIRST has been estimated (Cress *et al.* 1996): $w(\theta) \simeq 0.18\theta^{-1.1}$, with θ in arcminutes. Little is known about the correlations expected in the fluctuations in the contribution to the background radiation from unresolved radio sources.

It is clear from the foregoing discussion that both galactic and extragalactic continuum signals are likely to be so high that they would totally swamp the signal which we want to detect and therefore it is not possible to directly detect the radiation from HI unless we find some method for removing the foregrounds.

At present the most promising strategy is to use the proposed observations themselves to determine the foreground and remove this from the data, and we next discuss a possible method for doing this.

4.2 *Removing foregrounds*

We consider the GMRT band centered at 325 MHz for our discussion in this section. The total bandwidth of 16 MHz is divided in 128 channels each with $\Delta\nu =$ 1.25 kHz, and the signal in any frequency channel is expected to be dominated by the foregrounds.

Here we briefly review the standard method of continuum subtraction which is generally used in spectral line detections and then discuss how this method can be used for the analysis proposed here. The reader is referred to Subrahmanyam & Anantharamaiah (1990) and references therein for examples of how this method is applied in searches for HI emission from protoclusters.

We represent the observed signal $y_i(\mathbf{n})$ in the i th frequency channel in the direction $\mathbf{n}$ as:

$$y_i(\mathbf{n}) = x_i(\mathbf{n}) + f_i(\mathbf{n}) + N_i \tag{25}$$

where $x_i(\mathbf{n})$ and $f_i(\mathbf{n})$ are the contribution to the output signal from the HI and the foregrounds respectively, and N_i is the receiver noise.

We should at this stage remind ourselves that foregrounds are sources which are emitting continuum radiation—the primary of such source being the synchrotron radiation from our own galaxy. We also have the contribution from unresolved extragalactic radio sources which, as we have seen above, is a smaller contribution. The sum total of these along any line of sight is expected to be a smooth function of the frequency. On the contrary the contribution from the HI will come from individual damped Lyman α clouds along the line of sight with a velocity width $\simeq 200\,\mathrm{km\,sec}^{-1}$ (Prochaska & Wolfe 1998) and this will correspond to lines of width:

$$\Delta\nu \sim \frac{\Delta V}{c}\nu \simeq 0.2\mathrm{MHz}. \tag{26}$$

Although the total number of damped Lyman-α clouds in a $1^\circ \times 1^\circ \times 16\,\mathrm{MHz}$ field is expected to be quite large ($\simeq 3 \times 10^4$) we expect to have only one damped Lyman-α cloud along a single $20'' \times 20'' \times 16\,\mathrm{MHz}$ synthesized GMRT beam. The probability of two damped Lyman-α clouds occurring right next to each other in the same synthesized beam and causing confusion is quite small, and hence the signal we are looking for will come in the form of lines of width $\sim 0.2\mathrm{MHz}$ which we will not be able to detect as the individual lines will be swamped by both the foreground as well as the noise. What we can do is to fit the smooth component of the signal $y_i(\mathbf{n})$ by a function $F_i(\mathbf{n})$ and subtract this from the output signal to remove the effect of the foregrounds

$$S_i(\mathbf{n}) = y_i(\mathbf{n}) - F_i(\mathbf{n}) = x_i(\mathbf{n}) + N_i(\mathbf{n}) + E_i(\mathbf{n}) \tag{27}$$

where we call $S_i(\mathbf{n})$ the reduced signal and $E_i(\mathbf{n})$ is the possible error in the fitting procedure. If our foreground subtraction works correctly, the reduced signal should have contributions from only the HI signal and the noise.

We first determine the mean reduced signal

$$\bar{S}_i = \langle S_i(\mathbf{n})\rangle = \langle x_i(\mathbf{n})\rangle + \langle N_i(\mathbf{n})\rangle + \langle E_i(\mathbf{n})\rangle \tag{28}$$

where the angular brackets denote average over all lines of sight. If the errors in the foreground subtraction can be made smaller than the signal i.e. $\langle E_i(\mathbf{n})\rangle < \langle x_i(\mathbf{n})\rangle$ then this will give an estimate of the background brightness temperature due to the HI emission i.e. $\bar{T}(\nu) = \bar{S}_i$ where the index i refers to the channel with central frequency ν.

We next consider the quantity

$$\Delta S_i(\mathbf{n}) = S_i(\mathbf{n}) - \bar{S}_i \tag{29}$$

which gives the fluctuation in the brightness temperature. We can use this to estimate the cross-correlation in the fluctuations at different frequencies

$$w(\nu_1, \nu_2, \theta) = \langle \Delta S_i(\mathbf{n}) \Delta S_j(\mathbf{m})\rangle \tag{30}$$

where i and j are the channel with frequency ν_1 and ν_2 respectively, and $\mathbf{n}$ and $\mathbf{m}$ are two lines of sight separated by an angle θ and the angular brackets denote average over all such pairs of lines of sight.

5. Summary and Conclusions

We have investigated the contribution from the HI in unresolved damped Lyman-α clouds at high redshifts to the background radiation at low frequency radio waves (meter waves). The isotropic part of this radiation depends on the density of HI and the background cosmological model, while the fluctuations in this component of the background radiation have an added dependence on the fluctuations in the distribution of the damped Lyman-α clouds and their peculiar velocities.

We have used estimates of the HI density available from absorption studies to calculate the brightness temperature of this radiation. We find that this has a value $\sim$ 1 mK at 320 MHz which corresponds to $z \sim 3$. The distribution of damped Lyman-α clouds is assumed to trace the underlying dark matter distribution which also determines the peculiar velocities. Using this and the linear theory of density perturbations, we have calculated the relation between the fluctuation in this component of the background radiation and the density perturbations at high z. Observations of the cross-correlations of the fluctuations at different sight lines across images produced at different frequencies holds the possibility of allowing us to probe the two point correlation function (or power spectrum) at high redshifts. We have calculated the expected cross-correlations for two currently acceptable CDM models and find it to be in the range $10^{-7}\mathrm{K}^2$ to $10^{-8}\mathrm{K}^2$ at $\nu \sim 320$MHz for separations in sight lines and frequencies such that the corresponding spatial separation is in the range 10 Mpc and 40 Mpc. The cross-correlations are expected to be larger at smaller scales where the linear theory cannot be applied. Our results show that both the isotropic background (Fig. 2) and its fluctuations (Figs. 3 and 4) can be detected by GMRT which is the largest telescope operating at meter waves at present, provided this signal can be distinguished from other sources which contribute to the low frequency background radiation.

The biggest obstacles in detecting the HI contribution are the galactic and extragalactic foregrounds, both of which are many orders larger than the signal we want to detect. The fact that both those sources of contamination emit continuum radiation while the HI contribution is from individual damped Lyman-α clouds each of which emits a spectral line with a relatively small velocity width keeps alive the possibility of being able to distinguish this signal from the contamination. We have, in this paper, considered one possible approach which might allow us to model and subtract the foreground along any line of sight. More work is needed in this direction and work is currently underway in investigating other viable possibilities for foreground removal.

Acknowledgments

The authors would like to thank Jayaram Chengalur for many useful discussions on issues related to the GMRT and foregrounds.

References

Bagla, J. S. 1999, *ASP Conf. Ser.* **156**: Highly Redshifted Radio Lines, 9
Bagla J. S. Nath B., Padmanabhan T. 1997, *MNRAS*, **289**, 671
Barcons, X., Carrera, F. J., Ceballos, M. T., Mateous, S. 2000, *astro-ph/* **0001191**
Barcons, X., Fabian, A. C., Carrera, F. J. 1998, *MNRAS*, **293**,/ 60
Bond, J. R. 1996, *Observations of Large-Scale Structure in the universe*, Ed. R. Schaeffer *et al.* , Les Houches, Elsevier Science
Bardeen, J. M., Bond, J. R., Kaiser, N., Szalay, A. S. 1986, *ApJ*, **304**, 1
Bunn E. F., White M. 1996, *astro-ph*/9607060
Cress, C. M., *et al.* 1996, *ApJ*, **473**
Efstathiou, G., Bond, J. R., White, S. D. M. 1992, *MNRAS*, **250**, 1p
Gorjian, V., Wright E. L., Chary R. R., 1999, *ApJ*, in Press, *astro-ph*/9909428
Haslam, C. G. T., Stoffel, H. , Salter, C. J., Wilson, W. E. 1982, *ApJS*, **47**, 1
Kashlinsky, A., Mather, J. C., Odenwald, S. 1999, *astro-ph*/9908304
Kashlinsky, A., Mather, J. C., Odenwald, S. 1997, *astro-ph*/9701216
Katz, N., Hernquist, L., Weinberg, D. H. 1999, *ASP Conf. Ser.* **156**: Highly Redshifted Radio Lines, 1
Kumar A., Padmanabhan T., Subramanian K. 1995, *MNRAS*, **272**, 544
Lahav O., Lilje P. B., Primack J. R. and Rees M., 1991, *MNRAS*, **251**, 128
Lanzetta, K. M., Wolfe, A. M., Turnshek, D. A. 1995, *ApJ*, **430**, 435
Peacock, J. A. 1999, *Cosmological Physics* , Cambridge : Cambridge University Press
Peebles, P. J. E. 1993, *Principles of Physical Cosmology*, Princeton : Princeton University Press
Peebles, P. J. E. 1980, *The Large-Scale Structure of the Universe*, Princeton : Princeton University Press
Prochaska, J. X., Wolfe, A. M. 1998, *ApJ*, **507**, 113
Shaver, P. A., Windhorst, R. A., Madau, P. and de Bruyn, A. G. 1999, *A&A*, **345**, 380
Shectman, S. A. 1974, *ApJ*, **188**, 233
Storrie–Lombardi, L.J., McMahon, R.G., Irwin, M.J. 1996, *MNRAS*, **283**, L79
Subramanian, K., Padmanabhan, T. 1993, *MNRAS*, **265**, 101
Subrahmanyam. R., Anantharamaiah, K. R. *JAA*, 1990, **11**, 221
Sunyaev, R. A., Zel'dovich, Ya. B. 1975, *MNRAS*, **171**, 375
Swarup, G., Ananthakrishan, S., Kapahi, V. K., Rao, A. P., Subrahmanya, C. R., Kulkarni, V. K. 1991, *Curr. Sci.*, **60**, 95
Tegmark, M., Efstathiou, G. 1996, *MNRAS*, **281**, 1297
Tozzi, P., Madau, P., Meiksin, A. and Rees, M. J. 2000, *ApJ*, **528**, 597
White, R. L., Becker, R. H., Gregg, M. D.,Helfand, D. J. 1997, *ApJ*, **475**, 479

J. Astrophys. Astr. (2001) **22**, 35–50

GMRT Observations of Interstellar Clouds in the 21cm line of Atomic Hydrogen

Rekhesh Mohan,[1*] K. S. Dwarakanath,[1] G. Srinivasan,[1]
& Jayaram N. Chengalur[2]
[1]*Raman Research Institute, Bangalore 560 080, India*
[2]*National Center for Radio Astrophysics, Ganeshkhind, Pune 411 007, India*

Received 2000 October 23; accepted 2001 January 10.

Abstract. Nearby interstellar clouds with high ($|v| \geq 10\mathrm{km\,s^{-1}}$) random velocities although easily detected in NaI and CaII lines have hitherto not been detected (in emission or absorption) in the HI 21cm line. We describe here deep Giant Metrewave Radio Telescope (GMRT) HI absorption observations toward radio sources with small angular separation from bright O and B stars whose spectra reveal the presence of intervening high random velocity CaII absorbing clouds. In 5 out of the 14 directions searched we detect HI 21cm absorption features from these clouds. The mean optical depth of these detections is ~ 0.09 and FWHM is ~ 10 km s^{-1}, consistent with absorption arising from CNM clouds.

Key words: ISM: clouds, kinematics and dynamics – Radio lines: ISM.

1. Background and motivation

This study is a part of our continuing effort to detect interstellar clouds in the lines of sight to bright O and B stars in absorption in the 21cm line of neutral hydrogen. Such clouds have been extensively studied using absorption lines of singly ionized calcium. The most famous of such investigations is that by Adams (1949), who used the CaII absorption spectra towards 300 stars to determine their radial velocities. In an equally seminal paper Blaauw (1952) used Adams' data to obtain a histogram of the random velocities of interstellar clouds, often (roughly) allowing for the contribution to their radial velocity due to the differential rotation of the Galaxy. One of Blaauw's main conclusions was that interstellar clouds have

*e-mail:reks@rri.res.in

significant peculiar velocities, with the tail of the distribution extending upto 80 – 100 km s^{-1}. In an independent investigation, Routly & Spitzer (1952) found an interesting systematic behavior of the ratio of the column density of neutral Sodium to singly ionized Calcium (N_{NaI}/N_{CaII}). They found this ratio to decrease with increasing random velocity of the cloud. The ratio was less than 1 for the faster clouds ($|v| \geq 20$ km s^{-1}), but significantly greater than 1 in clouds with smaller random velocities. This seems to suggest two "classes" of interstellar clouds: those with negligible random velocities and those with substantial random velocities ($|v|$ > 15-20 km s^{-1}).

Soon after the 21cm line of the hydrogen atom was discovered, there were attempts to detect atomic hydrogen in the interstellar clouds along the lines of sight studied by Adams (Habing 1968,1969; Goldstein & MacDonald 1969). Interestingly, whereas many lines of sight towards the O and B stars studied by Adams showed the presence of several clouds – some with very small random velocities, while others with larger random velocities – only the low velocity ones ($|v| < 10$ km s^{-1}) were seen in emission in the 21cm line. The emission occurred at velocities that agreed well with the velocities of the CaII absorption line features. For some reason, there was no emission that could be attributed to the higher (random) velocity clouds. Although this was very intriguing, after some speculations it was soon forgotten. Recently Rajagopal *et al.* (1998a, 1998b) revived this question. Unlike in earlier 21cm studies, they attempted to detect the atomic hydrogen in these clouds in a 21cm *absorption* study. They selected some two dozen stars from the Adams' sample and used the VLA to do a 21cm absorption measurement against known radio sources whose angular separation from the star in question was within a few arc minutes. The idea was that such a line of sight to the radio source would pass through the same interstellar clouds that were detected earlier through the absorption lines of CaII. Surprisingly the conclusions of this absorption study were the same as that of the earlier emission studies: Only the clouds with random velocities less than $\sim$ 10 km s^{-1} were detected (and in each case the 21cm absorption velocity agreed with the velocity of the 21cm emission feature and also with the velocity of the CaII absorption line). No 21cm absorption was detected from the clouds with random velocities in excess of 10 km s^{-1} down to an optical depth of 0.1.

To explain this, Rajagopal *et al* (1998b) invoked the hypothesis that the peculiar velocities of interstellar clouds was due to their encounters with expanding supernova remnants. They argued that if this was the operative mechanism then the clouds accelerated to higher velocities would be warmer (due to their being dragged along by the hot gas behind the SNR shock front) and will also have smaller column densities compared to the slower clouds (due to evaporation). This would explain the small optical depth for the 21cm absorption (which is directly proportional to the column density and inversely proportional to the temperature). The Routly-Spitzer effect referred to earlier, will also have a natural explanation in this hypothesis. In clouds shocked by supernova blast waves, less of Calcium is likely to be locked up in grains due to sputtering of the grains.

Although shock acceleration of clouds seemed to provide satisfactory explanation, to strengthen that hypothesis it was important to observationally *establish* a correlation between the 21cm optical depth and the peculiar velocity. The present study is a part of a continuing effort towards this end. In this paper, we wish to report the results obtained from the first set of observations with the recently constructed Giant Meterwave Radio Telescope (GMRT). In these observations we obtained a limit on the optical depth roughly ten times better than that achieved by Rajagopal *et al* (1998a). The strategy for selecting the sources is outlined in the next section and some details pertaining to the observations are given in section 3. The results obtained by us are given in section 4 and a brief discussion in section 5.

2. Source selection

The basic finding list of stars with the CaII absorption line data was from Adams (1949) and Welty *et al.* (1996). The selection criteria was that the spectra of the stars should contain both low ($|v| < 10$ km s^{-1}) and high random velocity ($|v| > 10$ km s^{-1}) optical absorption features. Even though it is not possible to derive a sharp distinction between the low and the high random velocities, we have adopted the value 10 km s^{-1} as the dividing line (Spitzer 1978). The distances to the stars were obtained from the HIPPARCOS catalog (1997). The background radio sources towards which we measured HI absorption were selected from the National Radio Astronomy Observatory Very Large Array Sky Survey (NVSS, Condon *et al.* 1996). Rajagopal *et al* (1998a) chose their directions such that at half the distance to the star, the linear separation between the lines of sight towards the star and the radio source was ~ 3 pc. In the present observations, we have chosen the directions where this value is < 1 pc in most cases. This gives a better chance for both lines of sight to sample the same gas. Since our aim was to reach an rms of 0.01 in optical depth, only those radio sources with flux densities at 20cm greater than ~ 100 mJy were considered, so that we could reach the target sensitivity in a reasonable integration time. However, for a few directions we compromised the separation between the lines of sight for the higher flux density of the background source. Our final list consisted of 14 fields. Table 1 lists a summary of the fields observed. In a few cases, there was more than one radio source within the GMRT primary beam. Four out of the fourteen stars in our list have been previously studied by Rajagopal *et al* (1998) using the VLA.

3. Observations

3.1 *The Giant Meterwave Radio Telescope*

The Giant Meterwave Radio Telescope (GMRT) consists of 30 fully steerable dishes, of diameter 45 m with a maximum baseline of 25 km (Swarup *et al.* 1991). The aperture efficiency of the dishes is $\sim 40\%$ in the 21cm band, which implies an effective area of ~ 19000 m^2. This telescope is equipped with an FX correlator

Table 1. A summary of the observed directions: Column 1 lists the stars, whose spectra are known to contain high random velocity optical absorption lines. Those fields which were observed earlier by Rajagopal *et al.* (1998a) is marked with an asterix (*). Column 2 shows the distance to these stars obtained from the HIPPARCOS catalog. The flux density of the radio sources listed in column 6 are from the present observations. The angle θ (column 7) is the angle between the lines of sight to the star and the radio source. The linear separation between the two lines of sight at half the distance to the star is given in column 8.

Star	d	l	b	Radio source	S	θ	r
	pc	deg	deg		mJy		pc
HD 175754*	680.0	16.46	−10.02	NVSS J1856−192	67	$28'$	2.8
HD 159561	14.3	35.90	+22.58	NVSS J1732+125	174	$41'$	0.1
HD 166182	467.3	47.42	+18.03	NVSS J1809+208	383	$13'$	0.9
HD 193322	476.2	78.10	+2.78	NVSS J2019+403	310	$28'$	1.9
HD 199478*	2857	87.51	+1.42	NVSS J2056+475	180	$8'$	3.3
HD 21278*	174.8	147.52	−6.19	NVSS J0330+489	343	$28'$	0.7
				NVSS J0331+489	189	$22'$	0.6
HD 24760	165.0	157.35	−10.10	NVSS J0400+400	191	$30'$	0.7
HD 47839	313.5	203.00	+2.30	NVSS J0642+098	340	$8'$	0.4
HD 37128	411.5	205.26	−17.14	NVSS J0536−014	171	$18'$	1.0
HD 37742*	250.6	206.50	−16.49	NVSS J0542−019	408	$7'$	0.3
HD 37043	406.5	209.50	−19.60	NVSS J0535−057	299	$14'$	0.9
				NVSS J0536−054	215	$21'$	1.2
HD 38771	221.2	214.52	−18.50	NVSS J0549−092	170	$32'$	1.0
				NVSS J0549−092	97	$32'$	1.0
HD 143018	140.8	347.20	+20.14	NVSS J1559−262	328	$10'$	0.2
HD 147165	225.2	351.38	+16.90	NVSS J1623−261	287	$33'$	1.3

providing 128 channels per polarization per baseline. A baseband bandwidth ranging from 16 MHz down to 64 kHz variable in steps of 2 can be chosen. The 21 cm receiver is a wide band system covering the frequency range of 900 to 1450 MHz. It is a prime focus uncooled receiver with a characteristic system temperature of 70 K. The 21cm system has four sub bands, centered at 1060, 1170, 1280 and 1390 MHz, each with a 3 dB bandwidth of 120 MHz. Provision exists in the receiver to bypass the narrow bandpass filters to obtain the full 450 MHz band.

3.2 *Observing strategy*

The radio observations were carried out during the period April−May, and September, 1999. Only 8−10 antennas within the central square km of the array were used.

Table 2. The Observational Setup.

Telescope	GMRT
System temperature	~ 70 K
Aperture efficiency	$\sim 40\%$
Number of antennas	8 to 10
Base band used	2.0 MHz
Number of channels	128
Velocity resolution	3.3 km s^{-1}
On source integration time	$\sim$ 1 to 7 hour

We used a baseband bandwidth of 2 MHz, which translates to ≈ 422 km s^{-1} in velocity and a resolution of ~ 3.3 km s^{-1}. The center of the band was set at 1420.4 MHz. The observing band was found to be free from interference. We used one of the VLA primary flux calibrators (3C48/3C147/3C286) for setting the flux density scale. We observed a nearby secondary calibrator from the VLA calibrator manual for phase and bandpass calibration. The phase calibration was carried out once every hour. Bandpass calibration was carried out once every two hours for 10 minutes with the observing frequency shifted by 2 MHz below the band, which corresponds to a velocity shift of ≈ 400 km s^{-1}. This shift is adequate to move the observing band out of the velocity spread of the Galactic 21cm line spectral features. On source integration time ranged from $\sim$ 1 to 7 hours, depending on the strength of the background radio source. The rms sensitivity in optical depth varied from 0.02 to 0.007 towards different sources. A summary of the observational setup is given in Table 2.

The analysis of the data was carried out using the Astronomical Image Processing System (AIPS) developed by the National Radio Astronomy Observatory. The resulting data set consisted of 14 image cubes containing a total of 17 HI absorption profiles. Continuum subtraction was carried out by fitting a linear baseline to the line free channels in the visibility domain and subtracting the best fit continuum from all the channels. For the point sources amongst the list of program sources, the flux densities quoted in the NVSS (Condon *et al*, 1996) was found to agree with the flux densities obtained from the GMRT to within 10%. Separate line images of short and long baselines were made to convince ourselves that contamination due to HI emission was minimal. The rms noise level ranged from 1.5 mJy to 5 mJy/channel/beam depending upon the integration time. Out of the 17 directions, the lowest HI optical depth of ~ 0.007 was achieved towards the source NVSS J0542−019. In order to study the individual HI absorption components, multiple Gaussian profiles were fitted to the absorption line spectra using the Groningen Image Processing System (GIPSY).

4. Results

We have examined the HI absorption spectra towards 14 stars having optical absorption lines at both low and high random velocities. In all these fields, we have detected HI absorption at low random velocities. In all the directions, at low random velocities ($|v| < 10$ km s^{-1}) there is a good agreement between the velocities of the HI absorption features and that of the CaII absorption line components, within the limits of our velocity resolution (~ 3.3 km s^{-1}). In 5 out of the 14 fields, for the first time, we have detected HI absorption features coincident with the high random velocity CaII absorption lines.

The 21cm absorption profiles have a typical optical depth $\tau \sim 0.1$, and a FWHM $\sim$ 10 km s^{-1}. This velocity width is less than would be expected from thermal broadening in the WNM, and in any case, the path length of WNM required to produce an optical depth of ~ 0.1 is considerably larger than the distance to the star against which the NaI/CaII lines have been observed. The observed velocity width and optical depth are instead completely consistent with what would be expected from absorption in a CNM cloud. In contrast with the classical galactic emission/absorption line studies however, this cloud is too small to produce a clearly identifiable single dish emission signal. An estimate of the column density can however be obtained from the Leiden-Dwingeloo Survey (LDS) of Galactic neutral hydrogen (Hartmann & Burton 1995). Note that the column density as measured in this survey is at best indicative, since beam dilution causes it to underestimate the true N_{HI} of the cloud while contamination from the WNM causes it to overestimate the true N_{HI}. Nonetheless we have used the LDS HI column density to get a handle on the spin temperatures of the high random velocity clouds that we have detected. The N_{HI} was estimated by integrating over the FWHM of the HI absorption line. The same procedure was repeated for the low LSR velocity HI absorption features in the spectra and gave values that were consistent with earlier estimates. However, note that for the smaller clouds at higher velocity the fractional contribution from the WNM would be more in the HI emission spectra and would hence lead to greater errors in the estimation of N_{HI} and thus T_S.

Each of the five detections are discussed separately below. A summary of the detections is listed in Table 3. Since our velocity resolution is ~ 3 km s^{-1} and the optical absorption data for majority of the stars were obtained from a high resolution ($0.3 - 1.2$ km s^{-1}) survey (Welty *et al* 1996), the number of interstellar absorption features seen in the optical study is greater than those revealed by our HI absorption study. This is evident in figures 1 to 6 which display optical depth profiles.

4.1 *HI absorption detections from high random velocity clouds.*

HD37043/NVSS J0535−057: Towards the star HD37043, the high resolution CaII absorption line study by Welty *et al.* (1996) revealed 12 interstellar absorption features over the velocity range -22 to $+23$ km s^{-1}. The HI absorption was measured

Table 3. Detections of high random velocity HI absorption: Column 2 lists the high velocity ($|v| > 10$ km s^{-1}) CaII absorption lines seen towards the star. Column 3 gives the radial component of the Galactic rotation velocity at the distance to the star. Column 4 gives the HI optical depth at the velocity of the CaII absorption line and Columns 5,6 and 7 list the parameters of the gaussian fit to the HI absorption profile. Column 8 lists the HI column density in the respective line of sight derived from the Leiden Dwingeloo Survey (Hartmann & Burton 1995) and Column 9 gives the derived HI spin temperature.

Star HD no.	CaII V_{lsr} (kms^{-1})	v_{Gal} (kms^{-1})	τ_{HI}	Mean V_{lsr} (km s^{-1})	Peak τ_{HI}	FWHM (km s^{-1})	N_{HI} $\times 10^{20}$ (cm^{-2})	T_S (K)
37043	−16.86	+2.5	0.12	−15.1	0.12	12.8	0.2†	7†
	−12.34		0.10					
	+22.68		0.06	+24.0	0.06	20.4	1.8	78
159561	−14.07	+1.9	0.06	−13.0	0.06	11.6	0.5	40
193322	+21.68	+5.2	0.36	+24.0	0.24	6.3	2.6	89
143018	−26.48	−1.4	0.04					
	−21.63		0.07					
24760	+12.96	~ 0	0.06					

†: Upper limit, possibility of beam dilution.

towards NVSS J0535−057, which is 14′ in projection from the star. This angular separation is equivalent to a linear separation of 0.9 pc at half the distance to the star. The HI optical depth profile shows weak but significant absorption corresponding to the high random velocity CaII absorption lines (Fig. 1). This weak HI absorption persists over the velocity spread of the CaII absorption lines. The HI absorption profile was fitted with 5 gaussians, centered at +24, +12, +5, −2 and −15km s^{-1}. For the direction towards this star, negative velocities are forbidden by the Galactic rotation model (Brand & Blitz 1993). Presumably due to the lack of adequate velocity resolution in the 21cm spectra, the individual HI absorption features are spread over many optical absorption line components and it is difficult to obtain a one to one correspondence between them.

The HI absorption feature centered at around −15 km s^{-1} coincides with the optical absorption line at −16.86 km s^{-1}, well within the limits of our velocity resolution. The FWHM of this HI feature is $\approx$ 13 km s^{-1} and the peak optical depth is $\approx$ 0.12. In the LDS survey, there is no distinct HI emission feature at the velocity of the CaII and HI absorption lines, but only a shoulder of HI emission. If the gas associated with this cloud fills the Dwingeloo telescope beam, then the LDS provides an upper limit of 2.0×10^{19} cm^{-2} for the HI column density of this cloud. The upper limit on HI spin temperature implied by the N_{HI} from LDS is 7 K, which is about an order of magnitude lower than typical diffuse interstellar HI clouds. It seems highly likely therefore that the high random velocity optical and

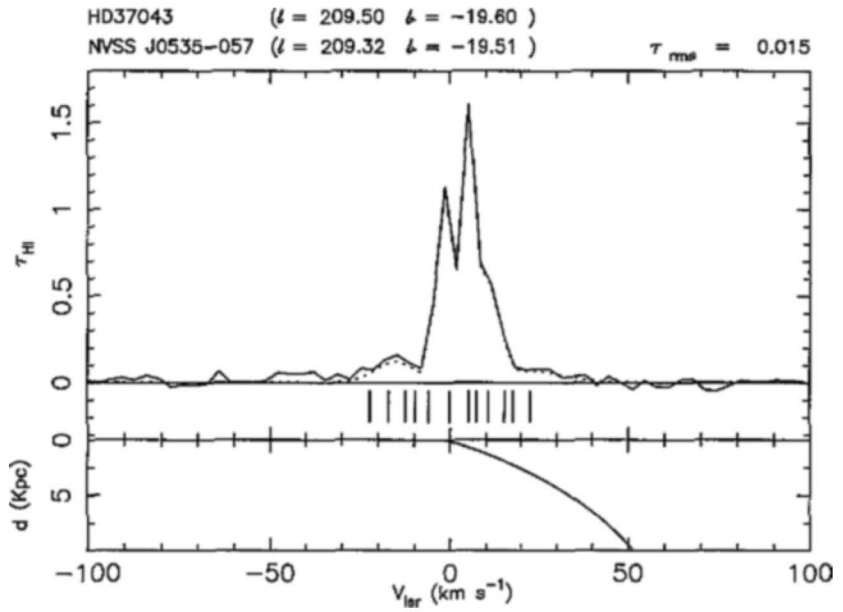

Figure 1. The HI optical depth spectrum (solid line) towards the radio source NVSS J0535−057. The vertical tick marks indicate the velocities of the CaII absorption lines in the spectrum towards the star HD37043. The radio source and the star are separated by $14'$ in the sky, which is equivalent to a linear separation of ~ 0.9 pc at half the distance to the star. The weak HI absorption extends over the velocity spread of the CaII absorption lines, with a distinct absorption feature at $v_{lsr} \sim -15$ km s^{-1}. The broken curve plotted along with the optical depth profile is the model from the Gaussian fitting to the absorption spectrum. The lower panel shows the radial component of Galactic rotational velocity for this direction as a function of heliocentric distance.

HI absorption arises from a cloud much smaller in size compared to the Dwingeloo telescope beam.

Corresponding to the CaII line at +22.68 km s^{-1}, the HI absorption feature at +24 km s^{-1} has a derived $N_{HI} \sim 1.8 \times 10^{20}$ cm^{-2} from the LDS. The implied spin temperature for this cloud is ~ 78 K.

The second radio source NVSS J0536−054 in the same field of view is at an angular distance of $21'$ from the star (corresponding to 1.2 pc at half the distance to the star). Interestingly, even though HI absorption is seen over a wide range of velocities towards this source, the correlation of CaII and HI absorption line positions at higher velocities is poor (Fig. 2). In fact, the high velocity feature at ~ -15 km s^{-1} seen clearly in Fig. 1 is absent in this figure. Obviously, this line of sight is outside the HI absorbing cloud.

HD159561/NVSS J1732+125: The CaII absorption line data obtained from Welty *et al* (1996) indicates three interstellar CaII absorption features, one of which is at a high random velocity of ≈ -14 km s^{-1} (Fig. 3). The background source for the

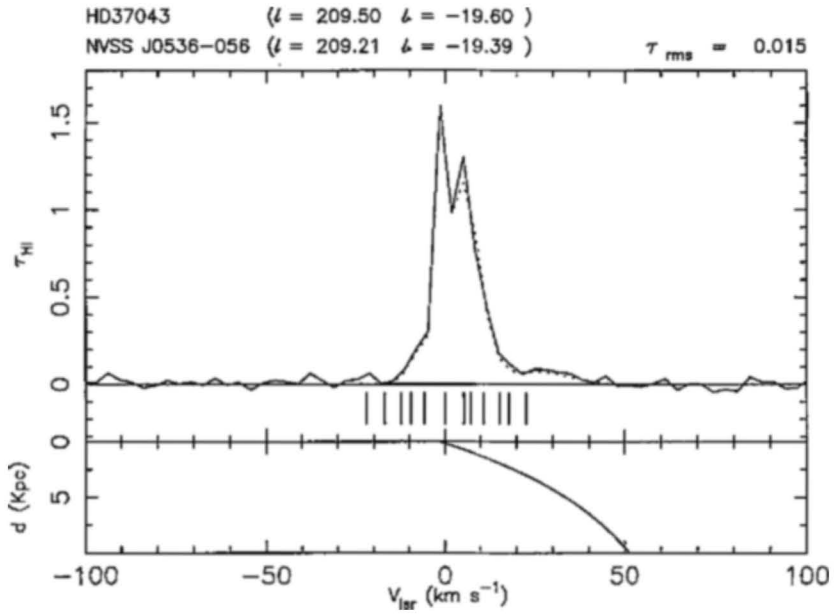

Figure 2. The HI optical depth profile towards the radio source NVSS J0536−054. The radio source is $\sim 21'$ away in projection from the star HD37043 which implies a linear separation of ~ 1.2 pc at half the distance to the star. The high random velocity HI absorption feature at ~ -15 km s^{-1} seen towards the radio source NVSS J0535−057 (Fig. 1) is not detected here.

HI absorption study was NVSS J1732+125, 41 in projection from the star. This angular extent is equivalent to a linear separation of 0.1 pc at half the distance to the star. Multiple gaussian fitting to the HI absorption profile provided 4 components, centered at +24, +12, −0.5 and −13 km s^{-1}. The feature at −13 km s^{-1}, with FWHM of 12 km s^{-1} and a peak optical depth of ~ 0.06 coincides with the CaII absorption line at −14 km s^{-1}. At a longitude of 36^o, this velocity is forbidden by the model of Galactic rotation (Brand & Blitz 1993). Given a distance to the star $\sim$ 14 pc, CaII and the HI absorption should be from a cloud in the local neighborhood. The HI column density estimated from the LDS is $\sim 5.3 \times 10^{19}$ cm^{-2}. This implies a spin temperature ~ 40 K.

HD193322/NVSS J2019+403: The star HD193322 was observed by Adams (1949) for interstellar CaII absorption lines. This direction is at a low Galactic latitude (b $\sim 2^o$) and hence the HI absorption profile towards an extra-galactic radio source can be complicated with a large number of absorption features arising from cold clouds in front of the star as well as from behind it. However it was chosen for our HI absorption study due to the presence of CaII absorption lines at velocities forbidden by the Galactic rotation. The HI absorption was measured towards NVSS J2019+403 which is $28'$ in projection from the star. This angular separation is equivalent to a linear separation of about 1.9 pc at half the distance to the star. The

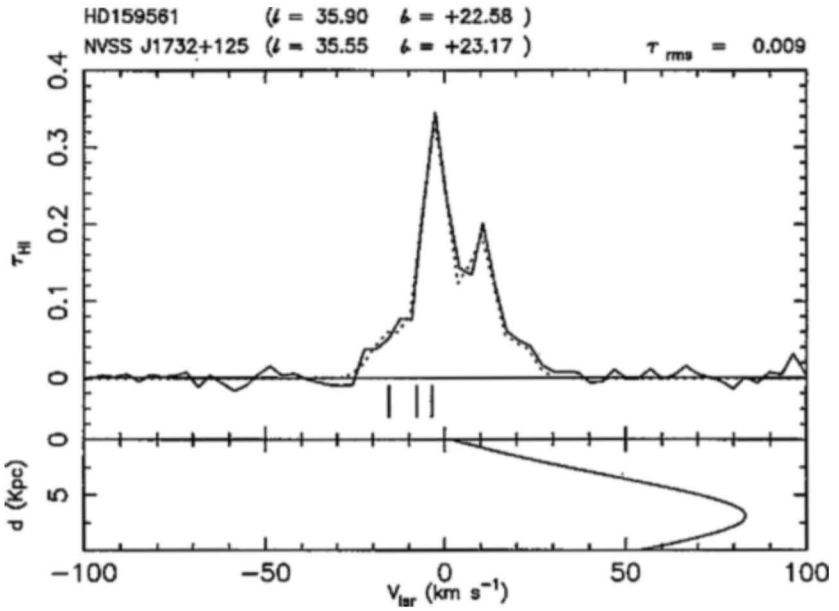

Figure 3. The HI optical depth profile towards the radio source NVSS J1732+125. The vertical tick marks indicate the velocities of the CaII absorption lines in the spectrum towards the star HD159561. The line of sight towards the radio source is separated by $\sim$ 0.1 pc from that towards the star at half the distance to the star. The HI absorption feature at ~ -13 km s^{-1} coincides well with the CaII absorption line. The dotted curve plotted along with the optical depth profile is the model from the gaussian fitting to the absorption spectrum. The lower panel shows the radial component of Galactic rotational velocity in this direction as a function of heliocentric distance.

HI optical depth profile is complicated as expected (Fig. 4). The absorption profile was fitted with 9 gaussian components. There is a prominent component at an LSR velocity of $\approx +24$ km s^{-1} near the CaII absorption component at +21.68 km s^{-1}. The FWHM of this HI absorption feature is ~ 6 km s^{-1} and the peak optical depth is ~ 0.24. The N_{HI} obtained from the LDS is $\sim 2.6 \times 10^{20}$ cm^{-2}, and the HI spin temperature ~ 89 K. However, we failed to detect HI absorption at the velocity of the CaII absorption line at +31 km s^{-1} (Fig. 4).

HD143018/NVSS J1559−262: The CaII absorption data for this star is from Welty *et al* (1996). The interstellar CaII absorption lines exist at negative LSR velocities upto -26 km s^{-1}. Since the star is located at a distance of 141 pc, the radial component of Galactic rotational velocity is only -1.4 km s^{-1} at the distance of the star. Hence, the CaII lines are arising from high random velocity clouds in the interstellar space. The HI absorption was measured towards NVSS J1559−262, $10'$ in projection from the star, which implies a linear separation of 0.2 pc at half the distance to the star. An HI absorption measurement towards an extragalactic

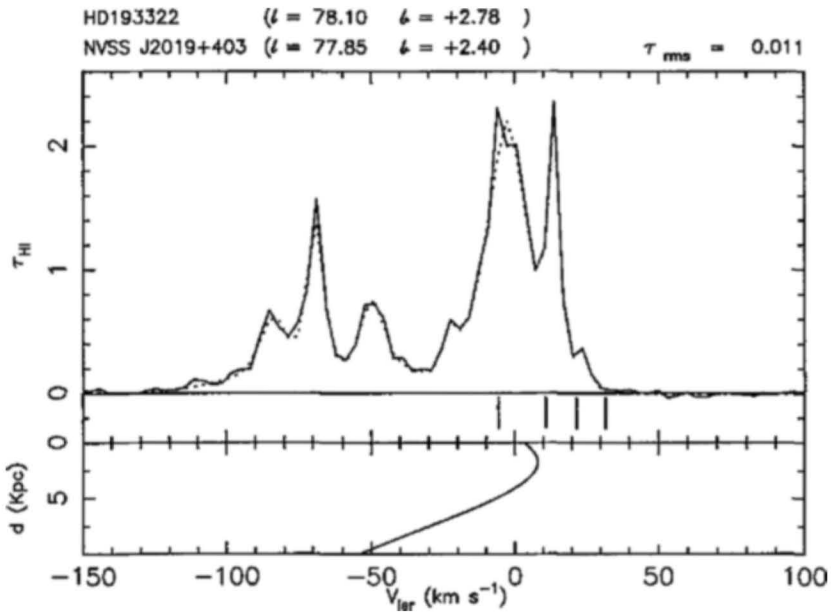

Figure 4. The HI optical depth profile towards the radio source NVSS J2019+403. The vertical tick marks indicate the velocities of the CaII absorption lines in the spectrum towards the star HD193322, which is at an angular separation of $\sim 28'$ from the radio source in the sky. The line of sight towards the radio source is separated by $\sim$ 1.9 pc from that towards the star at half the distance to the star. The CaII absorption line at $\sim$ 23 km s^{-1} has a coincident HI absorption feature. The dotted curve plotted along with the optical depth profile is the model from the gaussian fitting to the absorption spectrum. The lower panel shows the radial component of Galactic rotational velocity in this direction as a function of heliocentric distance.

source would sample gas all along the line of sight, even beyond the star. The HI optical depth profile is shown in Fig. 5. It is clear from the figure that

- There is non-zero HI optical depth at the positions of the high random velocity CaII absorption lines.
- The HI absorption decreases to zero beyond the highest velocity optical absorption line component.
- For the latitude $\sim +20°$, any low random velocity cloud (i.e. a cloud whose radial velocity is mainly due to Galactic rotation) with an LSR velocity of ~ -21 km s^{-1} should be at a distance of about 1 kpc above the Galactic plane, which places it in the Galactic halo. This appears unlikely. It is more likely that this HI cloud is in front of the star and has a high random velocity.

The Gaussian profile fitting provided three components, at velocities -12.5,

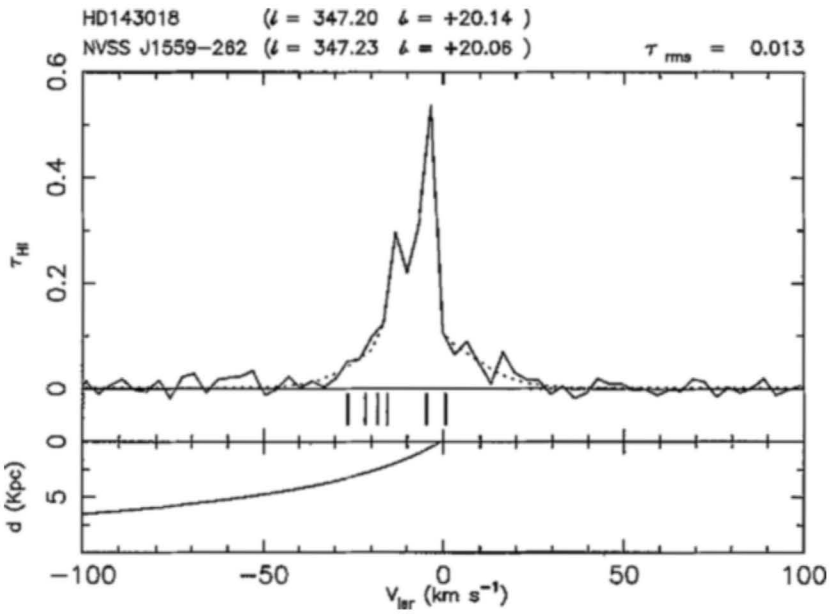

Figure 5. The HI optical depth profile towards the source J1559−262 at a distance of $\sim 10'$ in projection from the star HD143018 The vertical tick marks indicate the velocities of the CaII absorption lines in the spectrum towards the star. The lower panel shows the radial component of Galactic rotational velocity for the direction as a function of heliocentric distance. For the latitude of this direction, any low random velocity cloud at ~ -21 km s^{-1} should be at a distance of about 1 kpc above the Galactic plane, in the Galactic halo. Hence, any HI absorption at these velocities has to be from a nearer cloud with a large random velocity. The dotted curve plotted along with the optical depth profile is the model from the Gaussian fitting to the absorption spectra.

-7 and -4.5 km s^{-1}, with 5, 32 and 3.5 km s^{-1} respectively as the FWHM. The existence of non zero HI optical depth at the velocities of the CaII absorption lines makes this a detection of high random velocity clouds in HI absorption but the poor signal to noise ratio prevented a faithful Gaussian fit to this data. However, the non zero HI optical depth at the positive LSR velocities, extending beyond +20 km s^{-1} demands more attention.

HD24760/NVSS J1400+400: The CaII absorption data was obtained from Welty *et al.* (1996). There are 8 discrete interstellar absorption features seen in the line of CaII, out of which two at LSR velocities of +13 and +16.5 km s^{-1} are at high random velocities. These velocities are forbidden by the Galactic rotation model (Brand & Blitz 1993). The HI absorption towards the radio source NVSS J1400+400, which is $30'$ in projection from the star HD24760 is shown in Fig. 6. The HI optical depth profile indicate a non zero HI optical depth at the position of the CaII absorption line at +13 km s^{-1}, at a level of 0.06. However, as in the

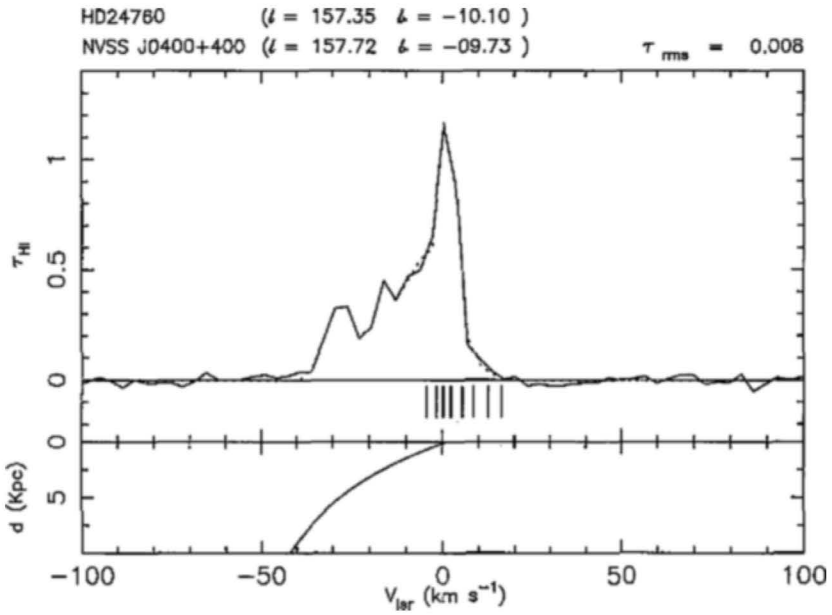

Figure 6. The HI optical depth profile towards the source NVSS J1400+400. This radio source is separated by $\sim 30'$ in projection from the star HD24760. The vertical tick marks indicate the velocities of the CaII absorption lines in the spectrum towards the star. There is a nonzero optical depth at the position of the CaII absorption line at $\sim +13$ km s^{-1}. However the gaussian fitting to the HI absorption data gave no discrete component to this high velocity feature. The dotted curve plotted along with the optical depth profile shows the model from the Gaussian fitting to the absorption spectra.

previous case, the gaussian fitting to this data gave no discrete component to the high velocity feature (see Table 3).

5. Summary and discussion

- We have obtained absorption spectra in the 21cm line of hydrogen in 14 directions which are close to the lines of sight of known bright stars against which optical absorption studies had been done earlier.
- We achieved an optical depth limit of approximately 0.01, which is about ten times better than the previous attempts in this context.
- The angular separation between the line of sight to the star and the line of sight to the radio source is also roughly two times smaller than in the earlier study.
- In 5 out of the 14 directions we have detected HI absorption at (random)

velocities in excess of 10 km s^{-1}. To recall, in their attempt Rajagopal *et al* (1998a) did not detect absorption from these faster clouds.

As mentioned earlier, our selection criteria restricted background radio sources to those with an angular separation from the star less than $\sim 40'$ (implying a linear separation less than ~ 1 pc at half the distance to the star). In the previous 21cm absorption search (Rajagopal *et al.* 1998a) larger angular separations (implying linear separations ~ 3 pc) were included in the sample. Our survey is also considerably more sensitive than that of Rajagopal *et al* (1998a). Four out of the 14 directions observed in this study – the fields containing the stars HD 175754, HD 199478, HD 21278 and HD 37742 respectively – were previously studied by Rajagopal *et al.* (1998a, 1998b). The rms optical depth levels achieved in their study in these directions were 0.09, 0.21, 0.08 and 0.03, respectively. Whereas in our study, these figures are 0.03, 0.015, 0.008 and 0.007, respectively. However, we too failed to detect any HI absorption from the clouds in all these four directions. This is intriguing since the results of our study indicate that about 30% of the high random velocity clouds are detectable (5 detections out of the 14 observed directions) at the sensitivity levels reached in this study ($\tau_{HI} \sim 0.01$). For more than 50% of the directions studied by Rajagopal *et al.* (1998a, 1998b), the rms optical depth level was *above* 0.1. The mean value of peak optical depth for our detections is ~ 0.09. Only one of the fields studied by Rajagopal *et al* (1998a) had the sensitivity level to detect this optical depth.

Earlier we recalled the conclusion by Blaauw (1952) *viz.* the distribution of random velocities of clouds extended beyond ~ 80 km s^{-1}. But this high velocity tail seemed distinct from the rest of the distribution that was well fit by a gaussian with a dispersion of ~ 5 km s^{-1}. Indeed, Blaauw was careful to remark on this. Later 21cm surveys of the Galaxy also yielded, as a byproduct, information about the velocities of the interstellar clouds. Unlike in the optical absorption studies towards relatively nearby stars (with good distance estimates), in the radio observation one did not have reliable distance estimates to the clouds and therefore one could not correct for the Galactic differential rotation to derive a distribution of random velocities. This was remedied by Radhakrishnan & Sarma (1980) who analyzed the HI absorption spectrum towards the Galactic center, for in this particular direction the observed radial velocities of clouds could be unambiguously attributed to random or peculiar velocities. Their analysis clearly showed that the distribution of random velocities could be well fit with a gaussian with a dispersion of 5 km s^{-1}, in excellent agreement with Blaauw's conclusion. Radhakrishnan & Srinivasan (1980) while interpreting the analysis of Radhakrishnan & Sarma (1980) suggested that whereas the narrow gaussian may represent the population of strongly absorbing clouds, there is possible evidence for a second population of weakly absorbing clouds, with a much larger velocity dispersion ~ 35 km s^{-1}. The peak optical depth of this distinct population (if at all one could decompose them into two population) was 0.3. Radhakrishnan & Srinivasan (1980) interpreted these high velocity, low optical depth clouds as those that have been shocked by

supernova remnants. The existence of a high velocity tail in the Galactic center observation has however, remained controversial (see, for example Schwarz *et al* 1982 and Kulkarni & Fitch 1985). Not withstanding this, we wish to assume that Radhakrishnan & Srinivasan (1980) were correct in their inference and ask if the results reported in this paper are consistent with their findings. Let us elaborate on this part. Given the statistics of clouds (the number of clouds per Kpc), and the long path length to the Galactic center, the profile of 21cm optical depth as a function of velocity can straightaway be interpreted as a velocity distribution of clouds. In the present observations, on the other hand, one encounters only a couple of clouds in any given line of sight. But it is worth asking if the optical depth of clouds we have detected with particular velocities is consistent with the optical depth versus velocity profile in the Galactic center observation.

The mean optical depth of our detections is $\tau \sim 0.09$, and the velocities ($|v|$ in the LSR) of the absorption features fall in the range 13 to 26 km s^{-1}. The distances to the stars towards which these detections were made are between 14 and 476 pc, implying a mean distance to the absorbing clouds ≥ 250 pc. The HI optical depth of the wide component discussed by Radhakrishnan & Srinivasan was ~ 0.25 in the velocity range referred above. This value is, of course, for a path length of $\sim$ 8 Kpc to the Galactic center, and would translate to an equivalent optical depth of ~ 0.01 for a distance ~ 250 pc. Such an estimate may be unwarranted in view of the uncertainties in the statistics of clouds. We merely wish to remark that the detections reported in this paper are not inconsistent with the existing data towards the Galactic center. As for the spin temperatures of the clouds we have detected in absorption, a mean value ~ 70 K would suggest that there isn't much difference between the slower and faster clouds at least as far as their spin temperatures are concerned. The tentative conclusion one can draw at this stage is that the much smaller optical depths of the faster clouds might be solely due to their smaller column densities.

Acknowledgements:
We wish to convey our deep gratitude to the large team of people associated with the National Center for Radio Astrophysics in Pune for their sustained and dedicated efforts which resulted in the Giant Meterwave Radio Telescope. We also wish to thank N.V.G. Sarma and his colleagues at the Raman Research Institute, Bangalore for designing and constructing the broad-band 21cm feeds for the GMRT.

References

Adams, W. A., 1949, *Astrophys. J.*, **109**, 354.
Blaauw, A., 1952, *Bull. Astr. Inst. Netherland.*, **11**, 459.
Brand, J., Blitz, L., 1993, *Astr. Astrophys.*, **275**, 67.
Condon, J. J., Cotton, W. D., Greisen, W. E., Yin, Q. F., Perley, R. A., Taylor, G. B., Broderick, J. J., 1996, *Astron. J*, **115**, 1693.
ESA, 1997, *The Hipparcos and Tycho Catalogues*, ESA SP-1200.

Goldstein, S. J., MacDonald, D. D., 1969, *Astrophys. J.*, **157**, 1101.
Habing, H. J., 1968, *Bull. Astr. Inst. Netherland.*, **20**, 120.
Habing, H. J., 1969, *Bull. Astr. Inst. Netherland.*, **20**, 171.
Hartmann, D., Burton, W. B., 1995, *An Atlas of Galactic Neutral Hydrogen*, Cambridge Univ. Press.
Kulkarni, S. R., Fich, M., 1985, *Astrophys. J.*, **289**, 792.
Radhakrishnan, V., Sarma, N. V. G., 1980, *Astron. Astrophys.*, **85**, 249.
Radhakrishnan, V., Srinivasan, G., 1980, *J. Astrophys. Astr.*, **1**, 47.
Rajagopal J., Srinivasan, G., Dwarakanath, K. S., 1998a, *J. Astrophys. Astr.*, **19**, 97.
Rajagopal J., Srinivasan, G., Dwarakanath, K. S., 1998b, *J. Astrophys. Astr.*, **19**, 117.
Routly, P. M., Spitzer, L. Jr., 1952, *Astrophys. J.*, **115**, 227.
Spitzer, L. Jr., 1978, *Physical Processes in the Interstellar Medium.*, New York:Wiley Interscience.
Swarup, G., Ananthakrishnan, S., Kapahi, V. K., Rao, A. P., Subrahmanya, C. R., Kulkarni, V. K., 1991, *Current Science*, **60**, 95.
Schwarz, U. J., Ekers, R. D., Goss, W. M., 1982, *Astron. Astrophys.*, **110**, 100.
Welty, D. E., Morton D. C., Hobbs, L. M., 1996, *Astrophys. J.Suppl.*, **106**, 533.

J. Astrophys. Astr. (2001) **22**, 51–80

Carbon Recombination Lines from the Galactic Plane at 34.5 & 328 MHz

N. G. Kantharia[1]* & K. R. Anantharamaiah [2]†
[1]*National Centre for Radio Astrophysics (TIFR), Pune 411007, India*
[2]*Raman Research Institute, Bangalore 560080, India*

Received 2000 September 14; accepted 2000 November 25.

Abstract. We present the results of a search for carbon recombination lines in the Galaxy at 34.5 MHz (C575α) made using the dipole array at Gauribidanur near Bangalore. Observations made towards 32 directions resulted in detections of lines in absorption at nine positions. Followup observations at 328 MHz (C272α) using the Ooty Radio Telescope detected these lines in emission. A VLA D-array observation of one of the positions at 330 MHz yielded no detection implying a lower limit of 10′ for the angular size of the line forming region.

The longitude-velocity distribution of the observed carbon lines indicate that the line forming regions are located mainly between 4 kpc and 7 kpc from the Galactic centre. Combining our results with published carbon recombination line data near 76 MHz (Erickson, McConnell & Anantharamaiah 1995), we obtain constraintson the physical parameters of the line forming regions. We find thatif the angular size of the line forming regions is $\geq 4°$, then the range of parameters that fit the data are: $T_e = 20 - 40$ K, $n_e \sim 0.1 - 0.3$ cm^{-3}and pathlengths $\sim 0.07 - 0.9$ pc which may correspond to thin photo-dissociated regions around molecular clouds. On the other hand, if the line forming regions are $\sim 2°$ in extent, then warmer gas ($T_e \sim 60 - 300$ K) with lower electron densities ($n_e \sim 0.03 - 0.05$ cm^{-3}) extending over several tens of parsecs along the line of sight and possibly associated with atomic HI gas can fit the data. Based on the range of derived parameters, we suggest that the carbon line regions are most likely associated with photo-dissociation regions.

Key words: Interstellar medium: clouds, lines, line profiles, radio lines.

*e-mail: ngk@ncra.tifr.res.in
†e-mail: anantha@rri.res.in

1. Introduction

Radio recombination lines have been extensively used to investigate the ionized component of the interstellar medium. Recombination lines of hydrogen, helium and carbon have been unambiguously identified in the spectra obtained towards H II regions. Since the ionization potentials of hydrogen (13.6 eV) and helium (24.4 eV) are relatively high, these elements are ionized by the strong UV radiation in the vicinity of O and B stars. Therefore radio recombination lines of H & He generally trace hot ionized regions ($T_e \sim$ 5000–10000 K). On the other hand, the first and second ionization potential of the fourth most abundant element, carbon are 11.4 eV and $\sim$ 24 eV. Carbon is likely to be doubly-ionized inside the H II regions. However, lower energy photons (E $<$ 13.6 eV) which escape from the H II regions can singly-ionize carbon both in the immediate vicinity of the H II region (if the H II region is ionization bounded) as well as in the interstellar clouds which may be farther away. In these regions where hydrogen, helium and oxygen are largely neutral and where carbon and few other elements with lower ionization potential (e.g. sulphur) are singly ionized, the temperatures are likely to be much lower i.e. less than a few hundred K. Radio recombination lines of singly-ionized carbon, thus, generally trace cooler regions of the interstellar medium.

The C II regions detectable in recombination lines can be categorized into two types. The first type are the ionized-carbon regions which occur in the immediate vicinity of some bright H II regions such as W3 and NGC 2024. We shall refer to such regions as classical C II regions since these are carbon Stromgren spheres around a central star. Carbon recombination lines were first detected from such classical C II regions by Palmer *et al.*(1967) at a frequency of $\sim$ 5 GHz and have subsequently been studied at $\nu >$ 1 GHz towards many H II regions using both single dishes and interferometers (e.g. Pankonin *et al.*1977, van Gorkom *et al.*1980, Roelfsema *et al.*1987, Onello & Phillips 1995, Kantharia *et al.*1998a). Carbon recombination lines from classical C II regions are narrow ($4-10$ kms^{-1}) and are sometimes comparable in strength to the hydrogen recombination line observed from the associated hot H II region. Both the narrow width and intensity of the line suggest that the carbon line originates in a cooler ($<$ few hundred K) region where stimulated emission of the background continuum is likely to cause enhanced line emission. Classical C II regions are generally observed in carbon recombination lines at frequencies $\nu \geq$ 1 GHz. To our knowledge no carbon recombination line from classical C II regions has been detected below 1 GHz.

A second class of C II regions, which we will refer to as diffuse C II regions, and which this paper is mainly concerned with, were discovered by Konovalenko & Sodin (1980). Using the UTR-2 low-frequency radio telescope in Ukraine, Konovalenko & Sodin (1980) observed an absorption line at 26.13 MHz in the direction of the strong radio source Cas A. This low-frequency absorption feature was later correctly identified by Blake, Crutcher & Watson (1980) as the C631α recombination line arising in a region at a temperature of $\sim$ 50 K and electron density $\sim$ 0.1 cm^{-3}. The region was tentatively identified with the diffuse neutral H I clouds in

the Perseus arm. Since then, the direction of Cas A has been observed in recombination lines of carbon at frequencies ranging from 14 MHz to 1420 MHz (Payne *et al.*1989, Payne *et al.*1994 and the references therein). The most recent results (Kantharia *et al.*1998b) suggest that the diffuse C II region in the Perseus arm towards Cas A could be at a temperature of ~75 K with an electron density of ~0.02 cm^{-3}, which supports the identification of these regions with neutral H I clouds. Interferometric observations of the spatial distribution of the C272α carbon line (near 332 MHz) over the face of Cas A also supports this association (Anantharamaiah *et al.*1994, Kantharia *et al.*1998b). The low-frequency recombination lines from diffuse C II region towards Cas A exhibit interesting characteristics. The lines which are in absorption below 150 MHz turnover into emission above 200 MHz. Moreover, the width of the lines increase dramatically towards lower frequencies because of pressure and radiation broadening. The variation of line strength and line width with frequency are important diagnostics of the physical conditions in the line forming regions.

If the diffuse C II regions which are detected in low-frequency recombination lines of carbon towards Cas A are associated with the neutral H I component of the interstellar medium, then it may be expected that such low-frequency lines are a widespread phenomenon. Detections have indeed been made in several other directions. Carbon recombination lines were detected in absorption near 25 MHz from the directions of G75.0+0.0 & NGC 2024 by Konovalenko (1984a) and towards L1407, DR21 & S140 by Golynkin & Konovalenko (1991). Anantharamaiah *et al.*(1988) detected absorption lines near 75 MHz towards M16 and the Galactic Center. With hindsight, it now appears that the carbon lines detected in emission near 327 MHz using the Ooty Radio Telescope towards 14 directions in the galactic plane by Anantharamaiah (1985) belong to this category. The first major fruitful search for low-frequency recombination lines of carbon was conducted by Erickson *et al.*(1995) at 76 MHz using the Parkes radio telescope in Australia. Absorption lines of carbon were detected from all the observed positions with longitudes $< 20^\circ$ in the Galactic plane. These observations showed that diffuse C II regions are a common phenomenon in the inner Galaxy.

In this paper, we present observations of recombination lines of carbon around 34.5 MHz made using the low-frequency dipole array at Gauribidanur (which is near Bangalore, India) and around 328 MHz made using the Ooty Radio Telescope (ORT). Out of the 32 directions, most of them in the galactic plane, that were searched at 34.5 MHz, lines were detected in absorption towards nine directions. At 327 MHz, twelve positions were observed and lines were detected in emission towards seven of these. Six of the detected lines are common to 34.5 MHz and 328 MHz. To obtain an estimate of the size of the line-forming region, observations were made with two angular resolutions ($\sim 2^\circ \times 2^\circ$ and $\sim 2^\circ \times 6'$) using the ORT. We also followed up one of the detections with observations near 332 MHz using the D-Configuration of the Very Large Array. All the six directions towards which lines were detected here at 34.5 MHz and 328 MHz, have also been detected at 76

MHz by Erickson *et al.*(1995). In this paper, we combine the results at these three frequencies to constrain the nature of the line forming region.

This paper is organized as follows. In Section 2, the observations at 34.5 MHz using the Gauribidanur dipole array, at 327 MHz using the Ooty Radio Telescope and at 332 MHz using the Very Large Array are described and the results are presented. In Section 3, we obtain constraints on the sizes of the line forming regions using line ratios observed with different angular resolutions. The probable location of the line forming region in the galactic disk is constrained using an $l - v$ diagram of the observed lines. In Section 3, we also derive constraints on the combination of electron density, temperature and radiation field surrounding the line forming region using the variation of line width with frequency. Section 4 is devoted to modelling the line forming region by fitting the observed variation of integrated optical depth with frequency. In Section 5, the results of modelling are discussed in the light of what we know about the interstellar medium. Finally the paper is summarized in Section 6.

2. Observations and Results

2.1 *Gauribidanur observations near 34.5 MHz*

The low-frequency dipole array at Gauribidanur which operates near 34.5 MHz (Deshpande *et al.*1989 and references therein) was used during July–October 1995 to observe several α–transitions (Δn = 1) with principal quantum numbers ranging from n = 570 to 580. The Gauribidanur radio telescope is a meridian transit instrument consisting of 1000 broadband dipoles arranged in a T-shaped configuration. The East-West (EW) arm consists of 640 dipoles, distributed over a distance of 1.38km whereas the North-South arm extends southwards from the centre of the EW arm and consists of 360 dipoles laid over a distance of 0.45 km. The present set of observations were carried out using the EW arm in total power mode, which gave an angular resolution of $\sim 21' \times 25°$ ($\alpha \times \delta$) at zenith. The effective collecting area of the EW arm is $160\lambda^2$ (λ=8.67 m).

The Gauribidanur telescope has limited tracking facility (Deshpande *et al.*1989) which enables the array to track a source with declination δ, for a period of 40secδ minutes about its transit time. Since these low-frequency recombination lines are weak, each position would have required several weeks of observations with the Gauribidanur telescope to reach the desired sensitivity. In order to reduce the total duration of the observations, we employed a multi-line receiver in which eight different transitions with $\Delta n = 1$ near $n = 575$ were observed simultaneously and the spectra averaged. The details of the multi-line receiver and the observing procedure have been described in Kantharia *et al.*(1998b).

The data collected were carefully examined and all those affected by interference were removed. The final spectrum was obtained by averaging all the observed transitions. The spectra are hanning smoothed and therefore have a resolution of 0.5 kHz. The total bandwidth is 32 kHz ($\sim$ 250 kms^{-1}).

Table 1. List of sources that were searched for carbon radio recombination lines at 34.5 MHz.

Position	α(1950)	δ(1950)	Central Vel setting	$\frac{\Delta T_{rms}}{T_{sys}}$	Effective int time
	hh mm ss	° ′ ″	kms^{-1}	$\times 10^{-3}$	hours
G342+00	16 50 34	-43 37 38	-20.0	0.35	63.5
G352+00	17 21 47	-35 37 25	-20.0	0.20	95.3
G00+00	17 42 27	-28 55 00	0.0	0.20	58.7
G05+00	17 54 00	-24 37 59	0.0	0.23	70.3
G10+00	18 04 47	-20 17 51	0.0	0.20	91.3
G14+00	18 12 59	-16 48 00	20.0	0.22	55.0
G16.5+00	18 17 57	-14 36 18	25.0	0.22	68.3
G25+00	18 34 12	-7 05 51	45.0	0.23	78.3
G45.2+00	19 11 44	10 48 50	20.0	0.23	45.8
G50+00	19 21 02	15 02 41	25.0	0.27	108.0
G55+00	19 31 08	19 25 32	25.0	0.23	50.7
G63+00	19 48 31	26 21 12	20.0	0.19	72.0
G75+00	20 19 02	36 26 46	0.0	0.15	188.0
G81+00	20 37 17	41 16 58	25.0	0.31	114.0
G85+00	20 23 08	21 22 05	25.0	0.34	41.7
G97+00	21 42 21	52 56 10	-20.0	0.29	91.5
G99+00	21 52 47	54 11 59	-20.0	0.33	169.5
G100+00	21 58 15	54 48 34	-20.0	0.20	178.3
G125+00	01 06 22	62 31 58	-20.0	0.37	88.8
G130+00	01 48 45	61 47 14	-20.0	0.37	128.5
G145+00	03 34 08	55 24 12	-20.0	0.37	100.0
S 140	22 17 36	63 04 00	-20.0	0.39	24.3
DR 21	20 37 13	42 09 00	0.0	0.35	28.3
Orion	05 32 48	-05 27 00	0.0	0.54	19.7
Cygnus Loop	20 49 30	29 50 00	25.0	0.16	99.8
Cygnus A	19 57 45	40 36 00	0.0	0.23	62.3
W3	02 21 50	61 53 20	-50.0	0.39	238.8
W49	19 08 51	09 02 27	60.0	0.46	42.9
W51	19 20 17	14 02 01	50.0	0.20	69.0
G203.1+2.1	06 38 17	09 43 20	8.0	0.5	12.0
G224.6-2.4	07 01 56	-11 23 55	15.0	0.22	49.1
Rosette Nebula	06 29 18	04 57 00	0.0	0.34	37.5

We observed 32 positions, most of these being in the Galactic plane. Table 1 gives the observational parameters. The observable positions were limited by the transit nature of the Gauribidanur telescope. Within the declination range accessible to the Gauribidanur telescope ($-45°$ to $75°$), the selection of positions was determined partly by the strong Galactic background in the inner Galaxy and partly by the positive results of other low-frequency observations (Konovalenko 1984a, Anantharamaiah 1985, Golynkin & Konovalenko 1991). Carbon recombination lines were detected in absorption from nine of these directions. At such high quantum levels, collisions thermalize the level populations and since the brightness temperature of the non-thermal background radiation field is much higher than the temperature of the thermal gas, the lines appear in absorption. The spectra obtained towards nine of the directions are shown in Fig. 1. The results from a high signal-to-noise ratio spectrum obtained towards Cas A have been presented in a separate publication (Kantharia *et al.*1998b). The peak line-to-continuum ratios observed towards the nine directions shown in Fig. 1 are of the order of a few times 10^{-4}. Gaussians were fitted to the detected spectra and the parameters are listed in Table 2. No lines were detected from the other positions to a 5σ limit of 5.0×10^{-4}. In almost all the cases, only a linear baseline had to be removed to obtain the final spectra.

A relatively strong absorption line of carbon was detected from the direction of the Galactic centre (G00 + 00) as shown in Fig. 1. Carbon recombination lines have been observed from this direction in absorption at 76 MHz (Anantharamaiah *et al.*1988, Erickson *et al.*1995), 42 MHz (Smirnov *et al.*1996) and in emission at 408 MHz (Pedlar *et al.*1978) and 328 MHz (Anantharamaiah 1985, Roshi & Anantharamaiah 1997).

Carbon lines were detected from all the six observed directions in the inner galactic plane ($l = 352°-17°$). This result is similar to that of Erickson *et al.*(1995) who detected carbon recombination lines near 76 MHz from all their observed positions in the longitude range 342° to 20°. We also detected lines near 34.5 MHz from DR 21, G63+00 and G75+00. The lines detected are either at positive velocities or close to 0 kms^{-1} . The line-to-continuum ratios of these lines range from a few times 10^{-4} to 10^{-3} and the width-integrated line-to-continuum ratio ranges from 1.5 to 4 s^{-1}. The lines have widely varying widths with the narrowest lines ($\sim$ 19 kms^{-1}) occurring towards DR 21 and the broadest lines ($\sim$ 54 kms^{-1}) towards G14+00. Erickson *et al.*(1995) have also observed line widths (near 76 MHz) ranging from 5 kms^{-1} to 47 kms^{-1} .

The carbon line observed towards G10+00 appears to be composed of two components. Parameters derived from a double component Gaussian fit to this profile are listed in Table 2. A similar trend is also seen in the profiles towards G05+00 and G14+00. However, the signal-to-noise is not adequate for a double component fit.

The rms noise and the effective integration time on the spectra with no detection are listed in Table 1. The spectra were smoothed to a spectral resolution corresponding to a typical line width ($\sim$ 20 kms^{-1}) and the spectra were again

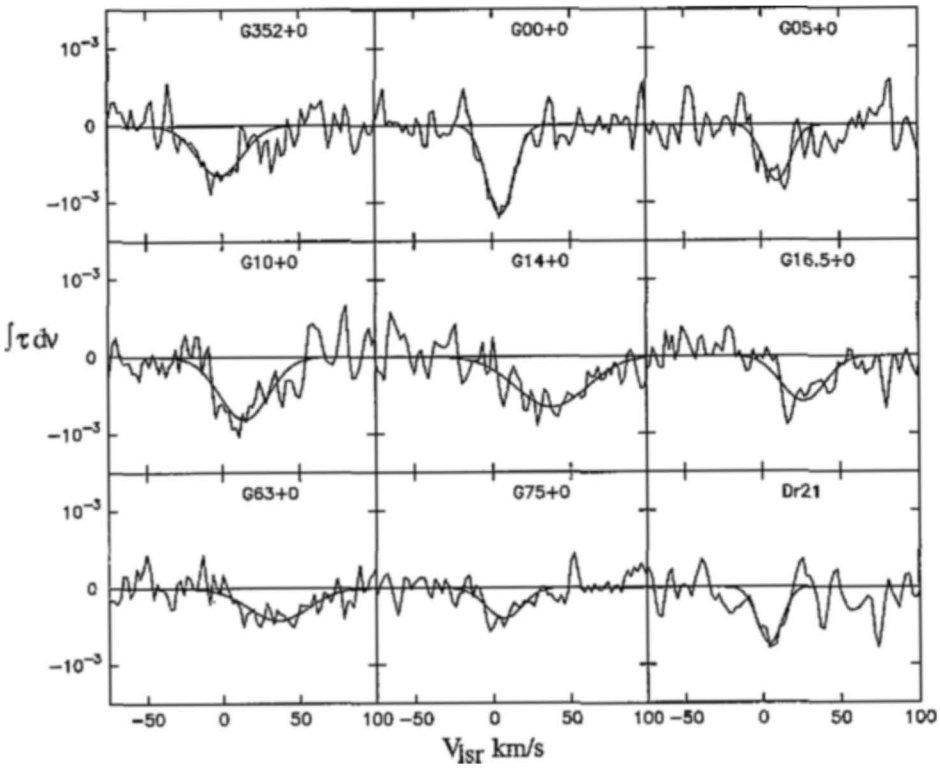

Figure 1. Carbon recombination lines detected near 34.5 MHz ($n \sim 575$). The smooth curve superposed on the observed spectrum is the Gaussian fit to the line profile.

examined for the presence of a spectral feature. A few of the spectra seem to suggest the presence of a weak signal *e.g.*, G342+00, G55+00 and G99+00. However further observations are required to confirm these.

2.2 *Ooty observations near 328 MHz*

The observations with the ORT (Swarup *et al.*1971) were carried out in two sessions: March–April 1995 and October 1995. The ORT is a 30m×530m (EW × NS) parabolic cylinder with an equatorial mount. The length of the telescope along the NS is divided into 11 north and 11 south modules. Since the main aim of these observations was to search for the emission counterpart of the carbon lines seen at 34.5 MHz, a subset of the positions observed at 34.5 MHz were observed with the ORT. Since the size of the carbon line-forming regions is not known, we undertook observations in two modes of operation of the ORT which yielded two different angular resolutions ($\sim 2^\circ \times 6'$ and $\sim 2^\circ \times 2^\circ$ at zenith).

In the first mode, 12 positions were observed with the resolution of the entire telescope (*i.e.* $\sim 2^\circ \times 6'$) whereas in the second mode, 10 of these positions were investigated with the resolution of a single module (*i.e.* $\sim 2^\circ \times 2^\circ$). The telescope

Table 2. Parameters of the lines detected at 34.5 MHz. ΔV is the FWHM. The quoted uncertainties are 1σ.

No.	Source	T_l/T_{sys} $\times 10^{-3}$	V_{lsr} kms^{-1}	ΔV kms^{-1}	$\frac{\int T_l d\nu}{T_{sys}}$ s^{-1}	T_{rms}/T_{sys} $\times 10^{-3}$
1	G352+0	−0.65(0.07)	−1.2(1.8)	34.8(2.6)	−3.3(0.3)	0.21
2	G00+00	−1.16(0.09)	5.3(0.8)	20.5(1.1)	−3.5(0.3)	0.21
3	G05+00	−0.74(0.10)	10.2(1.4)	21.2(2.0)	−2.3(0.3)	0.26
4	G10+00	−0.81(0.08)	14.3(1.7)	37.5(2.5)	−4.3(0.2)	0.29
4a	G10+00	−0.93(0.10)	9.6(1.5)	24.9(2.3)	−4.7(0.4)	0.28
		−0.47(0.11)	40.2(2.6)	18.4(3.7)		
5	G14+00	−0.66(0.07)	37.8(2.7)	54.0(3.8)	−5.1(0.4)	0.22
6	G16.5+0	−0.59(0.07)	26.4(2.0)	32.8(2.8)	−2.8(0.3)	0.22
7	G63+00	−0.42(0.06)	36.2(3.2)	46.0(4.5)	−2.8(0.4)	0.21
8	G75+00	−0.40(0.05)	6.9(1.8)	27.1(2.6)	−1.5(0.2)	0.18
9	DR 21	−0.74(0.13)	4.5(1.6)	18.8(2.2)	−2.0(0.3)	0.26

was used in the total power mode and each position was observed for at least 6 hours. In the higher resolution mode, data are collected simultaneously from two beams (which are labelled beams 5 and 7), separated by 6.6' in declination. Four successive recombination line transitions (C270α to C273α) were observed simultaneously from both the beams using a dual 4-line receiver developed for Galactic recombination line observations (Roshi & Anantharamaiah 2000). The four transitions were averaged to get the final spectra, which on the average have an effective integration time $\sim$ 30 hours. A spectral resolution of 2.1 kms^{-1} was obtained for each band after hanning smoothing. All the lines were detected in emission.

Table 3 shows the observational parameters. On the average, the rms noise on the spectra obtained using the full ORT was $T_{rms}/T_{sys} \sim 2 \times 10^{-4}$ and on the spectra obtained using a single module $T_{rms}/T_{sys} \sim 1.5 \times 10^{-4}$.

Totally, 12 positions (see Table 3) were observed near 328 MHz with the ORT. At the higher resolution, lines were detected from seven of these directions whereas in the low-resolution observations, lines were detected from six directions. The line profiles are shown in Fig 2.

The observed spectra were modelled by Gaussian profiles and the parameters

Table 3. Positions searched for carbon recombination lines at 328 MHz using the ORT.

Source	α(1950)	δ(1950)	Full Telescope		Single Module	
			$\frac{T_{rms}}{T_{sys}}$	t_{eff}	$\frac{T_{rms}}{T_{sys}}$	t_{eff}
	hh mm ss	° ′ ″	10^{-3}	hrs	10^{-3}	hrs
G355+00	17 29 54	-33 08 01	0.19	29.0	0.13	34.7
G00+00	17 42 27	-28 55 00	0.16	23.0	0.11	34.5
G05+00	17 54 00	-24 37 59	0.15	20.5	0.13	34.4
G10+00	18 04 47	-20 17 51	0.17	25.7	0.13	37.1
G14+00	18 12 59	-16 48 00	0.20	19.3	0.19	20.1
G16.5+00	18 17 57	-14 36 18	0.19	33.9	0.15	31.2
G30+00	18 43 29	-02 39 48	0.26	16.0	-	-
G50+00	19 21 02	15 02 41	-	-	0.17	28.2
G62+00	19 46 15	25 29 40	0.19	26.1	0.15	33.9
W49	19 08 51	09 02 27	0.20	20.7	0.17	42.9
W51	19 20 17	14 02 01	0.20	14.5	0.15	26.5
G75+00	20 19 02	36 26 46	0.20	30.7	-	-
NGC2024	05 39 11	-01 55 50	0.20	14.5	-	-

are listed in Table 4. The carbon lines detected in the Galactic plane are broader ($\Delta V \geq 20$ kms^{-1}) and weaker as compared to those detected towards Cas A (Payne *et al.*1989) at this frequency. The lines detected using the full ORT and using the single module had comparable strengths as is evident in Fig 2. No carbon line was detected towards other directions and the rms noise on the spectra are listed in Table 3.

2.3 *VLA observations at 332 MHz*

Observations made with the ORT with two different angular resolutions, provided some preliminary information regarding the angular size of the line-forming region. To obtain constraints on the possible clumpiness of the line-forming gas, we used the VLA to observe the carbon line emission near 332 MHz (270α) towards one of the positions in the Galactic plane which was detected with the ORT. The direction towards Galactic longitude 14° in the Galactic plane was observed for 4.5 hours in June 1995 using the D-configuration of the VLA. Details of this observation are given in Table 5. An amplitude calibrator was observed at the start of the observations. The phase calibrator which was also used for bandpass calibration, was observed once every 30 minutes. The four-IF mode of the correlator which consisted of two circular polarisations (Stokes RR and Stokes LL) and two IF frequencies, was used. Two recombination line transitions (270α & 271α) were observed simultaneously.

Table 4. Parameters of the carbon lines observed with the ORT. ΔV is the FWHM of the line. The numbers in the brackets are the 1σ uncertainty.

Source	T_l/T_{sys} $\times 10^{-3}$	V_{lsr} kms^{-1}	ΔV kms^{-1}	$\frac{\int T_l d\nu}{T_{sys}}$ s^{-1}
		ORT Beam 7		
G355+0	0.2(0.02)	-17.6(3.0)	45.0(7.1)	10.5(2.5)
G00+00	0.65(0.07)	-3.4(0.5)	18.7(1.1)	14.2(2.6)
G05+00	0.4(0.03)	10.7(0.8)	24.2(1.9)	11.1(1.0)
G10+00	0.3(0.02)	20.1(1.3)	32.8(3.0)	11.1(1.2)
G14+00	0.3(0.02)	27.7(1.0)	31.9(2.3)	10.9(0.9)
G16.5+0	0.2(0.02)	32.7(2.3)	39.1(5.3)	9.1(2.3)
G30+00	< 0.15	-	6.2	< 1.1
W49	0.3(0.06)	42.2(1.5)	30.7(3.6)	10.7(2.4)
W51	< 0.12	-	6.2	< 1.1
G62+00	< 0.14	-	6.2	< 1.2
G75+00	< 0.12	-	6.2	< 1.1
NGC2024	< 0.11	-	6.2	< 1.1
		ORT Beam 5		
G355+0	0.2(0.04)	-8.8(1.9)	21.9(4.4)	5.1(2.5)
G00+00	0.61(0.07)	-4.1(0.5)	20.6(1.1)	14.8(1.8)
G05+00	0.5(0.03)	12.3(0.6)	19.0(1.4)	10.9(0.9)
G10+00	0.4(0.02)	20.3(0.8)	29.9(2.0)	13.7(1.1)
G14+00	0.5(0.06)	24.6(1.7)	32.7(3.9)	18.8(1.2)
G16.5+0	0.45(0.1)	20.3(1.4)	11.4(3.3)	6.5(0.8)
G30+00	< 0.20	-	6.2	< 1.5
W49	< 0.17	-	6.2	< 1.2
W51	< 0.14	-	6.2	< 1.2
G62+00	< 0.13	-	6.2	< 1.1
G75+00	< 0.19	-	6.2	< 1.4
NGC2024	< 0.11	-	6.2	< 1.1
		ORT Single Module		
G355+0	0.3(0.02)	0.8(0.7)	20.1(1.7)	6.9(0.7)
G00+00	0.43(0.05)	0.5(0.6)	27.0(1.5)	13.5(1.8)
G05+00	0.52(0.02)	8.2(0.4)	16.2(0.9)	9.8(0.6)
G10+00	0.26(0.02)	21.7(1.2)	36.3(2.9)	10.7(1.0)
G14+00	0.2(0.04)	36.5(3.7)	54.6(8.7)	12.7(4.1)
G16.5+0	0.48(0.07)	20.0(0.8)	12.7(2.0)	7.0(0.6)
W49	< 0.10	-	6.2	< 1.0
G50+00	0.2(0.02)	50.5(1.9)	35.4(4.6)	8.3(2.5)
G62+00	<0.42	-	8.0	<3.7

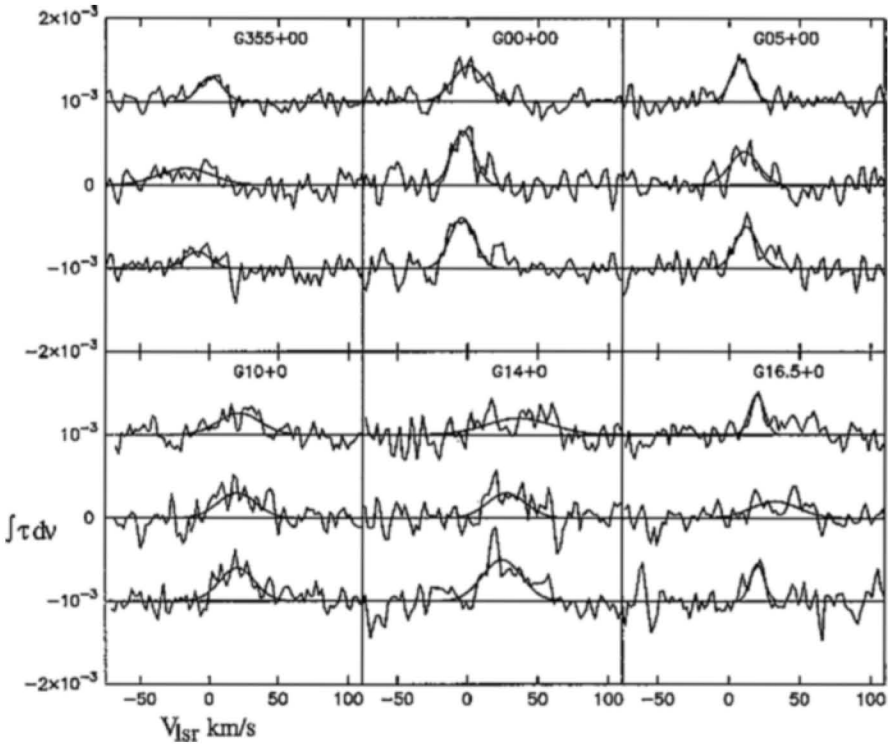

Figure 2. Spectra of carbon lines detected near 327 MHz using beam 5 and beam 7 of the full ORT and using a single module of the ORT are shown. In each frame, the lowermost spectrum is from beam 5 and uppermost is from a single module. These two spectra are offset along the y-axis from their zero-position. The vertical scale applies to all these spectra. The jagged line is the observed spectrum and the smooth line superposed on it is the Gaussian fit to the profile.

The UV data were processed using the standard procedures in the Astronomical Image Processing System (AIPS) developed by NRAO. The continuum image was generated by averaging the visibilities in the central three-quarters of the band. Natural weighting of the data gave a beam size of $5.4' \times 3.5'$ with P.A.$= 1.5°$. A line cube was obtained by Fourier transforming the residual visibilities after subtracting the continuum. To obtain the maximum possible signal-to-noise ratio, natural weighting was applied to the visibilities. Although we aimed at achieving an rms noise of 7-8 mJy/beam in the line images, severe problems due to interference forced us to discard more than 50 % of the data. The rms noise on the line images that we finally obtained was 25 mJy/beam.

The $2°$ field centred on $l = 14°, b = 0°$ which was imaged using the VLA at 332 MHz is shown in Fig. 3 (a). The rms noise in the image is 150 mJy/beam.

Table 5. Parameters of VLA observations.

Field Centre: α(1950)	$18^h12^m59^s$
δ(1950)	$-16°48'03''$
Observing Epoch	June 1995
Duration of Observations	4.5 hours
Observed Transitions	270α, 271α
Rest Frequencies (Carbon)	332.419 MHz
	328.76 MHz
Primary Beam	150'
Shortest spacing	0.035 km
Longest spacing	1.03 km
Observing Mode	4IF
Total bandwidth	781 kHz
	(693 kms^{-1})
Number of Channels	64
Frequency Resolution	12.207 kHz
Velocity Resolution	11 kms^{-1}
Amplitude Calibrator	3C286
Phase Calibrator	1827-360
Bandpass Calibrator	1827-360
Synthesized beam	321.4"×209"
(natural weighting)	
Rms noise, line	25 mJy/beam
Rms noise, continuum	150 mJy/beam

M17 (the bright source at the bottom-left corner of the image), a HII region, is the brightest source in the 2° field with a peak brightness of 40 Jy/beam. The central regions of this nebula are optically thick at low frequencies. The observed brightness temperature at 330 MHz indicates an electron temperature of 7885 °K for the peak emission of M17. which is comparable to the value 8000 K obtained by Subrahmanyan & Goss (1996). Counterparts of other features in Fig. 3 (a) are identifiable on the 5 GHz (Altenhoff *et al.*1979) and 2.7 GHz (Reich *et al.*1990) continuum maps.

The line images showed no emission to a 3σ limit of 75 mJy $beam^{-1}$. In Fig. 3 (b), the line emission integrated over the ORT beam and divided by the integrated continuum flux (19 Jy) is shown. No line emission is seen in the spectrum and the upper limit on the line-to-continuum ratio of carbon and hydrogen lines is 7.8×10^{-3} (3σ limit). This upper limit is consistent with the ORT results. The VLA observations place a lower limit of 10′ on the size of 'clumps', if any, in the ORT beam. This inference follows from a comparison of the results by Anantharamaiah (1985) who detected the C272α line with a peak flux of 160 mJy using a $2° \times 6'$

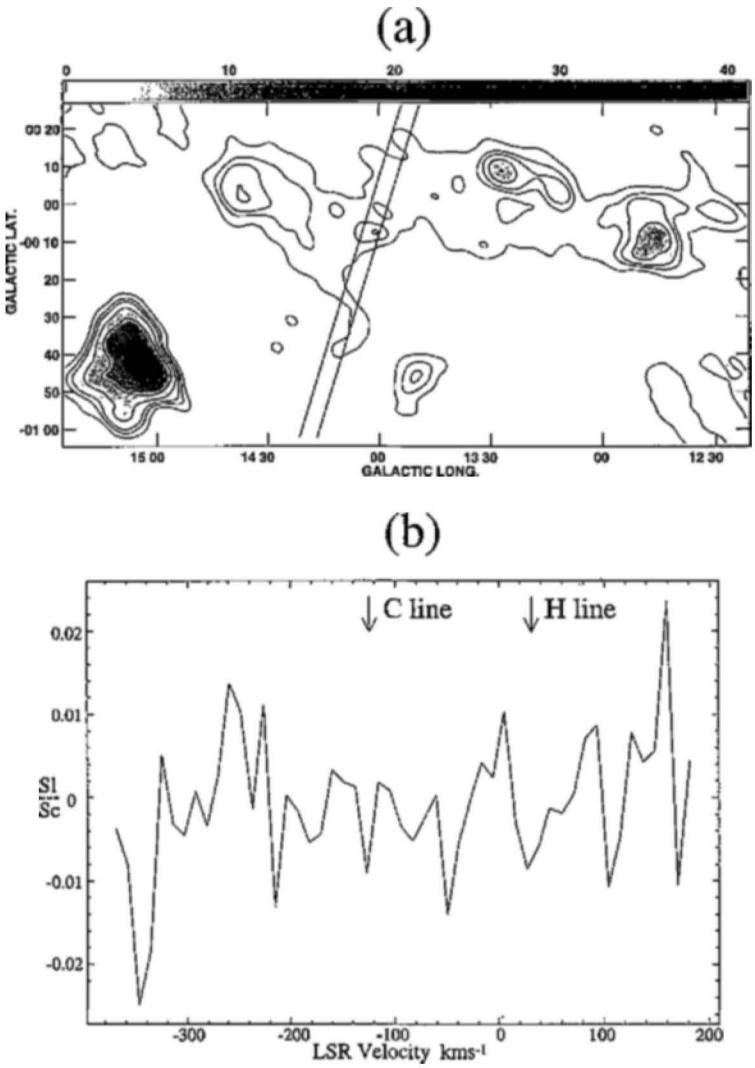

Figure 3. (a) VLA Continuum Image of G14+00 at 330 MHz in Galactic coordinates. The contour levels are 1,3,5,10,20,50,100,110 in units of 0.4 Jy/beam and the grey scale flux ranges from 0 to 41 Jy/beam. The full-ORT beam has been superposed on the continuum map. (b) Spectrum showing the line emission over the full-ORT beam. The arrows show the expected positions of the carbon and hydrogen recombination lines.

beam and the 3σ detection limit of 75 mJy obtained from the present VLA data with a beam of $5.4' \times 3.5'$.

3. Constraints on the physical properties of the carbon line regions

3.1 *Angular size of the line forming regions*

Since the interpretation of the observed recombination lines, in terms of the physical properties of the gas in which they arise, depends sensitively on the fraction of the beam that is filled by the thermal gas, it is necessary to obtain a preliminary idea of its angular distribution. Our observations have been made at different angular resolutions ranging from $21' \times 25°$ at 34.5 MHz to $2° \times 2°$ at 328 MHz and we also make use of the line data at 76 MHz (Erickson *et al.*1995) with a resolution of $4° \times 4°$. Unless the line radiation fills the beam or the distribution of the continuum intensity is highly concentrated and dominates the system temperature (*e.g.* Cas A), beam dilution effects will be significant, and the actual line optical depths will be very different from the apparent (observed) optical depths. Comparison of the line-to-continuum ratios integrated over the width, observed with the two different angular resolutions at 328 MHz (see Table 4) shows that, within the errors, the two ratios are almost equal for most of the positions. This equality indicates that the angular extent of the cloud giving rise to these lines in the inner Galaxy is $\geq 2°$ for most lines of sight. However, the possibility that the line-forming regions are made of a number of nearly uniformly distributed clumps within the field of view is not ruled out by the ORT observations. The VLA observations have placed a lower limit of $10'$ on the size of 'clumps', if any, in the ORT beam.

From their observation of carbon lines near 76 MHz as a function of Galactic latitude, Erickson *et al.*(1995) concluded that the angular extent of the carbon line-forming regions in the inner Galaxy must be approximately 4°. Very low-frequency (near 25 MHz) observation towards $l = 75°$ in the Galactic plane (Konovalenko 1984a) has also indicated that the carbon line-producing region is $\geq 4°$ in extent.

Thus, from the existing observational data on low-frequency carbon recombination lines, it appears that the ionized carbon gas is distributed in form of clouds or clumps with individual sizes $> 10'$ and with an overall extent of at least a few degrees.

3.2 *Constraints from the observed line widths*

One notable difference between the carbon lines observed towards Cas A and the lines observed from positions in the Galactic plane is the width of the lines (Table 6). While the lines detected towards Cas A (last row of Table 6) are seen to broaden with increase in quantum number, which is a clear indication of pressure & radiation broadening, no such trend is seen in the lines observed from the Galactic plane.

The lack of $n-$dependent line broadening towards the Galactic plane seems to

Table 6. Widths of carbon recombination lines observed at different frequencies.

Position	n∼686 25 MHz kms^{-1}	n∼575 34.5 MHz kms^{-1}	n∼443 76 MHz kms^{-1}	n∼271 328 MHz kms^{-1}
G352+0	-	36.4(3.6)	11(1)	20.1(1.7) (G355+00)
G00+00	-	20.5(1.2)	24(1)	27.0(1.5)
G05+00	-	21.0(2.5)	25(4) (G06+00)	16.2(0.9)
G10+00	-	37.0(3.2)	26(2)	36.3(2.9)
G14+00	-	56.0(4.5)	25(3)	54.6(8.7)
G16.5+0	-	32.6(3.4)	47(4)	12.7(2)
G63+00	-	45.9(4.4)	-	-
G75+00	15(0.9)[1]	24.4(2.8)	-	-
DR21	42(12)[2]	18.5(2.7)	-	-
Cas A	71.9(16.4)[3]	26.0(3.1)	6.7(0.4)[4]	5.0(0.5)

[1] From Konovalenko (1984a).
[2] From Golynkin & Konovalenko (1991).
[3] From Konovalenko (1984b).
[4] From PAE89.

indicate that lower electron densities and weaker ambient radiation fields prevail here compared to those in front of Cas A. However, the observed widths ($\geq$ 20 kms^{-1}) of the lines from the Galactic plane cannot be explained by thermal motions and micro-turbulence ($\sim$ few kms^{-1}) in the cool clouds. We suggest that the lines are broadened by the systematic motions owing to differential Galactic rotation and hence lack an $n-$dependence.

Since pressure (ΔV_P) and radiation (ΔV_R) broadenings are expected to be maximum at 34.5 MHz, the line widths at this frequency can be used to derive upper limits on the electron density and the ambient radiation field. We used Equations (1) and (2) from the paper by Shaver (1975) for deriving the limits which are listed in Table 7; and we reproduce them below for ready reference

$$\Delta V_P = 2 \times 10^{-8}\, exp\left(-\frac{26}{T_e^{1/3}}\right) \frac{n_e n^{5.2}}{T_e^{1.5}} \frac{c/(kms^{-1})}{\nu/(kHz)} \quad \text{kms}^{-1} \qquad (1)$$

$$\Delta V_R = 8 \times 10^{-20}\, W_\nu\, T_{R,100}\, n^{5.8} \frac{c/(kms^{-1})}{\nu/(kHz)} \quad \text{kms}^{-1} \qquad (2)$$

where ΔV_P and ΔV_R are the FWHM due to pressure and radiation broadening (kms$^-$1), T_e is the electron temperature (K), n_e is the electron density (cm^{-3}), n is the quantum number, c is the velocity of light (kms^{-1}), ν is the frequency (kHz), W_ν is the dilution factor, $T_{R,100}$ is the radiation temperature (K) at 100 MHz.

Table 7. Upper limits on the electron density and radiation temperature (at 100 MHz) from the observations at 34.5 MHz.

Position	ΔV_{obs} kms^{-1}	$n^1_{e,max}$ cm^{-3}	$T^1_{R100,max}$ K	T^2_{R100} K	ΔV^3_{exp} kms^{-1}
G352+00	36.4(3.6)	1.21(0.12)	5160(510)	3460	24.4
G00+00	20.5(1.2)	0.68(0.04)	2906(170)	5030	35.5
G05+00	21.0(2.5)	0.7(0.08)	2977(354)	5030	35.5
G10+00	37.0(3.2)	1.23(0.11)	5245(454)	5660	40.0
G14+00	56.0(4.5)	1.86(0.15)	7938(638)	5660	40.0
G16.5+0	32.6(3.4)	1.08(0.11)	4621(482)	5030	35.5
G63+00	45.9(4.4)	1.51(0.15)	6507(624)	2830	20.0
G75+00	24.4(2.8)	0.81(0.09)	3459(370)	2830	20.0
DR21	18.5(2.7)	0.61(0.09)	2622(383)	2680	19.0

[1] Upper limit derived from the observed line width at 34.5 MHz and using $T_e = 20$ K and $W_\nu = 1$.
[2] Averaged value over the Gauribidanur beam of 25° obtained from the continuum map at 34.5 MHz (Dwarakanath 1989) and extrapolated to 100 MHz using a spectral index $\alpha = 2.6$ where $T_B \propto \nu^{-\alpha}$.
[3] Expected line broadening at 34.5 MHz due to T_{R100} noted in column 6 and assuming $W_\nu = 1$.

The widths listed in Table 7 were calculated assuming that the entire width is due to either of the broadening mechanisms. The upper limits on the electron density in the medium were calculated for a nebula at 20 K.

The insignificant contribution of pressure and radiation broadening to the line width at 34.5 MHz indicates that the actual electron densities and radiation fields are much smaller than those listed in columns 4 and 5 of Table 7. Furthermore, the electron density decreases if the kinetic temperature is increased *e.g.* the values of n_e noted in column 4 will decrease by a factor of ~ 4 if T_e increased to 75 K. The derived upper limit for the radiation temperature in the Table assumes a dilution factor of unity which implies that the absorbing cloud is isotropically illuminated by the non-thermal radiation field. The actual radiation temperature seen by the cloud could be equal to or less than the values listed in column 6, which were obtained from the $26' \times 42'$ continuum map of Dwarakanath (1989) at 34.5 MHz. The widths of the carbon lines near 34.5 MHz as predicted by this radiation field are listed in column 7.

The limits listed in Table 7 are useful because they define the absolute boundaries of the parameter space that we use for modelling the observed recombination lines.

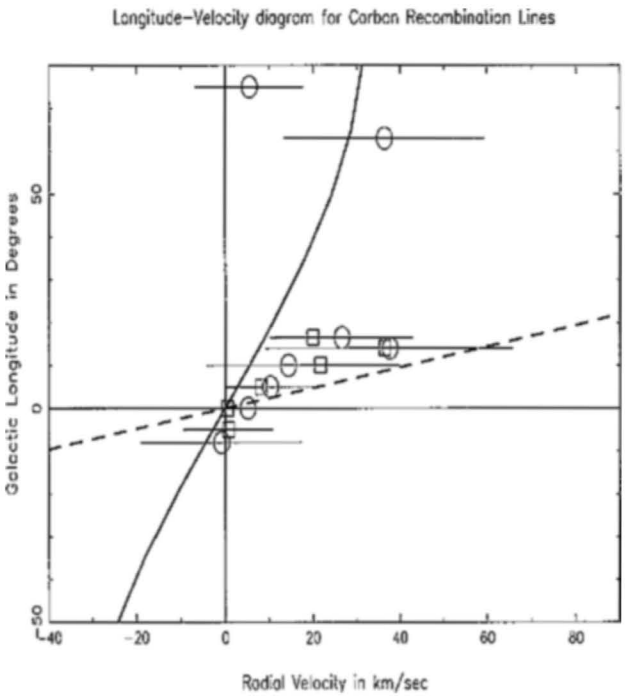

Figure 4. The Longitude-Velocity diagram of the carbon recombination lines at 34.5 MHz(circles) and 328 MHz(squares) from the Galactic plane. The horizontal lines about each point represent the observed widths of the lines. The solid line shows the variation of the radial velocity with longitude for a cloud placed at a Galactocentric distance of 7.5 kpc whereas the dashed line shows the expected l-v plot for a cloud at a distance of 4 kpc. These are obtained using the Galactic rotation model of Burton (1988).

3.3 *Longitude-Velocity diagram*

The l-v diagram for the carbon recombination lines observed at 34.5 and 328 MHz is shown in Fig. 4. The Galactic rotation model by Burton (1988) has been used. The kinematic nature displayed by gas at Galactocentric distances of 7.5 kpc (solid line) and 4 kpc (dashed line) is also shown in the figure.

All the observed points with $l > 0°$ lie between 4 and 7.5 kpc. This range coincides with the regions observed to be rich in molecular clouds (Scoville & Solomon 1975), H166α emission (Lockman 1976) and strong H II regions (Downes *et al.*1980). Broad lines of H I emission (Burton 1988) and absorption (Garwood & Dickey 1989), ^{12}CO (Bania 1977), H166α (Lockman 1976) and [C II] 158 μm (Mizutani *et al.*1994) emission are observed towards the Galactic centre. These broad (> 100 kms^{-1}) lines are due to non-circular motions near the Galactic centre. However, the low-frequency carbon recombination lines observed by us are relatively narrow (~ 20 kms^{-1}). The hydrogen recombination lines near 327 MHz observed by Anantharamaiah (1985) and Roshi & Anantharamaiah (1997) are also relatively narrow. Excluding the Galactic centre direction, the l-v distribution of

the carbon lines that we observe resembles that traced by H I absorption, diffuse H II (Lockman *et al.*1996) and ^{12}CO (except for the features due to the 3 kpc arm). Erickson *et al.*(1995) have a more continuous sampling of carbon lines near 76 MHz ($n \sim 445$) in the inner Galaxy and they also find that the gas responsible for the lines lies between galactocentric distances of 5 and 8 kpc. With the available data, we can only say that the gas giving rise to carbon lines in the inner Galaxy is likely to be distributed between galactocentric distances of 4 and 8 kpc and is likely to be associated with either the cold H I gas, or the molecular gas or the H II regions. From the similarity of the $l-v$ distributions of the emission lines observed near 328 MHz and the absorption lines detected near 34.5 MHz and 76 MHz from the inner Galaxy ($l < 17°$), we assume that all these lines arise in the same ionized carbon gas.

3.4 *Origin of carbon lines in cold, neutral gas*

Although the widths of the observed lines do not rule out an origin in classical H II regions, the low electron densities (previous section) and the absence of hydrogen recombination lines at low frequencies rule out such an origin. Hence, the lines are most likely associated with cold gas where only carbon is ionized. The possibilities are either the atomic H I gas (the cold neutral medium), the molecular gas or the low-excitation photodissociation regions in the interstellar medium. Interpretation of low-frequency recombination lines observed towards the direction of Cas A has shown that these lines are most likely to be associated with atomic H I gas. However, the different pressure and radiation broadening seen in the low-frequency lines observed from Cas A and the Galactic plane suggests that detectable low-frequency lines may arise in regions with a range of physical properties. In a review paper, Sorochenko (1996) discusses Cas A and other such directions towards which carbon lines have been detected and concludes that C II regions are formed on the surface of molecular clouds exposed to external ionizing UV radiation either close to H II regions or around isolated molecular clouds.

4. Modelling the line-forming regions

4.1 *Assumptions of the model*

We assumed a cloud of uniform density n_e , temperature T_e and emission measure EM illuminated by a non-thermal radiation field characterized by a brightness temperature T_{R100} at 100 MHz. Although this is a simplified model and the real cloud is likely to contain density condensations, it can be used to derive the average properties of the medium under consideration. The solution of the radiative transfer equation is (Shaver 1975):

$$T_l = T_\circ \left[e^{-\tau_c}(e^{-b_n\beta_n\tau_l^*} - 1)\right] + T_e \left[\frac{(b_n\tau_l^* + \tau_c)}{\tau_l + \tau_c}(1 - e^{-\tau_l+\tau_c}) - (1 - e^{-\tau_c})\right]. \quad (3)$$

In Equation (3), T_l is the line temperature, $T_\circ$ is the background temperature, T_e is the electron temperature, τ_c is the continuum optical depth at the given frequency, τ_l^* is the LTE line optical depth, τ_l is the non-LTE line optical depth and b_n and β_n are the departure coefficients which measure the deviation of the level populations from LTE values. Further simplifying assumptions which approximate the real system are made. At low frequencies, the lines are sensitive to tenuous, cool nebulae *i.e.* $T_e << T_\circ$. Since $\tau_c, \tau_l << 1$ at these frequencies, the second term in the above equation is much smaller than the first term and can be neglected. Hence, the line temperature can be expressed under these conditions as:

$$T_l = T_\circ \left[e^{-\tau_c}(e^{-b_n\beta_n\tau_l^*} - 1)\right]. \quad (4)$$

Since $T_c = T_\circ\, e^{-\tau_c}$ and $\tau_c << 1$, the line-to-continuum ratio can be approximated as

$$\frac{T_l}{T_c} = -b_n\beta_n\tau_l^* = -\tau_l. \quad (5)$$

The departure coefficients b_n and β_n quantify the non-LTE effects influencing the level populations. The true population of a level n is given as $N_n = b_n N_n^*$ where N_n^* is the expected LTE population. $\beta_n = 1 - \frac{kT_e}{h\nu}\frac{d(lnb_n)}{dn}$ depends on the gradient of b_n with n. A negative value of β_n signifies inverted populations and hence stimulated emission. A positive value of β_n means that the line at that frequency is likely to appear in absorption if the background temperature $T_\circ > T_e$. The RHS of Equation (5) is the non-LTE value of the line optical depth.

Rewriting Equation (5) in terms of antenna temperatures:

$$\tau_l = \frac{\Omega_c}{\Omega_L}\,\frac{T_{A,l}}{T_{A,c}} \quad (6)$$

where Ω_c, Ω_l are the solid angles subtended by the continuum and the line-forming regions. $\Omega_c, \Omega_l \leq \Omega_B$ where Ω_B is the solid angle subtended by the telescope beam. $T_{A,l}$ and $T_{A,c}$ are the line and continuum antenna temperatures. At 34.5MHz, the non-thermal background radiation dominates the continuum temperature. Since this background is all-pervasive in the Galaxy, $\Omega_c \geq \Omega_B$ and the main factor responsible for the unknown beam dilution factor is the extent of the line-forming gas within the observing beam.

At low frequencies, line-widths are likely to be affected by various n-dependent line broadening mechanisms, leading to reduction in the peak optical depths and increased widths. Therefore, the integrated optical depth is the correct physical quantity to compare at different frequencies. Theoretically, the integral of the line optical depth can be written as (Payne *et al.*1994):

$$\int \tau_l d\nu = 2.046 \times 10^6 \; T_e^{-5/2} e^{\chi_n} \; EM_l \; b_n \beta_n \quad s^{-1}. \tag{7}$$

Using this Equation, we attempt to fit the observed variation in the integrated optical depth given by Equation (5) with principal quantum number for plausible combinations of T_e and n_e .

4.2 *The modelling procedure*

We use carbon line observations at three frequencies to model the C II regions– our observations at 34.5 MHz and 328 MHz and the Parkes observations by Erickson *et al.*(1995) at 76 MHz. The angular resolution of these observations are different. We assume that the lines at the three frequencies arise in the same gas.

Each model is characterized by an electron temperature T_e, electron density n_e, emission measure EM, radiation temperature T_{R100} , carbon depletion factor δ_C and the angular size of the line-forming region. As discussed earlier, the upper limits on T_{R100} and n_e were determined from the widths of the lines observed at 34.5 MHz. We consider a range of possible temperatures for the line-forming region which include the typical temperatures of cold H I, H_2, and photo-dissociation regions which are all probable places of origin for the carbon lines. The lower limit on the electron densities is set from the maximum pathlengths through the Galaxy. We considered models with a carbon depletion factor of 0.5. Since observations indicate that the line-forming region could have an angular size $\geq 2°$, we explore models in which the line-forming region is (a) ubiquitous (*i.e.* fills all the beams that are used); (b) 4° and (c) 2°. The departure coefficients b_n and β_n which account for the non-LTE effects were calculated using the computer code, originally due to Salem & Brocklehurst (1979) and later modified by Walmsley & Watson (1982) and Payne *et al.*(1994).

The model integrated optical depths are calculated for different n using Equation (7) and the models are normalized to the observed integrated optical depth at 328 MHz. The ratio of line temperature to system temperature is considered to be equivalent to the line-to-continuum ratio, since the system temperature is dominated by the strong sky background at these low frequencies. Any model that we generate needs to satisfy the observed integrated optical depth $\frac{\int T_l d\nu}{T_{sys}}$ and be consistent with the upper limits on the physical conditions placed by the line data at 34.5 MHz. Since the observed width of the line is independent of frequency, we assumed that the contribution to the width at 34.5 MHz due to pressure broadening is < 5 kms^{-1} . This assumption translated to an upper limit on the electron density of 0.3 cm^{-3}. The lower limit was 0.001 cm^{-3}. The electron temperature space was varied from 20 K to 400 K. These models were generated for two values of the radiation temperature at 100 MHz which were 1250 K and 2500 K.

The non-LTE population is calculated assuming that the quantum levels are in statistical equilibrium so that the rate of population of a level n due to all possible physical processes is equal to the rate of depopulation of that level (Shaver 1975).

The main physical processes which determine the level populations are collisional and radiative excitation and de-excitation. The departure coefficients are calculated by solving a series of differential equations after imposing a boundary condition $b_n \rightarrow 1$ as n $\rightarrow \infty$ (Salem & Brocklehurst 1979) *i.e.* the levels are assumed to be in LTE at very large n. In case of carbon, it is necessary to also consider a dielectronic-like recombination process which significantly influences the high-n populations if the temperatures are around 100 K (Watson *et al.*1980)

4.3 *Results of modelling*

We examine the models which explain the observed variation in the integrated optical depth with frequency. The criteria used to select the possible physical models are (a) the observed behaviour of the integrated optical depth as a function of n, (b) the path lengths through the region which should be $\leq$ 5 kpc, as required by the observed line widths and (c) the turnover from emission to absorption which should occur at $n < 443$ as the lines are observed in absorption at 76 MHz (Erickson *et al.*1995). We classify the results on the basis of the assumed angular size of the line-forming regions. The angular size determines the beam dilution and the scaling from the observed to true optical depth. The data at the three frequencies have different angular resolutions and therefore different beam-filling factors. In all the cases, we assume, for simplicity, that the non-thermal radiation field uniformly fills the beams.

4.3.1 *Case 1: Cloud size > 4° or equal beam coverage by line and continuum*

We found that remarkably similar physical models reasonably explained the observed data towards the six positions in the inner Galaxy. The best-fitting models towards three of the positions, $l = 0°$, $l = 5°$, and $l = 14°$ are shown in Fig. 5 (panels on left) and the parameters are listed in Table 8(a). In all these models, we assumed $T_{R100} = 1250$ K. Similar physical properties were found if $T_{R100} = 2500$ K. All the models were constrained by the data at 328 MHz. The turnover from emission to absorption occurs around $n \sim 400$. We found no model which simultaneously explains the data at 76 MHz and 34.5 MHz, which is most likely due to the unknown beam dilution at 34.5 MHz. The models which explained the observed variation in $\frac{\int T_l d\nu}{T_{sys}}$ with n were within the temperature range $20 - 40$ K. Outside this range, the models predicted large optical depths at 76 MHz and 34.5 MHz. The electron densities in the acceptable models are 0.1 cm^{-3}. Although higher electron densities provided better fits to the data (e.g. the dashed line in Fig. 5 for G00+00 has n_e = 0.3 cm^{-3}), the resulting collisional broadening at 34.5 MHz exceeded the limit of 5 kms^{-1} and hence are not favoured.

The path lengths through the cloud range from 0.07 pc to 0.9 pc suggesting a sheet-like morphology for the regions and the emission measures are $\leq$ 0.01 pc cm^{-6}. Typical pressures in terms of $n_H T_e$ are a few tens of thousands cm^{-3}K,

Table 8. Model parameters for three positions for three assumed cloud sizes. T_{R100} = 1250 K.

Position	T_e K	n_e cm^{-3}	EM $pccm^{-6}$	$Size$ pc	$n_H T_e$ $cm^{-3}K$
		(a) Cloudsize > 4°			
G00+00	40	0.1	0.009	0.9	26680
	20	0.3	0.006	0.07	40000
G05+00	20	0.1	0.002	0.2	13340
	40	0.1	0.007	0.7	26680
G14+00	40	0.1	0.007	0.7	26680
		(b) Cloudsize = 4°			
G00+00	80	0.03	0.019	21.1	16000
	200	0.03	0.079	87.8	40000
G05+00	60	0.05	0.01	4.0	19980
	80	0.03	0.014	15.6	16000
G14+00	80	0.03	0.018	20.0	16000
	100	0.03	0.025	27.8	20000
		(c) Cloudsize = 2°			
G00+00	150	0.03	0.051	56.7	30000
	300	0.03	0.151	167.8	60000
G05+00	150	0.03	0.037	41.1	30000
	200	0.03	0.058	64.4	40000
G14+00	200	0.03	0.075	83.3	40000
	300	0.03	0.142	157.8	60000

which is higher than the average thermal pressure in the interstellar medium. We did not find any model which was in pressure equilibrium with H I. The relatively low temperatures in these models suggest association with molecular clouds.

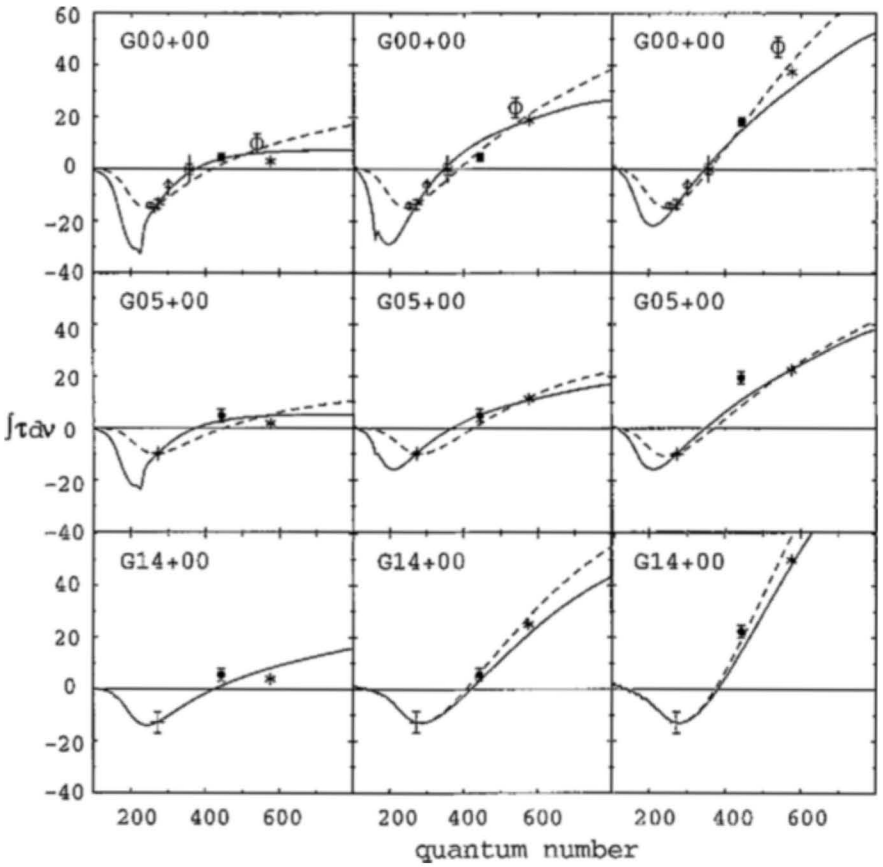

Figure 5. Model fits to observed carbon line data shown for three Galactic plane positions. The unbroken line and broken lines represent the two best-fit models for the two sets of parameters given in Table 8. The left panels show models for clouds assumed to be $\geq 4°$; the centrepanels show model fits for clouds assumed to be $= 4°$; and the panels on the right show models for clouds $= 2°$. Towards G00+00, the $n = 252, n = 300$ points are from Pedlar *et al.*(1978), $n = 356$ is from Anantharamaiah *et al.*(1988) and $n = 530$ is from Smirnov *et al.*(1996).

4.3.2 *Case 2: Cloud size* $= 4°$

These regions, if placed at a radial distance of 3.5 kpc from us, would have a linear size of 250 pc which is comparable to the scale height of the atomic gas. The best-fitting physical models have T_e in the range of $60 - 80$ K, n_e in the range of $0.03 - 0.05$ cm^{-3}, and path lengths range from 4 pc to 30 pc. Fig. 5 (centre panels) shows the models for the positions $l = 0°$, $l = 5°$ and $l = 14°$ and Table 8(b) lists the parameters. All the models are for $T_{R100} = 1250$ K. The turnover from

emission to absorption occurs around $n \sim 400$. The relatively warmer temperatures in these models favour association with atomic H I gas in the Galaxy. However, the thermal pressures are more than 3 times the average interstellar pressure ($n_H T_e \sim$ 5000 cm^{-3}K). There was no change in model parameters with $T_{R100} = 2500$ K except for a slight lowering of quantum number at which the turnover occurs.

4.3.3 *Case 3: Cloud size* $= 2°$

If these regions are placed at a radial distance of 3.5 kpc, then their linear size would be $\sim$ 125 pc. Models for three Galactic plane positions are shown in Fig. 5 (panels on the right) and the parameters are listed in Table 8(c). Best-fitting models have T_e between 150 K and 200 K and the electron density $n_e \sim 0.03$ cm^{-3}. Lower temperatures are possible if the upper limit on the electron density is relaxed i.e. the pressure broadening is > 5 kms^{-1} . The path lengths required by these models ranged from 40 to 170 pc. The models with $T_{R100} = 2500$ K slightly lowered the quantum numbers at which the turnover occurs, but the overall model parameters remained similar.

5. Discussion

The modelling described in the previous sections showed that most of the positions within $l = 352°$ to $l = 17°$ possess remarkably similar physical properties. Quantitatively, if the clouds along the line-of-sight are $> 4°$ in extent, then typically T_e $= 20 - 40$ K, $n_e \sim 0.1$ cm^{-3} and the pathlengths are tiny (< 1 pc). On the other hand, if the cloud is $4°$ in size then it is likely to be at a temperature between 60 and 200 K, with electron density between ~ 0.03 and 0.05 cm^{-3}. The path lengths through these clouds are in the range $4 - 90$ pc. If the cloud subtends an angle of $2°$, then they are likely to have $T_e = 150 - 300$ K and $n_e = 0.03$ cm^{-3} and pathlengths between 40 and 170 pc. All these models are able to reasonably explain the observed variation in the optical depth with n. Since the data is limited and the angular resolution is coarse, it is not possible to derive more stringent constraints on the parameters. It is entirely possible that the observed carbon recombination lines arise in clouds possessing a range of temperatures, electron densities and angular sizes. Here we discuss the plausibility of the above models using qualitative arguments.

The low temperature ($T_e = 20$ K) models give a good fit to the observed line strengths at two frequencies for most positions. If these models correctly explain the physical properties of the line-forming regions then their inability to explain the third data point is probably telling us about the beam dilution at the lowest resolution. However, these models require extremely short pathlengths through the ionized carbon gas. Since the widths of the lines detected at frequencies differing by a factor of ~ 10, are found to be very similar, it implies that pressure and radiation broadening, which are strong functions of n is not responsible for the line widths even at the lowest frequency (*i.e.* $\sim$ 34.5 MHz). The origin of the ob-

served width is, most likely, due to the differential Galactic rotation with the gas distributed between galactocentric distances of 4 and 7 kpc. However, the pathlengths required by the low-temperature models are tiny < 1 pc. If this pathlength is to be divided into smaller regions and distributed over ~ 3 kpc (to explain the line width), then it would require individual clouds to be < 0.1 pc thick which implies an extremely thin sheet-like geometry since the angular extent of the clouds is $> 4°$. This peculiar morphology for the clouds makes the models difficult to accept; however they are not entirely implausible. These thin sheet-like structures are reminiscent of ionization fronts near star-forming regions which typically have a thickness of ~ 0.02 pc suggesting a scenario where carbon is photo-ionized in a thin outer layer of molecular clouds by the ambient ultraviolet radiation field. However, to expect many such sheet-like objects to be distributed along every line-of-sight to generate the observed strength and widths appears too contrived. In the case of Cas A (the most-studied direction in recombination lines at low frequencies; Payne *et al.*, 1994 and the references therein), the low$-T_e$ models were ruled out since they failed to explain the observed variation in optical depth. Another interesting difference is that the carbon lines towards Cas A were distinctly affected by frequency-dependent line broadening whereas the lines from the Galactic plane positions hardly show any $n-$dependent broadening suggesting different physical conditions, especially the electron density and radiation field. The main drawback of the data we use here is that they are at only three frequencies, and with different and coarse angular resolutions which makes beam dilution an important issue. In contrast, for the data towards Cas A, the beam-size was determined by the continuum emission from Cas A since it dominates the system noise. One argument in favour of the low-temperature models is that the constraint on pressure equilibrium with the interstellar medium is lifted since the gas is assumed to coexist with molecular gas. Moreover, since the carbon lines seem to be widely detectable in the inner Galaxy, it also favours association with molecular gas which has maximum surface brightness in that region.

The higher temperature ($T_e \geq 60$ K) models, which indirectly assume coexistence of ionized carbon with atomic HI gas in the Galaxy, successfully fit the observed data towards most of the inner Galaxy positions if the angular size of the clouds is 4° or 2°. Due to the low electron densities (~ 0.03 cm^{-3}) in these models, they are sensitive to changes in the radiation temperature. For $T_{R100} = 5500$ K (such high radiation temperatures are ruled out by the observed line widths near 34.5 MHz), data from all the positions could be fitted assuming a cloud size of 4° or 2°, whereas for $T_{R100} = 1250$ K (which produces a radiation width of ≤ 5 kms^{-1} at 34.5 MHz for a dilution factor of 0.5), a few of the positions could not be fitted to the model. With the present data, we cannot obtain a more quantitative interpretation of this result. As mentioned before, the range of physical conditions in the clouds predicted by the warm models appears to be well-constrained. However, we had to relax the criterion of pressure equilibrium with HI to obtain good fits to most of the data. So, all the models in which the temperature favours association with HI have kinetic pressures which range from $3 - 10$ times the interstellar

pressures. These models do predict reasonable pathlengths for the line-forming clouds. Recall that towards Cas A, the warm models (Payne *et al.*1989, Payne *et al.*1994) satisfactorily explained the observed variation in optical depth over a wide frequency range. Thus, we favour the view that a significant fraction of low-frequency carbon recombination lines arise in warm HI gas in the photodissociation regions.

The range of physical parameters that we obtain in this analysis seems to favour an association of the CII gas with the photo-dissociation regions. A photo-dissociation region as defined by Tielens & Hollenbach (1985) are "regions where FUV radiation (6 – 13.6 eV) dominates the heating and/or some important aspect of the chemistry" and contains most of the atomic and molecular gas in the Galaxy. The low-excitation photo-dissociation region discussed by Hollenbach *et al.*(1991) are illuminated by the interstellar radiation field. These regions, according to them, include a warm (T$\geq$ 100 K) atomic region comprised of hydrogen, oxygen and ionized carbon near the surface. Beyond that, is a cool ($T \sim 50$ K) partially dissociated region and still further in the interior is a cooler ($T \sim 10 - 20$ K) region. The photo-dissociation regions encompass a wide range of physical properties. It appears highly probable that carbon recombination lines arise at various depths in the photo-dissociation region. From the present results, it appears that ionized carbon can be distributed in clouds of a range of angular sizes along the line of sight and possess a variety of physical properties resulting in detectable carbon lines.

However, the above argument also raises more questions. If the carbon lines arise in the neutral gas, probably within a low-excitation photo-dissociation region with temperatures ranging from 80 to 300 K (and possibly 20 K), then why are they not detected from many more directions in the Galaxy? It appears reasonable to expect the existence of stronger carbon lines from directions which show high HI optical depth or high ^{12}CO emission. However, this is not always the case. For example, inspite of the large HI optical depth observed towards $l = 30°$ in the Galactic plane, no carbon line near 328 MHz or 34.5 MHz has been detected. Another such interesting direction is towards the extragalactic source 3C 123. Although, this direction shows a high HI optical depth ($\tau_{\rm HI} \sim 2.5$), no carbon recombination line near 318 MHz ($n \sim 274$) (Payne *et al.*1984) have been detected down to an optical depth limit of 3×10^{-4}. Payne *et al.*(1994) explain that this non-detection could be due to the slightly higher temperature of the HI clouds in this direction which renders the lines undetectable. However, from the modelling in the previous section, we find that a range of temperatures (80 – 300 K in the warm models) for the carbon line-forming regions can give rise to detectable peak optical depths of $10^{-3} - 10^{-4}$ for a range of electron densities. If pressure equilibrium with HI gas is assumed, then the models we find have electron densities between 0.005 and 0.007 cm^{-3} implying atomic densities $n_H \sim 50$ cm^{-3}. Larger electron densities (~ 0.03 cm^{-3}) that we find for the best-fitting models cause the gas to move out of pressure equilibrium with HI. On the other hand, lower electron densities ($n_e < 0.003$ cm^{-3}) require extremely long pathlengths through the ionized-carbon gas to generate the observed line intensities. Therefore, if such electron densities

existed in the ionized-carbon gas then also the recombination lines would be undetectable. Hence it appears that detectablity of the low-frequency recombination lines is a sensitive function of both the electron density and temperature. At this point, it may be useful to note that low-frequency observations have detected carbon lines with line-to-continuum ratios ranging from a few times 10^{-4} to a few times 10^{-3}. It appears certain that lines very much stronger than a few times 10^{-3} are not common. However, the lower limit is set by the sensitivity of the observations conducted till date. Hence, lines intrinsically weaker than few times 10^{-4} might possibly exist and would require more deeper observations to detect them. It therefore appears that with the present sensitivity only a subset of the range of values possible for these parameters has so far been accessible through low-frequency recombination lines of carbon.

The physical properties of the gas in the inner Galaxy are remarkably uniform. Surprisingly, these lines which are so widespread in the inner Galaxy ($l < 17°$) appear to be difficult to detect in the outer Galaxy except towards a few directions ($l = 63°\&75°$). The reason possibly lies in the cloud sizes and also in the reduced background radiation field. Alternatively, since these observations have shown that the clouds in the inner Galaxy are $\geq 2°$, the non-detectability could be due to the different physical conditions that may exist in the photo-dissociation regions in the inner and the outer Galaxy. More sensitive multifrequency observations towards several directions in the outer and inner Galaxy are required to ascertain the widespread existence of low$-\nu$ carbon recombination lines.

5.1 *The site of formation of the [*C II *] 158 μm line and the low$-\nu$ carbon recombination lines*

The [CII] 158 μm line is a result of the radiative decay of the fine-structure transition, $^2P_{3/2} \rightarrow {}^2P_{1/2}$ in singly ionized carbon. The recombination lines, on the other hand, are a result of the electronic transitions of an electron which has most likely dielectronically recombined by exciting the same fine structure transition. The two lines are thus, intimately related and it is natural to look for a correlation between the two. However, although dielectronic-like recombination process is one excitation mechanism for the fine-structure line, it is not the only one. Recent advances in infrared observations have extensively detected the [CII] 158 μm line from the Galaxy and it has been inferred that a wide range of physical conditions are conducive to the formation of the fine-structure line. C^+ ions giving rise to the infrared line are found to exist in both neutral and ionized regions. Shibai *et al.*(1991) concluded from their balloon-borne experiments that the diffuse [CII] emission of the Galactic plane comes from the diffuse gas whereas Bennett & Hinshaw (1993) showed that the [CII] emission measured with COBE/FIRAS may originate in the photo-dissociation region. Petuchowski & Bennett (1993) and Heiles (1994), in separate studies, analysed the [CII] data and studied its correlation with the various possible sites of origin. Both the studies find that the extended low-density warm ionized medium which has a temperature around 10^4 K is the main global

contributor to the 158 μm fine-structure emission line, especially in the Galactic interior. Heiles (1994) argues that the next dominant contributor to the infra-red line is the cold neutral medium and the last is the photo-dissociation region. On the other hand, low-frequency carbon recombination line emission is detected only from cold neutral gas and probably molecular gas and not from the extended low-density warm ionized medium. The major contributor to the two species of lines, the C II 158μm and low-frequency carbon recombination lines seem to be different and hence we have not pursued a rigorous treatment of the correlation.

6. Summary

In this paper, we have presented observations of carbon recombination lines at 34.5 MHz and 325 MHz in the Galactic plane. The observations at 34.5 MHz ($n \sim 575$) were conducted using the low-frequency dipole array at Gauribidanur and at 328 MHz ($n \sim 272$) using the Ooty Radio Telescope. Carbon lines were detected from nine out of the 32 directions that were observed at 34.5 MHz. The lines at both the frequencies are weak with line-to-continuum ratios ranging from a few times 10^{-4} to 10^{-3} and line widths of $15 - 50$ kms^{-1}. The similarity of widths observed at the two frequencies suggest that the effect of radiation and pressure broadening is negligible and it is likely that the widths are due to differential Galactic rotation. Observations at 328 MHz, which were made with two angular resolutions, indicate that the angular size of the line-forming gas is $\geq 2^\circ$. Higher resolution VLA observations at 330 MHz towards one of the directions, $l = 14^\circ, b = 0^\circ$ failed to detect any carbon line emission to a 3σ level of 75 mJy beam^{-1}and implies a lower limit of $10'$ on the angular size of any possible clumps in the line-forming regions.

The l-v distribution of the carbon line data indicates that the line-forming regions are located between 4 and 7 kpc from the Galactic Centre. Combining the data at 34.5 MHz and 328 MHz with those of Erickson *et al.*(1995) at 76 MHz obtained using the Parkes telescope, we modeled the line-forming regions. Upper limits on the electron densities and the radiation fields were obtained from the observed line widths at 34.5 MHz. For different assumed angular sizes of the line-forming regions, we found combinations of temperature T_e , density n_e and pathlength l which could satisfactorily explain the observed variation of integrated line optical depth with frequency. The models were found to be sensitive to the assumed size of the line-forming region. In all the models, we assumed that the background continuum radiation uniformly fills the beam. Models were obtained for two values of the background radiation field $T_{R100} = 1250$ K and $T_{R100} = 2500$ K. For an assumed cloud size $> 4^\circ$, we found that the best-fitting parameters are $T_e \sim 20 - 40$ K, $n_e \sim 0.1$ cm^{-3} and $l < 1$ pc. For an angular size of 4°, models with T_e ranging from 60 K to 200 K, n_e between 0.03 and 0.05 cm^{-3}and l between 4 pc and 90 pc fitted the data. Finally, if the angular size of the clouds is 2° then

models with T_e ranging from 150 K to 300 K, $n_e \sim 0.03$ cm^{-3}and l between 40 pc and 170 pc could explain the observations.

The range of possible physical parameters suggest that the line-forming regions may be associated with photo-dissociation regions. Although photo-dissociation regions are known to be widespread in the Galactic disk, carbon lines are detected only in about 30% of the observed positions. We attribute the paucity of the detections to (a) limitation of sensitivity, (b) lack of strong background radiation in some directions and (c) variation in the physical parameters of photo-dissociation regions. Further observations of low frequency carbon recombination lines with higher sensitivity are likely to yeild many more detections.

Acknowledgements

This work was done when NGK was associated with the Raman Research Institute, Bangalore and the Joint Astronomy Programme, Indian Institute of Science, Bangalore. We thank A. Santhosh Kumar for the installation and testing of the 8-line receiver and the operational staff at Gauribidanur for assistance with the long observations. We thank Anish Roshi for his generous help with the observations with the Ooty Radio Telescope and also for valuable discussions and thank K. S. Dwarakanath for help with the VLA observations. The National Radio Astronomy Observatory is a facility of the National Science Foundation operated under cooperative agreement by Associated Universities, Inc.

References

Altenhoff, W. J., Downes, D., Pauls, T., Schraml, J. 1979, *Astr. Astrophys.*, **35**, 23.

Anantharamaiah, K. R. 1985, *J. Astrophys. Astr.*, **6**, 177.

Anantharamaiah, K. R., Payne, H. E., Erickson, W. C. 1988, *Mon. Not. R. Astr. Soc.*, **235**, 151.

Anantharamaiah, K. R., Erickson, W. C., Payne, H. E., Kantharia, N. G. 1994, *Astrophys. J.*, **430**, 682.

Bania, T. M. 1977, *Astrophys. J.*, **216**, 381.

Bennett, C. L., Hinshaw, G. 1993, *In Back to the Galaxy*, Holt, S. S., Verter, F., editors, AIP, 257.

Blake, D. H., Crutcher, R. M., Watson, W. D. 1980, *Nature*, **287**, 707.

Burton, W. B. 1988, In *Galactic and Extragalactic Radio Astronomy*, Verschuur, G. I. & Kellerman, K. I., editors, Springer-Verlag, 295.

Deshpande, A. A., Shevgaonkar, R. K., Shastry, CH. V. 1989, *JIETE*, **35**, 342.

Downes, D., Wilson, T. L., Bieging, J., Wink, J. 1980, *Astr. Astrophys.*, **40**, 379.

Dwarakanath, K. S. 1989, *Ph.D. Thesis*, Indian Institute of Science, Bangalore.

Erickson, W. C., McConnell, D., Anantharamaiah, K. R. 1995, *Astrophys. J.*, **454**, 125.

Garwood, R. W., Dickey, J. M. 1989, *Astrophys. J.*, **338**, 341.

Golynkin, A. A., Konovalenko, A. A. 1991, *Sov. Astron. Lett.*, **17(1)**, 7.

Heiles, C. 1994, *Astrophys. J.*, **436**, 720.

Hollenbach, D. J., Takahashi, T., Tielens, A. G. G. M. 1991, *Astrophys. J.*, **377**, 192.

Kantharia, N. G., Anantharamaiah, K. R., Goss, W. M. 1998a, *Astrophys. J.*, **504**, 375.
Kantharia, N. G., Anantharamaiah, K. R., Payne, H. E. 1998b, *Astrophys. J.*, **506**, 758.
Konovalenko, A. A., Sodin, L. G. 1980, *Nature*, **283**, 360.
Konovalenko, A. A. 1984a, *Sov. Astron. Lett.*, **10(6)**, 384.
Lockman, F. J. 1976, *Astrophys. J.*, **209**, 429.
Lockman, F. J., Pisano, D. J., Howard G., J. 1996, *Astrophys. J. Lett.*, **472**, L173.
Mizutani, K. *et al.*, 1994, *Astrophy. J. Supple. Ser.*, **91**, 613.
Onello, J., Phillips, J. A., 1995, *Astrophys. J.*, **448**, 727.
Palmer, P., Zuckerman, B., Penfield, H., Liley, A. E., Mezger, P. G. 1967, *Nature*, **215**, 40.
Pankonin, V., Walmsley, C. M., Wilson, T. L., Thomasson, P. 1977, *Astr. Astrophys.*, **57**, 341.
Payne, H. E., Salpeter, E. E., Terzian, Y. 1984, *Astr. J.*, **89**, 668.
Payne, H. E., Anantharamaiah, K. R., Erickson, W. C. 1989, *Astrophys. J.*, **341**, 890.
Payne, H. E., Anantharamaiah, K. R., Erickson, W. C. 1994, *Astrophys. J.*, **430**, 690.
Pedlar, A., Davies, R. D., Hart, L., Shaver, P. A. 1978, *Mon. Not. R. Astr. Soc.*, **182**, 473.
Petuchowski, S. J., Bennett, C. L. 1993, *Astrophys. J.*, **405**, 591.
Reich, W., Fuerst, E., Reich, P., Reif, K. 1990, *Astr. Astrophys. Supple. Ser.*, **85**, 633.
Roelfsema, P. R., Goss, W. M., Wilson, T. L. 1987, *Astr. Astrophys.*, **174**, 232.
Roshi, A. D., Anantharamaiah, K. R. 1997, *Mon. Not. R. Astr. Soc.*,**292**, 63.
Roshi, A. D., Anantharamaiah, K. R. 2000, *Astrophys. J.*, **535**, 231.
Salem, M., Brocklehurst, M. 1979, *Astrophy. J Supple. Ser.*, **39**, 633.
Scoville, N.Z., Solomon, P.M. 1975, *Astrophys. J.*, **199**, L10.
Shaver, P. A. 1975, *Pramana*, **5**, 1.
Shibai *et al.*1991, *Astrophys. J.*, **374**, 522.
Smirnov, G. T., Kitaev, V. V., Sorochenko, R. L., Schegolev, A. F. 1996, In *Annual Session of Sci. Council of Astrocosmical Center of P.N.Lebedev Phys. Inst., Puschino 1995, Collection of Reports*, 3.
Sorochenko, R. L. 1996, *Astr. Astrophys. Trans.*, **11**, 199.
Subrahmanyan, R., Goss, W. M. 1996, *Mon. Not. R. Astr. Soc.*, **281**, 239.
Swarup, G., Sarma, N. V. G., Joshi, M. N., Kapahi, V. K., Bagri, D. S., Damle, S. H., Ananthakrishnan, S., Balasubramanian, V., Bahve, S. S., Sinha, R. P. 1971, *Nature*, **230**, 185.
Tielens, A. G. G. M., Hollenbach, D. J. 1985, *Astrophys. J.*, **291**, 722.
van Gorkom, J. H., Goss, W. M., Shaver, P. A., Schwarz, U. J., Harten, R. H. 1980, *Astr. Astrophys.*, **89**, 150.
Walmsley, C.M., Watson, W.D., 1982, *Astrophys. J.*, 260, 317.
Watson, W. D., Western, L. R., Christensen, R. B. 1980, *Astrophys. J.*, **240**, 959.

J. Astrophys. Astr. (2001) **22**, 81–119

Hydrogen Recombination Lines near 327 MHz – II : A Galactic Plane Survey with a $2^\circ \times 6'$ Beam

D. Anish Roshi[1] * & K. R. Anantharamaiah [2]
[1]*National Centre for Radio Astrophysics, TIFR, Pune, India*
[Present Address: National Radio Astronomy Observatory, Green Bank, USA]
[2] *Raman Research Institute, Bangalore-560 080, India.*

Received 2000 October 6; accepted 2000 December 23.

Abstract. In a previous paper we presented a low-resolution ($2^\circ \times 2^\circ$) survey of radio recombination lines (RRLs) at 327 MHz in the longitude range $l = 330^\circ$ to 0° to 89°. In this paper, we present the results of a higher resolution ($2^\circ \times 6'$) survey of RRLs from seven 2°-wide fields and two 6°-wide fields in the same longitude range. Observations were made using the Ooty Radio Telescope (ORT). A total of 252 spectra that were obtained are presented. RRLs were detected in almost all the individual positions within the fields with $l < 35^\circ$ and at several individual positions within the fields in the longitude range $l = 35^\circ$ to 85°. Detailed analysis of the data towards the field centered at G45.5+0.0, shows that the line emission consists of discrete zones of ionized gas. The angular extent of these zones are likely to be one degree or more corresponding to a linear size of > 110 pc at the kinematic distance.

Key words: Galaxy: general – H II regions – ISM: clouds – ISM: general – ISM: structure – radio lines: ISM.

1. Introduction

Radio Recombination Lines (RRLs) are normally observed from compact, dense H II regions that are bright in radio continuum. Several surveys of RRLs at frequencies near 4.8 GHz (Downes *et al.* 1980, Caswell & Haynes 1987), 10 GHz (Lockman 1989) and 15 GHz (Wood & Churchwell 1989) have been made towards discrete H II regions in the Galaxy. The physical properties derived from these observations show that there exists a variety of H II regions. At one extreme are the ultra-compact H II regions with $n_e > 10^4$ cm^{-3} and sizes $\ll 1$ pc which are

*e-mail: aroshi@nrao.edu

formed around young, hot stars (Wood & Churchwell 1989). H II regions with densities between $n_e \sim 50$ and 1000 cm^{-3} and size ranging from few parsecs to few tens of parsecs are widely observed in the Galaxy. These regions have a relatively narrow range of temperatures ($T_e \sim 3000$–10000 K).

In early observations by Gottesman & Gordon (1970) and Gordon & Cato (1972), at frequencies < few GHz, RRLs were detected from several positions along the galactic plane which are free of discrete continuum sources. These low frequency RRLs do not originate in compact, dense H II regions due to the effects of continuum opacity, pressure broadening and beam dilution (Shaver 1975). These RRLs originate from low-density ionized gas ($n_e \sim 0.5 - 50$ cm^{-3}). Several surveys of RRLs near 1.4 GHz have been made (Hart & Pedlar 1976, Lockman 1976, 1980, Cersosimo 1990, Heiles, Reach & Koo 1996) to study this component of the Galaxy. RRLs from this gas were also observed by Anantharamaiah (1985a) near 325 MHz. These observations were used to study the distribution and physical properties of the low-density ionized gas (Hart & Pedlar 1976, Lockman 1976, 1980, Anantharamaiah 1985b, 1986) and also its association with other components of the Galaxy. Several suggestions have been made on the origin of this low-density ionized gas. Matthews, Pedlar & Davies (1973) and Shaver (1976) suggested that the low-density component is a population of "evolved H II regions". Mezger (1978) portrayed this gas as an ensemble of low-density H II regions which he referred to as "extended low-density" (ELD) ionized gas. Heiles *et al.* (1996) suggested a morphological model where the ELD gas is conflated with the "Warm Ionized Medium" and referred to it as "extended low-density warm ionized medium" (ELDWIM) (Petuchowski & Bennett 1993, Heiles 1994, Heiles *et al.*1996). Anantharamaiah (1986) suggested that the low-density ionized gas are associated with large, low-density envelopes of normal H II regions.

In a previous paper, Roshi & Anantharamaiah (2000) (hereafter paper I) presented a new, extensive low-resolution ($\sim 2° \times 2°$) observations of RRLs near 327 MHz from the Galactic plane. A part of the Ooty Radio Telescope (ORT) with a size of 23 m × 23 m, called a 'module', was used for these observations. RRLs were detected in more than 80 % of the observed positions in the longitude range l = 332° to 0° to 89° (inner Galaxy). The observed RRL emission showed large fluctuations as a function of galactic longitude indicating that the line emitting region may be clumpy (paper I). Higher resolution observations can help in studying the nature of the clumpiness and in determining the angular size of the line emitting region. With these objectives in mind, we observed a selected set of 2°-wide fields in the inner Galaxy using the full ORT (530m × 30 m) which gives a beam of 2° × 6′. This paper discusses these higher resolution observations and is organized as follows. The observations and results are described in Section 2. Comparison of the average spectra over a 2° × 2° region and the spectra obtained in the same direction in the low resolution survey is made in Section 3. Section 4 discusses the angular extent of the line emitting region inferred from the higher resolution observations. The paper is summarized in Section 5.

2. Observations and Results

The RRL survey was made using the ORT which is a 530 m x 30 m parabolic cylinder operating at a nominal center frequency of 327 MHz (Swarup *et al.* 1971). In the normal configuration of the ORT, the signals received by groups of 48 dipoles of the 1056 element linear array at the focal line are added in phase. 22 such groups, which are known as "modules", each having a half power beam width of $2^\circ.3$ (in RA) $\times$ $2^\circ.2$ sec(δ) (in Dec.), are combined later through a beam forming network to produce twelve beams of $\sim 2^\circ \times 5'.5$ sec(δ), δ being the declination. The twelve beams are spread along the north-south direction separated by $3'$sec(δ). The spectrometer used for the observations was configured (see below) to collect data from two such beams simultaneously. The two selected beams are separated in the sky by $6'$sec(δ).

The center frequency of operation of the ORT is 326.5 MHz. The RRL transitions from principal quantum numbers $n = 270$, 271, 272 and 273 with $\Delta n = 1$ fall inside the 15 MHz bandwidth of the ORT. A digital spectrometer which could simultaneously observe all the four transitions with a velocity resolution of ~ 1.0 km s^{-1} (Paper I) was used. The four RRL transitions from two beams were observed simultaneously using 2 such spectrometers. The reference spectrum was obtained by switching the frequency every second by half the bandwidth (i.e. 384 KHz). The velocity coverage is about 320 km s^{-1} after rejecting the edge channels. The final spectrum is obtained by averaging the four spectra corresponding to the four RRL transitions of each beam. Thus two final spectra from two sky positions, separated in declination by $6'$sec(δ), are obtained from each observing session. Details of the mode of observations and the data reduction procedure have been presented in paper I.

RRL at low frequencies are weak (line to system temperature ratio $\sim 10^{-3}$) and hence it is extremely time consuming to make a complete survey of the galactic plane with the $2^\circ \times 6'$ beam. Therefore we selected a set of seven fields which are 2° wide and two fields which are 6° wide in longitude. The selected fields were spread over the longitude range $l = 347^\circ$ to 0° to 67°. Fig. 1 (Appendix 2 contains all the figures of this paper) shows schematically all the positions in the galactic plane observed with the $2^\circ \times 6'$ beam. Except for the two 6°-wide fields, the beam centers were chosen so that a set of 20 adjacent positions in declination correspond to a $2^\circ \times 2^\circ$ region from which RRLs were observed in the low-resolution survey (paper I). For the two 6°-wide fields, the center of the two beams of the ORT, from which RRLs were observed simultaneously, is positioned at the galactic plane. Since the ORT is a north-south oriented telescope, the $2^\circ \times 2^\circ$ beam is inclined with respect to the galactic plane. Figs. 2 to 15 (Appendix 2) present all the observed spectra. In these figures, spectra are grouped such that they correspond, wherever possible, to a $2^\circ \times 2^\circ$ field observed at lower resolution using a single 'module' of the ORT (see paper I). A contour map of the 11 cm continuum emission (Reich *et al.* 1990) towards the $2^\circ \times 2^\circ$ field is also shown in each figure to compare the continuum emission within the observed fields. For example, field 9

is devoid of any bright, extended continuum emission (see Fig. 15). An average of all the individual spectra within the 2° field and the corresponding lower resolution spectrum (taken from paper I) are also given in each of these figures. The average spectrum, obtained from the 20 adjacent higher resolution observations should be equivalent to the spectrum observed in the low resolution survey towards the same direction (see Section 3). Table 1 (Appendix 1 contains all the Tables of this paper) gives a summary of the observations and the parameters derived from the line profiles shown in Figs. 2 to 15 in Appendix 2. The observed spectra are given in units of T_L/T_{sys}, where T_L is the line antenna temperature and T_{sys} is the system temperature. The velocity resolution to which the final spectra (shown in Figs. 2 to 15) are smoothed is given in column 6 of Table 1. Effective integration time for the spectra range from 8 hrs to 12 hrs. In many of the spectra, two emission features are detected. The feature at the higher velocity is the hydrogen line and the feature which is about -150 km s^{-1} from the hydrogen line is most likely a carbon recombination line. In many cases, the detected carbon lines are almost as strong as the hydrogen line in spite of the small C/H abundance ratio in the ISM ($< 3 \times 10^{-4}$) indicating that the two lines arise in regions with different physical properties. The carbon lines seen in Figs 2 to 15 most likely belong to the class of low-frequency recombination lines first observed in absorption at 26 MHz by Konovalenko & Sodin (1980). These RRLs were shown to turn over into emission above 200 MHz (Payne, Anantharamaiah & Erickson 1989) and to be widespread in the inner Galaxy (Erickson, McConnell & Anantharamaiah 1995, Kantharia & Anantharamaiah 2001). Carbon RRLs are not discussed further in this paper.

Hydrogen lines were detected in almost all the positions in the fields with $l < 35°$. In several cases, the line parameters seem to vary when the beam center is moved by $6'$ in declination. For example, the width of the lines detected towards G347.78−0.14 and G347.70−0.20 differ by more than a factor of two. These two positions are separated in declination by only 0°.1. The range in the central velocity of the lines observed towards fields with $l < 35°$ is typically 15 km s^{-1}. This difference is about half the typical line width observed in the survey. RRLs were not detected in many positions within the fields with $l > 35°$ (Figs 11 to 15 in Appendix 2).

2.1 *Line widths*

The width of the RRLs detected in these observations are in the range 20 – 45 km s^{-1}. Fig. 16 (Appendix 2) shows the histogram of the observed line widths. The median line width is 32.5 km s^{-1} which is somewhat large compared to the width of lines from normal H II regions ($\sim$ 26 km s^{-1}; Lockman *et al.* 1996). Line widths near 327 MHz can be affected by pressure broadening (Shaver 1975) and blending of lines from objects within the beam or from objects along the line of sight with different central velocities. In a few positions, the line width observed is less than 10 km s^{-1}, which constrains the kinetic temperature of the line emitting region to < 2200 K.

Comparison of the distribution of line widths obtained from the observations with $2° \times 2°$ (paper I) and $2° \times 6'$ beams shows that they are similar. The median widths from the low resolution observations is ~ 31 km s^{-1} (paper I). If the broadening is due to blending of lines from different objects either along the line of sight or within the beam, then we may expect larger widths in the low resolution survey. However, the low resolution observations are not sensitive to line emitting zones of relatively small angular extent due to beam dilution. On the other hand, such line emitting zones can contribute to line emission observed with the $2° \times 6'$ beam. Thus it is possible for the lines detected in the two observations to have similar median widths. Examination of the distribution of the widths, obtained from the two observations, shows that lines with width between 50 and 70 km s^{-1} are observed more frequently in the low resolution survey. These larger widths are most likely due to blending of lines from different objects within the coarse beam. Towards a few positions (e.g. G6.11+0.03), line with widths ~ 10 km s^{-1} has been observed in the high resolution survey. Such narrow lines are not detected in any of the positions in the $2° \times 2°$ observations.

2.2 l-v *Diagram*

An *l-v* diagram obtained from the data in Table 1 is shown in Fig. 17 (Appendix 2). Some confinement of line emission to the spiral arms 2 and 3 below $l = 50°$ is seen in the *l-v* diagram. On the other hand, at longitudes $l > 50°$, the line emission does not seem to be confined to any of the spiral arms. The *l-v* diagram shows good similarity with that obtained by Anantharamaiah (1985a) from the H272α line observations with similar resolution towards a selected set of sources in the longitude range $-2° < l < 50°$. The concentration of line emission towards galactocentric radius of ~ 5.0 kpc near longitude 15° and the extension of emission to negative velocities in the longitude range $l < 10°$ are evident in both the *l-v* diagrams. The *l-v* diagram obtained from the present observations shows, in general, good similarity with that obtained from the low resolution ($2° \times 2°$) survey (paper I). The line emission observed in the higher resolution survey at longitude $l > 50°$ shows extension towards the negative velocities in the *l-v* space which is not observed in the low resolution survey.

3. Comparison with the low resolution observations

With the higher resolution beam ($2° \times 6'$) used in these observations, 20 independent positions can be observed within the $2° \times 2°$ beam of the lower resolution survey presented in paper I. The higher resolution observations are therefore grouped into sets of 20 spectra. The aim is to average the 20 spectra in each of these sets and compare it with the spectrum obtained with the low resolution beam in the same direction and also to examine all the spectra within a 2° field for possible variations.

The average spectrum, obtained from the the 20 adjacent high resolution beam observations, should be equivalent to the spectrum observed in the low resolution

survey towards the same direction. The signal to noise ratio (SNR) of the two spectra will differ by the square root of the ratio of the total integration times involved. Two effects which can make the average spectrum different from the spectrum obtained in the low resolution survey in the same direction; (a) the 20 spectra are averaged without taking into account the angular response function of the low resolution beam, and (b) the integration time at different positions in the high resolution observation and the system temperature at different positions within the low resolution beam are not the same. The spectrum obtained by averaging the 20 spectra towards a given $2^\circ \times 2^\circ$ region and that observed in the same direction in the low resolution survey are also shown in Figs. 2 to 15. Table 2 (Appendix 1) gives the line parameters (columns 3,4,5) obtained from these spectra along with the spectral resolution (column 6) and the effective integration time (column 8). Examination of Table 2 shows that the parameters of the hydrogen line in the average spectrum in most of the fields agree, within the signal to noise ratio, with those of the spectrum obtained in the low resolution survey. In fields 1 and 8, the line width observed in the low resolution survey and that obtained from the average spectrum are different. The line emission appears to be complex in the field 6c, which makes it difficult to fit a proper baseline to the spectrum. A larger bandwidth is required for observation in this direction, since line emission seems to extend over a large velocity range.

In two fields, 6a and 9 (Figs. 10 & 15), the line structure in the average spectrum is different from that of the corresponding spectrum from the low resolution survey. The average spectrum towards field 6a consists of two hydrogen line features. The line feature with central velocity close to that observed in the low resolution survey has line width $\sim$ 30 km s^{-1} which is larger than the width of the line ($\sim$ 14 km s^{-1}) observed with the $2^\circ \times 2^\circ$ beam. If we assume that the line intensities (in units of T_L/T_{sys}) in the average spectrum and the spectrum obtained with the $2^\circ \times 2^\circ$ beam are similar, then the line features seen in the average spectrum should be at about the 2σ level in the spectrum obtained in the low resolution survey. Towards field 9, no line emission is detected in the low resolution survey whereas a line feature is detected (see Table 2) in the average spectrum. The line feature seen in the average spectrum should have been detected at $> 3\sigma$ level in the spectrum obtained in the low resolution survey if we assume that the line intensities in both spectra are similar. While the observations towards field 6a may be consistent within the signal to noise ratio, further investigation is required to understand the discrepancy observed towards field 9.

4. Angular extent of the line emitting region

In this section we will try to answer the question "do the RRL emitting regions consist of ionized clumps with emission confined to small angular regions or is the emission extended and uniform over a large area ? " The higher resolution observations show different behavior of line emission for $l < 35^\circ$ and for $l > 35^\circ$. While RRLs were detected in almost all the individual positions within the fields

with $l < 35°$, lines were not detected in several individual positions within the fields in the longitude range $l = 35°$ to $85°$.

If the line emission originates from a homogeneous, ionized region with angular extent of several degrees, then the line parameters observed at positions within this angular span are expected to be similar. Examination of the observed spectra shows that at several positions there is a considerable change in the line parameters when the beam center is moved by even $6'$ in declination. For example, towards the position G4.72+0.02, the detected line has a width of 49 km s^{-1} and a central velocity of ~ 2 km s^{-1} while the line parameters at G4.64−0.03 are $\Delta V = 27$ km s^{-1} and $V_{LSR} \sim 8$ km s^{-1}. The beam centers of these two positions differ by $0°.1$. This difference implies that the line emitting zones have structures on an angular scale of $\sim 0°.1$, which is ~ 10 pc, if the distance to the source producing the line emission is 5 kpc. This scale is smaller than the typical size of the line emitting regions estimated in Roshi & Anantharamaiah (2001). It seems that the line emission in fields with $l < 35°$ originate from ionized regions which may extend over several degrees but which may have clumps with angular structures as small as $0°.1$.

4.1 *Line emission towards the field G45.5+0.0*

We present a more detailed analysis of one of the observed fields, G45.5+0.0 (Fig. 13). The line of sight through the galactic disk over an angle of $2°$ towards G45.5+0.0 is shown in Fig. 18 (Appendix 2). The line-of-sight intersects the spiral arm 4 at one position and arm 3 at two places. The distances to the three regions of intersection are ~ 4.7 kpc, 7.8 kpc and 10.7 kpc. The expected radial velocities for these distances are 58, 56 and 17 km s^{-1} respectively. H II regions identified from higher frequency RRL observations in this field are listed in Table 3 (Appendix 1) along with the line parameters. RRL near 327 MHz is detected towards some of these positions and their parameters are also given in Table 3. The central velocities of the 327 MHz lines and those detected from H II regions at higher frequencies are comparable.

Examination of the 20 spectra obtained from this field (Fig. 13) shows unambiguous presence of lines in only 3 positions. If the line emission is confined to only these 3 positions, then the expected SNR of the spectrum obtained by averaging 20 spectra is 2.2. However the actual SNR of the line in the average spectrum is 5.9. This increased SNR clearly indicates that the line emission is not confined to only 3 positions but spread over a good fraction of the $2°$ region. To determine the actual angular extent of the line emission, the following analysis was made. Different subsets of the 20 spectra were averaged as shown in Fig. 19 (Appendix 2). The spectra in the left column are obtained by averaging the spectra at adjacent positions. Thus they are equivalent to observing with a beam of $2° \times 12'$. The spectra in the central column, obtained by averaging five adjacent spectra, have an effective beam of $2° \times 0°.5$. The rightmost column shows spectra with an effective beam of $2° \times 1°$. Line parameters of all possible emission features in these spectra are derived and tabulated in Table 4 (Appendix 1). A narrow (~ 11 km s^{-1}) feature appears

to be present in all the spectra in the longitude range G44.67−0.4 to G45.47−0.0 (Fig. 19). This feature does not seem to be present either in other individual spectra or in the spectrum averaged over 1° centered at G45.95+0.2 (see Fig. 19). Thus the region responsible for this line is less than 1° in extent. The central velocity of line emission indicates a kinematic distance to the line emitting region of 6.3 kpc and the estimated size of the region is $\sim$ 110 pc. The individual spectra towards the positions G46.35+0.4 to G45.56+0.0 of field 7 (see Table 1) do not seem to have a common component, although the integrated spectrum obtained by averaging them to an effective beam of 2° × 1° shows a broad feature ($\sim$ 35 km s^{-1}). Such broad features are also present in the spectra obtained by averaging over a 2° × 12′ region centered on G46.30+0.43 and G45.6+0.05 (see Fig. 19). These regions contain known H II regions. The 2.7 GHz continuum emission from the H II region G46.495−0.247 overlaps with the 2° × 12′ region centered on G46.30+0.43 (see Fig. 13). The 2° × 12′ region centered on G45.60+0.05 contains the H II regions G45.475+0.13 and G45.451+0.06. The central velocities of the features seen in the integrated spectra towards G46.30+0.43 and G45.60+0.05 are comparable with those obtained from the H II regions. We thus conclude that the line emission towards the field G45.5+0.0 consists discrete emission zones. Some of the discrete zones have an angular size as large as a degree or more. There is some evidence for the line emission zones to be associated with the H II regions in the field. Similar analysis of other fields (Figs. 2 to 15) will be presented elsewhere.

5. Summary

In an earlier paper (paper I) we presented a low-resolution (2° × 2°) survey of RRLs at 327 MHz in the inner Galaxy made using a single module of the ORT. In this paper, we discussed RRL observations at 327 MHz with the full ORT (i.e. all 22 modules), which gives an angular resolution of 2° × 6′. These observations are used to understand the spatial structure of the line emission observed in the low resolution survey. Seven 2°- wide fields and two 6°- wide fields in the inner Galaxy were observed with the 2° × 6′ beam. A total of 252 spectra were obtained from the higher resolution observations. RRLs were detected in almost all individual positions within the fields with $l < 35°$ and at several individual positions within the fields in the longitude range $l = 35°$ to 85°. The line width observed in these observations were in the range 20 km s^{-1} to 40 km s^{-1}. In most cases, the integrated spectrum obtained by averaging the 20 higher resolution spectra towards a 2° × 2° region is similar, to the spectrum observed at low resolution. Analysis of the line emission in the high resolution observations towards fields with $l < 35°$ indicates that the line emitting region is extended over several degrees but is clumpy. The clump size can be $\sim$ 10 pc or less. A more detailed analysis of the data towards one of the fields, G45.5+0.0, shows that the line emission consists of discrete zones of ionized regions. The angular extent of these zones are likely to be one degree or more corresponding to linear sizes of $>$ 110 pc at the kinematic distance obtained

from the central velocity of line emission. There is some evidence for the line emitting zones being associated with the H II regions in this field.

Acknowledgements

We are grateful to the technical and telescope operation staff at the Radio Astronomy Centre, Ooty, for generous help in conducting the long observations. DAR thanks the Raman Research Institute for generously allowing the use of their research facility. It is a pleasure to acknowledge V. Balasubramanian, A. Pramesh Rao and Jayaram N. Chengalur for many discussions and helpful suggestions. This work forms a part of the Ph.D. thesis of DAR.

APPENDIX 1.

Table 1. Summary of observations with the 2° × 6 beam.

l (°)	b (°)	T_L/T_{sys} × 10^3	ΔV (km s^{-1})	$V_{\rm LSR}$ (km s^{-1})	V_{res} (km s^{-1})	RMS[1] × 10^3	t_{int} (hrs)
Field 1 (G348.0+0.0)(see Fig. 2 for spectra)							
347.22	−0.56				8	0.14	6.9
347.30	−0.50				5	0.19	7.1
347.38	−0.44	0.55(0.02)	31.4(1.5)	−9.8(0.6)	8	0.15	8.1
347.46	−0.38	0.47(0.02)	39.4(2.3)	−16.1(1.0)	8	0.12	13.8
347.54	−0.32	0.50(0.03)	22.0(1.5)	−11.5(0.6)	5	0.14	12.2
347.62	−0.26	0.58(0.05)	29.3(2.7)	−11.7(1.1)	5	0.16	12.5
347.70	−0.20	0.61(0.03)	11.0(0.7)	−11.7(0.3)	5	0.13	14.2
347.78	−0.14	0.53(0.01)	37.5(1.1)	−13.3(0.5)	8	0.10	16.3
347.86	−0.08	0.52(0.02)	33.3(1.4)	−1.4(0.6)	8	0.12	9.5
347.94	−0.02	0.61(0.03)	35.7(2.2)	−13.1(0.9)	8	0.17	6.9
348.02	+0.03	0.48(0.02)	46.1(2.2)	−15.6(0.9)	8	0.14	10.3
348.10	+0.09	0.63(0.02)	31.0(1.1)	−14.5(0.4)	8	0.10	13.6
348.18	+0.15	0.64(0.02)	39.7(1.5)	−15.4(0.6)	8	0.13	10.7
348.26	+0.21	0.62(0.02)	29.6(0.9)	−19.0(0.4)	8	0.13	15.0
348.42	+0.33				8	0.24	11.3
348.51	+0.39	0.63(0.03)	34.9(2.0)	−18.1(0.8)	8	0.12	13.2
348.67	+0.51	0.55(0.02)	32.4(1.6)	−18.3(0.7)	8	0.14	9.7
348.75	+0.57	0.72(0.03)	31.8(1.5)	−16.1(0.6)	8	0.13	11.5
Field 2a (see Fig. 3 for spectra)							
0.43	−0.02	0.84(0.03)	40.8(1.8)	3.3(0.8)	8	0.17	10.2
0.52	+0.03	0.64(0.02)	44.2(1.6)	−2.3(0.7)	8	0.11	12.8
0.67	−0.00	0.53(0.02)	33.1(1.7)	4.8(0.7)	8	0.11	11.2
0.75	+0.05	0.77(0.04)	34.0(1.9)	0.2(0.8)	8	0.14	11.6
0.84	+0.10	0.72(0.02)	22.4(0.9)	4.5(0.4)	8	0.11	9.4
0.92	+0.16	0.78(0.03)	23.7(1.0)	5.1(0.4)	8	0.11	12.6
Field 2b (G2.3+0.0) (see Fig. 4 for spectra)							
1.12	+0.02	0.52(0.02)	40.4(1.6)	0.4(0.7)	8	0.13	10.2
1.21	+0.07	0.58(0.02)	45.9(1.9)	−4.3(0.8)	8	0.10	10.3
1.29	+0.13	0.40(0.02)	42.8(3.0)	−0.3(1.2)	8	0.12	9.9
1.38	+0.18	0.52(0.02)	41.9(2.1)	5.4(0.9)	8	0.12	10.1
1.58	+0.04	0.66(0.02)	28.3(1.3)	2.1(0.5)	8	0.13	11.8
1.66	+0.09	0.48(0.02)	37.8(2.3)	6.5(0.9)	8	0.12	12.2
1.75	+0.14	0.33(0.03)*	25.9(2.5)	3.2(1.1)	8	0.13	11.1
1.83	+0.20	0.51(0.03)	36.1(2.2)	7.8(0.9)	8	0.13	11.3
2.03	+0.06	0.57(0.02)	28.4(1.2)	1.0(0.5)	8	0.13	12.0
2.12	+0.11	0.46(0.03)	21.9(1.6)	3.6(0.7)	8	0.13	12.4
2.21	+0.16	0.43(0.02)	31.9(2.2)	1.2(0.9)	8	0.11	14.8

Table 1. (*Continued*).

l (°)	b (°)	T_L/T_{sys} $\times 10^3$	ΔV (km s^{-1})	$V_{\rm LSR}$ (km s^{-1})	V_{res} (km s^{-1})	RMS[1] $\times 10^3$	t_{int} (hrs)
2.29	+0.21	0.57(0.02)	21.0(1.4)	11.9(0.6)	8	0.10	14.9
2.54	−0.03				8	0.18	8.1
2.63	+0.02	0.44(0.02)	42.2(2.3)	6.9(1.0)	8	0.11	11.2
2.78	−0.03	0.64(0.02)	34.7(1.2)	7.8(0.5)	8	0.09	11.2
2.86	+0.02	0.44(0.02)	28.2(1.8)	8.5(0.8)	8	0.11	12.5
3.01	−0.03	0.65(0.03)	27.5(1.4)	5.2(0.6)	8	0.12	11.2
3.09	+0.02	0.40(0.03)*	21.4(1.8)	7.2(0.8)	8	0.11	11.7
3.24	−0.03	0.46(0.01)	34.5(1.3)	5.9(0.5)	8	0.15	10.1
3.33	+0.02	0.40(0.02)	26.7(2.0)	8.6(0.8)	8	0.11	11.5
Field 2c (G4.7+0.0) (see Fig. 5 for spectra)							
3.47	−0.03	0.36(0.02)*	33.6(2.4)	7.9(1.0)	8	0.13	9.2
3.56	+0.02	0.57(0.02)	24.7(0.9)	12.5(0.4)	8	0.09	10.4
3.71	−0.03	0.69(0.03)	27.0(1.3)	8.4(0.5)	8	0.14	8.8
3.79	+0.02	0.49(0.02)	34.4(2.0)	4.0(0.8)	8	0.12	11.6
3.94	−0.03	0.66(0.04)	18.3(1.4)	7.3(0.6)	6	0.15	8.4
4.03	+0.02	0.47(0.02)*	25.7(1.5)	11.0(0.6)	8	0.15	11.0
4.17	−0.03	0.47(0.02)	37.9(2.4)	8.6(0.9)	8	0.14	9.2
4.26	+0.02	0.45(0.03)	24.4(1.7)	11.9(0.7)	8	0.11	12.2
4.49	+0.02	0.55(0.04)	15.5(1.1)	9.1(0.5)	6	0.11	11.6
4.64	−0.03	0.45(0.02)	26.6(1.6)	8.4(0.7)	8	0.11	9.6
4.72	+0.02	0.62(0.02)	49.0(1.6)	1.8(0.7)	8	0.12	11.5
4.87	−0.03	0.72(0.04)	28.4(1.7)	8.0(0.7)	5	0.17	8.3
4.95	+0.02	0.49(0.02)	29.1(1.7)	12.4(0.7)	8	0.13	8.5
5.10	−0.03	0.54(0.02)	48.2(2.3)	10.6(1.0)	6	0.16	8.5
5.19	+0.02	0.81(0.02)	35.1(1.1)	9.4(0.5)	6	0.11	9.0
5.33	−0.03	0.61(0.02)	24.4(1.0)	12.2(0.4)	8	0.10	10.2
5.42	+0.02	0.59(0.04)	20.3(1.4)	12.1(0.6)	5	0.14	10.6
5.56	−0.03	0.59(0.03)	44.5(2.3)	8.9(0.9)	8	0.14	10.0
5.65	+0.02	0.69(0.03)	23.2(1.0)	11.2(0.4)	8	0.10	12.3
Field 2d (see Fig. 6 for spectra)							
5.80	−0.03	0.75(0.04)	22.8(1.3)	10.3(0.6)	6	0.16	7.4
5.88	+0.02	0.85(0.03)	30.9(1.1)	10.6(0.5)	8	0.13	8.6
6.02	−0.02	0.75(0.04)	25.0(1.5)	13.1(0.6)	8	0.16	4.2
6.11	+0.03	0.89(0.06)	9.6(0.8)	23.4(0.3)	6	0.18	4.2
6.25	−0.02	0.70(0.03)	30.8(1.8)	16.4(0.7)	6	0.16	5.6
6.34	+0.03	0.86(0.05)	29.4(1.9)	16.3(0.8)	5	0.22	5.6
6.48	−0.02	0.79(0.03)	29.0(1.3)	15.1(0.6)	8	0.15	8.0
6.57	+0.03	1.11(0.06)*	8.4(0.6)	6.6(0.2)	3	0.22	6.8
6.72	−0.02	1.02(0.03)	24.1(0.9)	14.5(0.4)	5	0.14	10.0
6.80	+0.03	0.94(0.02)	28.0(0.9)	15.4(0.4)	5	0.12	11.4

Table 1. (*Continued*).

l (^{o})	b (^{o})	T_L/T_{sys} $\times 10^3$	ΔV (km s^{-1})	$V_{\rm LSR}$ (km s^{-1})	V_{res} (km s^{-1})	RMS[1] $\times 10^3$	t_{int} (hrs)
Field 3 (G13.9+0.0) (see Fig. 7 for spectra)							
13.04	−0.46	0.77(0.03)	31.8(1.2)	26.0(0.5)	8	0.13	7.9
13.13	−0.41	0.41(0.02)	43.3(3.0)	28.7(1.2)	8	0.13	10.6
13.22	−0.36	0.61(0.03)	39.5(2.5)	26.0(1.1)	6	0.17	8.2
13.30	−0.36				6	0.18	8.4
13.39	−0.26	0.80(0.03)	39.4(1.7)	27.4(0.7)	8	0.14	8.4
13.48	−0.22	0.76(0.01)	34.3(0.8)	24.9(0.3)	6	0.12	11.2
13.57	−0.17	1.01(0.03)	40.9(1.4)	29.2(0.6)	5	0.16	9.3
13.65	−0.12	0.85(0.03)	32.5(1.3)	26.9(0.6)	6	0.14	9.1
13.74	−0.07	0.90(0.03)	31.5(1.3)	25.9(0.5)	8	0.18	8.0
13.83	−0.02	1.00(0.03)	38.3(1.5)	30.4(0.6)	5	0.21	8.8
13.92	+0.03	1.15(0.03)	48.4(1.4)	33.4(0.6)	8	0.19	6.3
14.00	+0.07	1.10(0.03)	27.1(0.8)	26.2(0.3)	6	0.17	6.7
14.09	+0.12	0.94(0.03)	30.3(1.1)	24.7(0.5)	5	0.15	10.0
14.18	+0.17	0.83(0.02)	40.2(1.4)	24.5(0.6)	6	0.13	10.9
14.27	+0.22	0.80(0.02)	36.6(1.0)	30.4(0.4)	8	0.13	9.9
14.36	+0.26	0.82(0.02)	38.4(1.4)	30.0(0.6)	5	0.13	11.7
14.44	+0.31	0.68(0.03)	26.3(1.4)	25.1(0.6)	8	0.14	7.5
14.53	+0.36	0.63(0.02)	34.9(1.3)	29.8(0.5)	8	0.13	8.0
14.62	+0.41	0.63(0.02)	34.8(1.4)	28.6(0.6)	8	0.14	10.1
14.71	+0.46	0.76(0.03)	22.6(0.9)	25.0(0.4)	6	0.11	11.8
Field 4 (G25.2+0.0) (see Fig. 8 for spectra)							
24.37	−0.44				8	0.13	10.2
24.46	−0.39	0.46(0.03)	19.1(1.3)	104.3(0.5)	8	0.10	10.6
24.55	−0.35				8	0.16	8.4
24.64	−0.30				8	0.14	9.3
24.73	−0.25	0.47(0.03)*	37.0(2.6)	107.2(1.0)	8	0.17	10.4
24.81	−0.21				8	0.16	8.3
24.90	−0.16	0.33(0.02)	61.1(4.7)	95.3(1.6)	8	0.13	14.3
24.99	−0.12				8	0.10	13.9
25.08	−0.07				8	0.15	8.4
25.17	−0.02				5	0.16	10.2
25.26	+0.03				8	0.13	12.4
25.35	+0.07				8	0.12	13.2
25.43	+0.12				8	0.14	10.7
25.52	+0.16				8	0.13	10.9
25.61	+0.21				8	0.13	9.5
25.70	+0.26				8	0.15	9.5
25.79	+0.30	0.55(0.02)	38.6(1.6)	110.6(0.7)	8	0.14	7.2
25.88	+0.35	0.56(0.02)	23.3(0.8)	102.1(0.4)	8	0.12	9.7
25.96	+0.40	0.57(0.03)	16.0(0.9)	99.4(0.4)	8	0.11	8.2
26.05	+0.44	0.47(0.03)	22.2(1.9)	103.2(0.8)	8	0.13	10.6

Table 1. (*Continued*).

l (°)	b (°)	T_L/T_{sys} $\times 10^3$	ΔV (km s^{-1})	$V_{\rm LSR}$ (km s^{-1})	V_{res} (km s^{-1})	RMS[1] $\times 10^3$	t_{int} (hrs)
Field 5 (G27.5+0.0) (see Fig. 9 for spectra)							
26.62	−0.43	0.63(0.01)	33.1(0.8)	95.9(0.3)	8	0.13	7.1
26.71	−0.39	0.35(0.03)	40.4(3.7)	90.4(1.5)	8	0.13	9.6
26.80	−0.34	0.45(0.02)	37.2(1.7)	100.3(0.7)	8	0.11	7.6
26.88	−0.30	0.40(0.03)	49.9(4.9)	101.4(1.7)	8	0.13	10.3
26.97	−0.25	0.61(0.03)	46.3(2.4)	90.3(1.0)	8	0.17	5.5
27.06	−0.20	0.68(0.03)	42.7(2.3)	92.8(1.0)	8	0.16	8.0
27.15	−0.16	0.38(0.02)	23.0(1.4)	88.4(0.6)	8	0.11	8.6
27.24	−0.11	0.60(0.02)	21.1(0.8)	95.0(0.4)	8	0.11	11.5
27.33	−0.06	0.53(0.02)	24.1(1.2)	94.5(0.5)	8	0.13	8.9
27.42	−0.02	0.52(0.03)	24.2(1.5)	90.8(0.6)	8	0.13	10.0
27.50	+0.03	0.59(0.05)	15.4(1.4)	94.5(0.6)	8	0.15	8.3
27.59	+0.07	0.61(0.04)	21.1(1.4)	94.5(0.6)	8	0.13	10.2
27.68	+0.12	0.50(0.03)*	16.3(1.2)	88.9(0.5)	8	0.13	8.5
27.77	+0.16	0.31(0.02)	33.0(2.9)	92.8(1.2)	8	0.10	10.1
27.86	+0.21	0.35(0.02)	39.8(3.1)	88.9(1.2)	8	0.17	6.8
27.95	+0.26	0.65(0.02)	29.8(1.1)	85.0(0.5)	8	0.10	8.2
28.04	+0.31	0.53(0.02)	34.8(1.9)	92.1(0.8)	5	0.14	15.0
28.13	+0.35	0.41(0.02)	31.1(1.4)	89.3(0.6)	8	0.08	18.6
28.21	+0.40	0.45(0.02)	48.7(2.9)	91.7(1.0)	8	0.14	7.6
28.30	+0.44	0.53(0.03)	24.2(1.8)	100.3(0.7)	8	0.14	9.2
Field 6a (G34.2+0.0) (see Fig. 10 for spectra)							
33.05	−0.02				8	0.13	12.4
33.14	+0.03				8	0.16	12.4
33.28	−0.02				8	0.14	11.1
33.37	+0.03				8	0.12	14.1
33.50	−0.02				8	0.13	15.2
33.59	+0.03				8	0.13	18.6
33.73	−0.02				8	0.13	10.8
33.82	+0.03				8	0.12	13.0
33.95	−0.02				8	0.16	10.6
34.04	+0.03				8	0.15	9.4
34.18	−0.02				5	0.18	9.7
34.27	+0.03	0.38(0.03)	16.8(1.4)	47.4(0.6)	8	0.10	13.1
34.40	−0.02				8	0.19	9.0
34.49	+0.03				8	0.14	12.2
34.63	−0.02				8	0.14	9.8
34.72	+0.03				8	0.10	13.3
34.85	−0.02				8	0.14	8.9
34.94	+0.03	0.35(0.02)	39.0(2.5)	56.5(1.0)	8	0.12	11.0
35.08	−0.02	0.30(0.02)	38.6(3.0)	52.4(1.2)	8	0.10	8.9
35.17	+0.03				8	0.20	11.9

Table 1. *(Continued).*

l (^{o})	b (^{o})	T_L/T_{sys} $\times 10^3$	ΔV (km s^{-1})	$V_{\rm LSR}$ (km s^{-1})	V_{res} (km s^{-1})	RMS[1] $\times 10^3$	t_{int} (hrs)
Field 6b (G36.5+0.0) (see Fig. 11 for spectra)							
35.31	−0.02	0.32(0.02)	45.4(3.4)	54.2(1.4)	8	0.11	11.1
35.40	+0.03	0.36(0.02)	45.1(2.3)	57.5(1.0)	8	0.10	14.3
35.53	−0.02	0.56(0.02)	36.7(1.6)	55.9(0.7)	8	0.16	7.2
35.62	+0.03				8	0.13	9.4
35.76	−0.02	0.21(0.02)*	31.6(3.8)	60.5(1.5)	6	0.10	10.7
35.85	+0.02				8	0.13	13.0
35.98	−0.02				8	0.13	11.7
36.07	+0.03				5	0.13	13.0
36.21	−0.02				8	0.12	10.6
36.30	+0.02				8	0.16	13.8
36.43	−0.02	0.61(0.03)	21.2(1.5)	82.0(0.6)	8	0.13	10.9
		0.46(0.03)	25.3(2.3)	47.5(0.89)	8	0.13	10.9
36.52	+0.02	0.27(0.02)	47.1(3.8)	71.9(1.5)	8	0.11	9.0
36.66	−0.02	0.43(0.03)	26.1(2.1)	79.3(0.9)	8	0.11	10.8
36.75	+0.02				8	0.12	13.0
36.89	−0.02				8	0.15	9.9
37.11	−0.02				8	0.17	12.2
37.20	+0.03	0.29(0.02)	46.2(3.4)	69.8(1.3)	8	0.11	14.2
37.34	−0.02	0.48(0.03)	31.5(2.2)	73.8(0.9)	8	0.17	5.4
37.43	+0.02				8	0.15	9.9
Field 6c (G38.7+0.0) (see Fig. 12 for spectra)							
37.56	−0.02				8	0.14	12.0
37.65	+0.02				8	0.15	15.5
37.79	−0.02				8	0.15	14.4
37.88	+0.02				8	0.17	8.4
38.01	−0.02	0.46(0.03)	46.7(3.3)	59.8(1.4)	8	0.14	9.3
38.10	+0.02				8	0.14	14.0
38.24	−0.03	0.33(0.02)	51.6(3.5)	58.6(1.4)	8	0.12	8.6
38.33	+0.02				8	0.16	9.1
38.46	−0.03	0.50(0.03)	21.5(1.6)	40.0(0.7)	8	0.13	9.7
38.55	+0.02				8	0.13	12.5
38.69	−0.03				8	0.19	6.8
38.78	+0.02				8	0.14	9.1
38.91	−0.03				8	0.15	10.9
39.00	+0.02				8	0.11	12.3
39.14	−0.02				8	0.26	2.6
39.22	+0.03				8	0.21	4.9
39.36	−0.02				8	0.20	4.3
39.45	+0.03				8	0.19	5.9
39.59	−0.02				8	0.18	4.2
39.68	+0.03				8	0.16	6.6

Table 1. *(Continued).*

l (^{o})	b (^{o})	T_L/T_{sys} $\times 10^3$	ΔV (km s^{-1})	$V_{\rm LSR}$ (km s^{-1})	V_{res} (km s^{-1})	RMS[1] $\times 10^3$	t_{int} (hrs)
Field 7 (G45.5+0.0) (see Fig. 13 for spectra)							
44.67	−0.44	0.30(0.03)*	28.3(2.9)	56.1(1.2)	8	0.12	9.0
44.76	−0.40				8	0.14	9.5
44.85	−0.35				8	0.12	10.4
44.94	−0.30				8	0.12	9.2
45.03	−0.25				8	0.13	10.5
45.12	−0.21				8	0.10	13.8
45.20	−0.16				8	0.10	10.3
45.29	−0.11				8	0.11	12.0
45.38	−0.07				8	0.10	10.5
45.47	−0.02	0.42(0.02)*	11.2(0.7)	55.1(0.3)	8	0.10	14.6
45.56	+0.03	0.38(0.02)	36.2(2.4)	44.9(1.0)	8	0.13	9.8
45.64	+0.08				8	0.12	15.1
45.73	+0.12				8	0.19	6.3
45.82	+0.17				8	0.14	11.0
45.91	+0.22				8	0.13	10.2
46.00	+0.26				8	0.16	10.3
46.08	+0.31				8	0.14	9.6
46.17	+0.36				8	0.11	9.7
46.26	+0.41	0.53(0.04)	16.0(1.3)	43.9(0.5)	8	0.10	9.5
		0.28(0.04)	17.0(2.5)	12.8(1.0)	8	0.10	9.5
46.35	+0.45				8	0.12	11.7
Field 8 (G56.9+0.0) (see Fig. 14 for spectra)							
56.08	−0.46	0.47(0.03)	32.7(2.7)	23.0(1.1)	8	0.13	12.8
56.17	−0.42	0.24(0.02)	30.6(3.5)	24.5(1.4)	8	0.10	13.7
56.26	−0.37	0.35(0.03)	54.8(6.8)	37.0(2.5)	8	0.15	9.9
56.34	−0.32				8	0.14	12.7
56.43	−0.27	0.33(0.03)*	25.2(2.8)	31.3(1.1)	8	0.13	12.5
56.52	−0.22				8	0.09	16.1
56.60	−0.17	0.37(0.02)	37.3(3.4)	24.3(1.2)	8	0.13	8.2
56.69	−0.12				8	0.13	12.4
56.78	−0.07	0.47(0.03)	27.6(2.4)	23.8(1.0)	8	0.14	10.1
56.86	−0.02				8	0.15	13.2
56.95	+0.03	0.21(0.01)*	32.4(2.5)	25.3(1.0)	8	0.08	13.1
57.04	+0.08	0.21(0.02)	49.5(7.0)	13.5(2.4)	8	0.10	16.8
57.12	+0.13	0.22(0.02)	64.3(11.2)	15.0(3.1)	8	0.11	11.1
57.21	+0.18				8	0.16	15.1
57.30	+0.23	0.39(0.02)	29.0(1.7)	12.5(0.6)	8	0.12	8.6
57.38	+0.28				8	0.10	11.6
57.47	+0.33				8	0.16	9.5
57.56	+0.38	0.27(0.02)	44.4(3.1)	17.2(1.3)	8	0.12	12.0
57.65	+0.42	0.30(0.02)	51.7(3.7)	19.7(1.4)	8	0.13	9.5
57.73	+0.47				8	0.15	11.4

Table 1. (*Continued*).

l (^{o})	b (^{o})	T_L/T_{sys} $\times 10^3$	ΔV (km s^{-1})	$V_{\rm LSR}$ (km s^{-1})	V_{res} (km s^{-1})	RMS[1] $\times 10^3$	t_{int} (hrs)
Field 9 (G66.2+0.0) (see Fig. 15 for spectra)							
65.39	−0.50	0.38(0.02)	44.7(2.8)	13.0(1.2)	8	0.10	11.6
65.48	−0.45	0.44(0.03)	37.5(3.1)	5.4(1.3)	8	0.13	12.1
65.56	−0.39	0.33(0.03)	44.7(4.4)	4.8(1.5)	8	0.13	8.9
65.65	−0.34				8	0.12	9.6
65.73	−0.29				8	0.15	5.8
65.82	−0.24				8	0.14	10.8
65.90	−0.18				8	0.13	12.1
65.99	−0.13				8	0.08	17.3
66.08	−0.08				8	0.16	4.8
66.16	−0.03				8	0.16	4.1
66.24	+0.03	0.67(0.02)	43.9(1.6)	14.9(0.7)	8	0.14	8.8
66.33	+0.08	0.42(0.04)	44.3(4.5)	3.2(1.8)	8	0.15	11.1
66.41	+0.13				8	0.22	7.5
66.50	+0.19				8	0.19	8.4
66.59	+0.24				8	0.13	11.5
66.67	+0.29				8	0.11	13.8
66.75	+0.35	0.33(0.03)*	38.2(4.2)	10.2(1.8)	8	0.15	7.7
66.84	+0.40	0.27(0.02)*	42.6(3.4)	8.3(1.4)	8	0.11	12.2
66.92	+0.45				8	0.16	8.5
67.01	+0.50				8	0.14	9.4

[1] RMS is in units of T_L/T_{sys}.

* Tentative detection.

Table 2. Line parameters from the low resolution observation and the average spectrum.

Field Name	l ($b = 0^o$) (^{o})	T_L/T_{sys} $\times 10^3$	ΔV (km s^{-1})	$V_{\rm LSR}$ (km s^{-1})	V_{res} (km s^{-1})	RMS[1] $\times 10^3$	t_{int} (hrs)
Field 1	348.0#	0.51(0.02)	35.9(1.5)	−15.5(0.6)	2	0.08	214.1
	348.0!	0.42(0.02)	53.6(2.9)	−22.6(1.2)	8	0.12	12.7
Field 2b	2.3#	0.43(0.01)	29.2(1.1)	5.1(0.5)	2	0.06	207.9
	2.3!	0.37(0.02)	26.0(2.0)	10.2(0.8)	8	0.10	10.7
Field 2c	4.7#	0.56(0.01)	34.3(1.0)	8.6(0.4)	2	0.06	199.5
	4.7!	0.67(0.02)	28.7(0.9)	11.3(0.4)	8	0.09	13.2
Field 3	13.9#	0.76(0.02)	34.9(0.8)	27.5(0.3)	2	0.07	182.9
	13.9!	0.90(0.02)	37.7(0.7)	26.7(0.3)	8	0.08	16.8
Field 4	25.2#	0.28(0.01)	30.0(1.7)	101.8(0.7)	3	0.06	205.8
	25.2!	0.44(0.01)	25.5(0.8)	98.2(0.4)	6	0.10	19.8
Field 5	27.5#	0.43(0.01)	31.9(1.0)	92.7(0.4)	3	0.05	189.7
	27.5!	0.39(0.02)	28.5(1.4)	91.6(0.6)	8	0.08	18.2
Field 6a	34.2#	0.15(0.02)	15.2(1.8)	90.4(0.8)	3	0.05	235.2
		0.17(0.01)	27.9(2.2)	50.8(0.9)	3	0.05	235.2
	34.2!	0.26(0.02)	14.2(0.9)	45.6(0.4)	5	0.08	38.4
Field 6b	36.5#	0.27(0.01)	55.6(2.4)	64.7(1.0)	5	0.06	209.1
	36.5!	0.25(0.01)	60.0(3.2)	65.2(1.2)	8	0.07	33.5
Field 6c	38.7#				3	0.09	181.1
	38.7!				8	0.07	27.6
Field 7	45.5#	0.18(0.01)	44.6(2.6)	47.5(1.1)	3	0.05	213.0
	45.5!	0.20(0.01)	40.5(2.2)	48.8(0.9)	8	0.05	53.5
Field 8	56.9#	0.24(0.01)	48.0(2.1)	21.2(0.9)	5	0.05	240.3
	56.9!	0.25(0.01)	21.2(1.6)	20.9(0.7)	8	0.06	46.2
Field 9	66.2#	0.25(0.01)	49.1(1.7)	9.9(0.7)	5	0.04	196.0
	66.2!				8	0.07	45.2

[1] RMS is in units of T_L/T_{sys}.

Parameters from the average spectrum.

! Parameters from the spectrum obtained with a 2° × 2° beam (paper I).

Table 3. H II regions and RRLs near 327 MHz in field 7 (G45.5+0.0).

l (^{o})	b (^{o})	T_L (mK).	ΔV (km s^{-1})	$V_{\rm LSR}$ (km s^{-1})	λ_{obs} (cm)	Note
44.786	−0.490	17(2.5)	30.0(5.5)	44.8(4.0)	9	L89
44.981	−0.646	14(2.0)	20.3(3.4)	67.3(1.4)	9	lph96
45.125	0.136	67(4.9)	31.6(2.7)	57.6(1.1)	3	L89
45.451	0.060	153(6.3)	27.9(1.3)	55.9(0.6)	3	L89
45.475	0.130	57(3.9)	27.5(2.1)	56.0(0.9)	3	L89
45.824	−0.290	16(2.0)	38.7(5.8)	62.3(4.2)	3	L89
46.495	−0.247	83(5.1)	22.4(1.6)	57.2(0.7)	3	L89
RRLs near 327 MHz in field 7						
l (^{o})	b (^{o})	T_L/T_{sys}	ΔV (km s^{-1})	$V_{\rm LSR}$ (km s^{-1})		Note
44.67	−0.44	0.30(0.03)	28.3(2.9)	56.1(1.2)		t
45.47	−0.02	0.42(0.02)	11.2(0.7)	55.1(0.3)		t
45.56	+0.03	0.38(0.02)	36.2(2.4)	44.9(1.0)		
46.26	+0.41	0.53(0.04)	16.0(1.3)	43.9(0.5)		
		0.28(0.04)	17.0(2.5)	12.8(1.0)		

Note: L89 – Lockman (1989); lph96 – Lockman *et al.*(1996);
t – Tentative detection.

Table 4. Line parameters from the set of average spectra in field 7 (G45.5+0.0).

l (°)	b (°)	T_L/T_{sys} $\times 10^3$	ΔV (km s^{-1})	$V_{\rm LSR}$ (km s^{-1})	V_{res} (km s^{-1})	RMS[1] $\times 10^3$	t_{int} (hrs)
Average over 2° × 12′							
46.30	+0.43	0.33(0.02)	33.0(1.1)	53.4(0.5)	8	0.09	21.1
46.12	+0.34				8	0.09	19.3
45.95	+0.24				8	0.10	20.5
45.77	+0.14	0.34(0.03)	13.6(1.3)	57.6(0.6)	5	0.13	17.3
45.60	+0.05	0.28(0.01)	39.8(2.5)	47.6(1.0)	8	0.08	24.8
45.43	−0.04	0.33(0.03)	11.7(1.1)	55.0(0.5)	3	0.12	25.2
45.25	−0.13	0.24(0.04)*	10.1(2.1)	53.2(0.9)	3	0.11	22.3
45.07	−0.23	0.18(0.02)*	26.4(3.8)	55.5(1.5)	5	0.09	24.3
		0.23(0.02)*	19.4(2.6)	18.4(1.0)	5	0.09	24.3
44.89	−0.33	0.29(0.03)*	11.6(1.2)	56.9(0.5)	3	0.11	19.5
44.71	−0.42	0.37(0.04)	10.4(1.4)	56.0(0.6)	3	0.12	18.5
Average over 2° × 30′							
46.17	+0.36	0.15(0.02)	9.1(1.2)	62.9(0.5)	8	0.06	50.7
		0.21(0.01)	15.8(1.2)	41.9(0.5)	8	0.06	50.7
45.73	+0.12	0.30(0.02)	14.2(1.0)	59.0(0.4)	6	0.07	52.4
		0.17(0.01)	29.3(3.2)	33.4(1.2)	6	0.07	52.4
45.29	−0.11	0.20(0.02)*	17.4(1.9)	54.9(0.8)	5	0.07	61.3
44.85	−0.35	0.30(0.03)	11.7(1.3)	56.0(0.5)	3	0.08	48.6
Average over 2° × 1°							
45.95	+0.24	0.14(0.01)	35.2(2.6)	47.5(1.1)	6	0.05	103.1
45.07	−0.23	0.24(0.02)	12.8(1.1)	55.3(0.5)	5	0.05	109.9

[1] RMS is in units of T_L/T_{sys}

* Tentative detection.

APPENDIX 2

This Appendix, beginning on the next page, contains all the figures (Fig. 1 to Fig. 19) referred to in this paper.

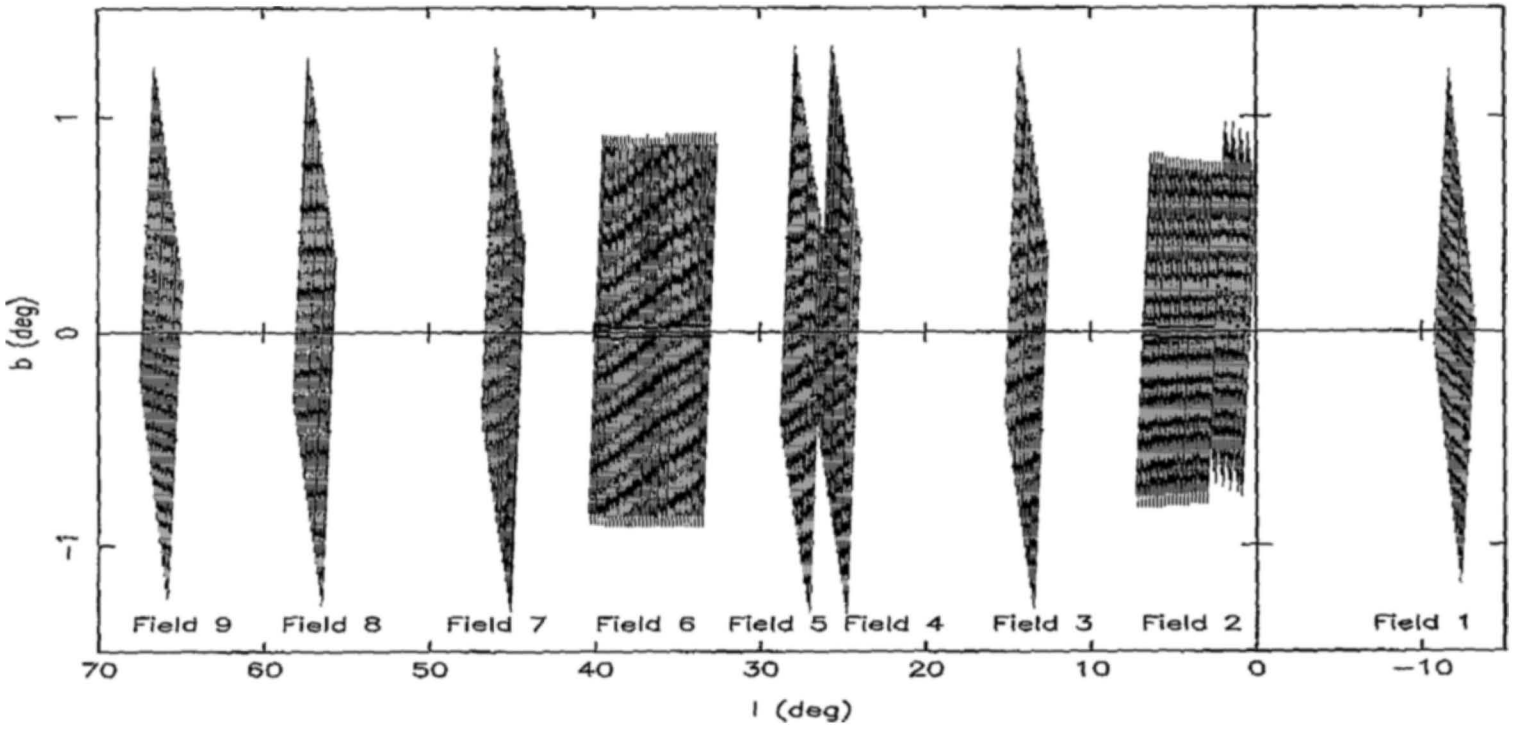

Figure 1. The positions observed in the galactic plane with the $2^\circ \times 6'$ beam of the ORT are shown schematically in galactic coordinates. The dots indicate the beam center and the length of the line represent the extent of the 2° beam of the ORT. Except for fields 2 and 6, the beam centers were chosen so that a set of 20 adjacent positions in declination correspond to a $2^\circ \times 2^\circ$ region from which RRLs were observed in the low-resolution survey (paper I). For fields 2 and 6, the center of the two beams, from which RRLs were observed simultaneously in this survey, is positioned along the galactic plane. Since the ORT is a north-south oriented telescope the $2^\circ \times 2^\circ$ beam is inclined with respect to the galactic plane.

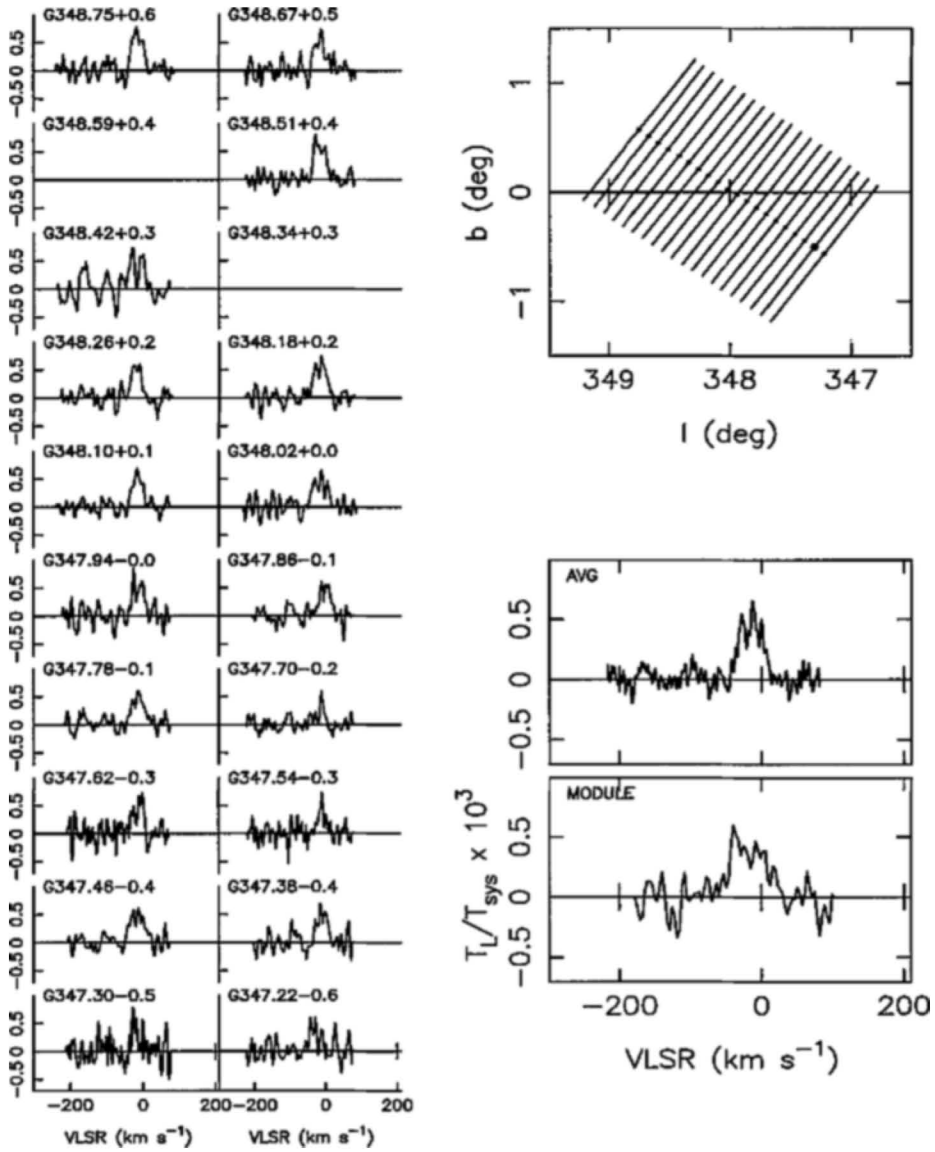

Figure 2. Spectra of recombination lines near 327 MHz observed with a beam of 2° × 6 towards various positions within field 1 centered at G348.0+0.0 are shown on the left. The positions observed are shown schematically in galactic coordinates in the top right corner where the dots indicate the beam center and the length of the line represent the extent of the 2° beam of the ORT. The spectrum (labeled as AVG) obtained by averaging all the 20 spectra and the spectrum (labeled as MODULE) obtained using a 2° × 2° beam covering the same region (taken from paper I) are shown in the bottom right corner. The ordinate of the spectra are in units of T_L/T_{sys} and abscissa are in LSR velocity with respect to the hydrogen line.

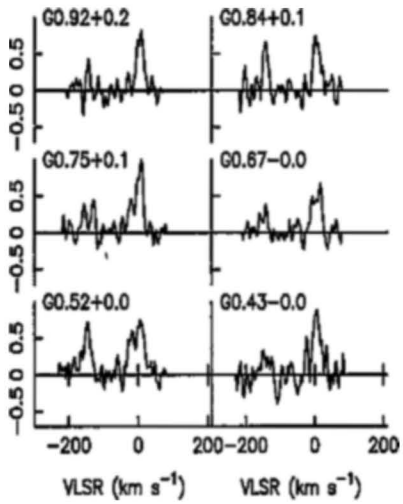

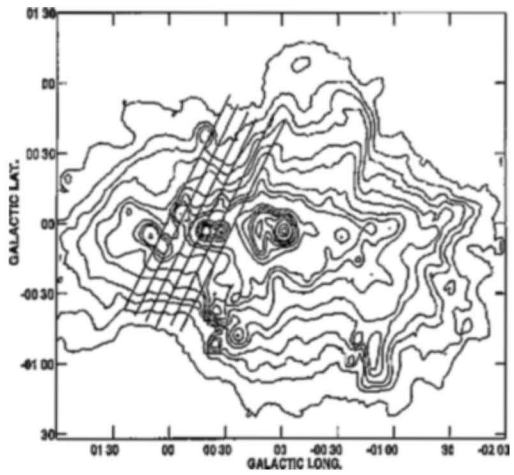

Figure 3. Spectra of recombination lines near 327 MHz observed with a beam of 2° × 6′ towards various positions within field 2a are shown on top. The observed positions are shown by slanted lines marked on the 11 cm continuum map with an angular resolution of 4′.3 taken from Reich *et al.* (1990) (bottom). The slanted line represent the 2° × 6′ beam of the ORT. The ordinate of the spectra are in units of T_L/T_{sys} and abscissa are in LSR velocity with respect to the hydrogen line. The contour levels for the 11 cm continuum map are in brightness temperatures of 0.5, 1, 1.5, 2, 3, 4, 5, 6, 8, 10, 20, 30, 40, 50, 70, 100, 200, 300 K.

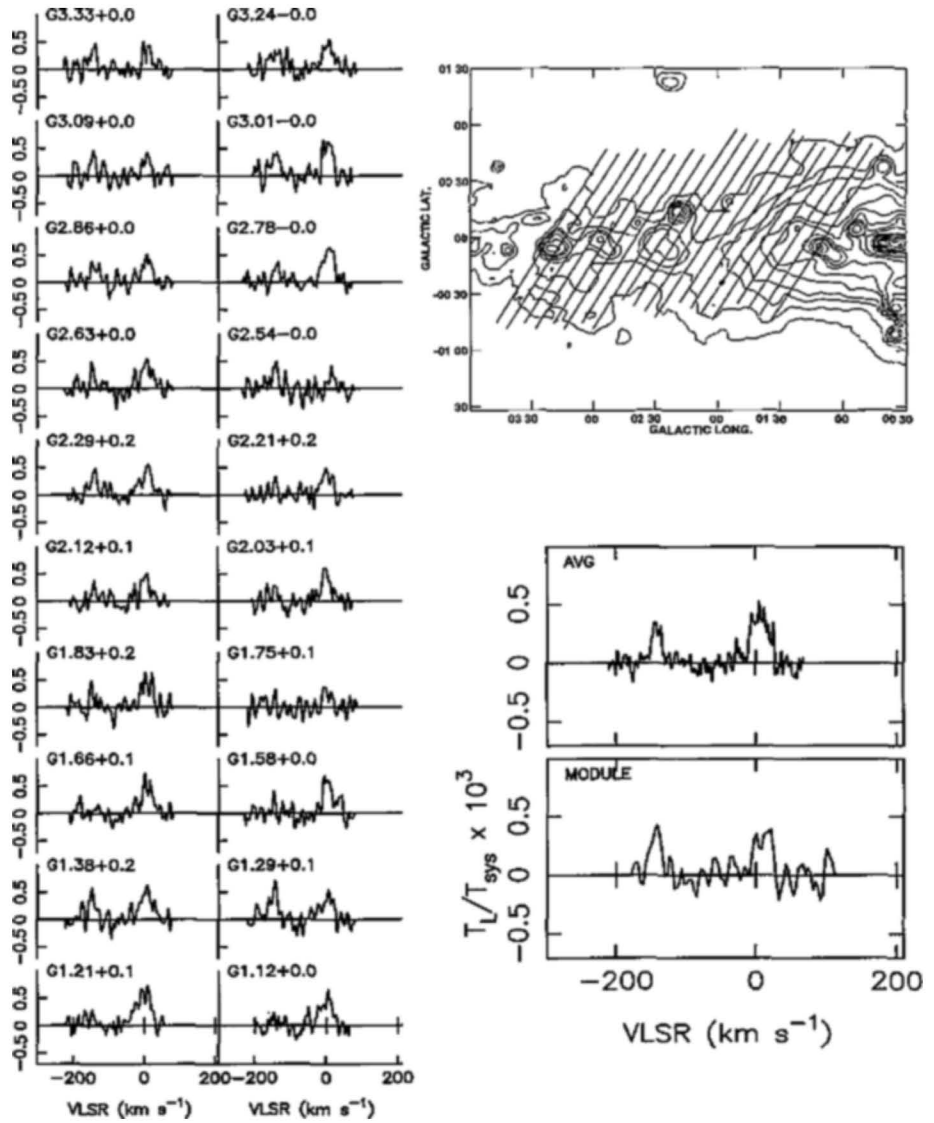

Figure 4. Spectra of recombination lines near 327 MHz observed with a beam of 2° × 6′ towards various positions within field 2b centered at G2.3+0.0 are shown on the left. The observed positions are shown by slanted lines marked on the 11 cm continuum map with an angular resolution of 4′.3 taken from Reich *et al.* (1990) (top right corner). The slanted line represent the 2° × 6′ beam of the ORT. The spectrum (labeled as AVG) obtained by averaging all the 20 spectra and the spectrum (labeled as MODULE) obtained using a 2° × 2° beam covering the same region (taken from paper I) are shown in the bottom right corner. The ordinate of the spectra are in units of T_L/T_{sys} and abscissa are in LSR velocity with respect to the hydrogen line. The contour levels for the 11 cm continuum map are in brightness temperatures of 0.5, 1, 1.5, 2, 3, 4, 6, 8, 10, 15, 20, 25, 30, 40, 50, 60 K.

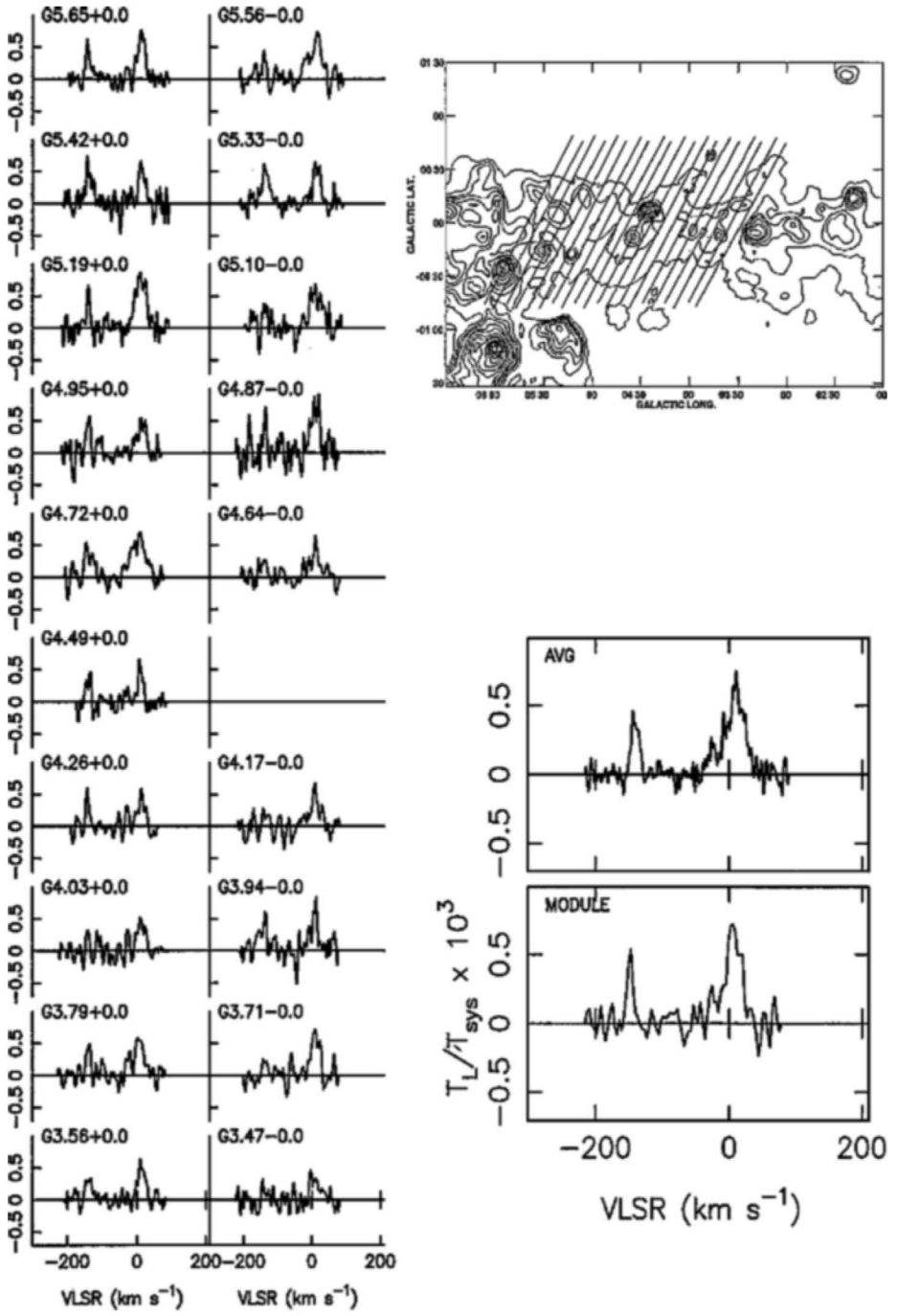

Figure 5. Same as Fig 4 for the field 2c centered at G4.7+0.0. The contour levels for the 11 cm continuum map are in brightness temperatures of 0.5, 1, 1.5, 2, 3, 4, 6, 8, 10, 15, 20, 25, 30, 40, 50 K.

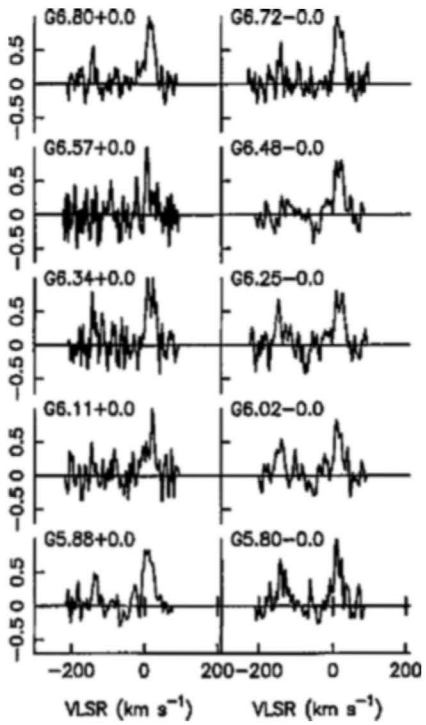

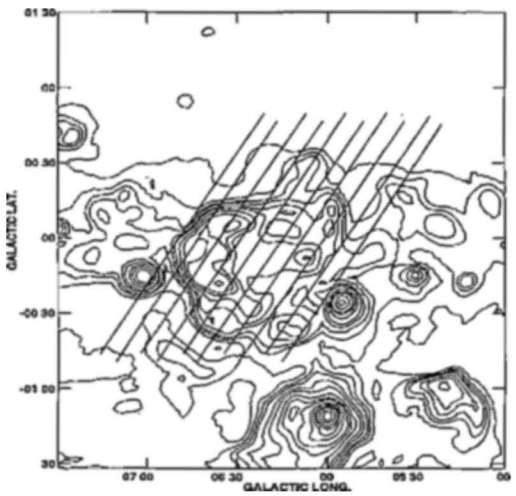

Figure 6. Same as Fig 3 for the field 2d. The contour levels for the 11 cm continuum map are in brightness temperatures of 0.5, 1, 1.5, 2, 3, 4, 6, 8, 10, 15, 20, 25, 30, 40, 50 K.

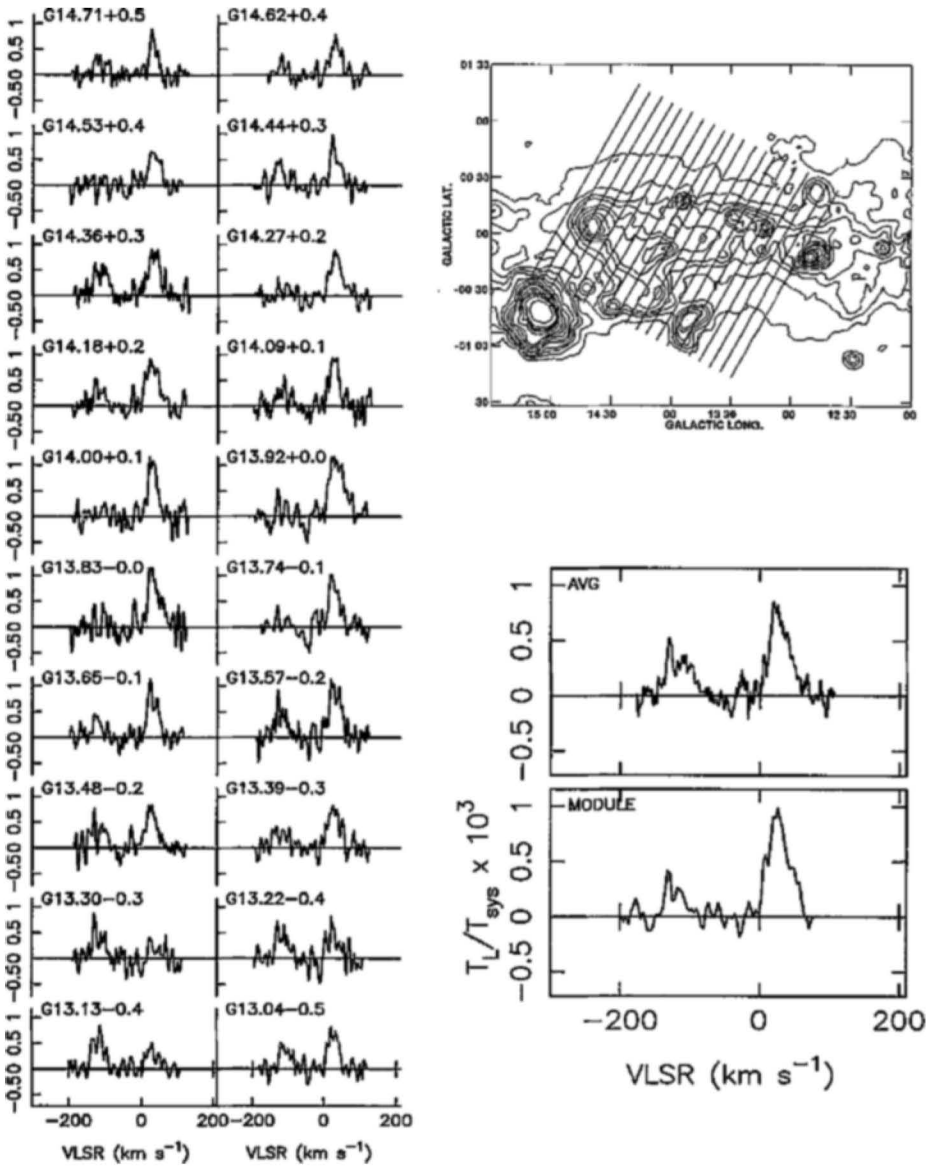

Figure 7. Same as Fig 4 for the field 3 centered at G13.9+0.0. The contour levels for the 11 cm continuum map are in brightness temperatures of 0.5, 1, 1.5, 2, 3, 4, 6, 8, 10, 15, 20, 25, 30, 40, 100 K.

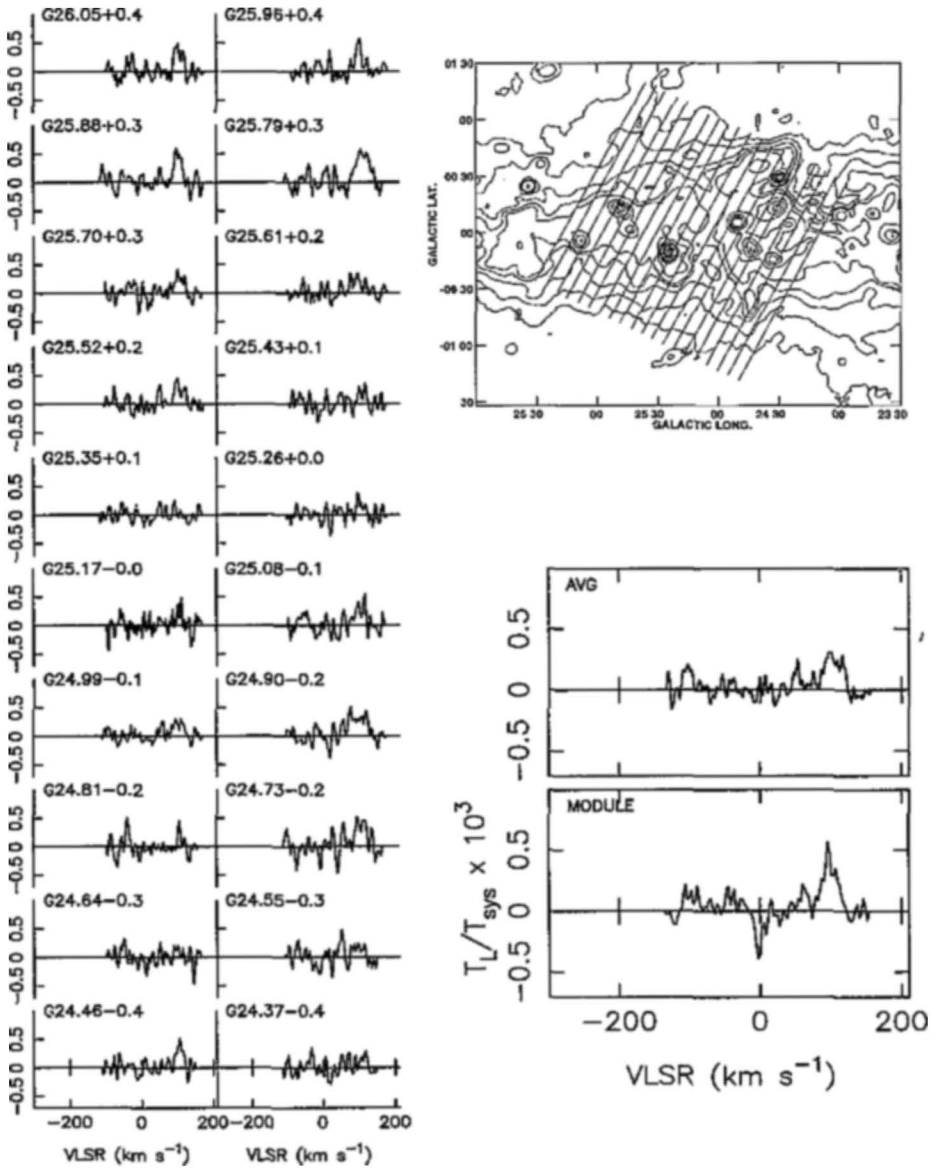

Figure 8. Same as Fig 4 for the field 4 centered at G25.2+0.0. The contour levels for the 11 cm continuum map are in brightness temperatures of 0.2, 0.5, 1, 1.5, 2, 4, 6, 8, 10, 15, 20, 25, 30 K.

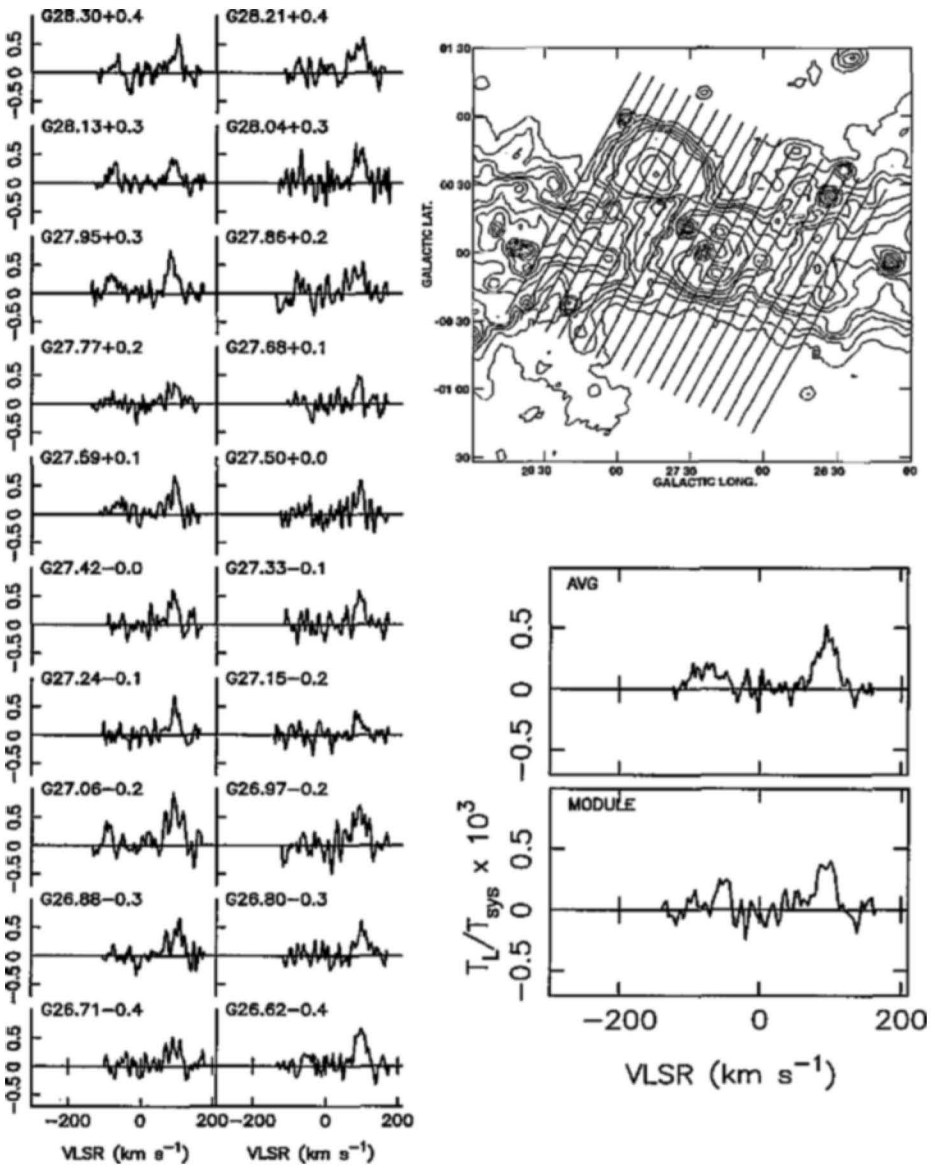

Figure 9. Same as Fig 4 for the field 5 centered at G27.5+0.0. The contour levels for the 11 cm continuum map are in brightness temperatures of 0.2, 0.4, 0.6, 0.8, 1, 1.5, 2, 3, 4, 5, 6, 7, 8 K.

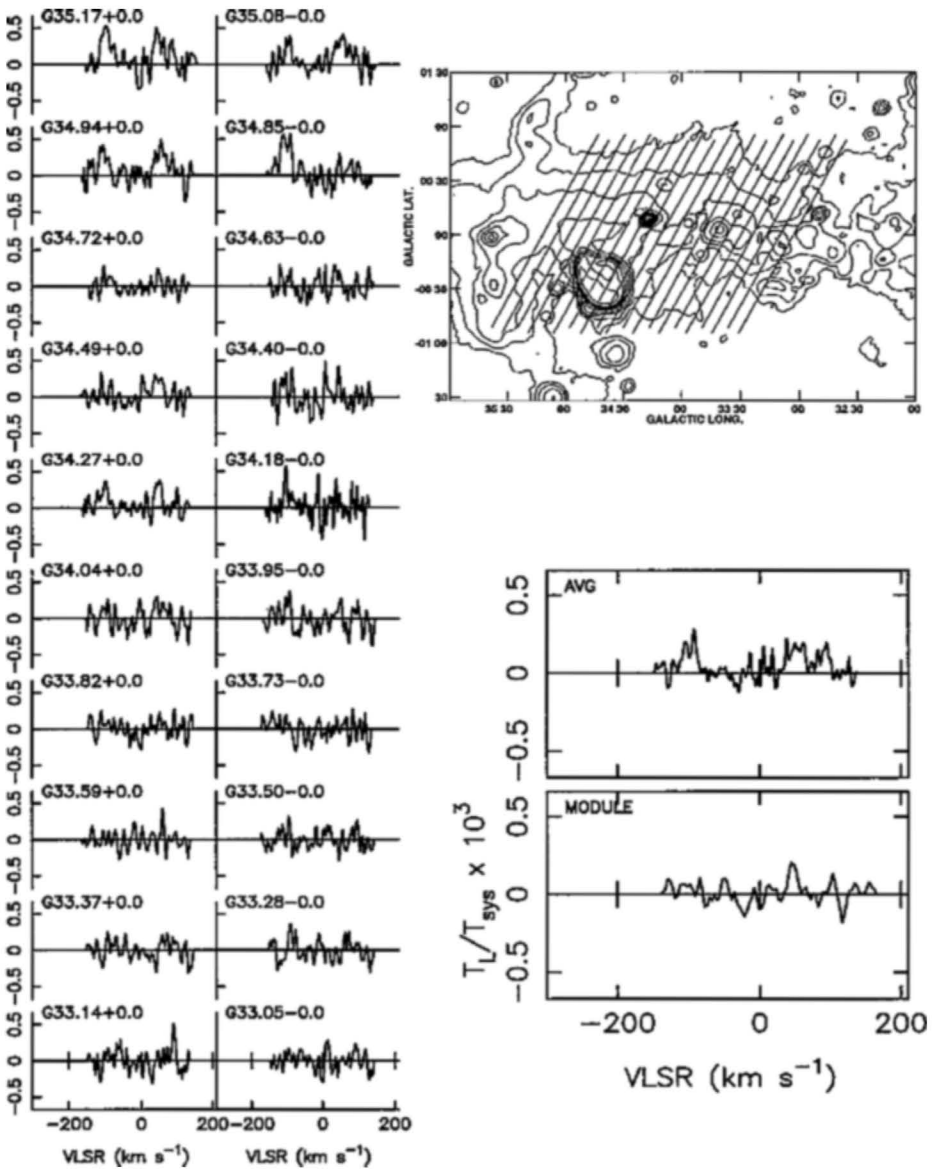

Figure 10. Same as Fig 4 for the field 6a centered at G34.2+0.0. The contour levels for the 11 cm continuum map are in brightness temperatures of 0.2, 0.5, 1, 2, 4, 6, 8, 10, 14, 18, 22, 24, 26 K.

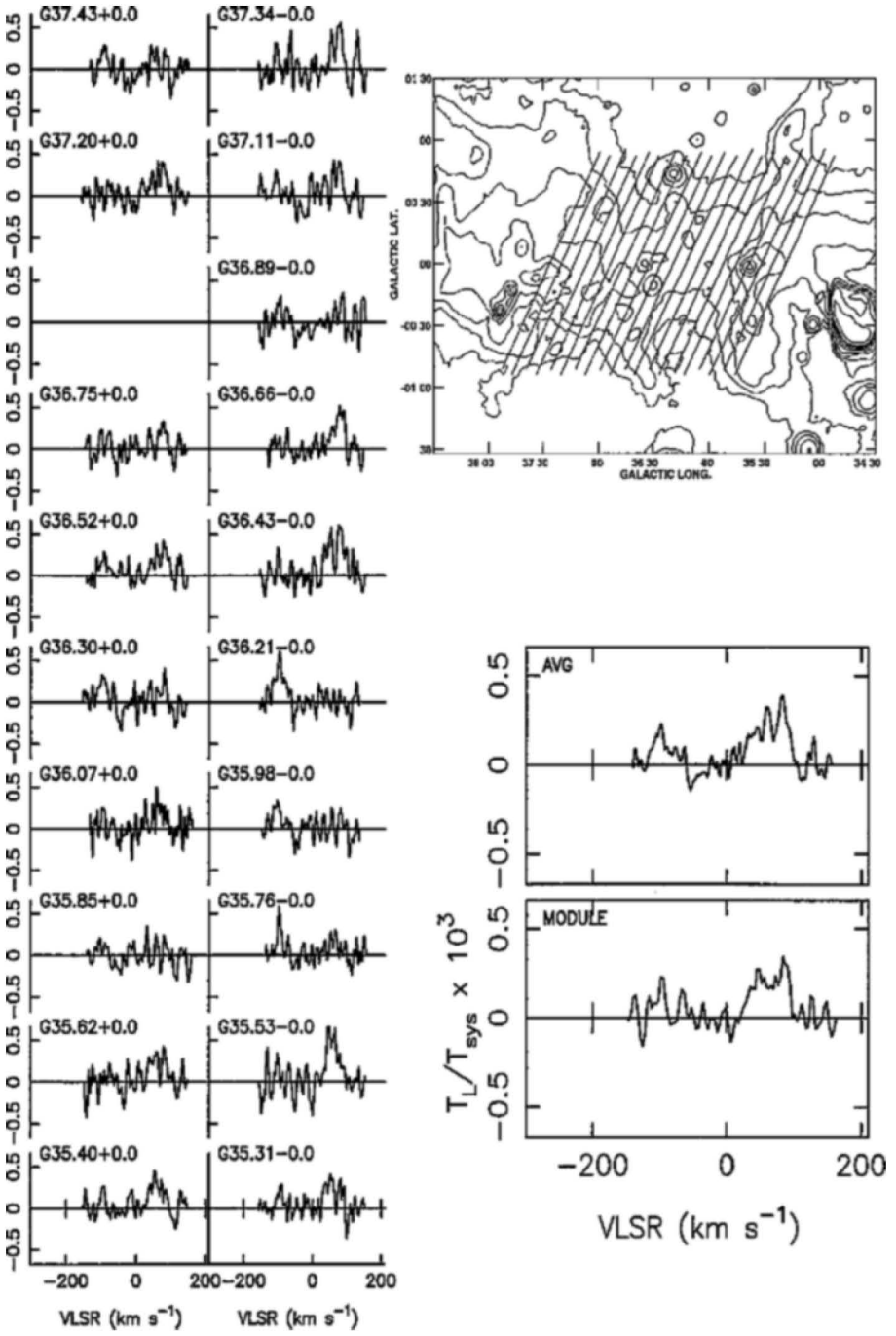

Figure 11. Same as Fig 4 for the field 6b centered at G36.5+0.0. The contour levels for the 11 cm continuum map are in brightness temperatures of 0.2, 0.5, 1, 2, 4, 6, 8, 10, 14, 18 K.

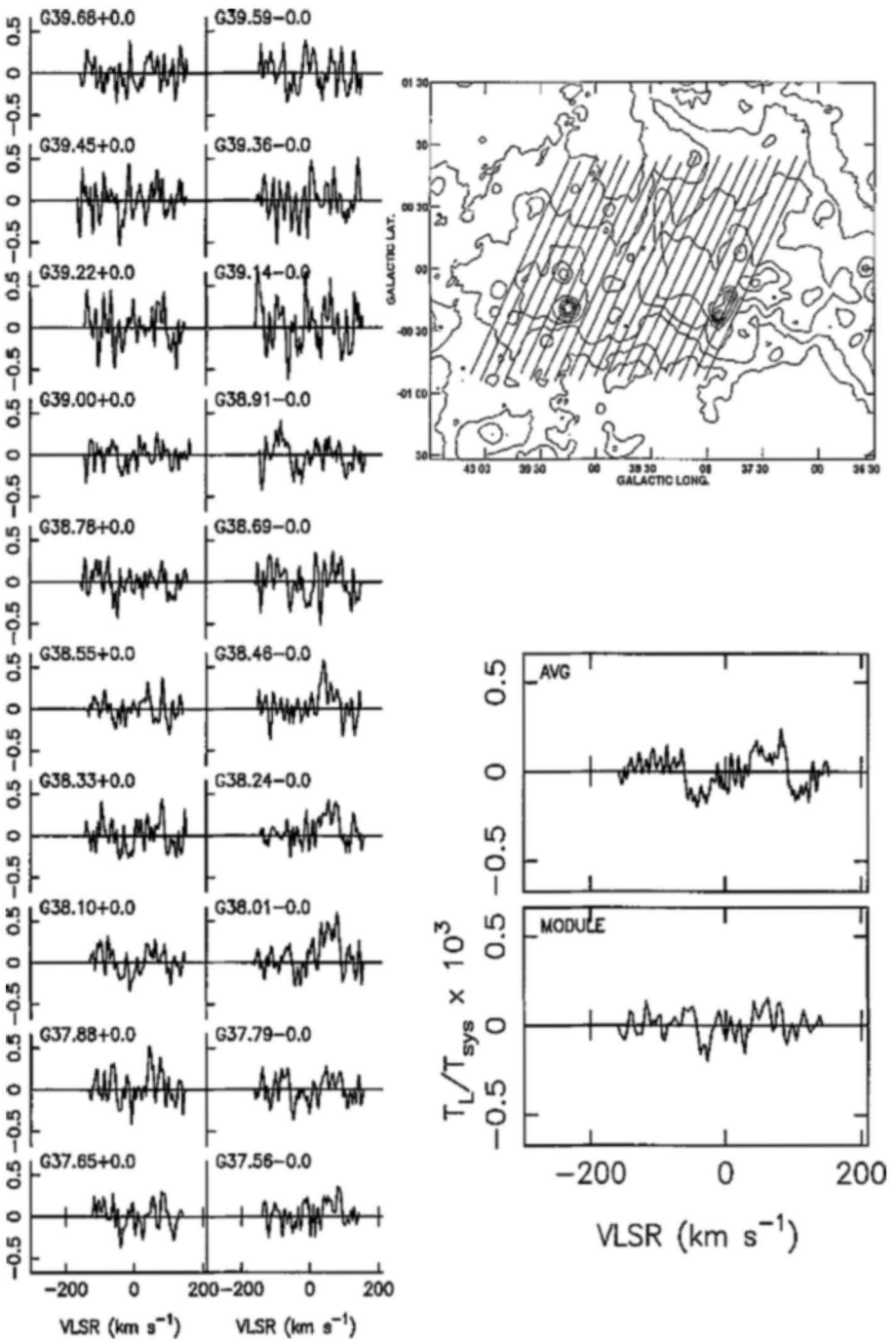

Figure 12. Same as Fig 4 for the field 6c centered at G38.7+0.0. The contour levels for the 11 cm continuum map are in brightness temperatures of 0.2, 0.5, 1, 2, 4, 6, 8, 10, 14, 18 K.

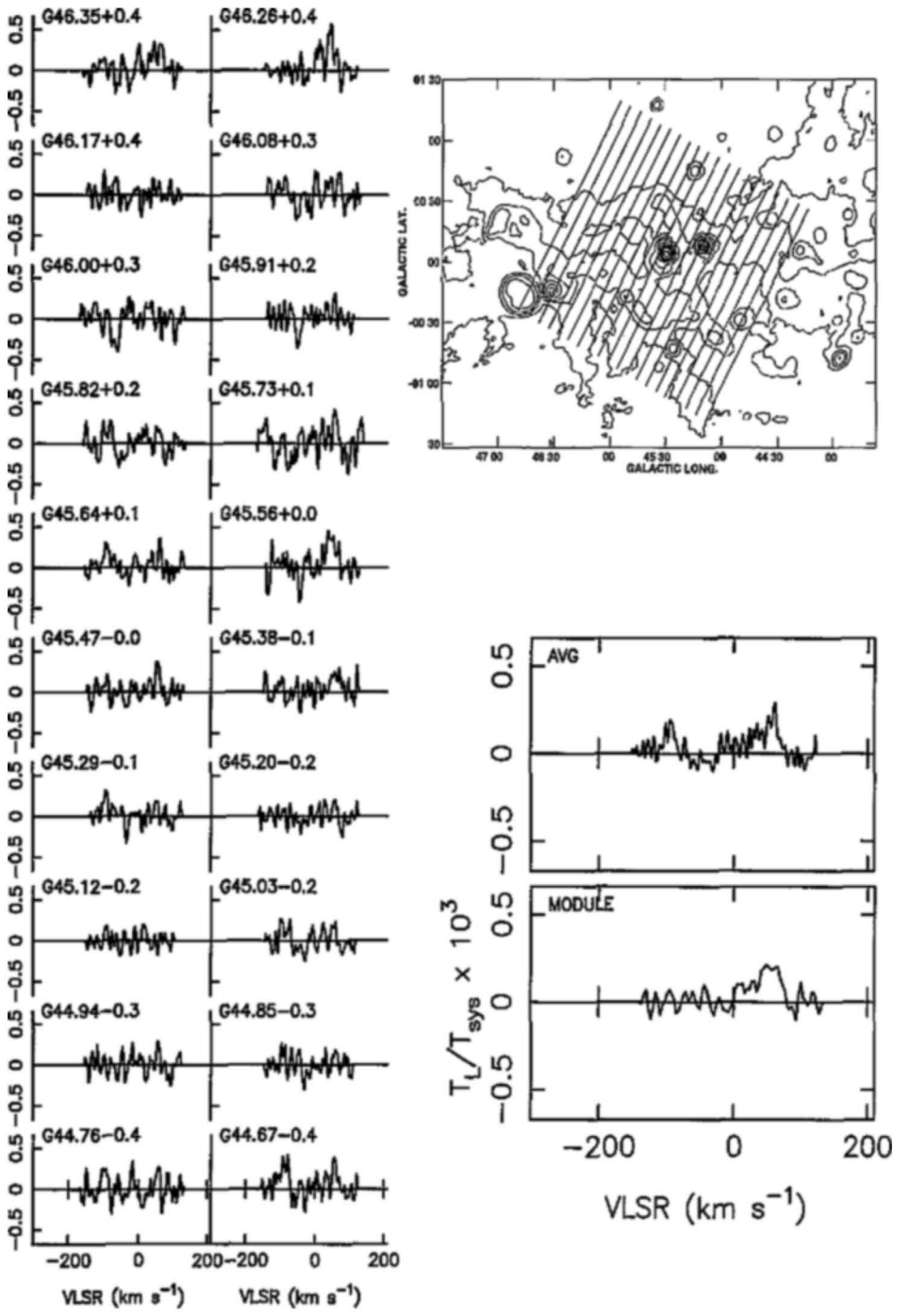

Figure 13. Same as Fig 4 for the field 7 centered at G45.5+0.0. The contour levels for the 11 cm continuum map are in brightness temperatures of 0.2, 0.5, 1, 2, 4, 6, 8, 10, 14, 18 K.

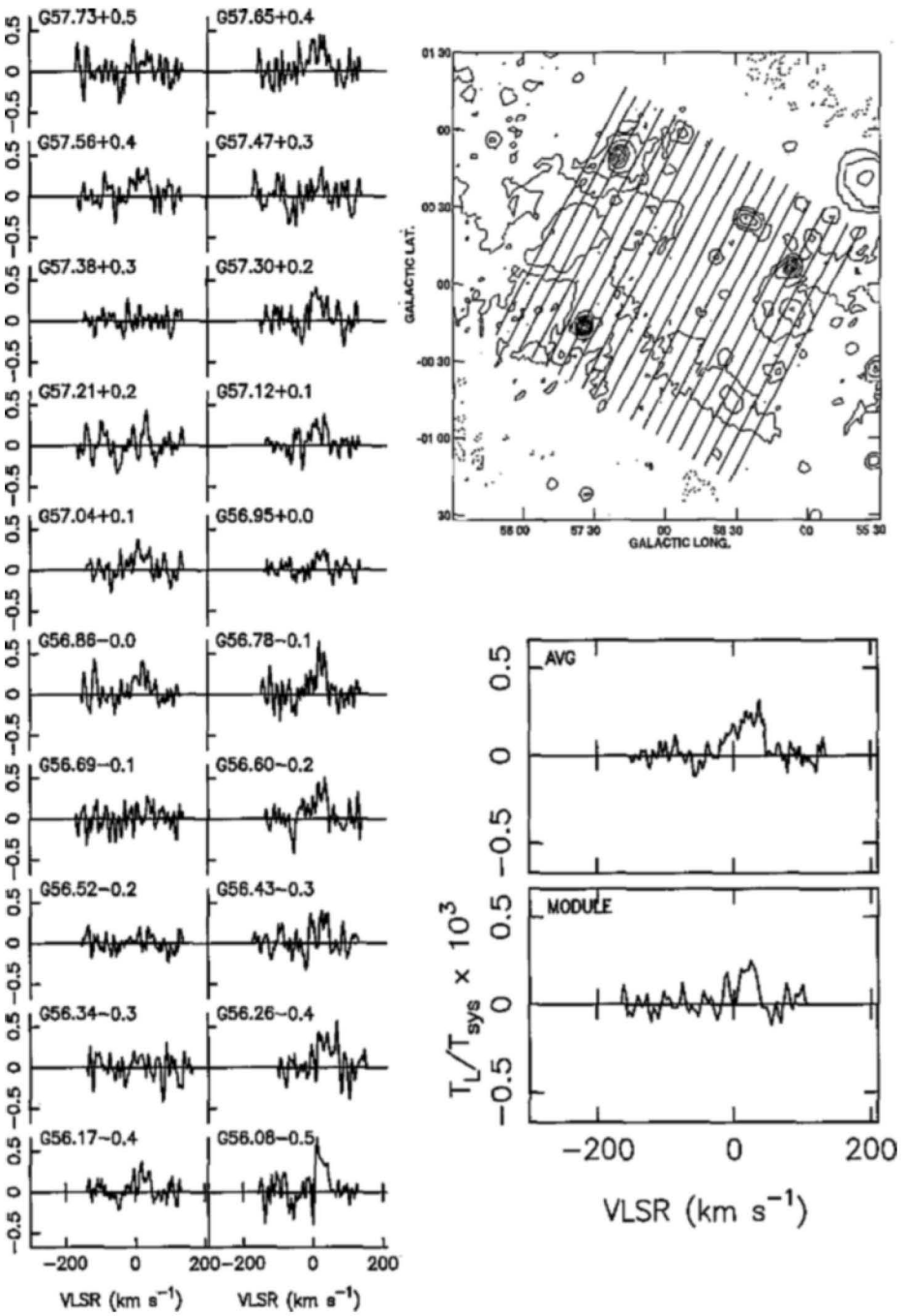

Figure 14. Same as Fig 4 for the field 8 centered at G56.9+0.0. The contour levels for the 11 cm continuum map are in brightness temperatures of −0.02, 0.1, 0.2, 0.4, 0.6, 0.8, 1, 1.2, 1.5, 1.9 K.

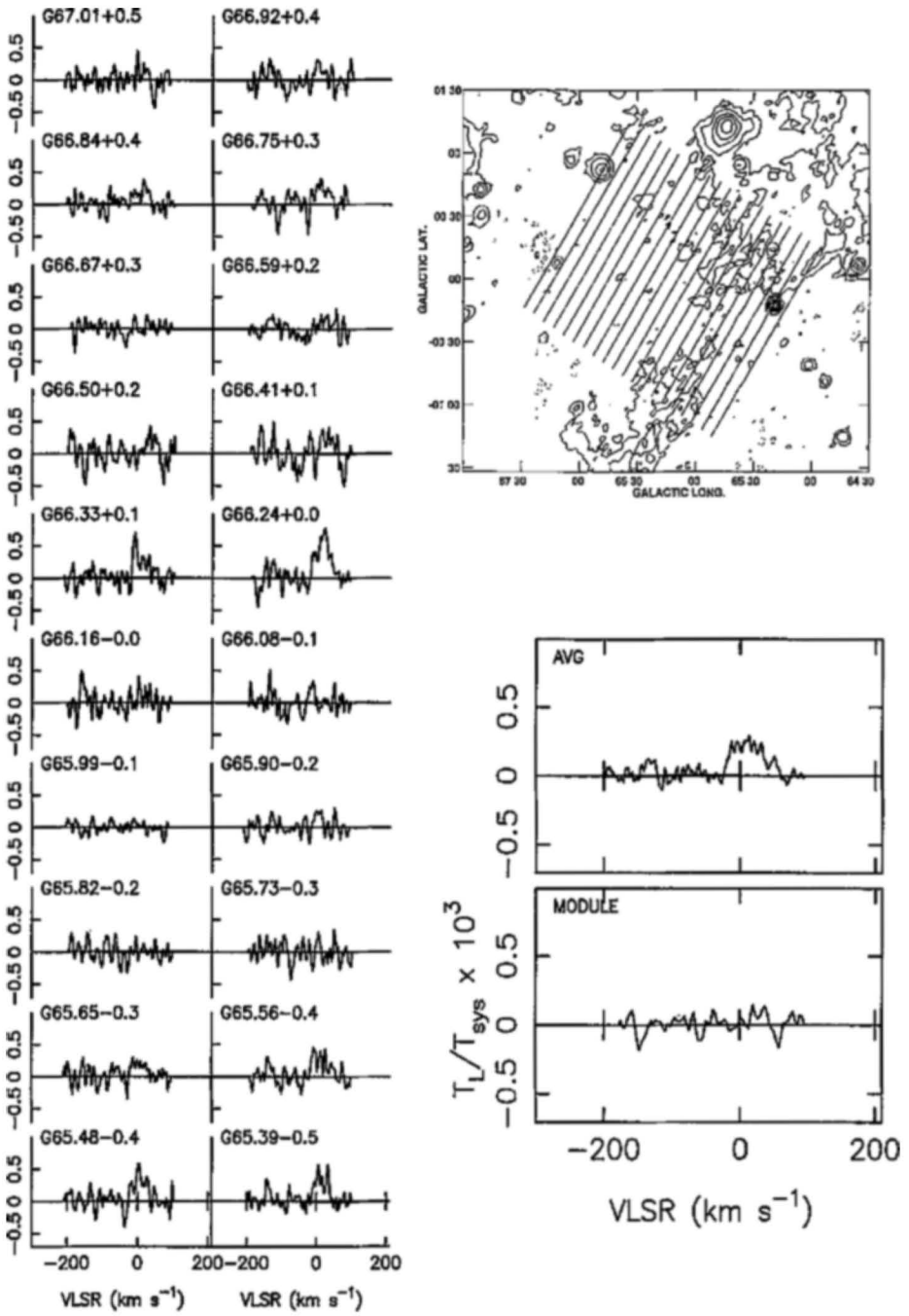

Figure 15. Same as Fig 4 for the field 9 centered at G66.2+0.0. The contour levels for the 11 cm continuum map are in brightness temperatures of −0.02, 0.1, 0.2, 0.4, 0.6, 0.8, 1, 1.2, 1.4 K.

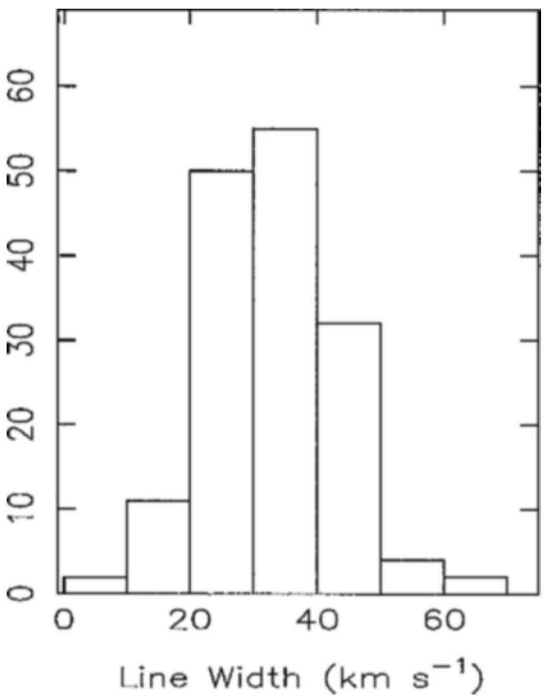

Figure 16. A histogram of the widths of hydrogen recombination lines near 327 MHz detected in the observations with a resolution of $2° \times 6'$.

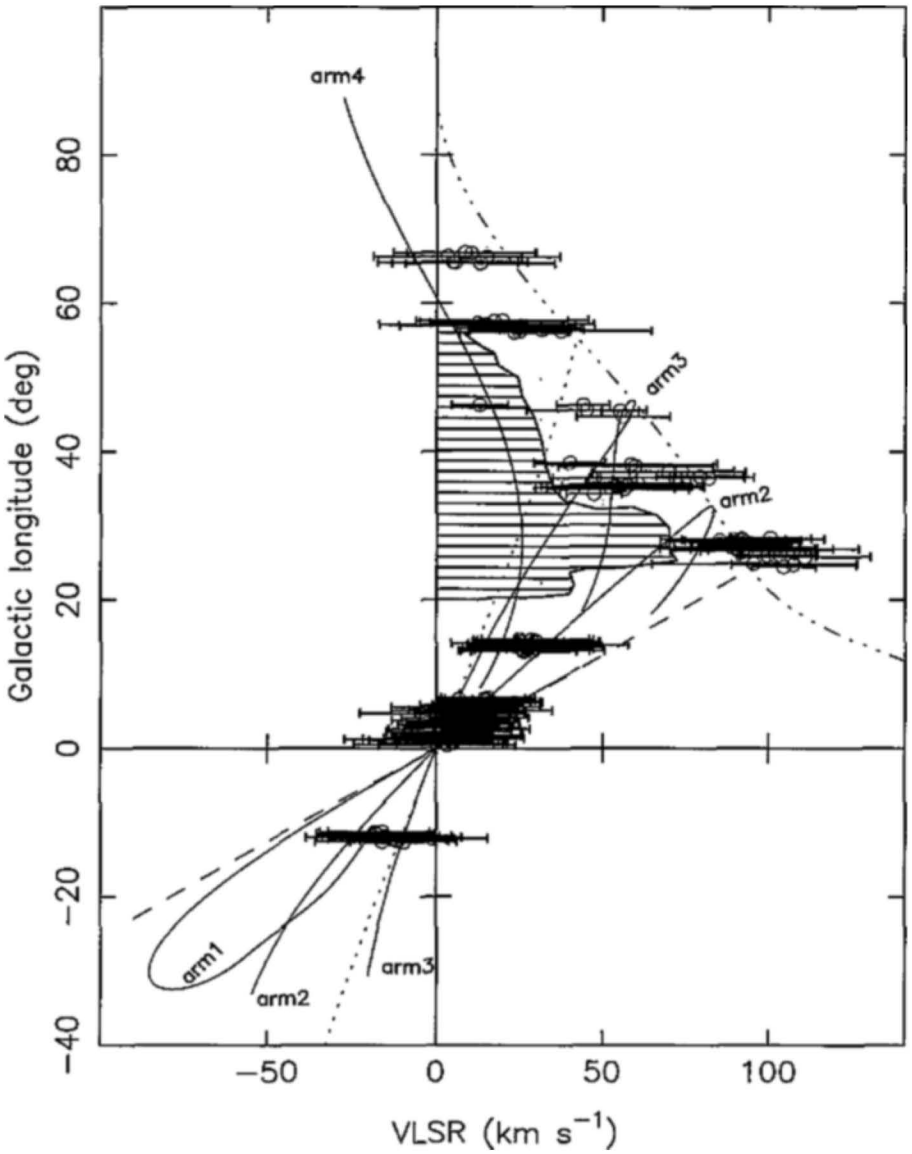

Figure 17. An *l-v* diagram obtained from the hydrogen line emission observed with the 2° × 6′ beam. The open circles represent the central velocity and the horizontal lines indicates the line width. The delineations (solid line) correspond to the four spiral arms (1 to 4 as designated by Taylor & Cordes 1993), the *l-v* diagram corresponding to an annulus of 3.5 kpc (dashed line) and 7 kpc (dotted line) and the terminal velocity at different galactic longitude (dash-dot-dot-dot line). Parameters of galactic rotation given by Burton & Gordon (1978) after scaling them to conform with $R_\odot$ = 8.5 kpc and θ_0 = 220 km s^{-1} are used to get these curves. The striped region corresponds to a region devoid of line emission near 327 MHz as observed in the 2° × 2° survey of Roshi & Anantharamaiah (2000).

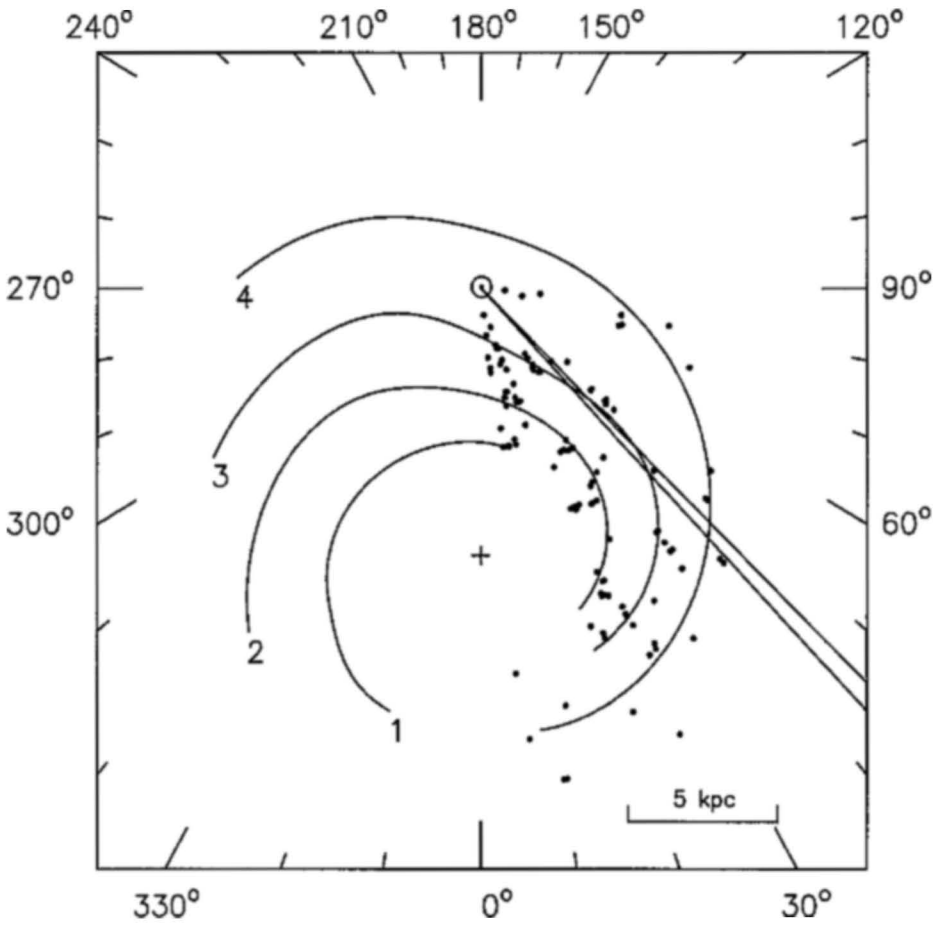

Figure 18. The line of sight through the galactic disk at $l = 45°.5$. The four spiral arms (curved solid lines) and the H II regions (dots) with known distances in the first quadrant are also marked.

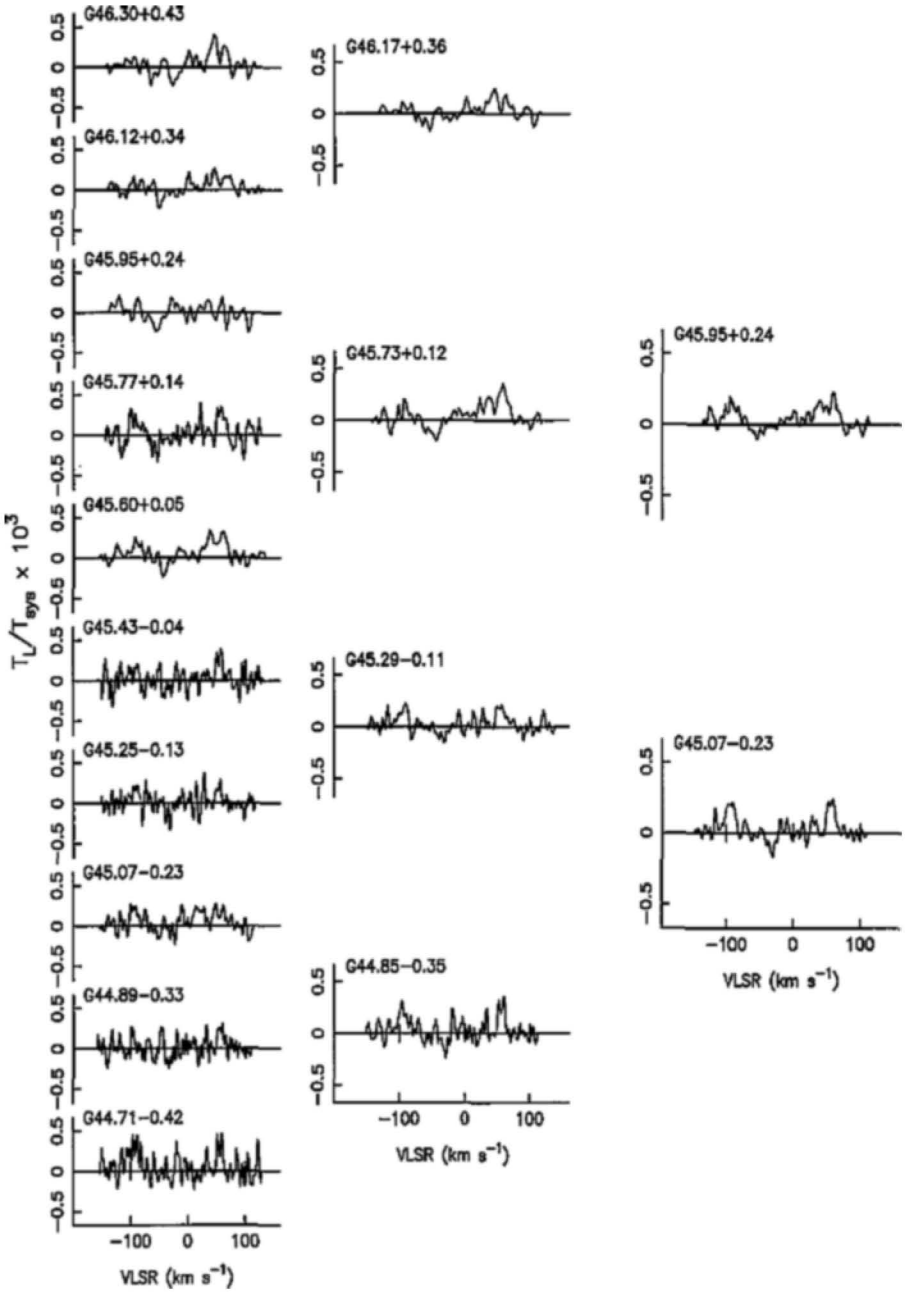

Figure 19. Spectra obtained by averaging different subsets of spectra observed towards field 7 (G45.5+0.0). The spectra shown in the left, center and right column are obtained by averaging over $2° \times 12'$, $2° \times 30'$ and $2° \times 1°$ area respectively. The galactic coordinates of the centers of these angular region are shown on the spectra.

References

Anantharamaiah K. R., 1985a, *JAA*, **6**, 177.
Anantharamaiah K. R., 1985b, *JAA*, **6**, 203.
Anantharamaiah K. R., 1986, *JAA*, **7**, 131.
Burton W. B., Gordon M. A., 1978, *A&A*, **63**, 7.
Caswell J. L., Haynes R. F., 1987, *A&A*, **171**, 261.
Cersosimo J. C., 1990, *ApJ*, **349**, 67.
Downes D., Wilson T. L., Bieging J., Wink J., 1980, *A&AS*, **40**, 379.
Erickson W. C., McConnell D., Anantharamaiah K. R., 1995, *ApJ*, **454**, 125.
Gordon M. A., Cato T., 1972, *ApJ*, **176**, 587.
Gottesman S. T., Gordon M. A., 1970, *ApJ*, **162**, L93.
Hart L., Pedlar A., 1976, *MNRAS*, **176**, 547.
Heiles C., 1994, *ApJ*, **436**, 720.
Heiles C., Reach W. T., Koo B.-C., 1996, *ApJ*, **466**, 191
Kantharia N. G., Anantharamaiah K. R., 2001, (this issue).
Konovalenko A. A., Sodin L. G., 1980, *Nat*, **283**, 360.
Lockman F. J., 1976, *ApJ*, **209**, 429.
Lockman F. J., 1980, in Shaver P. A., eds, Radio Recombination Lines, D. Reidel, Dordrecht, p. 185.
Lockman F. J., 1989, *ApJSS*, **71**, 469.
Lockman F., J., Pisano D., J., Howards G., J., 1996, *ApJ*, **472**, 173.
Matthews H. E., Pedlar A., Davies R. D. 1973, *MNRAS*, **165**, 149.
Mezger P. G., 1978, *A&A*, **70**, 565
Payne H. E., Anantharamaiah K. R., Erickson W. C., 1989, *ApJ*, **341**, 890.
Petuchowski S. J., Bennett C. L., 1993, *ApJ*, **405**, 591.
Reich W., Fürst E., Reich P., Reif K., 1990, *A&AS*, **85**, 633.
Roshi A. D., Anantharamaiah K. R., 2000a, 2000, *ApJ*, **535**, 231.
Roshi A. D., Anantharamaiah K. R., 2001, *ApJ* (submitted).
Shaver P. A., 1975, *Pramana*, **5**, 1.
Shaver P. A., 1976, *A&A*, **49**, 1.
Swarup G., *et al.*, 1971, *Nat. Phy. Sci.*, **230**, 185.
Taylor J., H., Cordes J., M., 1993, *ApJ*, **411**, 674.
Wood D. O. S., Churchwell E., 1989, *ApJS*, **69**, 831.

J. Astrophys. Astr. (2001) 22, 121–130

Spectroscopic Binaries near the North Galactic Pole Paper 23: HD 111154

R. F. Griffin
The Observatories, Madingley Road, Cambridge CB3 0HA, England.

Received 2000 June 27; accepted 2001 February 15

Abstract. HD 111154 is a member of the Coma Cluster. It is here shown to be a somewhat unequal pair of stars of approximately solar type. They are in an orbit that has a period of just under 27 days and quite a high eccentricity (0.442). Although the minimum masses (1.08 and 1.00 $M_\odot$) are large enough to encourage a search for eclipses, no such events have been detected.

Key words. Radial velocities—spectroscopic binaries—orbits—stars, individual—HD 111154.

1. Introduction

HD 111154 is seen as an eighth-magnitude solar-type star in Coma Berenices at a Galactic latitude above 85°; it is little more than 2° north-following 26 Com, the binary system with which this series of papers started (Griffin 1981). Its *Henry Draper Catalogue* type (Cannon & Pickering 1920) is G5.

The radial velocity of HD 111154 featured in a substantial list of North Galactic Pole stars measured by Sandage & Fouts (1987) from spectra obtained with an intensified reticon system on the coudé spectrograph of the Mount Wilson 100-inch reflector; they gave its value as -10 km s^{-1}. The presence of the star in that list led to some of its other properties being estimated by Knude (1989), who found (and gave to seemingly incredible accuracy) the absolute visual magnitude of $4^{\rm m}.325$ and the metallicity [Fe/H] = -0.040. He deduced its distance to be 64 pc. In their large survey that was published comparatively recently in this *Journal*, Yoss & Griffin (1997) gave the apparent magnitude and $(B-V)$ colour as $8^{\rm m}.40$ and $0^{\rm m}.56$ respectively, found $M_V = 4^{\rm m}.4$ and estimated an 'mk' type of G0 V from DDO-style photometry (McClure 1976 and references therein). On the basis of its being a single star they assigned a distance of 63 pc, corresponding to a distance modulus of exactly $4^{\rm m}$, but rather conflictingly they announced at the same time that it had been discovered to be a spectroscopic binary. The *Hipparcos* catalogue (1997) gives $m_V = 8^{\rm m}.38$, $(B-V) = 0^{\rm m}.59$, and a parallax of $0''.0130 \pm 0''.0011$, indicating a distance of 77 ± 7 pc and $(m-M) = 4^{\rm m}.44 \pm 0^{\rm m}.18$.

Quite recently, Odenkirchen, Soubiran & Colin (1998) listed HD 111154 as one of 40 stars (two of which seem to share an HD number) that they identified from *Hipparcos* as being kinematic members of the Coma Cluster. It is about 6½° from the cluster centre and is well outside the region featured in Trumpler's (1938) list of stars in that vicinity. The parallaxes of the members recognized by Odenkirchen *et al.* (1998) give a mean topocentric distance of 86 pc for the cluster members. Since the individually measured parallax of HD 111154 does not, however, indicate a radial distance from the cluster centre any larger than corresponds to its angular offset from that centre, there is no case for adopting the cluster parallax in preference to the individually determined one, which, in conjunction with the mean apparent magnitude of $8^{m}.39$, gives the integrated absolute magnitude of the binary system as $3^{m}.95$.

2. Radial-velocity measurements and orbit

The first attempt to measure the radial velocity of HD 111154 was made in 1971 with the original Cambridge spectrometer (Griffin 1967), and failed because no dips were recognized on the trace. That failure prompted Dr. (at that time Mr.) G. A. Radford and the writer to include the star in a list of troublesome objects whose natures might be elucidated by classification-dispersion spectrograms, which we took with the Cassegrain spectrograph of the Isaac Newton Telescope at Herstmonceux in the spring of 1974. HD 111154 was observed at a reciprocal dispersion of 62 Å mm^{-1} on 1974 April 1; the spectrum was classified as G0 V by Radford, who also noted that it had broad lines. In retrospect we can tell that there were two spectra, of mutually comparable intensities, with a separation at that time of more than 90 km s^{-1} (about 1.3 Å in the blue spectral region observed); the splitting of the lines would amount to about 20 μ on the plate, accounting for their somewhat diffuse appearance.

Some years later, in 1980, when there had been some improvement in performance of both the spectrometer and the observer at Cambridge, a fresh attempt to measure the velocity of HD 111154 was successful; a second measurement, which disagreed with the first, was made in 1984. It was noted on both occasions that the 'dip' was "very feeble". After a third observation, in 1987 March, had been made (with *Coravel* at Haute-Provence (Baranne, Mayor & Poncet 1979)) and disagreed with both the earlier ones, the object was observed relatively intensively in Cambridge. Very soon its double-lined nature was discovered, and the period of 27 days was established in that same observing season. As many as 86 observations (mostly consisting of measurements of both components) have now been accumulated of it. The majority (58) has been made at Haute-Provence, but 17 have come from Cambridge, 7 from the spectrometer (Fletcher *et al.* 1982) at the Dominion Astrophysical Observatory, Victoria, and 4 from the ESO *Coravel*. They have all been reduced as well as possible to the Cambridge zero-point (Griffin 1969) and are set out in Table 1; all but two (identified in the Table) were made personally

Table 1. Radial-velocity observations of HD 111154.

Heliocentric Date	HMJD	Velocity Prim. km s^{-1}	Velocity Sec. km s^{-1}	Phase	(O−C) Prim. km s^{-1}	(O−C) Sec. km s^{-1}
1980 Jan. 13.22*	44251.22	−42.1	—	0.187	−1.0	—
1984 Apr. 27.97*	45817.97	−32.0	—	58.277	+0.7	—
1987 Mar. 1.03	46855.03	+26.6	—	96.727	+0.1	—
20.03*	874.03	−15.0	—	97.432	−0.6	—
21.07*	875.07	−2.8		.470	—	—
22.01*	876.01	−2.1		.505	—	—
25.99*	879.99	+16.8	−17.7	.653	+1.9	−2.7
29.92*	883.92	+37.8	−40.2	.799	−1.0	+0.6
Apr. 27.98*	912.98	+53.2	−54.3	98.876	+1.7	+0.2
May 7.96*	922.96	−35.3	+39.9	99.246	+0.6	−0.1
8.97*	923.97	−31.8	+35.4	.283	+0.1	−0.3
19.99*	934.99	+22.0	—	.692	+1.1	—
1988 Jan. 23.51†	47183.51	+53.9	−58.4	108.906	−0.1	−1.2
26.41†	186.41	+1.0		109.014	—	—
27.57†	187.57	−24.9	+28.3	.057	+0.4	−0.2
30.52†	190.52	−42.8	+46.2	.166	−0.6	−0.6
31.43†	191.43	−40.4	+43.7	.200	−0.2	−0.9
Feb. 1.45†	192.45	−37.0	+40.6	.238	−0.2	−0.3
Mar. 11.09	231.09	+18.7	−17.6	110.670	+1.2	+0.2
12.00	232.00	+22.6	−23.0	.704	−0.2	+0.5
12.97	232.97	+27.3	−31.2	.740	−1.4	−1.4
13.95	233.95	+35.5	−35.9	.776	+0.6	+0.7
14.93	234.93	+40.6	−41.7	.813	−0.7	+1.8
16.91	236.91	+53.3	−55.0	.886	+0.6	+0.8
22.12*	242.12	−35.9	+39.3	111.079	−1.4	+0.9
23.08*	243.08	−43.0	+47.3:	.115	−1.7	+1.4
Apr. 9.91*	260.91	+35.3	−33.1	.776	+0.5	+3.4
12.95*	263.95	+52.1	−56.3	.889	−0.8	−0.2
13.93*	264.93	+53.4	—	.925	−0.1	—
May 6.92*	287.92	+33.5	−34.6:	112.777	−1.6	+2.2
Nov. 7.21	472.21	+9.0	−7.9	119.610	+0.3	+0.4
1989 Jan. 31.16[M]	47557.16	+32.0	−32.2	122.760	0.0	+1.3
Feb. 23.26‡	580.26	+9.6	−10.0	123.616	0.0	−0.8
24.24‡	581.24	+15.1	−15.4	.653	+0.2	−0.5
25.30‡	582.30	+21.0	−23.6	.692	+0.1	−2.2
Mar. 24.99	609.99	+24.8	−26.1	124.719	−0.3	−0.1
25.92	610.92	+30.7	−32.0	.753	−0.2	+0.2
27.02	612.02	+37.3	−38.4	.794	−0.7	+1.5

Table 1. (*Continued*)

Heliocentric Date	HMJD	Velocity Prim. km s^{-1}	Velocity Sec. km s^{-1}	Phase	(O−C) Prim. km s^{-1}	(O−C) Sec. km s^{-1}
1989 Mar. 27.94	47612.94	+42.8	−47.5	124.828	−1.2	−1.1
28.88	613.88	+50.0	−53.0	.863	+0.3	−0.4
30.10	615.10	+55.3	−57.6	.908	+1.3	−0.3
30.97	615.97	+51.1	−54.7	.940	0.0	−0.6
Apr. 27.86	643.86	+36.0	−37.1	125.974	−0.7	+1.5
28.05	644.05	+32.2	−33.3	.981	+0.2	+0.1
28.83	644.83	+8.8	−7.3	126.010	+0.4	+0.6
28.91	644.91	+5.3	−5.4	.013	−0.5	−0.3
28.97	644.97	+4.5	−4.3	.016	+0.6	−1.2
29.03	645.03	+3.3	−2.1	.018	+1.3	−1.1
29.10	645.10	−0.7	+3.4	.020	−0.5	+2.1
29.94	645.94	−22.2	+25.7	.052	+0.2	+0.3
30.08	646.08	−24.6	+28.2	.057	+0.6	−0.2
May 1.03	647.03	−37.7	+41.1	.092	+0.1	−0.9
1.94	647.94	−42.0	+47.1	.126	+0.2	+0.4
2.91	648.91	−42.9	+48.0	.162	−0.5	+1.0
1990 Jan. 20.22[P]	47911.22	+52.6	−56.8	135.887	−0.2	−0.9
27.04	918.04	−42.6	+47.1	136.140	0.0	−0.2
31.12	922.12	−31.1	+35.0	.291	−0.1	+0.3
Feb. 12.33[‡]	934.33	+29.5	−31.3	.744	+0.2	−0.7
1991 Jan. 28.13	48284.13	+24.4	−25.5	149.713	+0.1	−0.4
29.14	285.14	+30.5	−31.4	.751	0.0	+0.4
Feb. 5.01	292.01	+12.1	−13.3	150.006	−0.5	−0.9
6.15	293.15	−20.7	+23.1	.048	−0.5	+0.1
1992 Jan. 14.15	48635.15	+26.4	−28.0	162.728	−0.2	−0.3
16.12	637.12	+39.0	−40.8	.801	−0.2	+0.5
21.18	642.18	+26.6	−27.6	.989	−0.1	+0.1
Feb. 28.42[†]	680.42	−18.2:	+20.1:	164.406	−0.7	0.0
Apr. 22.02	734.02	−18.7	+23.4	166.394	+0.4	+1.6
23.04	735.04	−13.9	+17.5	.432	+0.6	+0.7
23.95	735.95	−10.4	+11.8	.465	−0.1	−0.5
29.06	741.06	+15.4	−14.9	.655	+0.2	+0.4
June 26.93	799.93	+45.7	−48.3	168.837	+0.1	−0.1
Dec. 19.20	975.20	−25.7	+29.1	175.336	+0.2	−0.1
21.21	977.21	−16.8	+19.9	.410	+0.3	+0.3
1993 Feb. 12.16	49030.16	−21.6	+24.5	177.374	−0.1	+0.1
14.13	032.13	−12.5	+14.9	.447	+0.1	+0.1
July 8.91	176.91	+41.5	−44.3	182.815	−0.1	−0.4
Dec. 25.24	346.24	−37.7	+42.7	189.093	+0.3	+0.5

Table 1. (*Continued*)

Heliocentric Date	HMJD	Velocity Prim. km s^{-1}	Velocity Sec. km s^{-1}	Phase	(O−C) Prim. km s^{-1}	(O−C) Sec. km s^{-1}
1994 Feb. 16.14	49399.14	−24.0	+26.9	191.054	−0.2	0.0
Aug. 4.84	568.84	−25.3	+27.5	197.346	−0.5	−0.4
Dec. 11.21	697.21	−40.8	+44.2	202.105	−0.6	−0.4
12.22	698.22	−42.3	+47.4	.143	+0.4	+0.1
1995 Jan. 4.19	49721.19	+22.0	−22.0	202.995	+0.1	+0.6
5.20	722.20	−8.5	+12.1	203.032	+0.9	+0.8
7.15	724.15	−39.7	+44.2	.104	+0.3	−0.3
June 2.99	870.99	+0.5		208.549	—	—
1996 Apr. 1.02	50174.02	+35.8	−38.3	219.784	−0.4	−0.3

*Observed with original Cambridge spectrometer.
†Observed with DAO 48-inch telescope.
‡Observed with ESO *Coravel*.
All others observed with Haute-Provence *Coravel*.
[M]Observed by Dr. J.-C. Mermilliod.
[P]Observed by Monsieur B. Pernier.

by the author. An example of a double-lined *Coravel* trace is shown as Fig. 1. Only a minority of the *Coravel* traces are of that form, however, because owing to the limited scanning range it was frequently necessary to observe the two components in separate integrations. In such cases both observations of a pair are listed together with the same mean time, because even near periastron the change of the components' velocities was never enough to be significant within the overall time taken to observe them both (normally less than 10 minutes).

Experimental orbital solutions showed first of all that it was appropriate globally to attribute half-weight to measurements of the secondary star, and that the Cambridge observations had twice the residuals, and therefore merited one-quarter of the weight, of *Coravel* and DAO ones. The residuals given by four observations in which the two 'dips' were closely blended together ($\Delta V < 15$ km s^{-1}) were noticed to contribute far more than a fair share towards the total of the squares of the residuals, so those few measures were rejected altogether. Four other observations (one *Coravel*, one DAO and two Cambridge) were so closely blended that they could be reduced only as single-lined, and so have not been used in the orbital solution. A few other velocities that were explicitly noted as uncertain at the time of measurement were arbitrarily assigned half the weight to which they would otherwise be entitled and are marked with a colon in Table 1. The final solution of the orbit is illustrated in Fig. 2 and has the following elements:

P	=	26.97128 ± 0.00013 days	$(T)_{143}$	=	MJD 48103.061 ± 0.012
γ	=	+0.55 ± 0.05 km s^{-1}	$a_1 \sin i$	=	16.09 ± 0.04 Gm
K_1	=	48.36 ± 0.10 km s^{-1}	$a_2 \sin i$	=	17.40 ± 0.05 Gm
K_2	=	52.30 ± 0.14 km s^{-1}	$f(m_1)$	=	0.2286 ± 0.0015 $M_\odot$
q	=	1.081 ± 0.003 ($= m_1/m_2$)	$f(m_2)$	=	0.2891 ± 0.0024 $M_\odot$
e	=	0.4422 ± 0.0013	$m_1 \sin^3 i$	=	1.071 ± 0.007 $M_\odot$
ω	=	76.08 ± 0.24 degrees	$m_2 \sin^3 i$	=	0.990 ± 0.006 $M_\odot$

R.m.s. residual (unit weight) = 0.51 km s^{-1}

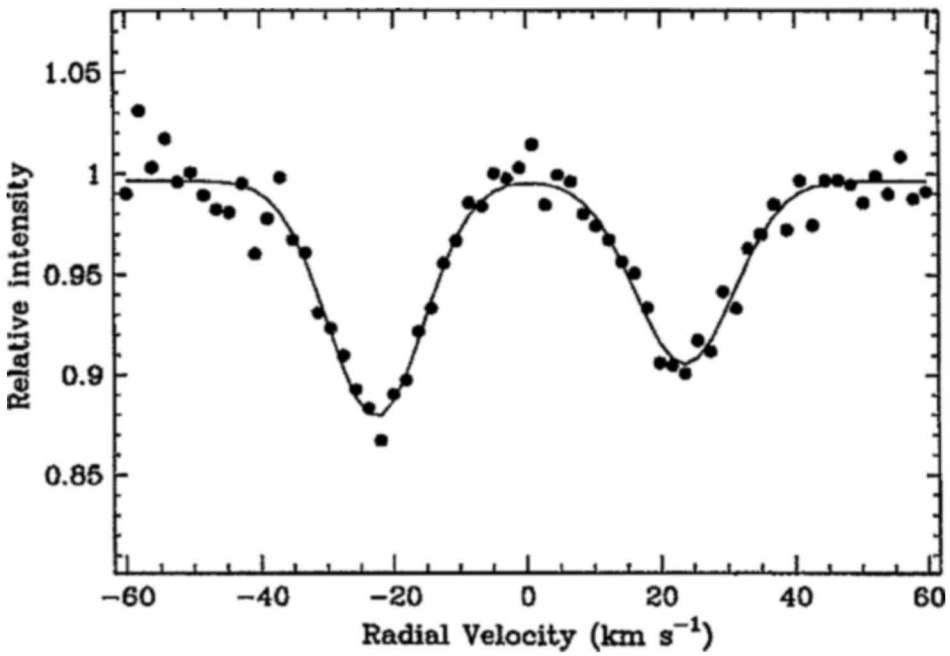

Figure 1. Double-lined radial-velocity trace of HD 111154, obtained with the Haute-Provence *Coravel* on 1993 February 12, illustrating the unequal dips. The number of counts per bin in the continuum is about 10,000.

3. Discussion

An obvious conclusion that can be made straight away from the orbital elements is that the γ-velocity is exactly the velocity of the Coma Cluster, amply confirming the system's cluster membership (Odenkirchen *et al.* 1998), which might have been considered questionable on the basis of the Sandage & Fouts (1987) radial velocity.

Another fact of immediate relevance is the mass ratio of 1.081 to 1, which, on the part of the main sequence in the vicinity of the observed integrated $(B - V)$ colour ($0^{\rm m}.58$) of HD 111154, corresponds (Allen 1973) to a difference of about $0^{\rm m}.4$ in visual luminosity.

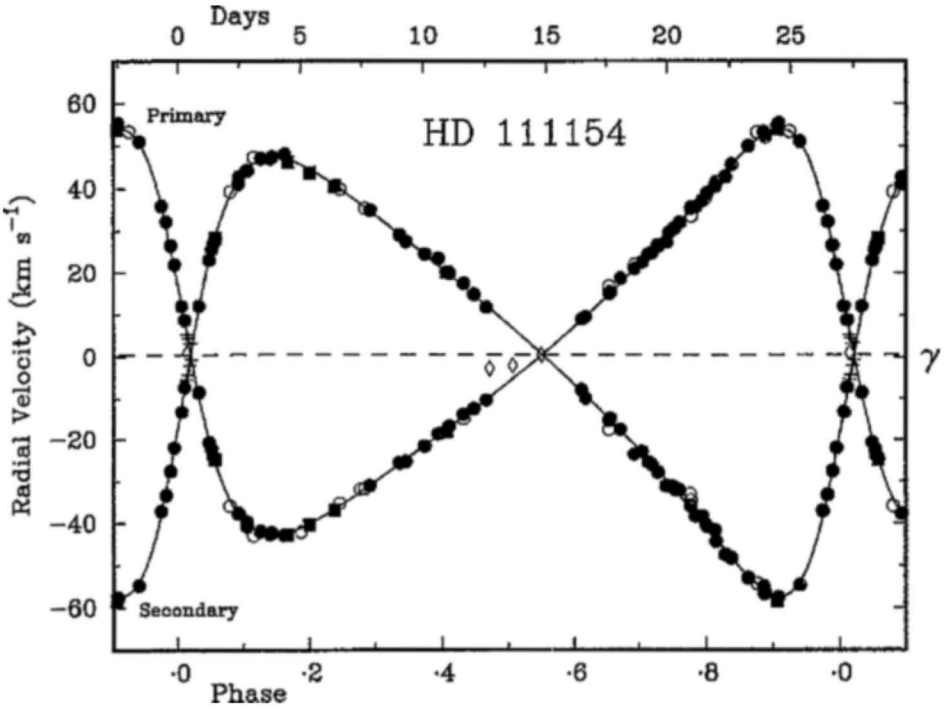

Figure 2. The observed radial velocities of HD 111154 plotted as a function of phase, with the velocity curves corresponding to the adopted orbital elements drawn through them. Filled circles represent observations made with the *Coravels* at Haute-Provence and ESO, squares indicate DAO data, and open circles are used for observations made with the original Cambridge spectrometer. Plusses show velocities that were not used in the orbital solution, having come from closely blended traces ($\Delta V < 15$ km s^{-1}) and being less reliable than those more clearly separated; open diamonds refer to four observations that were so closely blended that they had to be reduced as single-lined and omitted from the solution.

The disparity noticeable between the 'dips' given by the two component stars in Fig. 1 is a second factor that can be used to quantify the differences between their respective magnitudes and spectral types, again on the assumption that they follow the normal main-sequence relationships between luminosity, colour and spectral type. The mean equivalent widths found for the areas of the two dips on *Coravel* radial-velocity traces are 2.21 ± 0.03 and 1.49 ± 0.04 km s^{-1}. The total of 3.70 km s^{-1} tallies exactly with expectation for $(B - V) = 0^{\rm m}.58$, according to the graphical indication of equivalent widths of dips against colour index given in Fig. 21 of Baranne *et al.* (1979) for stars in the Coma Cluster. The ratio of the components' luminosities is rather larger than the ratio (1.48 ± 0.05; in magnitude terms $0^{\rm m}.42 \pm 0^{\rm m}.03$) of their equivalent widths because, as the cited graph shows, the intrinsic strength of dips increases with $(B - V)$. When due account

Table 2. Photometric model (absolute magnitudes, colour indices) for HD 111154.

Star		M_V m	(B−V) m	(U−B) m	M_B m	M_U m
Model	F9 V	4.20	0.55	0.04	4.75	4.79
	G1.5 V	4.60	0.62	0.08	5.22	5.30
	F9 V+G1.5 V	3.63	0.58	0.05	4.21	4.26
HD 111154 (observed)		8.39*	0.58			

**Apparent* magnitude; the implied distance modulus is $4^m.76$ (a distance of 90 pc).

is taken of that relationship, a magnitude difference, in the B photometric band that approximates to the spectral range used by *Coravel*, close to $0^m.5$ is determined. The V magnitude difference must then be close to $0^m.4$, in very good agreement with the difference obtained from the mass ratio, and the model set out in Table 2 is derived for the system. It is to be noticed that the integrated absolute magnitude expected for the system is $3^m.63$; it is a little brighter (though by less than two standard deviations) than the $3^m.95 \pm 0^m.18$ derived from the *Hipparcos* parallax, and in fact accords better with the $3^m.72$ that corresponds to the mean distance of 86 pc adopted by Odenkirchen *et al.* (1998) for the centre of the Coma Cluster.

The minimum masses, $m_{1,2} \sin^3 i$, demanded by the orbital elements are very close to the masses that stars of the relevant types are supposed (Allen 1973) to have. Accordingly, $\sin^3 i$, and *a fortiori* $\sin i$, must be expected to be close to unity, encouraging the idea of the possibility of eclipses. That possibility is enhanced by the fact that one of the conjunctions occurs very close to the time of periastron passage, when the stars are at only $(1 - e)$ times — little more than half — their mean separation. Eclipses will take place if $\tan i > (1 - e)(a_1 + a_2)(\sin i)/(R_1 + R_2)$, where the R's stand for the stellar radii; substituting the known values and estimated radii, we find that for eclipses to occur the inclination must be above about 85°.6. A 'self-help' effort to look for eclipses was made with the Haute-Provence *Coravel* on the night of 1989 April 28/29, when several measurements were made during a conjunction passage. In fact all four of the *Coravel* measures that have been rejected (see above) were made on that occasion, but their residuals are not systematically of the character to suggest that an eclipse was being witnessed.

An idiosyncrasy arising from the nearness of the period to an integral number of days is that in any particular observing season the opportunity to watch for eclipses is confined to a particular zone of terrestrial longitude, which migrates about 140° eastward from one season to the next. In 1989, when European longitudes were favoured, a call was put out to amateur astronomers possessing photoelectric photometric equipment to watch for eclipses at the known times of conjunction. Mr. J. Ells, of Bexleyheath, Kent, England, kindly observed the object during the conjunction of 1989 April 28.91 and again on the following night for comparison purposes. No eclipse took place. In the next season Mr. O. Ohshima, of the Bisei Observatory, Okayama, Japan, observed the conjunction of 1990 January 23.63, without

conclusive indication of eclipse. Much more recently it has been possible to search the *Hipparcos* 'epoch photometry' for evidence of eclipses, but there is none. The orbital inclination must therefore be less than the limiting value $i_{\max} = 85°.6$, and the minimum masses of the stars are correspondingly larger than those given directly by the orbital elements above, by the factor $(\sin i_{\max})^{-3}$ or about 1.009, to 1.081 and 0.999 $M_\odot$ for the primary and secondary respectively.

Projected rotational velocities, $v \sin i$, of 5.7 ± 0.5 km s^{-1} for the primary star and 3.2 ± 0.8 km s^{-1} for the secondary are found from the *Coravel* radial-velocity traces; the quoted errors are formal standard deviations of the mean values, and a lower limit to the real uncertainties is considered to be 1 km s^{-1}. The rotation periods corresponding to the observed velocities are approximately 10 ± 3 and 16 ± 6 days respectively. It is of interest to consider whether those values are consonant with synchronization between the axial rotations and the orbital motion. Normally rotation is not synchronized in main-sequence binaries with periods much above 10 days. The important quantity is, however, not the period but the separation of the stars — the *minimum* separation, $= a(1 - e)$, in the case of an eccentric orbit. The minimum separation of the components of HD 111154 is therefore about 0.56 times the semi-axis major of the relative orbit, and owing to the three-halves-power relationship between period and orbital radius it corresponds to the separation of stars in a *circular* orbit whose period is shorter than that of HD 111154 by the factor $(1 - e)^{3/2}$ — about 11 days; so synchronization would not be surprising, but neither would its absence. Hut (1981) has demonstrated how, in an eccentric orbit, tidal effects do not tend to equalize the axial and orbital periods but rotational 'pseudo-synchronization', which is basically related to the orbital angular velocity at periastron, is favoured. For the eccentricity of HD 111154, the pseudo-synchronized rotational period is shorter than the orbital period by a factor of nearly 2.9, making it a little under 10 days — which is within the (considerable) limits of uncertainty of the periods inferred from observation for both components, so we may conclude that the HD 111154 system probably *is* pseudo-synchronized.

Acknowledgements

I am most grateful to Dr. M. Mayor and the Observatoire de Genève for the provision of the 19 Haute-Provence observing runs during which the majority of the data in Table 1 were obtained, and to the late Dr. A. Duquennoy and to Dr. S. Udry who performed the reductions and produced Fig. 1. Additionally I thank the Dominion Astrophysical Observatory and ESO for two observing runs each. Travelling expenses were borne by the UK SERC and PPARC. I am much indebted to the late Mr. J. Ells and to Mr. O. Ohshima for observing HD 111154 at times of conjunctions in order to determine whether the system exhibits eclipses.

References

Allen, C. W. 1973, *Astrophysical Quantities* (London: Athlone), pp. 206, 209.
Baranne, A., Mayor, M., Poncet, J. L. 1979, *Vistas Astr.*, **23**, 279.
Cannon, A. J., Pickering, E. C. 1920, *Ann. Harv. Coll. Obs.*, **95**, 78.
Fletcher, J. M., Harris, H. C., McClure, R. D., Scarfe, C. D. 1982, *Publ. Astr. Soc. Pacific*, **94**, 1017.
Griffin, R. F. 1967, *Astrophys. J.*, **148**, 465.
Griffin, R. F. 1969, *Mon. Not. R. Astr. Soc.*, **145**, 163.
Griffin, R. F. 1981, *J. Astrophys. Astr.*, **2**, 115.
Hut, P. 1981, *Astr. Astrophys.*, **99**, 126.
Knude, J. 1989, *Astr. Astrophys. Suppl.*, **81**, 215.
McClure, R. D. 1976, *Astr. J.*, **81**, 182.
Odenkirchen, M., Soubiran, C., Colin, J. 1998, *New Astr.*, **3**, 583.
Sandage, A. R., Fouts, G. 1987, *Astr. J.*, **93**, 592.
The Hipparcos and Tycho Catalogues (ESA SP-1200) (Noordwijk: ESA), 1997, **7**, 1252.
Trumpler, R. J. 1938, *Lick Obs. Bull.*, **18** 167.
Yoss, K. M., Griffin, R. F. 1997, *J. Astrophys. Astr.*, **18**, 161.

J. Astrophys. Astr. (2001) **22**, 131–144

Development of a Three Channel Photometer for UPSO, Naini Tal

B. N. Ashoka[1], Kumar[1], V. C. Babu[1], S. Seetha[1], V. Girish[1], S. K. Gupta[2] , Ram Sagar[2], S. Joshi[2] & P. Narang[3]

[1] *ISRO, Satellite Center, Airport Road, Bangalore 560 017, India*
[2] *Uttar Pradesh State Observatory, Naini Tal 263129, India*
[3] *Sri Venkateswara College, University of Delhi, Delhi, India*

Received 2000 September 18; accepted 2000 November 30.

Abstract. The design and performance of a portable three channel photometer installed at the Uttar Pradesh State Observatory (UPSO), NainiTal is described. The photometer is modular and the whole unit can be disassembled as individual channels such that the system can also be used as a single channel or two channel photometer. The system also has provision to monitor a guide star. The instrument was put into operation since November 1999 on the 1m Sampurnanand telescope at UPSO, Naini Tal. Since then, it is used extensively for the 'Survey of rapidly oscillating Ap (roAp) stars in the northern sky' from UPSO. Observational results using this new photometer in its initial phase of operation are discussed. The advantage of having continuous sky measurement is demonstrated.

Key words: Photometry-light curves-variable stars.

1. Introduction

Conventional photometers use a single channel to get the light curve of a program star. Variations in the observed light curve can be interpreted as variations in the star if the observations are made under ideal observing conditions. However in practice, even at some of the best sites, under normal observing conditions, the variations seen in the light curve of the star are often contaminated by the variations caused due to 1) thin clouds, transparency variations, changes in the sky background 2) telescope tracking problems 3) instrument related problems such as electronic noise, misalignment of components and mechanical flexure 4) human errors such as improper centering and guiding. Therefore, in order to detect and eliminate most of the above variations from the genuine variations in the light curve, a 2nd channel is added to the single channel photometer to simultaneously monitor a nearby field star. Genuine variations in the program star can be seen only

in the 1st channel; any variations of terrestrial origin are included in both the channels. Thus, the two channel data enables distinguishing real and spurious variations in the time series data. If necessary, using the 2nd channel data, the 1st channel data can be corrected for cloud effects, transparency variations and extinction effects. It is also possible to make a good estimation of the extinction coefficient from the 2nd channel data for that night instead of using an average extinction coefficient. Thus, the addition of another channel to the single channel photometer results in a two-star photometer one of which we have developed (Venkata Rao *et al.* 1990) and have been using on telescopes at Vainu Bappu Observatory (VBO), Kavalur and UPSO, Naini Tal since 1988.

In a two star photometer, whenever sky measurements are needed, the stars have to be moved out of the diaphragm for a small interval of time in both the channels. This process has to be repeated several times during a night. This results in data breaks depending on the frequency and the length of the sky measurements needed. Such breaks in the data are in addition to those caused by inclement weather. The breaks in the data due to the above mentioned problems can cause aliases when we compute the discrete Fourier transform (DFT) of the data to search for periods. Also, in the two star photometer, the sky background is computed by interpolating the sky measurements made at different intervals assuming that the sky variations are always smooth. However, in practice, the sky background can abruptly vary due to changes in local conditions. A more serious problem arises during the times when the moon rises or sets. During this period the background varies nonlinearly making sky interpolation impossible. Even on dark nights, the sky background can vary non-uniformly from zenith to horizon. Sometimes zodiacal light can also cause considerable sky background variations. Therefore, it is clear that interpolating a few sky points in space and time to determine the sky background for the full night is inadequate. A solution is to have a 3rd channel attached to the two-star photometer to measure the sky background simultaneously. Thus, as a necessity, two star + sky, generally named as three channel photometers have evolved. In a three-channel photometer, sky measurements in all three channels are made only once at the beginning of the run and once more at the end if possible and rest of the time the sky is continuously recorded only in ch3. Using these sky measurements, the sky ratio of ch1/ch3 and ch2/ch3 is determined and using this ratio, the sky value at every point in the 1st and 2nd channel is determined using the corresponding 3rd channel sky data. Because the sky estimations are made for every data point, continuous sky variations are accounted for. Since the main channel data is not broken for sky measurements in between, we get continuous data on the program star. Using the three channel data, it is also possible to estimate, on each night, the limits of the scintillation noise and sky transparency noise which ultimately sets the limit on the range of frequencies which can be detected with a particular telescope at an observing site (Ashoka *et al.*2000).

Thus, in order to get reliable, continuous time- series data even under moderate sky conditions, a three-channel photometer is necessary. We have designed and developed a prototype three channel photometer in-house that is currently being

used at UPSO, Naini Tal and VBO, Kavalur, for the study of intermediate polars, pulsating white dwarfs and other rapid variables.

Recently, we have been involved in a program titled 'NainiTal-Cape Survey for pulsating chemically peculiar stars' with UPSO, Naini Tal and South African Astronomical Observatory/University of Cape Town, S. Africa. The survey involves extensive photometric observations and hence a dedicated three-channel photometer was necessary at UPSO, Naini Tal. Using funds from the Department of Science and Technology (DST) to UPSO, we have built a three channel photometer at Technical Physics Division, ISRO Satellite Center, Bangalore jointly with UPSO.

2. Design considerations

The points discussed below are some of the important criteria which have gone into the design of our present three channel photometer. The photometer is designed to suit our scientific objectives and other logistical requirements. The instrument is designed primarily for use at the Cassegrain focus of the 1m telescope at UPSO, Naini Tal. It can also be used on other similar telescopes. The focal ratio of the telescope at Naini Tal is f/13 with maximum available backfocal length of 300mm. Therefore, the size of the photometer is optimised to suit these numbers.

The program star is always observed through the 1st channel (main channel). Unlike the 2nd and 3rd channels, the 1st channel is designed with minimum transmitting optics and without any reflecting optics in order to minimize light loss from the program star. Even the Fabry lens is made thin and planoconvex and fabricated using BK-7 material for best transmission. The 2nd channel is made identical to the 1st channel except for an additional reflection using a prism to pickup a star in the 2nd channel. The 1st and the 2nd channel photometers therefore, can be interchanged if necessary.

The photomultiplier tube (PMT) is placed inside a housing which contains a Fabry and a shutter. Identical PMT housings with PMTs are made for all the three channels. Therefore, the PMT housings can be interchanged among the channels if necessary, and out of the three, the best (high gain, low noise) PMT is used in the 1st channel, the next best in the 3rd channel.

A suitable field star has to be always picked up in the 2nd channel without moving the telescope but by moving only the 2nd channel X-Y table within the photometer. Therefore, provision for scanning a large area (15 × 10)sq. arc min is provided in the 2nd channel so that stars are always available in any field to be picked up in the 2nd channel. Hence, even in rarified fields, stars can be picked up in the 2nd channel.

During observations, the stars have to be guided such that they stay within the diaphragm throughout the observations. If the tracking of the telescope is good, minimum guiding is sufficient. Generally, the offset guiding is done manually on the guide telescope using either a high power eyepiece or an autoguider. Since we need to guide on the same star throughout the night, the flexures between the main

and the guide telescope result in slow drift of the stars in the diaphragm. Perfect guiding is possible only if the guiding is done on a star in the main telescope. Provision is made on top of the photometer to pickup some arbitrary star in the field of view of the main telescope without disturbing the stars in other channels. Therefore, a guiding unit is attached to the photometer. In the guiding unit provision is made to scan large (50 × 50) sq. arc min to pick up any suitable bright star. The guiding is done using either a video CCD camera or a commercially available guiding CCD camera.

The photometer is designed to use Hamamatsu R647-04 photomultiplier tubes (PMTs) of half an inch diameter. They are blue sensitive tubes with quantum efficiency (QE) $\sim$ 30% and do not need any cooling since the dark counts are only $\sim$ 20 cps at room temperature. The tube response range (300–700 nm) and the region of the highest QE (400 nm) are optimal for observing blue stars such as A type stars, cataclysmic variables and white dwarfs. The usage of these tubes enabled us to make the unit compact and light weight.

All the three channels are made similar by using identical PMTs, filters and amplifier/discriminator. All electronics are powered by a single power supply and all PMTs are powered by the same high voltage (HV) source so that any electronics related variations should be reflected in all the three channels.

Since the optical observatories in India are situated throughout the country, a light weight, modular design is emphasised for transportation ease. All the three channels can be detached during transportation to fit in a suitcase and assembled easily at the telescope. The total weight of the photometer is $\sim$15 kgs. The entire photometer can be carried as a check-in baggage in an aircraft.

3. Description of the instrument

The three-channel photometer in the lab before shipment to UPSO is as shown in Fig. 1 (The circular plate at the bottom is attached to the telescope/guiding unit at the observatory). The schematic diagram is shown in Fig. 2. We discuss below, the different parts of the present photometer. As in the case of any conventional photometer, a wide angle eyepiece of 2 inch size and 32 mm focal length is used to identify the star fields, center the program star and select the star for the 2nd channel. The eyepiece can cover a field of 8 arc min at the focal plane of the 1m UPSO telescope. The 1st channel photometer is attached below the wide angle unit. The photometer has all the parts of a conventional single channel photometer such as a diaphragm plate, a microscope to view the star within the diaphragm and a filter wheel. An easily detachable type of a photomultiplier housing is attached to the photometer which consists of a shutter, a Fabry lens and a PMT with wired base. At the end of the housing, there are two connectors; one for the High Voltage (HV) input and the other for the signal output. The 2nd channel has got all the components as in the 1st channel with the addition of a pick-up prism before the diaphragm. The entire 2nd channel photometer is mounted on an X-Y table. The 2-

D motion of the photometer is used to pick up a star for the 2nd channel in the same field other than the program star. The movement of the 2nd channel is such that 15 $\times$ 10 sq. arc min area can be scanned to pick up a suitable star. The 2nd channel is mounted perpendicular to the 1st channel as shown in the figure. There is a dead region of 75 arc sec from the 1st channel where stars cannot be picked up in the 2nd channel. This is purposely introduced to avoid obscuration of the 1st channel star beam by the 2nd channel pick-up prism. The 3rd channel is a fixed channel which is used only for the sky background measurement. Similar to the 2nd channel, the 3rd channel also has a pick-up prism. To make the design simple unlike in the 1st and 2nd channel, the 3rd channel has a fixed diaphragm and provision for one filter. Since the sky variations are non gray, most of the time the sky measurements are made without a filter. The 3rd channel is also mounted perpendicular to the first channel and diametrically opposite to the 2nd channel. This channel measures the sky region close to the 1st channel at a distance of 90 arc sec. from the 1st channel star.

The 1st channel has three diaphragms of size 15, 23.5 and 30 arc sec. The 2nd channel has the same number of diaphragms but their sizes are 10% less than the corresponding ones in the 1st channel. This is done so that while guiding, any drift of the stars within the diaphragm can be detected first in the 2nd channel so that the telescope is guided in time such that no drift occurs in the 1st channel. The filter wheel consists of four holes in which three holes are fitted with Johnson UBV filters and one is left blank for observations without a filter. A neutral density filter can be used in the blank hole while observing very bright stars. The PMT housing has a Fabry lens whose focal length is 65mm such that at f/13 focus, it produces an image of 5mm in size on the 10 mm photocathode of the PMT. The 3rd channel has a fixed diaphragm (15 arc sec) and provision for one filter only since this channel is always used only for sky measurements. All the three PMT housings are made alike so that they can be interchanged among the three channels. The 1st and 2nd channel photometers are made modular so that they can be moved independently to get them focused on the stars.

4. Detector, instrumentation and data storage

The detector and the other electronics which are used here are similar to the Whole Earth Telescope (WET) standard photometer (Kleinman *et al.* 1995).

The detector is used in photon counting mode. We are interested in the intensity measurement of the star which is proportional to the number of photons detected. Photons striking the photocathode will produce pulses and the intensity of the source is determined by pulse counting. The detector is a Hamamatsu R647-04 PMT made for photon counting applications at low light levels. The tube is blue sensitive with S-11 response. The photocathode has a size of 10 mm and is made of bialkali material. It is an end window tube with anti magnetic shield coating on the outer glass. The tube has a gain of 2.2 x 10^6. The quantum efficiency is 30%

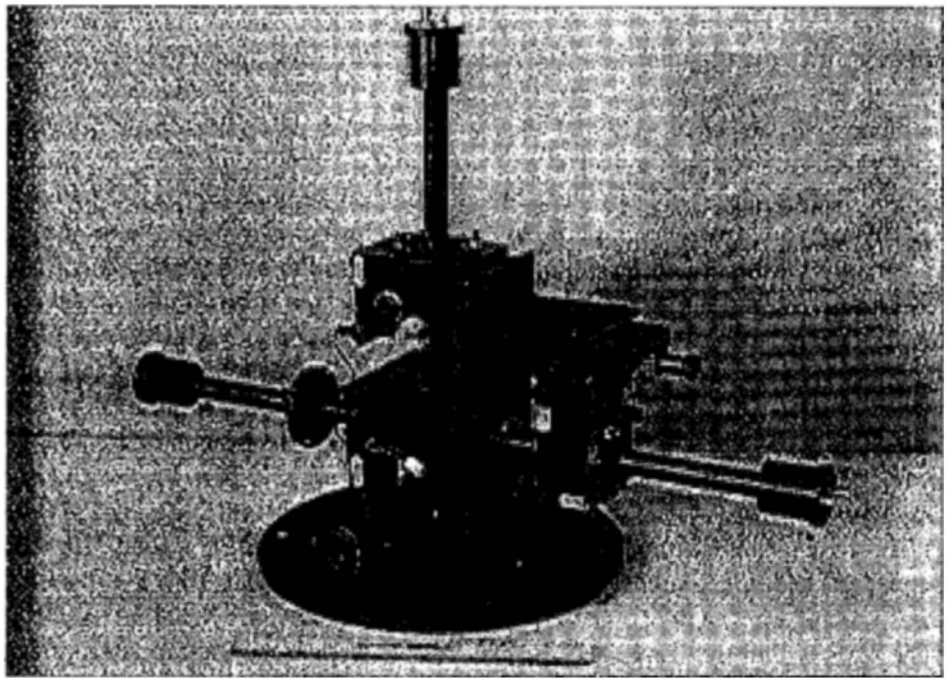

Figure 1. Three Channel Photometer.

around 400 nm. The operating HV is 1000V DC. Positive high voltage is used so that the cathode will be at ground potential and the magnetic shield is also kept at ground potential which reduces the noise. All the three PMTs are powered by single modular HV unit C4710-51 from Hamamatsu. It has an HV output adjustable in the range 200–1500V with maximum current of 0.1mA. It has a ripple of 0.005% (p-p) at maximum rating and voltage stability of 0.01% for 1V change in the input voltage. The output of the PMT goes to the amplifier/discriminator (PAD) EG&G PARC 1182 . The PAD amplifies the pulses coming from the PMT, discriminates the photon pulses from the dark noise pulses using a lower level threshold and then shapes the pulses suitable for counting. The pulse pair resolution is 20ns. The output is TTL pulse of width 10–75 nano secs. The PAD is well shielded and is free from EMI pickups. The output of the PAD is fed to an interface card. The present one we are using is CCLA three-channel interface card modified and marketed by the Vilnius team at Lithuania for all the WET participants as per the WET specified standards (Kalytis *et al.* 1995). The interface card is designed to operate as a computer interface to the photometer. It has timing circuits to ensure an accurate clock and integration times. The hardware of the card consists of a micro controller, counters, oscillator and EPROM. The interface card communicates with PC through a serial port.

The software which communicates between the PC and the interface card is the data acquisition software "Quilt-9" developed by the Texas group for the WET

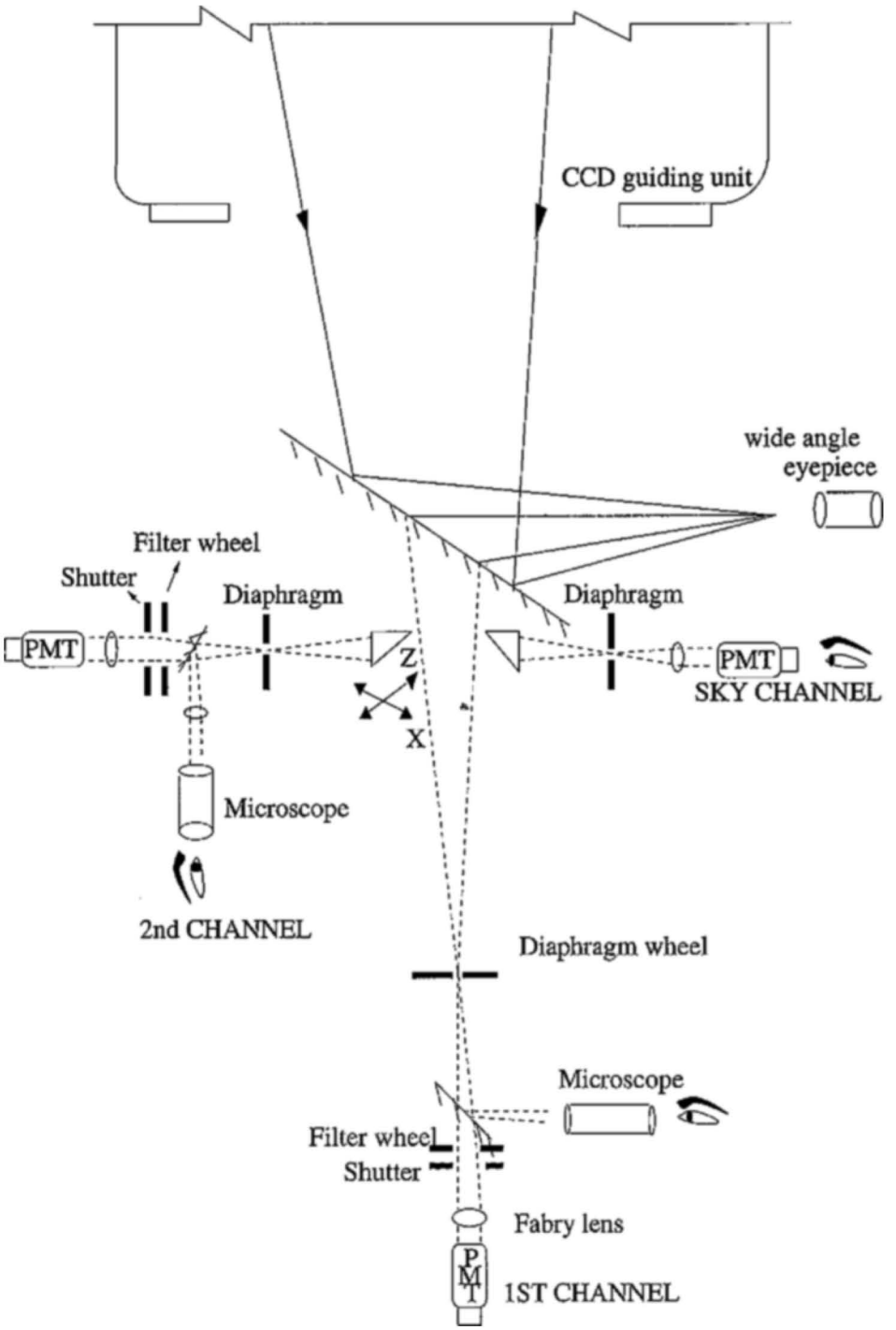

Figure 2. Schematic diagram of the three channel photometer.

program and distributed to all the "WET" participants (Nather *et al.* 1990). The software along with the interface card can acquire the data simultaneously from three channels. The software has provision for real time display of the data and its storage on hard disk and floppy. The data are stored as an ASCII file which contains header information and data. The header information includes relevant details such as the file name, name of the object, date of observation, start time of the run, integration time, filter used and the observatory name. After this the data follows. The data file can directly be read for further analysis.

A compact power supply unit is built to power the high voltage module, amplifier–discriminators, interface card and diaphragm illuminating lights. The power supply along with the interface card, HV unit, amp/disc. are mounted along with the photometer.

5. Calibration of the photometer

After assembling the photometer the following checks and measurements were made on it by attaching it to the telescope.

5.1 *Focusing of the three channels*

The instrument is designed such that when a star is focused in the diaphragm of the 1st channel, it will be almost focused at the diaphragm of the 2nd channel, diaphragm of the 3rd channel and at the wide angle eyepiece. Due to small mechanical errors, the focusing need not be perfect. Therefore, the 1st channel photometer is independently moved such that the star is focused perfectly in the 1st channel. Focusing in the wide angle eyepiece is made by moving the wide angle eyepiece itself. Focusing in the 3rd channel is nearly perfect and here the focus is not so critical since it measures only the sky. When the guiding unit is attached, the guide star is exactly focused on the detector plane of the guiding camera.

5.2 *Knife edge test*

The so called "knife edge test" is a method to ensure perfect focusing of the stars in the respective diaphragms of the photometer so that the beam width will be minimum at the diaphragm. Therefore, the star within the diaphragm could drift till the edge without the light being cut. The focussing is done as follows. The microscope eyepiece from the eyepiece holder is removed and a star image is put in the diaphragm such that part of the image is cut by the diaphragm edge. On changing the telescope focus, when the star is exactly focused at the diaphragm, the edge of the diaphragm shines like a knife edge. If the focus is before or after the diaphragm, this will not happen. Thus, the best focus is determined. After this, the eyepiece is replaced and focused on the star. This test has to be conducted once at the beginning of the observing run or whenever the telescope focus is changed. This test may not be needed in ch3 because it measures only the sky.

5.3 *High voltage setting*

As the high voltage is changed the gain of the PMT also changes. Generally the high voltage is fixed at the plateau region of the gain versus high voltage curve. The more effective way is to select the high voltage within the plateau region where the signal to noise is also maximum. This is done as follows. First only the dark signal at different high voltage values are measured. Next, the diaphragm is illuminated with a steady light source and the signal is measured at various voltages. The voltage in the plateau where the S/N is maximum is taken as the optimum high voltage for that tube. For the tube R647-04, the high voltage is thus fixed at 990V. Thus the high voltage is fixed at 990V. Since we are using similar tubes in 2nd and 3rd channel and the same HV unit has to be used for powering all the three channels, we fixed optimum value of HV as 990V for all the channels.

5.4 *Fabry check*

Fabry lens is used before the PMT to image the telescope primary mirror on the photocathode of the PMT. Since the Fabry focal length is much smaller compared to the telescope focal length, the drift of star due to improper tracking of the telescope will produce negligibly small drift on the photocathode. Fabry check is a method to check the optical alignment of Fabry lens and the PMT. Due to the presence of the Fabry even if the star drifts in the diaphragm from one end to the other, there should be no variations in the light curve. If there is some misalignment of Fabry lens, or any other obscuration in the path of the light or dust or finger prints on Fabry or on the filter, their presence can be seen as a variation in the output signal when the star is put at different places within the diaphragm. Such variations can be mistaken for actual star light variations and produce spurious results. Even in a best telescope it is practically impossible to make the tracking so perfect as to avoid trailing of the star within the diaphragm. Therefore, Fabry lens is made to image the primary mirror to half the area of the photocathode. Next, the Fabry should be perfectly aligned to the PMT. In order to check the perfectness, we conduct a test on the telescope using a star in the 1st channel. First, the star is moved across the diaphragm in one direction (in right ascension) from one end to the other with a very slow speed available on the telescope. During this, the star signal is recorded at a fast integration time of about 200ms. Next, this process is repeated in the perpendicular direction (declination). Each time the resulting light curve should produce a square wave pattern indicating that the star any where within the diaphragm will produce the same signal and the alignment is perfect at the diaphragm. Fabry check is the ultimate test for the perfect optical and mechanical alignment of all the components in the photometer.

5.5 *Dead time correction*

Since the experiment is basically a photon counting system, the brightness of the star is proportional to the number of photons detected. Due to their random arrival,

all the photons reaching the detector may not be counted if the count rate is high, resulting in dead time loss. This problem is obvious when bright stars are observed. Therefore, we have to estimate the dead time loss due to the overall system and correct for the loss. The dead time correction is determined by the aperture method (Clemens.J.C, private communications) as follows. Two apertures one small and another large are selected. Let S_1 and L_1 be the counts measured for a certain illumination in small and large apertures respectively. Let S_2 and L_2 be the respective measured counts for an increased illumination. From the four counting rates,

$$a = S_2 \times L_1, b = S_1 \times L_2, c = S_1 + L_2, d = S_2 + L_1$$

then the dead time is computed as (a-b)/(ac-bd). Using this method, the estimated dead time for the present system is 23 nano seconds.

5.6 *Selection of apertures*

Apertures in general are selected based on the telescope and observing conditions. As in the case of a single channel photometer, the 1st channel aperture is selected based on the telescope performance, sky brightness and the required S/N based on the brightness of the star. The aperture size should be such that star should not drift within a consecutive guiding interval. Otherwise frequent guiding will be required. In general, one prefers to use smallest aperture to reduce the background. However, if the star is bright, a bigger aperture is selected to allow the entire seeing disk to be well within the aperture. In a three star photometer, the 1st channel aperture is selected based on the above criteria. The 2nd channel aperture as a thumb rule, is kept 10% smaller than the corresponding 1st channel. The 3rd channel being a sky channel, its diaphragm size is kept same as the 1st channel.

The Fabry check and focusing checks have to be made every time before starting an observing run. The high voltage setting once made should remain unchanged.

6. Performance of the instrument

The photometer is installed on the 1m telescope at UPSO Naini Tal The photometer was used for the first time in three channel mode during a WET international campaign on a pulsating DAV white dwarf star HL Tau 76 (m_V=15.2) in November 1999. Excellent light curves from all the three channels were obtained. A sample light curve of one full night observation is shown in Fig. 3. The 1st channel light curve shows periodic variations of HL Tau 76. The dominant periods around 600s can be seen visually from the light curve of the star. A field star of comparable brightness to the program star is observed in the 2nd channel. The 2nd channel shows no other variations except for the extinction + sky variations which indicates that the variations seen in the 1st channel are real. The sky background is measured in the 3rd channel. We can notice from the figure that the sky variation is

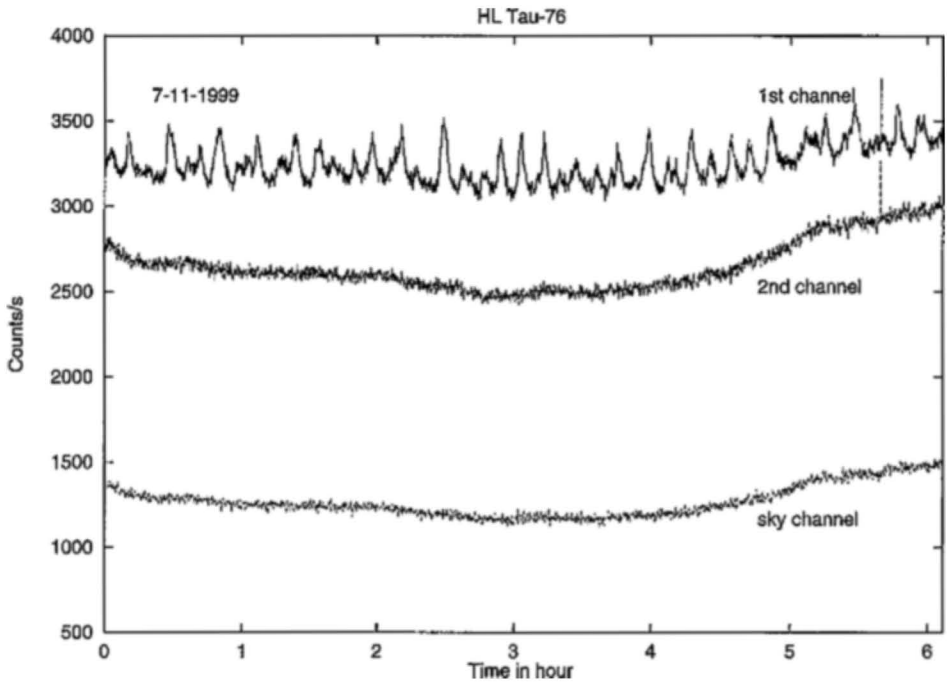

Figure 3. Three channel data on HL Tau 76.

not smooth throughout the night. In Fig. 4, the advantage of having continuous sky points instead of discrete sky measurements is demonstrated. The top panel in Fig. 4 shows the sky subtracted light curve of HL tau 76 with its DFT using the continuous sky background. The bottom panel in Fig. 4 shows the sky subtracted light curve and its DFT of the same data if we use only few sky points instead of continuous ch3 data. On comparing the two panels in Fig. 4, we can notice that the discrete sky points can introduce a long period trend in the light curve and thus few low frequency components in the DFT (bottom panel) which is not seen in the top panel. Therefore, it is clear that a continuous sky measurement is necessary whenever observations are made throughout the night. Thus, three channel photometer is a necessity for time series photometric studies.

The instrument is now continuously in use at UPSO, Naini Tal for a recently initiated program titled 'Naini Tal-Cape Survey for pulsating chemically peculiar stars'. The survey involves observing more than 300 potential stars in the northern hemisphere to discover new rapidly oscillating Ap stars and study them in detail. The survey was initiated on a trial basis in 1997. The program is taken up on a regular basis after having a three star photometer at the observatory. Since the survey involves observing many stars, initially each star is observed only for a duration of 1~2 hrs. Also, since these stars are bright (m_V=6-10), it is difficult to get an equally bright star for the 2nd channel. Therefore, the initial survey is

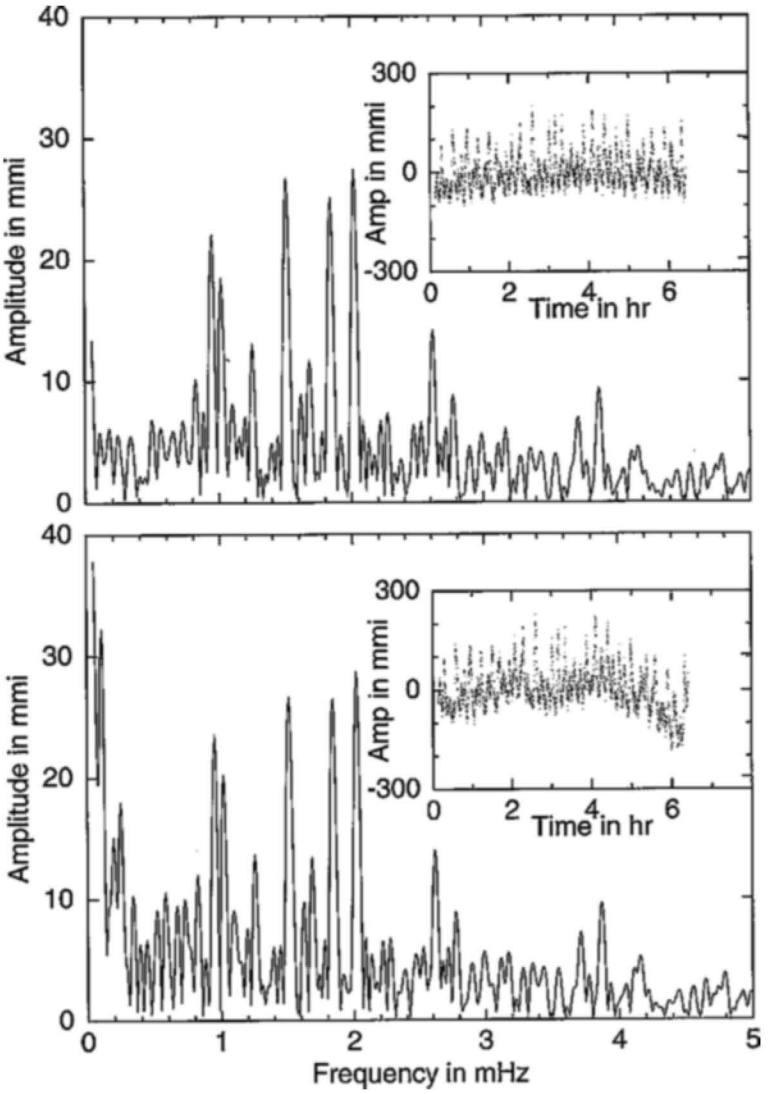

Figure 4. Amplitude spectrum of HL Tau 76.

made using a single channel mode. For a detailed study, the discovered variables are observed in three channel mode for long durations. The initial efforts resulted in the discovery of rapid oscillations in an Ap star HD12098. The initial analysis of the data indicated the presence of an oscillation at 7.61 min. with amplitude 1.5 mmag (Martinez *et al.* 2000) The light curve and its DFT are shown in Fig. 5 (top).

The survey also resulted in the discovery of a new delta Scuti star HD98851. Periods are detected at 79.4 min and 167 min (Joshi *et al.* 2000). The complex

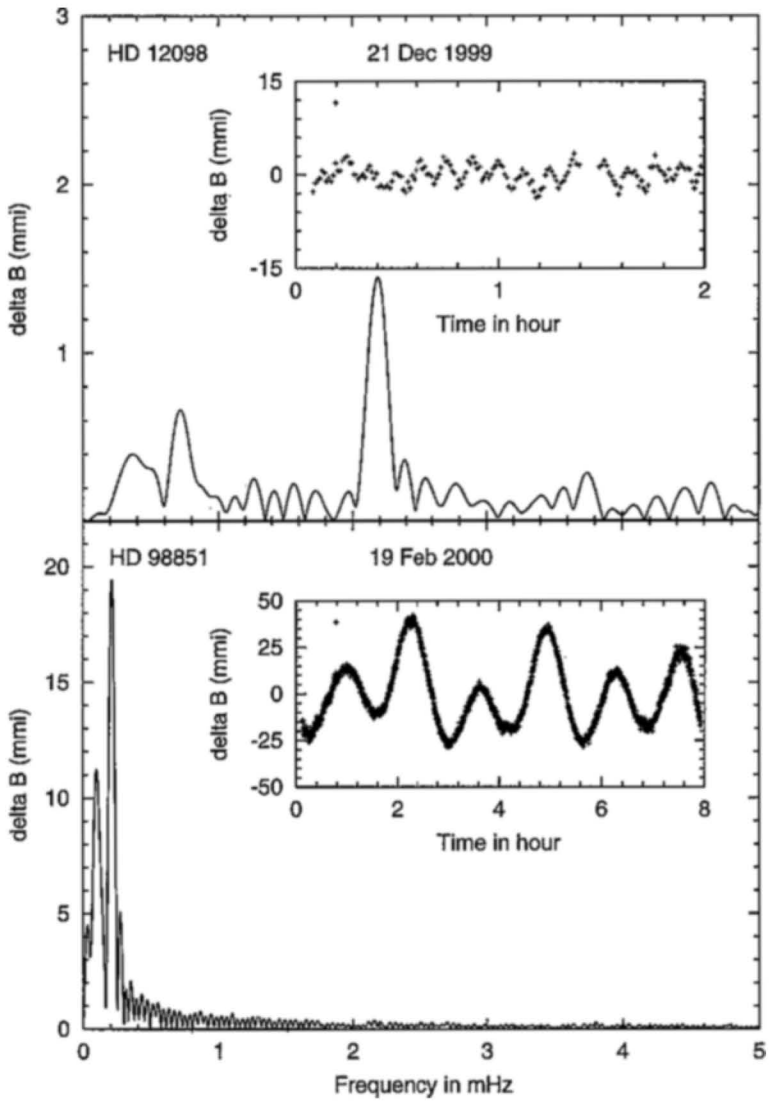

Figure 5. Fourier transform of the two variables HD 12098 (top) and HD 98851 (bottom). The respective light curves are shown in the inset.

light curve indicates the presence of multiple periods in this system. A sample light curve and its DFT is shown in Fig. 5 (bottom).

All the above results indicate the optimal functioning of the instrument during its operational phase.

7. Conclusion

The simultaneous monitoring of the program star, a field star and the sky background is essential to ascertain genuine variability during time series photometric studies. An instrument of this kind is also useful for the photometric study of the variables during a non photometric night where the variability can be retrieved from the 1st channel data using 2nd channel and 3rd channel data. Since the three channel photometer monitors the sky background continuously, the sky estimations could be made accurately even during moon-lit nights, dawn/dusk maximizing the utilization of telescope time. With this objective a 3 channel photometer was jointly built by the ISAC and the UPSO team. It has undergone all calibrations and its performance is excellent. It is at present being used at the 1meter telescope at UPSO Naini Tal.

Acknowledgements

The authors thank Mr. G. Venkata Rao and his colleagues for their help during mechanical fabrication of the photometer at the ISAC workshop. We also thank Dr. K. G. Gupta for his help in fabricating some optical components for the photometer at UPSO optical shop.

References

Ashoka B. N., Seetha S., Raj E., Chaubey U. S., Gupta S. K., Joshi S., Martinez P., Kurtz D. W., Ramsagar., Kasturirangan K. 2000, *Bull. Astr. Soc. India*, **28**, 251.

Joshi S., Girish V., Martinez P., Sagar R., Ashoka B. N., Gupta S. K., Seetha S., Kurtz D. W., Chaubey U.S. 2000, *IBVS* No. 4900.

Kalytis R., Meista E. G. 1995, *Baltic Astronomy*, **4**, 497.

Kleinman S. J., Nather R. E., Phillips T. 1995, *Baltic Astronomy*, **4**, 482.

Martinez P., Girish V., Joshi S., Kurtz D. W., Ashoka B. N., Chaubey U. S., Gupta S. K., Sagar R., Seetha S. 2000, *IBVS* No. 4853.

Nather R. E, Winget D. E., Clemens J. C., Hansen C.J., Hine B. P. 1990, *Astrophys. J.*, **361**, 360.

Venkat Rao G. *et al.* 1990, *Bull. Astr. Soc. India*, **18**, 79.

J. Astrophys. Astr. (2001) **22,** 145–154

Hard X-ray Spectrum of Mkn 421 during the Active Phase

R. K. Manchanda *Tata Institute of Fundamental Research, Colaba, Mumbai 400 005, India*
e-mail: ravi@tifr.res.in

Received 2001 July 27; accepted 2001 September 27

Abstract. Spectral measurement of Mkn 421 were made in the hard X-ray energy band of 20–200 keV using a high sensitivity, large area scintillation counter telescope on November 21, 2000 and these coincided with the onset of an active X-ray phase as seen in the ASM counting rates on board RXTE. The observed spectrum can not be fitted to a single power law similar to the PDS data of BeppoSAX. The data can be fitted both by a two component power-law function or a combination of an exponential function with a power law component at the high energies above 80 keV. We identify these components with those arising from the synchrotron self compton and the high energy power-law tail arising from the upgrading of the thermal photons due to multiple Compton scattering a la Cyg X-1. A comparison with the earlier data clearly suggests a spectral variability in the hard X-ray spectrum of the source. We propose a continuously flaring geometry for the source as the underlying mechanism for energy release.

Key words. X-rays; AGNs—BL Lac sources, massive black hole candidates, jet emission; individual—Mkn 421.

1. Introduction

Among the active galactic nuclei, blazers form a distinct class of highly luminous, radio loud and rapidly variable objects in the entire electromagnetic spectrum. The X-ray spectra of these sources extend from the soft X-ray region of < 1 keV to the TeV energy band. Mkn 421 is the brightest of the BL Lac objects in the X-ray band and the photon flux has been observed up to $> 10^2$ eV. This source was the first BL Lac object to be discovered in X-rays (Ricketts *et al* 1976) and hard X-ray spectrum up to 100 keV was first measured by Ubertini *et al* (1984). The source has been repeatedly studied in different wave band regions of radio, UV, X-rays, gamma rays and at TeV energies both individually and in coordinated campaigns for simultaneous multiwavelength monitoring of the source. These observations indicate a complex spectral variability of the source but a clear correlation of pronounced X-ray flares with the observation of TeV photons suggests a common emission mode for the two bands.

The low energy X-ray observations of the source below 10 keV with EXOSAT, ROSAT and ASCA during the quiescent state reveal that the variability of Mkn 421 in the soft X-ray band can be interpreted as small amplitude variations about a mean luminosity level which remains almost constant (George *et al* 1988). The time scale

of these variations is of the order of 10^5–10^6 sec. The temporal analysis of the X-ray photons during the 1998 flare from the BeppoSAX data suggests that hard photons between 3 and 10 keV band lag the soft photons below 3 keV by about 10^3 sec, which is in complete contrast with the observations in the other BL Lac spectra (Fossati *et al* 2000a). The combined multi-frequency observations of the source with EUVE, ASCA, RXTE and SAX-LECS and TeV band during the 1998 active phase (Macomb *et al* 1995) indicate both positive and negative lag in individual flares (Takahashi *et al* 2000). The measured time lag is also at variance with earlier reported data (Takahashi *et al* 1996). In summary, the temporal studies in the radio and low energy X-ray band do not constrain the X-ray emission models, however, the data does show a clear correlation between the soft X-ray photons and the TeV photons. No other underlying systematic feature has emerged to date (Maraschi *et al* 1999).

The spectral measurements of the source in the X-ray band below 10 keV with BeppoSAX during 1997 and 1998 flare period show a remarkable variability and spectral evolution during the flare. The observed spectra does not appear to fit either a single power law or even a broken power law (Fossati *et al* 2000b), a curved model has been thus applied to extract the model parameters. The ν-F_ν plot in the 0.1 to 10 keV energy band however, resembles a truncated parabolic shape in all the data sets. While the description of the spectral features in a narrow 10 keV band at low energies is limited due to the inherent problems of absorption within the source region, it is likely that the source spectrum may itself consist of both thermal and non-thermal components. In the hard X-ray region above 20 keV, the available spectral data on Mkn 421 is very limited. Entire data consists of mainly pre 1990 observations from balloon-borne instruments and the recent detection of the source up to 100 keV during a flare.

In the canonical models for blazars, the observed radiation in radio, UV and low energy X-ray band, is believed to arise in the synchrotron self compton (SSC) emission from the highly relativistic electrons in the jets which are fortuitously aligned to the line of sight (Ghisellini *et al* 1985). However, in these phenomenological models the acceleration of electrons to extremely high energies of about 10^{16} eV, their survival in a strong photon field and the required energy density of these high energy electrons, still remains unresolved. Similarly, the shape of the observed spectra of BL Lac sources does not provide a definite clue for any single fundamental mechanism in the X-ray emitting region. For example, in the low energy X-ray band of 0.1–10 keV, a convex spectral shape is seen for Mkn 421, while the spectrum of ON 231 exhibits a concave profile (Tagliaferri *et al* 2000). Therefore, the hard X-ray spectra from AGNs may be composed of a superposition of multiple components arising in both thermal and non-thermal processes consisting of the synchrotron tail, synchrotron self compton contribution and possibly a compton tail produced by upgrading of the low energy photons with thermal electrons in the hot regions.

A direct way to distinguish between the thermal and non-thermal components is to observe the AGNs in the hard X-ray and soft gamma ray energy band, where the spectral breaks are expected for the thermal and Compton models. The hard X-ray spectral measurements of galactic BHC X-ray sources do show that the non-thermal spectral component which dominates the flux for energies above 30 keV does not show spectral variability and therefore, the spectral properties of the thermal component

must be inferred by computing low energy residuals. In this paper we report the spectral measurements of Mkn 421 made during the active phase in the energy band 20–200 keV. The spectral variability is studied using other available data. We also propose a continuous flaring model and list different processes which may contribute efficiently in different energy regions.

2. Instrument and observations

The observations were made with a Large Area Scintillation counter Experiment (LASE) which is designed to study fast variations in the flux of X-ray sources in the hard X-ray energy region up to 200 keV. The payload consists of three large area X-ray detector modules mounted on a servo-controlled platform. The detectors are a specially designed combination of thin and thick large area NaI(Tl) scintillation counters configured in back-to-back geometry. Each of the detector modules has a geometrical area of 400 cm^2 and the thickness of the prime detector is 4mm. The active anti-coincidence shield is provided by a 30 mm thick crystal. The field of view of each module is $4.5^\circ \times 4.5^\circ$ and is defined by a slat collimator specially designed with a sandwiched material of lead, tin and copper. Each module along with the collimator is further encased with a passive shield. Each detector is designed as a stand-alone unit with independent on-board subsystems for HV power and data processing. The payload platform is servo-stabilized and the target X-ray source and the corresponding background region are tracked using an on-board micro-processor controlled star tracker.

The back-to-back configuration of the detector gives 80% reduction in the detector background in the operating energy range, most of which is produced due to partial energy loss by the Compton scattering of high energy photons in the main detector. The pre-flight calibration of the X-ray detectors is done at different energies using radioactive sources, Cd^{109} (22.1, 87.5 keV), Am^{241} (24.7 and 59.6 keV) and Ba^{133} (32.4 and 81 keV). In addition, an Am^{241} source is mounted on the payload for the calibration of the detectors during the flight using ground command. The accepted events are pulse-height analyzed, time tagged with a 25 μ sec resolution and transmitted to ground on a 40 Kbit PCM/FM link. The details of the detector design, associated electronics, control sub-systems and in-flight behaviour of the instrument are presented elsewhere (D'Silva *et al* 1998). A 3σ sensitivity of the LASE telescope in the entire energy range up to 200 keV is $\sim 1 \times 10^{-6}$ cm^{-2} s^{-1} keV^{-1} for a source observation of 10^4 sec.

The balloon flight was launched on November 21st, 2000 from Hyderabad, India (cut-off rigidity 16.8 GV) and reached the ceiling altitude of 42 km corresponding a residual atmosphere of 2.5 mbars. A number of X-ray sources in the right ascension band of 12^h to 20^h were observed during this experiment. Mkn 421 was in the field of view of three detectors for a total period of 60 min (two sightings of 20 and 40 min each) between 0215 UT and 0350 UT and the background was measured for 20 min each before and after the source observation and for 15 min midway the source pointings. The off-source pointing location was carefully selected blank field from the known X-ray source catalog. The X-ray light curve from the all sky monitor onboard RXTE, suggests that at the time of our observation the source had transited to the active flaring phase with source luminosity twice the lowest value.

3. Results and discussion

A total excess of 6960 counts due to Mkn 421 were recorded in the three detectors in the entire energy region. This corresponds to a combined statistical significance of $\sim 7.5\sigma$. The positive excess was seen up to 200 keV. The source contribution was divided in 12 energy bins and corrected for atmospheric absorption, window transmission, detector efficiency and energy resolution for each detector and co-added. The combined spectrum of the source is shown in Fig. 1. The errors on the data points correspond to 1σ statistical errors. A systematic error of $\sim$ 10% is estimated for the lowest energy channel and included in the plot.

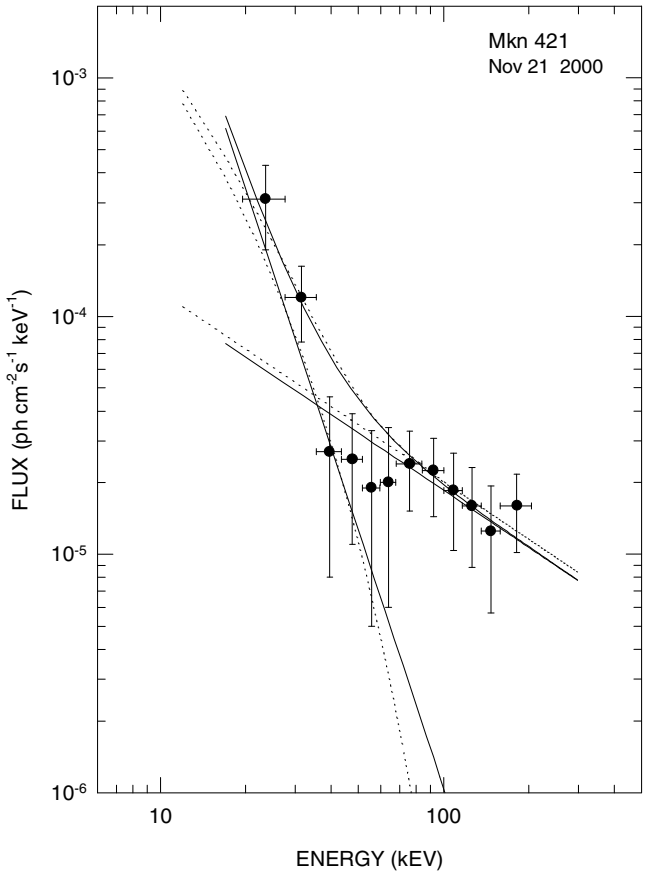

Figure 1. Hard X-ray spectrum of Mkn 421 in 20--200 keV. Solid lines represent a composite power law spectrum with two components α_1 and α_2. The dotted lines give the combination fit with α and kT.

It is clearly seen from Fig. 1, that a single power law fit of the form $\mathrm{d}N/\mathrm{d}E = K\,E^{-\alpha}$ photons $\mathrm{cm}^{-2}\mathrm{s}^{-1}\,\mathrm{keV}^{-1}$ does not fit the spectral data and the spectrum does consist of atleast two components. A broken power law or a composite fit with a thermal and non-thermal terms represent the data fairly well. The representative best fit model parameters for the two component power law model are; $\alpha_1 = -3.6 \pm 0.1$ and $\alpha_2 = -.86 \pm 0.15$ for a χ^2_4 value of 1.15 per dof. The solid line in the figure shows the power

law fit. A good fit to the data is also obtained for a composite power law + exponential function of the form $\frac{\mathrm{d}N}{\mathrm{d}E} = \frac{A}{E^{\alpha}} + \frac{B}{E}\, e^{-E/kT}$ ph cm^{-2} s^{-1} keV^{-1}. The best fit parameters obtained using gradient method (Bevington *et al* 1969) are $kT = 13.5 \pm 2.2$ keV and $\alpha = 0.86 \pm 0.07$ for χ^2_4 value of 1.2 per dof Lampton *et al* (1976). The estimated luminosity of the source in 20–200 band is 7×10^{42}–$10^{43} \left(\frac{D}{\mathrm{M\ pc}}\right)^2$ ergs s^{-1}.

The spectral data presented above corresponds to an active X-ray phase of the source. The long term behaviour of the source as seen in the ASM light curve on-board RXTE is shown in Fig. 2. The epoch corresponding to the present observations is marked with an arrow. A continuously varying nature of the source is quite apparent from the figure after MJD 51860, on which day the source made a transition from a lower luminosity state.

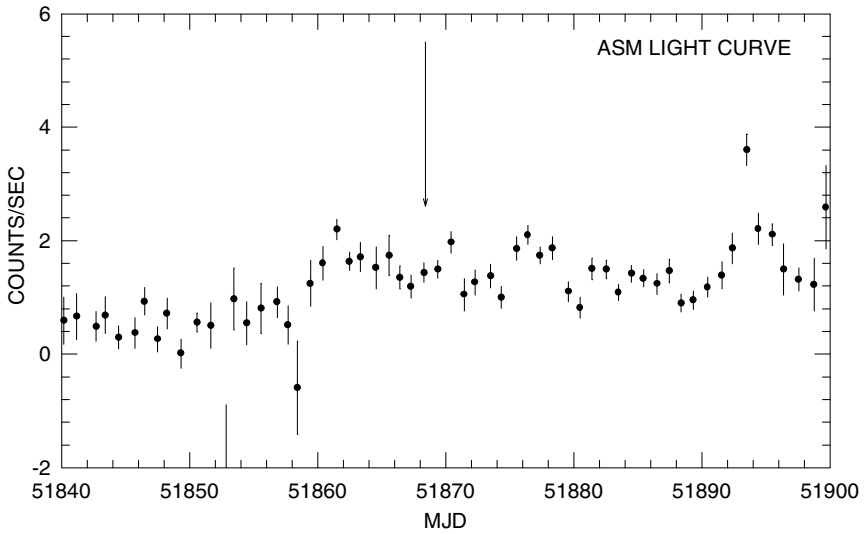

Figure 2. Long term variability of Mkn 421 in low energy range. The arrow marks the epoch for present observations.

In Fig. 3, we have plotted the available spectral measurements of the source between 1 and 200 keV band. The observations correspond to HXR 81 data (Ubertini *et al* 1984), OSO-8 data (Coe *et al* 1979) and HEAO-A2 data (Mushotzky *et al* 1979), Upper limits from OSSE observations (McNaron-Brown *et al* 1995) and the dotted line in the figure shows the single power law approximation to the BeppoSAX data (Guainazzi *et al* 1999). The hard X-ray spectral data obtained during present observations is in fair agreement with the earlier observations of Ubertini *et al* 1984, however the measured flux during the present epoch is factor of 20 higher than OSSE data in the 50–200 keV band. It is also seen from the figure that the present measurement can be construed as an extension of the OSO-8 data in the low energy band of 1–10 keV, but are in complete contrast with the HEAO-1 spectrum. Similarly, recent results of a flare spectrum in the 1–10 keV flare from BeppoSAX are also not consistent with the present measurements at higher energies. Although spectral evolution during the flare period is seen from the source in the low energy data, no simple functional form fits the data. The best fit power

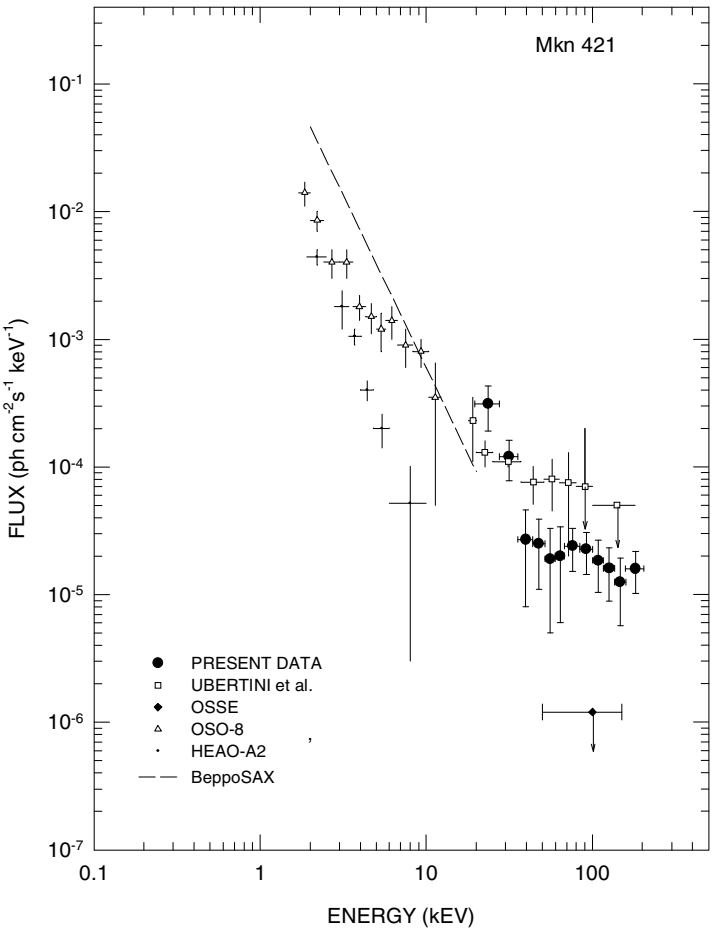

Figure 3. A comparison of the hard X-ray data of Mkn 421 with the other data in the 1.6–200 keV band.

index for a broken power law fit above 1.6 keV is $\alpha \sim 1.5$–1.8 (Fossati *et al* 2000a). It is also clear from the figure that a continuation of the low energy spectrum as shown in the dotted line, can not fit the present observations. A flattening in the spectrum above 30 keV is essential in any functional form. At the extreme high energy end, a combined fit to the hard X-ray observations and the EGRET data at GeV energies (Lin *et al* 1996) requires further steepening of the shape beyond 200 keV. In summary, a non-linear nature of the spectral shape between 1 keV and UHE energies, points to different emission mechanisms which cater to different energy regions.

4. Continuous flaring geometry

The present measurements made during the active phase clearly indicate that X-ray spectrum of the source in the 20–200 keV band is certainly not a simple power law as expected from the Synchrotron and Compton scattering models. Even if we assume that convex spectral shape in the 0.1–10 keV from BeppoSAX represents the high

energy end of the synchrotron emission, the high energy data points represent a new component. Added to this is the strong variability of the source in all wavebands. In the X-ray region, the percentage variation increases with increase in photon energies. It is therefore, necessary to examine alternate models and the possibility of thermal contribution to the X-ray spectrum. A new look is also necessitated, for the particle acceleration to higher energies. It is also essential that TeV photons must originate in a region where the magnetic field is extremely low, in order to avoid strong attenuation of these photons through magnetic pair-production process. An approximate limit is given by $\sqrt{B^2}[G] < 10^{12} \times \epsilon / E_{ph}$ (Bednareck 1991).

We therefore, propose a continuously flaring model in which the particle flux consisting of protons and electrons is squirted during each flaring episode and which is accelerated in the relativistic jets. Random nature of the intensity variations of Mkn 421 in different wavelength bands supports such a geometry. A steady emission from the source points to continuous injection of the particles into the jets.The active phase is therefore, analogous to the increase in the amplitude and the flare occurrence rate. Considering that the large flares are the high amplitude sub-set of continuum of low level flares and lead to a variability of the ambient particle flux, one can account for the observed temporal behaviour of the source even at ultra high energies.

4.1 *Particle acceleration and the photon emission*

The photon spectrum of Mkn 421 extends from radio emission to TeV ($> 10^{12}$ eV) gamma ray energies and is highly variable. The observation of a jet in the source provides a natural basis for radio emission as due to synchrotron emission from high energy electrons. The formation of the jet features, their morphology, extent and the speed of expansion are ultimately ascribable to either the accretion on to the central black hole or episodic ejection from the centre of the galaxy. The dynamical parameters including mass flow, momentum, collimation, energy, magnetic flux and the cooling depend upon the ambient environment and many hydro-dynamical models of the formation of narrow jets for AGN's and stellar scale compact objects have been proposed in literature (Begelman *et al* 1984, Colgate 1990). A continuous input to the jets as envisaged above does require the formation of accretion disk and the transfer of the material to the base of the jet. For synchrotron emission from relativistic electrons, the electron energy corresponding to the observed radio emission lie in the range $E \simeq 300 - 2000 \times [\nu / H_{\perp}]^{1/2}$ eV. Hence the detection of radio flux from the source is itself an evidence of the presence of relativistic particles and *in situ* acceleration.

The particle acceleration in the jets is believed to be due to shock wave at the interaction boundary of the expanding relativistic plasma and the ambient environment. During the shock acceleration a particle with velocity v gains a momentum $\simeq w/v$ every time it crosses the shock of velocity w. If the particles are scattered efficiently both sides of the shock and stay trapped, the particle can reach relativistic energies provided the adiabatic losses are negligible. In case of the diffusive shock the maximum proton energy $E^p_{\max} \sim 10^{15}$ eV is attainable for a shock compression ratio of 4 and reasonable values for other parameters (Ogelman 1986). Treating ultrasonic turbulent mass flow in the jet stream as analogous to the strong stellar winds the maximum energy may be even higher by ~ 100 at the shock boundary (Cesarsky & Montmerle 1991). In shock acceleration, the resultant spectrum of the particles is a power law and for a shock compression of $\sim 3 - 4$ the exponent lies between 2 and 2.5.

A large population of high energy electrons within a strong radio photon field can also give rise to high energy X-ray photons due to Inverse Compton collisions. This SSC mechanism is generally believed to be the main operative process for photon emission in the AGN sources. The SSC mechanism however, predicts very definite relationship between the spectral indices in the radio and the X-ray energy bands with the electron spectrum. If we take the spectral index for the electron spectrum to be $\gamma \sim 2.5$, then the power index for the synchrotron photon flux is given by $\alpha = \frac{(\gamma-1)}{2} - 1 \sim -1.75$. With the estimated value of $B \sim 0.03\,\mathrm{G}$, a break in the incident electron spectrum and a change of the power index by ≥ 1, due to steepening caused by the synchrotron and bremsstrahlung losses is expected at electron energies above 10^{14} eV. One can therefore, infer a further steepening in the photon spectrum by ≥ 0.5 at higher energies. Furthermore, the energetic constraints provide that the flux of X-ray photons produced in Compton collision of high energy electrons with radio photons increases, if value of B decreases, which in turn requires much higher electron energy for the production of radio photons. The observed X-ray spectrum below 20 keV can therefore, be identified with the tail end of the SSC photons. A flattening in the X-ray spectrum in hard X-ray region and a change of spectral index from 3.6 to 0.86 can not be therefore, ascribed to a non-thermal origin. As seen in Fig. 1. an additional component dominating the hard X-ray flux above 60 keV is essential. We propose that the high energy component arises due to upgrading low energy photons by thermal electrons.

It is well known that a localized non-radiative heating of the plasma can take place near the shock front. Therefore, a significant fraction of soft X-rays in the 2–10 keV region may arise due to thermal bremsstrahlung emission at the collision boundary of the jet since temperature of the hot gas behind the shock is $\sim 10^7 - 10^8\,\mathrm{K}$. The presence of an iron line at 6 keV in the spectrum clearly points to the existence of high temperature regions of thermal emission within the source volume. In addition, the observations of soft excess in bright quasars, without any obvious correlation with other spectral properties of the source is also indicative of a thermal component in the quasars spectra. Upgrading of the low energy seed photons due to multiple Compton collision with thermal electrons can lead to Compton tail in the 40–200 keV energy range as seen in the Mkn 421 spectrum. During Comptonization, if $4\,\mathrm{kT}_e > h\nu$, the seed photons will be upgraded in energy. The increase in photon energy on average during each scattering is given by $\Delta\epsilon = \frac{4}{3}[\gamma^2 - 1]\epsilon$, even for a Maxwellian distribution of electrons with $\mathrm{kT}_e \ll m_e c^2$. Therefore, multiple scattering even by a Maxwellian gas in hot spots can lead to very high photon energies. The emergent spectrum is a unified power law but the exact spectral shape is radically modified if the seed photons have a spectral distribution and there is a temperature gradient in the scattering electron cloud.

Since the correlated measurements have revealed beyond doubt that TeV gamma rays have a one-to-one correspondence with the low energy X-ray emission from the source, one is tempted to assume the TeV emission to be a simple extension of the SSC spectrum. However, an enhancement by a factor of 10^9 in the energy of electrons is needed to emit TeV photons and is far more difficult to achieve due to long acceleration time scale given by $t_a \sim (c/v)^2 t_c$, where t_c is the collision time, which is necessary to reach these energies, against the efficient cooling due to synchrotron and bremsstrahlung processes. Recently Dermer and Schlickeiser (1991) have shown that

production of UHE gamma rays by the inverse Compton process is not plausible even if one considers the 'triplet pair production' process. A much more efficient way of producing TeV gamma rays is from the protons. UHE photons can arise from the π° decay which are produced due to the collisions of the accelerated proton component. The production of gamma ray per target nuclei in pp collisions is given by Ozel & Ficktel (1988); $q[E_\gamma]\ \mathrm{d}E_\gamma = \mathrm{d}E_\gamma \int R(E_\gamma, E_p) N_p(E_p)\ \mathrm{d}E_p$; where R represents the integrated gamma ray production rate based upon the π° meson production and distribution function and N_p is the proton number density. The integral gamma ray flux from the source volume can be written as $S_\gamma \sim 2 \times 10^{25} \eta n_H V$, where V is the volume of the source, n_H is the number density of hydrogen nuclei and η is the ratio of the proton spectral density to that in the vicinity of the earth. Another possible source for the emission of TeV photons is due to $p\gamma$-photomeson photo production process. The gamma ray yield efficiency in this case is higher by a factor of ~ 2 since the square mass invariant in pp collisions is higher than the corresponding $p\gamma$ collision with X-ray photons. The estimated efficiency in the first process is only $\sim 8\%$. In addition, the multiplicity of pions in pp collisions increases with energy and this results in lower energy gamma ray photon for a given proton energy compared to $p\gamma$ process. The observable flux from the jet region will correspond to an oriented directional beam with a solid angle Ω. The required proton luminosity for a detectable gamma ray flux of $\sim 10^{-8}$ ph cm^{-2} s^{-1} keV^{-1} in the gamma ray region will require a number density of emitting protons given by $L_p \sim 3 \times 10^{44} \times \Omega \times \left(\frac{D}{\mathrm{Mpc}}\right)^2$. An apparent simultaneity of the TeV and X-ray photons is maintained in the proposed process as both the electron and protons are accelerated at the same time. This may also explain the observed feature that the decay of the TeV flux is faster than the keV flux.

In conclusion, the presence of jet in Mkn 421 does provide a self consistent basis for the acceleration of the electrons and protons within the source volume. The emission of ultra high energy photons can easily be produced in *pp* collisions. The observation of two component power-law X-ray spectrum of the source, with clear flattening at higher energies does not support a pure Synchrotron Self Compton emission model or the continually curved model proposed by Malizia *et al* (2000). The data points to an additional component possibly arising from thermal Comptonization in the hot regions within the emission volume.

Acknowledgements

I wish to thank the dedicated support of J. A. R. D'Silva, P. P. Madhwani, N. V. Bhagat, B. G. Bagade and Ms. N. Kamble. The BATSE and RXTE teams are gratefully acknowledged for their archival data.

References

Bednarek, W. 1991, 22nd ICRC Dublin, **1**, 549.
Begelman, M. C., Blandford, R. G. Rees, M. J. 1984, *Rev. Mod. Phys.*, **56**(2), 255.
Bevington, P. R. 1969, *Data reduction and Error analysis* (McGraw Hill).
Cesarsky, C. J., Montmerle, T. 1991, *Sp. Sci. Rev.* **36**, 173.
Coe, M. S., Dennis, B. R., Dolan, J. F. *et al* 1979, *Ap. Letters*, **20**, 63.

Colgate, S. A. *et al* 1990, *Astro. Lett. and Commun.*, **27**, 411.
Dermer, C. D., Schlickeiser, R. 1991, *Astron. Astrophys.*, **252**, 414.
D'Silva, J. A. R., Madhwani, P. P., Tembhurne, N. T., Manchanda, R. K. 1998, *NIM*, **A421**, 342.
Fossati, G., Celotti, A., Chiaberge, M. 2000a, *Astrophys. J.*, **541**, 153.
Fossati, G., Celotti, A., Chiaberge, M. 2000b, *Astrophys. J.*, **541**, 166.
George, I. M., Warwick, R. S. and McHardy, I. M. 1988, *MNRAS*, **235**, 787.
Ghisellini, G., Marascii, L., Treves, A. 1985, *Astr. Astrophys.*, **146**, 204.
Guainazzi, M., Vacanti, G., Malizia, *et al* 2000, *Astron. Astrophys.*, **342**, 124.
Lampton, M., Morgan, B., Boyer, S. 1976, *Astrophys. J.*, **208**, 177.
Lin, Y. C., Bertsch, D. L., Dingus, B. L. *et al* 1996, *Astr. Astrophys.*, **120**, 449.
Macomb, D. J., Akerlof, C. W., Aller, D, 1995, *Astrophys. J.* **449**, 99.
Malizia, A. *et al* 2000, *MNRAS*, **312**, 123.
Maraschi, L., Fossati, G. and Tavecchio F. 1999, *Astrparticle Phys.*, **11**, 189.
McNaron-Brown K., Johnson W. N., Jung, G. V. *et al* 1995, *Astrophys. J.* 575.
Mushotzky, R. F., Boldt, E. A., Holt, S. S., Serlimitsos, P. J. 1979, *Astrophys. J. (Letters)*, **232**, L17.
Ricketts, M. J., Cooke, B. A., Pounds, K. A. 1976, *Nature*, **259**, 546.
Tagliaferri, G., Ghisellini, G., Giommi, P. *et al.* 2000, *Astr. Astrophys.*, **354**, 431.
Takahashi, T. *et al.* 1996, *Astrophys. J.*, **470**, L 89.
Takahashi, T., Katoka, J., Madejski, G. *et al.* 2000, *Astrophys. J. (Letters)*, **542,** L105.
Ubertini, P., Bazzano, A., LaPadula, C., Polcaro, V., Manchanda, R. K. 1984, *Astrophys. J.*, **284**, 54.
Ogelman, H. 1986, in *Int. School of NS, AGN and Jets*, Erice.
Ozel M, Fichtel, C 1988, *Astrophys. J.*, **335**, 135.

J. Astrophys. Astr. (2001) **22,** 155–172

Hα Emission Line Morphologies in Markarian Starburst Galaxies

A. Chitre[1] & U. C. Joshi, *Physical Research Laboratory, Navrangpura, Ahmedabad 380 009, India*
[1]*Present address: Indian Institute of Science, Bangalore 560 012, India.*

Received 2000 December 4; accepted 2001 May 10

Abstract. We present broad band *R* and narrow band Hα emission line images of a sample of optically selected starburst galaxies from the Markarian lists. The emission line morphology is studied and global properties like luminosities, equivalent widths and star formation rates are derived. The radial distribution of Hα flux and the EW are determined using concentric aperture photometry on the emission line and the continuum images. Hα flux is generally found to peak in the nuclear region and fall off outwards. The EW is found to peak off-center in most of the cases implying that though the intensity of emission is maximum at the nucleus, the star formation activity relative to the underlying continuum often peaks away from the center in Markarian starburst galaxies.

Key words. Galaxies: starburst, photometry.

1. Introduction

Emission line fluxes of the Balmer series provide a measure of the integrated luminosity of galaxies short ward of the Lyman limit and can be used to provide a direct measurement of the star formation rate (SFR) for hot, massive stars that dominate the ionizing continuum. The Hα emission from giant HII regions in galaxies is a good tracer of OB star formation. The presence of Hα indicates that at least one massive star has formed there recently. Hence, Hα images are ideal for tracing the spatial distribution of hot, young stars in star forming regions of normal and starburst galaxies. Extensive Hα surveys of samples of normal galaxies were carried out by Kennicutt & Kent (1983). They found that the integrated emission of a galaxy is strongly correlated with its Hubble type and colour. They also inferred that the variation of emission among galaxies of a given type was due to real dispersion in star formation activity. Several Hα surveys of large samples of spirals using large apertures (Romanishin 1990) and CCD images (García-Barreto *et al.* 1996; Pogge 1989) were made. From a CCD Hα survey, Gonzalez Delgado & Perez (1997a, 1997b) report considerable circumnuclear emission in a large sample of active galaxies. Pogge & Eskeridge (1993) conducted an Hα imaging survey of a sample of neutral-gas rich S0 galaxies. Starburst galaxies and violently interacting systems show enhanced levels of star formation. The nuclear as well as the global properties of violently interacting galaxies were studied in detail by Bushouse (1986). Lehnert & Heckman (1996), hereafter LH96; studied a sample of

IR selected edge-on starburst galaxies using Hα images. In this paper, we present the Hα images along with the R band images of a sample of Markarian starburst galaxies and discuss the properties of the line emission. This paper is the second in a series of papers aimed at studying Markarian starburst galaxies in B, V, R, I and Hα. The optical B, V, R, I properties of a subset of the sample of Markarian starburst galaxies can be found in Chitre & Joshi (1999), hereafter, Paper I.

2. Observations and data reduction

The sample of galaxies was selected from the Markarian lists (Markarian, Lipovetskii & Stepanian 1979 and references therein) with the following criteria: Galaxies designated as starburst galaxies in the catalogue from CDS with m_v brighter than $14^m.5$ and angular sizes greater than $30''$ were selected. No consideration was made for any particular morphological type and the sample is unbiased towards the morphology of the galaxy. In this paper, we present results on 15 of the sample objects. All morphological types are represented in the present sample. Table 1 lists the global properties of the galaxies presented.

Table 1. Global properties of the sample galaxies.

			Type	Dist.	$S_{60\mu m}$	$S_{60\mu m}/S_{100\mu m}$	log L_{FIR}	B_T	log D_{25}
Mkn	NGC	UGC	CDS	Mpc	Jy		erg s^{-1}		RC3
(1)	(2)	(3)	(4)	(5)	(6)	(7)	(8)	(9)	(10)
14	–	4242	S0?	44	0.25	0.23	42.69	14.67	0.73
213	4500	7667	SBa	43.6	3.89	0.59	43.67	13.18	1.21
363	694	1310	Scp	41.5	2.4	0.65	43.40	14.28	1.58
439	4369	7489	Sa	14.5	5.91	0.53	42.92	12.65	1.32
449	5014	8271	Sap	15.4	2.27	0.56	42.54	13.45	1.23
602	–	2460	SBbc	38.2	3.55	0.63	43.50	13.50	1.09
603	1222	–	E	35.8	12.6	0.82	43.96	13.24	1.04
708	2966	5181	SB	21.2	5.37	0.672	43.16	12.53	1.35
743	3773	6605	E0p	11.7	1.48	0.83	42.06	13.19	1.07
781	4779	8022	SBc	36.6	1.82	0.44	43.25	13.07	1.33
1002	632	1157	E1	43.3	4.85	0.76	43.72	13.60	1.19
1134	7752	12779	I0	72	4.76	0.48	44.23	14.75	0.92
1194	1819	3265	SB0	62.1	6.95	11.40	44.23	13.23	1.22
1308	–	6877	–	11.9	0.99	1.29	41.84	14.04	0.82
1379	5534	–	SBbc dbl	36.5	4.73	0.68	43.58	13.29	1.15

Note. Cols. (1), (2) and (3) : The Mkn, NGC and UGC designations respectively of the objects. **Col. (4)** : The morphological type taken from the Markarian catalogue downloaded from CDS. **Col. (5)** : The adopted distance to the galaxy in Mpc. **Col. (6)** : The 60 μm flux density in Jy from IRAS. **Col. (7)** : The ratio of the 60 μm to the 100 μm flux density. **Col. (8)** : The logarithm of the FIR luminosity in ergs s^{-1} calculated using the formula from Lonsdale *et al.* (1985). **Col. (9)** : The total uncorrected B magnitude from Chitre (1999). This was derived by fitting an exponential disk to the outer part of the luminosity profile in the B band and extrapolating it to infinity to derive B_T. **Col. (10)** : The log of the diameter at 25 mag arcsec^{-2} in units of a tenth of an arc minute from RC3.

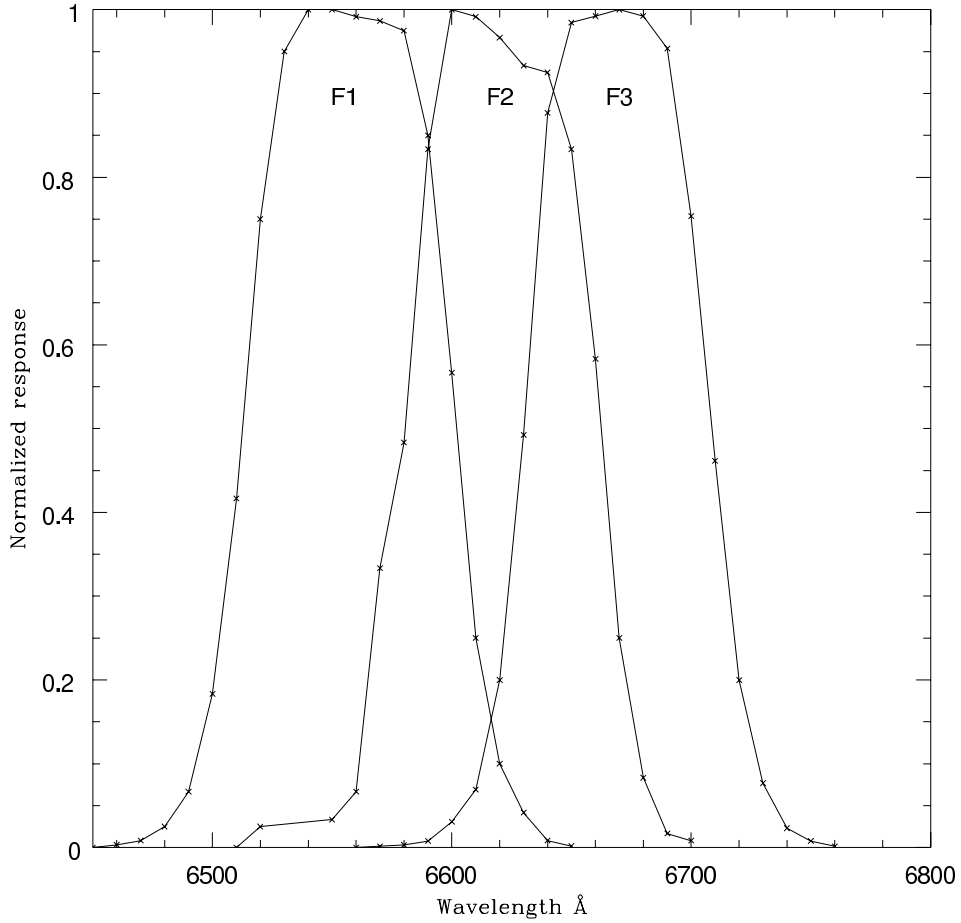

Figure 1. Normalized response curves of the narrow band filters.

Table 2. Narrow-band filter specifications.

Filter no.	λ_0 (Å)	Peak trans. (%)	W(eff.width) (Å)
F1	6556	60	91
F2	6618	60	84
F3	6669	65	81

The observations were carried out at the Cassegrain focus of the 1.2m telescope at Gurushikhar, Mt. Abu. The f-ratio of this telescope is f /13. A thinned, back illuminated Tektronix 1024 $\times$ 1024 pixels CCD chip providing a field of view ($5.2' \times 5.2'$) was used for imaging the galaxies. On chip binning of 2 $\times$ 2 was employed before recording the images to increase the signal-to-noise ratio. The final resolution was $0.63''$ /pixel which is sufficient to sample the point spread function (PSF) appropriately. The PSF

values during each galaxy observation are given in Table 3. Images were obtained through broadband Cousin's *R* and narrow band Hα filters. The sample of galaxies was observed using appropriately red shifted filters. The response curves of the narrow band filters used are given in Fig. 1. Table 2 gives the filter specifications viz., the mean wavelength (λ_0) the peak transmission and the effective width (the width of a rectangle with the same area as that under the response curve and height equal to the peak transmission; W) of each filter. About 3–4 exposures were taken in each filter. The exposure times are also given in Table 3. The data were reduced using IRAF[1] and standard reduction procedures viz., bias subtraction, flat fielding, cosmic ray correction were performed on the raw images. Airmass corrections were applied using the extinction coefficients obtained from the standard stars which were observed on the same nights together with the narrow band and the broad band images. The galaxy images in both *R* band and narrow band Hα were shifted and co-added to improve the signal-to-noise ratio. The sky background was computed from the mode of the histogram of the image since the field of view was large enough as compared to the size of the galaxy and the histograms were sky dominated. The galaxy images were subsequently sky subtracted and scaled for 1 second exposure. Figure 2 displays the *R* band continuum isophotal contours superimposed on the Hα emission line images.

Table 3. Observational details.

Mkn	t_R sec	$t_{H\alpha}$ sec	Filter no.	PSF $''$
14	480	2100	F2	3.0
213	660	2100	F2	2.3
363	360	1500	F2	2.2
439	360	1600	F1	2
449	450	1800	F1	1.8
602	240	2040	F2	1.7
603	320	1200	F2	1.7
708	1300	1500	F2	2.2
743	420	1500	F1	1.9
781	520	1200	F2	2.7
1002	300	1200	F2	2.0
1134	360	1320	F3	2.4
1194	300	1200	F3	1.9
1308	360	1800	F1	2.3
1379	360	1200	F2	1.9

[1]IRAF is distributed by National Optical Astronomy Observatories, which is operated by the Association of Universities Inc. (AURA) under cooperative agreement with the National Science Foundation, USA.

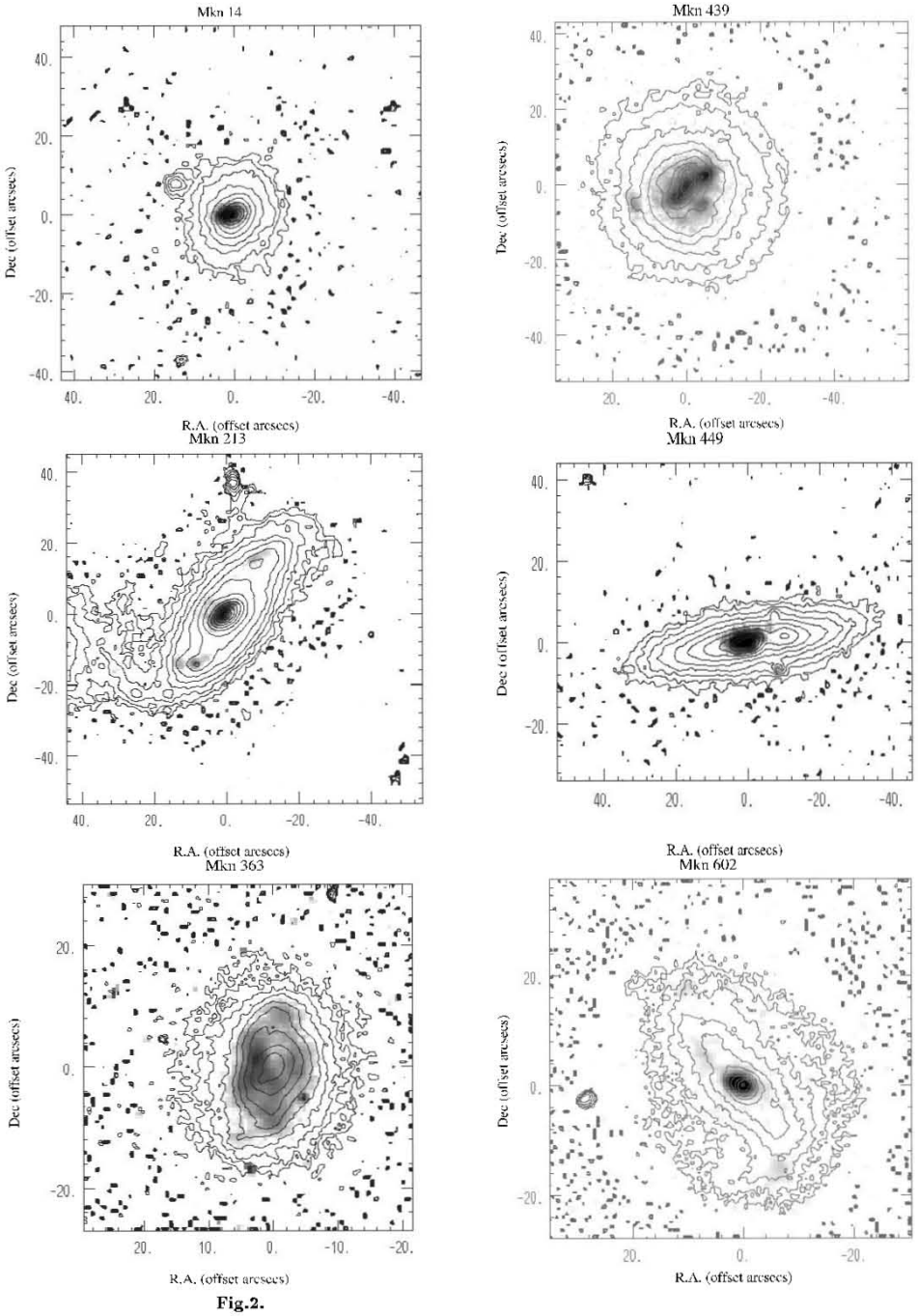

Figure 2. (*Continued*)

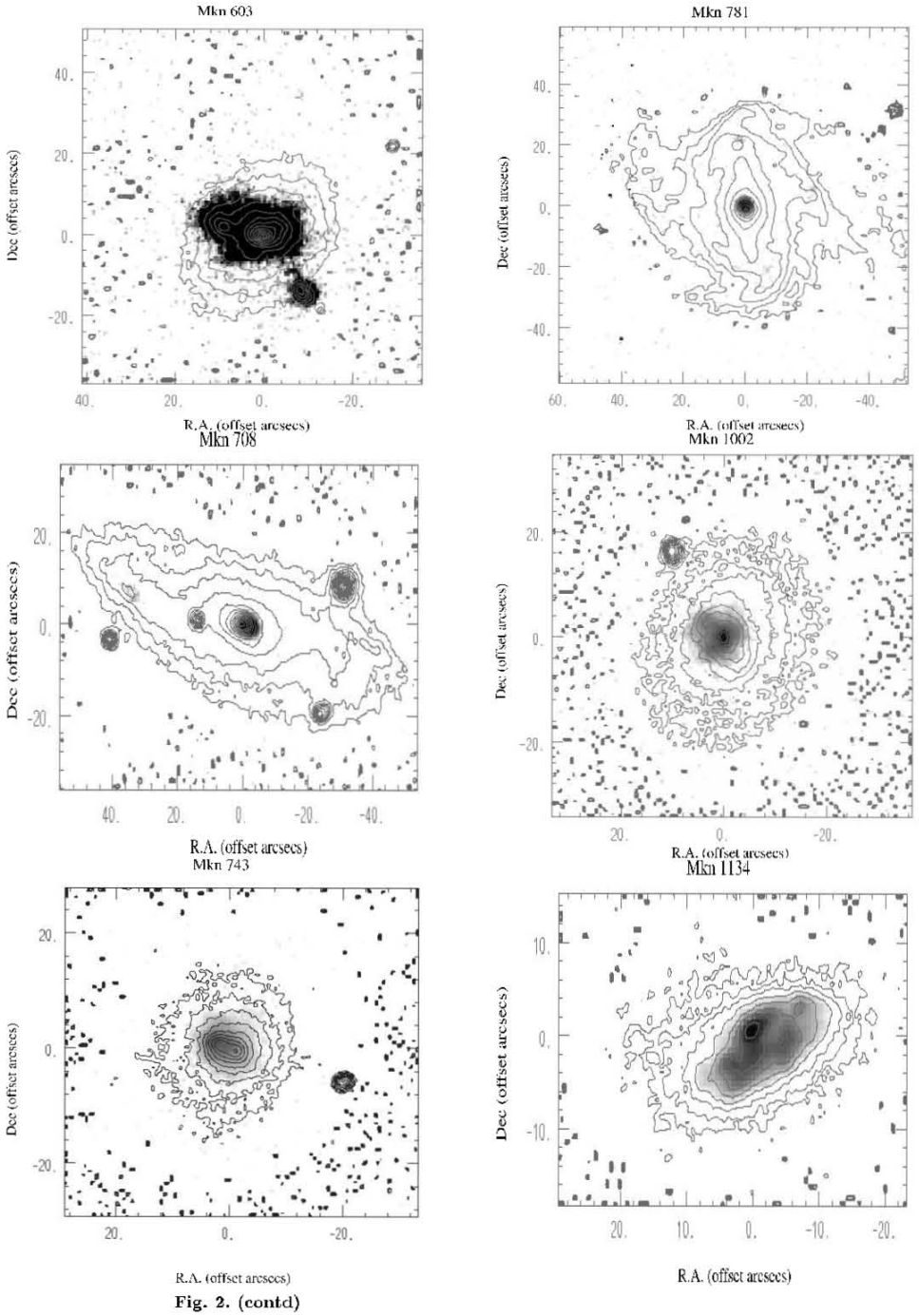

Fig. 2. (contd)

Figure 2. (*Continued*)

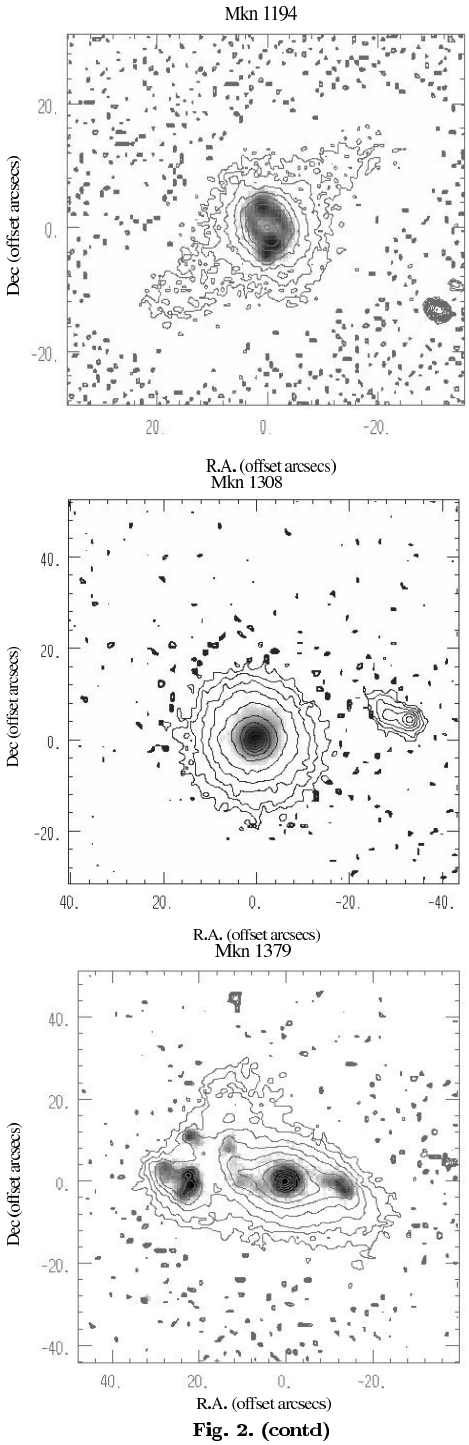

Fig. 2. (contd)

Figure 2. *R* band continuum isophotal contours superimposed on the Hα + [NII] emission line gray scale images. The gray scale has been chosen for best contrast. North is at the top and East is to the left. The *R* band contours are plotted on the magnitude scale at an interval of 0.5^m with the peak contours at 16.5 mag arcsec^{-2} for Mkn 213, Mkn 603 and Mkn 1379; 17.0 mag arcsec^{-2} for Mkn 439, Mkn 602 and Mkn 1194; 17.5 mag arcsec^{-2} for Mkn 449, Mkn 708 and Mkn 781; 18.0 mag arcsec^{-2} for Mkn 14, Mkn 363, Mkn 743, Mkn 1002 and Mkn 1308 and 18.5 mag arcsec^{-2} for Mkn 1134.

3. Generation and calibration of pure emission line images

The images obtained as discussed above were further reduced in the following way to obtain the pure emission line images. The FWHM of the stars in each set of R and Hα frames was examined and the better PSF was degraded to match the PSFs in R and the narrow band. The next step involved determining the scale factor between the broad band and the narrow band image. For this, all the foreground stars in each frame were used. Using synthetic aperture photometry, the counts within a fixed aperture were derived for stars in both the filters and their ratio was taken. The average scaling factor ϵ, between the R band and Hα was thus determined for each galaxy. The R band image was then scaled by the corresponding factor and subtracted from the narrow band images to yield the pure Hα+[NII] emission image.

The zero point R_0 for the continuum R band was determined using

$$R = R_0 - 2.5 \log N \tag{1}$$

where N is the number of counts and R is the corresponding instrumental magnitude. We used our broad band data (Chitre 1999) to determine the zero point for each observing night. The $H\alpha$ fluxes were determined using the equations explained in detail by Macchetto *et al.* (1996). These values were then corrected for galactic absorption using $E(B-V)$ from Burstein & Heiles (1984) and the Whitford (1958) form of the extinction curve as:

$$f_{\mathrm{H}\alpha\mathrm{corr}} = f_{\mathrm{H}\alpha\mathrm{obs}} \times \mathrm{dex}(0.969 \times E(B-V)). \tag{2}$$

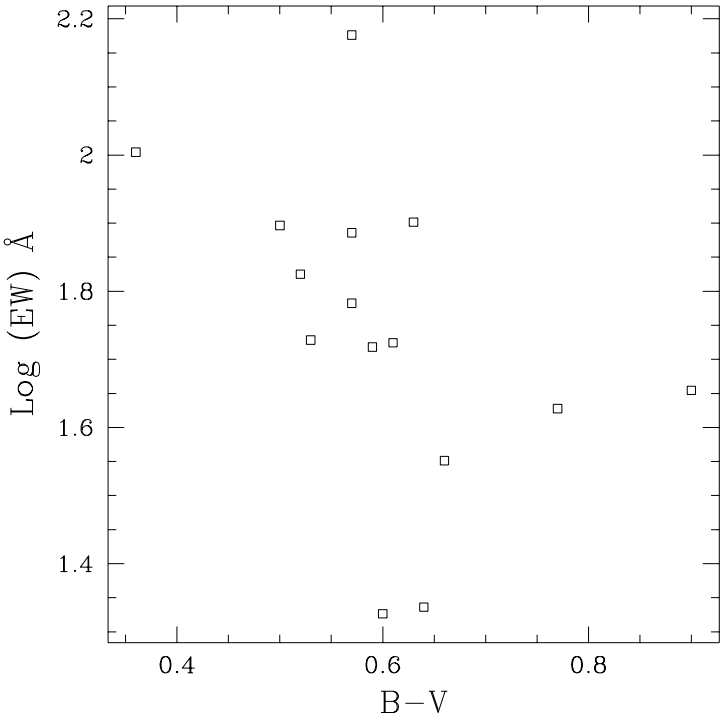

Figure 3. Hα equivalent widths (present study) vs. B–V colours (Chitre 1999).

Table 4. Derived properties of the sample galaxies.

Mkn	log $f_{H\alpha}$ (erg s^{-1} cm^{-2})	log $L_{H\alpha}$ erg s^{-1}	EW(Hα) Å	n / g	$r_{e,H\alpha}$ (kpc)	$r_{e,H\alpha}$ / $r_{e,R}$
(1)	(2)	(3)	(4)	(5)	(6)	(7)
14	−12.40	40.96	66	1.31	0.55	0.37
213	−12.29	41.21	21	1.94	0.98	0.43
363	−12.29	41.02	53.2	0.59	1.17	0.64
439	−11.65	40.74	52	1.38	0.61	0.92
449	−12.17	40.28	35	1.63	0.23	0.17
602	−12.04	41.20	45	–	0.939	0.31
603	−11.39	41.79	150	1.17	0.93	0.65
708	−12.14	40.79	53	1.89	1.25	0.255
743	−12.04	40.17	101	1.15	0.19	0.49
781	−12.27	41.08	21	–	3.52	0.60
1002	−11.95	41.36	76	1.50	0.643	0.256
1134	−12.35	41.44	60	1.10	1.87	0.748
1194	−11.97	41.69	42	0.80	1.42	0.57
1308	−12.07	40.16	78	1.21	0.21	0.39
1379	−11.54	41.66	79	1.47	1.98	0.83

Note. **Col. (1)** : The Mkn number. **Col. (2)** : The total Hα+[NII] flux of the galaxy corrected for galactic absorption using Eqn. 2. **Col. (3)** : The corrected luminosity of the galaxy in logarithmic units. **Col. (4)** : The global equivalent width in Å. **Col. (5)** : The ratio of the nuclear (central 1 kpc) to the global EW. **Col. (6)** : The half light radius in Hα. **Col. (7)** : The ratio of the half light radius in Hα to the half light radius in R band.

We have not applied corrections for the internal extinction within the galaxy. The corrected fluxes were converted to luminosities using the distances given in Table 1. The global equivalent widths of the galaxies were estimated by dividing the corrected Hα flux in the emitting region of the galaxy by the underlying R band continuum flux within D_{25}. The underlying R band continuum was determined by first subtracting the emission from the broad band image and then scaling it to the continuum in the narrow band. The global EW and the $B-V$ colours of the galaxy are plotted in Fig. 3. We do not find a strong correlation between the global EW and the $B-V$ colours of the galaxy. There is a large scatter in EW around $B-V$ of 0.6. All the derived quantities are presented in Table 4.

4. Discussion

4.1 *Spatial distribution of star formation*

The large-scale distribution of star formation can be studied in various ways. The simplest qualitative method is to visually examine the distribution of the emission line regions. On the basis of the emission line morphologies, the sample can be divided into the following four sub classes.

- Galaxies showing Hα emission in the central regions only. Mkn 14, Mkn 449 and Mkn 1308 belong to this sub class.
- Galaxies showing extended Hα emission or galaxies with extranuclear emission in addition to nuclear star formation. This includes most of the spirals which show

emission from either one or both the ends of the bar or along the bar. Mkn 213, Mkn 602 are examples of this sub class.

- Galaxies showing global massive star formation. Line emission is observed throughout the body of the galaxy in Mkn 363, Mkn 603 and Mkn 1134, indicating that these galaxies are undergoing a global starburst. The fact that massive star formation is not always confined to the nuclear region alone is best illustrated in these cases. Their strong stellar continuum at longer wavelengths (R band) points to the fact that these are not young systems experiencing their first phase of star formation, but are old systems with a younger burst of star formation.
- This sub class includes starburst galaxies with peculiar emission line morphologies. Mkn 439 and Mkn 1194 are examples of such systems. Mkn 439 shows extended Hα emission along a bar which is misaligned with the optical continuum isophotes (Chitre, Joshi & Ganesh 1999), while Mkn 1194 shows very faint emission from the central region but clearly shows a circumnuclear ring of intense massive star formation.

However, to study the emission line distribution in a quantitative manner and derive useful information from the results, synthetic aperture photometry was performed on the continuum subtracted Hα images to derive the radial flux distribution. Concentric apertures were used for this purpose. The apertures were centered on the nucleus, the position of which was determined from the R band continuum images. This convention was maintained irrespective of whether or not the Hα peak coincides with the R band peak. Circular apertures were considered up to the radius where the signal falls to the 3σ level of the background value. The radial distribution of the Hα flux thus obtained is plotted in Fig. 4.

To study the regions of current star formation relative to the underlying continuum contributed by older stars, the equivalent width (EW) was computed. This was done by dividing the Hα flux by the underlying stellar continuum flux at the same location estimated from the emission subtracted, scaled continuum images. It is a good measure for comparing relative levels of star formation from one galaxy to another. The EW provides a measure of the current star formation rate relative to the recent past star formation rate, since the line emission is due to massive stars with ages $< 10^7$ years while the stellar continuum at these wavelengths is due to G and K giants which are typically a few billion years old (Huchra 1977; Kennicutt 1983). A similar approach was used by Bushouse (1986) to derive pseudo equivalent widths for a sample of interacting galaxies.

An inspection of Fig. 4 reveals that most of the galaxies except Mkn 363 and Mkn 1194 show a peak in the flux at the center and a nearly exponentially falling behaviour outwards irrespective of their morphology. In some cases like Mkn 1308, the profile flattens out in the outer regions. In the case of Mkn 363 and Mkn 1194, the peak emission is off-centered from the nucleus. This is clearly seen in the gray scale images (Fig. 2) also. In general, galaxies with peculiar emission line morphologies or global emission show considerable deviations from the exponential profiles eg., Mkn 1134 and Mkn 439. However, the EW profiles show startling differences in their behaviour. The first two panels in Fig. 4 show galaxies with EWs peaking at the center and falling outwards. The next few panels have EWs peaking away from the center. The interesting point to be noted in these cases is that the EW peaks away from the center even in those cases where the peak Hα flux is maximum at the center. This indicates that though the flux levels are maximum at the center in some of these galaxies, the current star

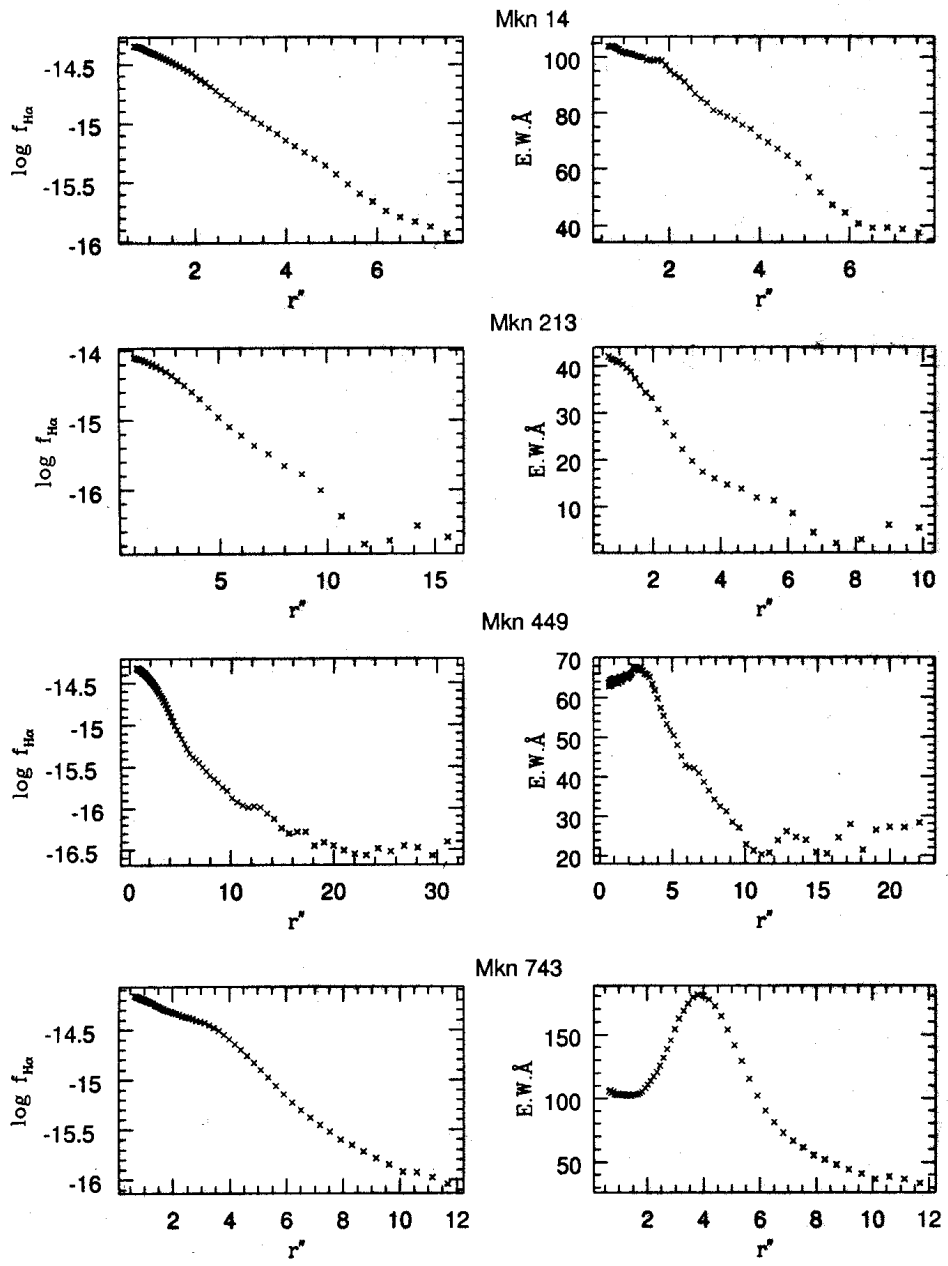

Figure 4. (*Continued*)

formation rate relative to the recent past star formation is maximum away from the center. The peak occurs in the inner half a kpc in most of these galaxies except in Mkn 363, Mkn 1134, Mkn 1194 and Mkn 1379 all of which show considerable extended extranuclear star formation. The peak is sharp in most cases except in Mkn 363 where it is broad and flattened. This is probably a result of the global star formation seen in

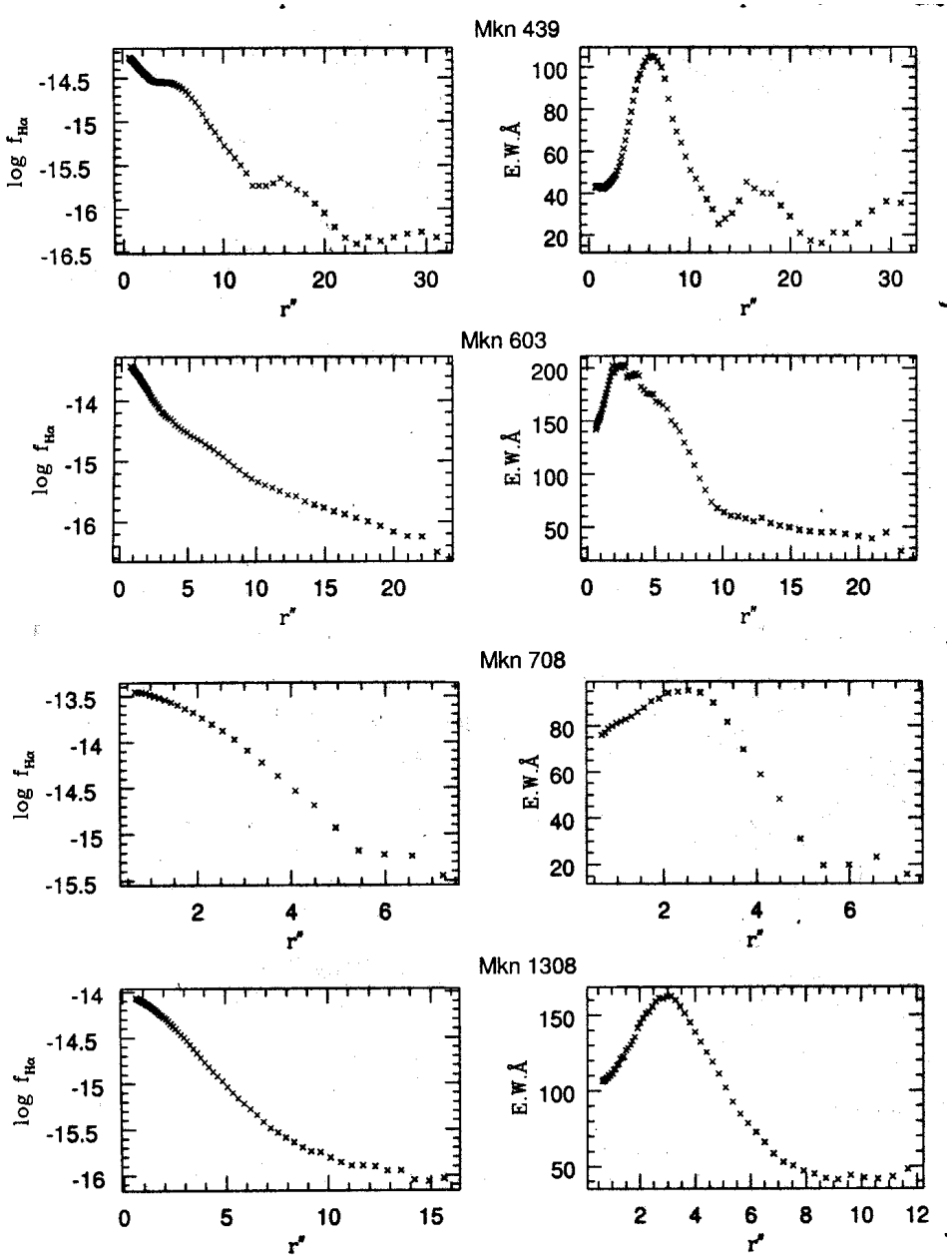

Figure 4. (*Continued*)

Mkn 363. The global EW listed in Table 3 was compared with the EW in the central 1 kpc of each galaxy except for Mkn 602 and Mkn 781. These galaxies were excluded because the signal-to-noise ratio was not good enough to derive the radial profiles and only global values were computed for these two galaxies. It was found that the central nuclear EW was higher than the global value in nearly all cases. This suggests that

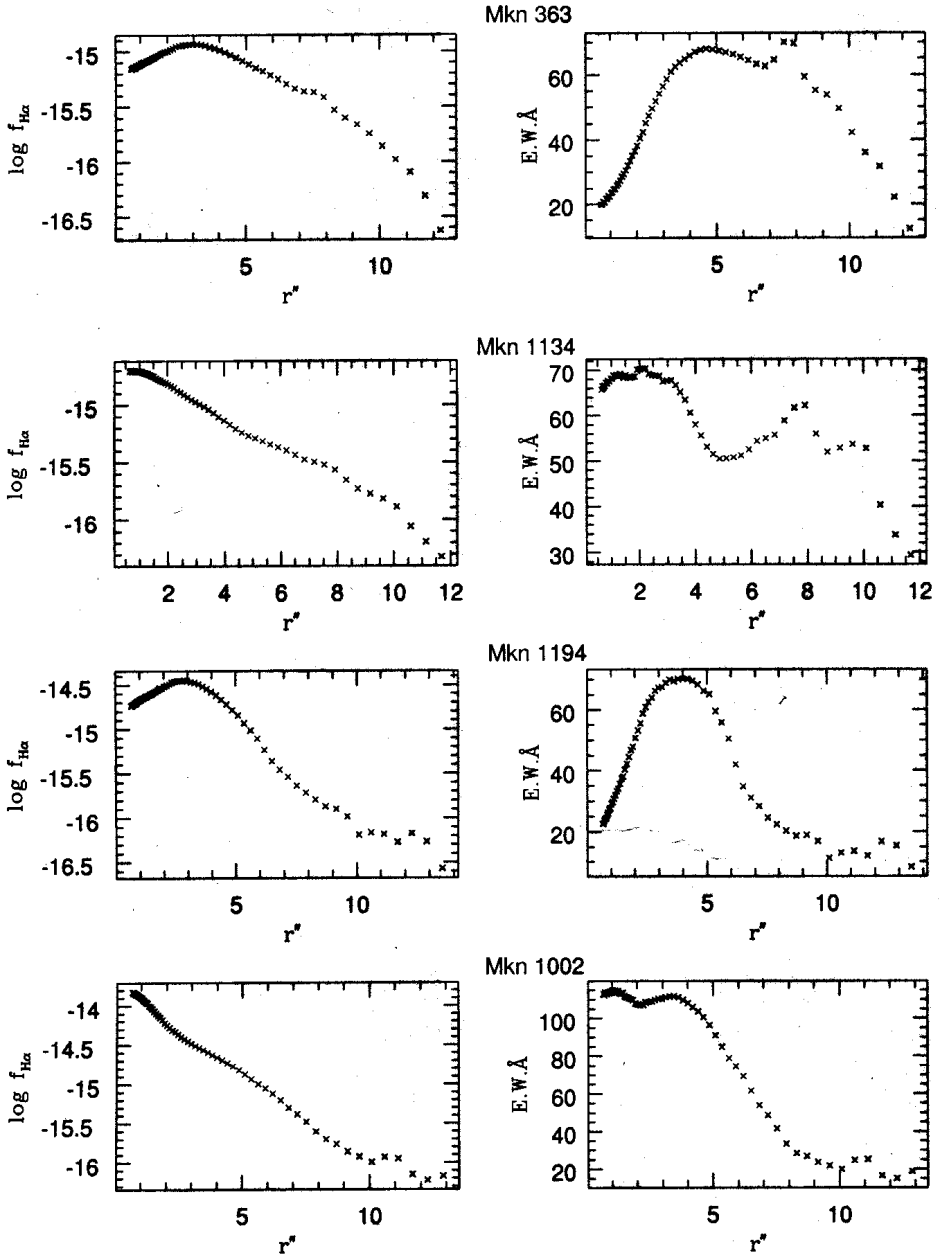

Figure 4. (*Continued*)

the star formation is more enhanced with respect to the underlying population in the central regions of these starburst galaxies. A few cases like Mkn 363 and Mkn 1194 have the ratio of the nuclear EW to its global value less than unity. Both these galaxies show a considerable amount of extranuclear star formation.

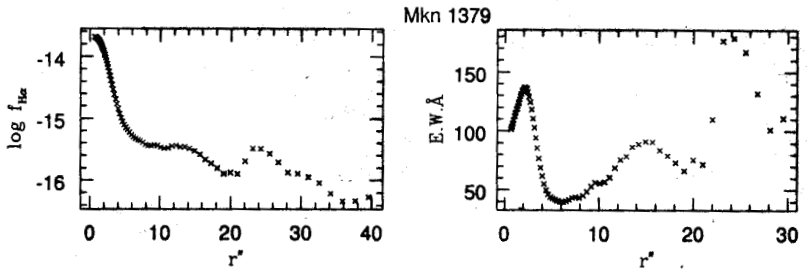

Figure 4. The radial variation of the logarithm of the Hα flux (erg s^{-1} cm $^{-2}$) and the EW (Å).

4.2 *Half-light radii and the relative concentration of star formation*

To compare the characteristic sizes of the star forming regions in the sample, we derived the half-light radius in Hα. This parameter enables us to define a model independent size of the emitting region especially while inter comparing data from a morphologically dissimilar sample as ours. The half-light radius in Hα ($r_{e,H\alpha}$) is defined as the radius enclosing half of the total line emission. For deriving this, the radius at which the counts in the image frame fall to 2σ of the background value is determined. The total flux inside this aperture is computed. A growth curve is constructed using concentric apertures of increasing radii and the half-light radius is determined from this curve. The values of $r_{e,H\alpha}$ derived in this manner are given in column (7) of Table 4. The mean value of log ($r_{e,H\alpha}$) derived from our sample is 2.88 in pc. The size of the emitting regions is directly proportional to the absolute luminosity of the galaxy. This

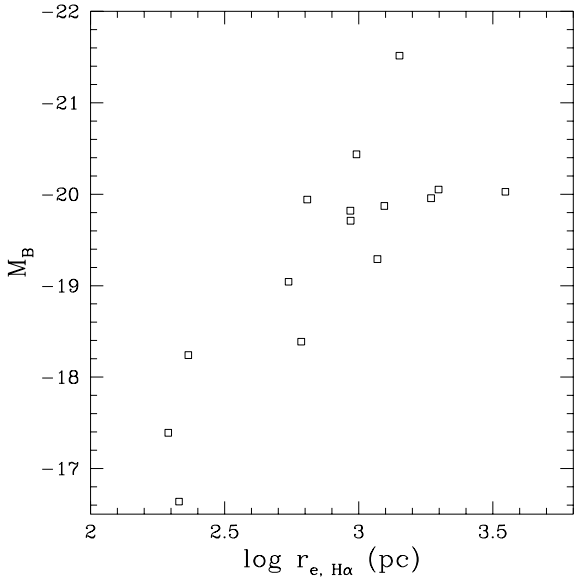

Figure 5. The absolute B magnitude as a function of the half-light radius in Hα.

is illustrated in Fig. 5 where the absolute blue luminosity M_B is plotted against the half-light radius in Hα, $r_{e,H\alpha}$.

To estimate the degree of concentration of the emission relative to the continuum, we calculated the ratio of the half-light radius in Hα to the half-light radius in R ($r_{e,R}$). The values of $r_{e,R}$ were taken from Chitre (1999). For our sample, this ratio is less than unity for all cases indicating that the emission is more centrally concentrated as compared to the continuum light. To compare the properties of our sample of optically selected, uv-excess starburst galaxies with other IR selected starburst galaxy samples, we have done a comparative study of our sample with LH96 sample. The LH96 sample was selected based on the following criteria: It contained starburst galaxies which were edge on, were IR bright ($S_{60\mu\mathrm{m}} > 5$ Jy) and IR warm ($S_{60\mu\mathrm{m}}/S_{100\mu\mathrm{m}}>0.5$. Our sample galaxies had a range of inclinations with Mkn 439 being nearly face on and Mkn 1194 being nearly edge on. Our sample galaxies were selected only on the basis of their redshifts and apparent magnitudes and were found to have $S_{60\mu\mathrm{m}}$ ranging from 0.25 Jy to 12.6 Jy with most galaxies having the value less than 5 Jy. Comparing the results derived by us with the results derived by LH96 (Table 5), we see that the average size of the emitting regions in the LH96 sample is nearly 1.8 times larger than that in our sample. The concentration of Hα in our sample is 45% with respect to the continuum while it is 60% for LH96. In other words, the line emission is more centrally concentrated in our sample of optically selected starburst galaxies than in the LH96 sample of IR selected starburst galaxies. We also find that on an average, LH96 galaxies are only 1.5 times brighter in Hα but are about 9 times brighter in FIR. One reason for this could be that the IR selected galaxies are much dustier and the star forming regions are hidden by large amounts of dust which could be responsible for the extinction of the line emission.

Table 5. Average properties of our sample and LH96 sample.

Parameter	This work	LH96
$S_{60\mu m}$(Jy)	0.25 – 12.6	>5
$S_{60\mu m}/S_{100\mu m}$	0.23 – 0.83	>0.5
Inclination	no limit	edge-on
Log $L_{H\alpha}$	41.06	41.23
Log L_{FIR}	43.25	44.22
Log $r_{e,H\alpha}$(pc)	2.88	3.15
Log ($r_{e,H\alpha}/r_{e,R}$)	−0.34	−0.22

Figure 6 shows a comparative study of the behaviour of log($L_{IR}/L_{H\alpha}$) versus $r_{e,H\alpha}/r_{e,r}$ for three samples, namely our sample, LH96 IR selected starburst galaxies sample and Usui *et al.* (1998) sample which consists of early-type spirals with log (L_{FIR}/L_B) higher than the average for early-type spirals. Our sample objects have smaller ratios of both log ($L_{IR}/L_{H\alpha}$) and $r_{e,H\alpha}/r_{e,R}$ as compared to LH96 while the values do not show much difference as compared to the Usui sample of early-type star forming galaxies.

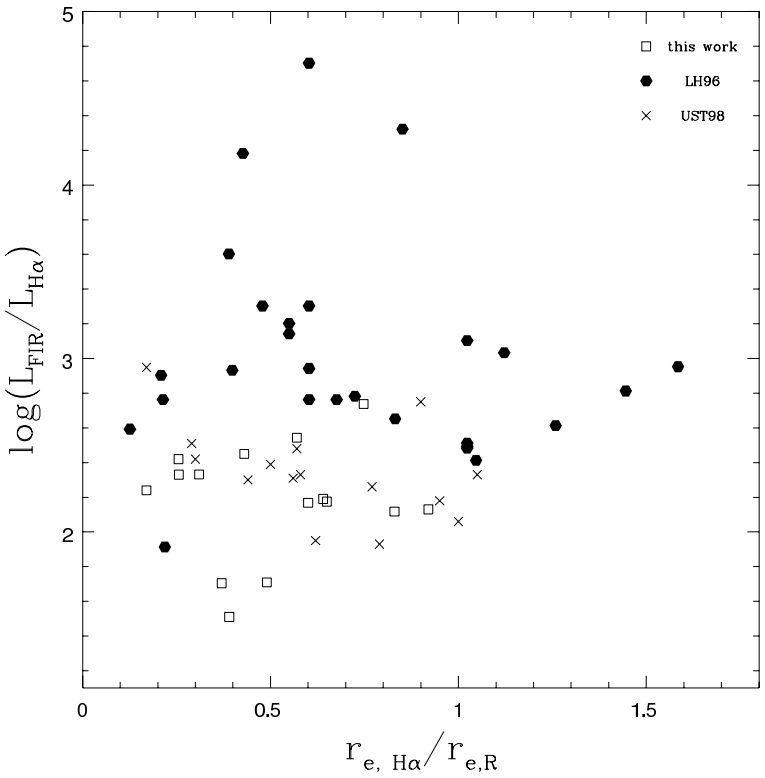

Figure 6. Log(L_{IR} /$L_{H\alpha}$) vs $r_{e,H\alpha}$ /$r_{e,r}$ for our sample compared with two other samples.

5. Conclusions

A study of a sample of Markarian starburst galaxies has shown that:

- The line emission peaks in the central region and falls nearly exponentially outwards in most of the cases.
- Unlike the emission, the radial variation of the equivalent width does not show a uniform behaviour. This indicates that though the intensity of star formation is maximum at the center, the relative level of star formation with respect to the underlying continuum shows different trends. We do not find any clear evidence for a relation between the radial behaviour of the equivalent width and the morphological type of the galaxy.
- The nuclear EW is greater than the global EW in most of the sample galaxies.

APPENDIX

Notes on individual galaxies

The emission line morphology of each galaxy is described below and compared with the optical colour maps from Paper I or Chitre (1999).

Mkn 14 : This S0 galaxy shows line emission in the central region. The emission appears to be more concentrated towards the eastern side of the nucleus (Fig. 2).

Mkn 213 : This spiral galaxy shows strong Hα emission in the central region fanning out towards the west and faint emission at the ends of the bar. The EWs are low compared to other galaxies in the sample indicating that the older stellar population is dominant in the inner region in this galaxy.

Mkn 363 : A peculiar emission morphology is seen in this galaxy. Hα emission is global but the morphology of the emission is disturbed and clumpy. The peak of emission off-centered from the nucleus. A comparison with the optical colour maps shows that the bluest region in this galaxy also lies 5″ away from the nucleus. The EW (Fig. 4) also reaches its peak value at this distance.

Mkn 439 : This galaxy is the most peculiar galaxy in the sample. The optical continuum contours and the emission line contours show completely different morphologies. The peak emission in Hα does not coincide with the bluest region seen in the optical colour maps. The line emission is along a bar misaligned with the optical contours of the galaxy (Chitre, Joshi & Ganesh 1999). The EW peaks 6″ away from the optical center of the galaxy.

Mkn 449 : Strong Hα emission is seen only in the central region in this galaxy.

Mkn 602 : This barred spiral shows emission in the nuclear region and very faint emission from the ends of the bar.

Mkn 603 : Mkn 603 is a part of an interacting system of galaxies. The main galaxy is an elliptical interacting with two small companions. This galaxy shows extended line emission while its companions show global line emission.

Mkn 708 : An elongated spiral galaxy with very broad ill-defined spiral arms, Mkn 708 shows line emission only in the central region. However, this galaxy gets redder inwards unlike other Markarian starburst galaxies which get bluer inwards. We do not find any clear indications for the presence of dust from isophotal analysis of the optical continuum images (Chitre 1999).

Mkn 743 : This double nucleus galaxy (Mazzarella & Boroson 1993) shows peak Hα emission in one of its nucleus. Emission is seen in the inner region in this galaxy.

Mkn 781 : The only flocculent spiral in the sample, this galaxy shows emission in the nuclear region and as a couple of very faint spots in the arms.

Mkn 1002 : Pogge & Eskridge (1993) have reported Hα emission in the nuclear region as well as clumps of emission in the circumnuclear region of this galaxy. Our studies show that the line emission does not follow the structure seen in colour maps but just shows extended emission in the central region.

Mkn 1134 : Global star formation is seen in this small irregular galaxy which is attached to the tip of the spiral arm of a larger spiral galaxy, NGC 7753. The peak emission is coincident with the off-centered nucleus of the galaxy.

Mkn 1194 : Star formation is enhanced in a circumnuclear ring in this galaxy. Two bright Hα spots are seen along the ring to the north and the south. The nucleus appears faint in emission. The ring lies at about 5″ from the nucleus. The EW is also found to peak in this region.

Mkn 1308 : This S0 galaxy has an elongated companion. Emission is seen in the nuclear region. However, the EW peaks 3″ from the optical center of the galaxy.

Mkn 1379 : Mkn 1379 forms a part of a system of interacting galaxies. Strong Hα emission is seen in the nuclear region and diffuse emission is seen along the bar. Blobs of Hα are seen at the ends of the bars and in the companion galaxies. Global

star formation is detected in the companions lying to the east. We measured the EWs in these eastern companions to be as high as 245Å. The companion to the west has a EW of about 105Å. These values are much higher as compared to the peak EW seen in Mkn 1379 (Fig. 4).

Acknowledgements

This work was supported by the Department of Space, Government of India. The authors are thankful to Mr. Shashikiran Ganesh for helping with observations and to Mr. A. B. Shah and Mr. N. M. Vadher for technical support. This research has made use of the Vizie R catalogue access tool, CDS, Strasbourg, France.

References

Burstein, D., Heiles C. 1984, *Astrophys. J. Suppl.* **54**, 33.
Bushouse, H. A. 1986, *Astr. J.* **91**, 255.
Chitre, A. A. 1999, *PhD thesis*, Gujarat University.
Chitre, A., Joshi U. C. 1999, *Astr. Astrophys. Suppl.* **139**, 105 (Paper I).
Chitre, A., Joshi U. C., Ganesh S. 1999, *Astr. Astrophys.* **352**, 112.
García-Barreto, J. A., Franco, J., Carrillo, R. *et al.* 1996, *Rev. Mex. Astron. Astrofis.* **32**, 89.
Gonzalez Delgado, R. M., Perez, E. 1997a, *Astrophys. J. Suppl.* **108**, 155.
Gonzalez Delgado, R. M., Perez, E. 1997b, *Astrophys. J. Suppl.* **108**, 199.
Huchra, J. P. 1977, *Astrophys. J.* **217**, 926.
Kennicutt, R. C. 1983, *Astrophys. J.* **272**, 54.
Kennicutt, R. C. J R., Kent, S. M. 1983, *Astr. J.* **88**, 1094.
Lehnert, M. D., Heckman, T. M. 1996, *Astrophys. J.* **472**, 546.
Lonsdale, C. J., Helou, G., Good, J. *et al.* 1985, *Catalogued Galaxies and Quasars in the IRAS Survey* (Washington: GPO)
Macchetto, F., Pastoriza, M., Caon N. *et al.* 1996, *Astr. Astrophys. Suppl.* **120**, 463.
Markarian, B. E., Lipovetskii, V. A., Stepanian D. A. 1979, *Astrofizika* **15**, 549.
Mazzarella, J. M., Boroson, T. A. 1993, *Astrophys. J. Suppl.* **85**, 27.
Pogge, R. W., 1989, *Astrophys. J. Suppl.* **71**, 433.
Pogge, R. W., Eskridge, P. B. 1993, *Astr. J.* **106**, 1405.
Romanishin, W. 1990, *Astr. J.* **100**, 373.
Usui, T., Saito M., Tomita A. 1998, *Astr. J.* **116**, 2166.
Whitford, A. 1958, *Astr. J.* **63**, 201.

J. Astrophys. Astr. (2001) **22,** 173–185

Far Infrared Mapping of Three Galactic Star Forming Regions: W3(OH), S209 & S187

S. K. Ghosh[1,2]*, B. Mookerjea[1,3], T. N. Rengarajan[4], S. N. Tandon[5] & R. P. Verma[1]

[1] *Tata Institute of Fundamental Research, Bombay 400 005, India.*
[2] *Institute of Space and Astronautical Science, Kanagawa 229, Japan.*
[3] *Joint Astronomy Programme, Indian Institute of Science, Bangalore 560 012, India.*
[4] *Department of Physics, Nagoya University, Nagoya 464-8602, Japan.*
[5] *Inter-University Centre for Astronomy & Astrophysics, Pune 411 007, India.*

Received 2001 April 7; accepted 2001 May 20

Abstract. Three Galactic star forming regions associated with W3(OH), S209 and S187 have been simultaneously mapped in two trans-IRAS far infrared (FIR) bands centered at ∼140 and 200μm using the TIFR 100 cm balloon borne FIR telescope. These maps show extended FIR emission with structures. The HIRES processed IRAS maps of these regions at 12, 25, 60 & 100 μm have also been presented for comparison. Point-like sources have been extracted from the longest waveband TIFR maps and searched for associations in the other five bands. The diffuse emission from these regions have been quantified, which turns out to be a significant fraction of the total emission. The spatial distribution of cold dust (T $<$ 30 K) for two of these sources (W3(OH) & S209), has been determined reliably from the maps in TIFR bands. The dust temperature and optical depth maps show complex morphology. In general the dust around S209 has been found to be warmer than that in W3(OH) region.

Key words. Interstellar dust—W3(OH)–S209—S187.

1. Introduction

The far infrared (FIR) continuum emission from the interstellar dust component allows one to probe deeper in to the denser regions of Galactic star forming regions. A long term programme of studying Galactic star forming regions is being pursued at the Tata Institute of Fundamental Research (TIFR) using its 100 cm balloon-borne FIR telescope. This programme aims at high resolution ($\sim 1'$) mapping in two FIR bands centered at wave-lengths ∼150 and 200 μm, beyond the longest waveband of IRAS survey. The trans-IRAS wavebands help in detecting colder component of the dust. Several Galactic star forming regions have been studied leading to detection of cold dust (up to 15K) and its spatial distribution

*e-mail: swarna@tifr.res.in

(e.g. Ghosh *et al*. 2000; Mookerjea *et al*. 2000). The present study deals with three regions selected on the basis of their association with powerful molecular outflow activity and their extended/complex morphology. These are: W3(OH), S209 and S187 regions.

The Galactic star forming region known as W3(OH), is a very unique and interesting source for several reasons. It is situated $\sim 13'$ SE of W3 (main) in the giant molecular cloud, along the prominent ridge of star formation in the Perseus arm at a distance of 2.3 kpc. It is one of the most luminous high emission measure compact HII region of shell type morphology (Dreher & Welch 1981). Surrounding the ionized gas, there exist dense molecular clumps which host spectacular sources of OH, H_2O and CH_3OH maser emission as well as a bipolar outflow source (Wink *et al*. 1994). Tieftrunk *et al*. (1998) have surveyed this region in the NH_3 line in which they have detected extended emission. A strong far infrared source is associated with the HII region (Campbell *et al*. 1989). W3(OH) has received a lot of attention recently from cm, mm and sub-mm waveband researchers, though mostly concentrating on the higher spatial resolution of the very central few arc sec region. Here we present the study of the distribution of dust in the general neighbourhood of W3(OH) (within a few parsec).

The S209 region is an evolved HII region with visible optical nebulosity in the outer Galaxy. The ionized region is very extended and luminous in radio continuum. The emission at 1.4 GHz has been detected over $12' \times 7'$ by Fich (1993). The associated molecular gas extends over a region of $\sim 14'$ diameter, as inferred from the CO survey of Blitz, Fich & Stark (1982). The CO line velocity places S209 complex at a Galactocentric distance of 21 kpc, one of the outermost sites of star formation in the Galaxy (Fich & Blitz 1984). Molecular outflow activity has been inferred from broad CO wings by Wouterloot, Brand & Henkel (1988). A H_2O maser source has also been detected in the vicinity by Cesaroni *et al*. (1988). The above indicators confirm that star formation is still in progress in the S209 complex. Despite its large heliocentric distance (12 kpc), S209 is expected to be detectable in infrared wavebands due to its high intrinsic luminosity. Surprisingly, no study of the far infrared continuum emission from the S209 region exists in the literature.

S187 is an optical HII region (Sharpless 1959) located at the near side of dark cloud L1317 at a distance of 1 kpc, belonging to the Orion arm in the Galaxy. High angular resolution radio continuum map of this region shows the ionized gas to extend over $\sim 6'$ with rich structures (Snell & Bally 1986). Association of this region with a large molecular cloud complex has been known since Blair *et al*. (1975) detected extended CO emission from this region. Bally & Lada (1983) found first evidence for high velocity molecular outflow from S187, later confirmed to be of extended and bipolar nature by Casoli, Combes & Gerin (1984a). The full extent of this molecular complex has become more evident from the large scale surveys (though with crude gridding), carried out in ^{12}CO and ^{13}CO lines by Casoli, Combes & Gerin (1984b) and Yonekura *et al*. (1997). Various evidences of recent star formation activity in this region have been presented by Zavagno, Deharveng & Caplan (1994). The structurally rich emission from the molecular as well as the ionized gas, prompted us to study the emission from the dust component in S187.

The next two sections describe the observations and the results.

2. Observations

2.1 *Balloon-borne observations*

The Galactic star forming regions associated with W3(OH), S209 and S187 were mapped using the 12 channel two band far infrared (FIR) photometer system at the Cassegrain focus of the TIFR 100cm (f/8) balloon-borne telescope. The photometer uses a pair of six element (2×3 close packed configuration) composite Silicon bolometer arrays cooled to 0.3K using a closed cycle ^{3}He refrigerator and it has been described in Verma *et al*. (1993). The same region of the sky was viewed simultaneously in two FIR bands with near identical fields of view of $1.'6$ per bolometer, thus instantaneously covering an area of $6.'0 \times 3.'4$ in each band. The sky was chopped along the cross-elevation axis at 10Hz with a throw of $4.'2$. Full details of the 100cm telescope system and the observational procedure can be found in Ghosh *et al*. (1988). These sources were observed in two different balloon flights with slightly different FIR passbands of the photometer. The journal of observations and other details are presented in Table 1. The spectral responses of the two bands, relative responses of the detectors, absolute calibration of the photometer and other details specific to these two flights in 1993 and 1995 have been presented in Ghosh *et al*. (2000) and Mookerjea *et al*. (1999) respectively.

Table 1. The journal and other observational details.

Flight date	FIR target	$\lambda_{\rm eff}$ Ch-I (μm)	$\lambda_{\rm eff}$ Ch-II (μm)	Planet used	Planet FWHM Ch-I	Planet FWHM Ch-II
18th Nov 1993	W3(OH)	148	209	Jupiter	$1.'0 \times 1.'4$	$1.'0 \times 1.'3$
12th Nov 1995	S209 S187	138	205	Saturn	$1.'6 \times 1.'9$	$1.'6 \times 1.'8$

The observed chopped signals have been deconvolved using an indigenously developed procedure based on the Maximum Entropy Method (MEM) similar to that of Gull & Daniell (1978) (see Ghosh *et al*. 1988, for details). The accuracy of the absolute aspect of the telescope was improved by using a focal plane optical photometer which detects stars (in an offset field) while the telescope scans the FIR target source. The achieved absolute positional accuracy is $\sim 0.'5$.

2.2 *IRAS Data*

The data from the IRAS survey in the four bands (12, 25, 60 and 100 μm) for the regions around the three target sources were HIRES processed (Aumann *et al*. 1990) at the Infrared Processing and Analysis Center (IPAC[1], Caltech). These maps have been used for extracting sources and quantifying interband positional associations and flux densities.

[1]IPAC is funded by NASA as part of the IRAS extended mission program under contract to JPL.

3. Results

3.1 *Intensity maps*

The MEM deconvolved TIFR maps at 148 and 209μm and the HIRES processed IRAS maps at 12, 25, 60 and 100 μm for the Galactic star forming region W3(OH) has been presented in Figs 1 and 2 respectively. Similarly, the intensity maps for S209 at 138, 205μm and the IRAS bands have been presented in a similar format in Figs 3 and 4. Due to limited dynamic range achieved in the 138μm band for S187, the intensity maps for this source are shown only at 205μm and the IRAS bands (Figs 5 and 6).

Whereas the IRAS maps have very high dynamic ranges ($>$1000), the same for the TIFR maps is restricted to $\sim$300 under the best circumstances. The contour levels displayed in TIFR maps for each programme source depend on the detector noise condition (which varied from time to time) at the time of the corresponding observations.

The angular resolution achieved in the TIFR bands is approximately represented by the deconvolved sizes of the point-like (planet) source in respective bands (see Table 1). All three programme sources, W3(OH), S209 and S187 show extended emission in both the TIFR bands.

The angular resolutions in the HIRES processed maps for each region are listed in Table 2, which depend on the observational details like relative orientation of scan tracks of the telescope boresight among different HCONs (Aumann, Fowler & Melnyk 1990). Although extensions are seen in many IRAS bands, the TIFR maps show superior angular resolution as a result of their smaller and circular beam.

Discrete sources have been extracted from the TIFR and HIRES maps using a procedure described in Ghosh *et al*. (2000). The longest wavelength channel (TIFR Ch-II) map has been used as the primary band. The sources detected in this are associated with sources in other bands if they satisfy the positional match criterion ($< 1'$ separation with TIFR Ch-I and $< 1.'5$ for HIRES bands). A total of nine sources in all three regions have been detected, details of which are listed in Table 3. Six of these have been detected in both the TIFR bands. All these nine sources have an association with

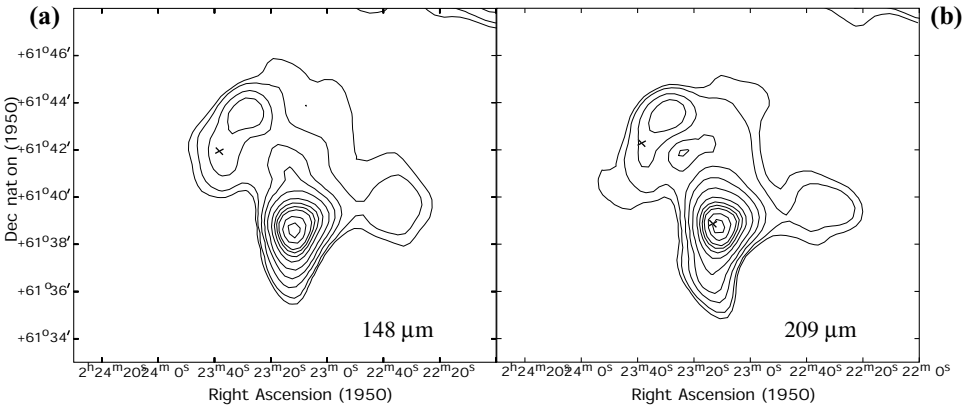

Figure 1. The intensity maps for the region around W3(OH) in TIFR bands :– **(a)** at 148 μm with peak = 3059 Jy/sq. arcmin, **(b)** at 209 μm with peak = 2101 Jy/sq. arcmin. The isophot contour levels in both (a) and (b) are 90, 70, 50, 40, 30, 20, 10, 5, 2.5, 1 & .5 % of the respective peaks. The crosses denote the positions of the IRAS PSC sources 02232 + 6138 (main source) & 02236 + 6142.

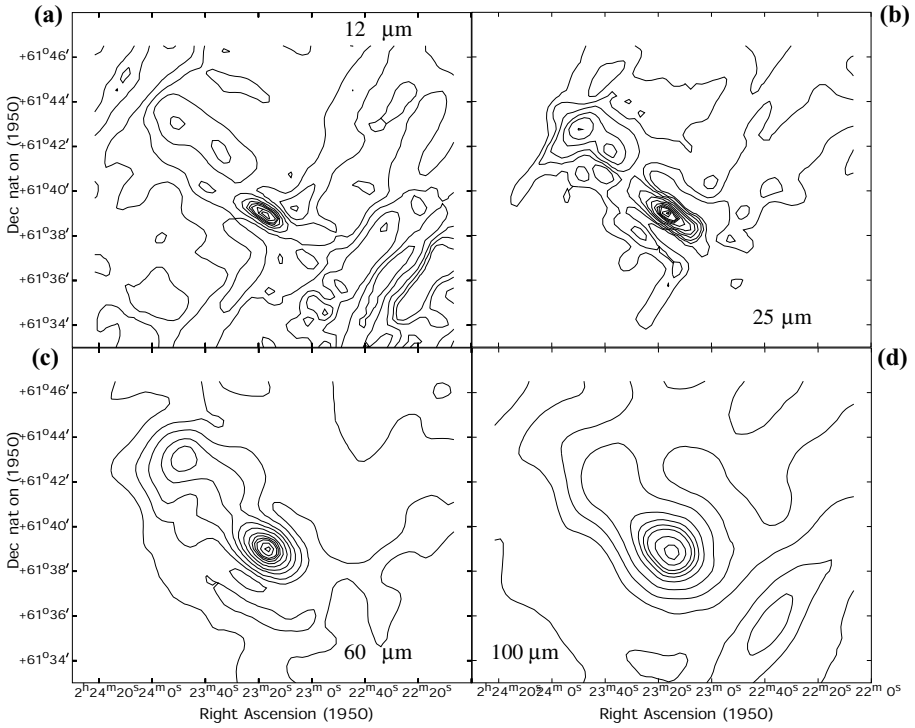

Figure 2. The HIRES processed IRAS maps for a similar region around W3(OH), as shown in Fig. 1, in the four bands :- **(a)** at 12 μm with peak = 66.9 Jy/sq. arcmin, **(b)** at 25 μm with peak = 1420 Jy/sq. arcmin, **(c)** at 60 μm with peak = 9870 Jy/sq. arcmin, **(d)** at 100 μm with peak = 3140 Jy/sq. arcmin. The isophot contour levels in (a) (b) & (c) are 90, 70, 50, 40, 30, 20, 10, 5, 2.5, 1, .5, & .25 % of the respective peaks. In (d), only the higher 11 of these contours have been displayed.

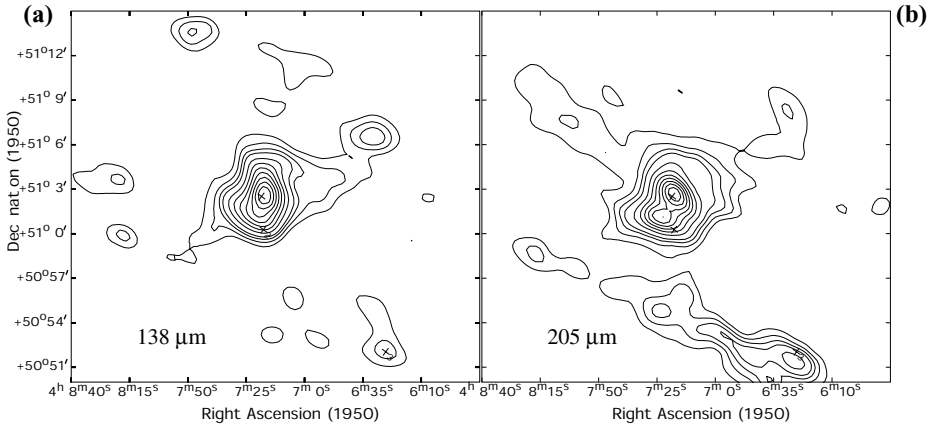

Figure 3. The intensity maps for the region around S209 in TIFR bands: **(a)** at 138 μm with peak = 441 Jy/sq. arcmin, **(b)** at 205 μm with peak = 213 Jy/sq. arcmin. The isophot contour levels in both (a) and (b) are 90, 80, 70, 60, 50, 40, 30, 20, 15, 10, & 5 % of the respective peaks. The crosses denote the positions of the IRAS PSC sources $04073+5102$ (amin source), $04072+5100$ (the nearby source which is resolved in 205 μm map) and $04064+5052$.

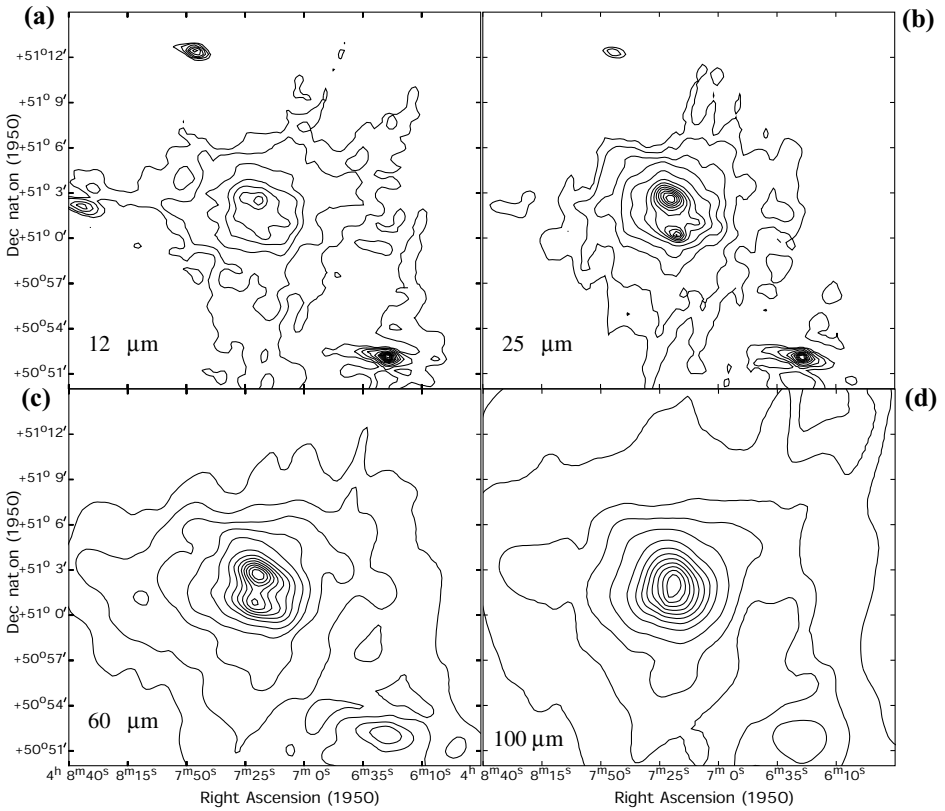

Figure 4. The HIRES processed IRAS maps for a similar region around S209, as shown in Fig. 3, in the four bands :- **(a)** at 12 μm with peak = 374 Jy/sq. arcmin, **(b)** at 25 μm with peak = 5470 Jy/sq. arcmin. **(c)** at 60 μm with peak = 12300 Jy/sq. arcmin. **(d)** at 100 μm with peak = 5830 Jy/sq. arcmin. The isophot contour levels in (a) are 30, 20, 10, 5, 2.5, 1 & .5 % of the peak, and in all the other three bands are 90, 80, 70, 60, 50 ,40, 30, 20, 10, 5, 2.5, 1 & .5 % of the respective peaks.

HIRES source in at least one band (8 have associations in 2 or more IRAS bands). The listed flux densities have been obtained by integrating over a circle of 3′ diameter. Six of these also appear in the IRAS Point Source Catalog (hereafter PSC). The PSC flux densities are also listed for comparison with those obtained from the HIRES maps. Four of these six PSC sources have upper limits in at least one IRAS band. This reflects the complexity of the morphology of these regions. The dust temperatures in the FIR, T_{FIR}, have been computed from the flux densities in the TIFR bands, assuming an emissivity law of $\epsilon_\lambda \propto \lambda^{-2}$. These are also listed in Table 3.

3.1.1 *W3(OH)*

Strong emission is seen in both 148 and 209 μm bands from W3(OH) and the peak position (S2) matches with that of the IRAS PSC source 02232 + 6138 (Fig. 1). The corresponding source is also the strongest in all the four HIRES maps (Fig. 2). Whereas in TIFR bands S2 is resolved, it is pointlike in the IRAS bands. There are two other sources detected in both the TIFR maps. The second brightest source (S3)

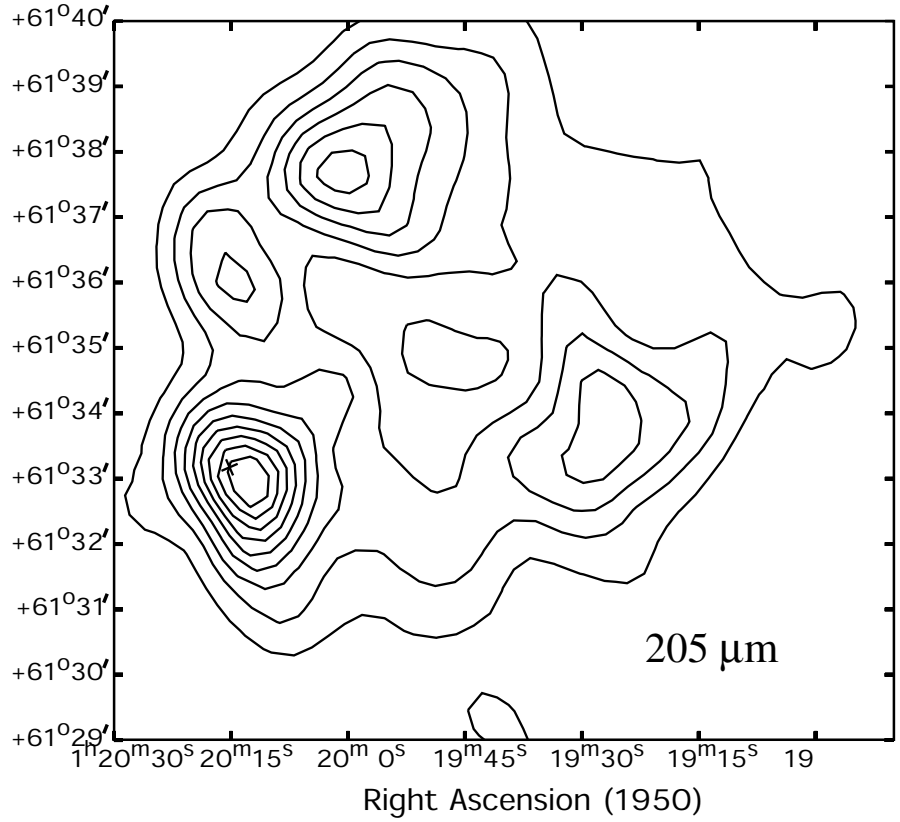

Figure 5. The intensity map for the region around S187 in TIFR band at 205 μm. The isophot contour levels are 90, 80, 70, 60, 50, 40, 30, 20 & 10 % of the peak intensity (388 Jy/sq. arcmin). The cross denotes the position of the IRAS PSC source 01202 + 6133 (main source).

has counterparts in 12, 25 and 60 μm maps and a clear extension in 100 μm map. The diffuse emission has been detected in all the six bands.

The extension of the isophot contours towards NE of W3(OH) in the TIFR bands, match remarkably well with the plume ($\sim$ 2pc $\times$ 1.3pc) seen in the recent mapping in NH_3 line by Tieftrunk *et al.* (1998). In fact they concluded that the W3(OH) core is much larger than thought earlier.

Combining TIFR data along with the sub-millimeter measurement of Chini *et al.* (1986), the dust emissivity index is found to be 1.8 between 200 and 350 μm.

The total emission from a circular region of 16′ diameter around the strong peak W3(OH), are 9601 and 6305 Jy at 148 and 209 μm respectively. The fraction of this in diffuse emission has been estimated to be 15% and 13% respectively by subtracting the contributions from the detected discrete sources (Table 3). A similar analysis of the IRAS-HIRES maps of the same region has quantified the diffuse emission to be 85, 55, 56 and 71% at 12, 25, 60 and 100 μm respectively. It may be noted that since the mapping in TIFR bands are carried out in sky chopped mode (in contrast to the IRAS bands), some part of the diffuse emission with low spatial gradient could have been missed in these bands. The total infrared luminosity estimated from the entire region is 1.91×10^5 $L_\odot$.

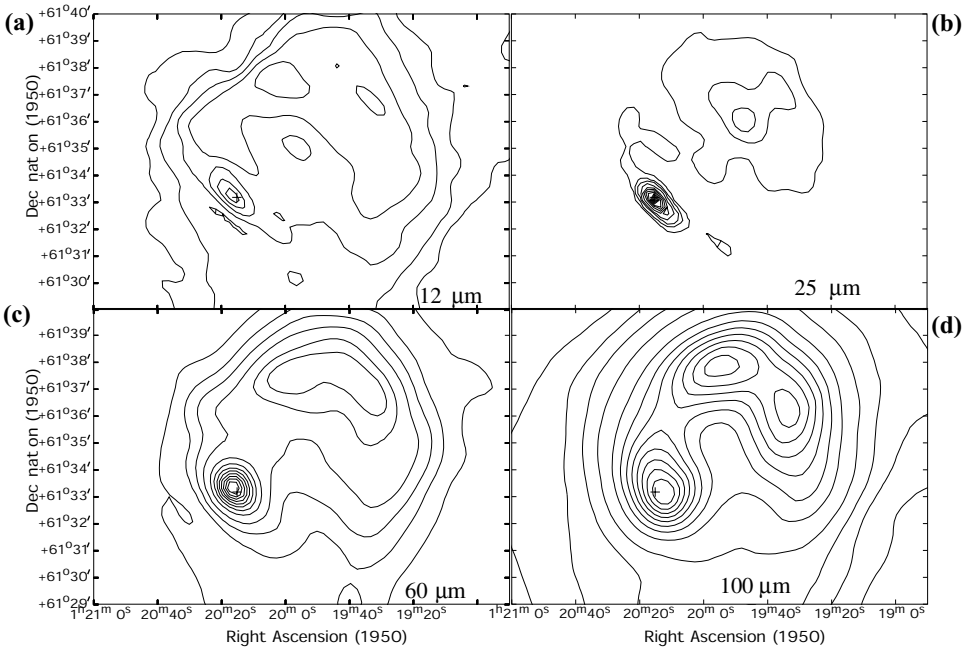

Figure 6. The HIRES processed IRAS maps for a similar region around S187, as shown in Fig. 5, in the four bands :– **(a)** at 12 μm with peak = 48.8 Jy/sq. arcmin, **(b)** at 25 μm with peak = 557 Jy/sq. arcmin, **(c)** at 60 μm with peak = 754 Jy/sq. arcmin, **(d)** at 100 μm with peak = 460 Jy/sq. arcmin. The isophot contour levels in (a) are 30, 20, 10, 5, 2.5 & 1% of the peak (the peak is outside the region displayed here) and in (b), (c) & (d) are 90, 80, 70, 60, 50, 40, 30, 20, 10, 5, 2.5, & 1% of the respective peaks.

Table 2. Angular resolutions in the HIRES maps.

Source region	Resolution at 12 μm FWHM	Resolution at 25 μm FWHM	Resolution at 60 μm FWHM	Resolution at 100 μm FWHM
W3(OH)	$74'' \times 29''$	$66'' \times 31''$	$114'' \times 57''$	$74'' \times 29''$
S209	$56'' \times 27''$	$54'' \times 28''$	$91'' \times 54''$	$110'' \times 64''$
S187	$39'' \times 27''$	$41'' \times 28''$	$76'' \times 46''$	$113'' \times 97''$

3.1.2 *S209*

There is a good correlation and structural similarity between the extended emission from the dust component in all the six bands. The complex emission structure has restricted the reliable source extraction for the IRAS Point Source Catalog as evident from inconsistent flux densities in different bands for the main source corresponding to S209, IRAS 04073 + 5102. However, numerical aperture photometry on HIRES processed IRAS maps provide reliable estimates of flux densities.

The main source in the S209 region is clearly resolved into two sources (S5 & S6) at 205 μm map and there is indication for the same in the 138 μm map (Fig. 3).

Table 3. Position and flux density details of the detected sources.

#	RA (1950) h m s	Dec (1950) ^{o} $'$ $''$	IRAS PSC associations	Flux Density (Jy) TIFR 209 / 205 μm	TIFR 148 / 138 μm	IRAS[a] 100 μm	IRAS[a] 60 μm	IRAS[a] 25 μm	IRAS[a] 12 μm	T^b_{FIR} (K)
	W3(OH)	**Region**								
S1	2 22 28.3	+61 39 32	...	128	260	–	–	35	30	30
S2	2 23 11.3	+61 38 54	02232+6138	4872	7198	10030	9488	683	66	22
	"	"	"			10600[c]	9269[c]	535[c]	40.6[c]	
S3	2 23 29.0	+61 43 34	02236+6142	476	744	1886	901	67	36	23
	"	"	"			<10600[c]	<1712[c]	<91[c]	12.3[c]	
	S209	**Region**								
S4	4 06 26.7	+50 51 18	04064+5052	323	224	190	149	48	30	15
	"	"	"			171.2[c]	83.4[c]	43.3[c]	25.4[c]	
S5	4 07 17.4	+51 02 45	04073+5102	970	2139	2298	2159	409	70	31
	"	"	"			2723[c]	<0.4[c]	97[c]	16[c]	
S6	4 07 22.6	+51 01 07	04072+5100	873	–	–	1905	236	38	–
	"	"	"			<2700[c]	<439[c]	41[c]	2.4[c]	
	S187	**Region**								
S7	1 19 25.7	+61 34 02	...	885	1770	–	829	–	41	28
S8	1 20 01.3	+61 37 45	...	1094	–	2005	1310	–	52	–
S9	1 20 13.6	+61 32 52	01202+6133	1304	–	1908	1400	211	32	–
	"	"	"			<1700[c]	882[c]	182[c]	10.4[c]	

[a] From HIRES processed maps unless specified otherwise. The flux densities are integrated over a circle of 3.′0 diameter.
[b] Determined using the flux densities in TIFR bands and assuming a gray body spectrum with emissivity $\epsilon_\lambda \propto \lambda^{-2}$.
[c] From IRAS Point Source Catalog.

The strongest peaks in both the TIFR bands (S5) coincide with the position of IRAS 04073 + 5102. The neighbouring source S6 is associated with IRAS 04072 + 5100. In 25 and 60 μm IRAS bands, S6 is clearly seen and an indication is present in the 12 μm map (Fig. 4). The 100 μm HIRES processed map does not resolve S5/S6.

Chini *et al*. (1984) have detected S209 in 1-mm continuum and presented the thermal emission from the dust after correcting for the expected free free emission from the hot gas. Using the flux densities at 205 μm and 1-mm, a very flat dust emissivity exponent of 0.64 has been found for this sub-mm region. In case the emission at 1-mm originates from a different colder dust component, then the above index is an underestimate.

The total emission from the S209 region presented in Fig. 3 is 5548 and 4000 Jy at 138 and 205 μm respectively. The fraction of this in diffuse emission has been estimated to be 57% and 46% respectively by subtracting the contributions from the detected discrete sources. A similar analysis of the IRAS-HIRES maps of the same region (Fig. 4) has quantified the diffuse emission to be 52, 44, 49 and 77% at 12, 25, 60 and 100 μm respectively. Hence right through the mid and far infrared region, a good part of the emission is in diffuse form. The total infrared luminosity estimated from the entire region is 2.0×10^6 $L_\odot$ (for distance = 12 kpc).

Balser *et al*. (1995) have modelled their 8.7 GHz radio continuum measurements of the S209 region ($8'\times8'$) and they conclude that the exciting source is either a ZAMS O6.5 star or a O5 star depending on the data used (VLA / MPIR). These stellar types correspond to a luminosity of 1.5 x 10^5 $L_\odot$ or 6.8 x 10^5 $L_\odot$ respectively (Thompson 1984).

3.1.3 *S187*

The dynamic range of the TIFR maps of S187 region is rather limited due to larger than usual noise in the bolometer channels during these observations (only the 205 μm map presented here). The strongest source (S9) associated with IRAS 01202 + 6133 is resolved at 205 μm (Fig. 5). The morphology of the diffuse emission in the TIFR band resembles the same in the HIRES maps (Fig. 6). This is despite the fact that TIFR observations used sky chopping whereas IRAS survey did not. The emissions in all the five bands are dominated by the source associated with IRAS 01202 + 6133. Most of the additional emission originates from an annular ring like structure of diameter $\sim 10'$. The ionized gas resides at the central cavity of the annular region as inferred from high resolution radio continuum map at 1.4 GHz (Snell & Bally 1986). The position of the high velocity molecular outflow lies about $2'$ west of S9. The H_2O maser source detected by Henkel, Haschick & Gusten (1986) is positionally very close to the outflow source. No local enhancement has been observed in any of the TIFR or HIRES bands at the location of the H_2O maser/outflow source. The position of the NH_3 core detected in the S187 region (Jijina, Myers & Adams 1999), also does not show positional match with any peak in the maps of dust continuum emission.

The total emission from the S187 region presented in Fig. 5 is 7256 Jy at 205μm. The fraction of this in diffuse emission has been estimated to be 55% by subtracting the contributions from the detected discrete sources. A similar analysis of the IRAS-HIRES maps of the same region (Fig. 6) has quantified the diffuse emission to be 66, 68, 53 and 69% at 12, 25, 60 and 100 μm respectively. For this source too, right through the mid and far infrared region, a large part of the emission is in diffuse form, which is

quite expected considering the complex morphology of the region. The total infrared luminosty estimated from the entire region is $1.7\times10^4\ L_\odot$ (for distance = 1 kpc).

Using the mass of the molecular cloud associated with S187, as estimated by Yonekura *et al*. (1997) from their ^{13}CO survey (their cloud # 164), we determine the average luminosity per unit mass to be $\sim$2.2 $L_\odot/M_\odot$. This value is very similar to that found for W 31 star forming complex (Ghosh *et al*. 1989).

3.2 *Distribution of dust temperature and optical depth*

Taking advantage of the nearly identical circular beams of the TIFR bands and the simultaneity of observations, reliable maps of dust temperature and optical depth (at 200 μm, τ_{200}) have been generated for W3(OH) and S209 regions. The available dynamic ranges in both the TIFR bands for these two sources allow us to meaningfully determine the dust temperature and optical depth distributions. These are presented in Figs. 7 and 8 respectively. A dust emissivity law of $\epsilon_\lambda \propto \lambda^{-2}$ has been assumed for this purpose. Details of the procedure can be found in Ghosh *et al*. (2000).

For W3(OH) region, the distribution of τ_{200} shows a peak near the intensity peak but the T(148/209) distribution shows a plateau there (Fig. 7). Some regions of higher dust temperature are also seen. The second peak in the optical depth map clearly corresponds to the matter distribution around 02236 + 6142. The dust temperature at the position of IRAS 02232 + 6138 is 21K, whereas the kinetic temperature of the NH_3 component has been found to be 27K (Tieftrunk *et al*. 1998). In addition, the shape of the τ_{200} distribution around IRAS 02232 + 6138 (within 2′) resembles the gas distribution traced by NH_3. A detailed comparison should help understanding the gas-dust coupling in denser regions of star formation, like the interstellar environment around W3(OH).

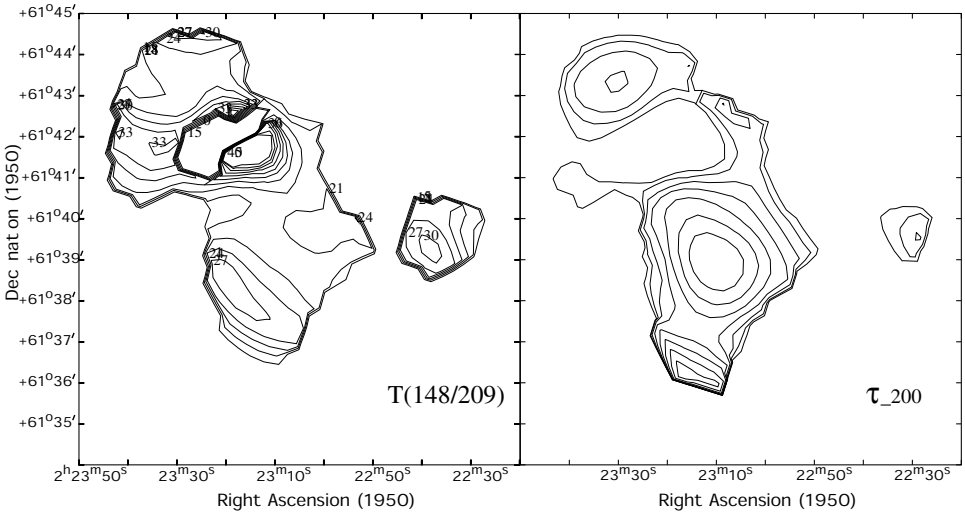

Figure 7. The distribution of dust temperature T(148/209), and optical depth at 200 μm, τ_{200}, for the region around W3(OH) assuming a dust emissivity law of $\epsilon_\lambda \propto \lambda^{-2}$. The isotherms correspond to 15K to 36K in steps of 3K, 40 & 45K. Temperature values are displayed near the contours. The highest contour of τ_{200} (innermost at the bottom) corresponds to a value of 0.16 and the successive contours represent values reducing by factor of 2.

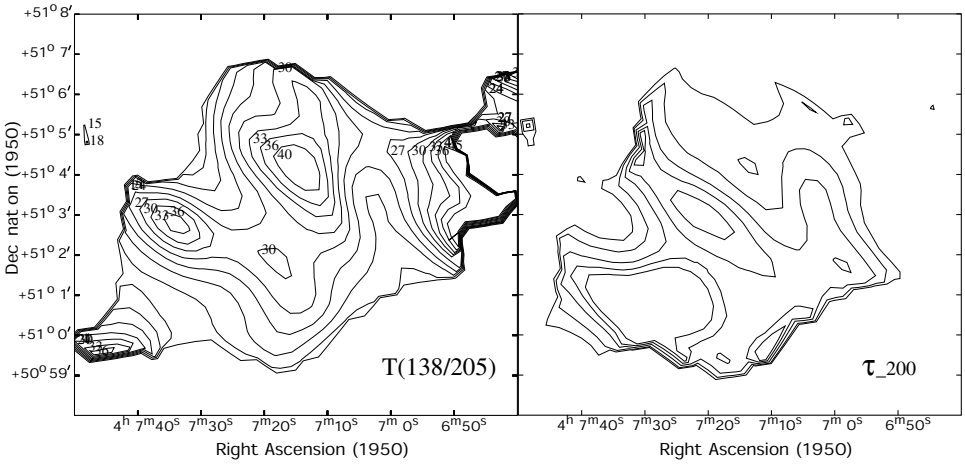

Figure 8. The distribution of dust temperature T(138/205), and optical depth at 200μm, τ_{200}, for the region around S209 assuming a dust emissivity law of $\epsilon_\lambda \propto \lambda^{-2}$. The isotherms refer to the same temperatures as in Fig. 7. The τ_{200} contours represent 100, 75, 50, 25 & 12.5 % of the peak value of 0.67.

The T(138/205) and τ_{200} distributions for S209 show an almost anticorrelation (Fig. 8). The hotspots are located near the two resolved sources in the 205 μm map. Most of the region in S209 has the dust temeparture higher than 27 K and the presence of colder dust is limited to the outermost periphery. This is in contrast to W3(OH) region where the dust is relatively cooler.

Acknowledgements

We thank S. L. D'Costa, M. V. Naik, S. V. Gollapudi, D. M. Patkar, M. B. Naik and G. S. Meshram for their support for the experiment. The members of TIFR Balloon Facility (Balloon group and Control & Instrumentation group), Hyderabad, are thanked for their roles in conducting the balloon flights. IPAC is thanked for providing HIRES processed IRAS data. SKG thanks the Institute of Space and Astronautical Science (ISAS), Japan, for their hospitality, where part of the work was done.

References

Aumann, H. H., Fowler, J. W., Melnyk, M. 1990, *Astr. J.* **99**, 1674.
Bally, J., Lada, C. J. 1983, *Astrophys. J* **265**, 824.
Balser, D. S., Bania, T. M., Rood, R. T., Wilson, T. L. 1995, *Astrophys. J. Suppl.* **100**, 371.
Blair, G. N., Peters, W. L., van den Bout, P. A. 1975, *Astrophys. J.* **200**, L161.
Blitz, L., Fich, M., Stark, A. A. 1982, *Astrophys. J. Suppl.* **49**, 183.
Campbell, M. F., Lester, D. F., Harvey, P. M., Joy, M. 1989, *Astrophys. J.* **345**, 298.
Casoli, F., Combes, F., Gerin, M. 1984a, *Astr. Astrophys.* **133**, 99.
Casoli, F., Combes, F., Gerin, M. 1984b, *Nearby molecular clouds*, G. Serra (ed.), Lecture Notes in Physics no. 237, p. 136, (Berlin-Heidelberg: Springer-Verlag).
Cesaroni, R. *et al*. 1988, *Astr. Astrophys. Suppl.* **76**, 445.
Chini, R., Krugel, E., Kreysa, E. 1986, *Astr. Astrophys.* **167**, 315.
Chini, R., Mezger, P. G., Kreysa, E., Gemund, H. P. 1984, *Astr. Astrophys.* **135**, L14.

Dreher, J. W, Welch, W. J. 1981, *Astrophys. J.* **245**, 857.
Fich, M. 1993, *Astrophys. J. Suppl.* **86**, 475.
Fich, M., Blitz, L. 1984, *Astrophys. J.* **279**, 125.
Ghosh, S. K., Iyengar, K. V. K, Rengarajan, T. N., Tandon, S. N., Verma, R. P., Daniel, R. R. 1988, *Astrophys. J.* **330**, 928.
Ghosh, S. K., Iyengar, K. V. K, Rengarajan, T. N., Tandon, S. N., Verma, R. P., Daniel, R. R., Ho P. T. P. 1989, *Astrophys. J.* **347**, 338.
Ghosh, S. K., Mookerjea, B., Rengarajan, T. N., Tandon, S. N., Verma, R. P. 2000, *Astr. Astrophys.* **363**, 744.
Gull, S. F., Daniell, G. J. 1978, *Nature* **272**, 686.
Henkel, C., Haschick, A. D., Gusten, R., 1986, *Astr. Astrophys.* **165**, 197.
Jijina, J., Myers, P. C., Adams, F. C. 1999, *Astrophys. J. Suppl.* **125**, 161.
Mookerjea, B., Ghosh, S. K., Karnik, A. D., Rengarajan, T. N., Tandon, S. N., Verma R. P. 1999, *Astrophys. J.* **522**, 285.
Mookerjea, B., Ghosh, S. K., Rengarajan, T. N., Tandon, S. N., Verma, R. P. 2000, *Astr. J.* **120**, 1954.
Sharpless, S. 1959, *Astrophys. J. Suppl.* **4**, 257.
Snell, R. L., Bally, J. 1986, *Astrophys. J.* **303**, 683.
Thompson, R. I. 1984, *Astrophys. J.* **283**, 165.
Tieftrunk, A. R., Megeath, S. T., Wilson, T. L., Rayner, J. T. 1998, *Astr. Astrophys.* **336**, 991.
Verma, R. P., Rengarajan, T. N., Ghosh, S. K. 1993, *Bull. Astron. Soc. India* **21**, 489.
Wink, J. E., *et al* 1994, *Astr. Astrophys.* **281**, 505.
Wouterloot. J. G. A., Brand, J., Henkel, C. 1988, *Astr. Astrophys.* **191**, 323.
Yonekura, Y., Dobashi, K., Mizuno, A., Ogawa, H., Fukui, Y. 1997, *Astrophys. J. Suppl.* **110**, 21.
Zavagno, A., Deharveng, L., Caplan, J. 1994, *Astr. Astrophys.* **281**, 491.

J. Astrophys. Astr. (2001) **22,** 187–211

Spectroscopic Binaries near the North Galactic Pole Paper 24: HD 106104, 109281, 109463 and 110743

R. F. Griffin, *The Observatories, Madingley Road, Cambridge CB3 0HA, England*

Received 2000 October 16; accepted 2001 February 15

Abstract. The four stars treated in this paper have been under observation with photoelectric radial-velocity spectrometers for many years. They have proved to be binaries with periods of 30, 1828, 1514 and 822 days respectively; the orbits are of modest eccentricity apart from that of HD 110743 which is indistinguishable from a circle. The mass functions are small, and no companion has been observed for any of the stars. HD 110743, a K dwarf, is much the nearest of the four, and its orbit is of short enough period for the photocentric motion to have been recognized by *Hipparcos*. An eleventh-magnitude star rather more than 1′ away from HD 106104 is shown to be a genuine physical companion, with practically identical radial velocity, proper motion and distance modulus, although the projected separation is about 13,000 AU.

Key words. Radial velocities—spectroscopic binaries—orbits—stars, individual—HD 106104—HD 109281—HD 109463—HD 110743.

1. Introduction

A fairly recent publication (Yoss & Griffin 1997) in this *Journal* described a comprehensive photometric and radial-velocity survey of the late-type stars that are in the North Galactic Cap ($b > 75^\circ$) and feature in the *Henry Draper Catalogue*. It was noted in that survey that no fewer than 125 of the 903 stars that were measured had been identified as spectroscopic binaries. The present author, in some cases with collaborators, had already published orbits for 33 of them and has subsequently provided one more (Griffin 2000), and three have been published by others. (One of those three (Jasniewicz, Duquennoy & Acker 1987) has since been implicitly withdrawn.) There remains, therefore, a formidable collection of the best part of a hundred loose ends needing to be tied up. The present paper represents a modest start upon that task, which is not made any easier by the fact that all of the stars reside within the same small area of sky and so in a sense compete for the same observing time. Many of them also have long periods, so the work could not be hurried beyond a certain point, no matter how much observing time might be available.

The four stars treated in this paper do not share any particular property apart from inclusion in the Galactic-Pole survey: they have been selected for publication because they are among the best observed of the binaries whose orbits remain to be determined. HD 106104, 109281 and 109463 are all in the constellation Coma Berenices, while

HD 110743 is at a higher declination and is in the south-western part of Canes Venatici. HD 109463 is sufficiently close to the Coma Cluster to have received a Trumpler (1938) designation, no. 189. It is also the brightest ($7^{m}.7$) and latest (K5) of the stars and gives very fine radial-velocity traces. At the other extreme, HD 106104 is remarkably faint ($10^{m}.3$) for an HD star; probably for that reason its HD number is overlooked in a catalogue (Hill 1982) specifically compiled to give cross-identifications of A- and F-type stars in the North-Galactic-Pole region, as well as in a photometric catalogue by Knude (1993). HD 106104 is also particularly early ($\sim$ F8) in type – much earlier than the ostensible limit of G5 imposed in the selection of late types from the *Henry Draper Catalogue* – and consequently is more troublesome to to observe. The other two stars are of intermediate character.

Table 1 recapitulates salient data from the survey paper (Yoss & Griffin 1997) about the four stars. It includes a fifth star, a visual companion (albeit a distant one, about $76''$ away in position angle 114°) to HD 106104; the object was included in the Galactic-Pole survey (Yoss & Griffin 1997) purely out of inquisitiveness because of its proximity to a star that was validly selected for the programme. The 'mk' spectral types in Table 1 were inferred from DDO-type photometry (McClure 1976, and see the survey paper cited above) and are not actual spectral classifications although they form a good substitute. Equally, the values for M_V, the implied z distances (which are for practical purposes equal to the line-of-sight distances to the stars, in view of the very high Galactic latitudes), and [Fe/H] are all derived from the DDO photometry.

Table 1. Properties of the stars discussed (Yoss & Griffin 1997).

HD	V m	B–V m	Type HD	Type 'mk'	M_V m	z pc	[Fe/H]
106104	10.34	0.53	G5	F9 V	+4.2	164	—
109281	8.68	1.01	K0	K0 III	+1.4	285	+0.02
109463	7.69	1.41	K2	K5 III–IV	+1.6	165	−0.02
110743	8.76	0.83	K0	K1 V	+6.1	34	+0.04
106104 B	11.27	0.62	—	G3 V	+4.9	182	—

Some additional photoelectric photometry in the V and B bands (but none in U) is available for the stars and is listed in Table 2; published spectral types are given in Table 3. There is a difference of opinion regarding the type of HD 110743, but it is readily resolved: the giant type proposed by Upgren (1962) was obviously wrong from the outset, because it implied a distance at which the star's large proper motion of about $0''.38$ per annum, which has been known since the nineteenth century (Porter 1895), would correspond to an unacceptable transverse velocity in the range 500–1000 km s^{-1}.

Rather surprisingly in view of the faintness of HD 106104 in particular, all four stars feature in the *Hipparcos* (1997) catalogue; their parallaxes and the corresponding distances, distance moduli and absolute magnitudes are set out in Table 4. The uncertainties of small parallaxes are reflected very asymmetrically in the derived distance estimates, so distances corresponding to $\pi \pm \sigma$ are given in brackets after the central

Table 2. Additional photoelectric magnitudes.

Star	V m	B−V m	Reference
HD 106104	10.352	—	Knude (1993)
	10.34	0.56:	Hipparcos (1997)
HD 109281	8.67	1.03	Ljunggren (1965)
	8.67	1.03	Hartkopf & Yoss (1982)
	8.71	—	Hansen & Radford (1983)
	8.68	—	Hipparcos (1997)
HD 109463	7.70	1.39	Häggkvist & Oja (1973)
	7.81	—	Hartkopf & Yoss (1982)
	7.69	—	Hipparcos (1997)
HD 110743	8.79	0.83	Ljunggren (1965)

Table 3. Additional spectral types.

Star	Type	Reference
HD 106104	g:F8	Schwassmann & van Rhijn (1951)
	F8	Hill (1982)
HD 109281	gG8	Malmquist (1960)
	K0 III	Upgren (1962)
	G9 II–III*	Hartkopf & Yoss (1982)
HD 109463	K5 III–IV*	Yoss (1977)
	K5 III–IV*	Hartkopf & Yoss (1982)
HD 110743	dK0	Malmquist (1960)
	G8 III	Upgren (1962)
	K1	Bidelman (1985) [*vice* Kuiper]

*From DDO photometry, not spectra

Table 4. *Hipparcos* parallaxes and derived distances and absolute magnitudes

Star	Parallax ms of arc	Distance pc	Dist. modulus m	M_V m
HD 106104	5.82 ± 1.73	172 (132–245)	6.17 ± 0.7	$+4.2 \pm 0.7$
HD 109281	0.44 ± 1.14	(> 630)	>9.0	<-0.3
HD 109463	2.58 ± 0.97	390 (290–620)	7.94 ± 0.9	-0.2 ± 0.9
HD 110743	22.90 ± 1.65	44 (41–47)	3.20 ± 0.16	$+5.59 \pm 0.16$

values; the asymmetries of the distance moduli are less serious and are glossed over in a representative uncertainty value.

2. Radial velocities

The first photoelectric radial-velocity measurements of the three brighter stars were made nearly (in one case more than) thirty years ago; HD 106104 was not observed until 1982. Because the stars were part of a large survey programme and the initial purpose was to obtain just two observations of each object, there was a deliberate delay in obtaining a second observation, and several years elapsed before velocity variability was established and the objects transferred to the spectroscopic-binary programme for systematic surveillance. Thus systematic observation has lasted only for intervals ranging from 12 to 22 years, but as even the longest orbital period is 5 years all the stars have been seen round several cycles and their orbits are very well established. The longest period belongs to HD 109281 and is so precisely an integral number of years (1828 $\pm$ 3 days, while 5 years is 1826 $\frac{1}{4}$ days) that the observing seasons correspond to exactly the same set of orbital phases cycle after cycle, causing the data to be unavoidably bunched in phase; the damage to the orbit determination is, however, more cosmetic than real, unlike the situation that can arise with periods that are very close to 1 or 2 years.

Radial-velocity spectrometers that have contributed measurements for this paper include the original instrument at Cambridge (Griffin 1967), the one made by Dr. J. E. Gunn and the writer for the Hale 200-inch telescope (Griffin & Gunn 1974), the Geneva Observatory's *Coravel*s (Baranne *et al.* 1979) at Haute-Provence and ESO, the instrument (Fletcher *et al.* 1982) at the Dominion Astrophysical Observatory's 48-inch coudé reflector at Victoria, and most recently a *Coravel*-like instrument at Cambridge. The numbers of observations made with the respective instruments are noted in Table 5.

Table 5. Usage of the various photoelectric radial-velocity spectrometers.

Spectrometer	HD: 106104	106104 B	109281	109463	110743	Totals
Cambridge (old)	2	—	55	28	47	132
Palomar	—	—	2	1	1	4
Haute-Provence	50	11	28	32	27	148
ESO	3	—	2	2	2	9
DAO	4	—	4	2	7	17
Cambridge (new)	5	2	11	11	8	37
Totals	64	13	102	76	92	347

Very few radial velocities have been published previously for any of the four stars. For HD 106104 there is none. HD 109281 was observed three times with the Kottamia 74-inch telescope by Woolley *et al.* (1981), who used a prismatic Cassegrain spectrograph which gave a reciprocal dispersion of 66 Å mm^{-1} at Hγ; Sandage & Fouts (1987) listed one velocity (+71.6 km s^{-1}), measured with a reticon detector at the Mount Wilson 100-inch coudé spectrograph, but they gave no date so it is not possible to include their observation in the discussion here. Heard (1956) reported a mean of four radial velocities obtained for HD 109463

with the David Dunlap 74-inch reflector at 66 Å mm^{-1}, but the observations were not given individually and did not suggest to Heard that the velocity was variable. Two measurements (only two days apart) were obtained of the star by Chériguene (1971), who used the coudé spectrograph of the Haute-Provence 193-cm telescope at a reciprocal dispersion of 25 Å mm^{-1}. Finally, HD 110743 is the subject of one observation published by Yoss, Neese & Hartkopf (1987), who noted that it was obtained with 'IRS', which they described by way of explanation as 'KPNO 0.9-m IRS'. All available radial velocities, already published or newly presented here, are listed in Tables 6(a)–(d).

It is a troublesome fact, but one that has to be faced, that radial velocities stemming from different sources are apt to exhibit different zero-points. *Coravel* measurements have been particularly troublesome in that regard, since their zero-point has seemed to possess a dependence on stellar colour (*e.g.* Scarfe, Batten & Fletcher 1990). That has recently been admitted, and a new reduction procedure and zero-point has been adopted (Udry, Mayor & Queloz 1999). The data in the Tables 6 are intended to be on the Cambridge zero-point used in the previous papers in this series; to that end, observations made at Cambridge, Palomar and Victoria have been standardized with respect to the Cambridge reference stars (Griffin 1969) — meaning in this case 41 Com alone, since that star is conveniently at hand in the Galactic-Pole field. All Haute-Provence and ESO *Coravel* observations are stored in a data base in Geneva, whence those needed for this paper were kindly retrieved by Dr. S. Udry. They are on the new zero-point and seem in the case of each star to need an adjustment of $+0.8$ km s^{-1} (which has already been applied to the velocities as given in Tables 6) to make them homogeneous with the other data. That is an agreeable finding, because it has long been considered (Griffin & Herbig 1981) that that is the offset usually needed to bring measurements that are on the 'IAU' zero-point into harmony with those on the Cambridge basis. For that reason, the same offset has been applied to the few published observations that feature in the tables.

The homogeneity of the observations made with the new Cambridge *Coravel* is possibly not above reproach: they agree all right in the case of the two red giants (HD 109281 and 109463), but for the two bluer stars they would agree more comfortably if altered by -0.3 km s^{-1}. Not enough experience has yet been gained with the instrument for there to be any certainty about any colour dependence of the zero-point; for present purposes the empirical correction of -0.3 km s^{-1} has been made to the relevant observations of HD 106104 and 110743, and of the visual companion of HD 106104, but no change has been made to those of HD 109281 or 109463.

3. Orbits

To obtain the best orbits it is necessary not only to coordinate the zero-points of different data sources but also to assign appropriate weights.

Preliminary orbits showed very clearly that *none* of the radial velocities gleaned from the literature stands comparison with those measured with the photoelectric spectrometers, so they have all been rejected from the orbital solutions although they are retained in the Tables 6 and plotted in the orbit diagrams in those cases where they fall within the boundaries of the plots.

It has been found in many previous analyses, as it has in this one, that radial velocities measured with the original spectrometer in Cambridge, upon which the photoelectric

Table 6a. Radial-velocity observations of HD 106104.

Date	MJD	Velocity km s^{-1}	Phase	(O − C) km s^{-1}
1982 Mar. 8.00*	45036.00	+12.8	0.501	−3.4
1984 Apr. 23.90*	45813.90	+18.9	26.488	+3.2
1988 Jan. 31.51†	47191.51	+15.7	72.511	−0.8
1989 Mar. 26.03	47611.03	+16.3	86.526	−0.8
May 1.88	647.88	+18.9	87.757	+1.3
1990 Jan. 27.11	47918.11	+14.8	96.785	−1.5
Feb. 12.29‡	934.29	+6.5	97.325	−0.2
14.36‡	936.36	+11.6	.394	+0.5
15.31‡	937.31	+13.2	.426	+0.4
1991 Jan. 28.11	48284.11	−8.7	109.012	−0.3
29.10	285.10	−9.8	.045	+0.4
30.05	286.05	−10.4	.077	+0.1
Feb. 3.17	290.17	−2.2	.214	−0.2
4.09	291.09	+0.2	.245	−0.4
5.09	292.09	+3.7	.278	+0.5
6.08	293.08	+6.0	.311	+0.3
Dec. 17.15	607.15	+14.7	119.804	−0.4
19.16	609.16	+9.5	.871	+0.4
19.21	609.21	+6.7	.872	−2.2
1992 Jan. 14.12	48635.12	+19.1	120.738	+0.8
15.08	636.08	+16.7	.770	−0.4
16.09	637.09	+15.1	.804	0.0
17.12	638.12	+12.7	.838	+0.3
18.12	639.12	+9.2	.872	+0.2
19.17	640.17	+4.9	.907	+0.3
20.15	641.15	+2.0	.939	+1.9
21.15	642.15	−4.3	.973	0.0
Feb. 26.49†	678.49	−3.5	122.187	+0.7
27.40†	679.40	−2.0	.217	−0.3
28.33†	680.33	+0.1	.248	−0.8
Apr. 21.97	733.97	−10.1	124.040	0.0
22.91	734.91	−10.6	.072	0.0
23.90	735.90	−9.6	.105	+0.1
24.92	736.92	−8.2	.139	−0.4
25.93	737.93	−5.9	.173	−0.5
26.95	738.95	−2.3	.207	+0.3
27.91	739.91	−0.9	.239	−1.0
29.89	741.89	+6.7	.305	+1.5

Table 6a. (*Continued*)

Date	MJD	Velocity km s^{-1}	Phase	(O − C) km s^{-1}
1992 Apr. 30.92	48742.92	+8.1	124.339	+0.4
June 27.92	800.92	+3.3	126.277	+0.2
Dec. 18.21	974.21	−10.5	132.066	+0.1
20.18	976.18	−7.4	.132	+0.9
1993 Feb. 12.13	49030.13	+0.6	133.934	−0.2
Mar. 19.04	065.04	−10.2	135.101	−0.3
Dec. 25.21	346.21	+15.5	144.494	−0.4
26.08	347.08	+17.8	.523	+0.8
27.15	348.15	+18.2	.559	+0.2
28.15	349.15	+18.1	.592	−0.7
29.16	350.16	+18.4	.626	−0.9
30.16	351.16	+20.0	.659	+0.6
1994 Jan. 1.24	49353.24	+18.6	144.729	0.0
3.16	355.16	+15.8	.793	0.0
8.13	360.13	−2.9	.959	−0.4
Feb. 21.05	404.05	+12.5	146.426	−0.3
Apr. 29.95	471.95	+20.3	148.694	+1.1
1995 Jan. 4.15	49721.15	−10.0	157.020	−1.0
June 2.95	870.95	−9.5	162.024	−0.2
1996 Apr. 2.98	50175.98	−2.8	172.214	−0.8
1997 Apr. 10.99§	50548.99	+19.6	184.676	+0.2
May 10.89§	578.89	+20.0	185.674	+0.6
1998 May 2.89	50935.89	+18.3	197.601	−0.6
2000 Jan. 9.14§	51552.14	−4.4	218.188	−0.3
Apr. 6.9§	640.96	−5.7	221.155	+1.0
May 30.92§	694.92	−2.0	222.958	+0.4

*Observed with original Cambridge spectrometer; not used in orbital solution.
†Observed with DAO 48-inch telescope.
‡Observed with ESO *Coravel*.
§Observed with Cambridge *Coravel*.
All others observed with Haute-Provence *Coravel*.

Table 6b. Radial-velocity observations of HD 109281.

Date	MJD	Velocity km s^{-1}	Phase	(O − C) km s^{-1}
1967 Mar. 30.88*	39579.88	+76.7	$\overline{1}$.343	−2.8
Apr. 13.82*	593.82	81.4	.350	+1.8
1970 May 11.80*	40717.80	69.8	$\overline{1}$.965	+2.6
1971 Feb. 27.08	41009.08	72.9	0.125	+0.4
1975 May 30.93	42562.93	66.5	0.975	−0.7
1977 Apr. 2.05	43235.05	79.0	1.343	−0.5
27.98	260.98	79.5	.357	−0.2
1978 Mar. 24.08	43591.08	78.0	1.537	−1.2
May 23.26†	651.26	79.6	.570	+0.9
June 18.93	677.93	79.5	.585	+1.1
1979 Jan. 3.25	43876.25	77.4	1.693	+1.8
Feb. 25.15	929.15	74.7	.722	+0.1
Mar. 8.10	940.10	76.7	.728	+2.3
Apr. 29.03	992.03	72.9	.757	−0.5
May 13.97	44006.97	72.3	.765	−0.8
June 22.94	046.94	71.5	.787	−0.7
Dec. 25.22	232.22	67.4	.888	−1.0
1980 Feb. 23.11	44292.11	66.1	1.921	−1.5
May 5.97	364.97	67.5	.961	+0.3
1981 Mar. 1.13	44664.13	72.5	2.125	0.0
Apr. 27.98	721.98	74.4	.156	+0.3
May 24.99	748.99	73.4	.171	−1.3
1982 Jan. 10.19	44979.19	79.0	2.297	+0.2
Mar. 4.06	45032.06	80.1	.326	+0.8
May 7.03	096.03	78.7	.361	−1.0
1983 Feb. 4.53‡	45369.53	80.0	2.510	+0.4
Mar. 7.08	400.08	80.9	.527	+1.5
June 12.93	497.93	76.8	.581	−1.7
Dec. 11.22	679.22	76.3	.680	+0.3
1984 Jan. 9.17	45708.17	75.2	2.696	−0.3
Apr. 3.01	793.01	74.0	.742	+0.1
May 10.94	830.94	73.3	.763	+0.1
Dec. 21.22	46055.22	68.7	.886	+0.2
1985 Jan. 24.13	46089.13	+67.2	2.904	−0.8

Table 6b. (*Continued*)

Date	MJD	Velocity km s^{-1}	Phase	(O − C) km s^{-1}
1985 Feb. 8.46‡	46104.46	+68.6	2.913	+0.8
Mar. 15.01	139.01	67.4	.932	0.0
May 31.90	216.90	68.2	.974	+1.0
1986 Jan. 25.10	46455.10	71.5	3.104	−0.1
Feb. 27.09	488.09	71.1	.123	−1.3
Mar. 7.04	496.04	71.7	.127	−1.0
Apr. 10.05§	530.05	73.9	.145	+0.3
May 12.95	562.95	75.0	.163	+0.6
June 14.91	595.91	75.7	.182	+0.5
Aug. 25.80§	667.80	77.0	.221	+0.3
Nov. 24.55†	758.55	78.9	.271	+0.7
1987 Jan. 6.18	46801.18	78.9	3.294	+0.2
Feb. 1.12	827.12	77.8	.308	−1.2
Mar. 1.13§	855.13	79.1	.323	−0.2
Apr. 27.91	912.91	78.9	.355	−0.8
May 31.92	946.92	80.3	.374	+0.5
June 22.93	968.93	79.2	.386	−0.7
Dec. 10.24	47139.24	79.1	.479	−0.8
1988 Jan. 8.22	47168.22	78.9	3.495	−0.8
Feb. 1.42‡	192.42	79.3	.508	−0.3
Mar. 11.07§	231.07	79.1	.529	−0.3
Apr. 12.91	263.91	+78.5	.547	−0.6

Table 6b. (*Continued*)

Date	MJD	Velocity km s^{-1}	Phase	(O − C) km s^{-1}
1988 May 6.90	47287.90	+79.6	3.560	+0.7
June 2.98	314.98	78.2	.575	−0.4
Nov. 5.20§	470.20	76.3	.660	−0.3
1989 Feb. 11.10	47568.10	73.7	3.713	−1.3
24.23¶	581.23	74.4	.721	−0.3
Mar. 18.03	603.03	74.6	.733	+0.3
Apr. 28.93§	644.93	73.6	.756	+0.2
May 26.91	672.91	73.2	.771	+0.4
June 19.91	696.91	71.9	.784	−0.4
1990 Jan. 31.09§	47922.09	68.3	3.907	+0.4
Feb. 12.31¶	934.31	68.0	.914	+0.2
Mar. 26.96	976.96	67.0	.937	−0.4
Apr. 30.87	48011.87	66.4	.956	−0.8
May 26.95	037.95	65.1	.971	−2.1
Dec. 27.20	252.20	71.5	4.088	+0.8
1991 Jan. 29.11§	48285.11	71.8	4.106	+0.2
May 2.93	378.93	73.9	.157	−0.2
Dec. 19.18§	609.18	77.9	.283	−0.6
1992 Jan. 16.11§	48637.11	78.8	4.298	0.0
Feb. 28.37‡	680.37	79.4	.322	+0.2
Apr. 23.91§	735.91	79.3	.352	−0.4
June 25.88§	798.88	+80.6	.387	+0.7

Table 6b. (*Continued*)

Date	MJD	Velocity km s^{-1}	Phase	(O − C) km s^{-1}
1992 Aug. 12.85§	48846.85	+79.9	4.413	−0.1
Dec. 20.26§	976.26	79.8	.484	0.0
1993 Feb. 15.10§	49033.10	80.0	4.515	+0.5
Mar. 23.08§	069.08	79.3	.535	0.0
July 6.89§	174.89	78.5	.593	+0.2
Dec. 30.20§	351.20	76.0	.689	+0.2
1994 Feb. 21.09§	49404.09	74.6	4.718	−0.2
May 3.00§	475.00	73.2	.757	−0.2
Aug. 1.83§	565.83	71.1	.807	−0.3
1995 Jan. 5.16§	49722.16	67.9	4.892	−0.4
June 4.93§	872.93	66.8	.975	−0.4
1996 Mar. 30.98§	50172.98	73.5	5.139	+0.3
1997 Mar. 29.06‖	50536.06	79.7	5.337	+0.2
Apr. 16.02‖	554.02	79.6	.347	0.0
May 11.00‖	579.00	79.4	.361	−0.3
July 19.90§	648.90	80.4	.399	+0.4
Sept. 9.78§	700.78	80.2	.428	+0.2
1998 May 1.99§	50934.99	79.3	5.556	+0.3
July 12.90§	51006.90	78.0	.595	−0.2
1999 Dec. 20.26‖	51532.26	68.6	5.883	0.0
2000 Jan. 9.18‖	51552.18	68.8	5.893	+0.5
Mar. 25.00‖	628.00	67.9	.935	+0.5
Apr. 30.98‖	664.98	67.5	.955	+0.3
May 30.91‖	694.91	67.1	.972	−0.1
June 19.94‖	714.94	67.6	.983	+0.3
July 16.91‖	741.91	67.7	.997	+0.2
Aug. 1.87‖	757.87	+67.0	6.006	−0.7

*Observed at Kottamia by Woolley *et al.* (1981); not used in orbital solution.
†Observed with Palomar 200-inch telescope.
‡Observed with DAO 48-inch telescope.
§Observed with Haute-Provence *Coravel*.
¶Observed with ESO *Coravel*.
‖Observed with Cambridge *Coravel*.
All others observed with original Cambridge spectrometer; weighted 1/4 in orbital solution.

Table 6c. Radial-velocity observations of HD 109463.

Date	MJD	Velocity km s^{-1}	Phase	(O − C) km s^{-1}
1968 Apr. 26.92*	39972.92	−33.2	0.080	−0.4
1969 Jan. 1.21†	40222.21	−23.8	0.245	+5.0
3.12†	224.12	−27.9	.246	+0.9
1982 Mar. 6.06*	45034.06	−29.9	3.423	−0.1
1984 Apr. 24.93*	45814.93	−37.9	3.939	+0.1
1985 Feb. 24.03*	46120.03	−30.9	4.141	−0.2
1986 Jan. 26.15*	46456.15	−29.5	4.363	−0.4
Mar. 7.04*	496.04	−30.0	.389	−0.6
Apr. 10.06	530.06	−29.6	.412	+0.1
May 7.90*	557.90	−30.0	.430	−0.1
June 4.91*	585.91	−29.5	.449	+0.7
Aug. 25.81	667.81	−30.6	.503	+0.7
Nov. 24.55‡	758.55	−32.6	.563	0.0
1987 Jan. 6.21*	46801.21	−33.8	4.591	−0.6
Feb. 1.11*	827.11	−32.9	.608	+0.7
Mar. 1.14	855.14	−33.6	.626	+0.5
Apr. 27.92*	912.92	−34.7	.665	+0.3
May 24.96*	939.96	−36.0	.682	−0.5
31.92*	946.92	−36.5	.687	−0.9
Dec. 10.25*	47139.25	−38.9	.814	−0.6
1988 Jan. 8.17*	47168.17	−37.4	4.833	+1.1
Feb. 1.43§	192.43	−38.7	.849	−0.1
Mar. 11.06	231.06	−38.7	.875	0.0
May 26.93*	307.93	−38.1	.926	+0.2
June 12.91*	324.91	−37.2	.937	+0.9
Nov. 5.21	470.21	−34.7	5.033	+0.1
1989 Jan. 18.17*	47544.17	−32.2	5.082	+0.6
Feb. 24.24¶	581.24	−32.5	.106	−0.7
Apr. 28.93	644.93	−30.0	.148	+0.4
May 26.91*	672.91	−29.8	.167	+0.2
June 19.92*	696.92	−28.4	.183	+1.2
July 3.92*	710.92	−28.7	.192	+0.7
1990 Jan. 31.09	47922.09	−28.7	5.331	+0.1
Feb. 12.31¶	934.31	−28.9	.339	0.0
Mar. 26.97*	976.97	−28.8	.368	+0.3
Apr. 30.88*	48011.88	−29.1	.391	+0.3

Table 6c. (*Continued*)

Date	MJD	Velocity km s^{-1}	Phase	(O − C) km s^{-1}
1990 May 26.94*	48037.94	−29.7	5.408	−0.1
Dec. 27.20*	252.20	−31.0	.549	+1.3
1991 Jan. 29.11	48285.11	−32.6	5.571	+0.1
Apr. 4.00*	350.00	−35.2	.614	−1.4
May 2.94*	378.94	−34.1	.633	+0.1
June 12.91*	419.91	−34.4	.660	+0.5
Dec. 19.18	609.18	−37.7	.785	+0.1
1992 Jan. 16.11	48637.11	−38.1	5.804	0.0
Apr. 23.91	735.91	−38.8	.869	−0.1
June 25.88	798.88	−38.7	.910	−0.2
Aug. 13.82	847.82	−37.7	.943	+0.3
Dec. 20.26	976.26	−34.8	6.028	+0.3
1993 Feb. 15.10	49033.10	−33.3	6.065	+0.1
Mar. 23.12	069.12	−31.9	.089	+0.6
July 7.92	175.92	−30.3	.160	−0.2
Dec. 29.20	350.20	−28.3	.275	+0.4
1994 Jan. 8.16	49360.16	−28.5	6.281	+0.2
Feb. 18.12	401.12	−28.9	.308	−0.2
May 3.01	475.01	−28.9	.357	+0.1
Aug. 2.85	566.85	−30.0	.418	−0.3
Dec. 14.21	700.21	−32.1	.506	−0.8
1995 Jan. 3.18	49720.18	−32.1	6.519	−0.5
June 2.96	870.96	−33.9	.619	0.0
Dec. 27.17	50078.17	−37.4	.756	−0.2
1996 Mar. 30.98	50172.98	−38.3	6.818	0.0
Nov. 21.27‖	408.27	−37.8	.974	−0.7
Dec. 15.26	432.26	−36.6	.989	0.0
1997 Mar. 29.07‖	50536.07	−33.6	7.058	+0.2
Apr. 17.94‖	555.94	−33.1	.071	+0.1
May 13.01‖	581.01	−32.9	.088	−0.4
July 20.90	649.90	−31.5	.133	−0.6
Dec. 25.18	807.18	−29.3	.237	−0.5
1998 May 2.90	50935.90	−28.7	7.322	+0.1
July 27.84	51021.84	−29.1	.379	+0.1
1999 Apr. 18.27§	51286.27	−32.4	7.554	−0.1
Dec. 20.26‖	532.26	−36.2	.716	+0.1

Table 6c. (*Continued*)

Date	MJD	Velocity km s^{-1}	Phase	(O − C) km s^{-1}
2000 Jan. 9.18‖	51552.18	−36.3	7.729	+0.3
Feb. 11.18‖	585.18	−37.1	.751	0.0
Mar. 25.00‖	628.00	−37.7	.779	0.0
Apr. 30.98‖	664.98	−38.4	.804	−0.3
May 30.91‖	694.91	−38.4	.824	0.0
June 19.95‖	714.95	−38.4	.837	+0.1

*Observed with original Cambridge spectrometer; weighted 1/4 in orbital solution.
†Observed at Haute-Provence by Chériguene (1971).
‡Observed with Palomar 200-inch telescope.
§Observed with DAO 48-inch telescope.
¶Observed with ESO *Coravel*.
‖Observed with Cambridge *Coravel*.
All others observed with OHP *Coravel*.

Table 6d. Radial-velocity observations of HD 110743.

Date	MJD	Velocity km s^{-1}	Phase	(O − C) km s^{-1}
1973 May 16.93	41818.93	−9.5	0.500	+0.5
1977 Apr. 30.98	43263.98	−4.8	2.258	−0.9
1978 May 23.29*	43651.29	−5.1	2.729	−0.7
1979 May 18.91	44011.91	−2.1	3.168	−1.7
1980 Jan. 2.16	44240.16	−9.8	3.446	−0.2
May 6.00	365.00	−8.3	.597	+0.5
1981 Mar. 1.13	44664.13	+2.5	3.961	−0.1
Apr. 27.99	721.99	+3.8	4.032	+1.1
May 31.95	755.95	−0.3	.073	−2.4
1982 Jan. 10.20	44979.20	−6.9	4.345	+0.3
Mar. 4.09	45032.09	−8.6	.409	+0.3
May 5.01	094.01	−10.1	.484	−0.2
1983 Feb. 3.56†	45368.56	−0.6	4.818	+0.3
23.07	388.07	+0.2	.842	+0.3
Mar. 7.09	400.09	−0.1	.857	−0.5
15.05	408.05	+1.6	.866	+0.9
Apr. 15.94	439.94	+2.8	.905	+1.1
May 9.94	463.94	+3.1	.934	+0.9
June 8.94	493.94	+3.0	.971	+0.3
Dec. 11.23	679.23	−1.8	5.196	−0.3
1984 Jan. 2.24	45701.24	−1.8	5.223	+0.7
Apr. 13.97	803.97	−9.3	.348	−2.0
27.94	817.94	−7.0	.365	+0.8
May 11.91	831.91	−8.6	.382	−0.3
20.13‡	840.13	−17.1	.392	−8.6
1985 Jan. 1.21	46066.21	−6.7	5.667	+0.1
24.16	089.16	−5.8	.695	0.0
Feb. 8.50†	104.50	−5.8	.713	−0.8
18.37†	114.37	−5.4	.725	−0.8
Mar. 15.04	139.04	−3.4	.755	0.0
May 31.93	216.93	0.0	.850	−0.2
1986 Jan. 25.17	46455.17	+0.2	6.140	−0.3
Feb. 27.11	488.11	−2.0	.180	−1.1
Mar. 7.08	496.08	−1.0	.190	+0.2
26.03	515.03	−3.4	.213	−1.3

Table 6d. (*Continued*)

Date	MJD	Velocity km s^{-1}	Phase	(O − C) km s^{-1}
1986 Apr. 10.08[§]	46530.08	−1.8	6.231	+1.0
May 5.95	555.95	−3.9	.263	+0.2
June 3.96	584.96	−4.8	.298	+0.7
Aug. 25.81[§]	667.81	−8.6	.399	+0.1
Dec. 12.24	776.24	−9.7	.531	+0.1
1987 Jan. 7.22	46802.22	−8.3	6.562	+1.2
31.16	826.16	−8.3	.591	+0.6
Feb. 21.10	847.10	−7.9	.617	+0.4
Mar. 3.09[§]	857.09	−7.9	.629	+0.1
20.02	874.02	−6.9	.650	+0.4
Apr. 27.93	912.93	−6.0	.697	−0.3
May 8.94	923.94	−4.9	.710	+0.3
Dec. 10.26	47139.26	+3.0	.972	+0.3
22.24	151.24	+2.2	.987	−0.6
1988 Jan. 23.49[†]	47183.49	+2.5	7.026	−0.2
Feb. 1.44[†]	192.44	+2.2	.037	−0.4
Mar. 11.08[§]	231.08	+2.3	.084	+0.4
Apr. 12.98	263.98	+0.8	.124	−0.1
May 29.95	310.95	−0.4	.181	+0.5
Nov. 5.21[§]	470.21	−8.4	.375	−0.3
1989 Feb. 11.15	47568.15	−10.3	7.494	−0.3
24.24[¶]	581.24	−10.4	.510	−0.5
Mar. 25.09[§]	610.09	−9.4	.545	+0.3
Apr. 28.95[§]	644.95	−9.1	.587	−0.1
May 26.94	672.94	−6.9	.621	+1.3
1990 Jan. 27.13[§]	47918.13	+1.8	7.920	−0.2
Feb. 12.33[¶]	934.33	+2.6	.939	+0.3
Mar. 27.01	977.01	+3.6	.991	+0.8
Apr. 30.92	48011.92	+2.7	8.034	+0.1
1991 Jan. 29.13[§]	48285.13	−8.2	8.366	−0.4
Feb. 6.14[§]	293.14	−8.6	.376	−0.5
1992 Jan. 16.12[§]	48637.12	−1.9	8.794	−0.1
Feb. 28.41[†]	680.41	+0.1	.847	0.0
Apr. 22.02[§]	734.02	+1.1	.912	−0.7
June 25.89[§]	798.89	+3.4	.991	+0.6
Dec. 20.25[§]	976.25	−2.3	9.207	−0.4
1993 Feb. 15.11[§]	49033.11	−4.3	9.276	+0.3

Table 6d. (*Continued*)

Date	MJD	Velocity km s^{-1}	Phase	(O − C) km s^{-1}
1993 Mar. 24.99§	49070.99	−6.5	9.322	−0.1
July 8.90§	176.90	−9.6	.451	+0.1
Dec. 27.19§	348.19	−7.0	.659	0.0
1994 Feb. 18.13§	49401.13	−4.5	9.724	+0.1
May 3.05§	475.05	−1.1	.814	0.0
Aug. 3.85§	567.85	+2.0	.927	−0.1
Dec. 14.22§	700.22	+1.0	10.088	−0.8
1995 Jan. 5.17§	49722.17	+1.6	10.114	+0.4
June 2.97§	870.97	−5.5	.295	−0.1
1996 Mar. 30.99§	50172.99	−5.6	10.663	+1.3
1997 Mar. 31.96‖	50538.96	+1.9	11.108	+0.5
Apr. 17.98‖	555.98	+1.1	.129	+0.3
May 13.02‖	581.02	−0.5	.159	−0.4
July 19.91§	648.91	−2.9	.242	+0.4
1998 July 8.87§	51002.87	−6.9	11.672	−0.3
1999 July 12.26†	51371.26	+1.5	12.120	+0.5
Dec. 29.21‖	541.21	−6.6	.327	0.0
2000 Mar. 4.10‖	51607.10	−8.5	12.407	+0.4
Apr. 7.01‖	641.01	−9.6	.448	0.0
May 29.94‖	693.94	−10.2	.513	−0.3
June 19.96‖	714.96	−9.7	.538	+0.1

*Observed with Palomar 200-inch telescope.
†Observed with DAO 48-inch telescope.
‡Observed at KPNO by Yoss, Neese & Hartkopf (1987); not used in orbital solution.
§Observed with Haute-Provence *Coravel*.
¶Observed with ESO *Coravel*.
‖Observed with Cambridge *Coravel*.
All others observed with original Cambridge spectrometer; weighted 1/4 in orbital solution.

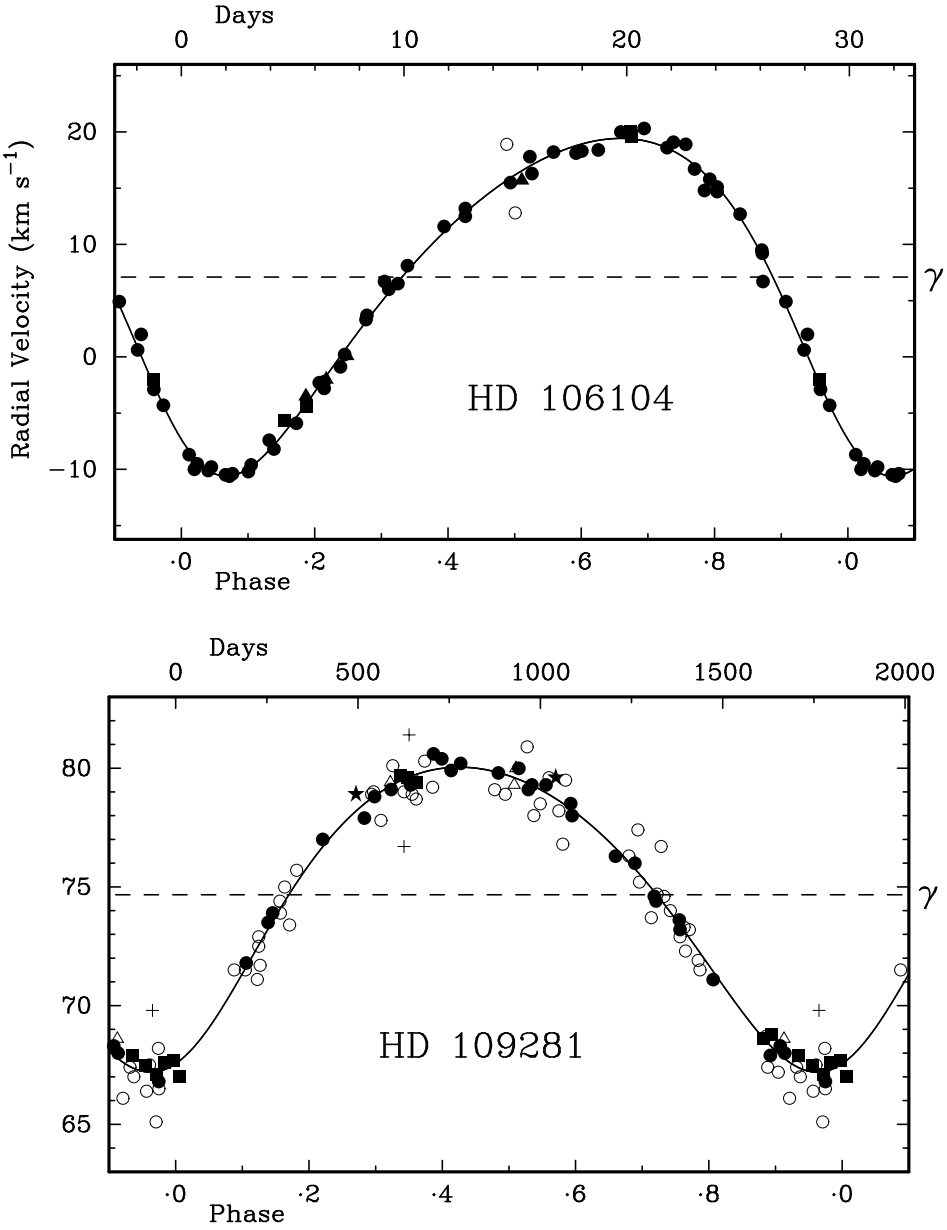

Figure 1. The observed radial velocities of the four stars plotted as functions of phase, with the velocity curves corresponding to the adopted orbital elements drawn through them. Filled circles represent measurements made with the Haute-Provence and ESO *Coravel*s, filled squares being used for the Cambridge one. Open circles refer to velocities obtained with the original Cambridge spectrometer; they were weighted $\frac{1}{4}$ in the orbital solutions, except in the case of HD 106104 where they were discarded altogether. Observations made at the Dominion Astrophysical Observatory are shown as filled triangles, those from Palomar as stars. Plusses and crosses represent the few measurements published by others, in cases where they fall within the confines of the diagrams; they are identified in Tables 6 and were not used in the solutions of the orbits.

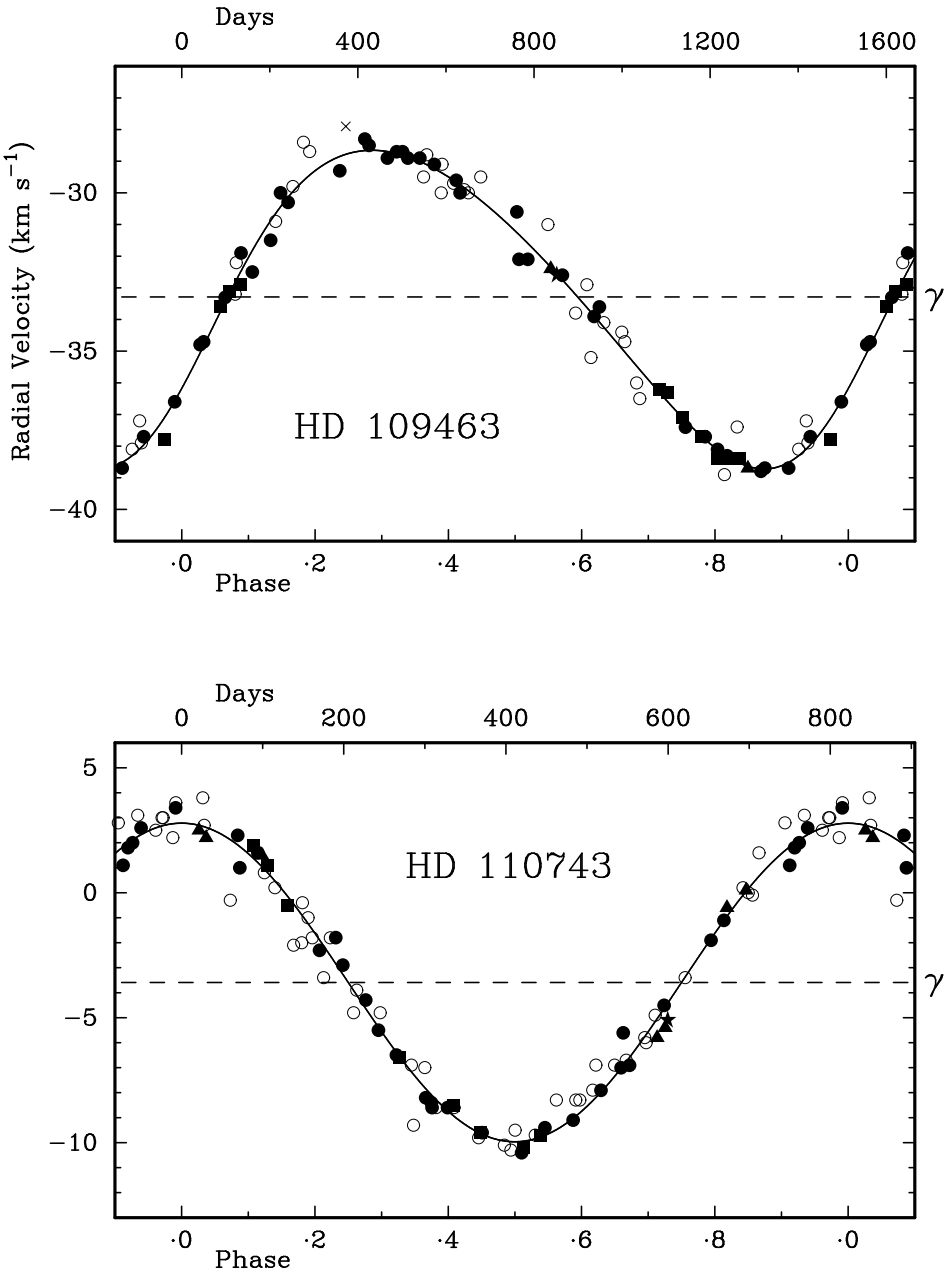

Figure 1. (*Continued*)

method was first developed, typically have (O – C) residuals about twice as large as those from the *Coravel* spectrometers, so they merit only $\frac{1}{4}$ of the weight. All the other instruments normally rate for unit weight, the same as the *Coravel*s. Some exceptions to the general rule have been made, as follows.

HD 106104. There are only two 'old Cambridge' measurements and they both give very bad residuals. The star is particularly faint and was difficult to measure with the

Table 7. Orbital elements for the four stars.

Element	HD 106104	HD 109281	HD 109463	HD 110743
P (days)	29.9335 ± 0.0013	1828 ± 3	1513.8 ± 2.4	822.1 ± 0.7
T (MJD)	48972.23 ± 0.19	48092 ± 22	48934 ± 19	47984.1 ± 1.7
γ (km s^{-1})	+7.10 ± 0.10	+74.67 ± 0.06	−33.29 ± 0.04	−3.59 ± 0.06
K (km s^{-1})	15.02 ± 0.13	6.42 ± 0.07	5.03 ± 0.07	6.37 ± 0.08
e	0.229 ± 0.008	0.173 ± 0.012	0.160 ± 0.010	0
ω (degrees)	141.4 ± 2.5	199 ± 4	240 ± 5	—
$a_1 \sin i$ (Gm)	6.02 ± 0.05	158.9 ± 1.9	103.4 ± 1.4	72.0 ± 0.9
$f(m)$ ($M_\odot$)	0.00970 ± 0.00026	0.0480 ± 0.0017	0.0193 ± 0.0008	0.0221 ± 0.0009

original instrument, which is why only two observations were made with it. They have been zero-weighted.

HD 109281. The scanning range of the Palomar spectrometer was fixed during any one series of measurements and could not be centred at will, star by star. HD 109281 has a high velocity which placed its 'dip' partly off the end of the two Palomar traces, impairing the accuracy of the resulting velocities, which have been given the same weight as the old Cambridge ones.

With those preliminaries settled, the orbits readily follow; they are plotted in Fig. 1 and their elements are set out in Table 7.

4. Discussion

4.1 *HD 106104*

At 30 days, the period of this star is by far the shortest of the four. *Coravel* traces show that HD 106104 is the only one of the four stars to have a significant rotational velocity — it is about 6 km s^{-1} . Since the spectral type is slightly earlier than that of the Sun and the orbital period is slightly longer than the Sun's period of rotation, synchronous rotation would necessitate an equatorial velocity almost identical with the solar one, *viz.* 2 km s^{-1} . The pseudo-synchronous velocity, that takes account of the eccentricity of the orbit, would be larger by about one-third (Hut 1981). Even so, and quite apart from the question of the unknown axial inclination, which would act to make the observed rotational velocity less than the true one, it is fairly certain that HD 106104 is spinning faster than synchronously with its orbital revolution.

The inclusion (purely out of curiosity) of the visual companion in the survey programme (Yoss & Griffin 1997), for which it did not meet the criteria for selection, provides an object lesson in serendipity. We have already seen, from Table 1, that the apparent magnitude of the companion is about $0^{m}.9$ fainter than that of HD 106104 itself; the companion is also slightly redder, and its DDO 'pseudo-spectral' type is G3 V against the principal star's F9 V, so the two objects would very well pass for a physical pair. In fact the deduced distances of 164 and 182 pc are equal to well within their joint uncertainty, and are uncannily close to the distance implied by the *Hipparcos* parallax (Table 4). The radial velocity of the companion has been measured thirteen times, with the results given in Table 8.

There is no strong evidence for variability, and the mean velocity of $+6.9 \pm 0.3$ km s^{-1} differs by only -0.2 ± 0.3 km s^{-1} from that of HD 106104 and makes it extremely likely that the two stars really *are* physically associated with one another. The matter is clinched by the accurate proper motion derived for the companion, from *Tycho* (*Hipparcos* 1997) and preceding astrometric catalogues, in the *Tycho 2* catalogue described by Høg *et al.* (2000): in Table 9 it is compared with the proper motions derived both by *Hipparcos* and by *Tycho 2* for the principal star, and is seen to be sensibly identical.

At the distance of the pair, taken to be about 170 pc, the observed angular separation of 76 seconds of arc represents a projected (*i.e.* minimum) distance of about 13,000 AU or $\frac{1}{16}$ of a parsec. The system could be only loosely bound at such a separation, but bound it must be: if for the sake of illustration we suppose the relative orbit to be more or less circular and its diameter to be not much greater than the observed

Table 8. *Coravel* radial-velocity observations of HD 106104 B.

Date	Velocity km s^{-1}	Date	Velocity km s^{-1}
1990 Feb. 14.36*	+6.4	1994 Apr. 29.95	+9.3
1991 Jan. 28.11	+7.2	1995 Jan. 4.16	+7.0
Feb. 5.09	+6.0	June 2.95	+8.1
1992 Jan. 15.09	+6.7	1997 May 10.89	+7.4
Apr. 26.95	+6.1	1998 May 2.89	+6.5
Dec. 20.19	+6.4	2000 Apr. 6.96	+6.7
1993 Dec. 29.16	+5.2		

Observed at: *ESO † Cambridge All others: OHP

Table 9. Proper motions of HD 106104 and its companion.

		Arc-milliseconds/year α	δ
HD 106104	Hipparcos	-35.0 ± 2.0	$+5.1 \pm 0.9$
	Tycho 2	-35.6 ± 1.3	$+4.9 \pm 1.3$
HD 106104 B	Tycho 2	-33.9 ± 1.8	$+7.5 \pm 1.8$

projected distance, the period is of the order of a million years and the relative orbital velocity about 0.3 km s^{-1}. If unbound, therefore, within at most a few million years — a time short compared with a revolution of the Galaxy — the system would disintegrate and not attract observers' attention (as it did ours) by the mutual proximity of its components. It would also seem to require a disturbance a great deal more localized than the general tidal field of the Galaxy to disrupt the system by giving the components differential accelerations sufficient to unbind them within a fraction of an orbital period.

4.2 *HD 109281*

The property that immediately catches attention concerning HD 109281 is its high γ-velocity of +74.7 km s^{-1} — fewer than a dozen of the 903 stars measured in the Galactic-Pole field proved to have velocities (taken without regard to sign) higher than that. Yet, according to the results derived from DDO photmetry, the high velocity is not accompanied by any diminution of metallic abundances in comparison with the Sun. The three radial velocities determined from Kottamia spectrograms by a Greenwich Observatory consortium under Woolley are excellent in their class and are consonant with the orbit derived from the photoelectric velocities, which have, however, only $\frac{1}{40}$ of the variance. The troublesome exactitude with which the orbital period equals an integral number of years was remarked upon in §2 above.

4.3 *HD 109463*

The V magnitude of $7^{\rm m}.81$ tabulated for HD 109463 by Hartkopf & Yoss (1982) in a paper that presents a great deal of photoelectric photometry would appear to constitute *prima facie* evidence for variability of that star; against that, the r.m.s. internal scatter in the *Hipparcos* magnitudes from the 87 individual transits is (at $0^{\rm m}.011$) the smallest for any of the four stars. Dr. Yoss has kindly informed me, however, that his magnitude was transcribed from the bibliographic catalogue of radial velocities by Abt & Biggs (1972) — a fact that cannot be divined from the published paper; it is my belief that Abt & Biggs copied that entry straight from the *Henry Draper Catalogue* (Cannon & Pickering 1920), which obtained it from visual photometry performed by Pickering (1890) in the spring of 1887. The unusual distance tabulated for HD 109463 (and the distances of all the other stars treated in the paper by Hartkopf & Yoss) arises from an error in the column headings and should be divided by a factor of a thousand.

The two radial velocities published by Chériguene (1971) do not agree with one another as well as might be expected of coudé velocities obtained at practically the same orbital phase; one of them falls well off the top of the plot in Fig. 1. The mean given by Heard (1956) for four (un-dated) velocities would also be above the top of the graph if the usual adjustment of $+0.8$ km s^{-1} were made in an effort to place them on the Cambridge scale. In a case in which eight radial velocities obtained with the same equipment (David Dunlap Cassegrain spectrograph, 66 Å mm^{-1} at Hγ) were known individually, however, it was found (Griffin 1980) that an offset of -5 km s^{-1} was needed to put them into systematic agreement with Cambridge measurements, and Heard himself was quoted there as having found in a substantial unpublished investigation of his own that his 66-Å mm^{-1} data needed such a correction. Such a change would place the mean of the four David Dunlap velocities at -31.1 km s^{-1}, which would be entirely reasonable. It may be inferred from the 'probable error' quoted for their mean that the individual values have an r.m.s. spread of 4.4 km s^{-1} around that value, but in the absence of information on the times of the observations it is not possible to tell how much the actual changes of HD 109463's velocity contributed to that spread.

4.4 *HD 110743*

HD 110743 is by far the nearest of the four stars treated in this paper; its proximity implies that the angular scale of its orbit as seen on the sky is much larger than in the cases of the other three objects. With the further circumstance, favourable from the point of view of the *Hipparcos* mission, that the orbital period is only a little shorter than the total duration of that mission, so the orbit is about as big as the satellite could have seen completely round a cycle, *Hipparcos* succeeded in discovering the duplicity of the star from the photocentric motion, from which was derived an orbital solution (*Hipparcos* 1997, **10**, p. DO2) entirely independent of the one given in the present paper. The astrometric orbit is in reasonable agreement with the radial-velocity one, as may be seen from the comparison given in Table 10; it is not nearly so precise, but it does provide values, which of course are not determinable spectroscopically, for the angular semi-axis major and the inclination.

The angular semi-axis of $0''.0221 \pm 0''.0016$ is practically identical with the parallax that was determined by *Hipparcos* at the same time, $0''.0229 \pm 0''.0016$, so the implied

Table 10. Comparison of orbital elements of HD 110743.

		Spectroscopic (This paper)	Astrometric (Hipparcos)
P	(days)	822.1 ± 0.7	799 ± 15
T	(MJD)	47984.1 ± 1.7	48039 ± 51
e		0	0.25 ± 0.13
ω	(degrees)	(0)	49 ± 30
a	(arcseconds)	—	0.0221 ± 0.0016
i	(degrees)	—	49 ± 12
$a_1 \sin i$	(Gm)	72.0 ± 0.9	—

linear measurement of the semi-axis is just about 1 AU. That dimension refers to the orbit of the photocentre, and could of course be smaller to any degree than that of the orbit of the visible star around the centre of gravity, depending on the contribution of the secondary star to the total luminosity. Comparison with the value of $a_1 \sin i$ determined spectroscopically is therefore fraught with uncertainty: the spectroscopic value is less than the true separation by the factor $\sin i$, the 1-σ limits of whose value according to *Hipparcos* (*cf.* Table 10) is 0.60–0.87, leading to the expectation that $a_1 \sin i$ is within those limits in terms of astronomical units, or could be larger if the apparent size of the astrometric orbit is diminished because of significant light from the secondary star. In fact it is only 0.481 ± 0.006 AU; the discrepancy seems to suggest that (*a*) there is little scope for the secondary star to contribute any substantial luminosity to the system, and (*b*) *Hipparcos* must have significantly over-estimated i and/or a, or under-estimated π. Among those parameters the proportional uncertainty of the inclination i is several times worse than that of the others, so it would be natural to lay the principal error at its door.

A noteworthy feature of the orbit of HD 110743 is its circularity, despite a period 50 to 100 times longer than the maximum at which tidal effects are supposed to circularize the orbits of lower-main-sequence stars (*e.g.* Mathieu *et al.* 1992). When the eccentricity is permitted as a free parameter in the orbital solution it takes the value 0.012, less than its own standard error, and in comparison with the result of the solution with the eccentricity fixed at zero the sum of the squares of the weighted residuals diminishes by barely 1% — far less than would constitute significance under Bassett's (1978) statistical tests. As a matter of general principle, therefore, since e is indistinguishable from zero and as a corollary ω is indeterminate, the exactly circular orbital solution is adopted. Astrophysically, however, the principle is hard to justify in this particular case: no mechanism of circularization can be proposed, so we are left to suppose that the HD 110743 system actually *formed* in a practically circular orbit. Even if the companion star has passed through its evolution as a giant — and to the best of the writer's knowledge no ultraviolet surveys have noticed evidence of a white dwarf in the system — it would have been unlikely to reduce the orbital eccentricity so very nearly (or quite) to zero: giant binaries are usually circularized up to periods only of the order of 200 days (Griffin 1990; Mermilliod & Mayor 1992), and even barium

stars, which are all supposed to include a highly evolved component, normally show non-zero eccentricities (McClure & Woodsworth 1990).

References

Abt, H.A., Biggs, E S. 1972, *Bibliography of Stellar Radial Velocities* (Tucson: Kitt Peak Nat. Obs.), p. 281.
Baranne, A., Mayor, M., Poncet, J L. 1979, *Vistas Astr.*, **23**, 279.
Bassett, E.E. 1978, *Observatory*, **98**, 122.
Bidelman, W. P. 1985, *Astrophys. J. Suppl.*, **59**, 197.
Cannon, A. J., Pickering, E.C. 1920, *Ann. Harv. Coll. Obs.*, **95**, 78.
Chériguene, M. F. 1971, *Astr. Astrophys.*, **13**, 447.
Fletcher, J. M., Harris, H.C., McClure, R.D., Scarfe, C.D. 1982, *Publ. astr. Soc. Pacific*, **94**, 1017.
Griffin, R. F. 1967, *Astrophys. J.*, **148**, 465.
Griffin, R. F. 1969, *Mon. Not. R. astr. Soc.*, **145**, 163.
Griffin, R. F. 1980, *J. R. astr. Soc. Canada*, **74**, 348.
Griffin, R. F. 1990, *J. Astrophys. Astr.*, **11**, 491.
Griffin, R. F. 2000, *J. Astrophys. Astr.*, **21**, 121.
Griffin, R. F., Gunn, J.E. 1974, *Astrophys. J.*, **191**, 545.
Griffin, R. F., Herbig, G.H. 1981, *Mon. Not. R. astr. Soc.*, **196**, 33.
Hipparcos and Tycho Catalogues 1997 (ESA SP-1200) (Noordwijk: ESA)..
Häggkvist, L., Oja, T. 1973, *Astr. Astrophys. Suppl.*, **12**, 381.
Hansen, L, Radford, G A. 1983, *Astr. Astrophys. Suppl.*, **53**, 427.
Hartkopf, W. I., Yoss, K M. 1982, *Astr. J.*, **87**, 1679.
Heard, J. F. 1956, *Publ. David Dunlap Obs.*, **2**, 105.
Hill, G. 1982, *Publ. Dominion astrophys. Obs.*, **16**, 87.
Høg, E. *et al.* 2000, *Astr. Astrophys.*, **355**, L27.
Hut, P. 1981, *Astr. Astrophys.*, **99**, 126.
Jasniewicz, G., Duquennoy, A., Acker, A. 1987, *Astr. Astrophys.*, **180**, 145.
Knude, J. 1993, *Astr. Astrophys. Suppl.*, **81**, 215.
Ljunggren, B. 1965, *Ark. Astr.*, **3**, 535.
Malmquist, K. G. 1960, *Uppsala astr. Obs. Ann.*, **4**, part 9, p. 40.
Mathieu, R. D., Duquennoy, A., Latham, D.W., Mayor, M., Mazeh, T., Mermilliod, J.-C. 1992, in *Binaries as Tracers of Stellar Formation*, Eds. A. Duquennoy & M. Mayor (Cambridge: Cambridge Univ.), 1992, p. 278.
McClure, R. D. 1976, *Astr. J.* **81**, 182.
McClure, R. D., Woodsworth, A.W. 1990, *Astrophys. J.*, **352**, 709.
Mermilliod, J -C., Mayor, M. 1992, in *Binaries as Tracers of Stellar Formation*, Eds. A. Duquennoy & M. Mayor (Cambridge: Cambridge Univ.), 1992, p. 183.
Pickering, E. C. 1890, *Harvard Ann.*, **24**, 67.
Porter, J. G. 1895, *Publ. Cincinnati Obs.*, no. 13, p. 34.
Sandage, A. R., Fouts, G. 1987, *Astr. J.*, **93**, 592.
Scarfe, C. D., Batten, A.H., Fletcher, J.M. 1990, *Publ. Dominion astrophys. Obs.*, **18**, 21.
Schwassmann, A., van Rhijn, P.J. 1951, *Bergedorfer Spektral-Durchmusterung der 115 Nordlichen Kapteynschen Eichfelder 68–91*, **4**, 152. [SA 80, no. 689.]
Trumpler, R. J. 1938, *Lick Obs. Bull.*, **18** 167.
Udry, S., Mayor, M., Queloz, D. 1999, in *Precise Stellar Radial Velocities*, Eds. J.B. Hearnshaw & C.D. Scarfe (*IAU Coll.*, no. 170) (*ASP Conf. Series*, **185**) (San Francisco: Astr. Soc. Pacific), p. 367.
Upgren, A. R. 1962, *Astr. J.*, **67**, 37.
Woolley, Sir R. *et al.* 1981, *Roy. Obs. Ann.*, no. 14, p. 73.
Yoss, K. M. 1977, *Astr. J.*, **82**, 832.
Yoss, K. M., Griffin, R F. 1997, *J. Astrophys. Astr.*, **18**, 161.
Yoss, K. M., Neese, C L., Hartkopf, W I. 1987, *Astr. J.*, **94**, 1600.

J. Astrophys. Astr. (2001) **22,** 213–227

Detection, Excision and Statistics of Interference at the Mauritius Radio Telescope

S. Sachdev[1,2] & N. Udaya Shankar[1,2,*]

[1]*Raman Research Institute, Sadashivanagar, Bangalore 560 080, India*
[2]*Department of Physics, University of Mauritius, Reduit, Mauritius.*

Received 2001 August 21; accepted 2001 September 28

Abstract. A technique to detect man-made interference in the visibility data of the Mauritius Radio Telescope (MRT) has been developed. This technique is based on the understanding that the interference is generally 'spiky' in nature and has Fourier components beyond the maximum frequency which can arise from the radio sky and can therefore be identified. We take the sum of magnitudes of visibilities on all the baselines measured at a given time to improve detectability. This is then high-pass filtered to get a time series from which the contribution of the sky is removed. Interference is detected in the high-pass data using an iterative scheme. In each iteration, interference with amplitudes beyond a certain threshold is detected. These points are then removed from the original time series and the resulting data are high-pass filtered and the process repeated. We have also studied the statistics of the strength, numbers, time of occurrence and duration of the interference at the MRT. The statistics indicate that most often the interference excision can be carried out while post-integrating the visibilities by giving a zero weight to the interference points.

Key words. Metre-wave radio telescope—Fourier synthesis—interference excision.

1. Introduction

Mauritius Radio Telescope (MRT) is a new metre-wave radio telescope operating at 150 MHz. The primary objective of the telescope is to produce a sky survey in the declination range -70° to -10° with a point source sensitivity of about 200 mJy (3σ). This will be the southern sky equivalent of the Cambridge 6C survey. A detailed description of the telescope is to be found in Golap *et al*. (1998). Mauritius was chosen as the site for the new telescope due to its strategic geographic location (latitude = -20.14°), where the Galactic Centre is almost overhead. The island was also considered a paradise for low frequency astronomy due to its interference-free environment. Unfortunately it no more remains an interference-free site due to the industrial growth in the country. This has confirmed the general belief that a totally interference-free

*email: uday@rri res.in

site may be a thing of the past, especially at low frequencies. In Mauritius the band around 150 MHz is not a primary allocation for radio astronomy. The Government of Mauritius has allocated only a 1 MHz band from 150 MHz to 151 MHz and not the band from 150.05 to 153 MHz, generally allocated to radio astronomy (Handbook on Radio Astronomy 1995). Emission from a new communication facility operating at 149 MHz, spills into the protected band making it unusable for radio astronomy. There is also interference from unidentified satellite(s) in this band. We have therefore moved the frequency of operation from the initially planned 150 MHz to 151.5 MHz. A narrow band around 151.5 MHz is relatively free of interference. Since this is not a protected band in Mauritius, an application for protection of this frequency has been forwarded to the Government of Mauritius.

In the mean time we have carried out observations with the MRT for more than 20,000 hours and data analyses are in progress. The section 2 of this paper briefly describes the Mauritius Radio Telescope and the observations carried out for the survey. The next section describes problems related to local interference and basic principles used for detection of external interference. Section 4 gives the description of the algorithm developed with a few illustrations of interference detection. In section 5 we give the statistics of the interference observed. Section 6 describes the principles used for interference mitigation in the final images.

2. The Mauritius Radio Telescope

The Mauritius Radio Telescope (MRT) is a Fourier synthesis T-shaped array with an East-West (EW) arm of length 2048m having 1024 helical antennas. The South (S) arm consists of a rail line of length 880m and 16 movable trolleys each with four helical antennas. The 1024 helices in the EW arm are divided into 32 groups of 32 helices each. All the EW groups are not at the same height, a situation imposed by the uneven terrain. Each trolley in the S arm constitutes one S group.

The 48 group outputs are amplified, heterodyned to 30 MHz in the field and brought separately to the observatory building via coaxial cables. In the observatory, the 48 group outputs are further amplified and down converted to a second IF of 10.1 MHz. The 32 EW and 16 S group outputs are fed into a 32×16 complex, 2-bit 3-level digital correlator sampling at 12 MHz. The 512 complex visibilities are integrated and recorded at intervals of 1 second. At the end of 24 hours of observation the trolleys are moved to a different position and new visibilities are recorded. The S baselines are sampled with a spacing of 1m, which is half a wavelength at 150 MHz. A minimum of 60 days of observing are needed to obtain the visibilities up to the 880m spacing. The Fourier Transform of the phase corrected visibilities obtained after the complete observing schedule, produces a map of the area of the sky under observation with a synthesized beam of $4' \times 4.6' \sec(\delta + 20.14^\circ)$. The expected root mean square (RMS) noise in the image made using an IF bandwidth of 1 MHz and an integration time of 8 seconds is $\approx$200 mJy(3σ).

The full width at half maximum (FWHM) of the primary beam of a S $\times$ EW interferometer at MRT is $2^\circ \times 60^\circ$. Due to this broad primary beam and its low operating frequency, the MRT is very susceptible to terrestrial interference. Interference causes spurious features in an image. If these effects are greater in strength than the noise fluctuations, they lead to misinterpretation. Hence, it is important to remove this interference. Interferences discussed in this paper can be classified as local and external

depending upon the locations of their sources. Here interference from sources which are located in-house are classified as local, while external refers to interference from sources remote to the telescope.

3. Local interference

Local interference is due to oscillators used in the observatory, whose harmonics fall in the observing band or the IF band.

We found the oscillators in switch mode power supplies of Personal Computers to be the main source of Radio Frequency Interference (RFI) emanating from the observatory building. These and the other parts of the receiver system were shielded by putting them in grounded Faraday cages. The analog and digital parts were grounded separately. Since the telescope site is rocky, the natural grounding is not good. Three pits, each 3m deep, with copper grounding plates buried in a mixture of coal and salt were used to improve the grounding. Two of these were used to separately ground the digital and analog parts of the receiver system. The third pit was used as ground for the air-conditioners and the computer systems outside the receiver room. The observatory building was not built with shielding. We reduced the effect of interference from the observatory by covering it with grounded stainless steel mesh.

To reduce the effect of common-mode interference picked up by the first IF cables and by the second IF signal lines, phase switching of the LO was implemented. We were also faced with the noise generated by the LO generator at 30 MHz, the first IF frequency. This leaked to the IF port at the first mixer and produced high correlations in some of the baselines. To reduce this, we used a band elimination filter centered around 30 MHz in the path of the Local Oscillator (LO).

The first IF at 30 MHz, is heterodyned with an LO of 40 MHz. In this conversion, stray signals centered around 50 MHz, picked up by long cables carrying the first IF to the observatory building, gets into the observing band. This resulted in increased noise in the observing band. To reduce their effects, we introduced band-pass filters centered around 30 MHz just before the heterodyning.

After sorting out most of the problems related to “in-house” interference, we still had interference in our data from external sources. The next section discusses the interference from external sources.

3.1 *Interference detection*

Some of the well known sources of external interference are communication systems, ignition systems of vehicles moving close to the telescope, high voltage power lines, satellites and the active Sun. Many of these produce short-interval, ‘spiky’ interference which have frequency components at a much higher frequency than that of the response of the antenna to celestial sources. Interference from man-made sources is highly polarized. Interference from communication systems is also generally narrow-band. However, interference with a broader spectrum is produced by arcing sources.

The front end of the receiver system has been built with sufficient bandwidth so that the observing frequency can be shifted (within 145–155 MHz) to an interference-free zone by tuning the LO. Presently the telescope is operated at 151.5 MHz which allows maximum interference-free observations.

At the MRT, since we do not measure the polarization of the signal, we cannot use this property of interference in differentiating the interference from the sky signal. Furthermore since we use XF correlators, we cannot reject parts of the observing band in which the interference occurs and use the rest of the band.

The 'spiky' nature of the interference is used for its detection at MRT. Interference which is 'spiky' in nature generally has Fourier components beyond the maximum due to the sky signal. In interferometer arrays, the visibility data are generally sampled in time at rates much faster than the rates required for a given baseline. This can be made use of in identifying interference which is 'spiky' in nature. For example, at the MRT the baseline with the longest east-west component ($\sim 512\lambda$) has a maximum fringe rate of about 0.04 Hz. We have sampled the data every one second which allows us to identify frequencies up to 0.5 Hz. Therefore interference can be identified by its contribution to frequencies in the range 0.04 Hz to 0.5 Hz.

The maximum frequency to which the sky contributes at the output of a complex correlator is given by $\omega_e x$, where $\omega_e = dH/dt = \frac{2\pi}{(24\times60\times60)} = 7.27 \times 10^{-5}$ radians per sidereal second and x is the east-west component of the baseline in wavelengths. Since x depends on the baseline used, the ability to distinguish interference from the sky signal decreases with increasing east-west component of the baseline. To overcome this baseline dependence, instead of detecting interference in the *cosine* and the *sine* channels separately, interference is detected in the magnitude of the visibility i.e., in $\sqrt{\cos^2 + \sin^2}$. The magnitude of visibility has a rate of change which is independent of the baseline used. This rate depends on the primary beam of the interferometer which is the product of the voltage patterns of a group of antennas (EW and S groups) forming the interferometer. At MRT the primary beam of the interferometer used for imaging is $2^\circ \times 60^\circ$. Thus the expected maximum frequency at the MRT in the magnitude of the visibility is $\sim$0.003 Hz.

The best method to ensure detection of interference in the *sum of magnitudes* would be to look for interference in the resultant obtained by summing all possible combinations of baselines. For example, if the interference had affected only two interferometers, then this interference would best be detected if the detection was carried out on the summation of magnitudes of these two baselines only, instead of adding the contribution of all the baselines. This, however, is not practical in terms of analysis time. We find that generally, interference affects all baselines simultaneously. Therefore, to improve the detectability of interference we add the magnitudes of all the visibilities used. We refer to this combined data as the *sum of magnitudes*.

The last group of the East array (E16) is fed to the correlator in the place of the 16th trolley of the S array. This gives a set of baselines formed between E16 and the E-W array on all observing days. This set of baselines is useful for calibration but reduces the number of usable trolleys to only 15. Thus only 480 ($15\times$ 32) baselines are used for imaging. If the magnitudes of all the visibilities of these 480 baselines are added, we will be able to detect interference at the level of $5\sigma_m/\sqrt{480}$ with a 5σ detection, where σ_m is the RMS noise on the $\sqrt{\cos^2 + \sin^2}$ of any baseline and σ is the RMS noise on the *sum of magnitudes*. For statistical considerations, a detection level greater than five times the RMS of the noise is used. Assuming interference affects all baselines with equal strength, we are able to detect interference down to $5\frac{\sigma_m}{\sqrt{480}}$, i.e., $\frac{\sigma_m}{4.4}$ per baseline. On the other hand if only n baselines are affected, then an interference of strength less than $\frac{5\sigma_m\sqrt{480}}{n}$ per baseline would go undetected.

At MRT images are made by adding 60 days of data. Further four images are post-integrated to get a final image. Assuming that there is interference on only one of the sixty days at a given sidereal time, the undetected interference will be of the order of the noise in this final image. This, in terms of flux density, is of the order of 100 mJy.

In principle, the process of combining visibilities of different baselines may also be extended to the data of different days to further detect interference which occurs at the same right ascension on some other day. Since this is very unlikely we decided to allow undetected interference of the order of $\frac{\sigma_m}{4.4}$ in the final images.

By detecting interference in the *sum of magnitudes* (incoherent detection), the sensitivity to detection is $\sqrt{2}$ times worse than detection carried out on phased visibilities (coherent detection). In using *sum of magnitudes*, there is the advantage of the simplicity of looking at one time series.

4. Implementation scheme

In the implementation of the detection of interference, the *sum of magnitudes* is low-pass filtered. This is done by applying a rectangular window function on the Fourier transform of the *sum of magnitudes* data. This retains only those frequencies corresponding to the sky contribution. The low pass filter allows a maximum frequency of $\omega_e x$, where x is the maximum east-west spatial frequency. For an EW $\times$ NS interferometer, $x = 36\lambda$. The output of this filter, which contains frequencies up to $\omega_e x$, is Inverse Fourier Transformed (IFT). This is then subtracted from the visibility data resulting in the 'difference' data from which the sky contribution has been removed. This 'difference' data is basically a high pass data with frequencies greater than $\omega_e x$, i.e., greater than the sky response. This therefore may be considered to consist only of contributions from the receiver noise and from the interference. The interference is detected in this 'difference' data. The detected points are stored in a file and are used to reject these points in subsequent processing. The flow diagram shown in Fig. 1 summarizes the technique used.

We now look at different ways of detecting the interference to minimize the time required without losing the reliability of the detections.

We started with a brute-force method in which the maximum deviation is located in the 'difference' data. If this deviation is greater than $k\sigma$, it is noted as interference. Here σ is the expected RMS deviation due to the receiver noise in the 'difference' data and k determines the threshold level of detection. This noted point is then removed from the time series and the remaining data are passed through the high pass filter again. This process is repeated till no points beyond $k\sigma$ are detected in the 'difference' data.

This method although simple and effective is prohibitively slow as it requires a filtering operation (involving an FFT and an IFT) for every interference point.

To reduce the time required we used an algorithm in which the interference is treated as a set of delta functions. In the 'difference' data a delta function appears convolved with the high pass function. In this algorithm, the maximum greater than $k\sigma$ is detected as earlier. However, instead of removing the marked out point in the time series and doing the whole process all over again, the high-pass response of a delta function of strength equal to the detected interference is subtracted from the 'difference' data. A delta function whose height equals the

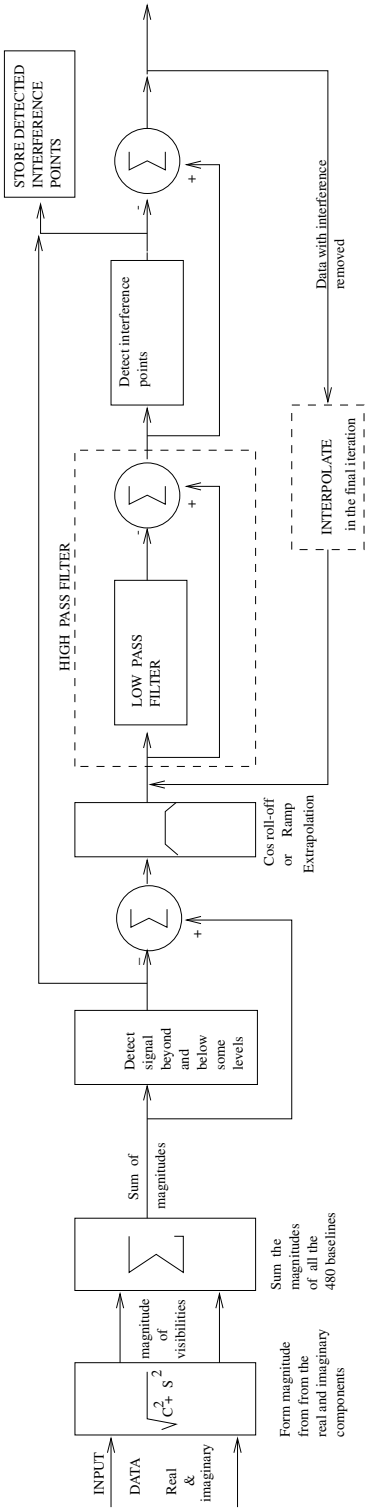

Figure 1. Block diagram illustrating the method adopted for interference detection.

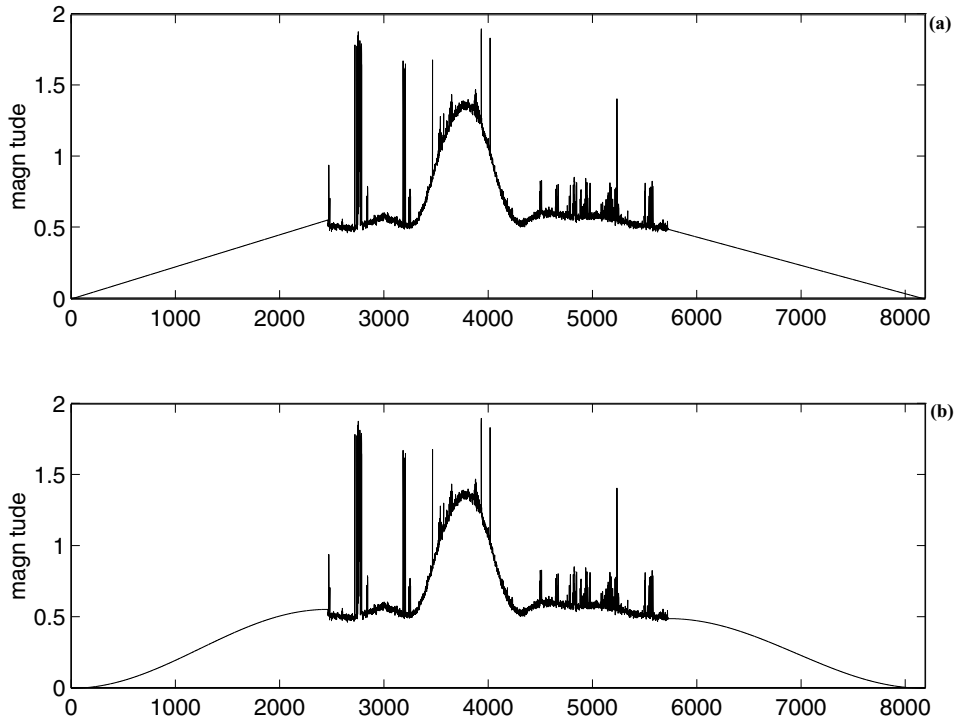

Figure 2. *Extrapolation*: The data at the beginning and at the end of a file are extrapolated with **(a)** a ramp function **(b)** cosine roll-off function.

maximum that has been subtracted is placed in a separate file. The next highest point in the residual difference data is then located and the procedure is repeated until a pre-determined level is reached in the residual difference. This is essentially performing a 'deconvolution' using the CLEAN algorithm (Hogbom 1974) on the 'difference' data. All detected points are then removed from the visibility data.

Some erroneous detections occur if there are strong, closely spaced interference which results in a very distorted 'difference' data. To overcome such a problem the following alternative algorithms were tried out:

(a) Whenever an interference point is found, a scaled high pass response due to the interference (which is the response of the high pass filter to a delta function) is removed. This is similar to introduction of a 'loop gain' in standard CLEAN algorithms.

(b) The interference is detected in the 'difference' data above a certain threshold level which is set depending on the maximum interference level. In each iteration interference points of strength greater than 80% of the peak interference detected are removed. We found that this method gives better results than the method (a) and is therefore used in the final implementation of interference detection.

A few practical aspects in interference detection are listed below.

1. Most correlators give a finite, non-zero correlation even for uncorrelated inputs. Because of these offsets, the magnitudes of the visibilities have higher frequency

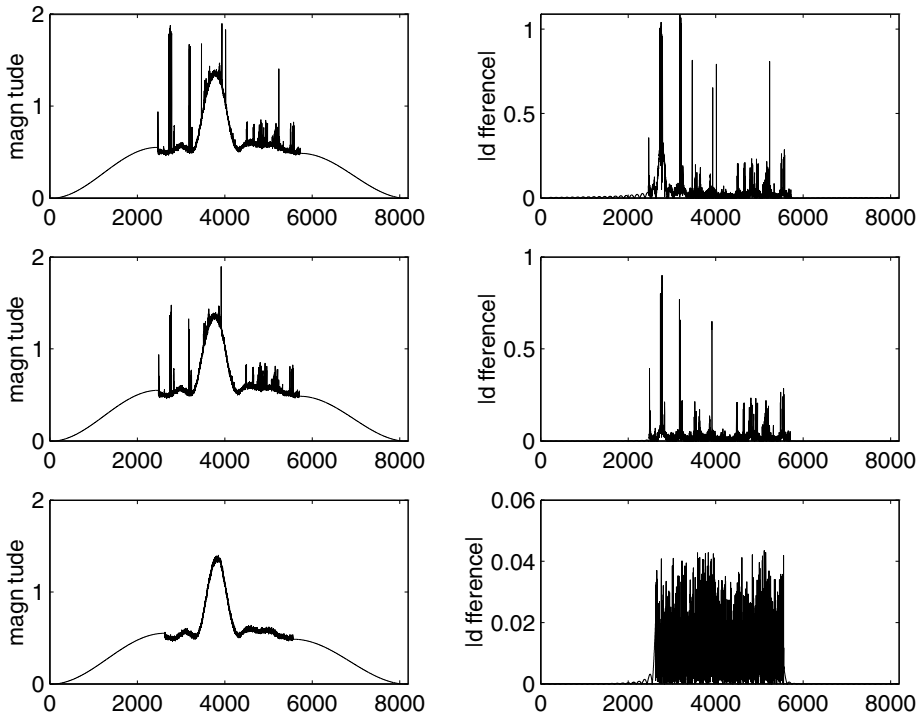

Figure 3. The different stages in interference detection. The left panels show the extrapolated *sum of magnitudes* and the right panels show the corresponding 'difference' data. The results of the 1st, 5th and the 15th, which is the last iteration, are shown.

components than the cut-off criterion used[1]. In the *sum of the magnitudes*, the contribution of these frequency components due to any given baseline is only $\frac{1}{480}$. Hence these are not detected as interference. But one would need to take this into account when applying the technique on a lesser number of baselines where the contribution of the fringing component produced by the offsets could be significant.

2. Using a DFT causes ripples whenever there is an offset between the beginning and the end of the patch being Fourier transformed [2]. Depending on the strength of the ripple, this may be detected as interference. To overcome this, the data at the beginning and at the end of the file are extrapolated with a smooth function before performing DFT. We find that using a cosine roll-off or a ramp function for extrapolation is generally sufficient. An example of the ramp extrapolation and cosine roll-off extrapolation is shown in Fig. 2. The cosine roll-off is better because it does not have a discontinuity at the edges. A larger extrapolation results in a smoother transform. The standard practice would be to use windowing which

[1] $\sqrt{(A+\cos(\omega t))^2+(B+\sin(\omega t))^2} = \sqrt{A^2+B^2+1+2A\cos(\omega t)+2B\sin(\omega t)} = \sqrt{A^2+B^2+1+K\cos(\omega t-\phi)}$. A and B are the offsets in the cos and the sin channels respectively. $\phi = \tan^{-1}\frac{B}{A}$ and $K = 2\sqrt{A^2+B^2}$.

[2] In a DFT algorithm the patch being transformed is treated as being periodic.

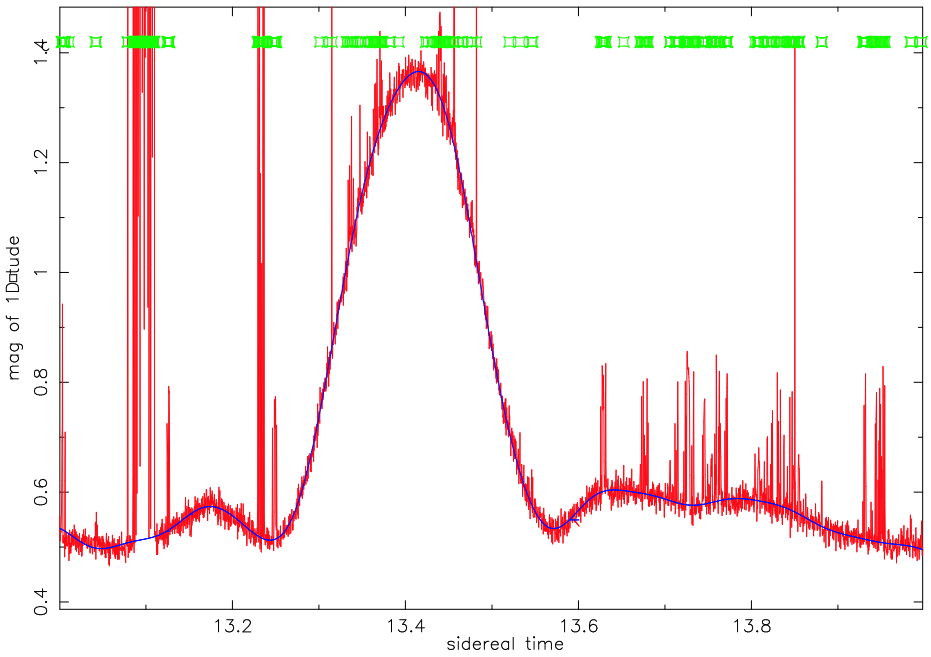

Figure 4. Interference detection on the *sum of magnitudes*: Detected interference points are marked out. Overlaid on the data is the fit to the data after removal and interpolation of the interference points from the *sum of magnitudes*.

would require data before and after the patch over which we are trying to detect interference. Using the 'smoothing' extrapolation we are able to process any size of data.

3. Response due to a strong source partially appearing at the beginning or at the end of a patch being processed will have a rate of change much higher than that expected from the sky and therefore would get removed as interference. This is prevented by increasing the length of the extrapolating function at the edge whenever a source of significant strength ($\geq 30\sigma$ in the *sum of magnitudes*) is encountered at the edge of a patch being processed.
4. An upper-cutoff and a lower-cutoff level are introduced based on *a priori* information of the highest and the lowest levels of the signals from the sky being processed. Any data point which is larger than, or less than, the limiting value is expunged from the data before any filtering is carried out. This reduces the time to process interference detection as the number of iterations are greatly reduced. The cut-off levels for any sidereal time take into account the changes in the Sun's right ascension.
5. We examined the difference between *sum of magnitudes* of two days (same trolley allocation) after removal of interference and interpolation to look for slowly varying interference not detected by our procedure.
6. As a final measure, the *sum of magnitude* plots after interference removal and interpolation are visually inspected and any suspicious looking data are manually identified.

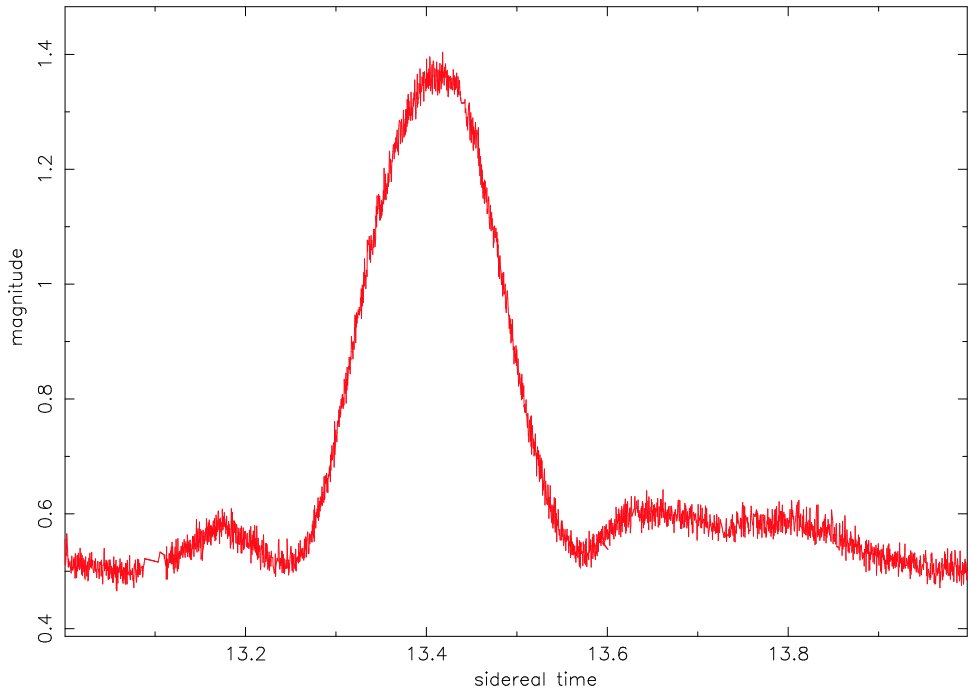

Figure 5. *Sum of magnitudes* after removal of interference and interpolation.

At the MRT, programs have been developed to implement the above algorithm (Sachdev 1999). The process of interference detection has been automated (except steps 5 and 6) and is carried out at the end of each sidereal hour. An example of the different stages in interference detection is shown in Fig. 3 with the column on the left showing the *sum of magnitudes* and the column on the right showing the corresponding 'difference' data. Fig. 4 shows all the interference points which have been detected. The *sum of magnitude* after removal of the interference points and interpolation is shown in Fig. 5.

5. Statistics of detected interference

We have data from observations over a year and have carried out interference detection on this data. We now look at the statistics of the detected interference.

- A typical histogram of the number of interference points against their strengths is shown in Fig. 6. From the histogram we note that most of the interference points have strengths less than 100σ ($\approx 85\%$). We find $N \; \alpha \; K^{-0.8}$, where N is the number of interference points with a strength K σ.
- Figure 7 is a histogram of interference points against strength of interference up to 500σ. The number of interference points do not fall monotonically and occasionally there is a large number of interference points at around 70σ and 100σ.
- Figure 8 shows the number of interference points against the number of consecutive seconds an interference lasts. We see that the largest number of interference

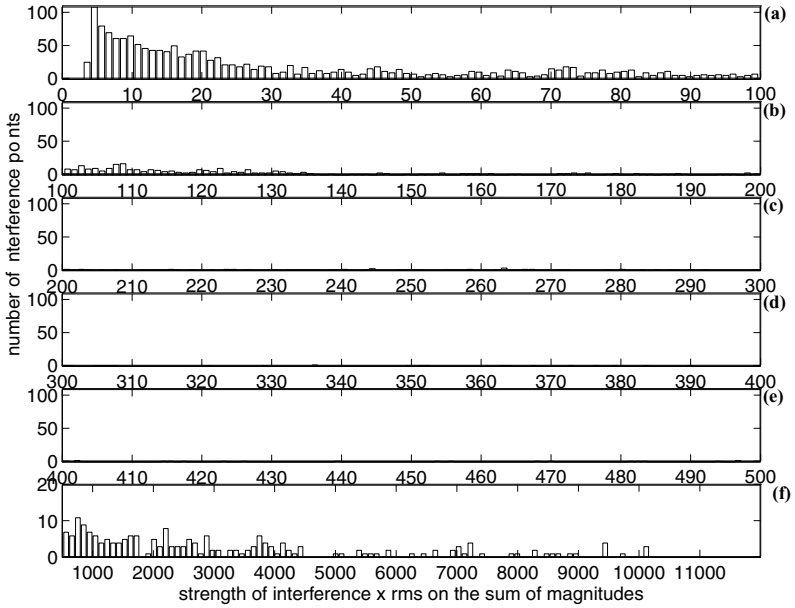

Figure 6. Histogram of number of interference points versus the strength of interference. All plots have 100 bins. **(a)** up to 100σ **(b)** from 100σ to 200σ **(c)** from 200σ to 300σ **(d)** from 300σ to 400σ **(e)** from 400σ to 500σ (f) from 500σ to max interference level

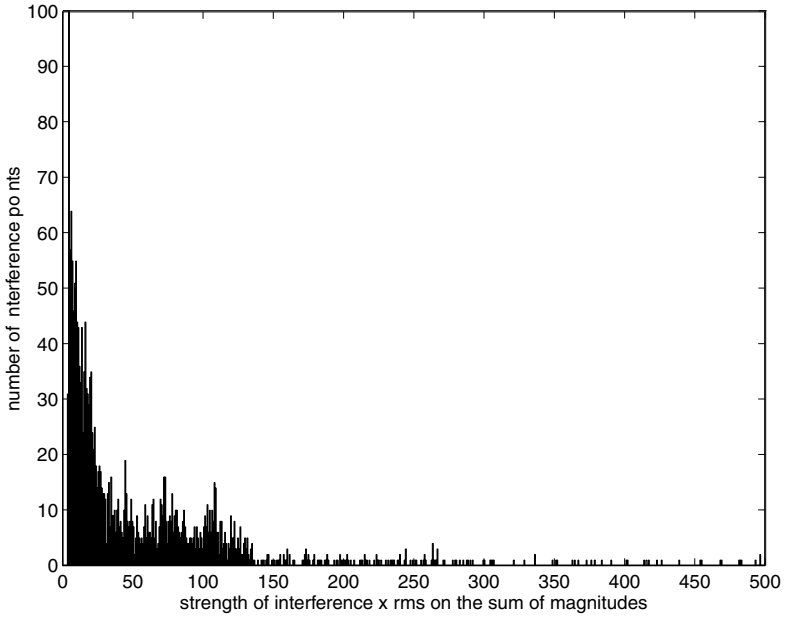

Figure 7. Histogram of number of interference points versus the strength of interference up to 500σ.

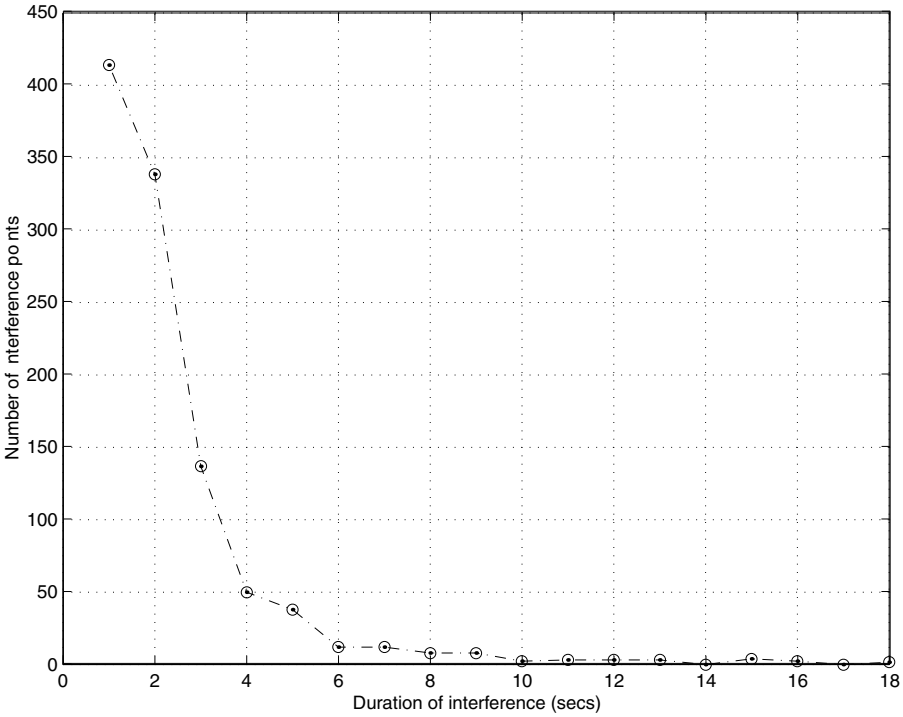

Figure 8. Statistics of the duration of interference.

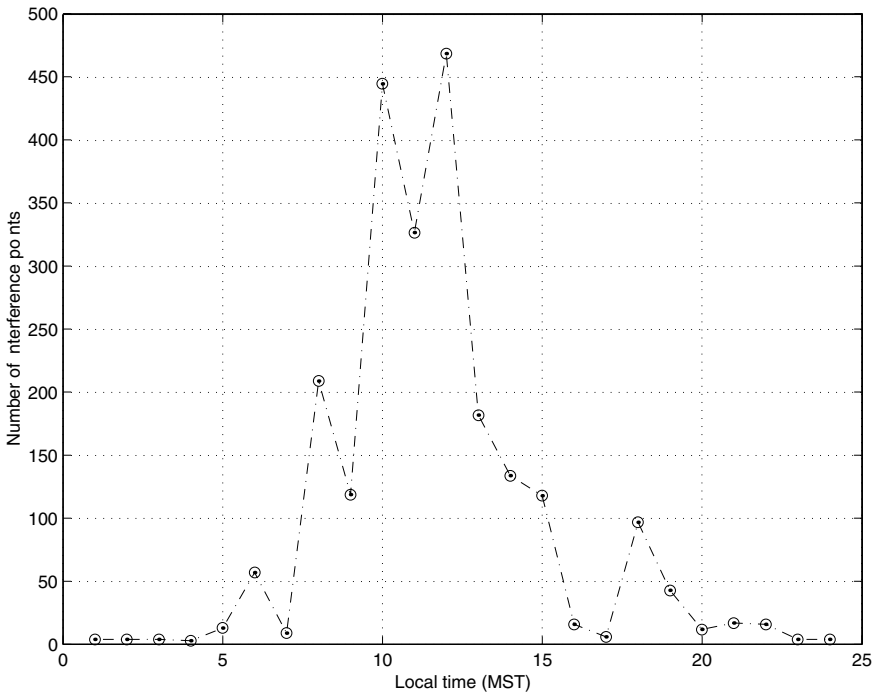

Figure 9. Number of interference points with MST.

occur for shorter durations ($\approx$ 80% with duration less than 6 seconds). There are generally less than 20 instances in the full 24 hours when the interference lasted 6 consecutive seconds. These statistics indicate that very often the interference excision can be carried out while post integrating the visibilities by giving a zero weighting to the interference points.

- A typical plot of number of interference points against local time (MST) in a given day is shown in Fig. 9. The interference is mostly during the day and is between MST 8:00hrs and 15:00hrs. These are the industrial working hours in Mauritius. This therefore indicates that interference is linked to the local industry.
- Figure 10 shows the number of interference points on different days during the observing period. We don't see any particular trend in the number of interferences over the year. A better indicator of any trend would require an analysis of statistics of a larger number of days.

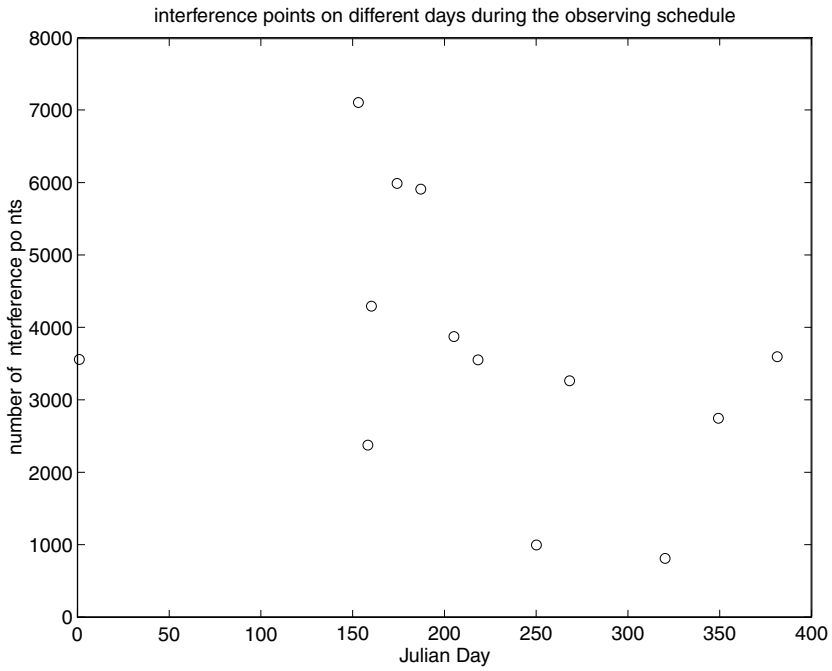

Figure 10. Number of interference points on different days during the observing schedule.The last three digits of the Julian Day are shown. The 0 on the x-axis corresponds to Julian day 2450150.

- We have found that the interference is reduced on Sundays and on other public holidays. As seen from Fig. 10, on Sunday the number of interference points could be as low as 1% of the data collected while it could be around 10% on other days.
- We note that we do not have any frequency information of the interfering signals. However we have found that the interfering signals are correlated in visibilities measured with different delay settings. The extent of the delay to which the interference is correlated gives an estimate of its bandwidth. Our measurements indicate that the interference is narrow-band ($\approx$ 10 kHz).

6. Interference excision

The raw data are not modified by the interference detection programs. The right ascension of the detected points are stored in a file and this information on interference is used in the subsequent calibration and imaging programs. As mentioned in the section on the observations, the visibilities are recorded with one second integration. While estimating the complex antenna gains, the file containing interference information is used to give zero weighting to the visibilities affected by interference. The measured visibilities are calibrated using the complex antenna gains estimated in the calibration process. The calibrated visibilities are box-car averaged for 4 seconds. Interference excision is incorporated at this stage by giving zero weighting to the points affected by interference. The averaged visibilities are phased appropriately to get an image on the meridian. The images of different days so obtained are precessed to a common epoch and then added. To obtain an optimum signal-to-noise ratio the images are convolved in the right ascension with a sinc function having a FWHM of 16 seconds in time. This is the FWHM in RA of the expected PSF of MRT in EW $\times$ S mode at zero degree declination. The simplicity of the method is due to the effective way the statistics of interference are used in its excision.

7. Conclusion

With the increasing demand for the commercial usage of the electromagnetic spectrum, it is becoming difficult to carry out radio astronomical observations, especially at low frequencies. In this environment it is most profitable to study the nature of interference at different observatory sites and develop techniques to obtain maximum interference-free observations or mitigate interference in the data recorded.

We have successfully developed a technique to detect man-made interference in the visibility data of MRT. This is a filtering technique based on the assumption that the interference is generally 'spiky' in nature and has Fourier components beyond the maximum frequency which can arise from radio sky and can therefore be identified. We take the sum of magnitudes of visibilities on all the baselines measured at a given time to improve detectability. The raw data are not modified by the interference detection programs. The right ascension of the detected points are stored in a file and this information on interference is used in the subsequent calibration and imaging programs. We have carried out statistical analysis of the interference detected. They indicate that most of the interference have strengths less than 100σ ($\approx$ 85%). The interference is largely during the day (MST 8–15 hours) and is linked to the local industry. A large fraction $\approx$80% of the interference occurs for durations less than 6 seconds. There are generally less than 20 instances in the full 24 hours when the interference lasted 6 consecutive seconds. This indicates that very often the interference excision can be carried out while post integrating the visibilities by giving a zero weighting to the interference points. The level of undetected interference is of the order of the noise in the final image. This, in terms of flux density is $\approx$100 mJy.

Acknowledgements

The MRT is operated jointly by the Raman Research Institute, Indian Institute of Astrophysics, and the University of Mauritius. We thank A. A. Deshpande, RRI for the many discussions we had with him.

References

Golap, K., Udaya Shankar, N., Sachdev, S., Dodson, R., & Sastry, Ch.V. 1998 A Low Frequency Radio Telescope at Mauritius for a Southern Sky Survey, *J. Astrophys. Astr.*, **19**, 35.

Handbook On Radio Astronomy, 1995, (Geneva: Radiocommunication Bureau).

Hogbom J.A.1974 Aperture Synthesis with a Non-Regular Distribution of Interferometer Baselines *Astrphys. J. Suppl. Ser.*, **15**, 417.

Sachdev. S., 1999, *Wide Field Imaging with the Mauritius Radio Telescope*, Ph.D. Thesis, Dept. of Physics, University Of Mauritius.

J. Astrophys. Astr. (2001) **22**, 229–249

Wide-Field Imaging With The Mauritius Radio Telescope.

S. Sachdev[1,2] & N. Udaya Shankar[1,2].
[1] *Raman Research Institute, Sadashivanagar, Bangalore 560080, India*
[2] *Department of Physics, University of Mauritius, Reduit, Mauritius*

Received 2001 August 21 ; accepted 2001 October 16*

Abstract.

The Mauritius Radio Telescope (MRT) is a Fourier Synthesis T-shaped array operating at 151.5 MHz. The primary objective of the telescope is to produce a sky survey in the declination range -70° to -10°. A 512 channel digital complex correlation receiver is used to measure the visibility function. The visibilities have to be measured with four different delay settings to image the entire declination range, keeping the effects of bandwidth decorrelation to less than 20% on the longest baseline. To have a reasonable surveying sensitivity this has to be done in one observation schedule. However the existing correlator system which can measure visibilities with only one presettable delay setting for each integration time, cannot meet this requirement. A recirculator system which enables visibility measurements with four different delay settings in one integration time using the existing correlator has been designed and installed to make the MRT an efficient surveying instrument. This paper describes the recirculator system, and the scheme that we use at MRT to calibrate the visibilities measured with different delay settings. The observations carried out for the full sky survey and a section of the wide field image made using the new system are described in this paper.

Key words:

Radio Telescope - Fourier Synthesis - Bandwidth decorrelation - Bandpass sampling - Single Side band system

1. Introduction

Very few surveys of the southern sky exist at frequencies below 1 GHz, and none which are as deep as the 6C survey of the northern sky (Baldwin *et al* 1985). The Mauritius Radio Telescope (MRT) was built to fill this gap. It is a Fourier

*Although this paper was accepted only on 16 October, we have included it because this issue was delayed due to other reasons.

synthesis instrument operating at 151.5 MHz and is situated in the north-east of Mauritius at a southern latitude of 20°.14. The aim of the survey using the MRT is to contribute to the database of southern sky sources in the declination range $-70° \leq \delta \leq -10°$ covering the entire 24 hours of right ascension, with a resolution of $4' \times 4'.6 \sec(\delta + 20°.14)$ and a point source sensitivity of $\sim$200 mJy(3σ).

The MRT is a T-shaped non-coplanar array consisting of a 2048 m long EW arm and a 880 m long south arm. In the EW arm 1024 fixed helices are arranged in 32 groups and in the south arm 16 trolleys with four helices on each, which move on a rail are used. The primary beams of the helices have a full width at half maximum (FWHM) of 60°, and they are mounted with a tilt of 20° toward the south, i.e., the peak of the primary beam is at $\delta = -40°$. This allows a better coverage of the southern sky including the Galactic plane. The outputs of the EW and the south groups are heterodyned to an intermediate frequency (IF) of 30 MHz in the field, and are brought to the observatory building through coaxial cables. In the observatory, these outputs are further amplified and down-converted to a second IF of 10.1 MHz. These are then quantized to 2-bit 3-levels and sampled at 12 MHz. These are further processed in a 512-channel digital complex correlation receiver to measure the visibility function. The 512 complex visibilities are integrated and recorded at intervals of 1 second. At the end of 24 hours of observation the trolleys are moved to a different position so as to sample the NS baselines with a spacing of 1m and new visibilities are recorded. A minimum of 60 days of observing are needed to obtain the visibilities up to the 880 m spacing. A detailed description of the telescope is to be found in Golap *et al* (1998).

A large part of the back-end including the correlator system was acquired from the Clark Lake Radio Observatory (CLRO) (Erickson *et al* 1982). We adapted and modified the CLRO system for use at the MRT. The modified system was then installed and tested with the rest of the system in Mauritius. In this paper we describe the need for a recirculator system to make MRT an efficient surveying instrument. Section 3 describes its design criteria, the hardware developed and its interface to a computer. The method developed for the calibration of the visibilities measured with four delay settings is described in the section 4. The steps involved in the analysis of the recirculator data and a wide field image with its analysis are described in the section 5.

2. Recirculator System

Although the use of larger bandwidths results in a better sensitivity (for continuum observations) of a telescope, it restricts the field of view of the image if the relative delays between the signals being correlated are not compensated. The loss in sensitivity at the edges of the field is appreciable if delays (τ) are comparable to the inverse of the bandwidth. This effect, known as bandwidth decorrelation, is also referred to by other names like chromatic aberration and fringe washing.

In the MRT the EW group has a narrow primary beam of two degrees in RA.

To obtain interference free observations, we restrict the bandwidth to 1 MHz. This bandwidth does not pose a problem for synthesizing the primary beam in the RA direction. However both the EW and the north-south groups have wide primary beams in declination extending from -70° to -10°. We will, therefore, be concerned with compensating geometric delays for zenith angles along the meridian za_o. The delay can be compensated for a zenith angle along the meridian, $za_o^{'}$, by introducing a delay of $\frac{y_\lambda sin(za_o^{'})}{c}$ where y_λ is the baseline (in wavelengths) along the north-south direction. The correlation response around this point in declination, for a rectangular passband from $\left(\nu_o - \frac{\Delta\nu}{2}\right)$ to $\left(\nu_o + \frac{\Delta\nu}{2}\right)$, is then graded by $sinc(\Delta\nu\Delta\tau)$. $\Delta\tau$ is the uncompensated delay in the direction za_0 given by $\Delta\tau = \frac{y_\lambda}{c}\left(\sin(za_o) - \sin(za_o^{'})\right)$ Thompson *et al* (1986). For a given delay compensation, we will be able to observe only a part of the sky with small decorrelation. This is referred to as the delay zone around the point at which the geometrical delay has been compensated. Our design goal is to image the declination range $-70^{\circ} \leq \delta \leq -10^{\circ}$, using a 1 MHz band keeping the bandwidth decorrelation to less than 20 % even on the longest north-south baseline. This requires visibility measurements with four delay settings.

The existing system measures visibilities with only one delay setting. Thus one has to collect data for different delay zones on separate days. So the number of days required to collect a set of data for survey would increase, thereby reducing the surveying sensitivity[1].

A minimum of 60 days of observing are needed to obtain the visibilities up to the 880 m spacing. We measure the visibilities on a given allocation for about 3 sidereal days to ensure interference free data. It therefore takes 180 days to obtain data for all the baselines. However, during this time the Sun moves through half the sky (12 hours in right ascension) thereby preventing full sky coverage with the 6 month data. We therefore carry out the observations in two rounds. In the second round we observe the same NS baselines after about 6 months interval. This ensures that we have night time observations for all the NS baselines.

Measurement of visibilities with four different delay settings on separate days makes the total time required for acquiring data for the survey to be of the order of four years. This would make the MRT a very inefficient surveying instrument.

Thus there is a need for a system which will allow visibility data to be collected for different delay zones on the same day without degradation in sensitivity. This requires a system which would store the samples for T seconds followed by a correlator system that would measure visibilities with each delay setting in $\frac{T}{N}$ seconds. Such a system wherein the data is sampled and stored at a slower rate and then facilitates the correlator to process data N times faster is called a recirculator. To implement this, a dual-buffer memory system is employed between the sam-

[1] Surveying sensitivity is the minimum flux density detectable in a survey of a particular region when the whole survey is completed in a total time t_s seconds. The sensitivity is expressed in terms of t_s rather than t, the time spent on the measurement in any one particular direction.

pler and the correlator. The data from the sampler is stored at a given rate in one bank while the data from the other bank is read and processed N times faster in the correlator. Figure 1 represents the basic principle of a recirculator system.

3. Design Criteria

The MRT receiver system provides an option of using 3.0 MHz, 1.5 MHz, 1 MHz and 0.15 MHz IF bandwidths. One would generally be interested in using the widest band available for more sensitivity. Higher sensitivity would also improve our calibration because we would be able to use weaker and therefore more number of sources for calibration. However, for wide field imaging the bandwidth decorrelation effect (described in the previous section) becomes more severe. Thus, a larger bandwidth would imply measurements of correlations at a larger number of delays to cover a large field of view.

In this section we discuss the choice of bandwidth used, the sampling frequency employed and the size of memory buffers used, and discuss the specifications and criteria for the design of a data acquisition system.

3.0.1 *Choice of bandwidth*

We begin by determining an appropriate bandwidth for use to maximize surveying sensitivity, given that we intend to map 60° of the sky using a correlator system which can work with clock rates of up to 12 MHz. Furthermore, we start with a design goal of letting the maximum loss due to bandwidth decorrelation to be 20% on the longest baseline.

The surveying sensitivity (Christiansen *et al* 1969), SS_{min}, is defined as:

$$SS_{min} = \sqrt{N_D} f_{os} \frac{\sqrt{2}\, 2k_B(\sqrt{T_{sys_{EW}} T_{sys_{NS}}})}{\sqrt{N_b} A_e \sqrt{\Delta\nu t}} \tag{1}$$

where f_{os} is the degradation factor for a digital correlator, N_D is the number of days required to cover the complete zenith angle range, $T_{sys_{EW}}$ and $T_{sys_{NS}}$ are the system temperatures of EW and NS groups respectively. N_D is given by:

$$N_D \geq int\left(\frac{N_{zn}}{N_{del}}\right) \tag{2}$$

where N_{zn} is the number of delay settings needed to cover the required zenith angle range, N_{del} is the number of delays with which the correlations can be measured using a correlator system that can run up to a maximum frequency of f_{corr}^{max} and *int* denotes the integer part of its argument.

N_{zn} depends on the delay range of interest, τ_{range}, and the maximum allowed decorrelation loss, x_{max}, and may be expressed as

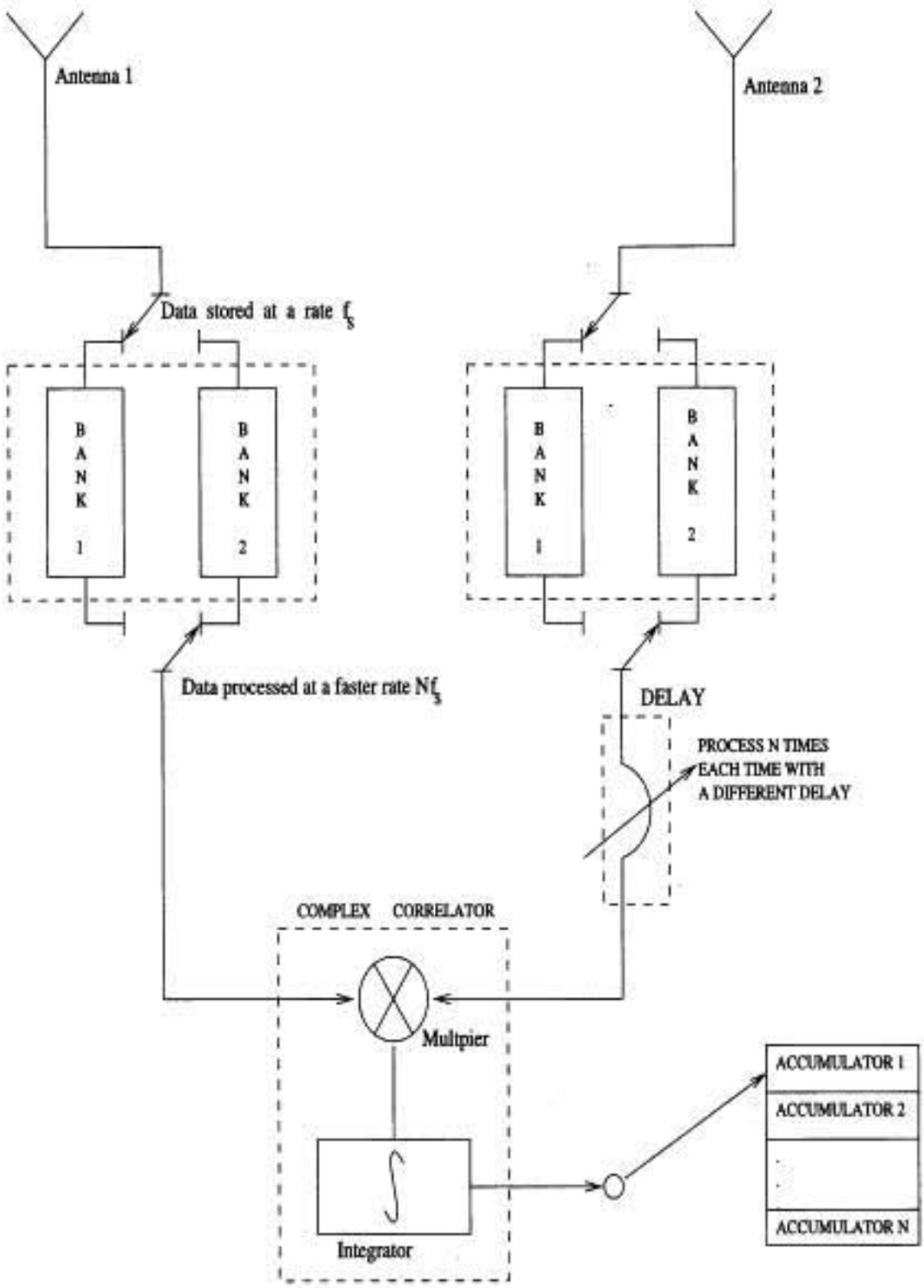

Figure 1. Schematic showing the basic principles of a recirculator. Data is stored at a rate f_s in a dual-buffer memory and is read out and processed at a rate Nf_s in the correlator, allowing data to be processed N times, each time with a different delay compensation.

$$N_{zn} \geq int\left(\frac{\tau_{range}\Delta\nu}{2sinc^{-1}(1-x_{max})}\right) \tag{3}$$

while N_{del} is given by

$$N_{del} \leq int\left(\frac{f_{corr}^{max}}{2\Delta\nu\,\eta}\right) \tag{4}$$

where η is the oversampling factor and $\Delta\nu$ is the bandwidth used.

We therefore note that for a given array, the surveying sensitivity depends upon the following:

(a) the bandwidth used ($\Delta\nu$).

(b) the delay range to be imaged (τ_{range}).

(c) the maximum decorrelation allowed (x_{max}).

(d) the maximum clock speed at which the correlator works (f_{corr}^{max}).

(e) the oversampling factor (η) and the degradation factor f_{os}.

The following have to be considered in obtaining an optimal surveying sensitivity.

(i) The sensitivity obtainable increases as the square-root of the bandwidth. However, the number of days required may increase with the bandwidth. These two factors affect the surveying sensitivity contrarily.

(ii) The sampling frequency has to be set considering

(i) the bandpass sampling criterion.

(ii) that the harmonics of the sampling clock should not fall inside the RF and first IF bands because these can cause spurious correlations.

(iii) The sensitivity also increases to a certain extent with larger oversampling factor for correlators with limited number of bits. However, a larger oversampling factor could reduce the number of delays covered with recirculation for a given correlator speed. This would increase the number of days required, and hence, reduce the surveying sensitivity.

Let us look at items (ii) and (iii) in more detail:

- For a bandpass signal, we need to sample keeping in mind the criterion for bandpass or harmonic sampling.

  The permissible sampling frequencies for a bandpass signal must satisfy the following criterion to avoid loss in sensitivity due to aliasing (Das *et al* 1986).

$$\frac{2}{n}\frac{f_h}{(f_h - f_l)} \leq \frac{f_s}{(f_h - f_l)} \leq \frac{2}{n-1}\left(\frac{f_h}{(f_h - f_l)} - 1\right) \tag{5}$$

where n is an integer such that $1 \leq n \leq \frac{f_h}{f_h - f_l}$, f_h and f_l being the highest and lowest frequencies in the bandpass. In Figure 2 the areas in between a broken line and the next solid line represent permissible sampling regions.

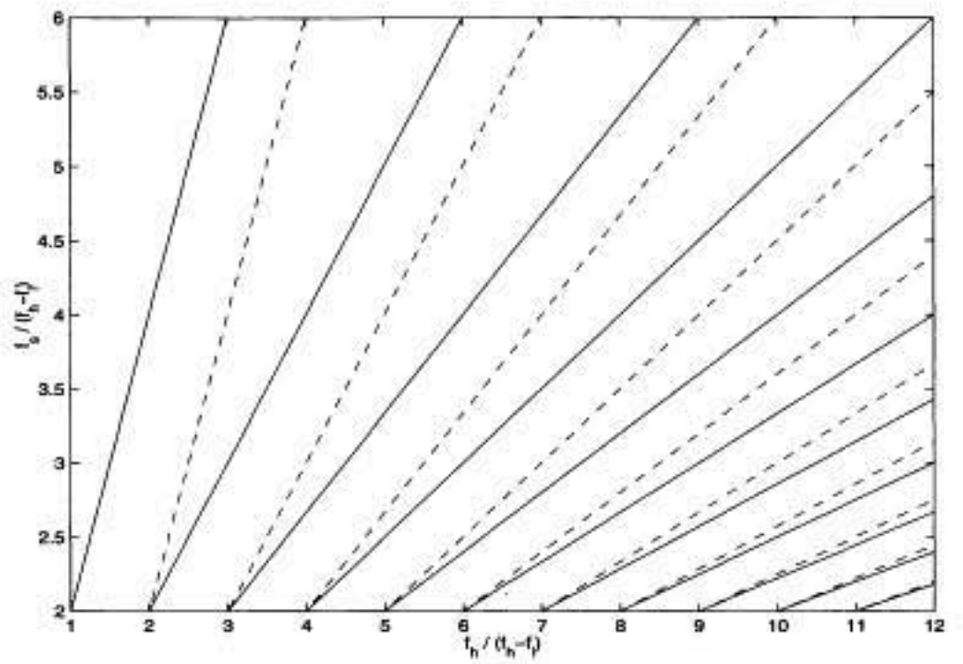

Figure 2. Bandpass sampling criteria: the areas between a broken line and the next solid line represent permissible sampling regions.

- The sampling frequencies that do not have harmonics in the RF (151.5 MHz) and first IF (30 MHz) signal bands.

  The basic system clock may have to be adjusted so that the harmonics of the sampling clock and other clocks used in the system do not fall in the 1 MHz bands about 151.5 MHz and 30 MHz. Harmonic pick-ups on the IF path (30 MHz) which vary faster than the LO switching period would cause spurious correlations and therefore need to be also considered. The duty cycle of the sampling clock also needs to be taken into account because the harmonic contents of the sampling clock depends on it.

- Dependence of sensitivity on the oversampling factor.

  A digital correlator has a lower sensitivity compared to that of an unquantized analog correlator. A band-limited signal that is quantized results in the generation of new frequency components in the waveform, In a digital correlator by sampling at rates higher than the Nyquist rate corresponding to the unquantized waveform, the loss of sensitivity can be reduced.

The dependence of the degradation factor, f_{os}, which is basically the deterioration of sensitivity (Klingler 1972) of a 3 × 3 correlator on the sampling rates is shown in Figure 3.

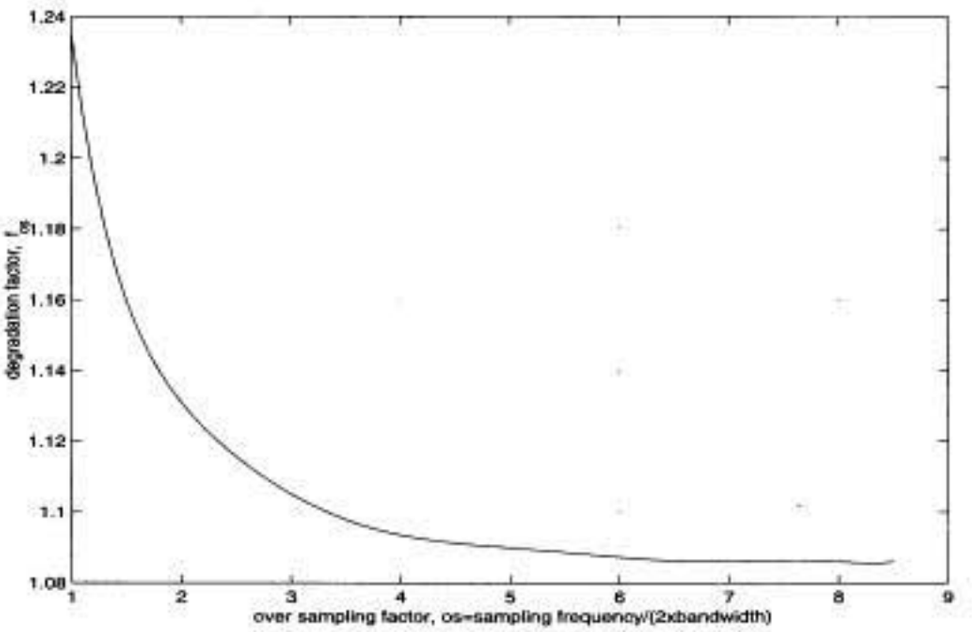

Figure 3. Degradation factor, f_{os}, versus over-sampling factor, η, for a 3 × 3 correlator (Klingler 1972)

We now calculate the surveying sensitivity obtainable with the MRT as a function of bandwidth to cover the full 60° ($-70° \leq \delta \leq -10°$) using a correlator system working at 12 MHz and allowing a maximum decorrelation of 20% on the longest baseline. We normalize the surveying sensitivity with that obtained using a 4 MHz bandwidth which would require 16 days of observations to cover $-70° \leq \delta \leq -10°$ with decorrelation not exceeding 20%. We choose 4 MHz to normalize the surveying sensitivity because this is the maximum bandwidth centered at 10 MHz that we can use with a sampling frequency of 12 MHz. Therefore the normalized surveying sensitivity may be represented as:

$$SS_N = SS_{min} / \left(\frac{1}{1.23} \sqrt{\frac{4 \text{ MHz}}{16 \text{ days}}} \right) \tag{6}$$

where 1.23 is the degradation factor (obtained from Figure 3) for Nyquist sampling in a 3×3 correlator system. The plot of normalized surveying sensitivity is shown in Figure 4.

The plot of surveying sensitivity against bandwidth is not a smooth curve. This is because at some bandwidths the number of days required to cover the entire declination range changes abruptly. From this plot we find that a bandwidth of about 1.1 MHz gives us the best surveying sensitivity. This requires 4 delay settings

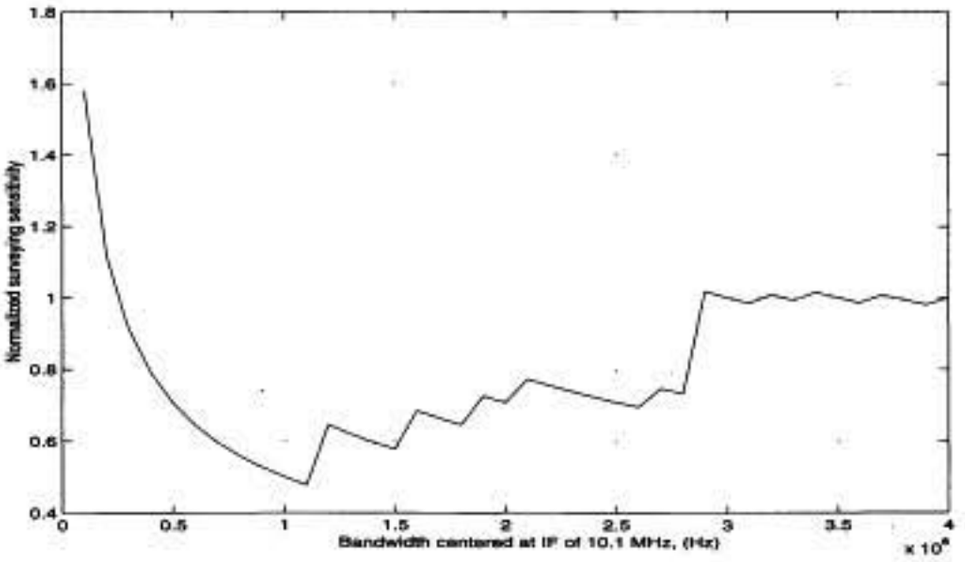

Figure 4. Normalized surveying sensitivity using different bandwidths to image $-70° \leq \delta \leq -10°$ with a 512-channel complex correlator which can work with a maximum clock frequency of 12 MHz.

($N_{del} = 4$), one day ($N_D = 1$) and an oversampling factor of 1.08 ($\eta = 1.08$). The bandwidth which gives surveying sensitivity closest to the above criterion is provided by the 1 MHz filters in the MRT receiver system. So even though the existing system can be used with a 3 MHz bandwidth, for surveying the declination range $-70° \leq \delta \leq -10°$ with the best surveying sensitivity using a 512-channel complex correlator system which can work with a maximum clock frequency of 12 MHz, we use a bandwidth of 1 MHz. This also satisfies our design goal of ensuring that the maximum loss of sensitivity due to bandwidth decorrelation on the longest baseline is 20%. The delay beam of the array which takes into consideration all the interferometers used for imaging will have a lower decorrelation in the different delay zones.

3.0.2 *Choice of sampling frequency*

The plots in Figure 5 show the allowed sampling frequencies according to different criteria for a band of 1 MHz centered at 10 MHz and sampled by a clock with 25% duty cycle, i.e., every fourth harmonic is suppressed. We see in Figure 5(a) the allowed sampling frequency according to the bandpass criterion for a 1 MHz band centered at 10 MHz. Figures 5(b) and 5(c) show the sampling frequencies which do not have harmonics within the 1 MHz band centered at 30 MHz and 151.6 MHz respectively. Figures 5(d) shows the maximum frequency usable to be 3 MHz to allow visibility measurements with four delay settings using a correlator that can work up to a clock frequency of 12 MHz. These different criteria are

finally ANDed to get the permissible sampling frequencies. Figure 5(e) shows the permissible sampling frequencies.

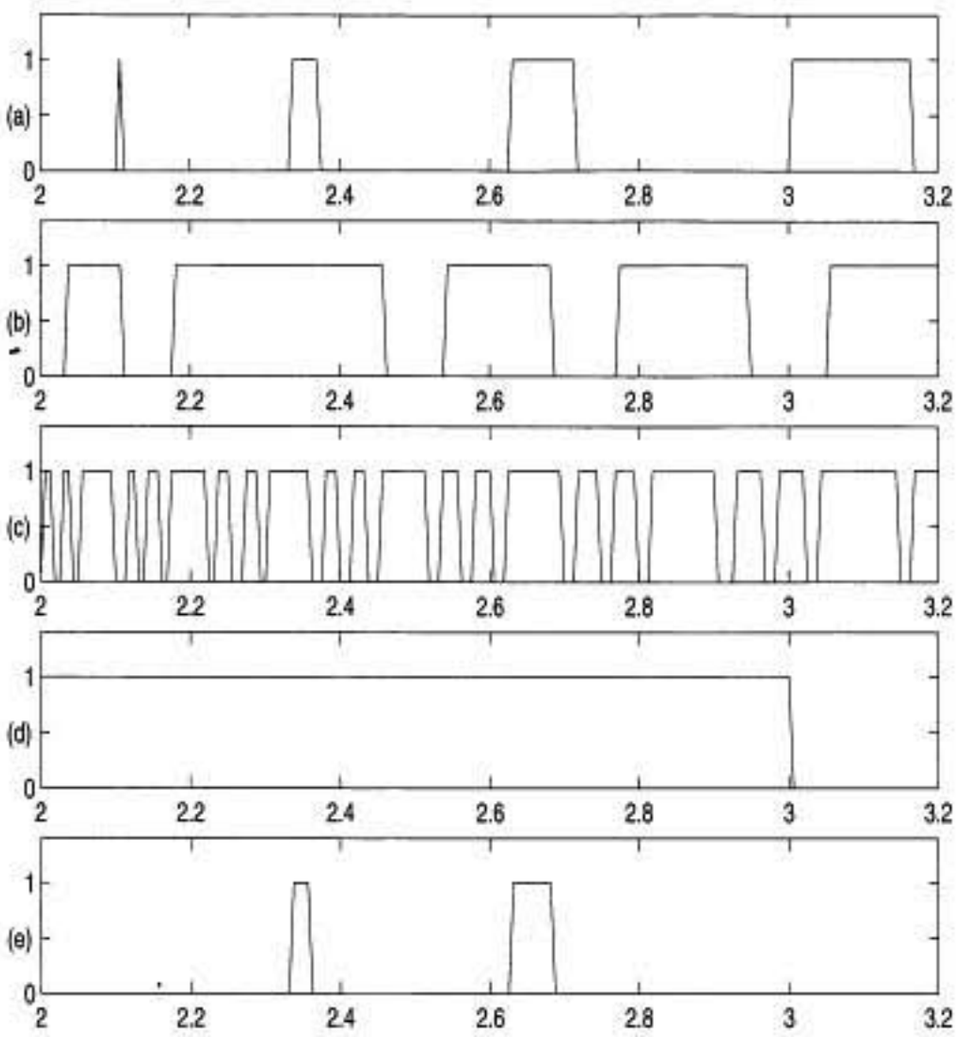

Figure 5. The above plots show the allowed sampling frequencies (a) according to the bandpass criterion for a 1 MHz band centered at 10.1 MHz. (b) which do not have harmonics within the 1 MHz band centered at 30 MHz (c) which do not have harmonics within the 1 MHz band centered at 151.5 MHz (d) for recirculating the data 4 times for the four delay zones using a 12 MHz correlator system (e) obtained after ANDing (a), (b), (c) and (d)

From Figure 5(e), we note that there are two permissible frequency ranges. One extends from 2.3333 MHz to 2.3750 MHz and the other from 2.6250 MHz to 2.7143 MHz. To get better sensitivity we chose a frequency in the higher band, i.e., in the range 2.6250 MHz - 2.7143 MHz. We finally chose a sampling frequency of 2.65625 MHz which is almost at the center of this allowed range of frequencies.

3.0.3 *Choice Of Memory Size*

The size of the memory available on the correlator boards is not enough to take care of the 4 delay zones. Thus it is necessary to transfer the integrated correlation values of each zone to an external memory and then process the other delay zone. The

size of the external RAM would be determined by the integration period required on the correlator boards.

The correlator system at present can output the required 1088 words (512 complex correlations and 64 self-correlations) in about 11 ms ($2^{13} \times 2^4$ clock cycles at 12 MHz $\approx$ 11 ms). For an 11 ms integration period, one needs an external RAM of size 128 K. Thus we undertook the design of a recirculator with external dual memory buffers each of 128 K.

3.1 *Hardware description*

The recirculator system is designed as a modular system consisting of several identical recirculator boards and a central control board for the generation of control signals. The block diagram of a recirculator board is shown in Figure 6.

The recirculator boards have the facility to select :

1. The number of delay zones. These are programmable to 2, 3, or 4 zones. This simultaneously selects the resampling frequency and the integration period.

2. Operation in bypass mode: the data in this mode does not go through the memory of the recirculator.

3. Operation in test mode: In the test mode, test data may be introduced into the recirculator system to test the working of an individual recirculator board. Test data is introduced through the test-buffer on the recirculator boards.

4. Operation in autocorrelation mode: This mode allows the correlator system to be used as a 128 channel auto-correlator directly and with some additional hardware, we can use it as a 4096 channel auto-correlator using the recirculator. The data for the autocorrelation is introduced through the auto-buffer on the recirculator boards.

5. The correlator can be configured in EW and NS fan beam configuration (NS+W)$\times$ NS and (E+W)$\times$E. With the recirculator one can observe in these modes in a time multiplexed mode with (E+W)$\times$S (pencil beam configuration).

3.1.1 *Design criteria for a Data Acquisition System (DAS)*

A PC based design was preferred, since it requires lesser implementation time. At the MRT site, 80386 PCs with ISA bus were readily available. Using a single PC, we were not able to complete all the steps of acquisition such as programming the delays every 11 ms, acquiring the 1088 words of correlation values, integrating them, acquiring the time information from a sidereal clock and then writing to the hard drive once every second. Therefore a data acquisition system employing a dual memory buffer shared by two 80386 PCs running on DOS were used. While one PC acquires and integrates the data onto one bank, the other PC has enough

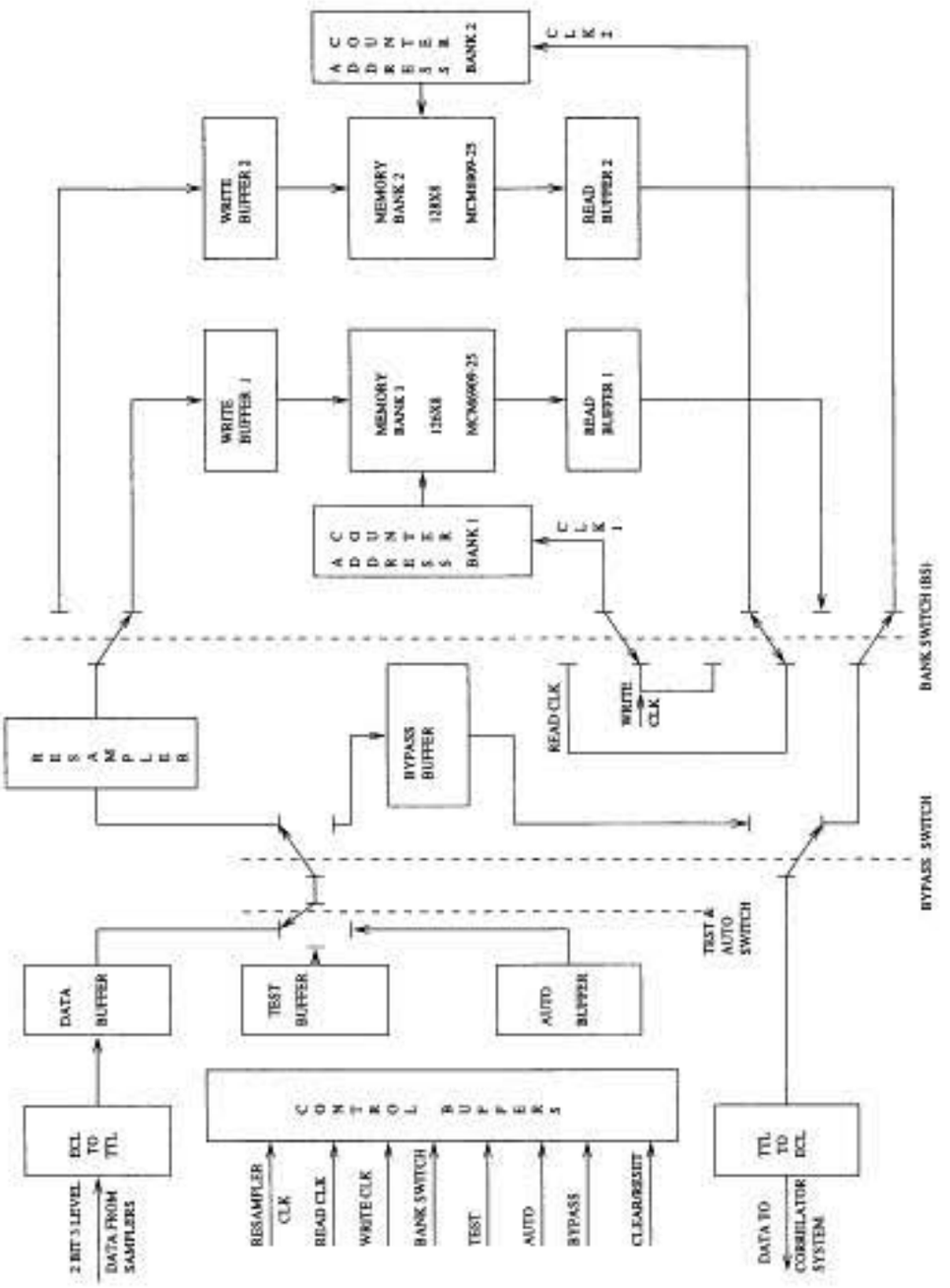

Figure 6. Block diagram of the MRT recirculator board.

time to transfer the data to the hard drive. The block diagram of the control and data acquisition system is shown in Figure 7.

3.2 *System tests*

The system was debugged using static inputs, carrier wave and noise signals as inputs. Finally, data on actual observations of the calibrator source MRC 1932-464 were used to compare the images made using the recirculator data with that

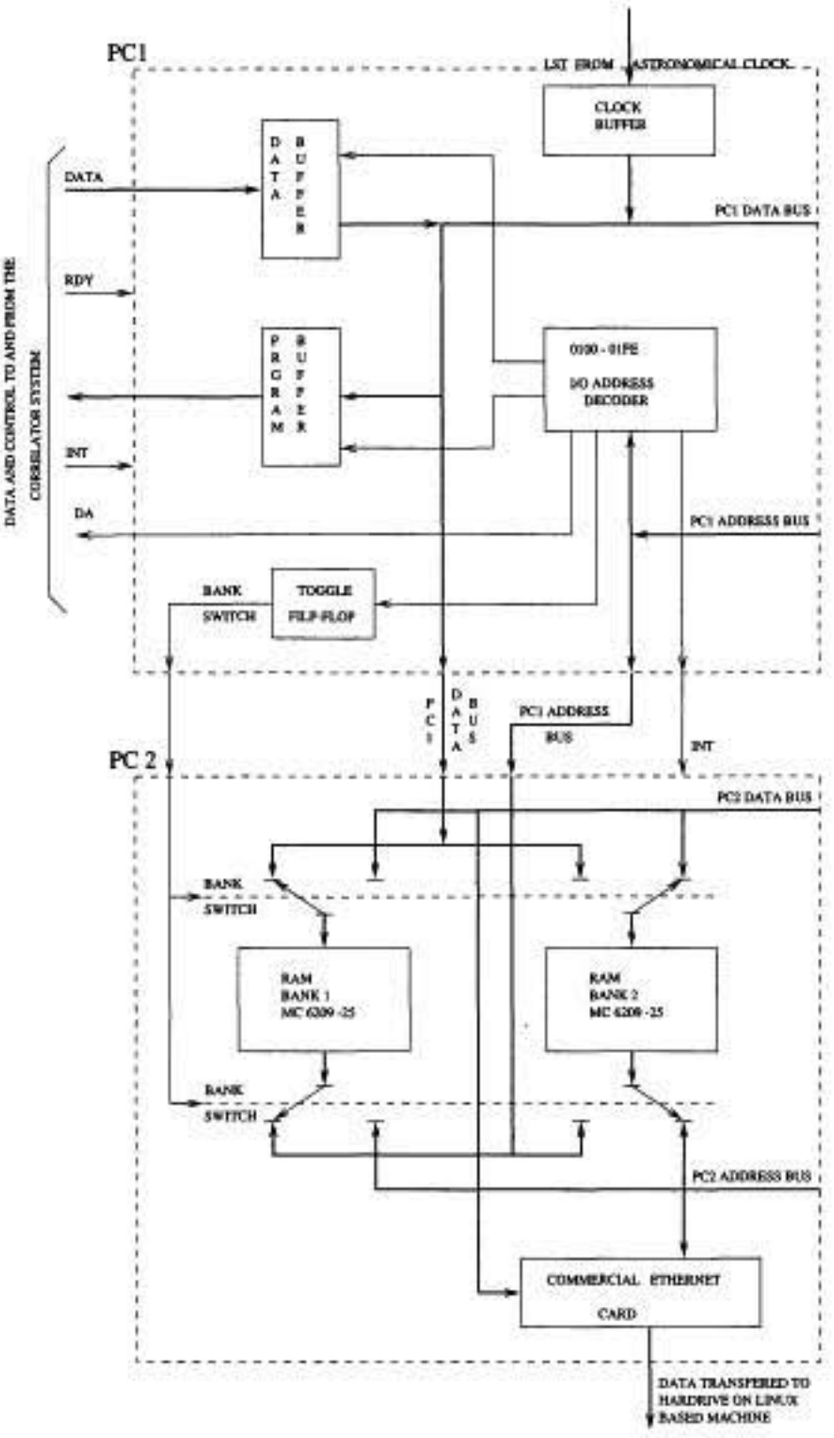

Figure 7. Block diagram of the control and data acquisition system.

obtained without the recirculator. We found the deterioration in the signal-to-noise ratio due to the recirculator to be less than 10%. Since the delays were identical in the two cases, the change in S/N expected was due to the reduced sampling from 12 MHz to 2.65625 MHz. This is of the order of 10%.

These tests and comparisons indicated satisfactory performance of the hardware systems developed.

4. Delay Zone Calibration

The recirculator system was designed to observe with different delay settings. Each delay setting maximizes the correlation in a given range of declination, which is called a delay zone. For imaging different delay zones, one has to calibrate visibilities measured with different delay settings. An ideal calibration scheme would be one in which we use separate calibrators in each declination zone. However we do not have sufficient number of strong calibrators in the southern sky to calibrate the visibilities in the different delay zones. Hence we were forced to use the complex antenna gains estimated for one zone, in which we have a strong calibrator, to calibrate the other zones.

The interferometer setup at MRT is shown in Figure 8. All the relevant equations for this interferometer are also given in this figure. The correlator response $C(\tau)$ of an interferometer obtained by integrating (Fomalont *et al* 1974) the single frequency response over the cross power spectrum may be written as:

$$C(\tau) = \gamma(|\tau_D - \tau|)|G|e^{j(2\pi\overline{\nu_{if}}(\tau_D-\tau)-2\pi(lo_1+lo2)\tau+\phi)} \quad (7)$$

where τ is the geometrical delay, τ_D is the compensating digital delay and $\gamma(|\tau_D - \tau|)$ is the bandwidth decorrelation term (fringe washing term). lo_1 and lo_2 are the first and the second local oscillator frequencies respectively. G is the complex gain of the interferometer expressed in terms of the magnitude $|G|$ and the phase ϕ_{inst}, i.e., $G = |G|e^{j\phi_{inst}}$. $\overline{\nu_{if}}$, is the centroid of the cross power spectrum.

From Equation 7 we see that a discrete change of τ_D produces a phase change equal to $2\pi\overline{\nu_{if}}\tau_D$. This result is used in estimating the complex antenna gains in all delay zones by instrumental calibration of any one of the zones with a strong calibrator.

4.0.1 *Measurement of the cross power spectrum*

We were concerned at the time of the design of the recirculator system about the possibility of unequal IF bandshapes of different antennas leading to variations in the centroids of different interferometers. Such variations limit the accuracy and the sensitivity of the instrument. We carried out measurements of the cross power spectrum of the 512 channels employed for synthesis to calculate the variations in the centroids.

The cross power spectrum is the Fourier transform of the cross correlation function[2]. This was measured using the recirculator system configuring the correlator in the auto/cross correlation mode. The distribution of the 512 band-centroids obtained are shown in Figure 9. It has a mean of 10.1 MHz and an RMS of 0.031 MHz. The measurement of the band-centroids was repeated four times at intervals of about 10 days. No noticeable changes in the band-centroids were seen.

[2]The cross correlation of two waveforms V_1 and V_2 is defined as $\int_{-\infty}^{\infty} V_1(t)V_2^*(t-\tau)\mathrm{d}t$

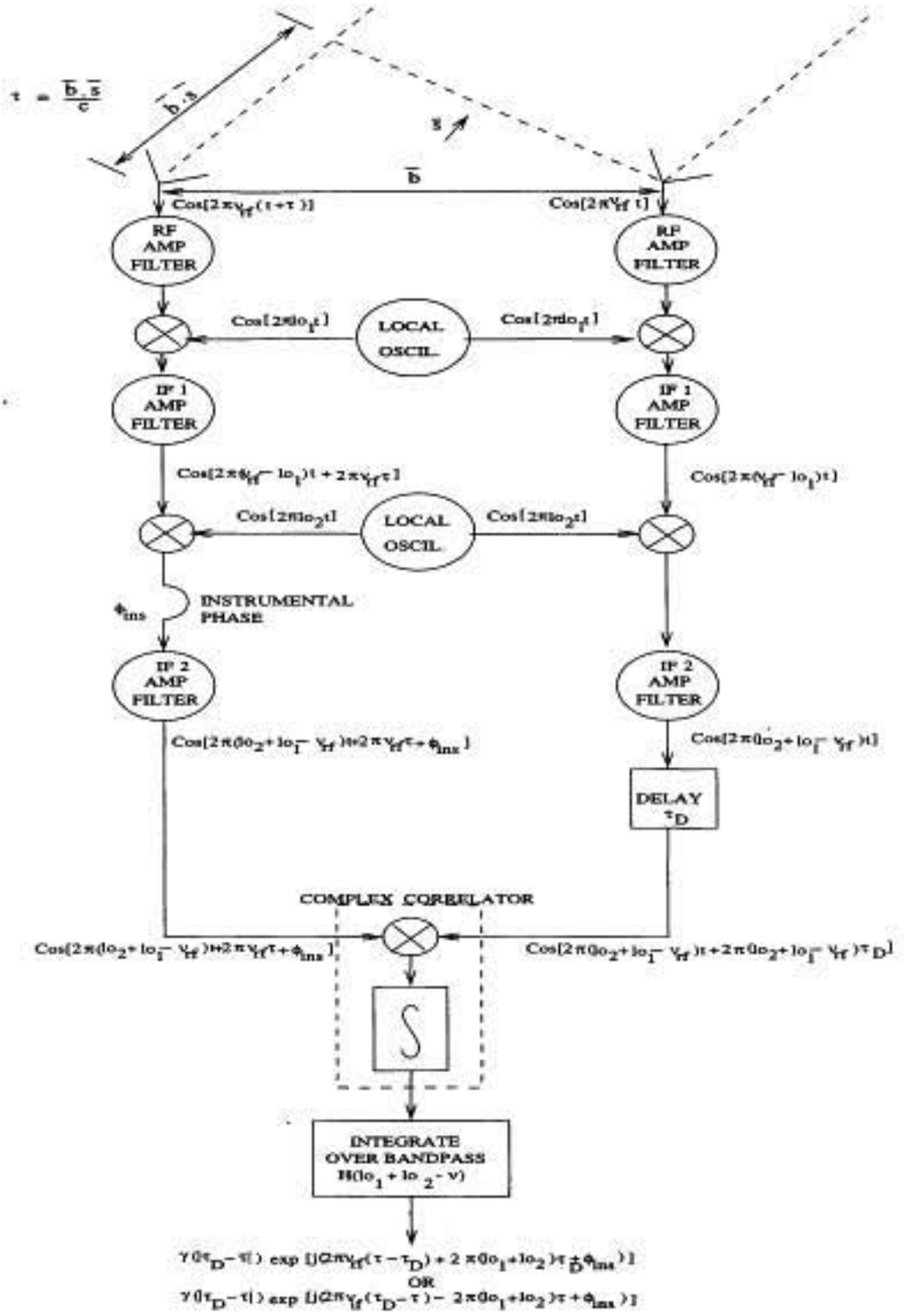

Figure 8. Schematic of the interferometer at the MRT.

The instrumental phase in two delay zones was measured using the calibrator MRC 1932-46 (Flux density $\approx$ 87 Jy) for south baselines less than $\sim$300 m. On these baselines, MRC 1932-46 has a good signal-to-noise ratio in two delay zones. We compared this with the instrumental phase obtained by using the centroid in-

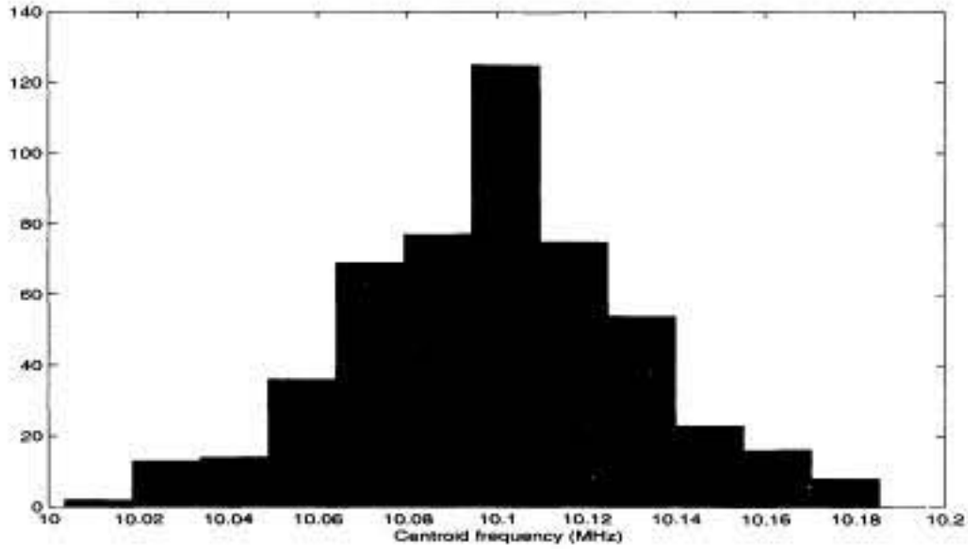

Figure 9. Histogram showing the distribution of the centroids estimated by feeding noise in the laboratory.

formation. A histogram of the difference between the instrumental phases obtained using the two different approaches is shown in Figure 10. The difference has an RMS of 5°. This is expected as the day-to-day phase variations of the instrumental phase estimated using MRC 1932-46 have an RMS of $\sim 10°$.

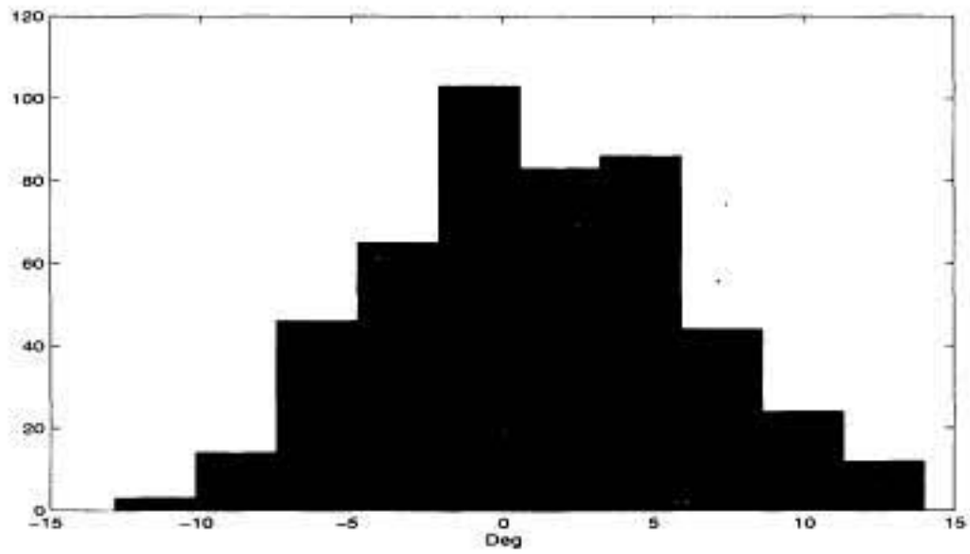

Figure 10. Histogram of difference in phase per delay as derived from the laboratory experiment and that from MRC 1932-46.

There will be phase errors if one uses a value of 10.1 MHz for the band centroids instead of the true values. An RMS variation of 0.031 MHz in the band

centroids leads to an RMS variation in phase of $\theta_1 = 5°$. The day-to-day and source-to-source phase variations are about $\theta_2 = 10°$. The net phase error therefore builds to $\sqrt{\theta_1^2 + \theta_2^2}$=11.18. Thus the spread in the centroid causes the phase errors to increase by only about 10%. The final image is made by combining 32 × 880 visibilities. The dynamic range limitation due to a phase error of 11° ($\frac{1}{1.52}$ radians) will be of the order of $\frac{1}{1.52} \times \frac{1}{\sqrt{32 \times 880}} \approx \frac{1}{850}$. This is quite acceptable. In fact we will be limited in dynamic range mainly due to errors in estimation of the point spread function used to deconvolve the images.

In the future, we plan to improve the calibration using multiple source and redundant baseline calibration techniques. These are expected to reduce phase errors to less than 5°. At that stage one can use the accurate knowledge of the band-centroids. Hence we incorporated the different band-centroid measurements in the calibration program and also in the imaging programs. Unequal bandshapes also limit the use of closure phase in calibration and in deriving antenna based gains from baseline based gains.

5. Wide-field images with a resolution of $4' \times 9'.2 \sec(\delta + 20°.14)$

For making the first wide-field images from the MRT using the recirculator data we chose the region between 19 hrs and 20 hrs in RA. This has the calibrator MRC 1932-464 in the field of view. This choice helped us in the flux density calibration of other sources in the image. Comparison of the estimates of the flux densities and the positional information of these sources with the existing data helps us gain confidence in various tools used for imaging. These images use north-south baselines only up to 441 m, i.e., about the mid-point of the north-south arm.

The flux density of MRC 1932-464 was adapted to be 87 Jy (Golap 1998; Slee 1995) . To obtain the estimates of positions and flux densities of point sources given in the Molongolo Reference Catalog (MRC) (Large *et al* 1981), the expected (theoretical) two-dimensional beam was least-square fitted around the position of the point sources given in the MRC.

A sample image in the right ascension range 19h19m to 19h40m and the declination range $-40°$ to $-29°$ chosen from the data analysed, (Sachdev 1999) is given in Fig.11. Since this is a dirty image, the corrections for the primary beam and for decorrelation have not been applied. 13 MRC sources in the flux density range 3-10 Jy are seen in the image shown. The parameters of the image presented here are summarized in Table 1.

The image is presented in J2000 coordinates. The contour levels are
–1.2, –2.0, –4.0, –6.0, –8.0, –1.5, –2.0, –1.2, –0.8, +0.8, +1.2, +2.0, +4.0, +8.0, +15, +20, +40, +60, +80, +100 Jy/beam.

Observing frequency	151.5 MHz
Minimum and maximum NS baselines	2m, 441m
No of visibilities used per second	$32 \times 440 = 14080$
Right ascension span	19h02m to 19h52m
Declination coverage	$-70°$ to $-10°$
Synthesized beam-width	$4' \times 9'.2 \sec(\delta + 20°.14)$
Point source sensitivity	550 mJy ($1\ \sigma$)

Table 1. Parameters of the images given in this paper.

5.1 *Analysis of the Images*

To estimate the noise in these images, we selected regions which appeared to be devoid of sources. The RMS measured in several such regions were then averaged to get an estimate of the noise. This is about 550 mJy.

We calculated the expected total noise in the image due to contributions from receiver noise, sidelobes of sources, undetected interference and confusion. This is ≈ 450 mJy. We have 20% of the noise which is unaccounted.

We estimated the flux densities and the positions of the sources given in the MRC catalogue. There are 54 sources in the MRC in the RA range 19h02m to 19h52m which are expected (assuming a spectral index of -0.7) to have a flux density $S_{150} \geq 3$ Jy/beam (5σ) in the MRT field of view. Out of these we have been able to detect 53 sources. Only the source MRC 1934-63 was not detected in our image due to its spectral index being different from -0.7. The positional discrepancies in declination are within 2 arcmin. The positional discrepancy in RA is within 0.8 arcmin. We find no systematic errors in position of the declinations and of the right ascensions. We also carried out positional analysis on artificial point sources of various strengths which were added to the images at different places. The errors in these detection were within 1.5 arcmin in declination and 0.7 arcmin in RA. From the ratios of the measured flux to the expected flux densities we have estimated the primary beam of our helix and the delay beam. The deviation from the expected is less than 10% in the declination range of interest.

6. Discussions and Conclusions

During the installation stage of the Mauritius Radio Telescope we identified the need for wide field imaging with this telescope to make it an efficient surveying instrument. We designed and built a recirculator system which allows us to measure visibilities with different delay settings in one observation schedule using the existing correlator. In the recirculator the digitised data is sampled at a rate of 2.65625 MHz, stored in a dual buffer memory and the correlations are measured at four times this rate (10.625 MHz). To program the correlator system and the recirculator boards, and also to acquire data from the correlators, we designed and

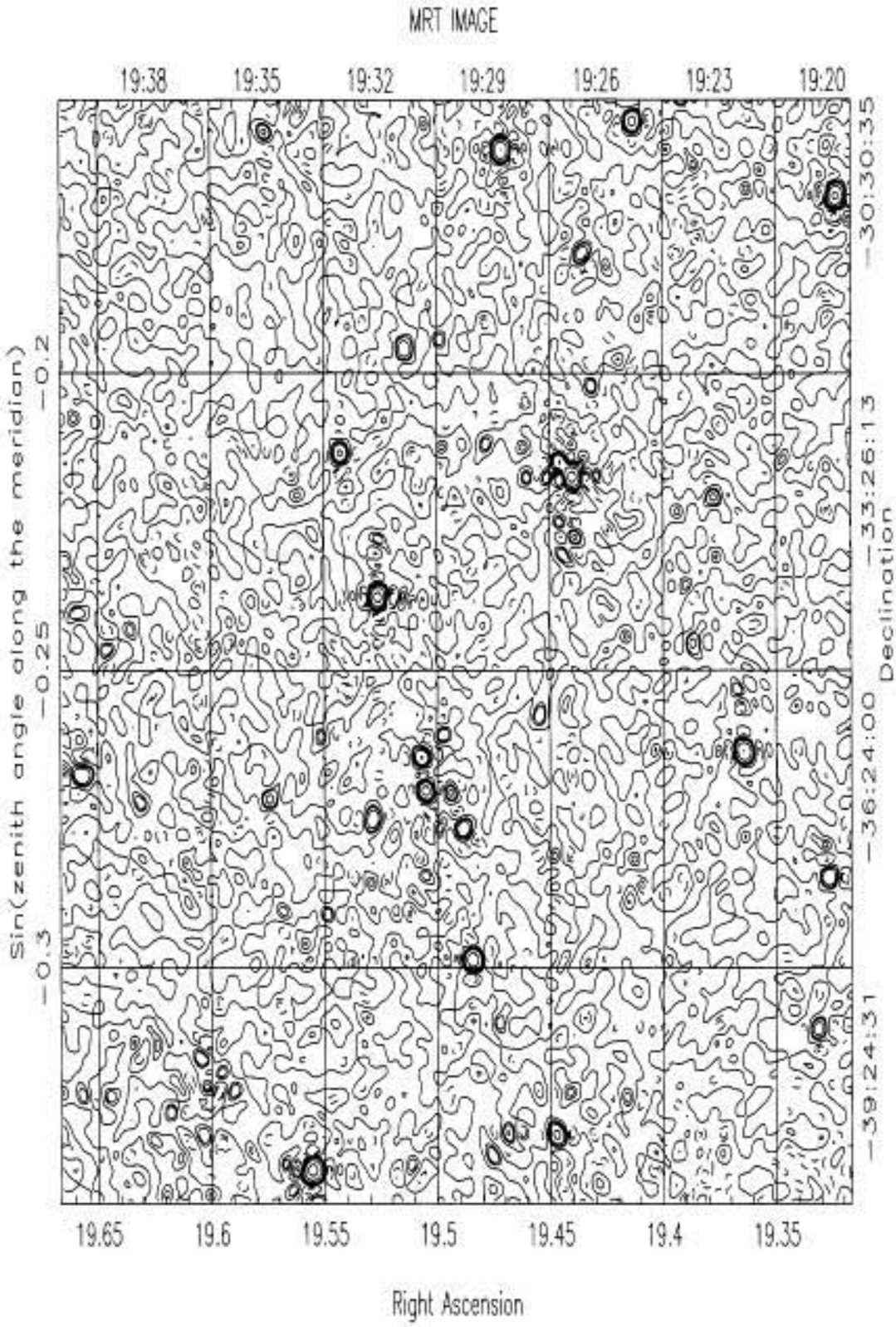

Figure 11. Image in the right ascension range 19h19m to 19h40m and declination range $-40°$ to $-29°$.

built a new data acquisition and control system (DAS). This data acquisition system comprises of a double bank of memories shared by two PCs running on DOS.

The recirculator system has been integrated into the receiver system at the MRT and tested. After ensuring satisfactory performance, we carried out observations for the survey using the recirculator system up to the longest north-south baseline, i.e., up to 880 m during the period September 1995 to October 1996.

The choice of the usable bandwidth and the sampling frequency for the recirculator has optimised the telescope performance. The methodology described here will also be useful in the design of modern receiver systems where digitisation very early in the receiver chain is preferred. The design has enabled us to measure visibilities with four delay settings, with the existing correlator with only a 10% loss in sensitivity. The hardware has added new features to the existing receiver system. The correlator system can now measure autocorrelation and cross correlation functions up to 128 clock delays. Using the recirculator in this mode the cross power spectrum of the 512 baselines was measured to establish the centroids of their bandpasses. The telescope can also be operated in a time multiplexed mode to measure EW X E and NS X NS baselines. This is useful in the calibration of the array using the Redundant Baseline Calibration technique. The second round of observations for the survey has been carried out in this mode, using $\approx 10\%$ of the observing time to obtain these correlations. With this many strong extended sources can be used for the array calibration and will help to improve the calibration of the visibilities.

Due to paucity of strong sources we have not been able to calibrate the visibilities measured with different delay settings. Using the receiver configuration we have devised a method of estimating the instrumental phase in the four delay zones using a calibrator in only one of the delay zones. This needs information about the centroids of the bandpass used. We measured the variation in the centroids of the bandpasses of the 512 baselines used for imaging and established that variation causes only a 5 degree RMS error in the instrumental phase calibration. Thus the hardware at MRT allows high dynamic range imaging (≈ 1000).

A one hour region around the calibrator MRC 1932-464 with the full declination range of the MRT has been imaged with a resolution of $4' \times 9'.2 \sec(\delta + 20^\circ.14)$. We have carried out some preliminary analysis of these images. The noise in our image is approximately 550 mJy and is only 20% higher than expected. We estimated the position and flux densities of the MRC sources in our image. We have been able to detect in the MRT image, all the 53 sources listed in the MRC catalog in the RA range 19h02m to 19h52m (J2000 coordinates) which are expected to have a flux density $S_{150} \geq 3$ Jy/beam (5σ) in the MRT field of view. The positional discrepancies in declination and in RA are well within the limits expected. We have also detected a number of sources which are not listed in the MRC. A detailed study of these sources will be undertaken in the future and will be published separately. We have thus demonstrated the wide-field imaging capability of MRT using the recirculator system. The usefulness of the recirculator in carrying out a survey with the MRT cannot be over-emphasized.

7. Acknowledgments

The MRT is operated jointly by the Raman Research Institute, Bangalore; Indian Institute of Astrophysics, Bangalore and the University of Mauritius. We thank K. Golap, University of Mauritius and R. Dodson, University of Durham for innumerable discussions during the design and installation of the recirculator; H. A. Ashwathappa, RRI, for his help in carrying out observations. We thank A. A. Deshpande, RRI, for many discussions regarding the design criteria of the recirculator. We thank K. S. Dwarakanath, RRI and Ch. V. Sastry for their valuable feedback on the manuscript. We would also like to thank V.N. Pandey and N. Oozeer for their help in preparing the manuscript.

References

Baldwin, J. E., Boysen, R. C., Hales, S. E. G., Jennings, J. E., Waggett, P. C., Warner, P. J., and Wilson, D. M. A., 1985, *MNRAS*, **217**,717.

Christiansen, W. N., and Hogbom, J. A., *"Radiotelescopes"*. Cambridge university press, 1969.

Das, J., Mullick, S. K., and Chatterjee, P. K., *"Principle of Digital Communication"*. Wiley Eastern Ltd., 1986.

Erickson, W. C., Mahoney, M. J., and Erb, K., 1982, *ApJS*, **50**,403.

Fomalont, E. B., Wright, M. C. H., in *"Galactic and Extragalactic Radio Astronomy"*, Ed. Vrshuur, G.L., Kellermann, K.I., Springer-Verlag, NY, 1974.

Golap, K., *"Synthesis Imaging at 151.5 MHz using the Mauritius Radio Telescope"*. PhD thesis, University of Mauritius, 1998.

Golap, K., Udaya Shankar, N., Sachdev, S., Dodson, R., Sastry, Ch. V., 1998, *J. Astrophys. Astr.*,**19**, 35.

Klingler, R. J. "Quantization noise of signal correlators". Master's thesis, University of British Columbia, 1972.

Large, M. I., Mills, B. Y., Little, A. G., Crawford, D. F., and Sutton, J. M., 1981, *MNRAS*, **194**,693.

Sachdev, S., *"Wide field Imaging with the Mauritius Radio Telescope"*. PhD thesis, University of Mauritius, 1999.

Slee, O. B., 1995, *AuJPh*, **48**,143.

Thompson, A. R., Moran, J. M. and Swenson, G. W. Jr. *"Interferometry and Synthesis in Radio Astronomy"*. John Wiley and Sons, 1986.

J. Astrophys. Astr. (2001) **22**, 251–262

Deconvolution of Wide-field Images from a Non-Coplanar T-Array

K. Golap[1] & N. Udaya Shankar[2,1].
[1] *Department of Physics, University of Mauritius, Reduit, Mauritius.*
[2] *Raman Research Institute, Sadashivanagar, Bangalore 560080, India.*

Received 2001 August 21 ; accepted 2001 October 16*

Abstract.

Deconvolution of wide-field images is a well-known problem with many interesting algorithms. In this paper we describe the solution developed for deconvolving wide-field images from the Mauritius Radio Telescope (MRT). MRT is a non-coplanar, Fourier synthesis T array operating at 151.5 MHz. The non-coplanarity of the MRT produces dirty images that are convolved by a position dependent point spread function (PSF). This paper mainly focuses on the methods developed for estimating the PSF of the array from the dirty images and translating the PSF estimated at a given declination to the PSF at any another declination.

1. Introduction

The Mauritius Radio Telescope (MRT) is a Fourier synthesis T-shaped array with an East-West (EW) arm of length 2048 m having 1024 helical antennas. The South (S) arm consists of a rail line of length 880m and 16 movable trolleys each with four helical antennas. The 1024 helices in the EW arm are divided into 32 groups of 32 helices each. The local terrain is rocky and uneven, especially along the EW arm with height differences of up to 35 m. To minimize the problems of non-coplanarity, it was decided to level the EW arm in multiples of 64 m (32λ) so that the antennas in each group will be at the same height. Each trolley in the S arm constitutes one S group. A detailed description of the telescope is to be found in Golap *et al* (1998).

The 48 group outputs are amplified, heterodyned to 30 MHz in the field and brought separately to the observatory building via coaxial cables. In the observatory, the 48 group outputs are further amplified and down-converted to a second IF of 10.1 MHz.

The 32 EW and 16 S group outputs are fed into a 32×16 complex, 2-bit 3-level

*Although this paper was accepted only on 16 October, we have included it because this issue was delayed due to other reasons.

digital correlator sampling at 12 MHz. The 512 complex visibilities are integrated and recorded at intervals of 1s. At the end of 24 hours of observations the trolleys are moved to a different position and new visibilities are recorded. The S baselines are sampled with a spacing of 1m, which is half a wavelength at 150 MHz. A minimum of 60 days of observing are needed to obtain the visibilities up to 880 m spacing.

The visibilities measured by an interferometer of baseline $\vec{b} \equiv (u, v, w)$ is given by Thompson *et al* (1986):

$$\tilde{V}(u,v,w) = \int\int \frac{A(l,m)B(l,m)}{\sqrt{1-l^2-m^2}} \exp(-i(lu+mv+nw))dldm. \quad (1)$$

where A(l,m) is the amplitude response of the array, B(l,m) is the sky brightness distribution and l,m,n are the direction cosines.

Let $B'(l,m) \equiv \frac{B(l,m)A(l,m)}{\sqrt{1-l^2-m^2}}$. Then the above equation becomes

$$\tilde{V}(u,v,w) = \int\int B'(l,m) \exp(-i(lu+mv+w\sqrt{1-l^2-m^2}))dldm. \quad (2)$$

where $B'(l,m)$ is the modified brightness distribution. For planar arrays this relationship can be simplified to a 2-dimensional Fourier transform.

The *u,v* coverage of MRT can be thought of as a pleated sheet, extended in both *u* and *v*, with discrete steps in *w* (height) as we move from one EW group to the other at a different height. As we are imaging a very large field of view ($\approx 6^0$), the approximate coplanar approach wherein the phase term due to the heights is assumed to be a constant over the synthesized field of view is invalid. Thus for MRT, a 3D imaging is required.

To avoid the grating response of the EW array, imaging is presently carried out on the meridian (Golap *et al* 1998). For meridian transit imaging, we transform the visibilities using a Fast Fourier Transform (FFT) along the regularly sampled *v* axis, apply a Direct Fourier Transform (DFT) along the *w* axis and finally sum along *u* to obtain the image on the meridian. A DFT on *w* is required as the sampling is not uniform. The direct transform corrects every term along the zenith angle on the meridian for the group heights. This is equivalent to phasing the groups to a common (and artificial) 2D plane and results in a dirty image convolved by a position dependent PSF.

We discuss in this paper a technique developed to deconvolve wide field images made using the MRT to obtain images with reasonable dynamic ranges ($\approx 1:100$). Our deconvolution method is based on the conventional CLEAN algorithm (Clark *et al* 1980; Hogbom 1974; Schwartz *et al* 1978). This needs knowledge of the Point Spread Function (PSF) of the array. The next section discusses the effect of the non-coplanarity of the array on the PSF and shows that it is a function of declination. Section 3 discusses the need and the method for the estimation of the PSF from the dirty images. Section 4 describes an algorithm to generate PSFs for

different declinations from the estimate at a given declination. Section 5 describes the application of the method developed to the deconvolution of images made using MRT for a low resolution survey ($17' \times 13'\sec(\delta - \phi)$).

2. The effect of non-coplanarity on the PSF

The PSF of a T-array is generally a complex function with a non-zero imaginary part. The real part of the PSF of a uniformly illuminated T- array is the same as that of a cross (Christiansen *et al* 1985). We use only the real beam and the corresponding real image for deconvolution. However, the imaginary part of the PSF is required when generating the PSF for a planar array with a non uniform illumination and for a non-coplanar array (Dwarakanath *et al* 1990).

Both the EW and the S arrays of the MRT are non-coplanar. The height profile of the EW array is shown in the Fig. 1.

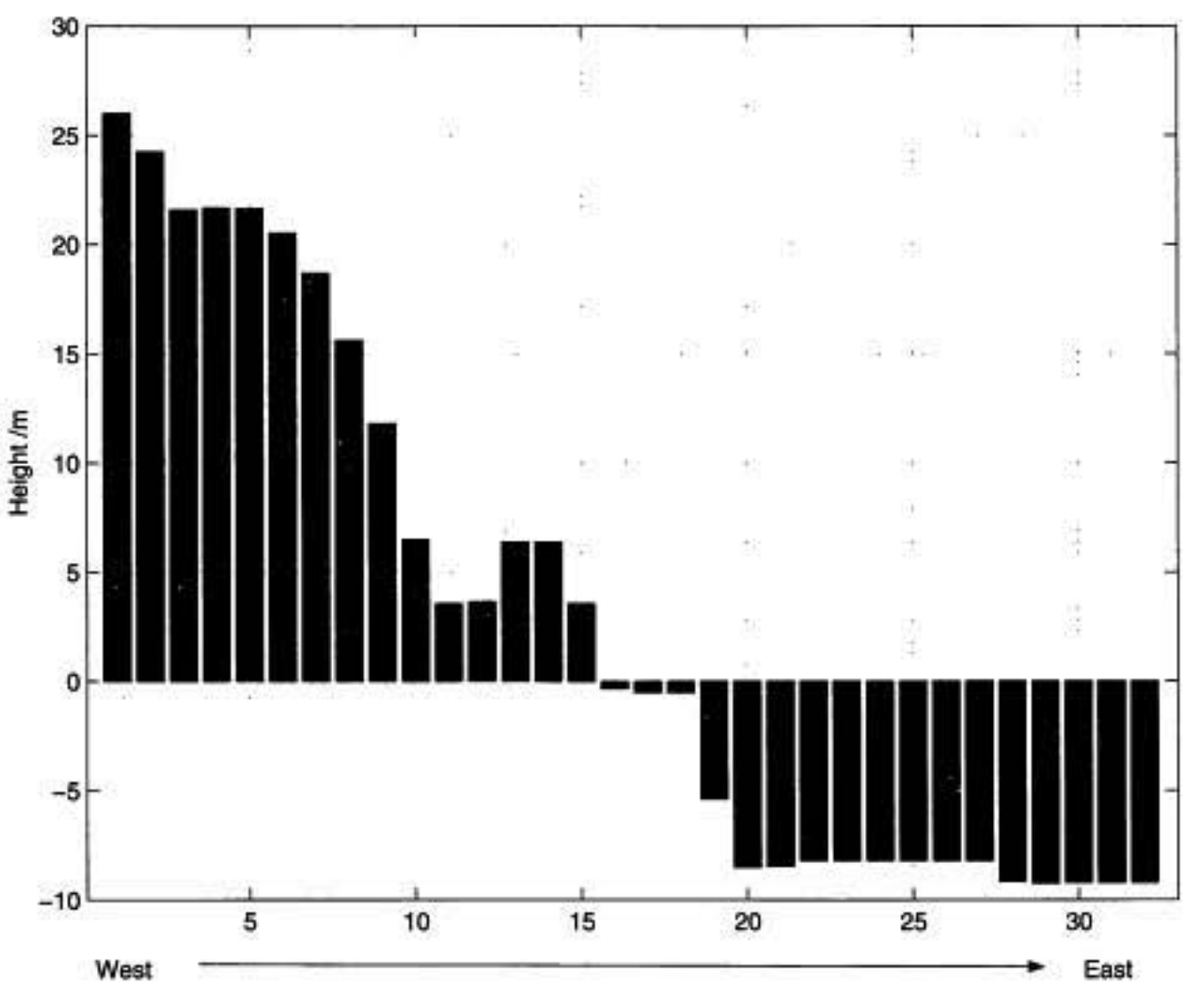

Figure 1. A plot showing the height profile of the EW array. Each bar represents a 64 m long EW group with 32 helices. The profile runs from west to east end.

An abandoned old railway line running North-South was rebuilt for use as the South arm. This arm slopes downwards at about $\frac{1}{2}^\circ$ to the horizontal till about 655 m, and then slopes upwards at about 1° to the horizontal. Visibilities measured

from these two parts are treated separately while transforming. The slope is taken into account by assuming an instrumental zenith appropriate to the slope of the track. While combining contributions from different parts we introduce necessary corrections to get an instrumental zenith equal to the latitude of the place. This treatment of visibilities does not result in a PSF substantially different from that of a co-planar T array. The deviation of the PSF of the MRT from that of a co-planar T array is mainly due to the non-coplanarity of the EW array.

Let us consider an EW group which is at a height h, from the NS array. Signal from a point source on the meridian, with a zenith angle (za) reaches the EW group with an extra path difference of $h \times \cos(za)$. While imaging, one compensates for a phase shift due to this path difference at each zenith angle along the meridian. This is carried out for all the baselines used for imaging. This results in the sidelobe of a source at za_1 appearing at za_2, getting compensated by a height phase equivalent to that at za_2. This causes a reduction in the level of the sidelobe at za_2. However the sidelobe around za_1 peaks at some other hour angle (HA) away from the meridian. Thus sidelobes of a source peaks at an RA which is different from its transit time. The position and the strength of the sidelobe depends upon how far it is from the source, the source declination and the EW height distribution. The dirty image around the source MRC2155-699 shown in the Fig. 2 clearly illustrates this effect.

The Fourier inversion of the visibilities measured by a non-coplanar array gives the function $F(l, m, n)$ (see, e.g. Cornwell *et al* 1992).

$$F(l,m,n) = \left[B'(l,m,n)\delta(\sqrt{1-l^2-m^2}-n)\right] * P(l,m,n), \qquad (3)$$

where $P(l, m, n)$ is the 3-D PSF. Equation(3) can be simplified to

$$F(l,m) = \int B'(l_o,m_o)P(l-l_o, m-m_o, \sqrt{1-l^2-m^2}-\sqrt{1-l_o^2-m_o^2})dl_o dm_o. \qquad (4)$$

Now let us consider an isolated point source in the sky. As the point source drifts in the sky transiting the meridian, its direction cosines l', m' change with the HA. The dirty image, when the point source is at l', m', is given by

$$F_{PSF}^{(l',m')}(l,m) = k \int \delta(l_o - l', m_o - m') \times P(l-l_o, m-m_o, \sqrt{1-l^2-m^2}-\sqrt{1-l_o^2-m_o^2})dl_o dm_o, \qquad (5)$$

$$= kP(l-l', m-m', \sqrt{1-l^2-m^2}-\sqrt{1-l'^2-m'^2}). \qquad (6)$$

For $l = 0$,

$$F_{PSF}^{(l',m')}(0,m) = kP(-l', m-m', \sqrt{1-m^2}-\sqrt{1-l'^2-m'^2}). \qquad (7)$$

Close to the meridian, m' can be simplified to $\sin(-za)$. Then the PSF is a one dimensional function F(0,m) for various values of l' given by

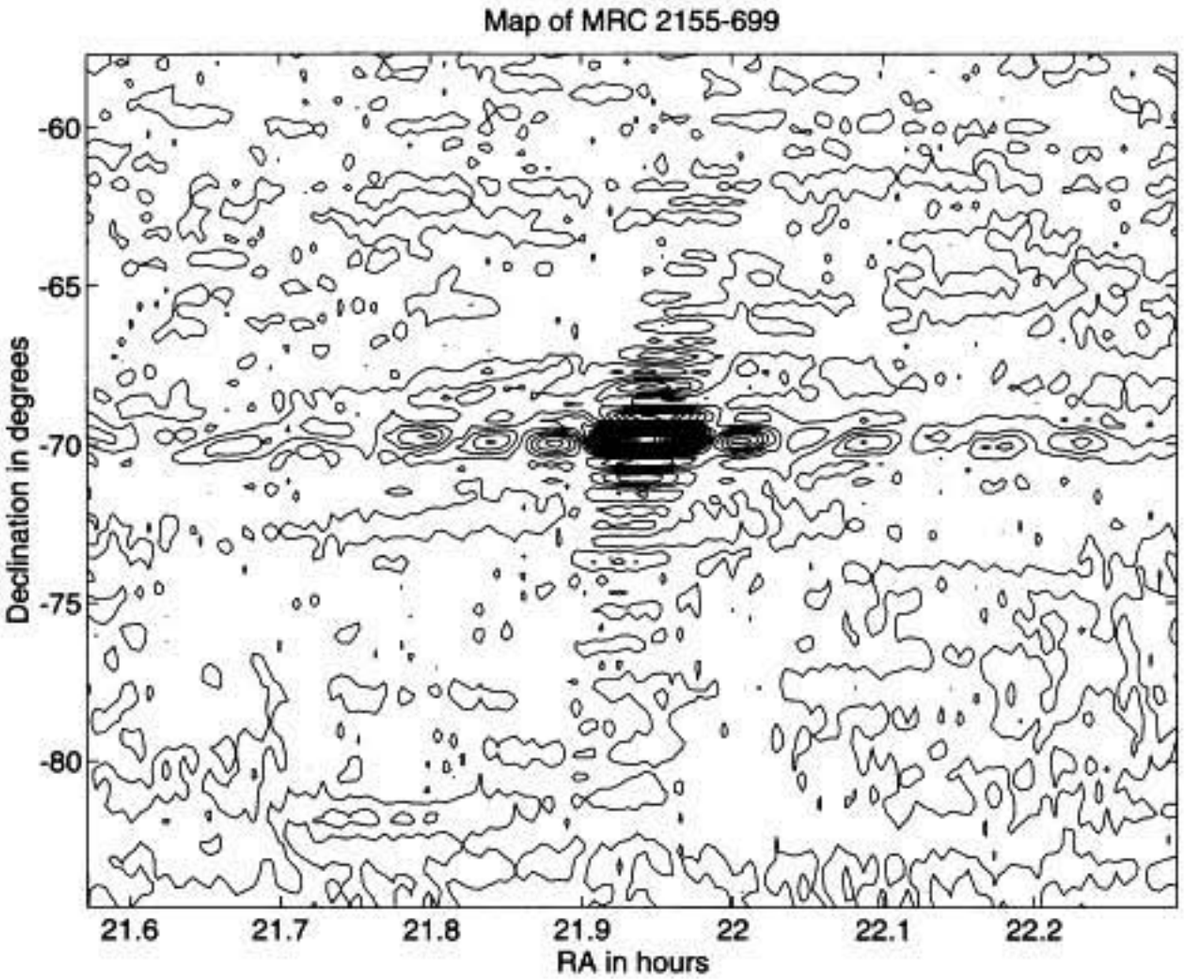

Figure 2. Dirty image around the source MRC2155-699. The twisted response of the array due to the non-coplanarity is clearly seen.

$$F_{PSF}^{(l',m')}(0,m) = kP(-l', m-m', \sqrt{1-m^2} - \sqrt{1-l'^2-m'^2}), \quad (8)$$

$$= kP(-l', sin(za') - sin(za), cos(za) - cos(za')). \quad (9)$$

Thus the two-dimensional PSF at m due to a point source at l', m' is not merely a function of $m - m'$ but also depends on m.

Thus the PSF will have different shapes depending on where the point source is centered. This implies that for deconvolution of the antenna response from the 2-D image we need different functions which depend upon the Zenith Angle of the source being deconvolved.

2.1 *Estimation of the PSF*

In the present work the imaging is restricted to making 1-D scans along the meridian. The 2-D image is time stacks of these 1-D scans. As a point source drifts across the meridian the 1-D stacks will give the point spread function. The T array

is used in a correlation mode in which the EW array is multiplied with the NS array. Thus the observed PSF is that of the NS array multiplied by the PSF of the EW array. Since the PSF and the aperture illumination are a Fourier transform pair, the PSF can be generated from the aperture illumination.

At MRT correlation of signals from groups of helices are performed. There are 32 helices in each of the EW groups and 4 helices in each of the NS groups. The calibration procedure used (Golap *et al* 1998) gives the phases and amplitudes of a group. The illumination pattern within each group is not estimated. This sets a limit to the extent of the PSF that can be estimated from the illumination pattern. For example, in the low resolution survey, only 8 central groups in the EW arm and trolley positions up to 178 m in the NS are used (Golap 1998). Thus using the aperture illumination from our calibration, we can estimate the PSF up to 4 sidelobes on each side of the main beam along the RA direction and 89 sidelobes along the declination on the meridian. The image will have a dynamic range of ≈ 12 if such a PSF is used for deconvolution (assuming a sinc pattern for the PSF). Hence CLEANing point sources stronger than 12 Jy would leave residues higher than 1 Jy in the final image; 1 Jy being the approximate noise level (1σ) of the low resolution survey. Hence we use the dirty image around a strong point source to estimate the PSF with an extent larger than four sidelobes on either side of the main lobe.

To achieve a dynamic range of, say, around 50 the PSF should have an extent of at least 16 sidelobes on either side of the main beam. In other words we need a field of $7.5^\circ \times 7.5^\circ$ with the point source in the centre. However such a field will have other sources apart from the point source under consideration. Such sources (especially if they lie along the same RA or declination) may not be distinguishable from the side lobes. Hence we may generate an unsatisfactory PSF. This effect can be minimised by averaging the PSFs estimated using point sources at different declinations.

The sky coverage of the low resolution survey is 18:00 to 24:00 hrs and 00:00 to 05:00 hrs in RA and from -70° to -10° in declination. There are not many strong point sources in this field to obtain the PSF at different declinations. The flux density of the strongest point source MRC1932-464 in this field is $\approx 80Jy$ and is just strong enough to determine the PSF.

The process of averaging of several PSFs of weaker sources will improve the estimation process. However since the PSF of the MRT is declination dependent it is not straight forward to sum the PSFs estimated at different declinations. This can be carried out if we are able to generate the PSF at a given declination δ_1 from the PSF estimated at some other declination δ_0. The next section discusses this.

3. Declination Shift Algorithm

If one plots the PSF of a planar array as a function of RA and $\sin(za)$, the declination scan of the PSF remains invariant with the zenith angle. The RA scan of

the PSF gets stretched by $\sec(\delta)$ as one moves to sources at different declinations. Because of the ease that m or $\sin(za)$ coordinate offers, the images were uniformly sampled in the $\sin(za)$ domain and the (RA, $\sin(za)$) coordinate system was used for the PSF and dirty images.

To sum the PSF estimated by sources at different declinations, we should be able to generate the PSF at any given declination δ_1 from the PSF at some other declination δ_0.

Let us consider the PSF of a source centered at δ_0, with its zenith angle $za_0 = \delta_0 - \phi$ and $m_0 = -\sin(za_0)$, where ϕ is the latitude of the telescope.

Any RA cut of the PSF, say at $m = m'_o$, which is different from the m of the source, is complex with non zero imaginary part. While imaging this declination, a phase correction corresponding to heights seen at the point $m = m'_o$ would have been put in. A Fourier transformation of this cut gives the "combined" spatial frequency response of the EW antennas used. Since in the EW×NS mode there are no redundant baselines, when the number of Fourier components estimated is equal to integral number of the EW groups, each Fourier component can be thought of as arising from a given EW group. Assuming that there is only one point source in the field of view, the entire signal comes from that source. Hence the Fourier components have been given a height correction due to m'_o, ($\Phi_{m'_o}(h) = h \times \cos(za'_o) = hn'_o$) while the signal has a phase due to height as seen at m_o ($\Phi_{m_o}(h) = hn_o$), where h is the height of the EW group corresponding to the Fourier component we are considering. Therefore there is a residual phase error corresponding to the path difference of $(\Phi_{m_o}(h) - \Phi_{m'_o}(h))$ in each Fourier component.

The process of declination shift consists of replacing these residual phase errors in Fourier components with the values expected if the source were centered at δ_1, which are proportional to $\Phi_{m_1}(h) - \Phi_{m'_1}(h)$. After this phase rotation the Fourier components are inverse transformed. This procedure is repeated across the declination range of the PSF to reconstruct it at δ_1. Reconstruction of the PSF at δ_1 also requires the RA section to be stretched or compressed to have a width proportional to $\sec(\delta_1)$.

The PSF at any declination can be made to look like the one obtained using a coplanar array by removing the residual phase errors mentioned above. This is equivalent of correcting for the heights at the declination of the source rather than the declination of the sidelobe. This would ensure that all the sidelobes, along the declination, peak on the meridian and the one dimensional stacks of the images would look similar to the one obtained with an array in which all the EW groups are at the same height. Then a pseudo PSF can be obtained by taking the real part of the complex product of the two one dimensional cuts across RA and declination. This is a reasonable approach since in the correlation mode one produces the 2-D response by multiplying the response of the EW and NS arrays (Dwarakanath *et al* 1990). Such a two dimensional PSF can later be transformed to the PSF of MRT at any declination by introducing the residual phase errors in its Fourier transform.

4. Low Resolution PSF and CLEAN

The declination shift algorithm was used to generate the PSF required for CLEANing the low resolution images ($17' \times 13'\sec(\delta - \phi)$). As already mentioned a low resolution survey using the observations covering the NS baselines up to 178 m has been carried out. To have nearly a symmetric beam for the images, data for baselines only with the central 512 m of the EW arm was used. The sky coverage of the low resolution survey is 18:00 to 24:00 hr and 00:00 to 05:00 hr in RA and from $-70°$ to $-10°$ in declination. The estimated noise in the image is around 1 Jy and is confusion limited (Golap 1998).

In the field of view of the survey four brightest point sources (flux density range 35-120 Jy) were used for estimating the PSF.

The following points were considered while constructing the PSF.

- The sources chosen are far from the Galactic plane but their fields are not devoid of large scale structures. We used a dirty image without zero spacing for the estimation of the PSF and also for the deconvolution. As regards the large scale structures in the PSF, we did not take any additional precautions. However, the averaging, of four regions for the estimation of the PSF, reduced the effect of the large scale structures from any single field.

- Interference affects the PSF estimation. An inspection of the images around the sources chosen did not show any interference.

After selecting a region $\approx 7.5° \times 7.5°$ around the sources. The following procedure was used to estimate the PSF:

1. Select a region with an extent of n sidelobes around the main beam. To get a dynamic range of d in an image with an *rms* noise σ, source should have a strength of at least $\sigma \times d$. If the PSF is approximately a sinc function, n should satisfy the condition $n < \frac{d}{\pi}$.
2. Subtract all identifiable sources in the field of view other than the central source of interest. For this we adopted a source detection program which identifies high points in the selected regions of the dirty image where gradients are negative in all directions, fits approximate RA and declination beams in the first step and a two dimensional beam later. Visual inspection is carried out using the apriori information available about the region from the Molongolo Reference Catalogue (MRC) (Large *et al* 1981) to ensure that the sidelobes of the central source are not mistaken for independent sources.
3. Phase rotate the Fourier transforms of the complex RA cuts of the above region to obtain the pseudo PSF of the array at zenith. This is nothing but the PSF of the MRT with its EW groups at the same height. While Fourier transforming an RA scan, its extent is chosen to give integral number of points within each group. Helices within each EW group

are at the same height. Hence each Fourier component will have one representative height

4. Repeat the steps 1, 2 and 3 for the four regions and average the pseudo PSF with suitable weighting factors.

5. Obtain two one dimensional complex scans of the above function with the source at the centre. The real part of the complex product of these two scans gives an improved average pseudo PSF.

6. While deconvolving this is transformed to the true PSF of MRT at the declination of interest using the declination shift algorithm.

We used the task APCLN in AIPS for deconvolution. The PSF at zenith generated by averaging PSFs of four sources with suitable weightages is shown in the Fig. 3. The PSF generated by cross multiplying the complex scans taken from this average PSF is shown in Fig. 4. The noise in the off-axes regions in this PSF is much lower than that shown in Fig. 3. The CLEANed image of Fornax A region is shown in Fig. 5. The source which is just below Fornax A is MRC0320-389 which has a flux density $\approx$ 4 Jy. The peak flux of the of the Fornax A is $\approx$ 290 Jy/beam. This gives a dynamic range $\approx$ 70.

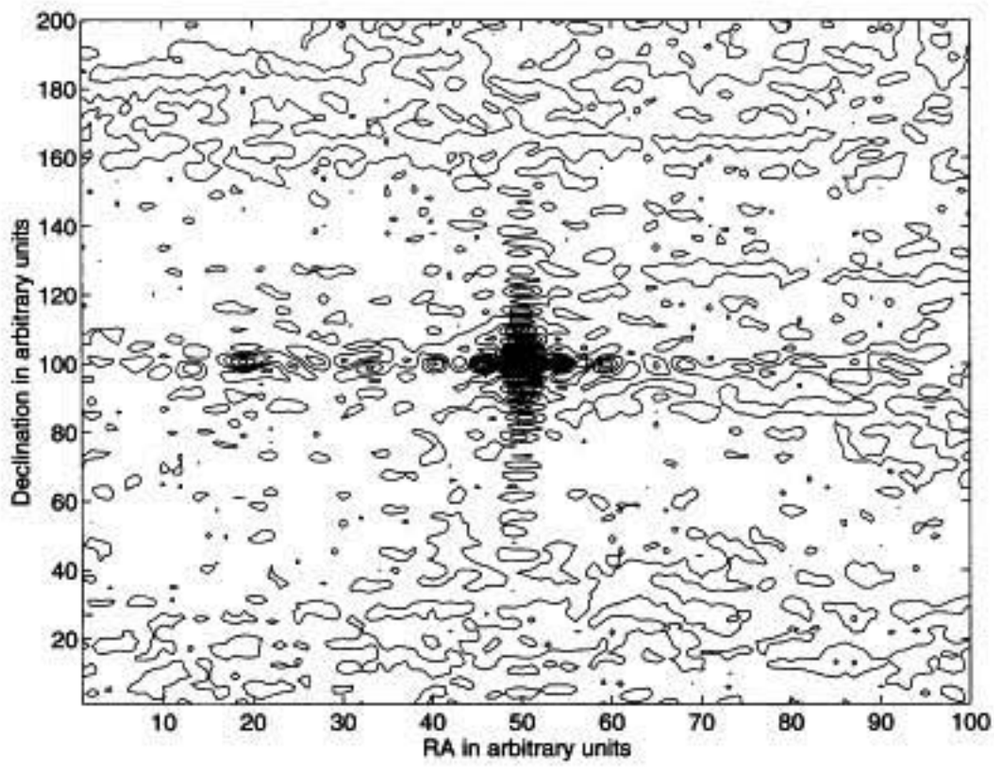

Figure 3. PSF at zenith generated by averaging the PSF of four sources. Note the noise in the off-axes region when compared to the PSF shown in Fig. 4.

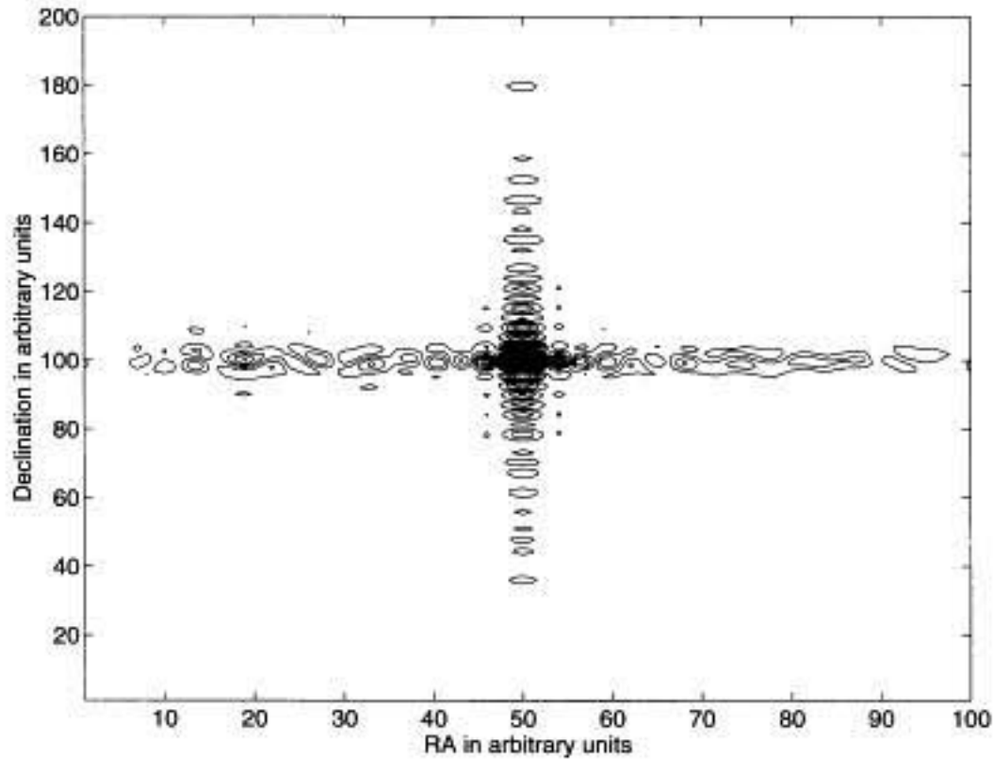

Figure 4. PSF generated by cross-multiplying the 1-D complex scans taken from the PSF of Fig.3

The dirty images from the low resolution survey have been CLEANed using the technique demonstrated here. The low resolution survey details will be discussed in a separate paper.

5. Conclusions

We have developed a technique to translate the position dependent PSF of a non-coplanar T-array. Employing this technique gainfully we are able to estimate the PSF required for deconvolution from the dirty images minimising the effects of off-axes sources by averaging the PSF of several sources. We have demonstrated the technique developed here by deconvolving a low resolution MRT image in the Fornax A region. This is one of the strong sources in the field of view of our survey. We have been able to achieve a dynamic range of 70, close to the axes of the source and a much higher dynamic range away from the axes. This technique has been put to use in preparing a low resolution survey of the southern sky. The sky coverage of the low resolution survey is 18:00 to 24:00 hr and 00:00 to 05:00 hr in RA and from -70° to -10° in declination. The estimated noise in several fields is ≈ 1 Jy. This is close to the expected sensitivity which is confusion limited. The next logical step is to develop techniques similar to hybrid imaging (Pearson *et al* 1997) for estimating antenna gains using these images as the first approximation for the field of view and hence re-calibrate the measured visibilities.

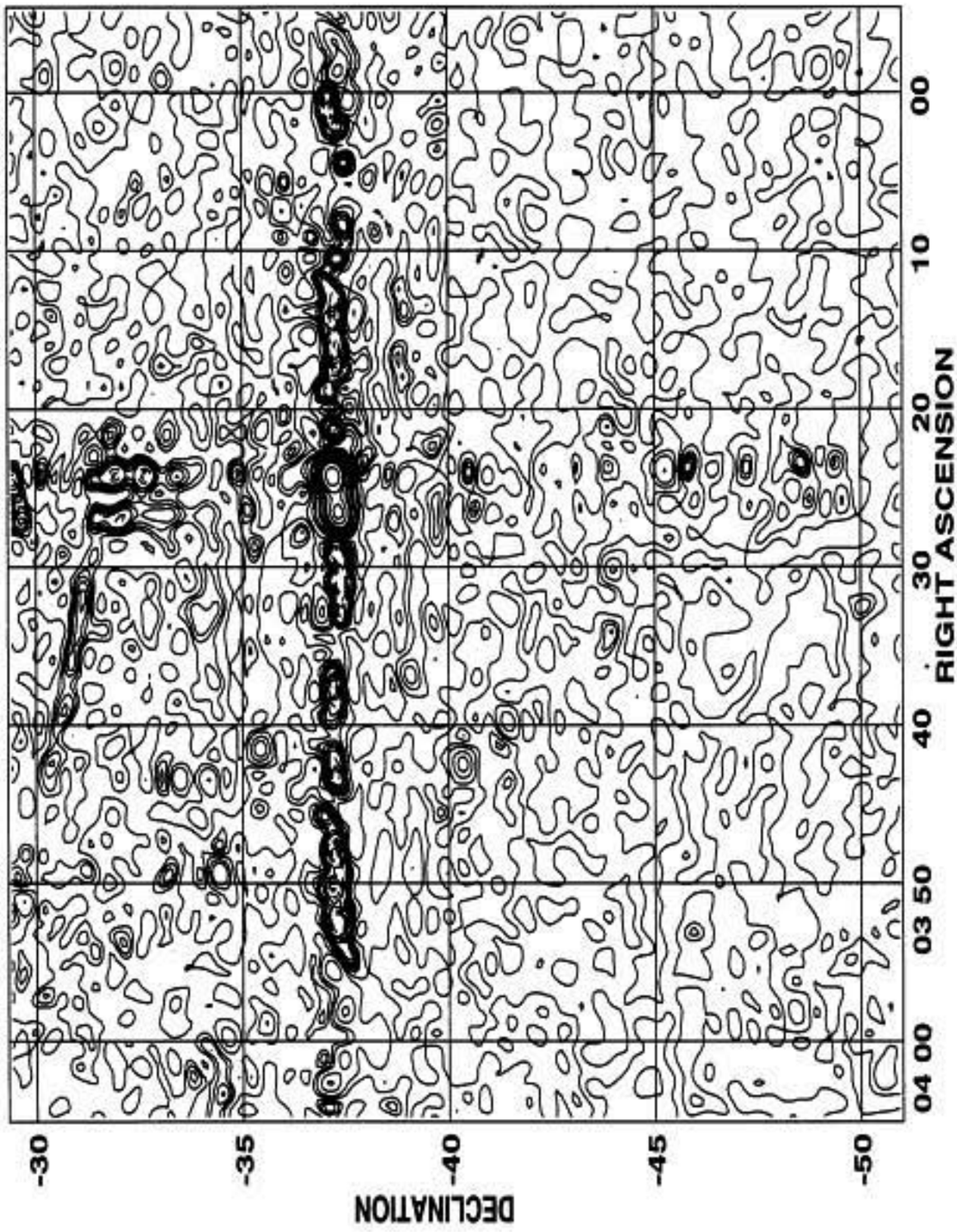

Figure 5. Fornax-A cleaned with a beam generated with 4 point sources

6. Acknowledgments

The MRT is operated jointly by the Raman Research Institute, Bangalore; Indian Institute of Astrophysics, Bangalore and the University of Mauritius. K.Golap wishes to thank the many people that helped but specifically would like to mention and dedicate this work to R. Somanah, H.A. Aswathappa and G. N. Rajasekar. R. Somanah helped in staving the many adminsitrative crises and the 'urgent paper work' that came along often. H.A.Aswathappa, specially, and G.N.Rajasekar provided dedicated technical support; which often meant trying to repair amplifiers and the correlator at 2:00 Am, after working in the field during the day.

References

Christiansen, W.N., and Hogbom, J.A., *"Radio Telescopes"*, Cambridge University press, 1985.

Clark, B.G., 1980, *Astron. Astrophys.*, **89**, 377.

Cornwell, T.J., Perley, R.A., 1992, *Astron. Astrophys.*, **261**, 353C.

Dwarkanath, K.S., Deshpande, A.A., Udaya Shankar, N., 1990, *J. Astrophys. Astr.*, **11** , 311.

Golap, K., *"Synthesis Imaging At 151.5 MHz Using The Mauritius Radio Telescope"*, Ph.D. Thesis, Dept. of Physics, University Of Mauritius, 1998.

Golap, K., Udaya Shankar, N., Sachdev, S., Dodson, R., Sastry, Ch. V., 1998, *J. Astrophys. Astr.*,**19**, 35.

Hogbom, J., 1974, *Astr. Astrophys. Suppl.*, **15** , 417.

Large, M. I., Mills, B. Y., Little, A. G., Crawford, D. F., Sutton, J. M., 1981, *MNRAS*, **194**, 693.

Pearson, T.J., Readhead, A.C.S., 1984, *ARA&A* , **22**, 97.

Schwartz, U.J., 1978, *Astron. Astrophys.*, **65**, 345.

Thompson, A. R., Moran, J. M., Swenson, G. W. Jr. *"Interferometry and Synthesis in Radio Astronomy"*. John Wiley and Sons, 1986.

J. Astrophys. Astr. (2001) **22,** 263–282

Variability of Extragalactic Objects in Relation to Redshift, Color, Radio Spectral Index and Absorption Lines

D. Basu *Department of Physics, Carleton University, Ottawa, ON K1S 5B6, Canada*
e-mail: basu@physics.carleton.ca

Received 2000 November 13; accepted 2001 December 11

Abstract. Optical variability of extragalactic objects, viz., QSOs, BL Lacs and Seyfert galaxies has been monitored systematically over an appreciable period of time and a large amount of data have accumulated. The present work reports results of investigations involving statistical analysis of updated data on relationships between variability and various observed properties of the objects, viz., redshift, color indices, radio spectral index and absorption lines. It is found that at high frequencies (rest frame) radio spectral index does not change significantly with the degree of variability. However, the degree of variability depends on redshifts. On the other hand, presence or absence of absorption lines is significantly associated with variability for QSOs with larger redshifts ($z > 1.0$), while no such relationship exists for QSOs at smaller redshifts ($z < 1.0$) or other objects. Correlation between color indices and redshifts depends on the degree of variability and the sample chosen for the color index.

Key words. Galaxies active: galaxies — quasars: general.

1. Introduction

Optical variability is one of the major criteria used in understanding the characteristics of QSOs and related extragalactic objects. Investigations of its association with other properties of different types of closely related objects are expected to throw light on the true nature of such objects and on any possible link between them. Optical variability of extragalactic objects has therefore been monitored systematically over an appreciable period of time.

Accordingly, objects have been classified into three types depending on their degree of variability (V) based on a criteria defined by Penston & Cannon (1970) and Basu (1973, 1980a), viz., $V = 0$ (non-variables, $\Delta m \leq 0^m.2$, the smallest value of Δm that can be detected without any ambiguity), $V = V$ (moderate variables, $0^m.2 < \Delta m < 1^m.0$, on a time scale of few weeks or months) and $V = OVV$ (optically violent variables, $\Delta m \geq 1.0$, over a period of few days or weeks). In the above classification, the magnitude change refers to peak to peak variations and the apparent magnitudes (m) are measured in photographic blue band or Johnson B filter. The degree of variability has been shown earlier to be related to redshifts, colors, radio spectral index, and presence or absence of absorption lines. Thus OVV quasars were found to exhibit flat radio spectra while the other two classes inclined to show steeper

Table 1. The data base.

Source	Name	Type	Var	z_e	z_a	$(B-V)^*$	$(U-B)^*$	α
$0003+158$	PHL 658	Q	OVV?	0.450	N	0.20	-0.83	-0.60
$0007+106$	III Zw2	S	OVV	0.090	-	0.51	-0.83x	0.99
$0017+154$	3C 9	Q	0	2.012	Y	0.46	-0.52	1.05
$0024+349$	OB 338	S	0	0.333	-	-	-	-0.32
$0035+121$		B	V	-	-	-	-	-
$0048-097$	PHL 856	B	V	>0.20	N	0.37x	-0.66x	0.43
$0056-001$	PHL 923	Q	0	0.717	N	0.20x	-0.73x	-0.46
$0058+019$	PHL 938	Q	0	1.961	Y	0.57	-0.66	-
$0106+010$	4C 01.02	Q	0	2.107	N	0.35	-0.53	0.69
$0109+224$		B	V	-	N	0.34x	-0.63x	1.19
$0119-046$	4C 04.04	Q	0	1.969	Y	0.67	-0.49	-0.38
$0127+233$	3C 43	Q	V	1.459	N	-	-	-0.71
$0128+074$	PHL 3375	Q	V	0.39	N	0.32	-0.50	-
$0130+033$	PHL 1027	Q	0	0.363	N	-0.03x	-0.77x	-
$0133+476$	OC 577	Q	V	0.859	N	-	-	-
$0134+329$	3C 48	Q	V	0.367	N	0.40	-0.52	-0.85
$0135-057$	PHL 1078	Q	V	0.308	N	-0.06	-0.65	-
$0137+012$	PHL 1093	Q	V	0.258	N	-0.03	-0.87	-0.37
$0139+061$	PHL 3632	Q	V	1.479	N	0.22	-0.63	-
$0141+339$	4C 33.03	Q	0	1.455	Y	-	-	-1.07
$0147+089$	PHL 1186	Q	V	0.27	N	-0.02x	-0.83x	-
$0148+090$	PHL 1194	Q	V	0.299	N	-0.14	-0.89	-
$0151+048$	PHL 1222	Q	0	1.923	Y	0.67	-0.57	-
$0151+045$	PHL 1226	Q	V	0.404	Y	0.41x	-0.78x	-
$0159-117$	3C 57	Q	V	0.680	N	0.25	-0.84	0.74
$0202-170$		Q	V	1.740	N	-	-	-0.13
$0215+015$		B	OVV	1.715	Y	-	-	0
$0219+428$	3C 66A	B	V	0.444	N	0.33x	-0.58x	-
$0222-234$	MSH $02-27$	Q	V	0.23	-	-	-	-
$0226-038$	PHL 1305	Q	0	2.064	Y	0.29	-0.60	-0.24
$0229+130$	4C 13.14	Q	0	2.065	Y	0.25x	-0.73x	-0.24
$0232-042$	PHL 1377	Q	V	1.434	Y	0.20	-0.66	0.49
$0235+165$	AO	B	OVV	0.94	Y	0.96x	0.14x	1.03
$0237-230$		Q	0	2.225	Y	0.35	-0.81	0.48
$0301-243$		B	V	-	-	-	-	-0.47
$0306+102$	OE 110	B	OVV	0.863	-	0.45x	-0.40x	0.56
$0323+022$		B	0	0.147	-	0.50x	-0.50x	-
$0333+321$	NRAO 140	Q	0	1.258	N	-	-	-0.19
$0336-019$	CTA 26	Q	V	0.852	N	0.55x	-0.82x	0.25
$0338-214$		B	V	-	N	-	-	0.21

Table 1. (*Continued*)

Source	Name	Type	Var	z_e	z_a	$(B-V)^*$	$(U-B)^*$	α
0340 + 048	3C 93	Q	V	0.357	N	0.35	−0.50	−0.95
0349 − 146	MSH 03−19	Q	0	0.614	N	0.43	−0.72	1.13
0350 − 073	3C 94	Q	0	0.968	N	0.44x	−0.68x	−0.94
0403 − 130		Q	OVV?	0.571	N	0.28x	−0.57x	0.04
0405 − 121	MSH 04−12	Q	V	0.574	N	0.18	−0.60	−0.28
0414 + 009		B	V	0.287	N	0.48x	−0.70x	-
0414 − 060	3C 110	Q	0	0.781	N	0.29	−0.70x	−0.83
0420 − 014	OF O35	Q	OVV	0.915	Y	0.48x	−0.32x	−0.80
0422 + 004	OF 038	B	OVV	-	N	0.10x	−0.49x	0.36
0433 + 052	3C 120	S	OVV	0.033	-	0.67x	−0.77x	0.09
0440 − 033	NRAO 190	Q	OVV	0.844	N	0.37x	−1.05x	−0.64
0454 − 220		Q	V	0.534	Y	0.06x	−0.62x	−0.97
0513 − 002	AKN 120	S	0	0.033	-	0.38x	−0.77x	-
0518 + 165	3C 138	Q	0	0.759	N	−0.04	−0.64	0.57
0538 + 498	3C 147	Q	V	0.545	N	−0.05	−0.82	0.73
0642 + 449	OH 471	Q	V	3.408	Y	1.08x	1.70x	−0.81
0710 + 118	3C 175	Q	V	0.768	N	0.13	−0.78	0.98
0711 + 356	OI 318	Q	V	1.626	N	-	-	−0.32
0725 + 117	3C 181	Q	V	1.382	Y	0.24	−0.88	−0.26
0735 + 170	DA 237	B	OVV	>0.424	Y	0.47x	−0.58x	0.05
0736 + 017	OI 061	Q	V	0.191	N	0.43x	−0.77x	−0.10
0738 + 313	OI 363	S	V	0.631	Y	0.07x	−0.61x	0.24
0740 + 380	3C 186	Q	V	1.063	N	0.19	−0.81	0.67
0752 + 258	OI 287	Q	V	0.456	N	0.55x	−0.35x	−0.27
0754 + 100	OI 090.4	B	V	0.66	N	0.43x	−0.66x	0.58
0802 + 103	3C 191	Q	0	1.952	Y	0.29	−0.72	0.91
0805 + 046	4C 05.34	Q	V	2.88	Y	0.37x	−0.04x	−0.63
0809 + 483	3C 196	Q	V	0.871	Y	0.45	−0.43	0.89
0812 + 020	4C 02.23	Q	V	0.402	N	0.18x	−0.77x	−0.63
0818 − 128	OJ 131	B	OVV	-	N	0.30x	−0.40x	−0.02
0829 + 046	OJ 049	B	OVV	0.18	N	0.70x	−0.37x	0.07
0833 + 654	3C 204	Q	0	1.112	N	0.58	−0.78	0.61
0837 − 120	3C 206	Q	OVV	0.200	N	0.02x	−0.85x	−0.56
0850 + 140	3CR 208	Q	V	1.11	N	0.26	−0.79	−0.93
0851 + 202	OJ 287	B	OVV	0.206	N	0.39x	−0.64x	0.11
0906 + 015	4C 01.24	Q	OVV	1.018	N	0.47x	−0.85x	0.11
0922 + 149	4C 14.31	Q	V	0.896	N	0.37	−0.51	−0.38
0953 + 254	OK 290	Q	V	0.712	N	0.25x	−0.53x	0.80
0955 + 326	3C 232	Q	OVV	0.530	Y	0.08	−0.68	0.22
0957 + 003	OK 096	Q	V	0.907	Y	0.29	−0.69	−0.62

Table 1. (*Continued*)

Source	Name	Type	Var	z_e	z_a	$(B-V)^*$	$(U-B)^*$	α
$0957+561$	A	Q	0	1.413	Y	-	-	-
$0957+561$	B	Q	V	1.425	Y	-	-	-
$1004+130$	OL 331	S	OVV?	0.24	-	0.07	-0.82	-0.70
$1019+309$	OL 333	Q	V	1.319	N	0.26x	-0.77x	-0.64
$1021-006$		Q	V	2.547	N	0.20x	-0.22x	-0.39
$1040+123$	3CR 245	Q	V	1.029	N	0.31	-0.67	-0.67
$1048-090$	3C 246	Q	V	0.344	N	0.09	-0.37	-0.94
$1049+215$	4C 21.28	Q	V	1.300	N	-	-	-0.19
$1055+018$	4C 01.28	Q	V	0.888	N	0.46x	-0.53x	0.13
$1055+201$	4C 20.24	Q	V	1.110	N	0.36	-0.84	0.82
$1100+772$	3C 249.1	Q	V	0.311	N	-0.09	-0.64	-0.97
$1101+384$	Mark 421	B	V	0.031	N	0.51x	-0.55x	0.33
$1116+128$	4C 12.39	Q	V	2.118	Y	0.35	-0.61	-0.33
$1119+183$	OM 133	Q	V	1.040	N	-	-	0.00
$1127-145$	OM 146	Q	0	1.187	N	0.23	-0.73	-0.19
$1137+660$	3C 263	Q	OVV	0.652	Y	0.29	-0.68	0.80
$1147+245$	OM 280	B	0	>0.20	N	0.52x	-0.60x	0.39
$1148-001$	4C 00.47	Q	V	1.980	Y	0.37	-1.20	-0.49
$1150+497$	4C 49.22	Q	0	0.334	N	0.30x	-0.97x	-0.58
$1156+295$	4C 29.45	Q	OVV	0.729	N	0.39x	-0.50x	-0.42
$1206+439$	3C268.4	Q	V	1.400	Y	0.58x	-0.69x	-0.94
$1215+303$	ON 325	B	OVV	0.237	N	0.46x	-0.61x	-0.19
$1217+023$	ON 029	Q	OVV	0.24	Y	-0.06	-0.77	0.04
$1218+304$	RS 4	B	V	-	N	0.65x	-0.50x	-
$1218+329$	3C 270.1	Q	0	1.519	Y	0.34	-0.65	0.85
$1219+285$	ON 231	B	OVV	0.102	N	0.61x	-0.54x	-
$1226+023$	3CR 273	Q	V	0.158	Y	0.13	-0.81	0.08
$1229-021$	4C 02.55	Q	V	1.038	Y	0.55	-0.66	-0.47
$1229+202$		S	V	0.064	-	0.27x	-1.02x	-
$1237-101$	ON 162	Q	V	0.753	N	-0.03x	-0.75x	0.00
$1246+377$	BSO 1	Q	V	1.266	Y	0.34	-0.49	-
$1246+346$	B 46	Q	V	0.271	N	0.35	-0.71	-
$1248+337$	BSO 2	Q	V	0.186	N	0.32	-1.02	-
$1252+119$	ON 187	Q	0	0.870	N	0.20	-0.75	-0.30
$1252+359$	B 114	Q	V	0.210	N	0.08	-0.77	-
$1253-055$	3C 279	Q	OVV	0.536	N	0.35	-0.71	-0.41
$1255+353$	B 154	Q	V	0.183	N	0.27	-0.72	-
$1256+357$	B 194	Q	0	0.894	Y	0.67	-0.58	-2.66
$1257+346$	B 201	Q	0	1.375	N	0.29	-0.53	-
$1259+344$	BSO 6	Q	0	1.956	N	0.29	-0.78	-

Table 1. (*Continued*)

Source	Name	Type	Var	z_e	z_a	$(B-V)^*$	$(U-B)^*$	α
1304 + 374	B 312	Q	0	0.450	N	0.28	−0.81	-
1308 + 3266	OP 313	B	OVV	0.996	Y	-	-	0.20
1311 + 362	BSO 11	Q	0	2.084	Y	0.28	−0.64	-
1318 + 290	Ton 155	Q	0	1.703	Y	0.12x	−0.90x	-
1318 + 290	Ton 156	Q	0	0.549	N	0.08x	−0.66x	-
1328 + 254	3C 287	Q	0	1.055	N	0.51	−0.47	0.54
1347 + 214	UM 614	S	0	0.033	-	0.89x	-	-
1354 + 195	4C 19.44	Q	OVV?	0.720	Y	0.25	−0.64	−0.06
1402 − 012	UM 632	Q	V	2.522	Y	0.21x	−0.27x	0.22
1418 + 546	OQ 530	B	V	0.152	N	0.66x	−0.50x	0.38
1442 + 101	OQ 172	Q	V	3.535	Y	0.80x	−0.37x	−0.71
1458 + 718	3C 309.1	Q	V?	0.905	N	0.29	−0.76	0.54
1502 + 036		Q	0	0.411	N	0.47x	−0.56x	-
1510 − 089	OR 017	Q	OVV?	0.361	Y	0.21	−0.65	-
1514 − 241	Ap Lib	B	OVV	0.048	N	0.80x	−0.29x	−0.16
1526 + 285	Ton 236	Q	0	0.450	N	0.00x	−0.60x	-
1532 + 01E		Q?	V	0.310	N	-	-	-
1532 + 01W	1532+016	Q	V	1.435	N	-	-	−0.26
1538 + 149	4C 14.60	B	V	0.605	N	0.52x	−0.60x	0.34
1545 + 210	3C 323.1	Q	OVV	0.264	N	0.07	−0.68	−0.56
1546 + 027	OR 078	Q	V	0.413	N	0.17x	−0.71x	0.17
1553 + 113		Q	V	0.360	N	-	-	-
1606 + 289		Q	V	2.560	N	-	-	−0.42
1611 + 342	OS 319	Q	V	1.401	N	-	-	0.19
1612 + 261	Ton 256	Q	V	0.131	N	0.65x	−0.78x	−2.29
1615 + 029		Q	0	1.339	N	−0.08x	−1.04x	−0.19
1618 + 177	3CR 334	Q	OVV	0.555	N	0.23	−0.94	1.32
1638 + 398	NRAO 512	Q	OVV	1.666	N	-	-	0.12
1641 + 399	3C 345	Q	OVV	0.594	N	−.39	−0.64	0.26
1652 + 398	MK 501	B	0	0.033	N	0.74x	−0.25x	0.06
1704 + 608	3CR 351	Q	OVV?	0.371	Y	0.11	−0.77	−0.85
1727 + 501	I ZW 187	B	0	0.053	N	0.63x	−0.52x	−0.18
1730 − 130	NRAO 530	Q	OVV	0.902	N	-	-	−0.25
1749 + 701		B	V	0.770	N	0.45x	−0.50x	0.25
1749 + 096	4C 09.57	B	V	0.322	N	0.52x	−0.42x	1.01
1807 + 698	3C 371	B	OVV	0.051	N	0.55x	−0.48x	0.14
1828 + 487	3C 380	Q	V	0.691	N	0.17	−0.79	0.47
1831 + 731		S	0	1.356	-	-	-	-
1845 + 797	3C 390.3	S	V	0.057	-	0.68x	−0.69x	−0.63
1901 + 319	3C 395	Q	V	0.635	N	-	-	−0.58

Table 1. (*Continued*)

Source	Name	Type	Var	z_e	z_a	$(B-V)^*$	$(U-B)^*$	α
$1929-293$	OV 236	Q	OVV	0.352	N	-	-	-
$2059+034$	OW 098	Q	V	1.013	N	0.35x	-0.84x	0.44
$2128-123$	PHL 1598	Q	V	0.501	Y	0.27	-0.82	-0.11
$2131-021$	4C 02.81	B	V	0.557?	N	-	-	0.13
$2134+004$	PHL 61	Q	0	1.936	N	0.30x	-0.94x	-
$2135-147$	PHL 1657	Q	OVV	0.200	Y	-0.03	-0.84	-
$2145+067$	4C 06.69	Q	0	0.990	Y	0.32	-0.76	0.40
$2154-184$		Q	0	0.668	N	-	-	-1.17
$2155-304$		B	V	0.116	Y	0.35x	-0.73x	1.77
$2200+420$	BL LAC	B	OVV	0.069	N	0.97x	-0.10x	-0.13
$2201+315$	4C 31.63	Q	0	0.298	Y	0.09x	-0.76x	-
$2209+080$	4C 08.64	Q	0	0.484	N	-	-	-0.51
$2216-038$	4C 03.79	Q	0	0.901	N	0.63x	-0.71x	-0.61
$2223-052$	3C 446	Q	OVV	1.404	N	0.48	-0.63	-0.08
$2223+210$	DA 580	Q	0	1.935	Y	-	-	-
$2230+114$	CTA 102	Q	V	1.037	N	0.28	-0.63	0.50
$2251+113$	4C 11.72	Q	0	0.323	N	0.15	-0.68	-0.70
$2251+158$	3C 454.3	Q	OVV	0.859	N	0.33	-0.66	-0.79
$2251+244$	4C 24.61	Q	V	2.237	Y	-	-	-0.94
$2251-178$		S	V	0.068	-	0.91x	0.05x	-
$2254+024$	OY 091.3	Q	0	2.091	N	0.083	-	0.17
$2254+074$	OY 091	B	OVV?	0.19	N	0.66	-0.44x	1.19
$2304+187$	4C 18.68	Q	V	0.313	N	0.13x	-0.75x	-0.42
$2335-181$		Q	V	1.441	N	0.07x	-0.91x	-0.18
$2344+092$	4C 09.74	Q	V	0.677	N	0.36	-0.71	-0.06
$2345-167$	OZ 176	Q	OVV	0.600	N	-	-	-1.82
$2349-014$	PB 5564	Q	V	0.174	N	0.12x	-0.90x	-0.60
$2354-117$		Q	0	0.960	N	-	-	-0.18
$2354+144$	4C 14.85	Q	V	1.816	Y	0.14x	-0.90x	1.61

Notes: **Q** = QSO; **S** = Seyfert; **B** = BL Lac; **Var** = degree of variability; z_e = emission line redshift; z_a = absorption line redshift; **N** = No; **Y** = Yes; $(U-B)^*$ and $(B-V)^*$ = continuum color indices; **x** under $(U-B)^*$ and $(B-V)^*$ columns = observed values of color indices; α = radio spectral index between emitted frequencies of approximately 3.0 GHz and 12.0 GHz.

spectra, and a distinct tendency was exhibited by the mean spectral index to approach flatness, while the percentage of quasars showing flat radio spectra was seen to increase with increase in optical variability (Basu 1973). On the other hand, optically variable QSOs demonstrated significant dependence of the degree of variability on the redshift (Basu 1980a). It was further suggested that the very long term variability of QSOs may be caused by changes in the intervening medium over the years along the line of sight through which light travels (Basu 1980b). Variability of QSOs was also shown

Table 2. Breakdown of data in Table 1.

	QSO				BL Lac				Seyfert				
Sec	T	0	V	OVV	T	0	V	OVV	T	0	V	OVV	Total
2	110(74)	27(23)	63(35)	20(16)	28	3	10	15	7	1	2	4	145
3	144(54)	44(19)	76(22)	24(13)	27	4	10	13	11	3	5	3	182
4	145(54)	45(24)	75(30)	25(0)	31	3	14	14	-	-	-	-	176
5(a)	71(48)	22(17)	35(19)	14(12)	-	-	-	-	-	-	-	-	71
5(b)	45	15	24	6	29	4	14	11	7	1	4	2	81

Note:

- Section numbers in the first column refer to the section where the data have been used. 5(a) refers to data for continuum color indices, and 5(b) refers to data for observed color indices.
- Numbers within parentheses under 'QSO' refer to those used in earlier analyses referred to in the text.
- T is 'Total', and 0, V, OVV are degrees of variability.

to be independent of the appearance of absorption lines (Basu 1985). On the other hand, statistically significant relations were found between continuum color indices and redshifts for $V = OVV$ QSOs, while no such relation existed for $V = 0$ and $V = V$ QSOs (Basu 1987).

However, the volume of data has increased enormously since the above analyses were performed. Furthermore, while the earlier works reported above were carried out mostly with QSOs, extensive data are now available for other types of extragalactic objects as well, viz., BL Lacs and Seyferts, which provide an opportunity to compare properties of these three types of objects. The importance of these objects in such studies will be appreciated as they exhibit many similar characteristics and also due to the possibility of existence of continuity in their properties (Thakur & Sapre 1980; Basu 1986). We were therefore prompted to re-examine the relationships mentioned above with the help of updated data involving the three types of extragalactic objects, viz., QSOs, BL Lacs and Seyferts, collectively known as Active Galactic Nuclei (AGNs). It may be mentioned in this connection that various aspects of AGN variability have been reviewed recently by Ulrich *et al* (1997).

Our data base presented in Table 1 has been prepared from Evans (1972); Basu (1973, 1980a); Burbidge *et al* (1997); Pica *et al* (1988); Webb *et al* (1988); Stickel *et al* (1991); Elvis *et al* (1994); Hewitt & Burbidge (1993); Padovani & Giommi (1995); Veron-Cetti & Veron (1996); Fan (1997) and Hall *et al* (1998). A breakdown of the number of different types of objects in different classes in the present analysis compared to the same in the earlier work is shown in Table 2. The purpose of this paper is to draw attention of researchers in the field to certain relationships that exist and/or do not exist although expected to exist, between various properties stated above of different types of extragalactic objects in relation to their variability. Throughout the work it has been assumed that the samples used are representative of their classes, even though the samples of different AGN classes are actually heterogeneously selected. Further, the samples comprising the three classes combined, viz., QSOs, BL Lacs and Seyferts, are hereinafter called Active Galaxies (AGs).

2. Optical variability and radio spectral index

A major contribution of optical monitoring of extragalactic objects has been the discovery of the OVVs which are now thought to possibly represent a separate class of objects that includes QSOs along with BL Lacs (the so called "Blazars") which are believed to be beaming their radiation toward the observer (Angel & Stockman 1980). One of the important properties of OVVs is that they show flat radio spectra, as mentioned above, based on which models have been proposed for these objects. Special attention is therefore needed as to how do OVVs particularly distinguish themselves, if at all, in respect of radio spectra from objects with $V = 0$ and $V = V$.

We calculated radio spectral index (α) from data at observed frequencies of 2.695 GHz and 5.0 GHz. The observed frequencies (ν_{ob}) are converted to emitted frequencies (ν_{em}) as $\nu_{em} = \nu_{ob}(1 + z)$, where z is the redshift of the object. α is defined as $S_\nu = \nu^\alpha$, where S_ν is the flux value at the frequency ν. This provided us with α values between emitted frequencies of approximately 3.0 GHz to 12.0 GHz for redshift values of the sample used here. α_2 values of Basu (1973) are used as α in the present analysis, and additional values of α have been calculated and/or obtained from data available in Stickel *et al*. (1991), Veron-Cetti & Veron (1996) and Hall *et al*. (1998).

Results are shown in Fig. 1 as the distribution of the radio spectral index for the three variability classes. For each class, individual samples of QSOs, BL Lacs, Seyferts and AGs are shown. The mean value of each distribution and the standard deviation (σ_n) are presented in Table 3.

Several features are seen in Table 3 and Fig. 1. The way the quantity α has been defined, a spectra will be called flat if α is more negative than 0.5 or more positive than -0.5, i.e., if α remains between ± 0.5. Based on this criteria, all the spectra are flat from consideration of the mean values of their distributions (with the exception of BL Lacs for $V = V$ which is also actually nearly flat). This is in contrast to earlier findings where flatness was found to be related to the degree of variability (Basu 1973). Furthermore, the present analysis indicates no statistically significant change in mean values of the radio spectral index at the high frequencies with the degree of variability, in either of the individual samples viz., QSOs, BL Lacs or Seyferts, or AGs. It is, however, noted in Table 3 that the standard deviation is quite high in all cases, as in the previous analysis.

Results presented in Table 4 demonstrates that almost the same proportion of objects in each of the three variability classes exhibit flat radio spectra, viz., 50 to 60 per cent of AGs, 40 to 50 per cent of QSOs and 70 to 80 per cent of BL Lacs, while the sample is too small for consideration for Seyferts.

The analysis confirms earlier findings (Basu 1973) that, contrary to the currently existing view, in which OVV objects are regarded as exhibiting flat radio spectra, this is really not a unique property of OVV objects, but the property is almost equally shared by objects of moderate variablity and non-variables as well.

3. Optical variability and redshift

The dependence of variability on redshift is complicated by the dependence of variability on absolute luminosity as well, while at the same time the absolute luminosity

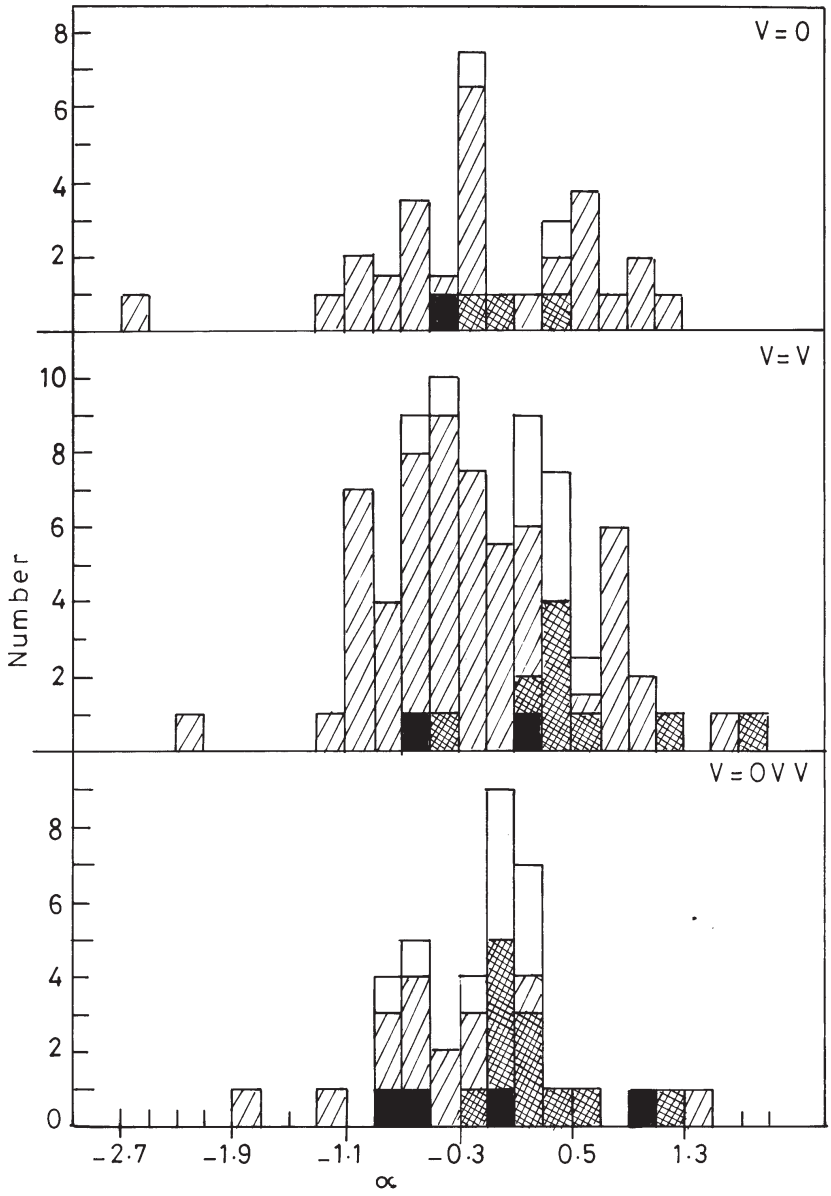

Figure 1. Distribution of mean radio spectral index (α) at high frequencies (rest frame) for three variability classes. White = AGs; Hatches = QSOs; Crossed hatches = BL Lacs; Dark = Seyferts.

itself is anti-correlated with redshift, and this "has resulted in a complex situation" (Cristiani *et al*. 1996). Cristiani *et al*. (1996) have developed a 'variability index' (IDX) which is a measure of the intrinsic variance and takes also photometric errors into consideration. They found that the IDX is anti-correlated with redshift, although correlated with absolute magnitude. However, since absolute magnitude, in its turn, is anti-correlated with redshift, these relations may not be real. In practice, it is difficult

Table 3. Mean values of α and corresponding σ_n.

Sample	Variability	No. of objects	α	σ_n
AG	0	51	−0.1484	0.7586
	V	91	−0.1681	0.6674
	OVV	40	−0.1263	0.6094
QSO	0	44	−0.1286	0.8093
	V	76	−0.1841	0.6674
	OVV	24	−0.3143	0.6342
BL Lac	0	4	0.0667	0.2494
	V	10	0.5200	0.5671
	OVV	13	0.2133	0.4097

Table 4. Percentage of objects with $\alpha = \pm 0.5$.

Sample/Variability	No. of objects	0	V	OVV
QSO	144	41	50	50
BL Lac	27	75	70	80
Seyfert	11	100	50	25
AG	182	47	53	59

to know the relative dependence of variability on redshift and on absolute luminosity, individually, and to separate the two from each other. No such attempt has been made in the present analysis.

Figure 2 shows the redshift distribution of the entire sample for the three different degrees of optical variability. As in the previous analysis, the striking feature of the diagram is that while the non-variable and, to some extent, the moderate variable objects are spread more or less uniformly along the redshift scale up to $z = 2.50$ to $z = 3.0$, OVV objects are concentrated at the lower range of the scale, mostly at $z < 1.0$.

Mathematically, χ^2 test is performed to determine any significant dependency of the degree of variability on the lower redshift range ($z < 1.0$) versus the higher redshift range ($z > 1.0$) (there is no object in Table 1 with $z = 1.0$) for AGs, QSOs and BL Lacs, the sample being too small for Seyferts for any such test. 2×3 contingency tables for three degrees of variability against redshifts of lower and higher ranges are shown in Table 5. The analysis is repeated with 2×2 contingency tables for nonvariables ($V = 0$) and variables ($V = V$ plus $V = OVV$) against lower and higher redshift ranges (Table 6). Results given in Table 7 show that the hypothesis of dependency is statistically significant at high levels for all samples, except for BL Lacs where the significance is marginal for variables against non-variables. This confirms the earlier result that optically variable QSOs exhibit statistically significant dependency of the

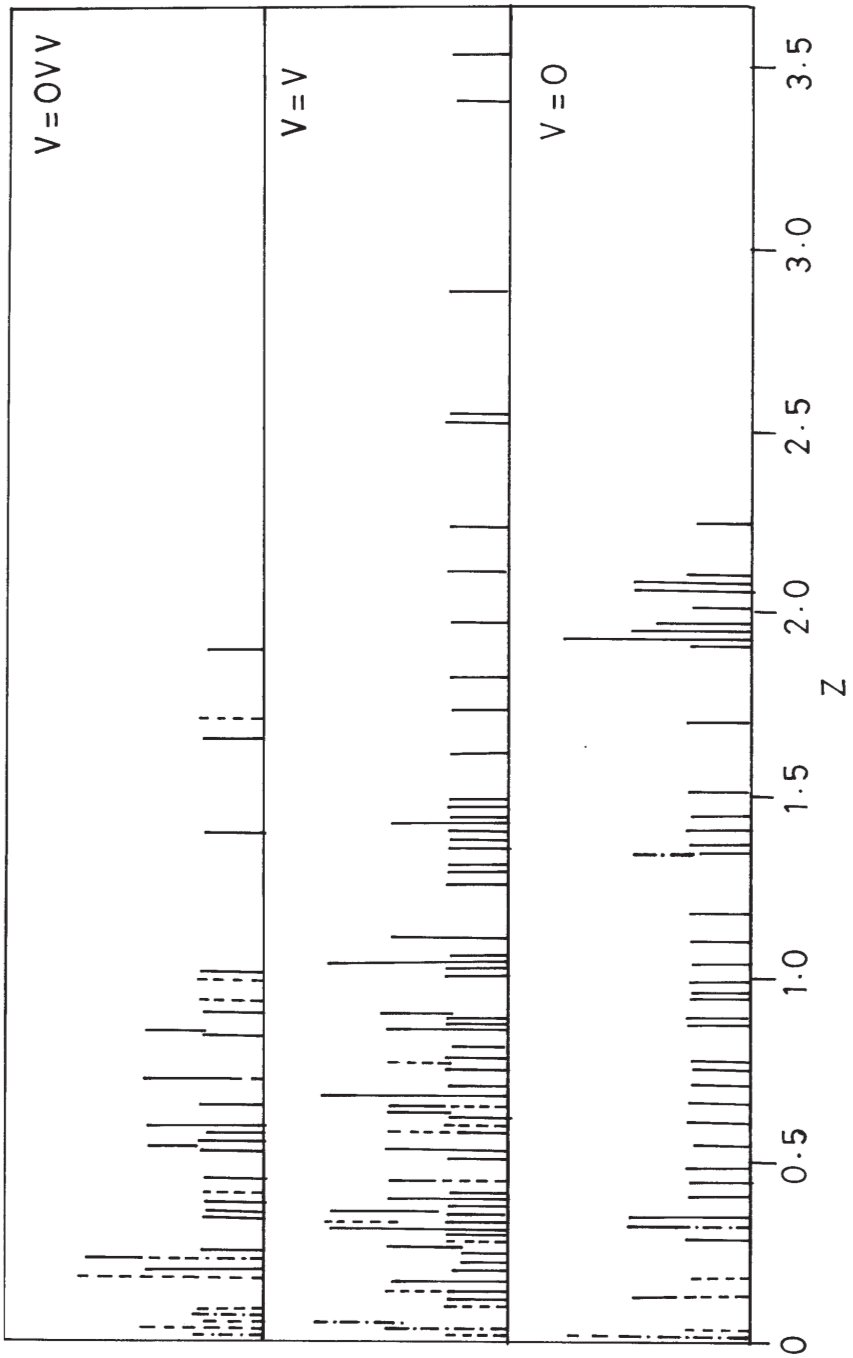

Figure 2. Distribution of redshifts for three variability classes. Each small bar represents an object with the corresponding redshift value. Solid line = QSOs; Dashed line = BL Lacs; Dashes and dots = Seyferts.

Table 5. 2×3 tables for variability against z.

Sample	z/Var	0	V	OVV
AG	$z < 1.0$	26	58	36
	$z > 1.0$	25	32	4
QSO + BL Lac	$z < 1.0$	24	53	33
	$z > 1.0$	24	32	4
QSO	$z < 1.0$	20	43	21
	$z > 1.0$	24	32	3
BL Lac	$z < 1.0$	4	10	12
	$z > 1.0$	0	0	1
Seyfert	$z < 1.0$	2	5	3
	$z > 1.0$	1	0	0

Table 6. 2×2 tables for variability against z.

Sample	z/Var	0	V + OVV
AG	$z < 1.0$	26	94
	$z > 1.0$	25	36
QSO + BL Lac	$z < 1.0$	24	86
	$z > 1.0$	24	36
QSO	$z < 1.0$	20	64
	$z > 1.0$	24	35
BL Lac	$z < 1.0$	4	22
	$z > 1.0$	0	1

degree of variability on redshift (Basu 1980a), and the finding is now extended to other objects like BL Lacs and possibly to Seyferts, and AGs, i.e., extragalactic objects in general.

This is of course expected, as $\Delta t_{\text{observed}} = (1 + z)\Delta t_{\text{intrinsic}}$, and observed high redshift sources will tend to be less variable in the observer's reference frame. This also explains why OVV objects seem to concentrate at low redshift regions. Moreover, the known correlation between variability time scales and luminosity (see e.g., Netzer *et al*. 1996) would support having less variable sources at higher redshift regions.

4. Optical variability and absorption features

Variability is measured as a change in optical magnitude of the object over a certain period of time. Such changes may result from physical phenomena occurring in the

Table 7. Results of χ^2 tests for var against z.

Sample	Table	χ^2	Sig level
AG	2×3	15.07	99.0
QSO + BL Lac	2×3	14.39	99.0
QSO	2×3	11.2	99.0
AG	2×2	7.62	99.5
QSO + BL Lac	2×2	6.52	99.0
QSO	2×2	4.83	95.0
BL Lac	2×2	1.09*	75.0
BL Lac	2×3	36.0	99.9

* Yeates correction applied.

source itself (intrinsic) or from changes occurring in the intervening medium along the line of sight. It is known that absorption lines may also originate intrinsically to the object itself or at the intervening medium. Thus the intervening medium may be the common cause associated with the occurrence of both variability and absorption lines, at least in some cases, in extragalactic objects.

Analysis of a sample of 54 QSOs taken out of 64 objects, "probably complete" to $m \leq 18.0$, demonstrated (Basu 1985) that optical variability is not associated with the presence or absence of absorption lines in QSOs. Thus, χ^2 test performed for the absence or presence of absorption lines against non-variable ($V = 0$) and variable ($V = V$ plus $V = OVV$) QSOs did not show any association of variability with the appearance of absorption features, even though Borra (1975) claimed optical variability to be more frequent among QSOs with absorption lines than those without any absorption feature.

Table 8. 2×3 tables for Abs lines against var.

Sample	Abs lines/Var	0	V	OVV
QSO + BL Lac	Yes	18	21	12
	No	30	68	27
QSO	Yes	18	20	8
	No	27	55	17
BL Lac	Yes	0	1	4
	No	3	13	10

Table 8 shows the 2×3 contingency tables for the presence and absence of absorption lines against the three degrees of variability for different samples. We also performed the χ^2 test with 2×2 contingency table for the presence or absence of absorption lines against non-variables ($V = 0$) and variables ($V = V$ plus $V = OVV$) with the same sample, and this is shown in Table 9.

As in the earlier work, we repeated the latter analysis by eliminating the objects with $z < 1.0$ from the sample, which left us with 59 QSOs (Table 9), in order to look

Table 9. 2×2 tables for Abs lines against var.

Sample	Abs lines/Var	0	0 + OVV
QSO + BL Lac	Yes	18	33
	No	30	95
QSO	Yes	18	28
	No	27	72
QSO ($z > 1.0$)	Yes	15	13
	No	9	21
BL Lac	Yes	0	5
	No	3	23

Table 10. Results of χ^2 tests for Abs lines against var.

Sample	Table	χ^2	Sig level
QSO + BL Lac	2×3	-20.95	0
QSO	2×3	1.94	< 75
BL Lac	2×3	-1.90	0
QSO + BL Lac	2×2	2.33	< 75
QSO	2×2	2.06	< 90
QSO ($z > 1.0$)	2×2	10.25	99.9
BL Lac	2×2	0.64	50

for any selection effect, as it has been pointed out (Basu 1982) that relatively more absorption lines are seen at $z > 1.0$.

Table 10 shows the χ^2 values and corresponding significance levels for these analyses. It will be seen that none of the samples considered is statistically significant, except QSOs with $z > 1.0$. Thus the presence or absence of absorption lines in extragalactic objects is, in general, independent of the variability of the object, and this confirms the earlier findings for QSOs in this respect (Basu 1985).

However, it also appears that the above mentioned selection effect may have influenced the result for the current sample of QSOs with $z > 1.0$, in which the presence or absence of absorption lines is significantly associated with the degree of variability. More observations are therefore needed.

On the other hand, BL Lac objects individually or in combination with QSOs, i. e., extragalactic objects in general (QSOs plus BL Lacs) exhibit absorption features in their spectra independent of their optical variability. The reason may be the low redshifts ($z < 1.0$) of the BL Lacs. No test was performed for BL Lacs with $z > 1.00$ as almost all BL Lacs have $z < 1.00$.

The number of Seyfert galaxies in the sample is too small for a separate analysis. Furthermore, there is no data available for their absorption features. Also, redshifts

of Seyferts are even smaller than those of BL Lacs, and hence it is very unlikely that Seyferts will influence the conclusion reached above in connection with extragalactic objects in general.

Assuming redshift is cosmological, $z > 1.0$ corresponds to objects at very large distances implying a larger light path through the intervening medium. It may be worth investigating (which is of course beyond the scope of the present work) whether the two phenomena, viz., variability and absorption lines for objects with $z > 1.0$, if there is no selection effect for the close association between the two, may have a common origin in the intervening medium, as was pointed out by Basu (1987). It is known that variability is observed at other wavelength bands as well, e.g., hard x-ray and infra-red, which are much less affected by absorption. Variability in such cases may be assigned to be an intrinsic phenomenon.

5. Optical variability and color-redshift relation

Variation of color indices with redshifts is known to be complex and does not exhibit any correlation (McCrea 1966; Strittmatter & Burbidge 1967; Goldsmith 1972; Basu 1981, 1986, 1990). The importance of such study lies in the fact that a simple relationship between the redshift and color indices may lead to the prediction of redshifts from photometric observations, a rather much easier way of determination of redshifts. Derivation of energy distribution function is another possibility, although continuum color indices have to be used for the purpose. The effect of variability, if any, in such investigations would certainly throw more light on the phenomena involved.

Basu (1980b) analysed continuum color indices (Evans 1972) and found a statistically significant correlation between redshift and continuum color indices for OVV QSOs, although no such correlation was exhibited by the other two classes, viz., $V = 0$ and $V = V$. As was indicated in Basu (1974, 1980b, 1986), continuum color indices are better suited for such analyses since observed indices are contaminated with the presence of emission lines.

Nevertheless we have also added observed color indices in Table 1 for objects for which continuum indices are not available. As far as is known to us, continuum color indices have not been determined other than the work of Evans (1972), and more recently, that of Elvis *et al* (1994), used in the present analysis. Published data and work with observed color indices are actually more common in catalogues and literature (e.g., McCrea 1966; Strittmatter & Burbidge 1967; Goldsmith 1972; Hewitt & Burbidge 1993; Veron-Cetti & Veron 1996). The present study with observed color indices may provide a comparison.

Figures 3 to 5 show plots of color indices, both observed ($(U-B)x$, $(B-V)x$) and continuum ($(U-B)^*$, $(B-V)^*$), against redshifts for QSOs, BL Lacs and Seyferts separately, for the three degrees of variability. The plots may appear random distribution of points, but following up individual symbols would demonstrate some significant correlations, and these are presented in Table 11 (we did not consider any correlation for samples with total number of objects less than 15).

In case of AGs, significant correlation is established for redshift against $(U-B)^*$ for $V = 0$ and $V = OVV$, and $(B-V)^*$ for $V = V$. As for QSOs, whereas the previous analysis showed significant correlation for $(U-B)^*$ and $(B-V)^*$ against redshifts only for OVVs, the present analysis demonstrates such relation for $(U-B)^*$ for $V = 0$, and $(B-V)^*$ for $V = V$ and $V = OVV$.

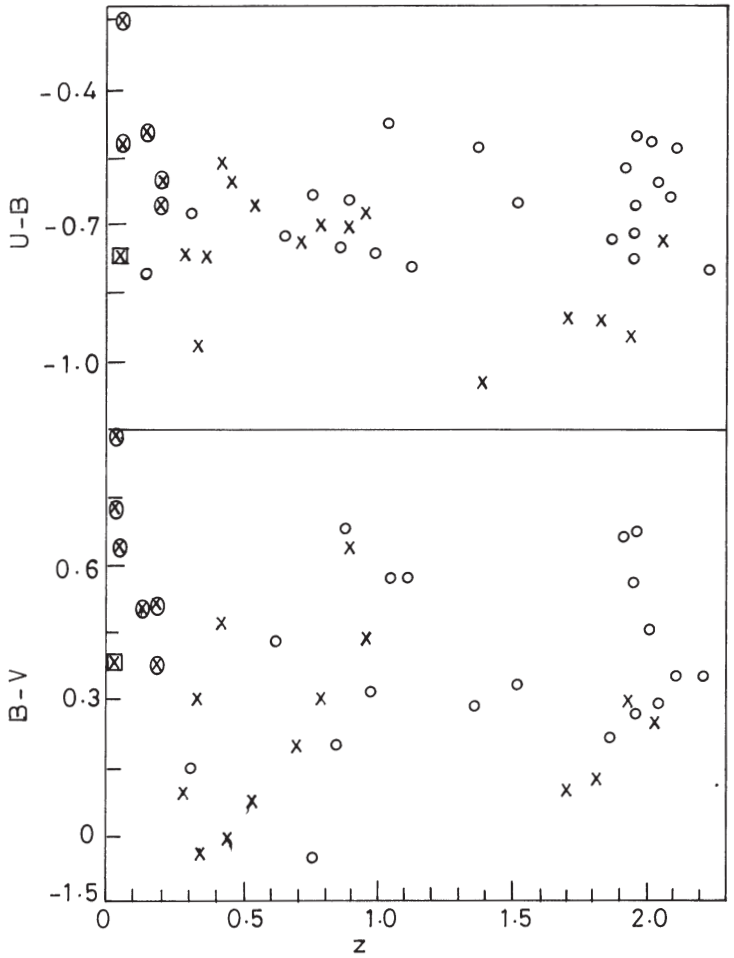

Figure 3. Plots of color indices against redshifts for variability class $V = 0$. Circles and crosses = QSOs; filled circles and crossed circles = BL Lacs; squares and crossed squares = Seyferts. Crossed symbols = $(U - B)x$ or $(B - V)x$; Non-crossed symbols = $(U - B)^*$ or $(B - V)^*$.

On the other hand, observed color indices $(U - B)x$ and $(B - V)x$ show significant correlation for $V = V$ and $V = 0$ (latter, although negative) respectively for AGs. As for QSOs, such relations are demonstrated by both $(U - B)x$ and $(B - V)x$ for $V = V$, and $(B - V)x$ for $V = OVV$.

Significant correlation of color indices against redshift is therefore not limited to OVV objects only, as was found in the earlier analysis (Basu 1986).

The relationships shown by the observed color indices against redshifts are important from the practical point of view in the sense that redshifts can be predicted and/or determined from photometric observations. A statistically significant relationship between the two quantities has long been sought for in the past (see Basu 1986, in this respect). In general, extragalactic objects do not show such a relation. However, Table 11 would demonstrate that for non-variable ($V = 0$) and moderate variable ($V = V$) objects highly significant linear relations do exist for the observed color indices $(U - B)x$

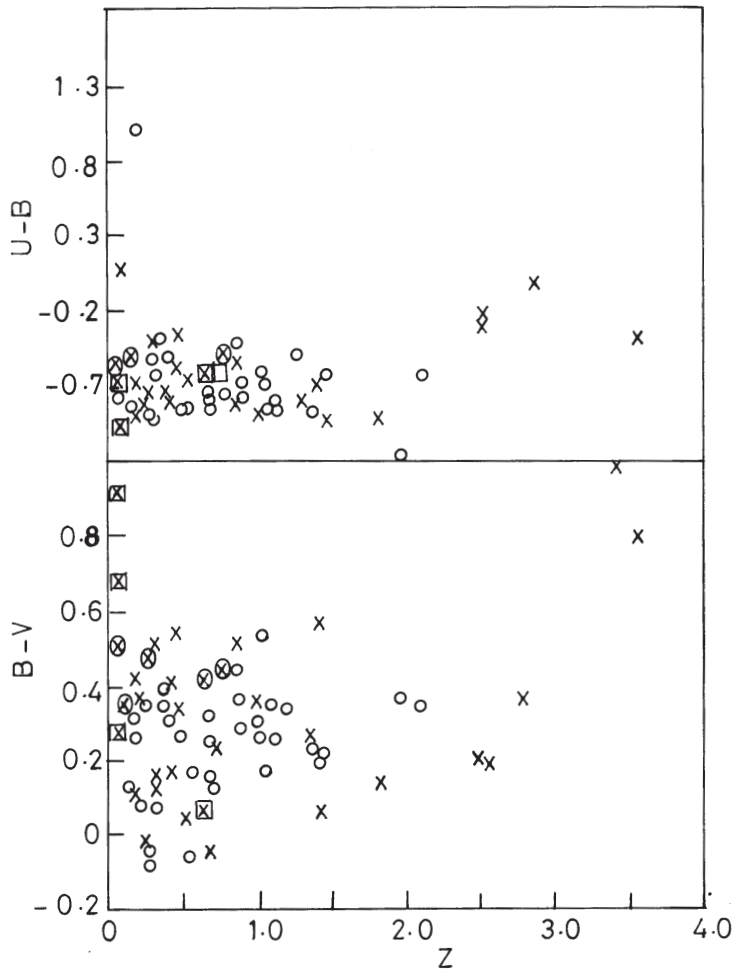

Figure 4. Same as Fig. 3, for variability class $V = V$.

and $(B - V)x$. As mentioned earlier, such prediction and/or determination of redshifts from photometric measurements is a much simpler and easier method and should be exploited.

We can represent a significant linear relation between a color index (CI) and redshift (z) by CI = A + Bz, where CI can be $(U - B)x$ or $(B - V)x$ and A, B are constants. Determination of A and B from data in Table 1 shown in Figs. 3 and 4 leads to

$$(U - B)x = -0.7955 + 0.2678z \text{ for AGs for } V = V, \quad (1)$$

$$(B - V)x = 0.4365 + 0.1578z \text{ for AGs for } V = 0, \quad (2)$$

$$(U - B)x = -0.9453 + 0.3343z \text{ for QSOs for } V = V, \quad (3)$$

$$(B - V)x = 0.1981 + 0.1133z \text{ for QSOs for } V = V. \quad (4)$$

Equations (1) to (4) can be used for prediction and/or determination of redshifts from values of color indices obtained by photometric measurements. This can be demon-

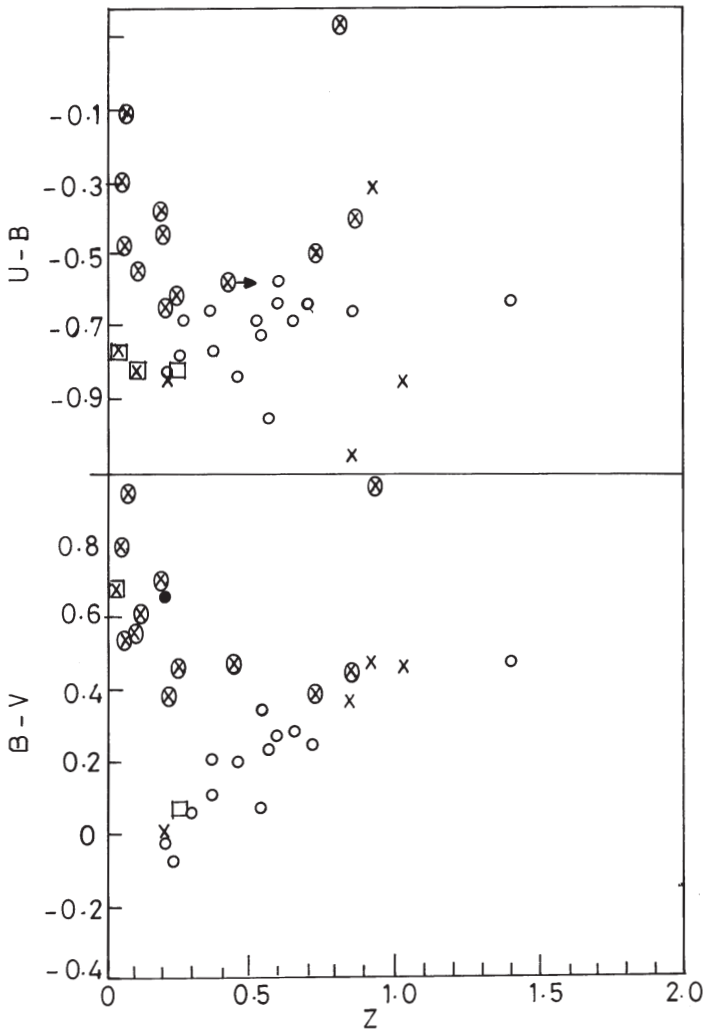

Figure 5. Same as Fig. 3, for variability class $V = OVV$.

strated for individual objects of our own sample. Thus redshifts computed from the above equations are 0.9914 (object 1055 + 018), 2.0057 (object 1328 + 290), 2.708 (object 0805 + 046) and 1.3407 (object 2059 + 034), the spectroscopic values being 0.888, 1.703, 2.88 and 1.013, and hence accuracies 11.6, 17.8, 6.4 and 32.3pc respectively. Accuracies appear reasonable and better for $(U - B)x$ values than those for $(B - V)x$ values, which can also be seen from the relatively larger correlation coefficients of $(U - B)x$ versus z than those for $(B - V)x$ versus z.

It is, however, admitted that although the statistical significance levels are high, appreciable scatters are present in Figs. 3 and 4. More data obtained from future observations would probably make less scatters in the diagrams, and hence better prediction and/or determination of redshifts from such relations. Furthermore, equations (1) to (4) obtained for the present sample can be used for prediction and/or determination of

Table 11. Correlation coefficients with redshift.

Sample	Parameter	Var = 0			Var = V			Var = OVV		
		r	L	Sig?	r	L	Sig?	r	L	Sig?
AG	$(U-B)^*$	0.3554	95	Y	0.1056	0	N	0.4832	>95	Y
	$(B-V)^*$	0.2859	90	M	0.4089	99	Y	0.2923	85	N
	$(U-B)x$	-0.3306	93	M	0.5714	99	Y	-0.0071	0	N
	$(B-V)x$	-0.4012	97	Y	0.1791	88	N	-0.1814	<80	N
QSO	$(U-B)^*$	0.3554	95	Y	0.1056	0	N	0.4443	99.9	Y
	$(B-V)^*$	0.2851	90	M	0.4089	99	Y	0.5600	99.9	Y
	$(U-B)x$	-0.4182	92	M	0.6664	99	Y	0.1171	0	N
	$(B-V)x$	0.0667	0	N	0.4061	98	Y	0.9748	99.9	Y

Notes: r = Correlation coefficient; **L** = Level of significance; **Sig?** = whether significant; **Y** = Yes; **N** = No; **M** = Marginal.

redshifts from photometric measurements for $(U-B)x > -0.7955$, $(B-V)x < 0.4365$, $(U-B)x > -0.9453$ and $(B-V)x > 0.1981$ respectively.

6. Conclusion

The foregoing analyses lead us to make the following important conclusions with respect to optical variability of extragalactic objects in relation to their redshifts and other properties. It is, however, admitted that some selection effects have not been taken into consideration. As an example, low redshift objects are likely to be nearer and brighter and hence better studied than high redshift ones which are expected to be fainter. Some degree of caution is therefore suggested with respect to the conclusions stated below.

• Radio spectral index at high frequencies (rest frame) does not change significantly with the degree of variability of extragalactic objects. OVV objects which have drawn special attention in this respect exhibit flat radio spectra at high frequencies (rest frame), but this is not an exclusive property of OVVs only, as has so far been considered, since objects of lower categories of variability and non-variables also show such spectra.

• The degree of variability of AGs depend significantly on redshifts in the sense that smaller redshift objects exhibit a higher degree of variablity.

• Presence or absence of absorption lines in AGs does not depend on the degree of variability except for QSOs at larger redshifts (> 1.0).

• Correlation between color indices and redshift depends on the degree of variability and the sample considered. Thus:

(a) For AGs, in general, continuum color index $(U-B)^*$ exhibit significant correlation for non-variables and violent variables and $(B-V)^*$ for moderate variables. For QSOs, $(U-B)^*$ is significantly correlated for non-variables while $(B-V)^*$ for moderate and violent variables.

(b) Observed color indices $(U-B)x$ and $(B-V)x$ exhibit significant correlations with redshifts for moderate variable and non-variable AGs respectively, and moderate variable QSOs. This is an important property and can be utilized for predicting/determining redshifts from photometric observations.

In view of the above findings with respect to variability, continued observations involving monitoring of all types of extragalactic objects is suggested and the relationships checked as more and more data are available.

Acknowledgement

The author is grateful to an anonymous referee for helpful suggestions that led to major improvement of the work.

References

Angel, J., Stockman, H. 1980, *ARAA* **18**, 321.
Basu, D. 1973, *The Observatory* **93**, 184.
Basu, D. 1974, *The Observatory* **94**, 61.
Basu, D. 1980a, *Ap. Letts.* **21**, 63.
Basu, D. 1980b, *A& SS* **72**, 241.
Basu, D. 1981, *Ap. Letts.*, **21**, 85.
Basu, D. 1982, *Ap. Letts.*, **22**, 139.
Basu, D. 1985, *The Observatory* **105**, 210.
Basu, D. 1986, *Astr. J.* **91**, 226.
Basu, D. 1987, *A & SS* **132**, 207.
Basu, D. 1990, *Ap. Letts. & Comm.* **27**, 393.
Borra, E. 1975, *The Observatory* **95**, 141.
Burbidge, G., Crowne, A., Smith, H. 1977, *Astrophys. J. Suppl.* **33**, 133.
Cristiani, S., *et al*. 1996, *Astr. Astrophys.* **306**, 395.
Elvis, M., *et al*. 1994, *Astrophys. J. Suppl.* 95, 1.
Evans, A. 1972, *Mon. Not. R. Astr. Soc.* **160**, 407.
Fan, J. H. 1997, *Ap. Letts. & Comm.*, **35**, 361.
Goldsmith, S. 1972, *Nat. Phys. Sci.* **236**, 122.
Hall, J. C., *et al*. 1998, *Astrophys. J. Suppl.* **119**, 228.
Hewitt, A., Burbidge, G. 1993, *Astrophys. J. Suppl.* **87**, 451.
McCrea, W. 1966, *PASP* **78**, 49.
Netzer, H., *et al*. 1996, *Mon. Not. R. Astr. Soc.* **279**, 429.
Padovani, P., Giommi, P. 1995, *Mon. Not. R. Astr. Soc.* **277**, 1477.
Penston, M. V., Cannon, R. D. 1970, *Roy. Observ. Bull.*, **159**.
Pica, A. S., Smith, A. G., Webb, J. R., Leacock, S. C., Gambola, P. P. 1988, *Astr. J.* **96**, 1215.
Stickel, M., Padovani, P., Urray, C. M., Fried, J. W., Kuhr, H. 1991, *Astrophys. J.* **374**, 431.
Strittmatter, P., Burbidge, G. 1967, *Astrophys. J.* **147**, 13.
Thakur, R. K. and Sapre, A. K. 1980, *A & SS* **70**, 281.
Ulrich, M.-H., *et al*. 1997, *ARAA* **35**, 395.
Veron-Cetti, M. P., Veron, P. 1996, *ESO Sci. Rep.* No. 17.
Webb, J., Smith, A. G., Leacock, R. J., Fitzgibbons, G. L., Gombola, F. P., Shepherd, D. W. 1988, *Astr. J.* **95**, 329.

J. Astrophys. Astr. (2001) **22,** 283–292

Soft X-ray Variability of the Bright Quasar 3C273

Chulhee Kim *Department of Earth Science Education, Chonbuk National University, Korea.*
e-mail:chkim@astro.chonbuk.ac.kr

Received 2001 July 20; accepted 2001 November 2

Abstract. We present the results from ROSAT observations of 3C273 in the soft X-ray band. The light variation of 3C273 was investigated for three different energy bands of soft, medium, and hard. The maximum variability with a factor of 2 for 551 days was confirmed at all three different bands. This appears to be a periodic variation within the period of roughly 6 months. However, the short-term or micro variation was not so distinct and the light variation of each band did not show any correlation between them. The hardness ratio for hard and soft bands shows irregular variation but there was no correlation between them. There is no distinct variation of the photon index in the case of simple power law model fitting. For power law + free absorption model fitting, the average photon index (Γ) is 2.08.

Key words. Galaxies: individual (3C273), quasar—X-rays: galaxies.

1. Introduction

Bright quasar 3C273 ($z = 0.158$) is one of the most extensively observed extragalactic objects and has been tested by many theories of active galactic nuclei. Bowyer *et al*. (1970) detected X-rays from 3C273 for the first time. Turner *et al*. (1990) observed it with the EXOSAT and Ginga and they determined the photon index value of $1.40 < \Gamma < 1.55$ using the simple power law model. The fact that this value does not correlate with the flux variation in the 2–10 keV band region was also confirmed.

They also found the existence of soft excess below 1 keV from the analysis of the EXOSAT data and this was confirmed by Courvoisier *et al*. (1987); Masnou *et al*. (1992), and Wilkes & Elvis (1987) who analyzed the Einstein data. Furthermore, it was found that this soft component flux varies during a one week period. The existence of a soft excess component was again confirmed by Staubert (1992) from the analysis of the ROSAT and Ginga data.

Hence there has been no doubt about the existence of the soft excess component to 3C273, but there has been no agreement with the spectral model fitting to it. Based on the analysis of the Einstein data, it was argued that the broken power law or power law + black body model is better than other models. However it was reported that the black body, steep power law, or thermal bremsstrahlung model is good for the EXOSAT data.

Leach *et al*. (1995) analyzed the ROSAT PSPC data through 14 times of observations for 25 days and they found that the variations of the overall count rate is 20 per cent in

2d and the count rates, when split into hard (1.5–2.4 keV) and soft (0.1–0.3 keV) energy bands, are not correlated, showing that two physically distinct emission components are present. They also reported that the spectra are modelled best by a combination of two power laws with absorption at the galactic value, the spectral index of the softer power law ($\Gamma_{\rm soft}$) is 2.7 when the photon index ($\Gamma_{\rm hard}$) of the harder power law is fixed at 1.5, and there are small but significant variations in $\Gamma_{\rm soft}$ which do not correlate with the soft count rate.

Fan *et al* (2001) used a database of measurement of 110 years in the B-band in order to search periodicity of 3C273 and they argued the existence of periods of 2.0 years. By encouraging this discovery, we try to analyze the four ROSAT PSPC data sets of 3C273 which were not included in the investigation by Leach *et al*. (1995) in order to search any periodic long-term soft X-ray variation. We present the observation in section 2, an analysis and the results in section 3, and discussion and conclusion in section 4.

2. Observations and data analysis

The X-ray data described here are from observations carried out at four epochs between December 15th, 1991 and June 17th, 1993 using the X-ray telescope on board the ROSAT Observatory (Trümper 1983) with the position sensitive proportional counter (PSPC; Pfeffermann *et al*. 1987). The bandpass of the PSPC is $\sim$ 0.1–2.4 keV and the field of view was $\sim 2^\circ$ diameter. The energy resolution is $\Delta E/E = 0.43(E/0.93)^{-0.5}$ (FWHM) where the unit of E is keV. The spatial resolution at the central part is $\sim 25''$ (FWHM) (Hasinger *et al*. 1992). To eliminate the shadow effect due to the grid in front of the detector window, the satellite was wobbled at a period of $\sim$ 400 sec with a wobbling angle of $\sim 7'$–$8'$.

In order to investigate the long-term variation, we searched all the ROSAT PSPC archive data for 3C273. The selection criteria were first, observations should cover a long enough duration – at least more than one year – and, second, the count rate should be higher than about 10 (c/s) for more reliable timing and spectral analysing results. We selected four sources observed by different observers from 1991/12 to 1993/06 for about one and half years. 3C273 was at the center of the PSPC field of view during two of the observations. In the other two it was at different off-axis angles. We will refer to them as P1, P2, etc. The log of observations is presented in Table 1 where the source number, observation date, exposure time and count rate are given.

All data sets were analyzed using the MIDAS-EXSAS software package (Zimmermann *et al*. 1994). The imaging analysis, background subtraction and various detector corrections like vignetting and dead time corrections are included in data reduction. The source was extracted from a circular region of 1.5 arcmin. The background was computed in an annulus between 2.0 and 3.4 arcmin centered on the source cell. For the off-axis sources, a larger circular region was taken for source extraction and other nearby regions without faint sources instead of an annulus centered on the source were taken for the background subtraction.

3. Analysis and results

Because the typical X-ray spectra of AGNs show a distinct structural pattern caused by the soft excess, absorption by cold material in the host galaxy, and Kα line etc.,

Table 1. Log of ROSAT-PSPC observations.

Source name	Source number	Start time [UT]	End time [UT]	Exposure time (sec)	Count rate (cts/s)	Off-axis
P1	700191P	91/12/14/08:54:56	91/12/15/04:10:01	6140	14.64	no
P2	600242P	92/07/21/21:47:36	92/07/11/21:55:43	3078	31.05	yes
P3	600242P-1	92/12/24/15:31:36	92/12/26/22:16:59	24830	19.90	yes
P4	141509P	93/06/06/16:07:08	93/06/17/11:33:57	3330	26.63	no

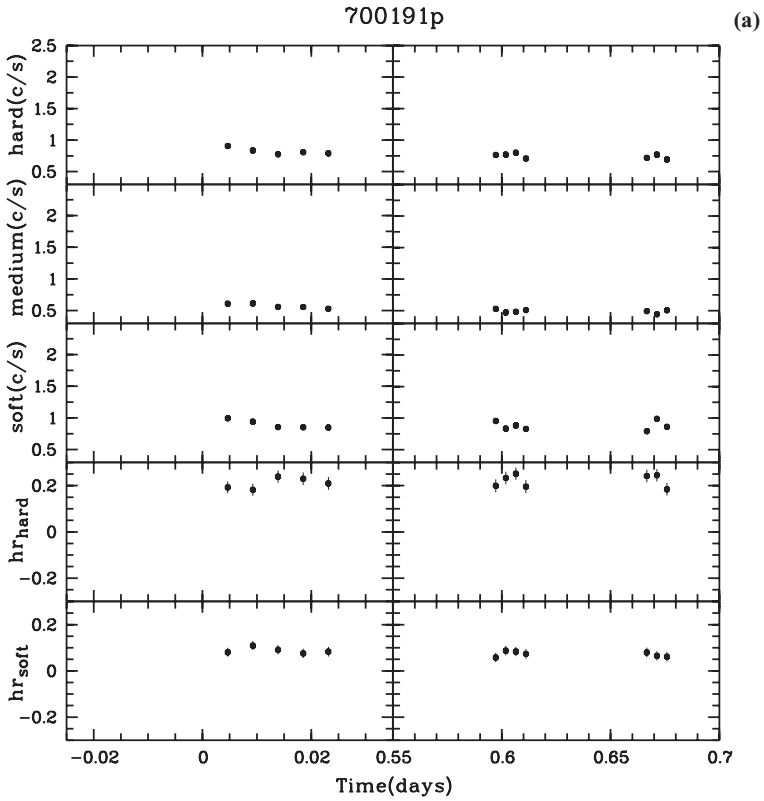

Figure 1(a–d). The X-ray light curves in the three X-ray bands (top three panels) and hardness ratios of 3C371. Note that the scale of X-axes is not the same for all observations.

it is necessary to investigate the light variation for different energy bands. Figure 1 shows the X-ray light curves for the three energy bands of soft, medium, and hard energy regions. These three bands correspond to channels 11–19, 52–69, and 132–201, respectively. Data were rebinned into 400 sec bins. Note that the scale of X-axes is different for each.

Figure 1 does not exhibit any distinct short-term variation. However it can be seen that the count rate in the three different bands varies alternately for four data sets. Table 2 represents the mean count rate for different bands.

Table 2. Mean count rate for soft, medium, and hard band as well as the hardness ratio for four data sets.

	700191p	600242p	600242p-1	141509p
Hard(c/s)	0.8	1.2	0.7	1.2
Medium(c/s)	0.5	0.9	0.5	0.9
Soft(c/s)	0.9	2.0	1.3	2.0
$hr_{\rm hard}$	0.2	0.2	0.2	0.2
$hr_{\rm soft}$	0.1	−0.2	−0.2	−0.1

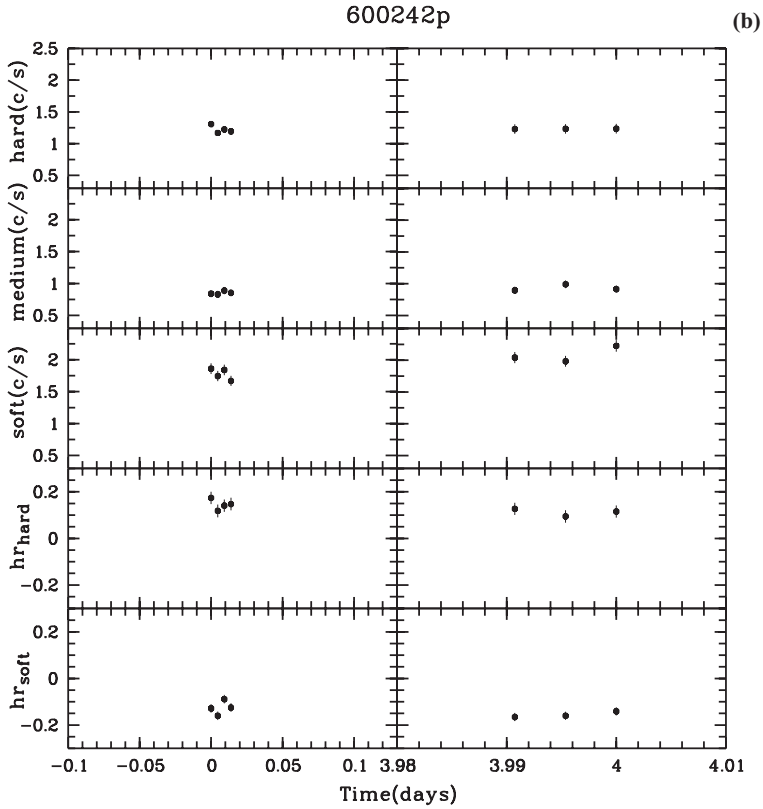

Figure 1(b). (*continued*)

The mean count rate for the hard band varies from 0.8 (c/s) in 700191p to 1.2 (c/s) in 600242p, then recovered to 0.7 (c/s) in 600242p-1. Again the count rate increased to 1.2 (c/s) in 141509p. For medium and soft bands, the light variation shows a similar pattern. Because the observation of four data sets carries out with crudely every half year interval, this alternate variation seems to be a periodic phenomenon. Also the amount of increment or decrement is largest for the soft band. And, in addition, the soft flux varies more largely than the hard flux especially for 600242p-1. A more detailed discussion will be given in the last section.

In order to investigate the presence of any correlation between the hardness ratio and light variations, we calculated the hardness ratio of $hr_{\rm soft}$ and $hr_{\rm hard}$. The hardness ratio is defined as equation (1) and (2) below where $band_1$, $band_2$, $band_3$, and $band_4$ are the count rates in channels 11–41, 52–201, 52–90, and 91–201 respectively.

$$hr_{\rm soft} = \frac{(band_2 - band_1)}{(band_2 + band_1)}, \tag{1}$$

$$hr_{\rm hard} = \frac{(band_4 - band_3)}{(band_4 + band_3)}. \tag{2}$$

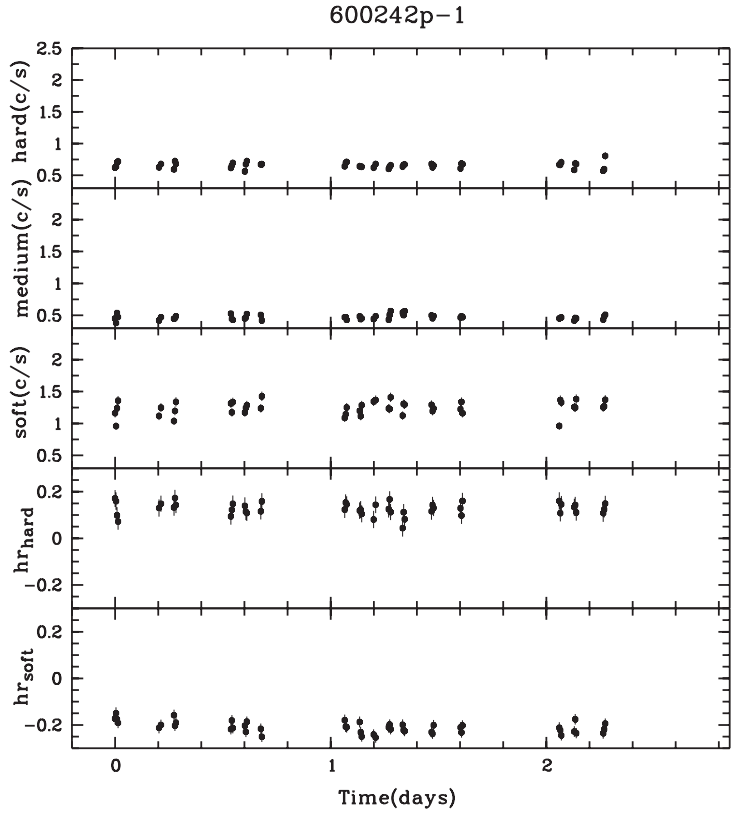

Figure 1(c). (*continued*)

The lower two panels for four data sets in Figs. 1 show $hr_{\rm soft}$ and $hr_{\rm hard}$ versus time. We can see that both $hr_{\rm soft}$ and $hr_{\rm hard}$ varied irregularly on short time scales. For all four data sets $hr_{\rm hard}$ varied from 0.14 to 0.22, but $hr_{\rm soft}$ varied strongly from 0.08 to -0.19. A variation in the hardness ratio exhibits spectral variability during the observations. However, any correlation between the hardness ratio and the light variation cannot be seen. Furthermore it was also found that there is no correlation between the variation of the $hr_{\rm soft}$ and $hr_{\rm hard}$.

The X-ray spectra of AGNs are complex (see Turner *et al*. 1993; Nandra & Pounds 1994; Page *et al*. 1999). The energy source below ~ 10 keV is composed of at least two parts, i.e., a power law component which reaches to the higher energy region (> 40 keV) and a soft X-ray component appearing in the lower (< 1.0 keV) energy region. The power law component seems to be produced in the hot corona surrounding the relativistic accretion disk (see Nandra *et al*. 1997).

For the spectral analysis we excluded bad PSPC channels 1–9 and 241–256 and the data were rebinned to have a S/N ratio of 8. A simple power-law + absorption model was fitted and the best-fit parameters are presented in Table 3. In Fig. 2, we show the observed spectra for all four sources with the best-fit model and residuals between the spectra and the model are shown in the lower panels of this figure. We can see from the χ^2 statistics that this model provides acceptable fits to all data sets except the spectrum of 600242p-1.

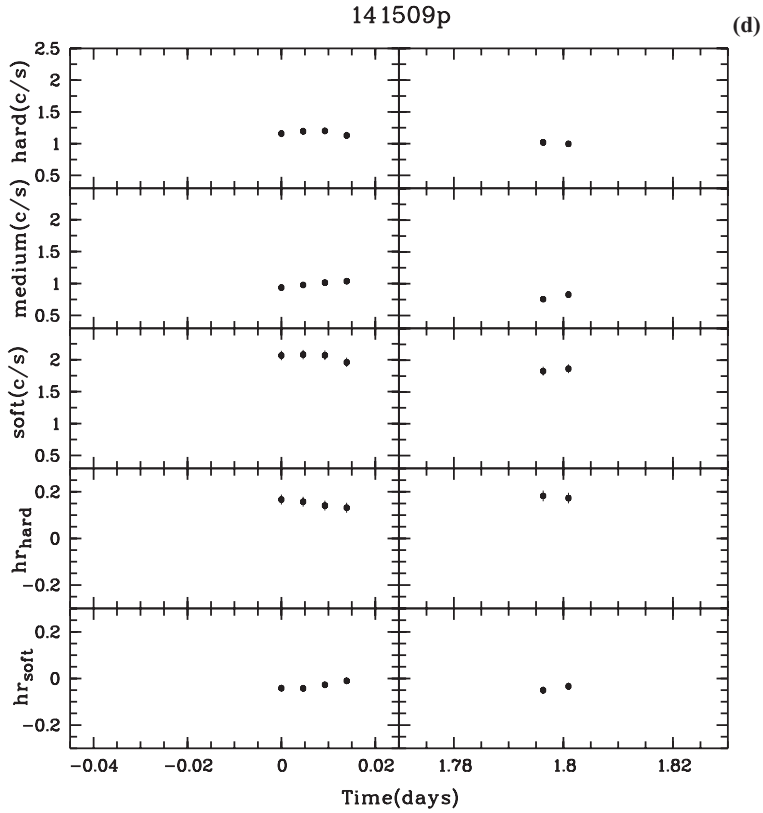

Figure 1(d). (*continued*)

The column density values of the hydrogen (N_H) along the line of sight to 3C273 are smaller than the Galactic value of $1.79 \times 10_{20}$ H-atom/cm^2 (Dicky & Lockman 1990). This lower N_H, i.e., "Negative N_H", implies a "soft excess" due to ionization. Residuals of this figure clearly show the existence of the "soft excess" and the soft emissions are variable. Because our main purpose is the investigation of the long-term variation, we did not try to apply other models for a better fit except a few models such as power law + fixed absorption, black body, exponential, thermal bremsstrahlung,

Table 3. Spectral fits to the spectra of 3C273: Power-law + absorption model.

Source name	γ^a	N^b	N_H^c	χ^2/d.o f	L^d
P1	1.92 ± 0.04	1.85 ± 0.03	1.67 ± 0.10	1.16 ⁄198	1.03
P2	2.18 ± 0.05	2.81 ± 0.06	1.62 ± 0.12	1.62 ⁄174	2.00
P3	2.18 ± 0.05	1.57 ± 0.02	1.67 ± 0.05	4.40 ⁄206	1.23
P4	2.05 ± 0.04	2.86 ± 0.04	1.46 ± 0.09	1.15 ⁄190	1.78

[a] Photon index.
[b] Normalization at 1 ke V.
[c] Column density (N_H) 10^{20} H-atom/cm^2.
[d] Luminosity[10^{46} erg/s].

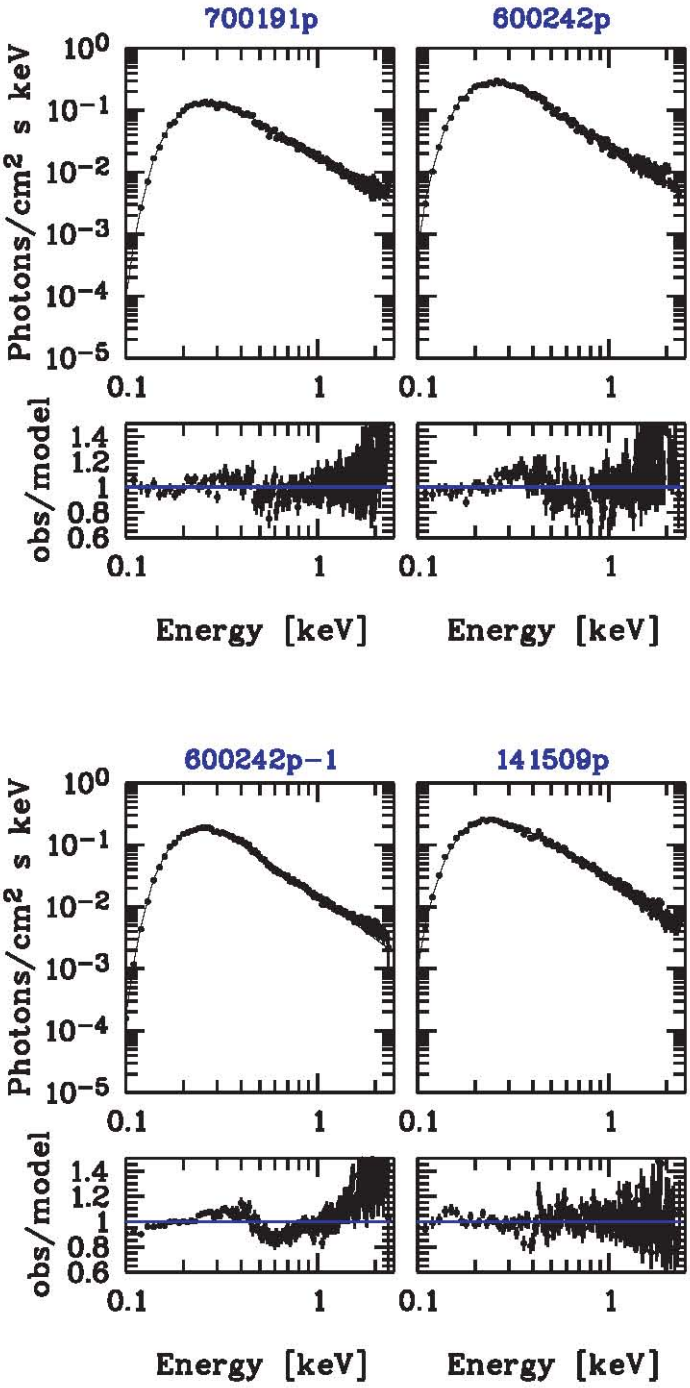

Figure 2. Observed spectra of 3C371 along with the best-fit model (power law + absorption). Residuals between the spectrum and the model are shown in the lower panels.

and power law + exponential. From the χ^2 statistics for these models, it was found that the simple power-law + absorption model gives the best fit.

The photon index varies from $\Gamma = 1.92$–2.18 which is not much different from 2.1 by Leach, *et al*. (1995). However this value is different from $\Gamma = 1.4$–1.55 from the EXOSAT ME and Ginga spectra for 2–10 keV band (Turner *et al*. 1990), and also $\Gamma = 1.3$ from the Einstein spectra for 0.2–3.5 keV band (Wilkes & Elvis 1987). This difference can be understood by the fact that the spectral slope of AGNs is flatter as the band is towards hard X-ray.

Using the relation of Schmidt & Green (1986), assuming $H_0 = 50$ km/s/Mpc and $q_0 = 0.5$, the luminosity of 3C273 was determined. The result is given in Table 3 and again light variation is evident.

4. Discussion and conclusions

In order to search for short- and/or long-term variations and spectral properties of 3C273, we have examined the soft X-ray emissions using hardness ratios and spectral analysis of four ROSAT data sets. It was found that light variation for all three different bands during 551 days was in the order of two, but short-term or micro variation was not confirmed. Interestingly light increment alternates with light decrement and the amount of variation is almost the same. It would be difficult to say that this is a periodic phenomenon occurring about every six months because the total number of data sets is only four. However this is different from the gradual decrease in X-ray brightness over about three years detected in Mrk 926 by Kim & Boller (2002).

The long-term variation is difficult to explain. One possibility is a change in the accretion rate which is expected to occur on a time scale of the radial infall of matter onto the central masssive black hole. The infall time scale of the order of months to years can be estimated (see Kim & Boller 2002). If the alternate variation in 3C273 is periodic, the plausible explanation can, therefore, be a periodic accretion rate variation. In order to confirm this as well as the periodicity of 3C273, observation of this object for a longer time for multi-wavelength bands is absolutely required.

On the other hand the variation of the soft hardness ratio is evident from 0.08 to -0.19, but this variation does not show any correlation with that of brightness. However soft hardness varies from 0.08, -0.15, -0.19, to -0.05 for four sources in Table 2, but the photon index varies from 1.92, 2.18, 2.18, to 2.05 in Table 3, i.e., variation of soft hardness ratio is the reverse of that of the photon index. Similar variation pattern can be seen for hard hardness ratio, but the amount of variation is much smaller. However the meaning of this is not so evident.

Because photon index is an indicator of a soft excess, a variation of soft hardness ratio reflects a physical and/or morphological variation in the original source of a soft excess. If the soft excess is due to the most promising mechanism of the thermal radiation from the accretion disk surrounding a super massive blackhole (see Arnaud *et al*. 1985; Ross, Fabian & Mineshige 1992), variation of the soft hardness ratio can be understood as a variation of thermal radiation output caused by a variation of the amount of gas infalling on the accretion disk. However because the soft hardness ratio does not correlate with the variation of brightness, the variation of infalling gas on the accretion disk is too small to have an effect on the change of brightness.

Acknowledgements

CK thanks Prof. J. Trümper for the kind hospitality at the Max-Planck-Institut für Extraterrestrische Physik and Dr. Thomas Boller for his assistance and close collaboration. This research has made use of the NASA/IPAC Extragalactic Database (NED) which is operated by the Jet Propulsion Laboratory, California Institute of Technology, under contract with the National Aeronautics and Space Administration.

References

Arnaud, K. *et al*. 1985, *MNRAS*, **217**, 105.
Bowyer, C. S., Lampton, M., Mack, J., de Mendonca, F. 1970, *Ap. J.*, **161**, L1.
Courvoisier, T. J. -L, *et al*. 1987, *A& A*, **176**, 197.
Dicky, J. M., Lockman F. J., 1990, *Ann. Rev. Astron.*, **28**, 215.
Fan, J. H., Romero, G. E., and Lin, R. G., 2001, *Acta Astronomical Sinica*, **42**, 9.
Hasinger, G., Turner, T. J., George, I. M., Boese, G. 1992, Legacy 2 (OGIP Calibration Memo CAL/ROS/92-001), 77
Leach, C. M., McHardy, I. M., Papadakis, I. E. 1995, *MNRAS*, **272**, 221L.
Kim, Chulhee, Boller, Th. 2002, *Ap & SS* (accepted)
Masnou, J. L., Wilkes, B. J., Elvis, M., McDowell, J. C., Arnaud, K. A. 1992. *A& A*, **253**, 35.
Nandra, K., Pounds, K. A. 1994, *MNRAS*, **268**, 405.
Nandra, K., George, I. M., Mushotzky, R. F., Turner, T. J., Yaqoob, T., 1997, *ApJ*, **477**, 602.
Pfeffermann, E., *et al*. 1987, *Proc. SPIE*, **733**, 519.
Page, M. J., Carrera, F. J., Mittaz, J. P. D., Mason K. O. 1999, *MNRAS*, **305**, 775.
Ross, R. R., Fabian, A. C., Minesshige, S. 1992, *MNRAS*, **258**, 189.
Schmidt, M, Green, R. F. (1986) *Ap. J*, **269**, 352.
Staubert, R. 1992, in *MPE report no. 235*, W. Brinkmann & J. Trümper (eds)
Turner, T. J., George, I. M., Mushotzky, R. F. 1993, *Ap. J*, **412**, 72.
Turner, M. J. L, Williams, O. R., Courvoisier, T. J. -L. *et al*. 1990, *MNRAS*, **244**, 310.
Trümper, J. 1983, *Adv. Space Res.* **2**, 241.
Wilkes, B. J., Elvis, M., 1987, *Ap. J*, **323**, 243.
Zimmermann, H. U. *et al*. 1994, *EXSAS Users' Guide, MPE Report*.

J. Astrophys. Astr. (2001) **22,** 293–307

HI Fluctuations at Large Redshifts: I–Visibility correlation

Somnath Bharadwaj[1] & Shiv K. Sethi[2*]

[1]*Department of Physics and Meteorology & Center for Theoretical Studies, I.I.T. Kharagpur, 721 302, India*
email: somnath@phy.iitkgp.ernet.in
[2]*Raman Research Institute, C. V. Raman Avenue, Sadashivnagar, Bangalore 560 080, India*
email: sethi@rri.res.in

Received 2002 March 15; accepted 2002 May 31

Abstract. We investigate the possibility of probing the large scale structure in the universe at large redshifts by studying fluctuations in the redshifted 1420 MHz emission from the neutral hydrogen (HI) at early epochs. The neutral hydrogen content of the universe is known from absorption studies for $z \lesssim 4.5$. The HI distribution is expected to be inhomogeneous in the gravitational instability picture and this inhomogeneity leads to anisotropy in the redshifted HI emission. The best hope of detecting this anisotropy is by using a large low-frequency interferometric instrument like the Giant Meter-Wave Radio Telescope (GMRT). We calculate the visibility correlation function $\langle V_\nu(\mathbf{U}) V_{\nu'}(\mathbf{U})\rangle$ at two frequencies ν and ν' of the redshifted HI emission for an interferometric observation. In particular we give numerical results for the two GMRT channels centered around $\nu = 325$ MHz and $\nu = 610$ MHz from density inhomogeneity and peculiar velocity of the HI distribution. The visibility correlation is $\simeq 10^{-10}$–10^{-9} Jy^2. We calculate the signal-to-noise for detecting the correlation signal in the presence of system noise and show that the GMRT might detect the signal for integration times $\simeq 100$ hrs. We argue that the measurement of visibility correlation allows optimal use of the uncorrelated nature of the system noise across baselines and frequency channels.

Key words. Cosmology: theory, observations, large scale structures — diffuse radiation.

1. Introduction

Various observations indicate that around 90% of the HI mass in the redshift range of 2 to 3.5 is in clouds which have HI column densities greater than 2×10^{20}atoms/cm^2 (Lanzetta, Wolfe & Turnshek 1995; Storrie-Lombardi, McMahon & Irwin 1996; Peroux *et al.* 2001). These high column density clouds are responsible for the damped

*On leave from Harish-Chandra Research Institute, Chhatnag Road, Jhusi, Allahabad 211 019, India.

Lyman-α absorption lines observed along lines of sight to quasars. The flux of HI emission from individual clouds ($\lesssim 10\mu$Jy) is too weak to be detected by existing radio telescopes unless the image of the cloud is significantly magnified by an intervening cluster gravitational lens (Saini, Bharadwaj & Sethi 2001). Although we may not be able to detect individual clouds, the redshifted HI emission from the distribution of clouds will appear as background radiation in low frequency radio observations. Bharadwaj, Nath and Sethi (2001; hereafter referred to as BNS) have used existing estimates of the HI density at $z \simeq 3$ to infer the mean brightness temperature of $\simeq 1$ mK at $\nu \simeq 320$ MHz for this radiation. The fluctuations in the brightness temperature of this radiation arise from fluctuations in the HI number density and from peculiar velocities. As shown in BNS, the cross-correlation between the temperature fluctuations across different frequencies and different lines of sight is related to the two-point correlation function (or equivalently the power spectrum) of density perturbations at the redshift where the radiation originates. The possibility of measuring this provides a new method for studying large scale structures at high redshifts. Estimates indicate the expected values of the cross-correlations in the brightness temperature to vary from $10^{-7}\,\mathrm{K}^2$ to $10^{-8}\,\mathrm{K}^2$ over intervals corresponding to spatial scales from 10 Mpc to 40 Mpc for some of the currently-favoured cosmological models. Estimates of the different contributions to the flux expected in a pixel of a radio image show the contribution from galactic and extragalactic sources and the system noise to be substantially higher than the contribution from the HI radiation. The task of devising a strategy for extracting the signal from the various foregrounds and noise in which it is buried is a problem which has still to be solved. A possible strategy based on the very distinct spectral properties of the foregrounds as against the HI emission is discussed in BNS.

An alternate strategy for using the HI emission from high redshifts to study large scale structures has been discussed by many authors (Subramanian & Padmanabhan 1993; Kumar, Padmanabhan & Subramanian 1995; Bagla, Nath & Padmanabhan 1997; Bagla 1998). This is based on detecting the HI emission from individual protoclusters at high redshifts. There have also been observational efforts in this direction (see Subrahmanyan & Anantharamaiah 1990 and reference therein). No detections have been made till date. This strategy suffers from the disadvantage that the protoclusters correspond to very large overdense regions which are very rare events. Protoclusters with flux in the range 3 to 5 mJy are predicted to occur with abundances in the range $10^{-8} - 10^{-7}\,\mathrm{Mpc}^{-3}$ in the CDM model (Subramanian and Padmanabhan 1993). In the statistical approach proposed in BNS fluctuations of all magnitude in the HI distribution contribute to the signal. The statistical approach allows optimum use of the signal present in all the pixels of the images made at different frequencies across the bandwidth of a typical radio observation. In this paper we take up various issues related to the statistical approach originally proposed in BNS.

The main focus of this paper is the choice of an appropriate statistical estimator to quantify the properties of the signal and the system noise. The statistical estimator proposed in BNS is the cross-correlation between the temperature fluctuations along different lines of sight in radio map made at different frequencies. While this quantity is conceptually very simple, complications arise when it is applied to images produced by radio interferometry, as is the case with most low frequency radio telescopes. Such observations measure the coherence between the signals arriving at any two antennas, a quantity known as the visibility $V(\mathbf{U})$. This is measured for all pairs of antennas in the interferometric array. Here $\mathbf{U}$ refers to the vector joining a pair of antennas,

measured in units of λ, projected on the plane perpendicular to the direction which is being imaged.

The image is produced by a Fourier transform of the visibility

$$I_\nu(\vec{\theta}) = \int V(\mathbf{U}) \exp[2\pi i\, \vec{\theta} \cdot \mathbf{U}]\, d^2\mathbf{U} \tag{1}$$

where $\vec{\theta}$ refers to different positions in the small patch of the sky which is being imaged, and $I_\nu(\vec{\theta})$ is the specific intensity. The contribution of system noise to the signal from each antenna is independent, and the visibilities measured by each pair of antennas are uncorrelated. The noise in the pixels of a radio image constructed from the visibilities is not independent. The correlations in the noise in the pixels depend on the detailed distribution of the different separations (baselines) **U** for which the visibility has been measured. Any strategy based on the statistical analysis of radio images will be faced with the problem of distinguishing the correlations in fluctuations of the HI emission from the correlations in the noise. This complication can be avoided by dealing directly with the visibilities. In this paper we investigate the possibility of detecting the fluctuations in the HI emission using a statistical estimator constructed directly from the visibilities measured in a radio interferometric observation, without making an image.

We next present a brief outline of this paper. In section 2 we calculate the relation between the statistical properties of the HI fluctuations and the visibilities produced by these fluctuations. In section 3 we present numerical estimates of these quantites for some of the currently favoured cosmological models for the system parameters of GMRT (Swarup *et al.* 1991). In section 4, we calculate statistical properties of the visibility correlations arising from the system noise. In section 5 we present the conclusions and discuss possible directions for future work.

2. From density fluctuations to visibility

We consider radio-interferometric observations of a small patch of the sky whose center is in the direction of the unit vector **n** (Fig. 1). A small patch of the sky may be treated as a plane, and the angle $\vec{\theta}$ which refers to different directions in the sky (Fig. 1) may be treated as a two dimensional vector. Observations at a frequency ν would measure the HI emission from a redshift $z = (1420\,\mathrm{MHz}/\nu) - 1$ or equivalently a comoving distance r_ν. The specific intensity of the redshifted HI emission arriving from any direction $\vec{\theta}$ may be decomposed into two parts

$$I_\nu(\vec{\theta}) = \bar{I}_\nu + \Delta I_\nu(\vec{\theta})\,, \tag{2}$$

where $\bar{I}_\nu$ and $\Delta I_\nu(\mathbf{n})$ are the isotropic and the fluctuating components of the specific intensity. The isotropic component $\bar{I}_\nu$ is related to $\bar{n}_{\mathrm{HI}}(z)$, the mean comoving number density of HI atoms in the excited state at a redshift z and we have

$$\bar{I}_\nu = \frac{A_{21}\, h_P\, c\, \bar{n}_{\mathrm{HI}}(z)}{4\pi\, H(z)} \tag{3}$$

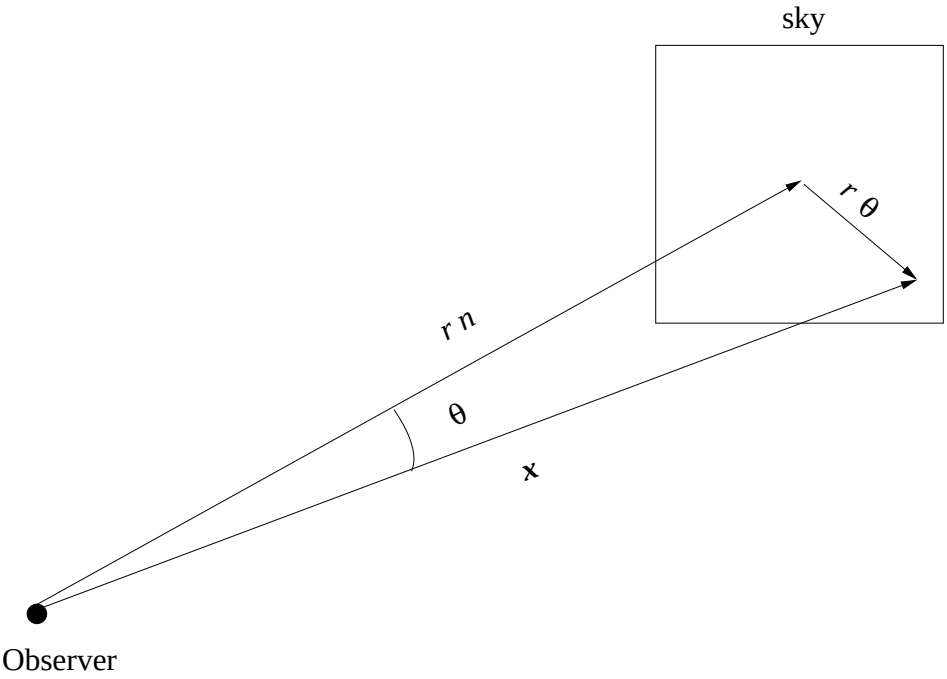

Figure 1. The geometry for the flat-sky approximation is shown.

where A_{21} is the Einstein coefficient for the HI hyperfine transition, h_P the Plank constant, c the speed of light and $H(z)$ the Hubble parameter. This is a slightly rearranged version of equation (11) of BNS.

The fluctuations in the specific intensity $\Delta I_\nu(\vec{\theta})$ arise from fluctuations in the HI number density $\Delta n_{\rm HI}(\mathbf{x})$ and the peculiar velocity $\mathbf{v}(\mathbf{x})$, where $\mathbf{x}$ refers to the comoving position $\mathbf{x} = r_\nu(\mathbf{n} + \vec{\theta})$ The details of the calculation relating these quantities are presented in BNS, and we use a slightly rearranged version of equation (12) of BNS

$$\Delta I_\nu(\vec{\theta}) = \bar{I}_\nu \left[\frac{\Delta n_{\rm HI}(\mathbf{x})}{\bar{n}_{\rm HI}} + \frac{(\mathbf{n}\cdot\nabla)(\mathbf{n}\cdot\mathbf{v}(\mathbf{x}))}{aH} \right] \tag{4}$$

where a is the scale factor. It should be noted that all the quantities in the right hand side of equation (4) should be evaluated at the epoch when the radiation was emitted.

In this paper we wish to calculate the contribution from the redshifted HI emission to the visibilities $V_\nu(\mathbf{U})$ that would be measured in radio-interferometric observations. The relation between the specific intensity and the visibilities is

$$V_\nu(\mathbf{U}) = \int d^2\theta\, A(\vec{\theta})\, \Delta I_\nu(\vec{\theta})\, e^{-i2\pi \mathbf{U}\cdot\vec{\theta}}\,. \tag{5}$$

Only the fluctuating part of the specific intensity contributes to the visibility, and we have dropped the isotropic component from eq. (5). Here $A(\vec{\theta})$ is the beam pattern of

the individual antennas in the array (primary beam). We use equations (4) and (5) to relate the visibilities to the fluctuations in the HI distribution.

It is convenient to work with $\Delta_{\rm HI}(\mathbf{k})$, the Fourier transform of the density contrast of the HI number density $\Delta n_{\rm HI}(\mathbf{x})/\bar{n}_{\rm HI}$. We assume that on sufficiently large scales $\Delta_{\rm HI}(\mathbf{k})$ can be related to $\Delta(\mathbf{k})$, the density contrast of the underlying dark matter distribution, through a linear bias parameter b i.e., $\Delta_{\rm HI}(\mathbf{k}) = b_{\rm HI}\Delta(\mathbf{k})$. We also assume that the scales we are dealing with are sufficiently large that we can apply linear theory of density perturbations (Peebles 1980) to relate the peculiar velocities to the fluctuations in the dark matter distribution, $\mathbf{v}(\mathbf{k}) = (-iaHf(\Omega_m)\mathbf{k}/k)\Delta(\mathbf{k})$, where $f(\Omega_m) \approx \Omega_m^{0.6} + \frac{1}{70}[1 - \frac{1}{2}\Omega_m(1+\Omega_m)]$ in a spatially flat universe (Lahav *et al.* 1991). These assumptions allow us to express the fluctuations in the specific intensity as

$$\Delta I_\nu(\vec{\theta}) = \bar{I}_\nu \int \frac{d^3k}{(2\pi)^3}\left[1 + \frac{\beta k_\parallel^2}{k^2}\right]\Delta_{\rm HI}(\mathbf{k})\, e^{ir_\nu(k_\parallel + \mathbf{k}_\perp\cdot\vec{\theta})} \tag{6}$$

where we have decomposed the wave vector $\mathbf{k}$ into two parts $\mathbf{k} = k_\parallel\mathbf{n} + \mathbf{k}_\perp$ where $k_\parallel\mathbf{n}$ refers to the component of the Fourier mode $\mathbf{k}$ along the line of sight to the center of the patch of sky being observed, and $\mathbf{k}_\perp$ refers to the component of $\mathbf{k}$ in the plane of the sky. We use equation (6) in equation (5) to express the visibility $V_\nu(\mathbf{U})$ in terms of $\Delta(\mathbf{k})$. This allows us to carry out the integral over $\vec{\theta}$ which gives us

$$V_\nu(u, v) = \bar{I}_\nu \int \frac{d^3k}{(2\pi)^3}\Delta_{\rm HI}(\mathbf{k})\left[1 + \frac{\beta k_\parallel^2}{k^2}\right] e^{ir_\nu k_\parallel}\, a\left(\mathbf{U} - \frac{\mathbf{k}_\perp r_\nu}{2\pi}\right) \tag{7}$$

where $a(\mathbf{U})$ is the Fourier transform of $A(\vec{\theta})$ the primary beam,

$$a(\mathbf{U}) = \int d^2\vec{\theta}\, A(\vec{\theta})\, e^{-i2\pi\mathbf{U}\cdot\vec{\theta}}\,. \tag{8}$$

For a Gaussian primary beam pattern $A(\theta) = e^{-\theta^2/\theta_0^2}$ the Fourier transform also is a Gaussian and we have

$$a(\mathbf{U}) = \pi\theta_0^2 \exp\left[-\pi^2\theta_0^2 U^2\right] \tag{9}$$

which we use in the rest of this paper.

Equation (7) relates the contribution to the visibilities from fluctuations in the HI number density. These fluctuations are assumed to be a Gaussian random field, or equivalently the different modes $\Delta_{\rm HI}(\mathbf{k})$ have independent, random phases. This allows us to predict all the statistical properties of $\Delta_{\rm HI}(\mathbf{k})$ in terms of the power spectrum of the fluctuations in the HI distribution $P_{\rm HI}(\mathbf{k})$ which is defined as $\langle\Delta_{\rm HI}^*(\mathbf{k})\Delta_{\rm HI}(\mathbf{k}')\rangle = (2\pi)^3\delta^3(\mathbf{k} - \mathbf{k}')P_{\rm HI}(\mathbf{k})$ where $\langle\rangle$ denotes ensemble average. We use this to calculate the correlation between the visibilities at different baselines $\mathbf{U}$ and $\mathbf{U}'$ and two different

frequencies ν and $\nu + \Delta\nu$. Here we assume that the bandwidth over which the observations are being carried out is small compared to the central frequency i.e., $\Delta\nu \ll \nu$ and $r_{\nu+\Delta\nu} = r_\nu + r_\nu^{'}\Delta\nu$ where $r_\nu^{'} = \frac{dr_\nu}{d\nu}$. Using these inputs to calculate the visibility correlation function we obtain

$$\langle V_\nu(\mathbf{U}) V^*_{\nu+\Delta\nu}(\mathbf{U}^{'})\rangle = \left[\bar{I}_\nu \theta_0^2 \pi\right]^2 \int \frac{d^3k}{(2\pi)^3} P_{\rm HI}(k) e^{ik_\parallel r_\nu^{'}\Delta\nu} \left[1 + \beta\frac{k_\parallel^2}{k^2}\right]^2 \times \exp\left[-\frac{q^2 + q'^2}{(2/r_\nu\theta_0)^2}\right] \tag{10}$$

with $q = \mathbf{k}_\perp - 2\pi\mathbf{U}/r_\nu$ and $q' = \mathbf{k}_\perp - 2\pi\mathbf{U}^{'}/r_\nu$. The assumption of linear bias allows us to relate $P_{\rm HI}(\mathbf{k})$ to $P(\mathbf{k})$ the power spectrum of density fluctuations in the dark matter distribution through the linear bias parameter $P_{\rm HI}(\mathbf{k}) = b^2 P(\mathbf{k})$. We use this in later sections to obtain numerical estimates for different cosmological models.

We next turn our attention to a qualitative analysis of equation (10) to determine the nature and extent of the correlations between the visibilities measured at different baselines. This is largely governed by term $\exp\left[-\frac{(\mathbf{k}_\perp - 2\pi\mathbf{U}/r_\nu)^2 + (\mathbf{k}_\perp - 2\pi\mathbf{U}^{'}/r_\nu)^2}{(2/r_\nu\theta_0)^2}\right]$ which arises because the observations have a limited sky coverage determined by the primary beam pattern. This term is very small for all values of $\mathbf{k}_\perp$ unless $\mid \mathbf{U} - \mathbf{U}^{'} \mid < 1/\theta_0$. The parameter θ_0 is related to the FWHM of the primary beam and $\theta_0 \approx 0.6\,\theta_{\rm FWHM}$, which allows us to relate θ_0 to D the diameter of the individual antennas as $\theta_0 \approx \lambda/D$. We also express $\mathbf{U}$ and $\mathbf{U}^{'}$ in terms of $\mathbf{d}$ and $\mathbf{d}^{'}$, the physical separations between the pairs of antennas as $\mathbf{U} = \mathbf{d}/\lambda$ and $\mathbf{U}^{'} = \mathbf{d}^{'}/\lambda^{'}$ It should be noted that here and throughout we assume that $\lambda^{'} = \lambda(1 - \Delta\nu/\nu)$ with $\Delta\nu << \nu$. Using these we see that the condition for the visibilities to be correlated can be expressed as $\mid \mathbf{d} - \mathbf{d}^{'} \mid < D$. This implies that the visibilities measured by a pair of antennas separated by the displacement $\mathbf{d}$ will be correlated to the visibilities measured by another pair separated by a displacement $\mathbf{d}^{'}$ only if difference in the two displacements $\mathbf{d}$ and $\mathbf{d}^{'}$ is less than the antenna diameter. The consequences of this for a typical antenna configuration are

- The visibilities measured at various frequencies by the same pair of antennas are correlated.
- The visibilities measured by different pairs of antennas are uncorrelated.

For the rest of the paper we shall consider only the correlation between the visibilities measured at various frequencies by the same pair of antennas. We use the notation $\langle V_\nu(\mathbf{U}) V^*_{\nu+\Delta\nu}(\mathbf{U})\rangle$ to denote the correlation between the visibilities measured at two different frequencies by the pair of antennas at a physical separation $\mathbf{d} = c\mathbf{U}/\nu$. The fact that this physical separation $\mathbf{d}$ will correspond to a different baseline $\mathbf{U}^{'} = (\nu+\Delta\nu)\mathbf{d}/c$ at the frequency $\nu + \Delta\nu$ is ignored throughout as $\Delta\nu \ll \nu$. Equation (10) can now be used to obtain

$$\langle V_\nu(\mathbf{U}) V^*_{\nu+\Delta\nu}(\mathbf{U})\rangle = \left[\bar{I}_\nu \theta_0^2 \pi\right]^2 \int \frac{d^3k}{(2\pi)^3} P_{\rm HI}(k) e^{ik_\parallel r_\nu^{'}\Delta\nu} \left[1 + \beta\frac{k_\parallel^2}{k^2}\right]^2 \times \times \exp\left[-\frac{(\mathbf{k}_\perp - 2\pi\mathbf{U}/r_\nu)^2}{2(1/r_\nu\theta_0)^2}\right]. \tag{11}$$

The role of the Gaussian in equation (11) arising from the primary beam pattern is to ensure that most of the contribution is from Fourier modes for which $\mathbf{k}_\perp \approx (2\pi/r_\nu)\mathbf{U}$. Equation (11) is further simplified if we approximate the Gaussian with a Dirac Delta function

$$\exp\left[-\frac{(\mathbf{k}_\perp - 2\pi\mathbf{U}/r_\nu)^2}{2(1/r_\nu\theta_0)^2}\right] \approx \frac{2\pi}{r_\nu^2\theta_0^2}\delta^2\left(\mathbf{k}_\perp - \frac{2\pi}{r_\nu}\mathbf{U}\right) \tag{12}$$

whereby only Fourier modes for which $\mathbf{k}_\perp = (2\pi/r_\nu)\mathbf{U}$ contribute. This allows us to do two of the integrals in equation (11) giving us

$$\begin{aligned}\langle V_\nu(\mathbf{U})V^*_{\nu+\Delta\nu}(\mathbf{U})\rangle \;&=\; \frac{\left[\bar{I}_\nu\theta_0^2\right]^2}{2}\int_0^\infty dk_\parallel \frac{P_{\rm HI}(k)}{r_\nu^2\theta_o^2}\cos(k_\parallel r_\nu^{'}\Delta\nu)\;\times \\ &\times\left[1+\beta\frac{k_\parallel^2}{k^2}\right]^2 \text{ with } k=\sqrt{k_\parallel^2+(2\pi/r_\nu)^2U^2}.\end{aligned} \tag{13}$$

Equations (11) and (13) represent the main results of this section. They relate the correlation in the visibilities to the power spectrum of fluctuations in the HI distribution. The visibility correlations at any baseline U are seen to be sensitive to Fourier modes $\geq 2\pi U/r_\nu$. It comes from the fact that each visibility measurement is sensitive to one Fourier mode in the plane of the sky, which arises from the projection of three-dimensional Fourier modes making different angles with the plane of the sky. The typical length scales $\simeq \pi/k$ that contribute to the measurement for any baseline U are $\lesssim 30h^{-1}\,\mathrm{Mpc}(100/U)$.

In the next section we use these equations to make predictions for the visibility correlations expected in the currently favoured cosmological models and we discuss the possibility of observing these.

3. Results

Equation (3) can be calculated to give:

$$\bar{I}_\nu = \frac{5.4\,h\,\mathrm{Jy}}{\mathrm{degree}^2}\Omega_{\rm gas}(z)\left[\Omega_{m0}(1+z)^3+\Omega_{\Lambda 0}\right]^{1/2}(1+z)^{-3} \tag{14}$$

for a spatially flat cosmological model. Here $(1+z) = 1420/\nu$, ν being the observed frequency. We use $\Omega_{\rm gas}(z) = 10^{-3}$ as a fiducial value throughout for $z \geq 1$ (Peroux *et al.* 2001). We give results for the currently-favoured cosmological model: spatially-flat with $\Omega_{\Lambda 0} = 0.7$ and $\Omega_{m0} = 0.3$ (Perlmutter *et al.* 1999; de Bernardis *et al.* 2000). We use $h = 0.7$ whenever quoting a numerical value (Freedman *et al.* 2001).

For GMRT $\theta_{\rm FWHM} = 1.8^\circ \times (325\,\mathrm{MHz}/\nu)$. We plot the visibility correlation function in Figs. 2 and 3 for the GMRT channels centered around $\nu = 325\,\mathrm{MHz}$ and

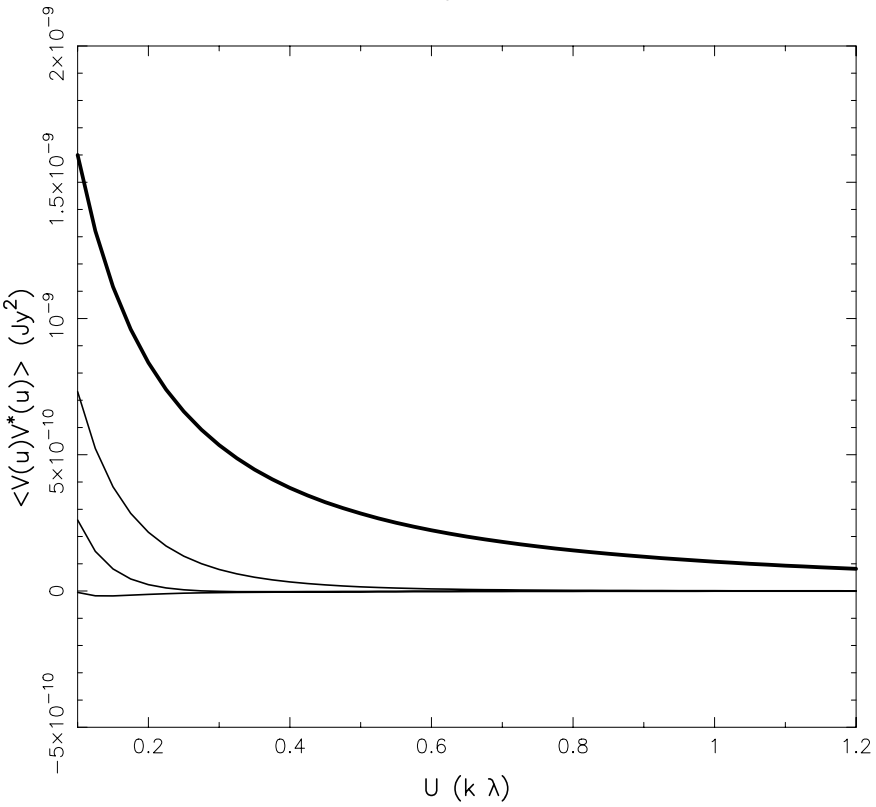

Figure 2. For the central frequency $\nu = 320$ MHz, this figure shows the visibility correlation function as baseline U varies. The thick curve shows the visibility correlation for $\nu = \nu'$. The other three curves show, from top to bottom, the visibility correlation for $\nu' - \nu = \{0.5, 1, 2\}$ MHz, respectively.

$\nu = 610$MHz for COBE-normalized power spectrum (Bunn & White 1996) and $b = 1$. GMRT has a total bandwidth of 16 MHz at these frequencies in 128 channels. The visibility correlation function shown in the figures is averaged over one of these channels with $\Delta\nu = 1.25$ kHz. The correlation function is not very sensitive to the width of the channel so long as the channel width is $\lesssim$ a few kHz.

For $\nu = \nu'$, the signal $(\sqrt{\langle V_\nu(\mathbf{U}) V_{\nu'}(\mathbf{U})\rangle})$ is 10–50 μJy for baselines $|\mathbf{U}| \simeq$ 100–1000. GMRT has 15 antennas in a central array within a radius of $\simeq$ 1 km. Antenna pairs formed from these antennas will be most sensitive to the signal.

For $\nu \neq \nu'$, the correlation signal is seen to dip sharply as frequency separation is increased. The signal is anti-correlated and drops below $\simeq 1\,\mu$Jy for $\nu' - \nu \geq 2$ MHz. For $\nu' - \nu \leq 0.5$ MHz the signal is 5–30 μJy for baselines $\lesssim 500$.

In Figs. 2 and 3 we assume that the HI distribution follows the underlying dark matter distribution, i.e., $b = 1$. However this may not be true; observed structures at any redshift are expected to be biased with respect to the underlying mass distribution (see e.g., Bardeen *et al.* 1986). This bias is expected to be higher at larger redshifts and the observed strong clustering of high redshift galaxies is at least partly owing to this fact (Steidel *et al.* 1998). In this paper we adopt a simple model of bias and assume it

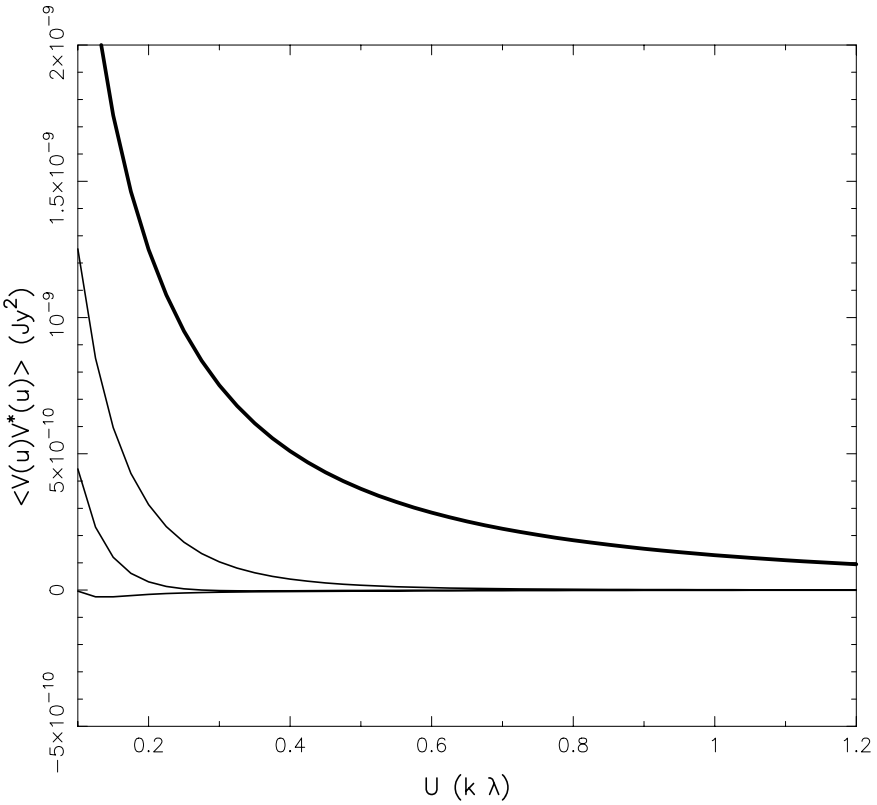

Figure 3. Same as Fig. 2 for the central frequency $\nu = 610$ MHz.

to be linear and independent of the Fourier mode. Though the exact dependence of the HI signal on the bias is complicated (equation 13), the signal scales roughly linearly with bias. This means that for a moderately biased HI distribution $b \leq 2$ the signal could be higher by a factor of two.

4. Noise

For each visibility measurement in the UV plane, the contribution comes from both the signal from HI fluctuations S_ν, the detector noise N_ν, and various galactic and extragalactic foregrounds. We consider here the contribution from only the HI signal and the noise. The visibility measurement gives:

$$V_\nu(\mathbf{U}) = S_\nu(\mathbf{U}) + N_\nu(\mathbf{U}). \tag{15}$$

Both S and N are complex quantities with both real and imaginary parts distributed as Gaussian random variables (see e.g., Crane & Napier 1989 for properties of noise). The signal is a Gaussian random field because it is linear in density perturbation $\Delta(\vec{k})$ which is expected to be a Gaussian random field for large scales (small k) (see e.g., Bardeen *et al.* 1986; Peacock 1999). The signal and noise are uncorrelated with each other. The reality condition of the surface brightness (equation 1) and the noise in the

real space implies $S(-\mathbf{U}) = S^*(\mathbf{U})$ and $N(-\mathbf{U}) = N^*(\mathbf{U})$ Our aim is to construct bilinear combinations like $V_\nu(\mathbf{U})V^*_{\nu'}(\mathbf{U})$ and to detect $S_\nu(\mathbf{U})S^*_{\nu'}(\mathbf{U})$. ν and ν' will in general be different. The average signal $\langle S_\nu(\mathbf{U})S^*_{\nu'}(\mathbf{U})\rangle$ is calculated in the previous section. The average noise correlation, for $\nu = \nu'$:

$$\langle N_\nu(\mathbf{U})N^*_\nu(\mathbf{U})\rangle = \left[\frac{T_{\rm sys}}{K\sqrt{\Delta\nu\Delta t}}\right]^2. \tag{16}$$

Here $T_{\rm sys}$ is the system temperature, $\Delta\nu$ is the bandwidth, K is the antenna gain, and Δt is the time of integration for one visibility measurement. For $\nu \neq \nu'$ the noise correlation vanishes as the noise in different frequency channels is uncorrelated.

Estimator of the signal: From the measured visibility it is possible to write several estimators of the signal. The simplest such estimator is:

$$\hat{S} = V_\nu(\mathbf{U})V^*_{\nu'}(\mathbf{U}) - \langle N_\nu(\mathbf{U})N^*_\nu(\mathbf{U})\rangle. \tag{17}$$

This estimator is clearly unbiased, i.e.,

$$\langle\hat{S}\rangle = \langle S_\nu(\mathbf{U})S^*_{\nu'}(\mathbf{U})\rangle.$$

The quantity of interest to us is the variance of the estimated signal: $\sigma(\hat{S})^2 = \langle\hat{S}^2\rangle - \langle\hat{S}\rangle^2$. This quantity is calculated to be (see Appendix A for a derivation):

$$\sigma^2(\hat{S}) \simeq \frac{q}{n}\langle N_\nu(\mathbf{U})N^*_\nu(\mathbf{U})\rangle^2 \tag{18}$$

$q = 2$ for $\nu = \nu'$ and $q = 1$ for $\nu \neq \nu'$. n is the total number of visibility measurements. The signal-to-noise for the detection of the HI fluctuation signal is $\langle\hat{S}\rangle/\sigma(\hat{S})$.

The value of n for a given $|\mathbf{U}|$ in general depends on the antenna positions, frequency coverage, and the position of the source in the sky. To calculate the value of n we first consider the case when $\nu = \nu'$.

Case I – $\nu = \nu'$: To get a simple estimate, assume that a pair of antennas describes circular tracks in the UV plane with radius $|\mathbf{U}|$ and that these tracks do not overlap with the tracks of other antenna pairs, then $n = T/\Delta t$ for each frequency channel, where T is the total time of observation. (The actual observation is more complicated because the antenna tracks cross in the UV plane.) For this case, equation (18) gives, using equation (16):

$$\sigma^2(\hat{S}) = \left[\frac{2T_{\rm sys}}{K\sqrt{\Delta\nu\,T}}\right]^2. \tag{19}$$

Before proceeding further it is useful to calculate the expected noise for the GMRT. We shall take the fiducial observing frequency to be $\simeq 320$ MHz. At this frequency the GMRT system temperature $T_s \simeq 110$ K. GMRT has a total bandwidth of 16 MHz at this

frequency in 128 channels. To calculate the quantity in equation (16) we take one channel ($\Delta\nu = 125$ kHz) and an integration time of $\Delta t = 30$ sec for one 'instantaneous' measurement for a given baseline. The antenna gain at this frequency $K = 0.32\,\mathrm{K\,Jy^{-1}}$. Using this equation (16) gives the noise correlation to be $\simeq 175$ mJy. As this is much larger than the expected signal calculated in the last section, we are justified in neglecting the signal term in equation (26) in the Appendix. For total time of integration $T = 10$ hrs, equation (19) gives $\sigma(\hat{S}) \simeq 5$ mJy.

As each frequency channel gives a realization of the signal, the noise can be reduced further by using all the frequency channels. This gives $n = N_{\mathrm{chan}} \times T/\Delta t$ with $N_{\mathrm{chan}} = 128$ for GMRT; equation (19) gives $\sigma(\hat{S}) \simeq 0.45$ mJy. Even though we made a few simplifying assumptions in calculating the noise, this is the typical value obtainable in a real experiment. The expected noise is much larger than the expected signal from the HI fluctuations and therefore an experiment like GMRT cannot detect the HI fluctuation for a given $|\mathbf{U}|$ or by using a single pair of antennas in a reasonable amount of integration time.

To reduce the noise further one must consider averaging the signal over more than one pair of antennas. One such estimator is the map RMS which uses information from all possible baselines. The total number of 'instantaneous' baselines for an experiment with N antennas is $N(N-1)/2$. This gives $n = N_{\mathrm{chan}} N(N-1)/2 \times T/\Delta t$ and gives a further decrease of a factor $\simeq N/\sqrt{2}$ in the sensitivity. In the previous section we showed that much of the contribution to signal comes from baselines $\leq 1000\lambda$. GMRT has 15 antennas in the central array within a radius of $\simeq 1$ km. Much of the contribution to the signal will come from these antenna pairs.

Taking $N = 15$ in the calculation of noise sensitivity, we get $\sigma(\hat{S}) \simeq 40\,\mu$Jy for 10 hours of integration. The average signal (averaged over 15 antennas of the central GMRT array) is $\simeq$ 20–40 μJy. This means that a few sigma detection of the signal might be feasible in integration time ≤ 100 hrs using the central array of GMRT.

Case II – $\nu \neq \nu'$: In this case, $\langle N_\nu(\mathbf{U}) N_\nu^*(\mathbf{U})\rangle = 0$ and the variance of the signal estimator is smaller by a factor of 2 (equation (18)). The rest of the calculations proceeds similar to the first case. The number of distinct pairs for two different frequencies will depend on the separation of the frequencies. However, one must also take into account the line width of the damped Lyman-α clouds which is $\simeq 200\,\mathrm{km\,sec^{-1}}$ (Prochaska & Wolfe 1998). The line width of each GMRT channel is $\simeq 120\,\mathrm{km\,sec^{-1}}$. This means that one damped Lyman-α cloud will spill over in many frequency channels, thereby creating a correlation in the signal for nearby channels. This correlation must be accounted for before the HI fluctuation signal can be extracted. It is hard to do it analytically and this issue will be addressed in future using simulations of the HI signal. However it is possible to get the typical noise sensitivity for this measurement.

The total number of frequency channel pairs is $N_{\mathrm{chan}}(N_{\mathrm{chan}}-1)/2$. Each pair gives a different realization of noise. If we average the signal over all baselines and all frequency pairs, we get $n = N(N-1)/2 N_{\mathrm{chan}}(N_{\mathrm{chan}}-1)/2$. This is larger than the maximum value of n in the first case by a factor of $\simeq N_{\mathrm{chan}}/2$. However it would be meaningful to average over all channel-pairs if the signal is significant for all such cross-correlations. As seen in the previous section, the correlation between different channels falls rapidly for separation ≥ 1 MHz, therefore the number of useful channels pairs is less than the maximum possible. The value of n however is still likely to be more than in the previous case. For example if we average the sig-

nal over all the frequency channels with $\nu' - \nu \leq 0.5\,\mathrm{MHz}$, the expected signal is $\simeq$ 10–20 μJy. The number of frequency pairs are $\simeq 5N_{\mathrm{chan}}$ in this case. This gives $\sigma(\hat{S}) \simeq 15\,\mu\mathrm{Jy}$ for ten hours of integration. From this discussion we can conclude that it might also be possible to extract this signal for integration time ≤ 100 hrs using GMRT.

The noise in detecting the HI signal $\sigma(\hat{S})$ is comparable to the sensitivity for detecting continuum sources. This is so even though the HI clouds emit line radiation. Therefore the method of observing fluctuations in HI radiation makes more optimal use of all the frequency width available in the experiment. The individual clouds are very faint (flux $\lesssim 10\,\mu$Jy (Saini *et al.* 2001)) and cannot be detected using GMRT because the line sensitivity $\simeq 50\,\mu$Jy for 100 hrs of integration needed to detect the HI fluctuations.

5. Conclusions and discussion

Our main results are:

- The correlation in measured visibilities owing to density inhomogeneities and peculiar velocities of the HI distribution at high redshifts can be related to the power spectrum of the HI distribution (equation (13)). The visibility correlation for any baseline U is sensitive to Fourier modes $\geq 2\pi U/r_\nu$. This means that the typical length scales probed for any baseline are $\lesssim 30h^{-1}\,\mathrm{Mpc}(100/U)$.
- The signal is strongest for baselines $\lesssim 1000$ and for $\nu = \nu'$, i.e., on the same two-dimesional map, the correlation is between 2×10^{-9} Jy^2 and 10^{-10} Jy^2.
- For $\nu \neq \nu'$, i.e., cross-correlation signal, the correlation signal is 10^{-9}–10^{-11} Jy^2 for baselines $|\mathbf{U}| \lesssim 500$ for $\nu' - \nu \lesssim 0.5\,\mathrm{MHz}$. The correlation is negative for most baselines for $\nu' - \nu \gtrsim 2\,\mathrm{MHz}$ and falls below 10^{-12} Jy^2.
- GMRT might detect these signals for integration times $\lesssim 100$ hrs. We argue that measuring visibility correlations in the presence of system noise makes optimal use of the fact that the noise is uncorrelated across baselines and frequency channels. The error for these measurements is comparable to and can even be smaller than the continuum sensitivity of the instrument.

The signal and noise analyses given in this paper are for the system parameters of the currently-operational GMRT. However it can be easily extended to future telescopes like Square Kilometer Array (SKA)* and Low Frequency Array (LOFAR)†. Our analysis can also be extended to higher redshifts ($z \simeq 5$) as the HI content of the universe at these redshifts is beginning to be known (see e.g. Peroux *et al.* 2001).

In this paper we neglected two other contributions to the visibility correlations: galactic and extra-galactic foregrounds and the Poisson fluctuations owing to point-like nature of HI clouds. The galactic foregrounds are expected to be dominated by the fluctuations in the synchrotron radiation from the Galaxy. The only existing all-sky map at low radio frequencies is the 408 MHz Haslam map (Haslam *et al.* 1982). This map has an angular resolution of $\simeq 1^\circ$ and therefore cannot give much information

*See `http://www.nfra.nl/skai/`

†See `http://www.astron.nl/lofar`

on the angular scales of interest to us. The extra-galactic foregrounds get most of its contribution from the radio point-sources. Little is known about the radio point sources at sensitivity levels ($\lesssim 100\,\mu$Jy) and frequencies of relevance in this paper.

Even though not much is known about Galactic and extra-galactic foregrounds at angular scales and sensitivity levels relevant to this paper, extrapolation from known foregrounds suggest that these foregrounds are likely to dominate over the HI signal (BNS 2001). A possible strategy to remove foregrounds was discussed in BNS (2001). Long GMRT baselines ($\gtrsim 1$ km) will be useful (the signal is negligible at such baselines) in removing the radio point sources and galactic foreground at angular scales $\lesssim 1'$. Any strategy to remove the foregrounds might degrade the signal-to-noise for the detection of the HI signal. This issue will be discussed in a later paper by using simulations of the HI signal and the foregrounds.

The HI at large redshift is locked up in discrete clouds. This will give rise to visibility correlations even in the absence of gravitational instability. This signal also depends on the mass function of the HI clouds (Saini *et al.* 2001) and therefore the detection of this signal can give an important clue about how the HI at high redshift is distributed. We shall attempt to estimate this signal from simulation of the high redshift HI in a later publication.

Acknowledgements

The authors would like to thank Jayaram Chengalur for many useful discussions. We are thankful to the late K. R. Anantharamaiah for helpful comments on the noise properties of interferometric experiments.

APPENDIX A

The HI fluctuation signal and the noise satisfy the following conditions:

$$\langle S_\nu(\mathbf{U}) S_{\nu'}(\mathbf{U}')\rangle = \langle S_\nu(\mathbf{U}) S_{\nu'}(\mathbf{U})\rangle \delta_D(\mathbf{U}-\mathbf{U}') \tag{20}$$

$$\langle N_\nu(\mathbf{U}) N_{\nu'}(\mathbf{U}')\rangle = \langle N_\nu(\mathbf{U}) N_\nu(\mathbf{U})\rangle \delta_D(\mathbf{U}-\mathbf{U}')\delta_D(\nu-\nu'). \tag{21}$$

Note that the signal is correlated across frequency channels while the noise is not. Let us assume that any interferometric experiment makes n measurements of the visibility for given $|\mathbf{U}|$ and the quantities (like visibility correlation function) are estimated by averaging over these measurements. Using this it is seen that the signal (for $\nu = \nu'$) and the noise can be treated as n uncorrelated, random variables with the same mean and variance. In such a case, the estimated average equals the average of any of the random numbers and the variance of the estimated 'signal' is $1/n$ times the variance of any of the random variables (see e.g., Papoulis 1984; this result is independent of the probability distribution functions of the individual variables). Of particular interest to us is the variance of the estimator in equation (17) for a given $|\vec{u}|$. The variance is estimated from n realizations of the random variable $\hat{S}$. It is given by:

$$\sigma^2(\hat{S}) = \frac{\sigma^2}{n}. \tag{22}$$

Here $\sigma^2 = \langle \hat{S}^2 \rangle - \langle \hat{S} \rangle^2$ is the variance of any realization of $\hat{S}$.

It is given by, using the definitions of V and N from equation (15):

$$\sigma^2 = \langle V_\nu V_{\nu'} V_\nu V_{\nu'} \rangle + \langle N_\nu N_{\nu'} \rangle^2 - 2\langle N_\nu N_{\nu'} \rangle \langle V_\nu V_{\nu'} \rangle - \langle S_\nu S_{\nu'} \rangle^2. \tag{23}$$

To simplify this expression further we use the fact that for a Gaussian random process, the expectation value of four random numbers is given by

$$\langle x_1 x_2 x_3 x_4 \rangle = \langle x_1 x_2 \rangle \langle x_3 x_4 \rangle + \langle x_1 x_3 \rangle \langle x_2 x_4 \rangle + \langle x_2 x_4 \rangle \langle x_1 x_3 \rangle.$$

We first consider the case when $\nu = \nu'$. Equation (23) then reduces to:

$$\sigma^2 = 3\langle V_\nu V_{\nu'} \rangle^2 + \langle N_\nu N_{\nu'} \rangle^2 - 2\langle N_\nu N_{\nu'} \rangle \langle V_\nu V_{\nu'} \rangle - \langle S_\nu S_{\nu'} \rangle^2. \tag{24}$$

Again using equation (15) for the definition of $\langle V_\nu V'_\nu \rangle$, this simplifies to:

$$\sigma^2 = 2 \times (\langle S_\nu S_\nu \rangle + \langle N_\nu N_\nu \rangle)^2 . \tag{25}$$

The case when $\nu = \nu'$ is slightly more complicated. Making a simplifying assumption that the signal contribution can be dropped while calculating the four-point functions in equation (23) (for justification see the text), we get:

$$\sigma^2 \simeq \langle N_\nu N_\nu \rangle^2. \tag{26}$$

Equations (25) and (26) along with equation (22) gives equation (18).

References

Bagla, J. S. 1998, ASP Conf. Ser. 156: Highly Redshifted Radio Lines, **9**.
Bagla, J. S., Nath, B., Padmanabhan, T. 1997, *MNRAS*, **289**, 671.
Bharadwaj, S., Nath, B., Sethi, S. 2001, *JAA*, **22**, 21.
Bardeen, J. M., Bond, J. R., Kaiser, N., Szalay, A. S. 1986, *ApJ*, **304**, 1.
Bunn E. F., White M. 1996, *ApJ*, **460**, 1071.
Crane, P. C., Napier, P. J. 1989, in *Synthesis Imaging in Radio Astronomy*, ASP series, volume 6
de Bernardis, P. *et al.* 2000, *Nature*, **404**, 995.
Freedman, W. *et al.* 2001, *ApJ*, **553**, 47.
Haslam, C. G. T., Stoffel, H. , Salter, C. J., Wilson, W. E. 1982, *ApJS*, **47**, 1.
Kumar A., Padmanabhan T., Subramanian K. 1995, *MNRAS*, **272**, 544.
Lahav O., Lilje P. B., Primack J. R., Rees M., 1991, *MNRAS*, **251**, 128.
Lanzetta, K. M., Wolfe, A. M., Turnshek, D. A. 1995, *ApJ*, **430**, 435.
Papoulis, A. 1984, *Probability, Random Variables, and Stochastic Processes*, (McGraw-Hill)

Peacock, J. A. 1999, *Cosmological Physics* , (Cambridge: Cambridge University Press)
Peebles, P. J. E. 1980, *The Large-Scale Structure of the Universe* , (Princeton: Princeton University Press)
Perlmutter, S. *et al.* 1999, *ApJ*, **517**, 565.
Péroux, C., McMahon, R. G., Storrie-Lombardi, L. J., Irwin, M. J. 2001, *MNRAS*
Prochaska, J. X., Wolfe, A. M. 1998, *ApJ*, **507**, 113.
Saini, T., Bharadwaj, S., Sethi, S. 2001, *ApJ*, **557**, 421.
Steidel, C. *et al.* 1998, *ApJ*, **492**, 428.
Storrie–Lombardi, L. J., McMahon, R. G., Irwin, M. J. 1996, *MNRAS*, **283**, L79.
Subramanian, K., Padmanabhan, T. 1993, *MNRAS*, **265**, 101.
Subrahmanyam. R., Anantharamaiah, K. R. 1990, *JAA*, **11**, 221.
Swarup, G., Ananthakrishan, S., Kapahi, V. K., Rao, A. P., Subrahmanya, C. R., Kulkarni, V. K. 1991, *Curr. Sci.*, **60**, 95.

J. Astrophys. Astr. (2001) **22,** 309–319

A Map for a Group of Resonant Cases in a Quartic Galactic Hamiltonian

N. D. Caranicolas *Department of Physics, Section of Astrophysics, Astronomy and Mechanics, University of Thessaloniki, 540 06 Thessaloniki, Greece*
e-mail: caranic@helios.astro.auth.

Received 2000 October 11; accepted 2001 November 29

Abstract. We present a map for the study of resonant motion in a potential made up of two harmonic oscillators with quartic perturbing terms. This potential can be considered to describe motion in the central parts of non-rotating elliptical galaxies. The map is based on the averaged Hamiltonian. Adding on a semi-empirical basis suitable terms in the unperturbed averaged Hamiltonian, corresponding to the 1:1 resonant case, we are able to construct a map describing motion in several resonant cases. The map is used in order to find the $x - p_x$ Poincare phase plane for each resonance. Comparing the results of the map, with those obtained by numerical integration of the equation of motion, we observe, that the map describes satisfactorily the broad features of orbits in all studied cases for regular motion. There are cases where the map describes satisfactorily the properties of the chaotic orbits as well.

Key words. Galaxies: elliptical-orbits-regular and chaotic motion—maps: averaged Hamiltonian—stability.

1. Introduction

Resonant orbits are very important for systems of 2 degrees of freedom. Stable resonant tori give birth to families of regular orbits with similar shape to that of the parent resonant periodic orbit. On the other hand, unstable resonant tori are connected with a breakdown of regularity and with chaos.

One of the modern and quick methods to study the properties of orbits in a dynamical system is to use a map in order to construct the Poincare phase plane of a given Hamiltonian system. This technique was successfully used both in celestial mechanics and galactic dynamics (see Caranicolas 1990, 1994; Hadjidemetriou 1991, 1993; Sidlikovsky 1992; Hadjidemetriou & Lemaitre 1997; Caranicolas & Karanis 1999).

In this article we shall use the potential

$$V = \frac{1}{2}(\omega_1^2 x^2 + \omega_1^2 y^2) - \varepsilon \left[\beta(x^4 + y^4) + 2\alpha x^2 y^2\right], \tag{1}$$

where ω_1, ω_2 are the unperturbed frequencies of oscillation along the x and y axis respectively, α and β are positive parameters while $\varepsilon > 0$ is the perturbation strength.

This potential can be considered to describe the motion in the central parts of non rotating elliptical galaxies. We are particularly interested in resonant motion and for the study of the properties of resonant orbits we shall use a map. We aim to construct a map describing several resonant cases. The details for the construction of the map are given in section 2. Section 3 contains some applications while a discussion and the conclusions of this work are presented in section 4.

2. A map for a group of resonant cases

The Hamiltonian to the potential (1) is

$$H = \frac{1}{2}(p_x^2 + p_y^2) + V = h, \tag{2}$$

where p_x, p_y are the momenta per unit mass conjugate to x and y while h is the numerical value of H. In order to obtain the averaged Hamiltonian we follow the steps described in Caranicolas (1990). The averaged Hamiltonian in the resonant case $\omega_2 : \omega_1 = 1 : 1$ reads

$$\varepsilon\beta\left[\frac{3J^2}{2\omega_1^2} + \frac{3(\Lambda - \omega_1 J)^2}{2\omega_2^4}\right] + \frac{2\varepsilon\alpha J(\Lambda - \omega_1 J)}{\omega_1\omega_2^2}\left[1 + \cos 2\left(\theta - \frac{\pi}{2}\right)\right], \tag{3}$$

where we have set $\Lambda = h$. In order to study general resonance cases, say $\omega_2 : \omega_1 = r : s$, where r, s are integers, we must modify the Hamiltonian (3). A reasonable choice is to replace the term $\cos(2\theta - \pi)$ which characterizes the 1:1 resonance with the term $\cos(2r\theta - s\pi)$. In this way we obtain generally the Hamiltonian

$$\varepsilon\beta\left[\frac{3J^2}{2\omega_1^2} + \frac{3(\Lambda - \omega_1 J)^2}{2\omega_2^4}\right] + \frac{2\varepsilon\alpha J(\Lambda - \omega_1 J)}{\omega_1\omega_2^2}\left[1 + \cos 2\left(r\theta - s\frac{\pi}{2}\right)\right], \tag{4}$$

which gives (see for details Caranicolas 1990) generally the map

$$\begin{aligned} J_{n+1} &= J_n + f(J_{n+1}, \theta_n) \\ \theta_{n+1} &= \theta_n + S(J_{n+1}) + g(J_{n+1}, \theta_n), \end{aligned} \tag{5}$$

where

$$\begin{aligned} f(J,\theta) &= \pm\frac{2\varepsilon\alpha r J(\Lambda - \omega_1 J)\sin 2r\theta}{\omega_1\omega_2^2}, \\ S(J) &= \frac{3\varepsilon\beta J}{\omega_1^2} - \frac{3\varepsilon\beta\omega_1(\Lambda - \omega_1 J)}{\omega_1^4} - \frac{2\varepsilon\alpha J}{\omega_2^2} + \frac{2\varepsilon\alpha(\Lambda - \omega_1 J)}{\omega_1\omega_2^2}, \\ g(J,\theta) &= \pm\frac{\varepsilon\alpha(\Lambda - 2\omega_1 J)\cos 2r\theta}{\omega_1\omega_2^2}. \end{aligned} \tag{6}$$

We use the plus sign when $s = 2k$ and the minus sign when $s = 2k+1, k = 0, 1, 2\ldots$ and return to the original x, p_x variables through $x = (2J/\omega_1)^{1/2}\cos\varphi$, $p_x = -(2J\omega_1)^{1/2}\sin\varphi$.

The fixed points of (5) are at

$$\begin{aligned}
&\text{(i)} \quad J = \frac{\omega_1(\beta\omega_1^2 - \alpha\omega_2^2)\Lambda}{\beta\omega_1^4 - 2\alpha\omega_1^2\omega_2^2 + \beta\omega_1^4}\,, \qquad \theta = 0, \pi,\\
&\text{(ii)} \quad J = \frac{\omega_1(3\beta\omega_1^2 - \alpha\omega_2^2)\Lambda}{3\beta\omega_1^4 - 2\alpha\omega_1^2\omega_2^2 + 3\beta\omega_1^4}\,, \qquad \theta = \pm\frac{\pi}{2}, \qquad (7)\\
&\text{(iii)} \quad J = 0, \qquad \text{any } \theta.
\end{aligned}$$

Here we must make clear that we have the above positions of the resonant fixed points (i) and (ii) when $s = 2k$ while, for $s = 2k+1$, the fixed points (i) and (ii) interchange their θ positions.

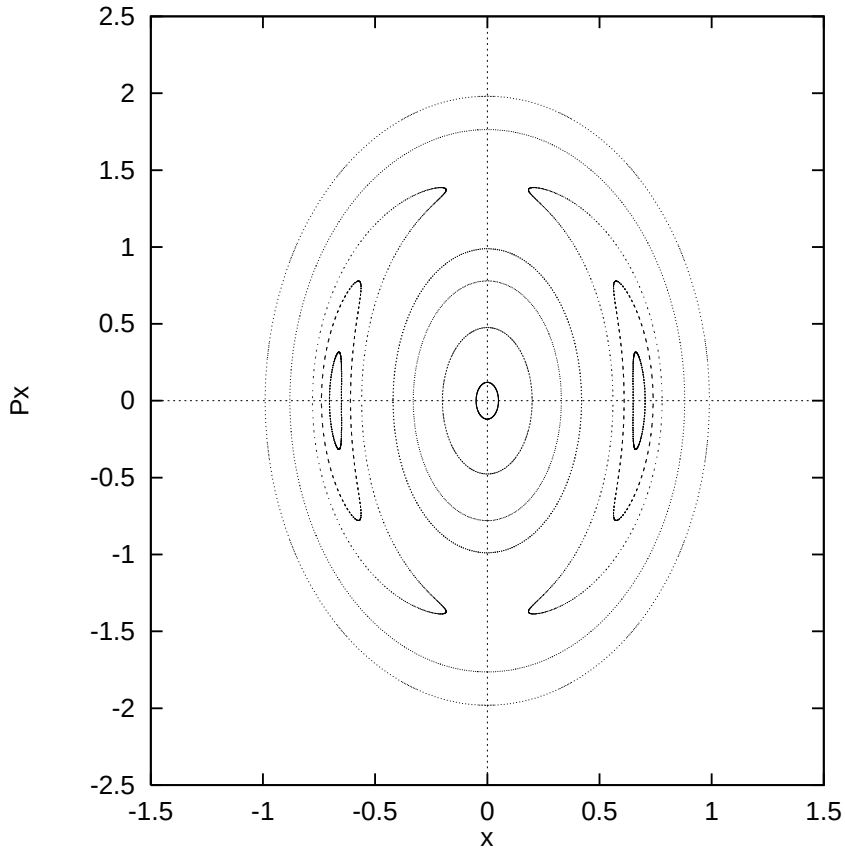

Figure 1. The $x - p_x$ phase plane, in the case of the 2:1 resonance, derived by numerical integration. The values of the parameters are $\varepsilon = 0.1,\ h = 2,\ \alpha = 1.2,\ \beta = 0.01$.

3. Applications

The general map (5) gives very good results in the 1:1 resonance case. This case has been studied in detail by Caranicolas & Vozikis (1999). In the following we shall use the map (5) in order to study the properties of orbits in two additional resonance cases: the 2:1 and the 3:1 resonant case.

3.1 *The 2:1 resonance*

In order to make things simple we use the values $\omega_1 = 2, \omega_2 = 1$. In this case the positions of the resonant periodic points are given by

$$\begin{aligned} &\text{(i)} \quad J = \frac{2(\alpha - 4\beta)\Lambda}{8\alpha - 17\beta}, \qquad \theta = 0, \pi, \\ &\text{(ii)} \quad J = \frac{2(\alpha - 12\beta)\Lambda}{8\alpha - 51\beta}, \quad \theta = \pm\frac{\pi}{2}. \end{aligned} \tag{8}$$

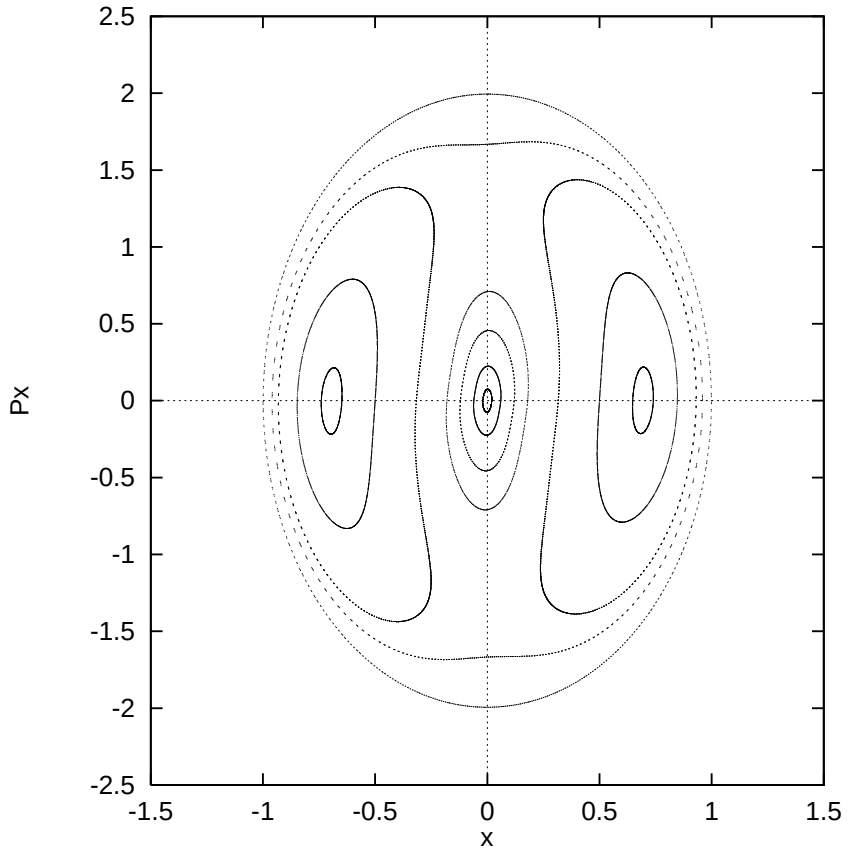

Figure 2. The $x - p_x$ phase plane, in the case of the 2:1 resonance, derived by the map. The values of the parameters are as in Fig. 1.

It is evident that the existence, position and stability of the resonant periodic orbits depends on the particular values of the parameters α and β. An elementary analysis shows that both resonant periodic orbits (i) and (ii) are present when

$$\alpha > 12\beta \tag{9}$$

while only the resonant periodic points (i) are present when

$$\frac{51\beta}{8} < \alpha < 4\beta. \tag{10}$$

The indices of stability (see Caranicolas 1990) for the resonant periodic orbits (i) and (ii) are

$$\begin{aligned} \delta_1 &= \left| 2 + \frac{3\alpha}{8\alpha - 17\beta} \left[9\alpha\beta - 4(\alpha - \beta)^2 \right] \varepsilon^2 \Lambda^2 \right|, \\ \delta_2 &= \left| 2 + \frac{\alpha}{8\alpha - 51\beta} \left[4(\alpha^2 + 9\beta^2) - 51\alpha\beta \right] \varepsilon^2 \Lambda^2 \right| \end{aligned} \tag{11}$$

respectively. When $\delta < 2$ the orbit is stable, otherwise it is unstable.

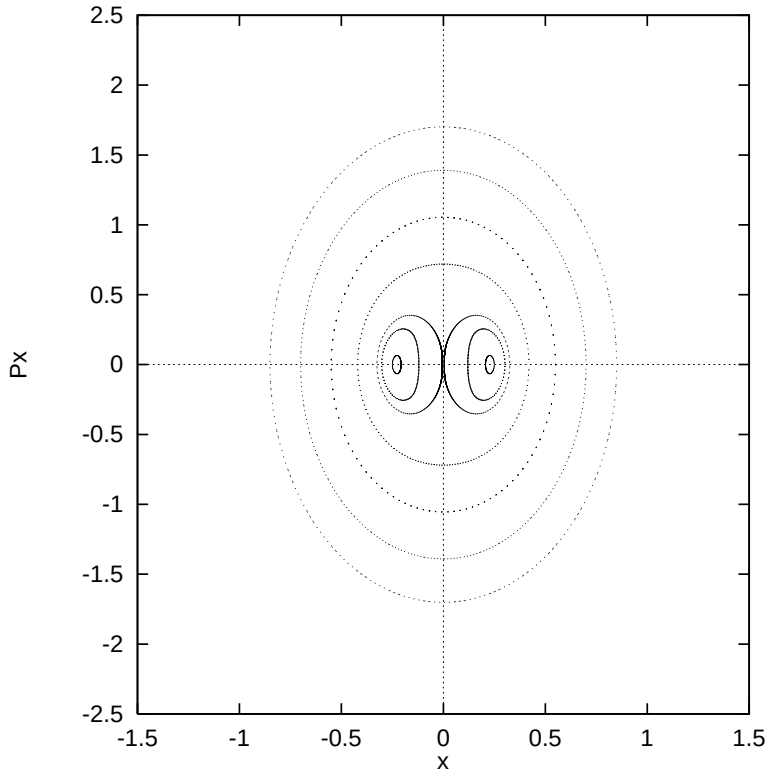

Figure 3. Same as Fig. 1 when $\beta = 0.1$.

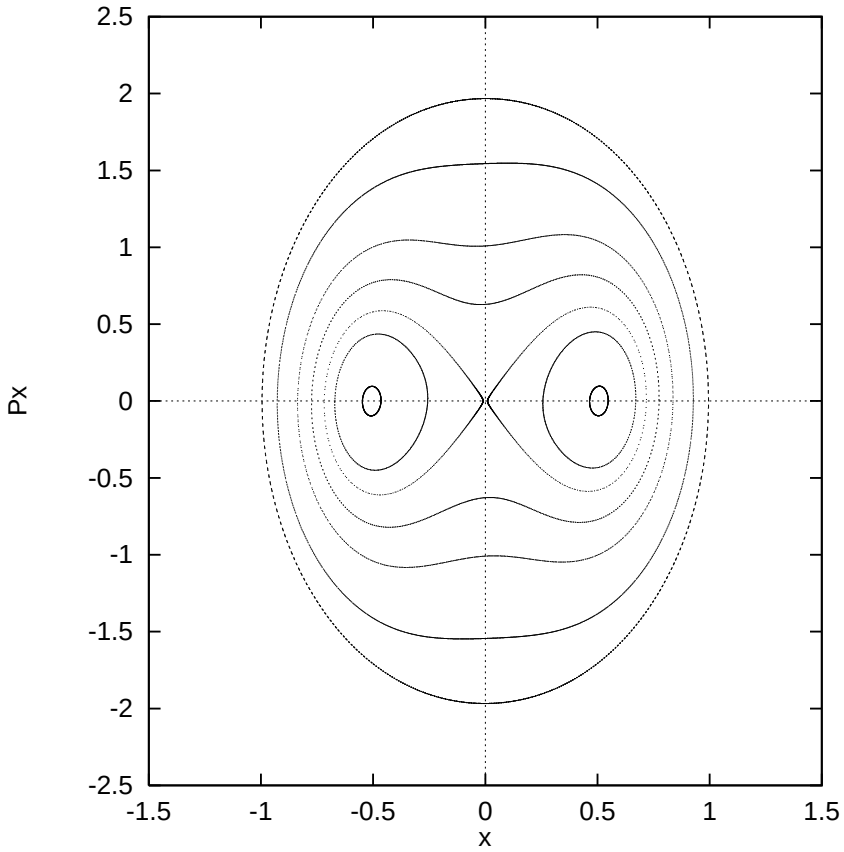

Figure 4. Same as Fig. 2 when $\beta = 0.1$.

Figures 1 and 2 show the x-p_x phase plane, when $\alpha = 1.2,\ \beta = 0.01,\ h = 2,\ \varepsilon = 0.1$, found by numerical integration and the map respectively. As one can see the basic characteristic, that is position of periodic points and stability, are satisfactorily described by the map. It is evident that we are in the case (9) where both fixed points (i) and (ii) are present. As, in this case, β is at least two orders of magnitude smaller than α, relations (11) give $\delta_1 < 2,\ \delta_2 > 2$, which means that fixed points (i) are stable while fixed points (ii) are unstable. Figs. 3 and 4 are similar to 1 and 2 when $\beta = 0.1$. One observes that the resonant periodic points (ii) are not present now, because for this value of β relation (10) is valid. We see that the position of the periodic orbits is not the same in the two patterns. Nevertheless the general topology and the stability features of the phase plane derived by the map is similar to that given by the real system.

3.2 *The 3:1 resonance*

In what follows we shall study the 3:1 resonance. Here we use the values $\omega_1 = 3,\ \omega_2 = 1$. The position of the resonant periodic points, which become again functions of the parameters α and β are at

$$\begin{aligned} &\text{(i)} \quad J = \frac{(\alpha - 27\beta)\Lambda}{2(8\alpha - 41\beta)}, \qquad \theta = 0, \pi, \\ &\text{(ii)} \quad J = \frac{3(\alpha - 9\beta)\Lambda}{2(9\alpha - 41\beta)}, \qquad \theta = \pm\frac{\pi}{2}. \end{aligned} \tag{12}$$

Both resonant periodic orbits (i) and (ii) are present when

$$\alpha > 27\beta \tag{13}$$

while only the resonant periodic points (i) are present when

$$9\beta < \alpha < 27\beta. \tag{14}$$

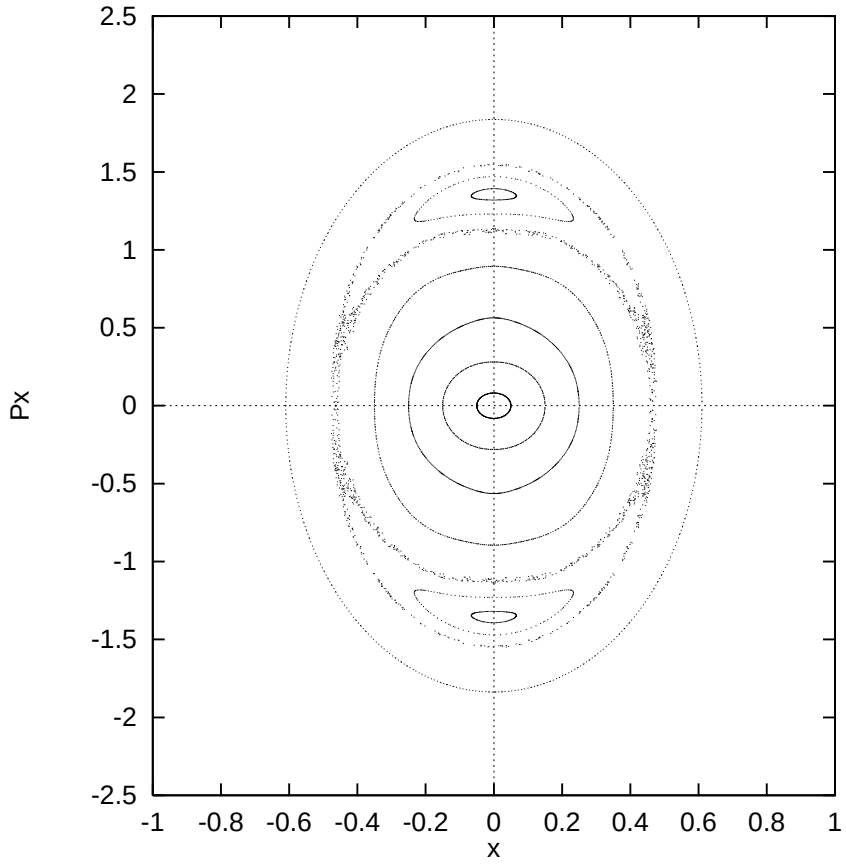

Figure 5. The $x - p_x$ phase plane, in the case of the 3:1 resonance, derived by numerical integration. The values of the parameters are $\varepsilon = 0.4,\ h = 2,\ \alpha = 1.2,\ \beta = 0.01$.

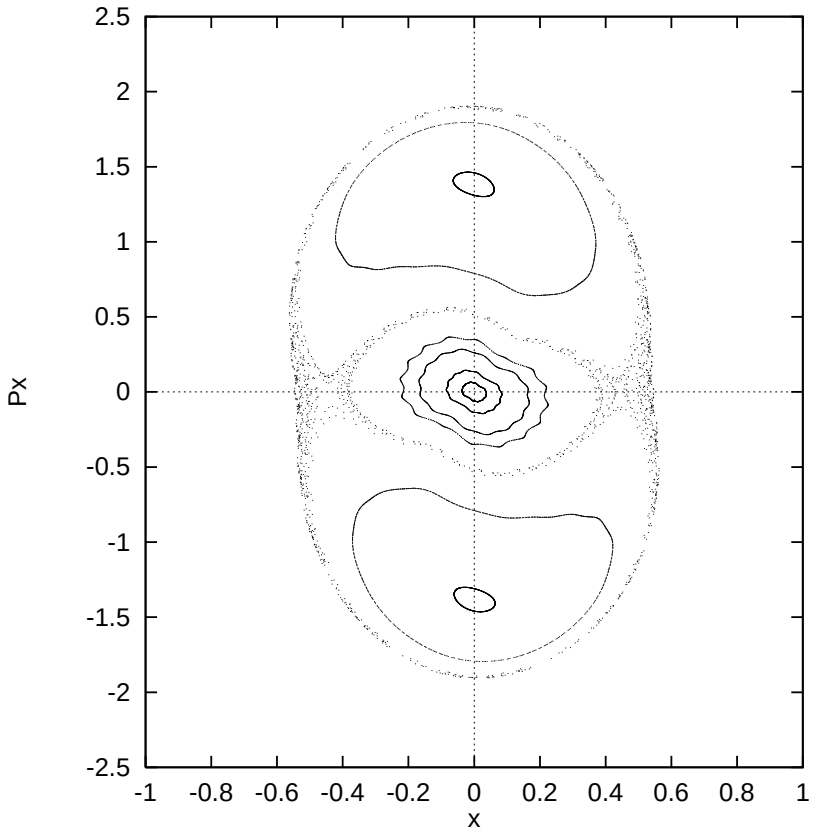

Figure 6. The $x - p_x$ phase plane, in the case of the 3:1 resonance, derived by the map. The values of the parameters are as in Fig. 5.

In this resonant case the indices of stability, for the resonant periodic orbits (i) and (ii), become

$$\delta_1 = \left| 2 + \frac{2\alpha}{9(3\alpha - 41\beta)} \left[3(\alpha - \beta)^2 - 4\beta(19\alpha - 6\beta) \right] \varepsilon^2 \Lambda^2 \right|,$$
$$\delta_2 = \left| 2 + \frac{2\alpha}{3(9\alpha - 41\beta)} \left[64\alpha\beta - 9(\alpha - \beta)^2 \right] \varepsilon^2 \Lambda^2 \right|, \tag{15}$$

respectively.

Figures 5 and 6 show the $x - p_x$ phase plane found by numerical integration and the map respectively. The values of the parameters are $\alpha = 1.2,\ \beta = 0.01,\ h = 2,\ \varepsilon = 0.4$. Here one observes that part of the phase plane appears chaotic. This chaotic behavior is also described by the map. Finally Figs. 7 and 8 are similar to Figs. 5 and 6 but when $\beta = 0.1,\ \varepsilon = 0.25$. Here the motion is regular, the central point is unstable while the resonant points (i) are not present. As one can see the position of the resonant points is different in the two patterns. On the other hand, we observe that the structure of and the stability characteristics are the same for the two phase planes.

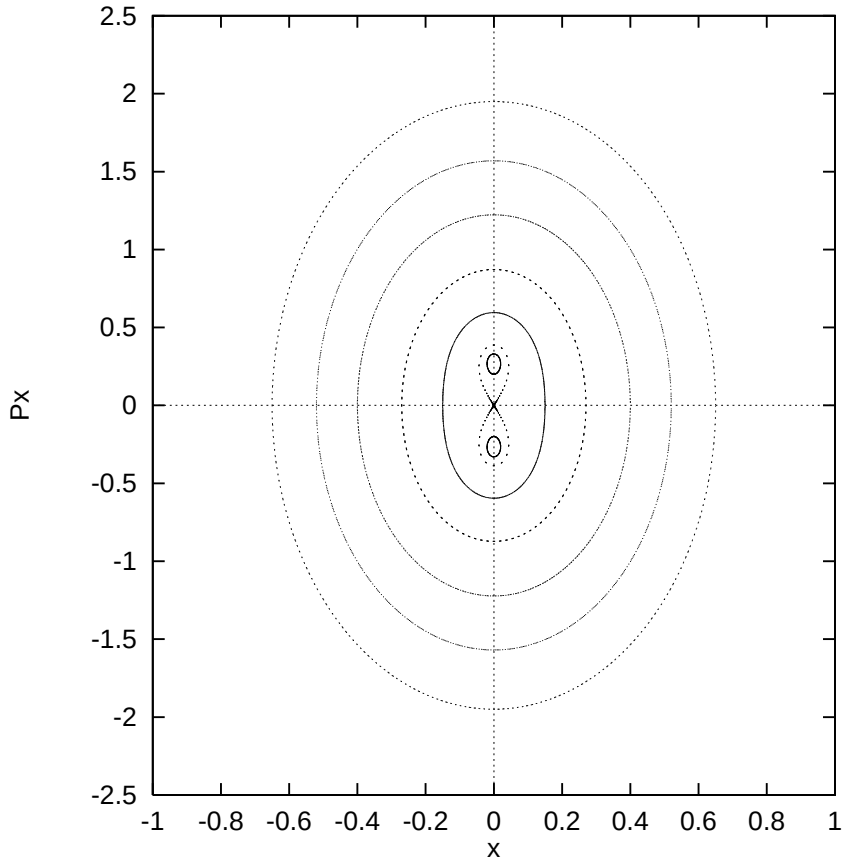

Figure 7. Same as Fig. 5 when $\varepsilon = 0.25,\ \beta = 0.1$.

4. Discussion

In this paper we have tried to present a map describing three different resonant cases. Of course it is not easy to find a map describing all resonance cases. In an earlier paper (Caranicolas & Vozikis 1999) we have constructed a map, describing the Hamiltonian system (2) in the 1:1 resonant case. That map gave results that are in very good agreement with those found by numerical integration. The construction of the map, in the 1:1 resonant case was easy because, for the particular resonance, the Hamiltonian to the potential (1) had suitable terms that favored the above resonant case. On the other hand numerical evidence suggests that the quartic Hamiltonian (2) gives interesting results for other resonant cases as well.

On this basis we decided to construct a map that will be adequate to cover several resonant cases instead of one single resonance. One additional reason for this decision was that the map gives analytic expressions for the position and stability of the resonant periodic orbits of the system. Furthermore, the idea to have a tool, that is the map, that describes a group of resonances seems interesting and attractive.

What we have presented here is a semi-analytical method. In fact we have replaced in the averaged Hamiltonian (3) the term depending on the angle θ by a general term,

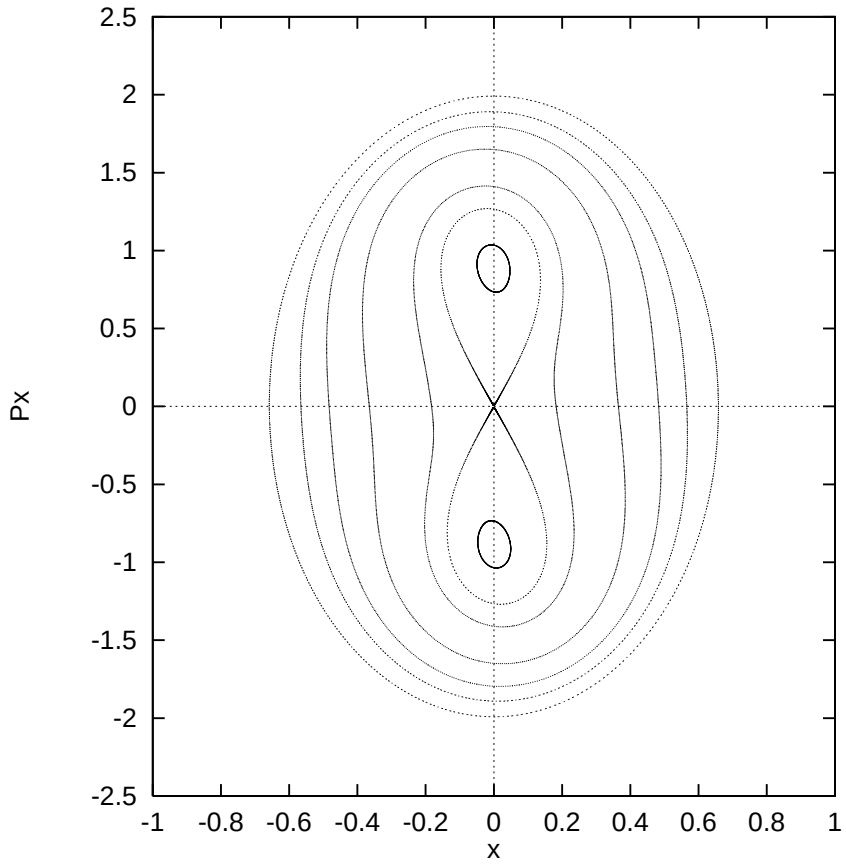

Figure 8. Same as Fig. 6 when $\varepsilon = 0.25,\ \beta = 0.1$.

containing the integers r and s, in such a way as to cover some additional resonant cases. This was made in a complete empirical basis and our choice was justified by the satisfactory results. Here we must emphasize that semi-analytical or semi-numerical methods are of importance and have been frequently used both in galactic dynamics and celestial mechanics during the last years (see Henrard & Lemaitre 1986, 1987; Henrard 1990; Henrard & Sato 1990; Caranicolas & Innanen 1992; Caranicolas 1993).

The results of this work suggest that maps can give fast, interesting and analytical information for systems made up of harmonic oscillators not only for a particular resonance but for several resonant cases. We believe that it is not too difficult to construct a map, for any resonant case, in systems made up of perturbed harmonic oscillators. What we have to do is to replace or to add suitable terms in an averaged Hamiltonian coming from the real system. This will make maps more useful and stronger tools for the study of the nice properties of harmonic oscillators. The reader can find interesting information on the construction and use of maps in Lichtenberg & Lieberman (1983) and Hadjidemeriou (1991). Another interesting and powerful tool, for systems made up of harmonic oscillators, is the extension of the lissajous transformation for the study of the phase space of the above systems in any resonant case (see Elipe & Deprit 1999; Elipe 2000).

Acknowledgement

The author would like to thank an anonymous referee for useful comments.

References

Caranicolas, N. D. 1990, *Cel. Mech.* **47**, 87.
Caranicolas, N. D. 1993, *Astr. Astrophys.* **267**, 388.
Caranicolas, N. D. 1994, *Astr. Astrophys.* **287**, 752.
Caranicolas, N. D., Karanis, G. I. 1999, *Astr. Astrophys.* **342**, 389.
Caranicolas, N. D. Vozikis, Ch. 1999, *Astr. Astrophys.* **349**, 70.
Caranicolas, N. D. 2000, *New Astron.* **5**, 397.
Caranicolas, N. D., Innanen, K. A. 1992, *Astron. J.* **103**, 1308.
Elipe, A., Deprit, A. 1999 *Mech. Res. Com.* **26**, 635.
Elipe, A. 2000 *Phys. Rev. E.* **61**, 6477.
Hadjidemetriou, J. D. 1991 *Mapping Models for Hamiltonian Systems with application to Resonant Asteroid Motion*, in *Predictability, Stability and Chaos in N-Body Dynamical Systems*, A E Roy (ed.) 157, (Kluwer Publ.)
Hadjidemetriou, J. D. 1993, *Cel. Mech.* **56**, 563.
Hadjidemetriou, J. D., Lemaitre, A. 1997, *The dynamical behaviour of our planetary system*, p.277, (Kluwer Academic Publishers)
Henrard, J. 1990, *Cel. Mech.* **49**, 43.
Henrard, J., Lemaitre, A. 1986, *Cel. Mech.* **39**, 213.
Henrard, J., Lemaitre, A. 1987, *Icarus* **69**, 266.
Henrard, J., Sato, M. 1990, *Cel. Mech.* **47**, 391.
Lichtenberg, A. J., Lieberman, M. A. 1983, *Regular and stochastic motion*, (Berlin Heidelberg; New York: Springer)
Sidlichovsky, M. 1992, *Astron. J.* **87**, 577.

J. Astrophys. Astr. (2001) **22,** 321–342

Real-Time Signal Processor for Pulsar Studies

P. S. Ramkumar* & A. A. Deshpande *Raman Research Institute, C. V. Raman Avenue, Bangalore 560 080, India.*
* *Present address: Intel Technology India Pvt Ltd, No. 65, 13th cross, III phase, JP Nagar, Bangalore 560 078.*

Received 2002 April 1; accepted 2002 May 8

Abstract. This paper describes the design, tests and preliminary results of a real-time parallel signal processor built to aid a wide variety of pulsar observations. The signal processor reduces the distortions caused by the effects of dispersion, Faraday rotation, doppler acceleration and parallactic angle variations, at a sustained data rate of 32 Msamples/sec. It also folds the pulses coherently over the period and integrates adjacent samples in time and frequency to enhance the signal-to-noise ratio. The resulting data are recorded for further off-line analysis of the characteristics of pulsars and the intervening medium. The signal processing for analysis of pulsar signals is quite complex, imposing the need for a high computational throughput, typically of the order of a Giga operations per second (GOPS). Conventionally, the high computational demand restricts the flexibility to handle only a few types of pulsar observations. This instrument is designed to handle a wide variety of Pulsar observations with the Giant Metre Wave Radio Telescope (GMRT), and is flexible enough to be used in many other high-speed, signal processing applications. The technology used includes field-programmable-gate-array(FPGA) based data/code routing interfaces, PC-AT based control, diagnostics and data acquisition, digital signal processor (DSP) chip based parallel processing nodes and C language based control software and DSP-assembly programs for signal processing. The architecture and the software implementation of the parallel processor are fine-tuned to realize about 60 MOPS per DSP node and a multiple-instruction-multiple-data (MIMD) capability.

Key words. Stars: neutron—pulsars; interstellar medium: dispersion—Faraday rotation; telescope: GMRT; instrumentation.

1. Introduction

Pulsars are highly magnetized rapidly-rotating neutron stars radiating predominantly linearly polarized electromagnetic radiation beamed along its magnetic poles. As the pulsar rotates, its radiating beam sweeps across the line of sight of the observer periodically, much like a rotating beacon, resulting in a periodic train of narrow pulses of broad-band radiation, which can be detected using a radio telescope. Different types of observable parameters, such as the pulse periodicity, its rate of change, the pulse

width, pulse energy, pulse shape and its structures, polarization of radiation received at different positions within the pulse, and their spatial and temporal variations are of great interest, besides the characterization of some of the properties of the interstellar medium through which the pulsar signal propagates. This paper describes the design, tests and preliminary results of a real-time parallel signal processor built to aid a wide variety of pulsar observations planned using the GMRT (Swarup *et al.* 1991; Deshpande 1995; Ramkumar 1998). Pulsar signals appear as a train of highly periodic pulses, with period typically in the range of a few milliseconds to a few seconds and are usually very weak and buried in the noise contributed by the background sky and the receiver of the radio-telescope (typically 20 to 40 dB below the noise level). During their propagation through the intervening medium, these signals are distorted due to dispersion, scattering and Faraday rotation (see Manchester & Taylor 1977; Hankins & Rickett 1975 for details). Also, due to the relative motion of the earth and the pulsar, the Doppler acceleration changes the apparent period of the pulses. To correct some of these distortions in real-time (as the telescope tracks the pulsar), and process the signal to enhance the signal-to-noise-ratio (SNR), the computations required demand rates of several Giga-operations per second. Many operations that are common in the methods used to correct each type of distortion were identified. These redundancies were removed and a common signal processing algorithm was designed to handle one or more of the corrections within a single framework. A parallel processing machine was designed based on ADSP 21020 processors, to implement the algorithm and perform the corrections in real-time and the algorithm was then fine-tuned to exploit the architectural advantages of the DSP chip.

2. Hardware architecture

The front-end receiver system (Swarup *et al.* 1991), which supplies data to the Signal Processor, consists of RF/IF sections for the signals (with a bandwidth of 32 MHz) received from two polarization channels of each of the thirty dishes. Each of these two bands is split further into two sub-bands and converted individually to baseband outputs, each 16MHz wide, and are processed separately in the FX system that follows. The Signal Processor for Pulsar Studies (SPPS) will use two identical systems to cater to the two sub-bands separately. The further description will detail the instrumentation for only one sub-band (the other being identical). The inputs to the SPPS appear as two parallel digital streams of complex voltages (corresponding to the frequency spectra of two orthogonal polarization channels). The input specifications of the SPPS for one sub-band are summarized below.

Signal source: Combined (sub-band) output spectra (Prabu 1997; Ramkumar 1998) from a selected number of GMRT antennas with 16 MHz band-width and two polarizations.

Nature of input: 256-channel complex frequency-spectrum (per polarization); data over frequency channels sent in time-multiplexed form at a rate of 16M samples/sec, new spectra available every 16 μs.

Data format: 1-bit sign, 8 bit magnitude each, for real/imaginary part of the complex voltage for any frequency channel, polarization.

The block diagram shown in Fig. 1 outlines the different sections of the SPPS for one sub-band.The SPPS has four basic blocks: A Data Input Module (DIM), DSP parallel-processing nodes, a Result Collection Module (RCM) and the Control and

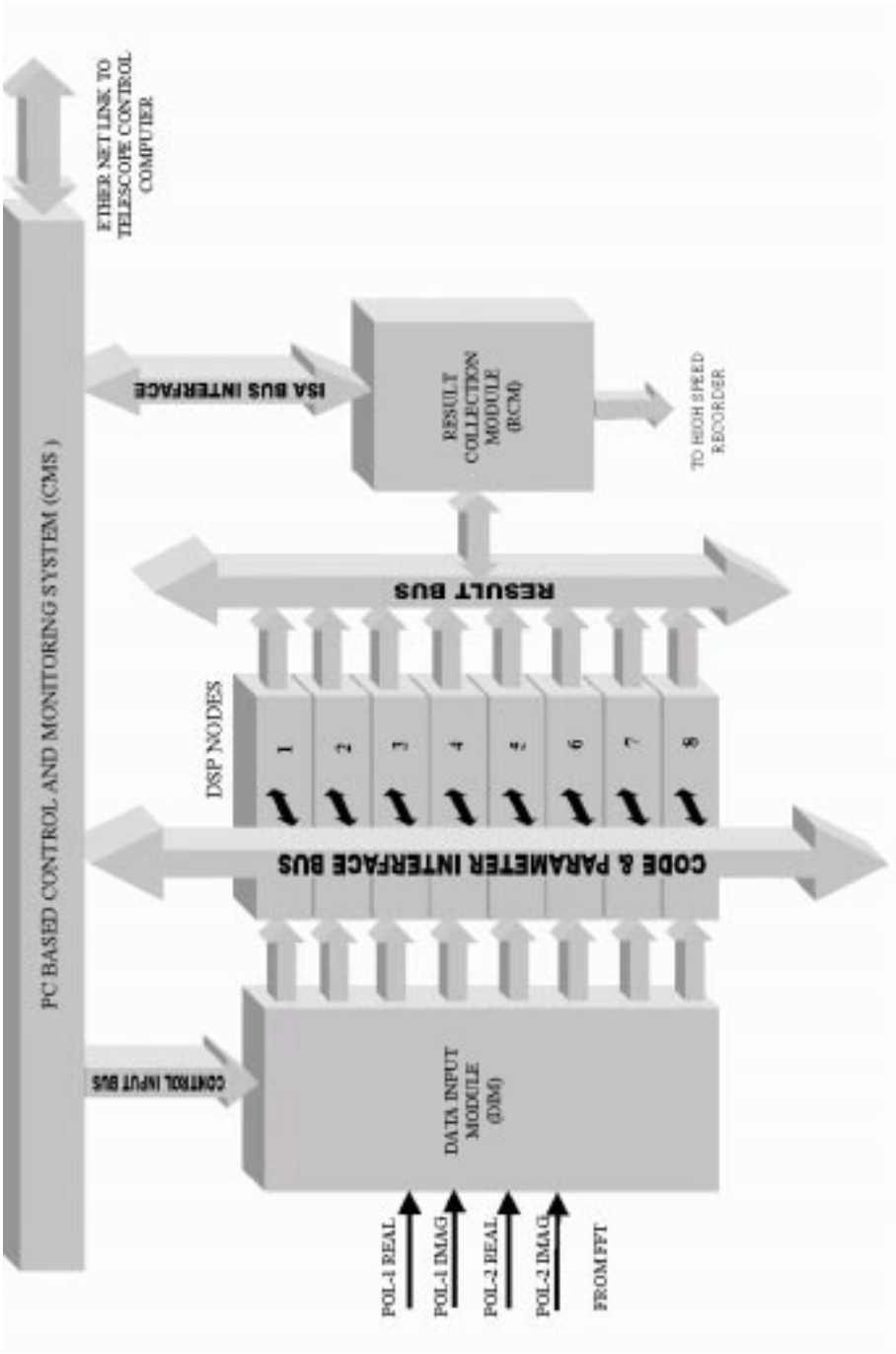

Figure 1. Basic blocks of SPPS of one sub-band (the other sub-band SPPS is identical, and the CMS is shared by both the sub-bands).

Table 1. Computations corresponding to different Stokes parameter derived from dual-polarization inputs.

Computation	Products	Additions	Stokes parameters for linear (circular) polarization inputs [e_1, e_2]
$e_1e_1^* + e_2e_2^*$	8	5	I (I)
$e_1e_1^* - e_2e_2^*$	8	5	Q (V)
Real($2e_1e_2^*$)	3	1	U (Q)
Imag($2e_1e_2^*$)	3	1	V (U)
Total = 34	22	12	

Monitoring System (CMS). The DIM links the front end to the parallel processor. It receives complex-voltage spectra from FFTs over differential-ECL links, computes the Stokes parameters (I,Q,U,V) for each frequency channel, and distributes the channels to the DSP processing nodes at a uniform rate. Each of the eight DSP processing nodes receives all 4 Stokes parameters of a selected band of 32 channels and performs operations such as pulse folding, Faraday de-rotation, dedispersion, Doppler acceleration correction, averaging of adjacent sample in time and frequency, pulse gating, data formatting, etc.. The RCM collects the results from each of the DSP nodes and renders the blocks of results at high speed to a fast recorder. In parallel, the same data are buffered to the CMS, which performs set-up, diagnostic and monitoring operations. The CMS also down-loads the processing codes and parameters to the DSP nodes, acquires and stores low-speed outputs (results) from the RCM, performs adaptive modifications to process parameters and feeds them back to the DSP nodes in real-time.

2.1 *Data input module*

As shown in the block diagram (see Fig. 2), the DIM has two major blocks, one for computation of Stokes parameters and another for distributing the Stokes parameters of different frequency channels to eight different data output paths. The effective data rate of the first block is about 128 Mbytes per second. The second block splits the data into multiple paths, so that individual DSP nodes in the following block can accept data for a smaller number of frequency channels at a slower, uniform rate and process the data independently in each module. The basic equations (e.g., Kraus 1966) relating the complex voltage samples (e_1, e_2) to the Stokes parameters are as listed in Table 1. For the specified bandwidth, the total computation rate amounts to about 544 million operations per second (MOPS) for calculating all four Stokes parameters.

This function has been implemented as a hybrid design involving the use of both look-up tables and dedicated high-speed logic built into EPLDs. The product of the magnitudes is calculated separately using EPROM-based look-up tables, while the resulting sign is from the exclusive-or (XOR) operation of the sign bits of the two numbers. The product terms are rounded to upper-most 16-bits to fit within the registered EPROMs. The addition and subtraction of the product terms, is performed using dedicated pipelined adders, designed and hosted within a pair of EPLDs. The outputs of these EPLDs represent the Stokes parameters I, Q, U and V. The summation/subtraction requires pipelined adder/subtractor logic modules (hosted in two EPLDs, consuming

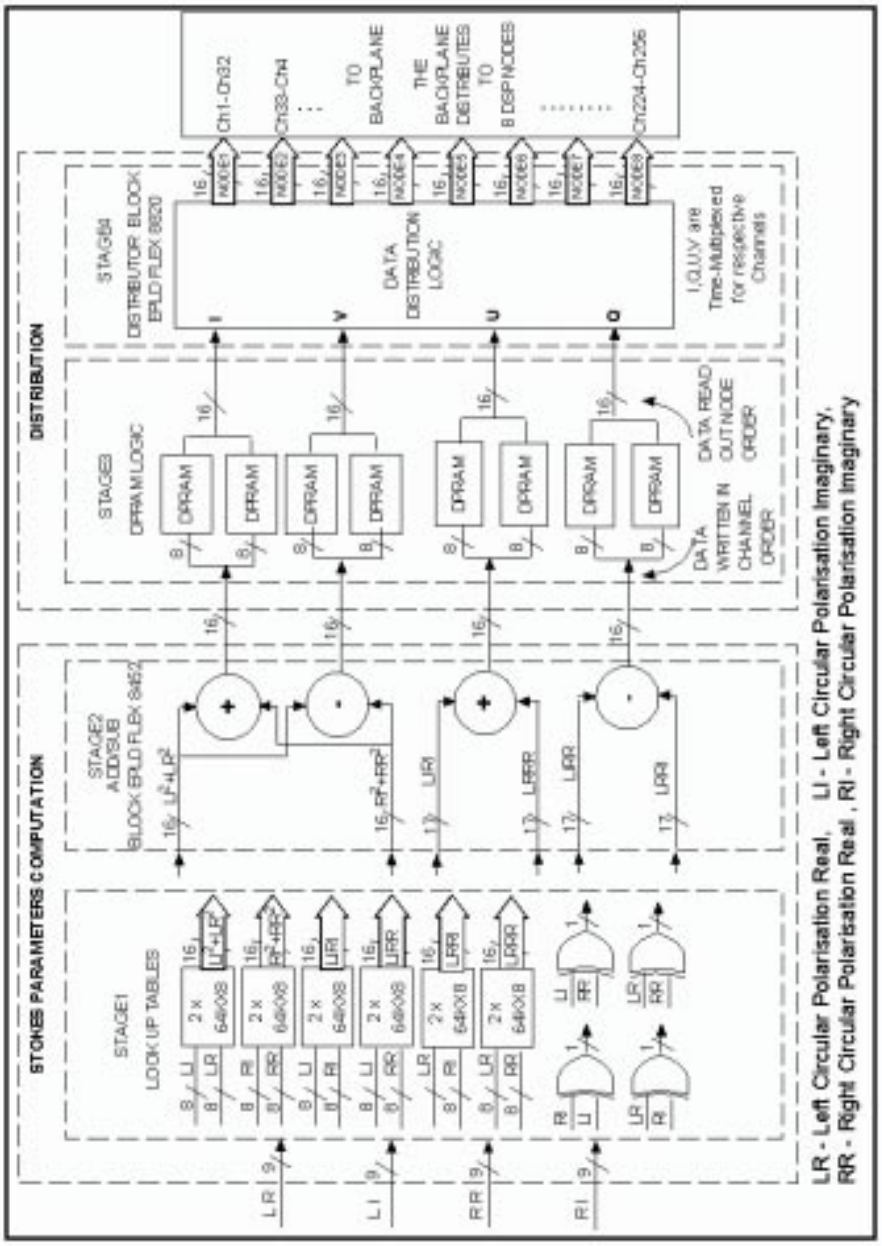

Figure 2. Architecture of Data Input Module.

about 3500 gates). A PASS-THROUGH mode is also provided, in which the look-up table and EPLD outputs are just replicas of their inputs, so that the raw data can be directly fed to further stages, if needed. Further, the 256 channels are split into eight paths of 32 consecutive channels, so as to supply to eight DSP nodes. To avoid burst - transfers to the DSPs, the Stokes parameters of various channels are written into a set of DPRAMs as they appear (1, 2, 3,..255, 1, 2.. etc.). After a full spectrum is written, the read out is started, in a node-sequential channel order (0, 32, 64, .. 224, 1, 33, 65,... 225, 2, 34,.. etc.). Thus the DSP nodes share the data at a slower, uniform rate. After the first spectrum is written, the read and write operations continue simultaneously without contention, in two alternating halves of the DPRAMS, through two ports of the DPRAMs. The four Stokes parameters of each node are latched in separate set of parallel-in, serial-out shift registers for each node, and are shifted out with the Stokes parameters time-multiplexed. After the initial pipeline delay, data appear concurrently on all the eight data paths, at a uniform speed of 8 Mwords/second. Write-strobe pulses are transmitted to each node along with the respective data and are synchronized to start after the pipeline delays in their respective data paths. This entire circuit is designed to fit in a pair of EPLDs (about 8000 gates), and is down-loaded into the EPLDs from a PC at setup time. Separate design files for different channel order, node order, etc., can be programmed, to route the DPRAM data to any node in any sequence.

2.2 *DSP nodes*

To perform all operations such as folding, adjacent sample integration, gating, Faraday de-rotation, dedispersion and Doppler acceleration correction, a suitable scheme is needed where the available memory resource can be redistributed between Stokes parameters, frequency channels and time frames depending on the type of observation. A parallel processing architecture based on DSP chips with an efficient signal processing algorithm was an optimal choice for design. Given below is a description of the architecture of one DSP-node (8 such nodes are to handle one sub-band of the GMRT) . The corresponding block diagram is shown in Fig. 3.

- The input data are available for the DSP node from a memory located on the program memory (PM) side. The data flowing in gets written into this memory at a steady speed, while the processor reads them out as and when required by the processing algorithm. Since the data flow from the DII to the DSP node is unidirectional and the writing/reading operations are independent as well as being at different speeds, this memory is chosen to be a 32-bit FIFO block. The write port of the FIFO block is interfaced to the DII and the read side is connected to the DSP node.
- The parameters required by the DSP nodes for processing are available from a separate memory on the PM side. The instruction code for the DSP node is also located in this memory. This allows the necessary update of the process parameters on-line, without disturbing the processor in the DSP node, and provides a common control block for all DSP nodes from which the instruction code and process parameters can be down loaded and updated on-line. The controller must be able to read back and check what it has written into this memory, before letting the DSP use it. The controller-DSP node communication protocol requires many semaphores. These semaphores may be bi-directional and are also located in the same memory for simplicity. A 48-bit dual port RAM block is chosen to hold the

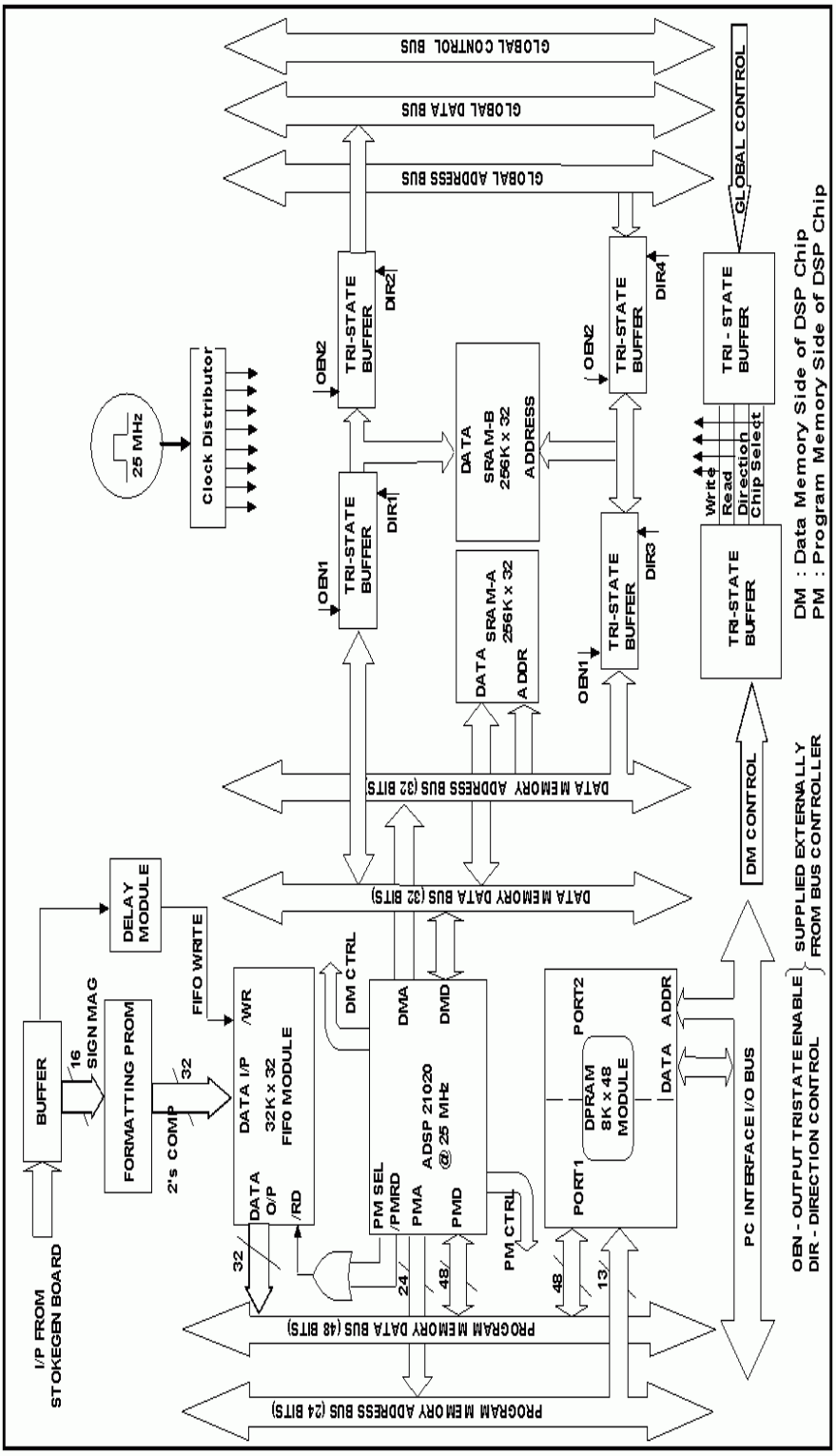

Figure 3. Architecture of a single DSP node.

instructions, parameters and semaphores. One port of the DPRAM is connected to the controller, while the other is interfaced to the PM side of the DSP node.

- A memory block in the data memory side of the DSP node holds the temporary results during the data processing. This memory has to be fast enough to match the DSP read/write speeds without requiring any wait cycles and is dedicated to the processor. This is realized in the form of a 256K location, 32-bit SRAM module designated SRAM-A which is interfaced to the data memory (DM) side of the DSP node. This memory is logically organized into two halves (banks) which alternate so that when one half is used for processing the previous results available in the other half can be read out by another task.
- The processed results in one of the two logical partitions of SRAM-A are copied into a continuous block of another SRAM module designated SRAM-B. This module is interfaced to the DM side of the DSP through tri-state buffers, such that it can be attached to or detached from the processor bus under software control. This SRAM is connected through another set of tri-state buffers to an output bus, common to all DSP nodes. When the DSP node wants to copy results from SRAM-A to SRAM-B, the buffers only on the DSP-node side are turned-on. After the results are written, SRAM-B (about 25 ns access time) is disconnected from the DSP node by tri-stating these buffers. Control logic ensures that the output-bus buffers are enabled only when the DSP node is not accessing SRAM-B and when the data acquisition system needs to acquire data from this particular node. The handshake between the DSP node and the RCM is explained later. Even though the flow of results is always from the DSP node to the RCM, SRAMs are chosen instead of FIFOs to provide flexibility for inter-node communications, such that the results of one node can be read and processed further by another node, if required, for other types of processing. With this feature, the architecture provides a loosely coupled, multiple instruction, and multiple data (MIMD) parallel processing system, which could be a very advantageous configuration for a variety of applications. The handshake for inter-node communications has been worked out, but is not necessary for the present requirements of pulsar signal processing. A memory mapped port on the DM side of the DSP node brings all status flags to the processor, which can be polled during processing.

Each DSP node operates at a 25 MHz clock rate. The code memory of all nodes are physically bussed together as shown in Fig. 4. All nodes are controlled by a central controller, implemented on a PC/AT platform, with suitable interface through parallel I/O ports hosted on the ISA bus of the PC/AT. The parallel ports are grouped to form the program bus, consisting of address, data, control and status buses which connect to the DPRAMs in the DSP nodes. The DPRAMs are 16-bit wide with 8K locations each, needing a 13-bit address bus and 16-bit data bus. There are 24 DPRAMs per sub-band and are organized as separate pages. Initially, the page number is latched in to a page-selector and subsequent addresses refer within a selected DPRAM until the page number is changed.

2.3 *Result collection module*

Two hand-shake signals, namely BUS-FREE and ENGAGED, are dedicated to each node for communication between the RCM and the nodes. Whenever a DSP node has its results ready in its SRAM-B, it activates its BUS-FREE line indicating that the RCM

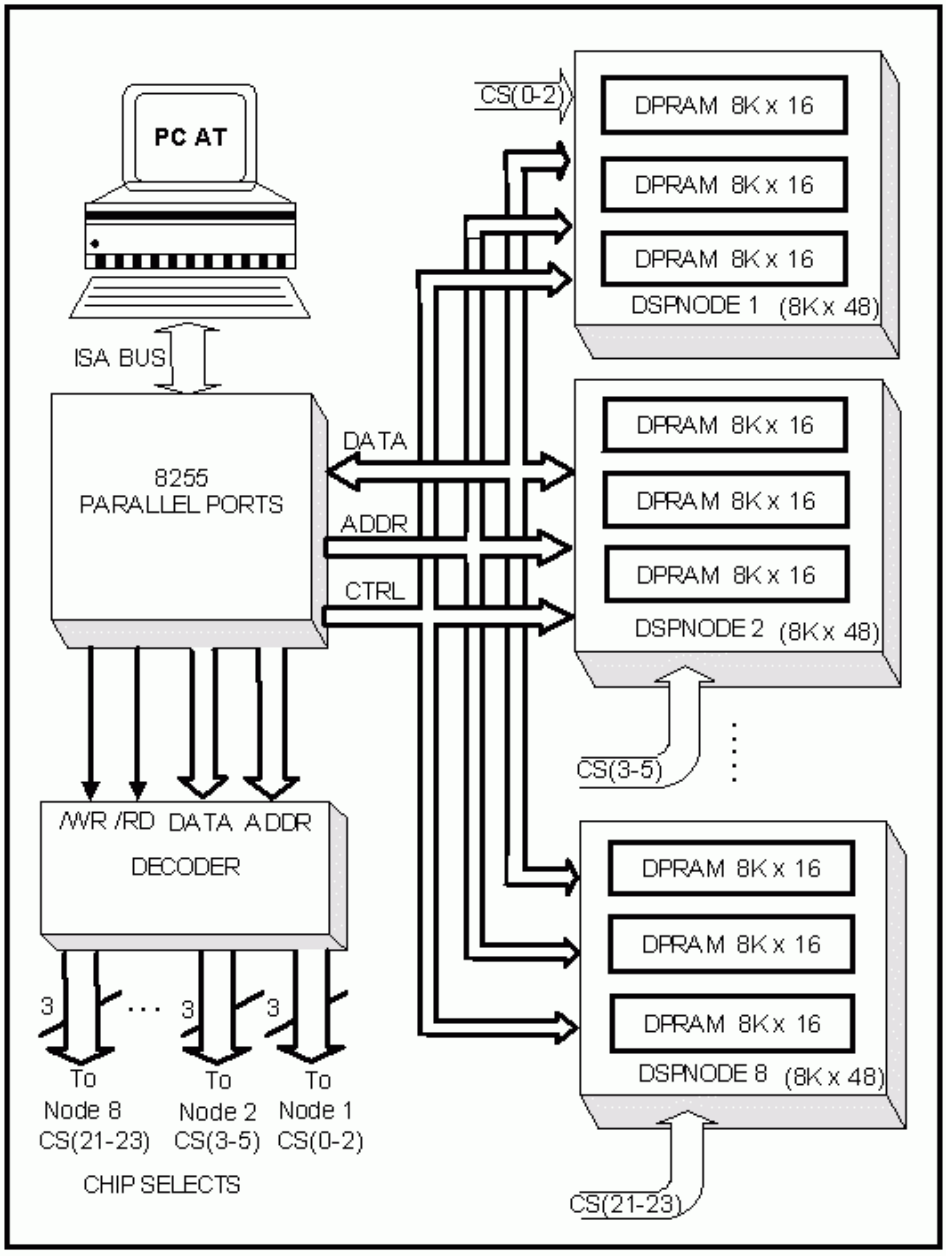

Figure 4. PC I/O interface to code memory of DSP node.

can access its SRAM-B. The RCM polls the BUS-FREE line and if found active, it sets the ENGAGED line to indicate to the DSP that it has taken over the bus and SRAM-B. Then it sends a sequence of addresses on the result-address-bus within a preset range. After asserting each address, it sets a chip-select signal (called OE) for that node, upon which the data from the SRAM flows onto the “result-bus". The RCM latches this data

into a 32-bit register and then sequences the address further. After completing the range specified for each node, it deactivates the ENGAGED line, indicating to the DSP node that it has finished transactions with its SRAM-B. This signal is tied to a hardware interrupt of the DSP chip, and an interrupt is issued whenever the ENGAGED line goes from active to deactivated state. An interrupt service routine in the DSP routine gets activated immediately and removes the BUS-FREE signal, disengages the SRAM-B from the result bus, and reclaims the connection to the memory. Meanwhile, the RCM polls the BUS-FREE line of the next node to set, after which it acquires data from that node in a similar manner as explained above. This process goes on, and suspends only when all nodes deactivate their BUS-FREE lines. After each 32-bit result gets latched in the RCM, it is split into two halves of 16-bits each and is loaded into a local FIFO block (32 K x 16). The FIFO block is memory mapped onto the PC via ISA bus. The PC monitors the FIFO flags and initiates a block transfer to the hard disk from the FIFOs whenever the half-full flags are set. The acquisition is stopped when the control PC finds that the time specified for ending the observation is reached.

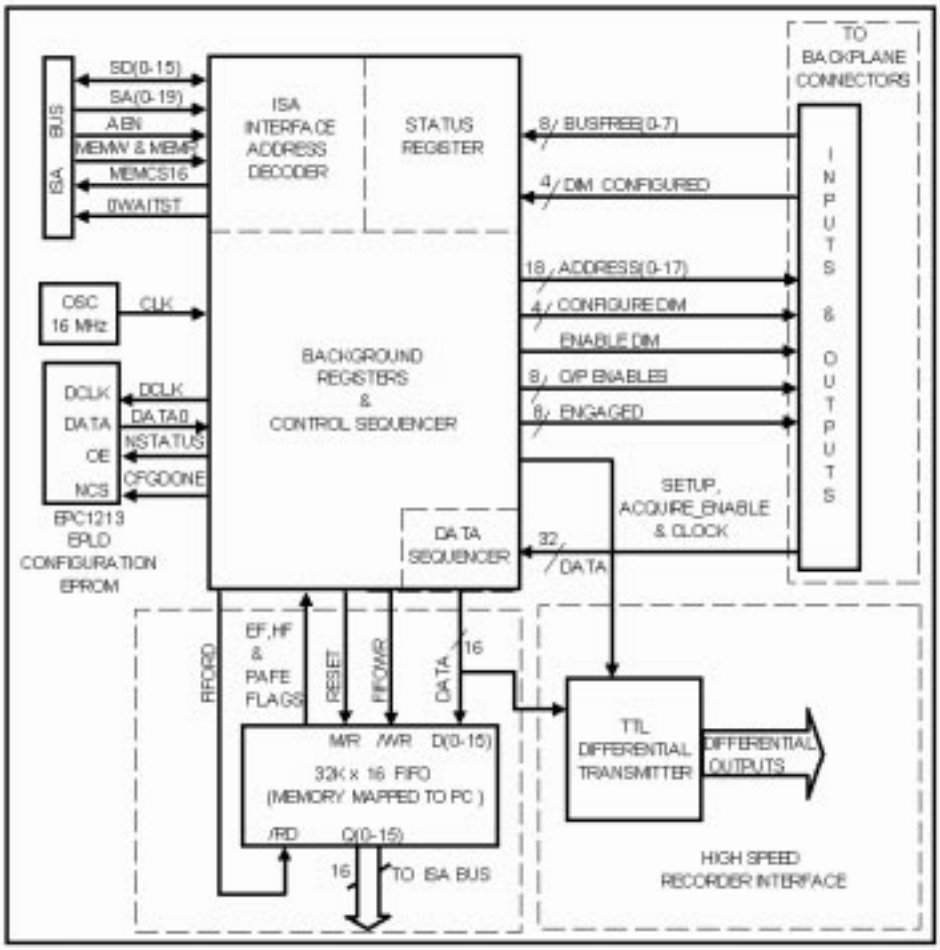

Figure 5. Architecture of Result Collection Module.

The block diagram of the RCM is shown in Fig. 5. The DCS is memory mapped through the PC's ISA bus. A space of 32 KBytes is mapped to the FIFO bank from which the results filled by the DCS can be read out. In the upper half, many control registers are mapped. A decoder generates the appropriate read/write pulses when the PC presents the respective address of different registers or memory, depending on the read/write signals of the ISA bus. The DCS is capable of working in a zero-wait state, 16-bit data transfer mode of ISA BUS. To specify the range of memory locations in each node from where results are to be collected, two registers, called lower- and upper-bound registers, are to be loaded with the start and end address of the result block in SRAM-B (the results are expected to fall in the same address range in all nodes). Through a programmable counter, the speed of acquisition from DSP nodes can be varied from 32 Kbytes/sec to 8 Mbytes/sec. Some times all of the eight nodes are not used or may have to be accessed in a different order to collect the results. To indicate the number of nodes and the node sequence for collecting results, a separate 32-bit register is loaded by a pattern, which uniquely defines every combination of number of nodes and node sequence. A 29-bit counter, clocked continuously at 16 MHz, forms the basic control sequencer. The lower most 8-bit section of the counter can be used to program the data acquisition rate. The next section of the counter chain is a 3-bit state counter. For every location to be read out from any DSP node, the eight states of this counter are decoded to produce the control signal sequence to complete reading out one 32-bit location, and loading it into two 16-bit locations of the local FIFO bank of DCS. The 16-bit words going to the FIFO bank are brought out in parallel along with a write strobe through an ECL differential link to a connector, which can be linked to a remote recorder for acquiring data at speeds higher than the PC's capability. The next stage in the counter chain is an 18-bit address counter, which generates an address sequence for read-out from the DSP nodes in a preset address range (maximum of 256 K locations). The next section in the counter chain is a Node sequencer, based on a set of shift registers. The node sequence and the number of nodes are loaded initially into background registers and the node sequencer cycles through this sequence and order. The state sequencer uses the node number to route the control signals to the appropriate node. The entire logic explained above has been built into a single FLEX EPLD chip (4000 gates).

3. Signal processing algorithm

It can be assumed that the input complex spectra are obtained with sufficient frequency and time resolution, and that consecutive spectra can be arranged to form a matrix, with the profile in each channel being located in fixed number of memory locations, say $N_{\mathrm{per-chan}}$ (which is equal to N_{bins} when folding at the pulsar period is performed). Consecutive spectra come in at time intervals of T_{frame} seconds. The basic operations required for various corrections are grouped as addition of incoming data to the matrix at suitably indexed locations. The calculation of index for various corrections is explained below:

a) De-dispersion (channel based data alignment): Due to interstellar dispersion, the arrival time of pulsed radiation at different frequencies (f_k) within the observed bandwidth is different and the delay difference ($\Delta\tau$) can be calculated relative to

the arrival of the pulse at the highest frequency ($f_{\rm high}$), and expressed in units of the sampling interval as,

$$\Delta N(f_k) = \frac{\Delta\tau}{T_{\rm frame}} = \frac{\beta.{\rm DM}}{T_{\rm frame}}[{f_k}^{-2} - {f_{\rm high}}^{-2}] \quad (1)$$

where DM, the dispersion measure, is the column density of electrons along the sight-line to the pulsar, and β is a known constant. This offset $\Delta N(f_k)$ can be subtracted from the time index and the data sample can be added into the memory location addressed by the modified time index. This way, as the data of different frequencies get written into the memory, the dispersive delay is automatically compensated and the matrix will contain aligned pulse profile sequences. If pulse folding is not required, the relative delay between channels is compensated by just skipping the corresponding number of samples in respective channels initially, before starting to write/add the incoming samples in the output data matrix. In such a case, the matrix data (over the allocated $N_{\rm per-chan}$ locations per output channel) are read out well before they can be overwritten by new data.

However, when pulse folding is required, each frequency channel is allocated $N_{\rm bins}$ locations to hold its average profile (over a pulse period P). Here, for a given input sample of $i^{\rm th}$ time frame and $k^{\rm th}$ frequency channel, the linear memory destination address can be found by the relation $A(i,k) = (k.N_{\rm bins}) + {\rm REM}[(i - \Delta N(f)).Ph_{\rm inc}/N_{\rm bins}]$, where the first term $(k.N_{\rm bins})$ forms the base address (B_k) of the corresponding frequency channels and the REM operator extracts the remainder of the operand ratio. The remainder in the second term indicates that the result will be modulo $N_{\rm bins}$, ensuring wind back into the $N_{\rm bins}$ space for the $k^{\rm th}$ channel. The $Ph_{\rm inc}$ denotes the input frame interval in units of the profile bin-width $(P/N_{\rm bins})$.

b) Spectral integration (channel summation): If there are $N_{\rm ch-in}$ input frequency channels that are to be grouped into $N_{\rm ch-out}$ bunches of adjacent channels that are added together, then the memory can be split into $N_{\rm ch-out}$ banks of $N_{\rm bins}$ each. It is reasonable to let $N_{\rm ch-in}$ be a binary multiple of $N_{\rm ch-out}$. Then the input and output channel indices (i.e., k and j respectively) are related as $j = INT(k.N_{\rm ch-out}/N_{\rm ch-in})$, where both indices start from zero. The destination index in the matrix for any given output channel j is given as $A(i,j) = (j.N_{\rm per-chan}) + {\rm REM}[(i - \Delta N(f_k)).Ph_{\rm inc}/N_{\rm per-chan}]$, where k = 0 to $N_{\rm ch-in} - 1$, j = 0 to $N_{\rm ch-out} - 1$, i = 0 to $N_{\rm per-chan} - 1$. In cases where profile folding is also required, the index is given by a similar expression where $N_{\rm per-chan}$ is replaced by $N_{\rm bins}$.

c) Pulse folding: If a pulsar has an apparent period P and the interval between consecutive frequency spectra is $T_{\rm frame}$, then the number of time samples within one period is simply $R_{\rm bins} = (P/T_{\rm frame})$. This $R_{\rm bins}$ value is generally a real number, consisting of a fractional and an integer part (a default choice for $N_{\rm bins}$). Since the profile has to be hosted only in an integer number of locations ($N_{\rm bins}$), the fractional part is the residual time width that has to be accounted for. A pulse-phase (in units of profile bin-width) pointer is incremented every time a new sample (i.e., spectral frame) arrives and its integer part is used to address the memory as already indicated in the index computations above. The phase increment per data sample (frame) can be estimated as $Ph_{\rm inc} = (N_{\rm bins}/R_{\rm bins})$, and is ≤ 1. In general, when there are multiple frequency channels, this phase increment is common to all frequency channels. When folding is not required, the $Ph_{\rm inc}$ would be equal to unity, unless integration over successive time-samples is required.

d) Doppler correction: The apparent period at a given epoch and observing location may be different from the “true" period of the pulsar due to the Doppler shifts in the observed pulse frequency because of the relative motions of the Earth and the pulsar and is estimated using standard algorithms. The correction of interest amounts to compressing or stretching the profile (before folding) in a direction opposite to that due to the Doppler effect, so as to ensure that every new profile is in phase with the old ones as folding progresses, and thus avoids time-smearing of the details within the folded pulse. Once the new period P_{new} is known, the compression or expansion can be implemented by changing the phase increment (Ph_{inc}) value adaptively, as ${Ph_{\text{inc}}}^{\text{new}} = {Ph_{\text{inc}}}^{\text{old}}.(P_{\text{old}}/P_{\text{new}})$. Typically, the interval between updates in Ph_{inc} values will be in the order of a few seconds, to ensure that the phase error never accumulates to more than a sample interval.

e) Successive time-sample integration (smoothing): This integration can be implemented in a simple manner while folding by just changing (reducing) the number of bins (N_{bins}) into which the profile has to be fit, thus reducing Ph_{inc} correspondingly. Then the suitable value for N_{bins} would be the integer part of ($R_{\text{bins}}/N_{\text{smooth}}$), where N_{smooth} is the number of time samples to be integrated. In the absence of folding, such an integration can be effected by defining $Ph_{\text{inc}} = 1/N_{\text{smooth}}$.

f) Pulse gating: A time window within a pulse period is specified as that containing the pulse (plus more), so that the data within the on-pulse window are processed retaining the required resolution, when the samples outside the window can be rejected. Initially, the window width is set equal to the full period. The input data are folded until a significant deflection above noise (corresponding to the pulse-peak) is detected, and the window is then shrunk around the “on-pulse" region to a suitable width. This adaptive phase-locking of the window is automated under software control. Within the window, the matrix address is extracted from the phase pointer every time it gets incremented. However, during the off-pulse window region, the phase increment proceeds, but the index address is jammed to a constant value, so that all the time frames outside the window get added onto a single bin, which may be ignored.

It is clear from the above discussion that all these operations can be clubbed together, by simply manipulating the index to the time-frequency matrix and adding the incoming sample to the matrix at that index.

g) Faraday de-rotation: Initially, a known approximate value of Rotation Measure (RM) is used to find the differential Faraday rotation of the polarization position angle at a given channel (frequency f_k) with respect to one of the edge channels (say, at f_{high}) in the band as

$$\theta(f_k) = c^2.\text{RM}.({f_k}^{-2} - {f_{\text{high}}}^{-2}) \tag{2}$$

where c is the speed of light. Then the rotation θ can be corrected for by equivalently rotating the phase of the Stokes parameter combination $Q + jU$, in each frequency channel, by an amount ϕ = -2θ, such that $(Q + jU)_{\text{corrected}} = (Q + jU)_{\text{observed}}(\cos\phi + j\sin\phi)$. Thereafter, the time averaged Stokes parameters Q and U can be used to find the residual error, so that the corrections can be adaptively changed.

h) Parallactic angle correction: In case of an alt-azimuth mount telescope (at latitude L), the parallactic angle change as a function of Hour Angle (HA) can be expressed as

$$\theta_{\text{par}} = \tan^{-1}\left[\frac{\cos(L).\sin(HA)}{\cos(\delta).\sin(L) - \sin(\delta).\cos(L).\cos(HA)}\right] = -(\phi_p/2) \tag{3}$$

where δ is the declination of the source. The parallactic angle is corrected for, by rotating the phase angle of $(Q + jU)$ by ϕ_p in all channels, since it is purely a geometrical effect and is independent of frequency.

4. Software architecture

A BOOT routine has been developed to perform the basic house-keeping functions such as memory checks, allocation of logical memory partitions for data, code and parameters, identifying and short-listing working nodes, and forming the node-sequence, etc.. After booting the DSP nodes, the control PC loads the signal processing code and associated parameters into the dedicated regions of DPRAMs and releases the “reset" for only the short-listed nodes. Each DSP starts executing the outer shell of the signal processing task immediately. The DPRAM memory space is logically partitioned into Code, Semaphore and Parameter space. The parameter space is further partitioned into several tables and values. Initially, the DSP node clears its SRAM memories and initializes its FIFOs and disables the bus transaction for SRAM-B and establishes a header table in SRAM-B. The header is recorded along with the results, to help in tracking any data loss. The DSP then loads some ‘constants’ required for processing into its computational registers. As a next step, the DSP initializes its internal Data Address Generation (DAG) index registers with pointers to the FIFO, SRAMs and the different tables within the parameter space of the DPRAM. The beginning addresses of the profiles in each output channel are pre-stored into a circular table to allow fast generation of pointers while processing. Two such tables are established to contain the starting addresses in the two alternate processing banks of SRAM-A. A register is initialized to contain the total number of folds to be performed before switching the SRAM-A banks for fresh processing. Once these initial configurations are setup, the DSP sends a config-done semaphore to the Control PC through its DPRAM ports. Upon receiving the semaphore, the PC enables clocks to flow to the entire system. The DSP nodes await the onset of their FIFO half-full flags and then invoke further processing. The signal processing routine was split into two tasks, one for data processing and another for data communication to update process parameters on-line and send the results to a data recording system. To facilitate fast context switching, two sets of registers, called the primary and alternate registers, are used, to hold data corresponding to Task 1 and Task 2 respectively.

TASK 1: This task is the core routine for processing the data from the FIFOs using SRAM-A for temporary storage of intermediate results and using the parameters from DPRAMs. The code packed into this task is a highly optimized, parallel instruction sequence which loops for every channel. The data of parameters I and V are directly added to their old profiles in SRAM-A, but parameters U and Q are multiplied with a Faraday correction factor read from a table and then added to their old profiles in SRAM-A. In each iteration, the ‘phase’ index is checked for completion of a fold. On completion of a fold, the phase pointer is wrapped around by subtracting N_{bins} from the current value and the fold count is decremented. Once the required number of folds are completed, the banks are switched and information is set up for Task 2 regarding the result data size and starting location from where the results have to be copied to SRAM-B and sent to RCM. Then, Task 1 loops back to begin a new fold in the alternate bank with fresh data. Successive folds continue in a phase-synchronous manner. The folding proceeds

until the data of one half FIFO size is read out, and then the FIFO address register rolls back to the beginning address of the FIFO block. This generates an internal interrupt automatically and the interrupt service routine branches to Task 2 after clearing the interrupt. The process returns from Task 2 only when the FIFO half-full flags indicate the availability of the next block of input data. On return from Task 2, Task 1 continues operation from exactly where it had branched to Task 2.

TASK 2: This task performs the phase error correction, profile rotation, parameter update and transfer of results.

a) Pulse Phase error correction: The current phase pointer has its upper 16-bits corresponding to an integer bin address and the lower 16-bits to a fractional bin. Thus the indicated position is accurate only to (1/65536) of a bin. The residual error accumulates with every sample, and has to be corrected to avoid pulse-smearing during folding. The phase error is separately accumulated in a register and when it exceeds a preset limit, then the accumulated error is subtracted from the current position for all channels. At this point another facility is provided to add an integer value to the integer part of the current phase, to force a new position from which the folding can proceed, so that the profile gets rotated within the N_{bins} span, if required. The rotation value is fed by the PC and can be altered on-line.

b) Transfer of results: Each time Task 2 is executed, the value of 'residual' result size is examined. If it is a non-zero number, then the DSP node immediately deactivates its BUS-FREE flag to indicate to the RCM unit that it is going to access the SRAM-B and disables the bus-buffers of SRAM-B, enables the buffers on its own side. The results are transferred in small enough blocks such that the time required for each of these transfers does not exceed the intervals between two FIFO-half-full events. The DSP updates the 'residual' size in successive transfers. When the residue eventually reaches zero, the DSP buffers are disconnected and the bus-side buffer enabled, and the BUS-FREE flag is activated, to indicate to the RCM that the results are ready to be collected. As the data gets transferred from SRAM-A to SRAM-B, the old locations of SRAM-A are initialized to zeros so that, consequently, the bank can be re-used for a fresh set of folds by Task 1.

c) Parameter update: The parameters used by the DSP may change with time and are updated periodically. The control PC computes the parameters and the time at which the update is needed. At such a time, the PC stores the parameters in an update table in the DPRAMs of all nodes and sets up a semaphore to the DSP. This semaphore is written at a dedicated DPRAM location which automatically generates an interrupt to the DSP. The DSP may be in the middle of processing data, so the interrupt service routine just sets a flag, indicating that there are new values. During Task 2, this flag is checked for and if found 'set', the corresponding tables used routinely by the DSP during processing are changed using the update-table. An acknowledgment semaphore is then sent to the control PC to indicate that the new parameters have now been accepted by the node.

After completing the above tasks, the DSP waits in a loop polling for the FIFO-half-full flag to get set again. Once the flags appear, the DSP switches the alternative set of registers to primary set, returns from the interrupt service and continues with the execution of Task 1, from where it left on receiving its internal interrupt.

4.1 *Time budget*

Each DSP node runs at 25 MHz, executing one instruction every 40 ns and processes 8 Msamples per second. This means that on the average only about three instruction cycles are available for every data point to perform all the functions mentioned in Task 1 and Task 2! To speed up the code the instructions were heavily parallelized. The architectural advantages of the DSP chip that were exploited in implementing the signal processing code are:

- Zero-overhead branching and looping,
- Address-based interrupt generation,
- Intelligent caching to use effectively the 3 bus architecture,
- Parallel multiply,
- Add and data access instructions,
- Single-cycle task switching,
- Circular-buffer addressing with auto increment,
- Rolled coding for core loop,
- External hardware interrupt service for I/O handshake with DCS, and
- Use of on-chip decode lines to interface zero-wait-state memories.

With these optimizations, the core loop takes 11 cycles to process 4 Stokes parameters and perform the index calculations. This means about 2.75 cycles, or 110ns per data point. Since a new data point is available every 125ns, the savings is only about 0.375 cycles, or 15ns per data point. This loop iterates “half FIFO size" number of times before getting an internal interrupt, and the net time ‘saved’ within such intervals is given by X = half-FIFO-size * 15 (nsecs). This time must be sufficient to execute the outer loops of Task 1 and all operations of Task 2. Considering the computational load for folding, de-dispersion, Faraday correction, adjacent sample integration, channel integration, Doppler correction of a 1-millisecond period pulsar (in a fast binary),

Table 2. Time bugdet for the tasks and estimation of free-cycles.

Operation/Task	No. of cycles per half FIFO
Task 1	
Core loop	$11 \times 4096 = 45056$
Outer loop 1 overheads (after 1 profile is over)	$3 \times 32\text{ch} \times 2$ periods $= 192$ cycles
Outer loop 2 overheads (after N-folds are over)	8×2 period $= 16$ cycles
TASK 1: Total cycles required	45264 cycles
Task 2	
Error correction	600 cycles
Transfer of results (block of 256 locations)	820 cycles
Parameter update	240 cycles
TASK 2: Total cycles required	1650 cycles
Free cycles	4350 cycles

the number of cycles consumed by these instructions is outlined in the following table. A set of 4 FIFOs are chosen to form a 32-bit memory of 32K locations so that the time saved for these operations will be about 6000 instructions cycles between every two FIFO half-fulls which is sufficient for all the remaining operations. To include pulse gating, two operations are added in each outer loop 1. This overhead is well within the limits of the available free time.

5. Tests and results

Initially, a digital ramp pattern starting at value 0 and increasing up to 255 was fed repeatedly to the DII module at 16 Msamples/sec, such that each of the 256 frequency channels gets a constant number every 16 μsec, and adjacent channels have the ramp pattern. The polarimeter outputs were obtained satisfactorily on all 8 output paths at full speed. Subsequently, two DSP nodes were populated and used for tapping the DII data to check the signal processing algorithms and the communication links. The Stokes parameters of 64 frequency channels from DII were time-averaged independently to check for long-term stability and the outputs were obtained satisfactorily. Then, a periodic pulse-pattern with 1-sample pulse-width and period of 256 time frames was fed and the DSP nodes were run to fold the pulses for 16384 periods with correction for different RM values (while the input pattern does not simulate any of these effects). The resultant profile reflected the corrections put in, as an opposite handed rotation of the “linear polarization" position angle across the band as expected. Similarly, tests were made using a range of DM values and the resultant profiles showed corresponding de-dispersion delay gradients across the band as expected.

While the GMRT telescope was getting ready, the SPPS was interfaced to the Ooty Radio Telescope (ORT) to conduct the primary field tests. Since the ORT is a single polarization telescope, the FFT outputs of the north and south halves of the ORT antenna array (same polarization) were connected to two polarization input channels (e.g., treating them as they were dual circular polarization channels). In this mode of connection the Stokes parameters calculated by the polarimeter do not represent polarization characteristics, but represent physically different terms, namely, the Stokes I gives the sum of the total powers from the two halves of the telescope, V gives the difference in the power from North and South halves and $(Q + jU)$ represents the complex correlation between the North and South array voltages. This method of connection was sufficient to allow us to critically evaluate the performance of the machine even though the ORT does not possess dual polarization facilities. The two DSP nodes together tap a total of 64 channels out of the 256-point spectrum corresponding to a total of 4 MHz. The power levels of the North and South halves were matched by adjusting the gains of respective receivers such that the average spectra of parameter V was minimized. The difference in the arrival time of the signals in the two halves is reflected in the cross-correlation phase, defined as $\phi = \tan^{-1}(U/Q)$, showing an apparent phase gradient across the band. From this measurement, the delay was equalized at the IF stage of the two receivers. After phase equalization, a strong pulsar (B1749-28, Average flux density $\sim$1.3 Jy) was observed and the pulses were de-dispersed and folded on-line. The resultant profile showed that the deflections corresponding to the pulse are about the same in I and Q parameters, while the contributions in V and U are very small, indicating that the gains and phases were matched adequately.

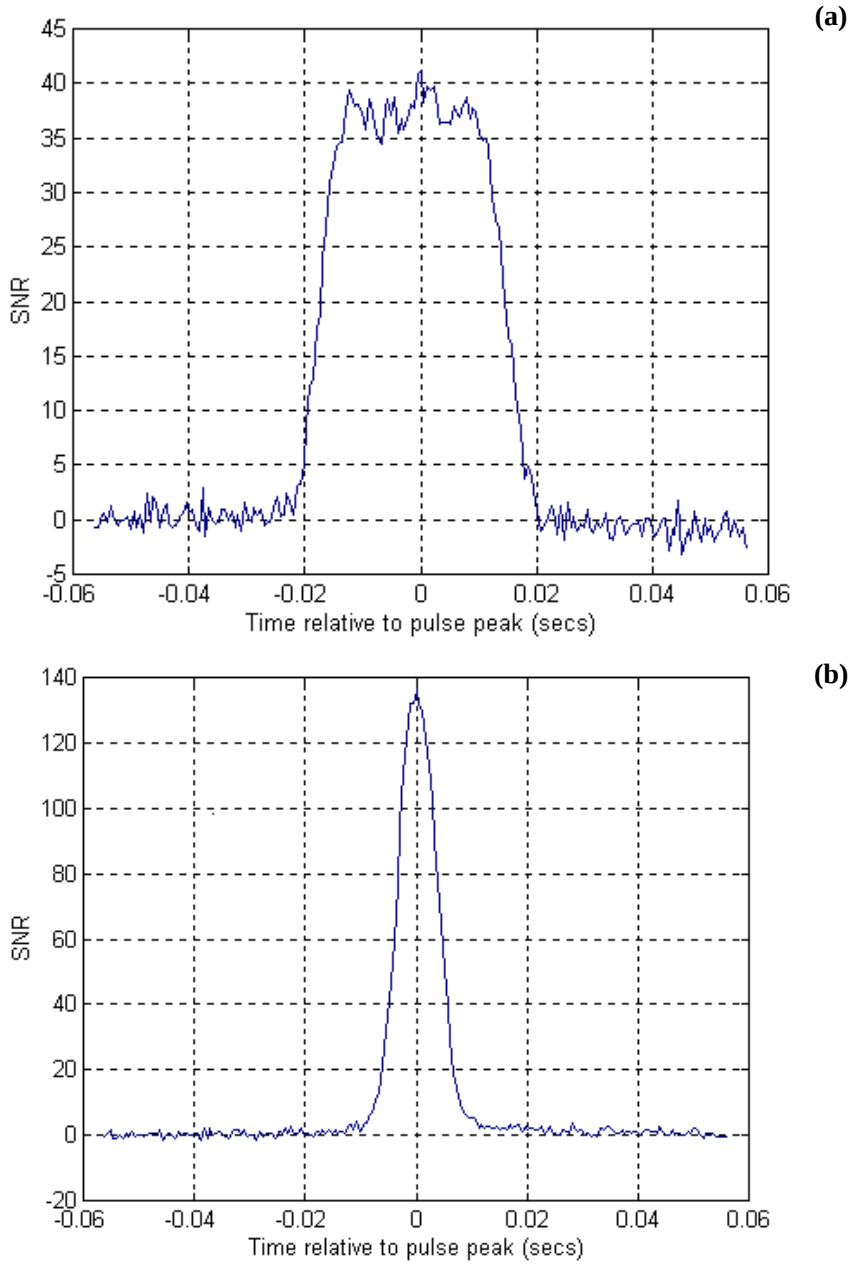

Figure 6. Folded total-power (I) profile of pulsar B1749-28 observed on 5th October 1997 using the Ooty Telescope. (period $\sim$ 0.562 s; DM $\sim$ 50.88 pc/cc; $S_{average} \sim$ 1.3 Jy; equivalent pulse width $\sim$ 7.5 ms; No. of pulses averaged = 580; No. of adjacent samples integrated per time bin in the profile = 27; 64 channels averaged after dispersion correction) Note: The delay difference across the observed band at 327 MHz is about 64 ms. The plots in the top **(a)** and bottom **(b)** panels show the results of the runs without and with the on-line dispersion correction respectively. In both cases the pulse-phase error was allowed to accumulate without correcting it. Significant smearing due to lack of this correction is still present in (b).

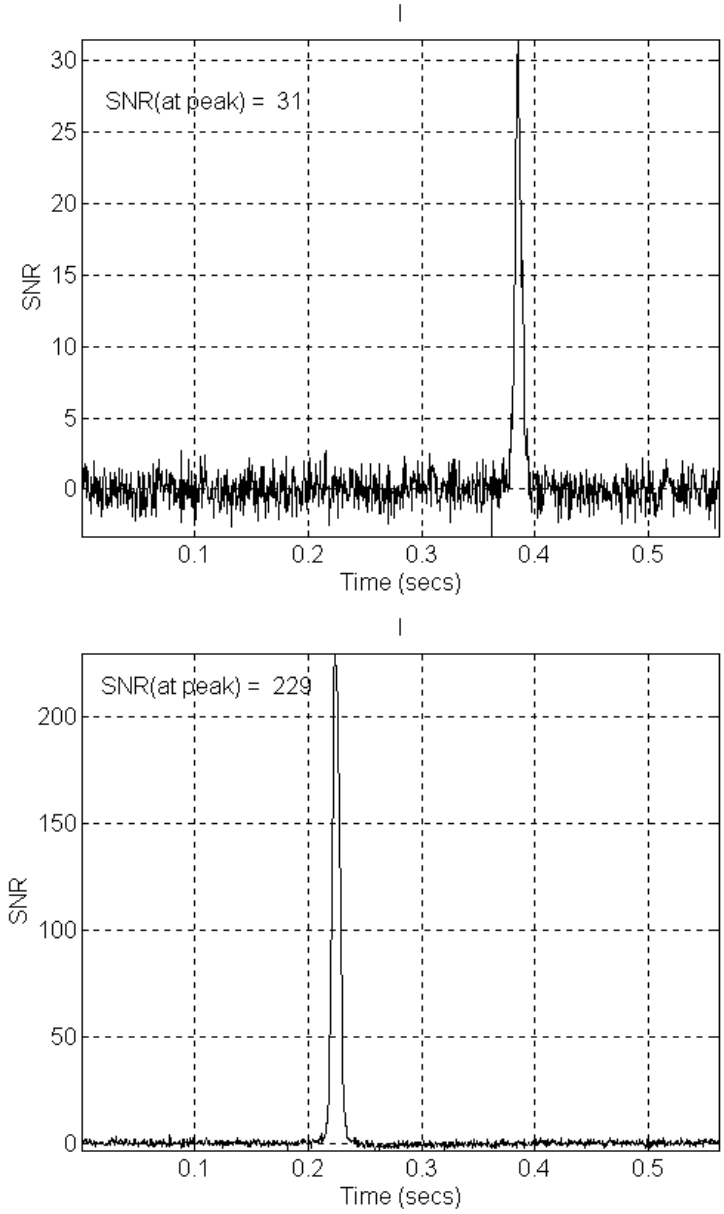

Figure 7. Folded profile (signal-to-noise ratio versus pulse phase) of pulsar B1749-28 observed on 13th December 1997 using the Ooty Telescope. Here, the time resolution is ~ 550 μs (27 sample smoothing) and both dispersion and pulse-phase error corrections were enabled during folding. No. of folds: (top) 18 and (bottom) 1160.

The clock was derived from a programmable frequency generator, which was phased locked to a stable reference signal from a Rubidium oscillator to obtain high accuracy (about 1 part in 10^{12}) and stability. As mentioned earlier, due to finite representation of the pulse phase (32 bit), the residual error will accumulate as the folding pro-

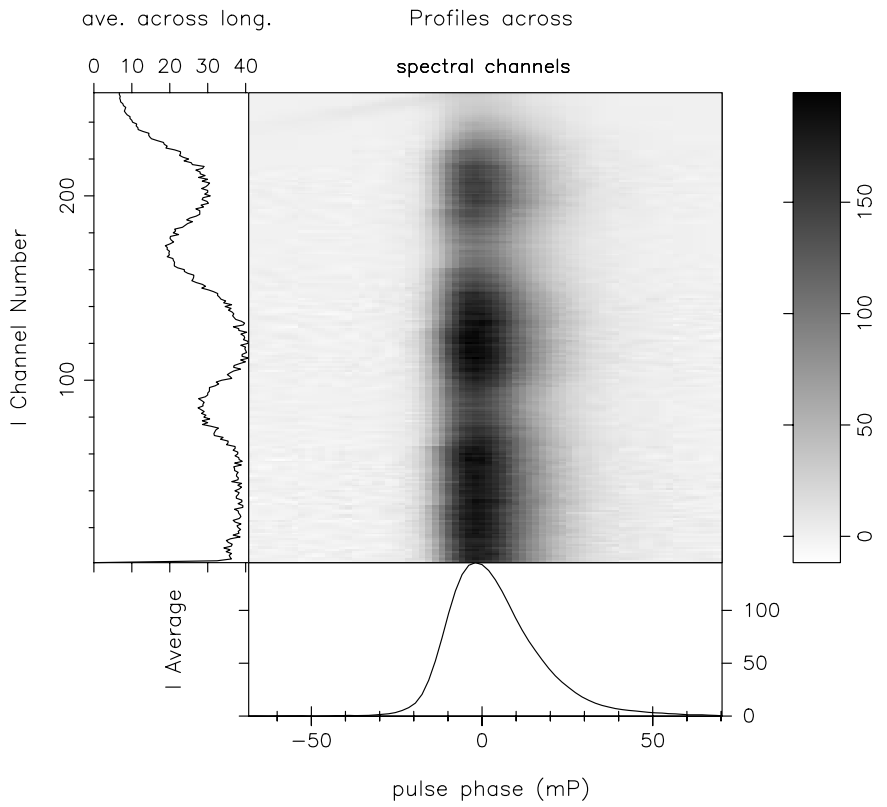

Figure 8. Average pulse profiles (across a 16-MHz band at 610 MHz; 256 channels) from an observation of the Vela pulsar (B0833-45) using one dish of GMRT are shown in the central panel and the average over the entire spectral band is given in the bottom panel. The profiles shown are for the Stokes parameter I (uncalibrated), where the relative delays due to dispersion (DM $\sim$ 68 cm^{-3}pc) have been corrected. The x-axis scale is in milli-periods where the pulsar period is $\sim$ 89 ms (with 512 bins across the period). The left panel shows the apparent intensity variation across the spectral channels, and reflects primarily the spectral gain response of the analog (RF/IF) system. The polarization data (for all the 4 Stokes parameters) were recorded after on-line folding over 3000 pulse periods ($\sim$270 seconds integration). The two polarizations channels input to the system were dual-circular.

gresses, which is corrected periodically. The data of pulsar PSR 1749-28 was processed (dedispersion + folding) with and without the phase-error correction and a significant change in the pulse shape was observed (see Fig. 6). After this, the phase increment value was updated every second so as to adapt to any changes in the period. Further observations were conducted in this mode. To test the spectral-integration function, pulsar PSR 1749-28 was observed with dispersion correction and all frequency channels added together and folded over the pulsar period. Such observations were repeated for different lengths of time and a corresponding improvement in signal to noise ratio (SNR) was as expected (see Fig. 7). Subsequently, many other pulsars were observed covering a wide range of periods, flux-densities and DMs (Ramkumar 1998).

Subsequent tests checked another feature of the instrument, namely, the pulse-gating operation. Also, the feedback from these tests was used in improving the performance

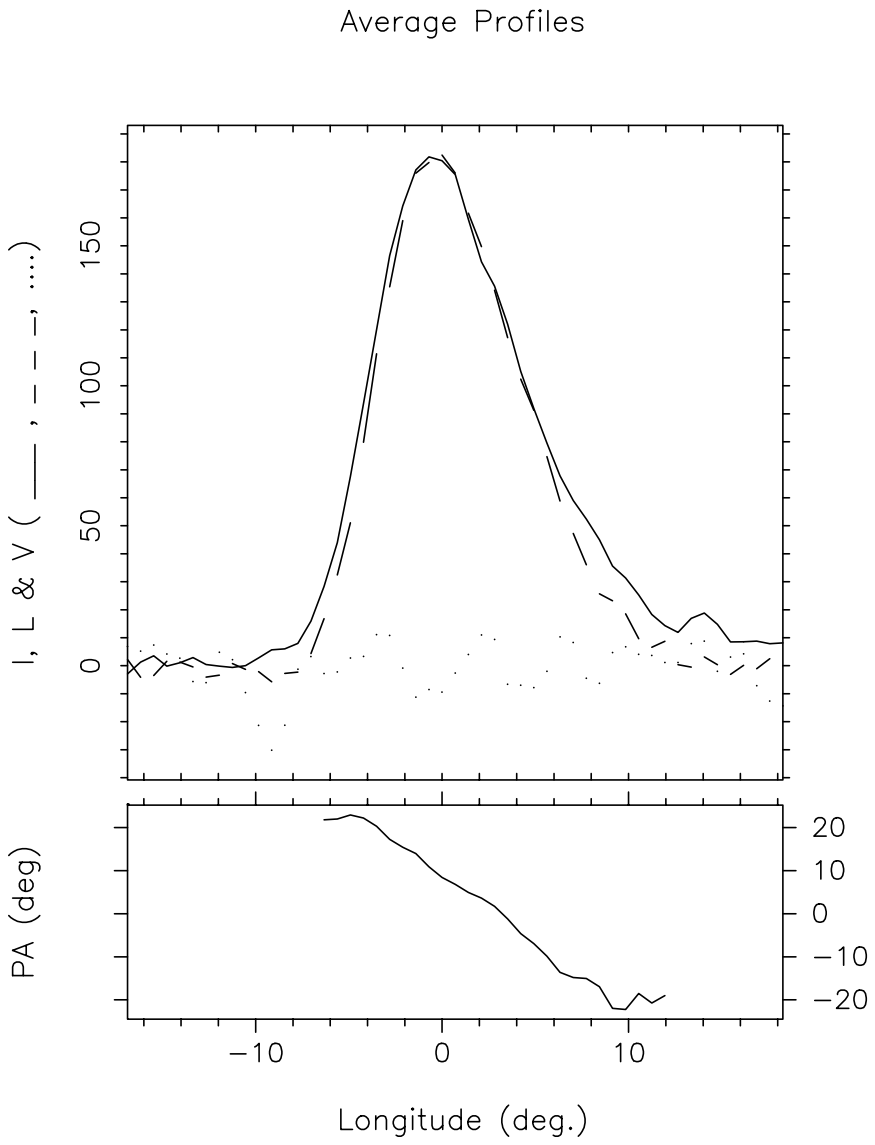

Figure 9. A full set of Stokes parameters for one of the 256 channels from the observation mentioned above (i.e. Fig. 8) is used to compute profiles in total intensity (Stokes I), the linear and circular polarized intensities (L & V) and are shown in solid, dashed and dotted lines respectively. The lower panel shows the corresponding position angle (PA) profile. Please note that these profiles are shown only as an example of typical raw data output from the processor and are not corrected for any (complex) gain differences between the input polarization channels (and their possible coupling). However, the high degree of linear polarization and the PA sweep rate apparent in the raw data are generally consistent with known polarization properties of the Vela pulsar (see, for example, Radhakrishnan & Cooke 1969). The PA profile shown includes the offsets due to Faraday rotation and the (feed) parallactic angle.

of the system. While an enhanced version of the SPPS system was being reproduced to handle full 32 MHz bandwidth at GMRT, the two-node 4-MHz system was used for conducting further tests with the dual polarization antennas of the GMRT array. A result from a series of test observations with the final full bandwidth system commissioned later at GMRT, and now available for observations, is shown in Figs. 8 and 9. A user-friendly software package for the post processing of pulsar data recorded by this processor has been developed.

The system can be used, in general, as a networked, high-speed parallel (SIMD OR MIMD) signal processing computer for many other signal processing applications. Program development tools provided by third-party vendors can be used to develop software in C/Assembly languages and downloaded to a chosen set of nodes. The resources of each node are scalable in terms of the depth of a FIFO and SRAM modules. Provision has been made for additional dynamic RAM interfaces on both the programme and data memory sides of the DSP chip allowing for larger size applications. A separate shared, scalable memory module can be added and shared by all the nodes, if required, by suitably designing a memory bank with an interface that mimics the hand-shakes of a DSP slave node. With such an interface, the memory bank can be treated as an additional node of the parallel processor and this memory can be directly accessed by other DSP nodes in the system. The PCBs are capable of performing at higher clock rates and the frequency of operation can be scaled up with the availability of suitable devices. With minimum modifications in the control software, the DSP nodes can be configured to execute together and perform either parallel (identical) tasks or different tasks/jobs that can be arranged for parallel execution.

Acknowledgements

It is a great pleasure to acknowledge individual and collective contributions from all the members of the GMRT-pulsar project team at the Raman Research Institute and the staff at the Ooty Radio Telescope. We also thank V. Radhakrishnan, G. Swarup and V. Balasubramanian for their constant support, encouragement and for many useful discussions. PSR gratefully acknowledges many useful discussions with K. Kishan Rao.

References

Deshpande, A. A. 1995, Proceedings of the 6th Asia Pacific Regional Meeting of IAU (1994), Supplement to *J. Astrophys. Astr.*, **16**, 225.

Hankins, T. H., Rickett, B. J. 1975, in *Methods in Computational Physics*, (New York: Academic Press, 1975), Vol. 14, page 56.

Kraus, J. D. 1966, *Radio Astronomy* (McGraw-Hill Book Company: 1966).

Manchester, R. N., Taylor, J. H. 1977, *Pulsars*, (San Fransisco: W. H. Freeman and Co.)

Prabu, T. 1997, *Array Combiner for GMRT*, M.S. Thesis, Dept. of Electrical Communication Engineering, I.I.Sc., Bangalore, India.

Radhakrishnan V., Cooke D. J. 1969, *Astrophys. Lett.*, **3**, 225.

Ramkumar, P. S. 1998, *Real-Time Signal Processing Instrumentation for Search and Studies of Pulsars*, Ph.D. Thesis, Regional Engineering College, Warangal, India.

Swarup, G., Ananthakrishnan, S., Kapahi, V. K., Rao, A. P., Subramanya, C. R., Kulkarni, V. K. 1991, *Curr. Sci.*, **60**, 95.